



SAPIENZA  
UNIVERSITÀ DI ROMA

DEPARTMENT OF INFORMATION ENGINEERING  
ELECTRONICS AND TELECOMMUNICATIONS



INSTITUT D'ÉLECTRONIQUE ET DE  
TÉLÉCOMMUNICATIONS DE RENNES

# ADVANCED RADIATING SYSTEMS BASED ON LEAKY WAVES AND NONDIFFRACTING WAVES

**Walter Fuscaldo**

PhD Thesis in Information and Communication Technology  
*- Applied Electromagnetics -*

Supervisor at Rome  
Prof. Alessandro Galli

Supervisor at Rennes  
Dr. Mauro Ettore

*Examination Committee*

Dr. Mauro Ettore  
Prof. Alessandro Galli  
Prof. Giuseppe Schettini  
Prof. Alessandro Toscano  
Prof. Francisco Medina-Mena

Rome, February 27<sup>th</sup>, 2017



# CONTENTS

ABSTRACT xxxi

ACKNOWLEDGMENTS xxxiii

INTRODUCTION xliii

## I RECONFIGURABLE LEAKY-WAVE ANTENNAS FOR THZ FAR-FIELD APPLICATIONS 1

### 1 CONVENTIONAL LEAKY-WAVE ANTENNAS 3

1.1 Introduction 3

1.2 Leaky-Wave Theory 5

1.2.1 Nature of waves 5

1.2.2 Physical significance of leaky waves 6

1.2.3 Mathematical significance of leaky waves 8

1.2.4 The transverse resonance technique 13

1.2.5 Classification of leaky-wave antennas 17

1.3 1-D Leaky-Wave Antennas 20

1.3.1 Historical examples of 1-D LWAS 20

1.3.2 Radiating properties of 1-D unidirectional LWAs 22

1.3.3 Radiating properties of 1-D bidirectional LWAs 24

1.4 2-D Leaky-Wave Antennas 26

1.4.1 Historical examples of 2-D LWAS 26

1.4.2 Radiating properties of 2-D LWAs 28

1.4.3 Design rules for dielectric-based 2-D LWAs 29

1.4.4 Motivation for the study of unconventional 2-D LWAs 30

1.5 Conclusion 32

### 2 FORMULAS FOR LEAKY-WAVE ANTENNAS 33

2.1 Introduction 33

2.2 Formulas for 1-D Unidirectional Leaky-Wave Antennas 35

2.2.1 Analytical framework 35

2.2.2 Fitting procedure 38

2.2.3 Numerical results 42

2.2.4 Comparison with Oliner's formula 47

2.2.5 Beamwidth evaluation at endfire 51

2.3 Formulas for 1-D Endfire Leaky-Wave Antennas 53

2.3.1 The modified Hansen-Woodyard condition for 1-D LWAs 53

2.3.2	Analytical investigation about the limitations on the choice of an optimum phase constant	55
2.3.3	Beamwidth and SLL evaluation for endfire 1-D LWAs	59
2.3.4	Definition of a suitable objective function for taking into account the $\Delta\theta_h$ vs. SLL tradeoff	61
2.3.5	Approximate formulas for the beamwidth and the sidelobe level	62
2.3.6	Investigation for extremely-efficient endfire leaky-wave antennas	65
2.4	Formulas for 1-D Bidirectional Leaky-Wave Antennas	69
2.4.1	Beamwidth formulas for uniform and infinite apertures	69
2.4.2	Beamwidth formulas for finite apertures	73
2.5	Conclusion	80
3	RECONFIGURABLE LEAKY-WAVE ANTENNAS	81
3.1	Introduction	81
3.2	Graphene-based Leaky-Wave Antennas	83
3.2.1	Graphene properties	85
3.2.2	Graphene plasmonics	91
3.2.3	Graphene planar waveguide	95
3.2.4	Graphene substrate-superstrate antenna	105
3.2.5	Graphene strip grating antennas	118
3.2.6	Technological aspects	121
3.3	Fabry-Perot Cavities Based on Liquid Crystals	124
3.3.1	Introduction	124
3.3.2	Liquid crystals	125
3.3.3	Electromagnetic model for nematic liquid crystals	126
3.3.4	Tunable THz Fabry-Perot cavity leaky-wave antenna based on NLCs	130
3.4	Conclusion	139
II	GENERATION OF NONDIFFRACTING BEAMS AND PULSES FOR NEAR-FIELD APPLICATIONS AT MILLIMETER WAVES	141
4	NONDIFFRACTING WAVES	143
4.1	Introduction	143
4.2	Mathematical framework	145
4.3	Bessel Beams	152
4.3.1	History, definition and properties	152
4.3.2	Potential applications	154
4.3.3	Realizations	155
4.4	X-Waves	158
4.4.1	History, definition and properties	158
4.4.2	Potential applications	160



4.4.3	Realizations	161
4.5	Conclusion	164
5	BESSEL-BEAM LAUNCHERS	165
5.1	Introduction	165
5.2	Microwave Bessel-Beam Launchers	166
5.2.1	Theoretical analysis	166
5.2.2	Numerical results	171
5.2.3	Experimental results	173
5.2.4	Millimeter-wave design	175
5.3	Millimeter-wave Bessel-Beam Launchers	178
5.3.1	Design of the structure	179
5.3.2	Numerical validation	186
5.3.3	Prototype	189
5.3.4	Measurements	190
5.3.5	Use of a LRW as an X-wave launcher	194
5.4	Conclusion	196
6	X-WAVE LAUNCHERS	197
6.1	Introduction	197
6.2	Zeroth-Order X-Wave Generation Through Finite Apertures	198
6.2.1	Metric of confinement	199
6.2.2	Ideal X-waves	201
6.2.3	Dispersive X-waves	209
6.2.4	Dispersive-finite X-waves	212
6.3	Higher-Order X-Wave Generation Through Finite Apertures	220
6.3.1	Analytical framework	221
6.3.2	Monochromatic higher-order Bessel beams	222
6.3.3	Polychromatic superposition of higher-order Bessel beams	223
6.3.4	Numerical results	225
6.4	Conclusion	227
A	A POSSIBLE PROOF ABOUT THE DEFINITION OF THE POINTING ANGLE IN LWAS	229
B	SIMULATION MODEL FOR THE FULL-WAVE ANALYSIS OF GRAPHENE-BASED LWAS	231
	BIBLIOGRAPHY	233
	LIST OF PUBLICATIONS	257
	LIST OF AWARDS	261

## LIST OF FIGURES

- Figure 1.1 (a) A closed and (b) an open region with respect to the vertical  $x$ -axis. In the electric/magnetic case the boundaries would represent *perfect electric/magnetic conductor* (PEC/PMC) walls. 6
- Figure 1.2 Ray interpretation of the physical significance of (a) a *forward* and (b) a *backward* leaky wave in a waveguiding structure of finite extent. Within a wedge-shaped region (highlighted in light blue) limited by the shadow boundary, the leaky-wave field dominates the near-field region. It is worth noting the capability of backward leaky waves to focus radiation in the near field. 7
- Figure 1.3 Classification of forward waves in open regions with respect to their propagating features. When  $\alpha_z = 0$  two kinds of waves exist: uniform plane waves  $\alpha_x = 0$ , and surface waves  $\alpha_x \neq 0$ . Surface waves might be proper or improper, depending on the sign of  $\alpha_x$ . When  $\alpha_z \neq 0$ , physical leaky waves exist only when  $\alpha_z > 0$ . Even more interestingly, in order to describe a radiation mechanism  $\beta_x > 0$ , a forward leaky wave must be improper. 8
- Figure 1.4 (a) Real  $\Re\{\hat{k}_z\}$  part and (b) imaginary  $\Im\{\hat{k}_z\}$  part of  $\hat{k}_z$  vs.  $f$  for a SW mode (black solid line) evolving in a LW mode (dotted green line), after ‘crossing’ the *spectral gap* (improper real SW are there represented with green and black dashed lines) in a typical GDS covered with a PRS. The nonphysical LW solution (which is the complex conjugate of the potentially physical one) is represented in dotted black line. 9
- Figure 1.5 The top and bottom sheets (i.e.,  $k_z$ -planes) of the *two-sheeted Riemann surface* for  $k_x$ . The Sommerfeld branch cuts are represented in blue dashed-dotted lines. Color styles and line styles are the same of Fig. 1.4. The arrow indicates the direction for which the frequency is decreasing. A path of integration, labeled as  $P$ , is also shown in red solid line on the top Riemann sheet. 10

- Figure 1.6 The deformation of the path  $P$  into  $P'$  (solid red lines). The LW poles are represented with dotted circles since they lie on the bottom Riemann sheet and thus they are not captured during the path deformation. 11
- Figure 1.7 Steepest descent  $\phi$ -plane. The eight quadrants (from T1 to T4 for the top sheet and from B1 to B4 for the bottom sheet) constituting the two sheets are mapped in a single strip onto the  $\phi$ -plane. The original path  $P$  (red solid line) is deformed into the SDP (black solid line) for any angle of observation  $\theta$ . The *extreme* SDPs (ESDPs) are obtained for  $\theta = \pm\pi/2$ , and are reported in black and white dashed line for the positive one (ESDP<sup>+</sup>) and the negative one (ESDP<sup>-</sup>), respectively. Only the poles which lie within ESDP<sup>+</sup> and ESDP<sup>-</sup> may contribute to the radiated field. 12
- Figure 1.8 2-D section and TEN model of (a) a PPW and (b) a GDS. 14
- Figure 1.9 Dispersion diagram  $\hat{k}_z$  vs.  $f$  of a PPW. Dispersion curves are found for  $\epsilon_r = 1$  and  $h = \lambda_0/2$  where  $\lambda_0 = 300 \mu\text{m}$ . Evanescent modes  $k_z = -j\alpha_z$  in dashed lines and guided modes  $k_z = \beta_z \in \mathbb{R}$  in solid lines. Since the structure is not simply-connected, a TEM mode (black solid line) propagating from DC frequency is obtained for  $m = 0$  (green lines are for  $m = 1$  and blue lines are for  $m = 2$ , TE-TM modes, respectively). Yellow dots indicates the cutoff frequencies  $f_c^{(m)}$ . 15
- Figure 1.10 Dispersion diagram  $\hat{k}_z$  vs.  $f$  of a GDS. Dispersion curves are found for  $\epsilon_r = 2.17$  and  $h = \lambda_0/2$  where  $\lambda_0 = 300\mu\text{m}$ . The light line  $k_z = k_0$  sets the boundary between the *radiating region* (just below, highlighted in blue) where *leaky waves* ( $\hat{\beta}_z$  in dashed blue lines and  $\hat{\alpha}_z$  in dotted blue lines) may describe radiation, and *propagating region* (just above, highlighted in green) where *surface waves* ( $\hat{\beta}_z$  in solid blue lines) may describe surface propagation. 16
- Figure 1.11 Two well-known examples of 1-D LWAs. (a) An example of 1-D uniform LWA: the *slitted rectangular waveguide* [24]. (b) An example of 1-D quasi-uniform LWA: the *holey waveguide* [25]. 20
- Figure 1.12 Comparison between the far-field distributions of a uniform aperture distribution and a leaky aperture distribution. The directivity of LWAs increases as long as the leakage rate  $\alpha_z$  is low. 21

- Figure 1.13 2-D section of a unidirectional LWA with an equivalent magnetic (electric) surface current that models an aperture field with the typical exponentially-decaying distribution of forward leaky waves. An absorber is usually put at the end of the structure to avoid back-reflection from the forward leaky wave. 22
- Figure 1.14 2-D section of a bidirectional LWA centrally-fed by a coaxial cable. When the two beams approaches each other, they merge in a single beam which points exactly at broadside. 25
- Figure 1.15 The original ray explanation proposed by von Trenini in [49] for FPC-like antennas. At that time, these kind of antennas were not recognized as 2-D LWAs. 26
- Figure 1.16 Several examples of different types of PRS. The PRS consists of a single (a) dielectric layer, (b) a multistack of alternating dielectric layers, (c) a 2-D periodic array of metallic patches, and (d) its complementary version, i.e., slots in a thin metal plate. 27
- Figure 2.1  $t_h$  vs.  $a$  calculated numerically (black solid lines). The behavior of  $t_h$  has been reported for (a)  $0 \leq a \leq 1$ , (b)  $0 \leq a \leq 3$ , (c)  $0 \leq a \leq 10$ , and (d)  $0 \leq a \leq 30$ . In (b)  $t_h$  has been fit with a cubic spline curve (blue circles). 38
- Figure 2.2 Evolution of the third-order polynomial coefficients of the spline interpolation. 39
- Figure 2.3 Comparison of data fitting of  $t_h$  vs.  $a$  by means of different fitting functions in the range  $0 \leq a \leq 0.25$  (top-left corner),  $0 \leq a \leq 0.5$  (top-right corner),  $0 \leq a \leq 1$  (bottom-right corner), and  $0 \leq a \leq 3$  (bottom-left corner). 41
- Figure 2.4 (a) Asymptotic behavior of  $t_h$  vs.  $a$  for the various fitting functions in the range  $0 \leq a \leq 3$ . (b) Absolute percent error (APE) vs.  $a$  of the various fitting functions in the range  $0 \leq a \leq 3$ . 41
- Figure 2.5  $\Delta\theta_h$  vs.  $e_r$  for  $\theta_0 = 5^\circ, 15^\circ, 45^\circ, 90^\circ$  (in order in red, yellow, green, blue) Comparison between aBW (in solid lines) and eBW (in circles) results for the evaluation of  $\Delta\theta_h$  for  $L = 10\lambda$  (top-left corner),  $L = 20\lambda$  (top-right corner),  $L = 2\lambda$  (bottom-left corner),  $L = 100\lambda$  (bottom-right corner). 43

- Figure 2.6  $\Delta\theta_h$  vs.  $\theta_0$  for  $e_r = 50\%, 75\%, 90\%, 99\%$  (in order in red, yellow, green, blue). Comparison between aBW (in solid lines) and eBW (in circles) results for the evaluation of  $\Delta\theta_h$  for  $L = 10\lambda$  (top-left corner),  $L = 20\lambda$  (top-right corner),  $L = 2\lambda$  (bottom-left corner),  $L = 100\lambda$  (bottom-right corner). 44
- Figure 2.7 APE (calculated as  $100 \cdot |aBW - eBW|/|eBW|$ ) vs.  $e_r$  for  $\theta_0 = 5^\circ, 15^\circ, 45^\circ, 90^\circ$  (in order in red, yellow, green, blue) for  $L = 10\lambda$  (top-left corner),  $L = 20\lambda$  (top-right corner),  $L = 2\lambda$  (bottom-left corner),  $L = 100\lambda$  (bottom-right corner). 44
- Figure 2.8 APE vs.  $\theta_0$  for  $e_r = 50\%, 75\%, 90\%, 99\%$  (in order in red, yellow, green, blue) for  $L = 10\lambda$  (top-left corner),  $L = 20\lambda$  (top-right corner),  $L = 2\lambda$  (bottom-left corner),  $L = 100\lambda$  (bottom-right corner). In black dashed lines the location of  $\theta_m$  defined as the minimum  $\theta_0$  for which the APE is less than 5%. 45
- Figure 2.9 APE (calculated as  $100 \cdot |aBW - eBW|/|eBW|$ ) vs.  $\theta_0$  and  $e_r$ . White dashed lines highlight the boundaries set by  $\theta_m$ . 45
- Figure 2.10 (a) APE (calculated as  $100 \cdot |eF_1BW - eBW|/|eBW|$ ) vs.  $\theta_0$  for  $e_r = 50\%, 75\%, 90\%, 99\%$  (in order in red, yellow, green, blue) and (b) APE vs.  $e_r$  for  $\theta_0 = 5^\circ, 15^\circ, 45^\circ, 90^\circ$  (in order in red, yellow, green, blue). The  $eF_1BW$  is calculated using either the  $F_1$  (solid lines) or the  $F_2$  (dashed lines) formulas. Results are shown only for  $L = 10\lambda$ . 46
- Figure 2.11 APE (calculated as  $100 \cdot |eBW - eF_1BW|/|eBW|$ ) vs.  $\theta_0$  and  $e_r$ . 47
- Figure 2.12  $\bar{P}(\theta)$  vs.  $\theta$  (in linear scale) for different values of  $\theta_0$  and  $e_r$ . 48
- Figure 2.13  $\bar{P}(\theta)$  vs.  $\theta$  (in linear scale) for different values of  $\theta_0$  when  $e_r = 90\%$ . Lighter colored region represent the estimation of the single-sided beamwidth when using Oliner's formula. The red solid line is reported for helping the reader to find the half-power value. 49
- Figure 2.14 An example of a 1-D LWA. A leaky mode is excited at the source location  $z = 0$ . The metallic top wall of a rectangular waveguide is replaced by a partially reflecting screen to allow the propagating mode to leak out along the  $z$ -axis. The antenna is terminated with a matched load at  $z = L$ . 54

- Figure 2.15  $\bar{P}(\theta)$  vs.  $\theta$  (in dB scale) for  $e_r = 0\%$ ,  $l = 10\pi$ ,  $b = l$  (solid blue line) and  $b = l + \Delta b_{\max}$  (solid green line), respectively. The first sidelobe for  $b = l$  occurs around  $\theta_{\text{SL}} \simeq 31^\circ$  (dashed blue lines). When  $b = l + \Delta b_{\max}$  the first sidelobe (dashed green line) reaches the same intensity of the main lobe. 57
- Figure 2.16  $\bar{P}(\theta)$  vs.  $\theta$  (in dB scale) for  $e_r \in \{0\%, 50\%, 75\%, 90\%, 95\%, 99\%\}$ ,  $l = 10\pi$ ,  $b = l$  (solid blue line) and  $b = l + \Delta b_{\max}$  (dashed grey line), respectively. 58
- Figure 2.17 (a)  $\bar{P}(\theta)$  vs.  $\theta$  for  $e_r = 85.8\%$ ,  $l = 20\pi$ , when  $\Delta b = 0$  (blue line) and  $\Delta b = 1.47$  (green line). (b) Fig. 4 of Reference [45] reported here for convenience. Case 1 and Case 2 perfectly match the blue and green curves, respectively. 59
- Figure 2.18  $\bar{P}(\theta)$  vs.  $\theta$  for  $e_r \in \{0\%, 75\%, 90\%, 95\%\}$ ,  $l = 10\pi$ ,  $\Delta b = 0$  (red line),  $\Delta b = 0.8$  (green line),  $\Delta b = 1.6$  (blue line), and  $\Delta b = 2.4$  (black line) respectively. 60
- Figure 2.19  $\Delta\theta_h$  and SLL vs.  $b$  for  $e_r \in \{0\%, 50\%, 75\%, 90\%, 95\%\}$ ,  $L = 10\lambda$ . 61
- Figure 2.20 The optimizing function vs.  $\Delta b$  for  $e_r \in \{0\%, 75\%, 90\%, 95\%, 99\%\}$ , and for  $w = 0, 0.25, 0.5, 0.75, 1$  when  $L = 10\lambda$ . Obviously, the extreme cases  $w = 0$  and  $w = 1$  would lead to the same  $b$  which minimizes the beamwidth and the SLL, respectively. 62
- Figure 2.21  $\overline{\Delta\theta}_h$  and SLL vs.  $\Delta b$  for  $e_r = 0\%, 75\%, 90\%, 95\%$ . The magenta dot indicates the value of  $\Delta b$  for which the SLL improves as  $e_r$  increases. 63
- Figure 2.22 (a)  $\overline{\Delta\theta}_h$  and (b) SLL vs.  $\Delta b$  in the range  $0 \leq \Delta b \leq 2.4$ . A family of  $a$ -parametric curves (solid lines) shading from blue to red is generated for  $a$  going from 0 to 0.8. Fitting curves are reported in circles in both figures. 64
- Figure 2.23 (a)  $v_i$  and (b)  $w_i$  vs  $a$  for  $i = 0, 1, 2$  (in order blue, green, and red solid lines) and their linear interpolations (dashed lines). 64
- Figure 2.24  $\bar{P}(\theta)$  vs.  $\theta$  (in dB scale) for  $L = 10\lambda$  for  $e_r \in \{99\%, 99.5\%, 99.9\%, 99.95\%, 99.99\%, 100\%\}$ ,  $b = l$  (blue line) and  $b = l + \Delta b_{\max}$  (grey line), respectively. A blue dot highlights the location of the first sidelobe encountered from the main lobe for  $b = l$ . 65

- Figure 2.25  $\bar{P}(\theta)$  vs.  $\theta$  (in dB scale) for (a)  $L = 1\lambda$ , (b)  $L = 5\lambda$ , (c)  $L = 100\lambda$ , (d)  $L = 1000\lambda$  for  $e_r \in \{99\%, 99.5\%, 99.95\%, 100\%\}$ ,  $b = l$  (blue line) and  $b = l + \Delta b_{\max}$  (grey line), respectively. A blue dot highlights the location of the first sidelobe encountered from the main lobe for  $b = l$ . 66
- Figure 2.26 (a)  $t_h$  vs.  $a$ . A family of curves shading from blue to red is generated for  $r$  going from 0 to 1. The black solid line represent the result obtained through Eq. (2.12). (b)  $t_h$  vs.  $r$ . A family of curves shading from blue to red are generated for  $a$  going from 0 to 10. 74
- Figure 2.27 (a)  $t_h$  vs.  $a$ . A family of curves (solid lines) shading from blue to red is generated for  $r$  going from 0 to 1. The fitting curves are reported in circles. (b)  $w_1$  vs.  $r$  (blue solid line) and  $w_2$  vs.  $r$  (green solid line). The corresponding interpolations are reported in dashed lines. 75
- Figure 2.28  $t_h$  vs.  $a$ . A family of curves (solid lines) shading from blue to red is generated for  $r$  going from 0 to 1. The fitting curves are reported in circles. 76
- Figure 2.29 Contour plot of APE vs.  $a$  and  $r$ . Left panel: APE is calculated after the first fitting procedure (see Fig. 2.27). Right panel: APE is calculated after the second (last) fitting procedure (see Fig. 2.28). 76
- Figure 2.30 (a)  $t_h$  vs.  $a$ . A family of curves (solid lines) shading from blue to red is generated for  $r$  going from 0 to 1. The fitting curves are reported in circles. (b)  $w_1$  vs.  $r$  (blue solid line),  $w_2$  vs.  $r$  (green solid line), and  $w_3$  (red solid line). The corresponding interpolations are reported in dashed lines. 77
- Figure 2.31  $t_h$  vs.  $a$ . A family of curves (solid lines) shading from blue to red is generated for  $r$  going from 0 to 1. The fitting curves are reported in circles. 78
- Figure 2.32 Contour plot of APE vs.  $a$  and  $r$ . Left panel: APE is calculated after the first fitting procedure (see Fig. 2.30). Right panel: APE is calculated after the second (last) fitting procedure (see Fig. 2.31). 78

- Figure 3.1 (a) The hexagonal lattice of a graphene monolayer. The unit cell of graphene with lattice constant  $a$  has two carbon atoms per unit cell, A and B. (b) Electronic dispersion (energy vs.  $k_x$  and  $k_y$ ) obtained in the frame of the *tight-binding model* [91]. Note the conical shape (linear dispersion) of the diagram in proximity of the  $K$  points of the first Brillouin zone of graphene. Around the  $K$  points the Fermi velocity. The figure is a concession of [91]. 85
- Figure 3.2  $E_0$  vs.  $\mu_c$  in the range  $0 \leq \mu_c \leq 1$  eV, obtained from 3.8, for  $\epsilon_r = 1$  (air). 87
- Figure 3.3 Real part (in red) and imaginary part (in blue) of the graphene surface conductivity as a function of the frequency. Comparison between the expressions of the non-local model, i.e.,  $\sigma_\rho$  (circles) and  $\sigma_\phi$  (in squares), and the Kubo formula  $\sigma$  (solid line). Results are shown for  $\mu_c = 0$  eV and (a)  $k_\rho = k_0$ , (b)  $k_\rho = 200k_0$ . 88
- Figure 3.4 Comparison between  $\sigma = \sigma_{\text{intra}} + \sigma_{\text{inter}}$  (solid lines) and  $\sigma_{\text{intra}}$  (dashed lines) in the low THz range  $0.3 \leq f \leq 3$  THz for  $\mu_c = 0.1$  eV and  $\tau = 3$  ps. The agreement remains good for reasonable values of  $\mu_c$  and  $\tau$ . 89
- Figure 3.5 (a) Graphene surface conductivity vs. chemical potential in the range  $-1$  to  $1$  eV at the frequency for frequency raising from  $0.3$  THz to  $3$  THz (colors shade from blue to cyan for  $\sigma_J$  and from red to yellow for  $\sigma_R$ , respectively). (b) Graphene surface conductivity vs. frequency in the band  $0.3$ - $3$  THz for chemical potential raising from  $0$  to  $1$  eV (colors shade from blue to cyan for  $\sigma_J$  and from red to yellow for  $\sigma_R$ , respectively). 90
- Figure 3.6 (a) Graphene  $\text{Re}[\sigma]$  and  $\text{Im}[\sigma]$  vs.  $\tau$  at  $f = 1$  THz for  $\mu_c$  ranging from  $0$  eV to  $1$  eV.  $\text{Re}[\sigma]$  and  $\text{Im}[\sigma]$  curves gradually shade from red to blue and from gray to black, respectively, as  $\mu_c$  increases from  $0$  eV to  $1$  eV. 90



- Figure 3.7 Intensity of plasmonic dissipation losses  $\hat{\alpha}_{\text{SPP}}$  in the range  $[0,1]$  in the  $\sigma$  complex plane. The dynamic range of  $\hat{\alpha}_{\text{SPP}}$  has been saturated to values greater than 1 for readability purposes. The paths followed by the graphene surface conductivity in the complex plane have been reported for values of  $f$  ranging from 0.75 THz to 1.25 THz (size of the symbols increases),  $\tau$  ranging from 0.1 ps to 3 ps (symbols change shape in the following order:  $\circ, \times, \nabla, *$ ) and  $\mu_c$  ranging from 0.25 eV to 1 eV (color of the symbol change in the following order: red, green, blue, and yellow). The black region represents the area characterized by the highest dissipation losses and is attained by graphene samples with both lower  $\mu_c$  and  $\tau$ . 92
- Figure 3.8 SPP figures of merit: (a)  $M_2 = (\hat{\beta}_{\text{SPP}} - 1)/\hat{\alpha}_{\text{SPP}}$  and (b)  $M_3 = \hat{\beta}_{\text{SPP}}/(2\pi\hat{\alpha}_{\text{SPP}})$  vs.  $\sigma_R$  and  $\sigma_I$  in the dynamic range shown in Fig. 3.5(a). The former (Fig. 3.8(a)) gives a measure of the confinement of a suspended SPP for 1-D and 2-D waveguide structures. The latter (Fig. 3.8(b)) is strictly connected to the quality factor  $Q$  [149]. 94
- Figure 3.9 (a) 2-D sketch of the GPW structure ( $\epsilon_{r1} = 3.8$ ). The biasing scheme is not reported. (b) Normalized field configurations of the tangential component of the electric field  $E_z$  at  $f = 0.92$  THz for the fundamental TM leaky mode (red line) and the SPP (blue line) in a GPW antenna. Grey and white regions represent the substrate and the air, respectively, whereas the black diamonds stand for the graphene sheet. The  $x$ -axis is normalized to the height of the substrate  $h_1$ . 95
- Figure 3.10 2-D sketch, TEN model, and ABCD-matrix representation of a GPW antenna. 96
- Figure 3.11 Dispersion curves of SWs and LWs within the band 0.25 – 2 THz for a GDS (blue lines), a GPW (red lines), a BGPW (green lines), and a PPW (gray lines). In dashed lines improper waves, in solid lines proper waves. In (a)  $\hat{\beta}_z$ , in (b)  $\hat{\alpha}_z$  for TE modes, and in (c)  $\hat{\beta}_z$ , in (d)  $\hat{\alpha}_z$  for TM modes. 97

- Figure 3.12 Dispersion curves of SWs and LWs within the band 0.25 – 1.5 THz for three different values of the chemical potential. In dashed red line improper leaky poles, in dashed blue line improper non-physical poles, in solid red line SWs for the fundamental TM mode and in solid blue line the remaining SWs. In (a)  $\hat{\beta}_z$ , in (b)  $\hat{\alpha}_z$  for TE modes, and in (c)  $\hat{\beta}_z$ , in (d)  $\hat{\alpha}_z$  for TM modes. 98
- Figure 3.13 Dispersion curves of the TE<sub>1</sub>, TM<sub>2</sub> fundamental LWs (a) within the band 0.75 – 1.1 THz for  $\mu_c = 0.5, 0.75, 1$  eV, and (b) within the range  $0.2 \leq \mu_c \leq 1$  eV for  $f = 0.92$  THz. In (a)  $\hat{\beta}_z$  and  $\hat{\alpha}_z$  are both represented in dashed lines for the TE<sub>1</sub> mode and in solid lines for the TM<sub>2</sub>. In (b)  $\hat{\beta}_z$  and  $\hat{\alpha}_z$  are represented in solid lines and dashed lines, respectively, for both modes. 100
- Figure 3.14 Dispersion curves of (a)  $\hat{\beta}_z$ , (b)  $\hat{\alpha}_z$  for the plasmonic mode SPP. Lines become brighter (red to yellow, and blue to cyan) as  $\mu_c$  increases from 0 to 1 eV. Note that as  $\mu_c$  approaches 1 eV the SPP mode approaches the PPW TEM mode. 100
- Figure 3.15 (a) 2-D section of the structure and its transverse equivalent networks: (b) using the lossless model, (c) using the approximate Leontovich boundary condition, and (d) using the transition boundary condition. 101
- Figure 3.16 Effects of the introduction of losses and spatial dispersion in the curves of the fundamental LWs in the band 0.9 – 0.95 THz for (a) TE and (b) TM modes. The red and green-blue lines consider the effect of dielectric losses and ohmic losses, respectively. The yellow ones consider the effect of a spatially dispersive model in addition to dielectric and ohmic losses. 101

Figure 3.17 (a) Illustrative example of the typical scannable conical beam-scanning feature of a GPW antenna. In (b) and (c), the radiation patterns normalized to the overall maximum (achieved at broadside) vs. elevation angle  $\theta$  for the GPW antenna represented in (a), are reported for the H-plane and E-plane, respectively. Analytical results are plotted in black solid lines, whereas full-wave results obtained with the tool CST Microwave Studio [159] are given by blue circles. The scanning behavior at a fixed frequency ( $f_c = 0.922$ ) is shown for beam maxima at  $\theta_p = 0^\circ, 15^\circ, 30^\circ, 45^\circ$ . The corresponding chemical potentials are reported in the legend. 103

Figure 3.18 2-D sketch, TEN model, and ABCD-matrix representation of a GSS antenna. 105

Figure 3.19 (a) The dispersion curve ( $\hat{\beta}_z$  and  $\hat{\alpha}_z$  vs.  $f$  in black solid and dashed lines, respectively) of the fundamental TM leaky mode of the unperturbed SS is reported in the frequency range  $0.75 \leq f \leq 1.25$  THz. On the same plot the values of the splitting condition ( $\hat{\beta}_z = \hat{\alpha}_z$ ) are shown for different positions of the graphene sheet starting from the interface  $x_0/h_1 = 1$  to the ground plane  $x_0/h_1 = 0$ . The color of the dots shades from red to blue as the graphene sheet moves from  $x_0/h_1 = 1$  to  $x_0/h_1 = 0$ . An optimum position is found at  $f = 1.132$  THz for  $x_0/h_1 = 0.82$  (black dot). Note that the frequency  $f_c$  at which splitting condition occurs ranges approximately from 1 THz to 1.5 THz. (b) Cutoff frequency  $f_c$  (blue solid line) and relevant value of  $\hat{\beta}_z(f_c) = \hat{\alpha}_z(f_c)$  (red dashed line) as a function of the normalized distance  $x_0/h_1$  of the graphene sheet from the ground plane, for the fundamental TM mode in the GSS structure. 107

Figure 3.20 (a) The dispersion curve ( $\hat{\beta}_z$  and  $\hat{\alpha}_z$  vs.  $f$  in black solid and dashed lines, respectively) of the fundamental TE leaky mode of the unperturbed SS is reported in the frequency range  $0.75 \leq f \leq 1.25$  THz. An optimum position is found at  $f = 1.148$  THz for  $x_0/h_1 = 0.805$  (black dot). Note that the frequency  $f_c$  at which splitting condition occurs ranges approximately from 1 THz to 1.5 THz. (b) Cutoff frequency  $f_c$  (blue solid line) and relevant value of  $\hat{\beta}_z(f_c) = \hat{\alpha}_z(f_c)$  (red dashed line) as a function of the normalized distance  $x_0/h_1$  of the graphene sheet from the ground plane, for the fundamental TM mode in the GSS structure. 108

Figure 3.21 Cutoff frequency  $f_c$  (blue to cyan solid lines) and relevant value of  $\hat{\beta}_z(f_c) = \hat{\alpha}_z(f_c)$  (red to yellow solid lines) as a function of the distance of the graphene sheet from the ground plane  $x_0$  normalized to the substrate thickness  $h_1$ , for the fundamental TM leaky mode in the GSS. Similar results are found for the fundamental TE leaky mode. As the dielectric contrast spans the following values  $d_{1,2} = 2, 5, 10, 20, 50$ , the curves shade from blue to cyan and from red to yellow for values of  $f_c$  and of  $\hat{\alpha}_z(f_c)$ , respectively. 109

Figure 3.22 Normalized phase constants and attenuation constants of the fundamental TM (in black) and TE (in grey) leaky modes of a GPW (dashed lines) with parameters as in [114] (i.e., with graphene placed at the interface between the air and a dielectric layer at a fixed frequency  $f_c = 0.92$  THz) and of the proposed GSS (solid lines) with parameters as in Fig. 3.19, with graphene placed at the optimum position  $x_0 = 0.82h_1$  at a fixed frequency  $f_c = 1.132$  THz, as a function of the chemical potential in the range  $1 > \mu_c > 0$  eV. 110

Figure 3.23 (a) Illustrative example of the typical conical beam-scanning feature of a GSS antenna. In (b) and (c), the radiation patterns normalized to the overall maximum (achieved at broadside) vs. elevation angle  $\theta$  for the GSS antenna represented in (a), are reported for the H-plane and E-plane, respectively. Analytical results are plotted in black solid lines, whereas full-wave results obtained with the tool CST Microwave Studio [159] are given by blue circles. The scanning behavior at a fixed frequency ( $f_c = 1.132$  THz) is shown for beam maxima at  $\theta = 0^\circ, 15^\circ, 30^\circ, 45^\circ$ . The corresponding chemical potentials are reported in the legend. 112

Figure 3.24 H-plane radiation patterns, normalized to the overall maximum (achieved at broadside), vs. elevation angle  $\theta$  for a GSS antenna (solid lines) with parameters as in Fig. 3.22 and for an equivalent GPW (dashed lines), excited by a HMD placed on the ground plane. The scanning behavior at a fixed frequency ( $f_c = 1.132$  THz for the GSS and  $f_c = 0.92$  THz for the GPW) is shown for four theoretical pointing angles  $\theta_p = \sin^{-1}(\hat{\beta}_z^2 - \hat{\alpha}_z^2)^{1/2} = 0^\circ, 15^\circ, 30^\circ, 45^\circ$ . The chemical potentials for the GPW and the GSS are reported in the legend. 112

Figure 3.25 (a) Efficiency  $\eta$  vs. graphene positions in the substrate  $x_0/h_1$  (red lines), and directivity at broadside normalized to its maximum  $\bar{D}_0$  (blue lines). Both  $\eta$  and  $\bar{D}_0$  have been calculated at the corresponding cutoff frequency for each graphene position  $x_0/h_1$ . The grey dashed line, representing the efficiency of an equivalent GPW antenna, has been reported for comparison. (b) The function  $f$  vs.  $x_0/h_1$  of Eq. (3.38) for different values of  $w$ . Color of the lines shades from blue to red as  $w$  ranges from 0 to 1. Colored dots highlight the positions of the maxima of  $f$  as  $w$  ranges from 0 (blue dot) to 1 (red dot). Maxima are located closer to the interface as the efficiency is weighted more than the directivity. 114

- Figure 3.26 Field configurations of the tangential component of the electric field  $E_z$  for the fundamental TM leaky mode (red line) in a GSS antenna (a) at  $f = 1.13$  THz when graphene is placed at  $x_0 = 0.82h_1$  and (b) at  $f = 1.00$  THz when graphene is placed at the interface  $x_0 = h_1$ . Light grey, dark grey, and white regions represent the substrate, the superstrate, and the air, respectively, whereas the black diamonds stand for the graphene sheet. The  $x$ -axis is normalized to the height of the overall structure  $h = h_1 + h_2$ . 115
- Figure 3.27 2-D section of the GSG antenna and its TEN model. 118
- Figure 3.28 Dispersion diagrams of  $\hat{\beta}_z$  and  $\hat{\alpha}_z$  vs.  $f$  for (a)-(c) TE and (b)-(d) TM fundamental leaky modes of a (a)-(b) graphene-based planar single-slab antenna (solid lines) and a (c)-(d) graphene-strip grating antenna (dashed lines). The values of the chemical potentials  $\mu_c$  are reported in the legends. 119
- Figure 3.29 Normalized radiation patterns  $P(\theta)/P_{\max}$  vs.  $\theta$  for (a) TE and (b) TM fundamental leaky mode of a GPW (blue lines) and a GSG (red lines). 120
- Figure 3.30 Representation of NLC molecules twisting in a LC cell. The optical axis of the NLC switches under the effect of an applied bias voltage. 125
- Figure 3.31 2-D section (a) on the  $xy$ -plane and (b) on the  $xz$ -plane of the THz fishnet MM. Further details on the unit-cell are available in [96]. 126
- Figure 3.32 Real part of the diagonal terms  $\varepsilon_{ii}(x, y, z = 0)$  vs.  $xy$ -plane of the relative permittivity tensor for  $V_{\text{bias}} = 0 - 7$  [V]. First column ( $i = x$ ), second column ( $i = y$ ), and third column ( $i = z$ ). Starting from the first row the driving voltage takes the following values:  $\{0, 1.5, 2, 3, 4, 7\}$  [V]. 127
- Figure 3.33 Real part of the off-diagonal terms  $\varepsilon_{ij}(x, y, z = 0)$  vs.  $xy$ -plane of the relative permittivity tensor for  $V_{\text{bias}} = 0 - 7$  [V]. First column ( $i = x, j = y$ ), second column ( $i = y, j = z$ ), and third column ( $i = x, j = z$ ). Starting from the first row the driving voltage takes the following values:  $\{0, 1.5, 2, 3, 4, 7\}$  [V]. 128
- Figure 3.34 Real part of the diagonal terms  $\varepsilon_{ii}(x = x_0, y = y_0, z)$  vs.  $z$  for  $V_{\text{bias}} = 0 - 7$  [V]. First column ( $i = x$ ), second column ( $i = y$ ), and third column ( $i = z$ ). Starting from the first row the  $(x_0, y_0)$  position takes the following values:  $(0, 0)$   $\mu\text{m}$ ,  $(54, 54)$   $\mu\text{m}$ , and  $(75, 75)$   $\mu\text{m}$ . 129

- Figure 3.35 Imaginary part of the diagonal terms  $\varepsilon_{ii}(x = x_0, y = y_0, z)$  vs.  $z$  for  $V_{\text{bias}} = 0 - 7$  [V]. First column ( $i = x$ ), second column ( $i = y$ ), and third column ( $i = z$ ). Starting from the first row the  $(x_0, y_0)$  position takes the following values:  $(0, 0)$   $\mu\text{m}$ ,  $(54, 54)$   $\mu\text{m}$ , and  $(75, 75)$   $\mu\text{m}$ . 130
- Figure 3.36 2-D section view of the proposed device and its equivalent transmission-line representation. The NLC layers are biased through a pair of extremely-thin moderately-conductive polymer films (not reported in the picture), e.g., PEDOT:PSS [99], whose absorption is neglected here. 131
- Figure 3.37 Dispersion curves ( $\hat{\beta}_z$  and  $\hat{\alpha}_z$  vs.  $f$ ) of the fundamental TM leaky mode for (a) Layouts 1, (b) 2, (c) 3, and (d) 4 (see Table 3.5) when the NLC layer is biased at  $V_\infty$  (blue lines) and when is unbiased 0 V (red lines). Colors gradually shades from blue to red as  $V_b$  decreases from  $V_\infty$  to 0 V. 133
- Figure 3.38 Radiation patterns predicted considering only the LW pole contribution (dashed lines) and by means of reciprocity theorem (solid lines) for (a) Layouts 1, (b) 2, (c) 3, and (d) 4 (see Table 3.5) when the beam points at broadside (blue lines) and when is steered at the maximum pointing angle (red lines). 135
- Figure 3.39 Dispersion curves ( $\hat{\beta}_z$  and  $\hat{\alpha}_z$  vs.  $f$ ) of the fundamental TM leaky mode for (a) Layout 2 and (b) Layout 4 (see Table 3.5) in the lossy case, when the NLC layer is biased at  $V_\infty$  (blue lines) and when is unbiased 0 V (red lines). Colors gradually shades from blue to red as  $V_b$  decreases from  $V_\infty$  to 0 V. 136
- Figure 3.40 Radiation patterns for (a) Layout 2 and (b) Layout 4 for radiation at broadside (solid) and at the maximum pointing angle (dashed). The radiation patterns have been calculated by means of reciprocity theorem in both the lossless (in red) and the lossy (in black) case, and then compared with those given by means of LWA theory (blue). Full-wave simulations with CST are also reported for the lossy case for radiation at broadside (filled green circles) and at the maximum pointing angle (empty green circles). 137
- Figure 4.1 Wavevectors  $\kappa = k_\rho \hat{\rho}_0 + k_z \hat{z}_0$  lying on the surface of a cone with axicon angle  $\theta_0$ . 147

- Figure 4.2 (a) Modulus and (b) phase of a higher-order Bessel beam of order  $n = 1$  generated by an aperture of 25 cm at 12.5 GHz. The phase follows the typical spiral path, whereas the modulus exhibits a central dark spot. 149
- Figure 4.3 Intensity distribution of a zeroth-order Bessel function of the first kind (black solid line) and its envelope (blue dashed line) decaying as  $\rho^{-1}$ . 152
- Figure 4.4 Contour-plot of a zeroth-order Bessel beam generated by an (a) infinite aperture and (b) a finite aperture of radius  $\rho_{\text{ap}} = 3\lambda$  and with an axicon angle  $\theta_0 = 45^\circ$ . 153
- Figure 4.5 (a) A sketch of the experimental setup used by J. Durnin for the first generation of a Bessel beam in optics [189]. (b) A sketch of the experimental setup for generation of a Bessel beam through an axicon lens as presented in [223]. The axicon element allows for converting a Gaussian beam in a Bessel beam within a rhomboidal region located in the near field. The dashed red line is located at  $z = z_{\text{ndr}}/2$ . In the far-field, the Fourier-Transform of the aperture field gives rise to the expected annulus shape. 155
- Figure 4.6 (a) 2-D and (b) 3-D plot of the normalized amplitude of an X-wave as a function of  $\rho$  and  $z - v_z t$  where  $v_z$  is the group velocity of the wave. Since for an ideal X-wave cone dispersion is neglected, the group velocity  $v_z$  coincides with the phase velocity  $v_{\text{ph}} = c / \cos \theta_0$ . As a consequence the variable  $z - v_z t$  gives a measure of the spatio-temporal confinement of the pulse. In this example, we have considered a wide uniform frequency spectrum and an axicon angle  $\theta_0 = 45^\circ$ . The X-shape of the pulse follows the inclination dictated by the axicon angle, as emphasized by the boundaries in both figures. 159
- Figure 4.7 (a) A sketch of the experimental setup used by Lu and Greenleaf for the first generation of X-waves in acoustics [264]. (b) A sketch of the experimental setup for the first measurement of the 3-D field distribution of X-waves in optics [265]. Except for a system of converging lenses and a pinhole, the mechanism of generation was equal to the one originally proposed by Durnin [189] for the Bessel beam generation. 161



- Figure 5.1 Geometrical view of a leaky-wave radial waveguide of thickness  $h$ . A metallic rim is placed at  $\rho = \rho_{ap}$ . The PRS is represented by a square lattice of metallic patches. 167
- Figure 5.2 The mechanism of generation of a Bessel beam through the superposition of an inward Hankel wave and an outward Hankel wave. An outward Hankel wave is generated at the center by a coaxial feed and is then reflected back by the circular metallic rim to create an inward Hankel wave. If the circular rim is placed in one of the zeros of the Bessel function and the incident wave is slowly-attenuated, the two Hankel waves constructively interfere each other and create the Bessel beam. 168
- Figure 5.3 (a) 2-D section of the LRW and its (b) transverse equivalent network (TEN) model. 170
- Figure 5.4  $\beta_{\rho}/k_0$  vs. frequency ( $f$ ). The intersections between the transverse (solid blue lines) and the radial (black dashed lines) resonances define the operating points. 171
- Figure 5.5  $\beta_{\rho}^{(n)}/k_0$  vs.  $f$ . The intersections between the transverse (solid blue lines) and the radial (black dashed lines) resonances define the operating points of the launcher. The radial resonance are reported only for  $4 \leq n \leq 6$ . 172
- Figure 5.6 Contour plot of the electric field  $|E_z|$  along the  $\rho z$ -plane for the proposed LRW at the operating frequency  $f = 10$  GHz. The five nulls are clearly distinguishable, as expected from theory. 173
- Figure 5.7 Final prototype. The array of vias comprising the outer metallic rim is shown in the inset. Courtesy of Mauro Ettore [235]. 173
- Figure 5.8 Normalized component  $E_z$  of the electric field. (a) Comparison between measured and simulated results at  $z = 0.75\lambda_0$  for different  $\phi$ -cuts. (b) 2D field distribution over the  $xy$ -plane at  $f = 9.6$  GHz at  $z = 0.75\lambda_0$ . (c) 2D field distribution over the  $xz$ -plane at  $f = 9.6$  GHz at  $y = 0$ . Courtesy of Mauro Ettore [235]. 174
- Figure 5.9 2-D section of a PPW with lossy metallic plates. 175
- Figure 5.10  $\alpha_c$  vs. frequency ( $f$ ). At  $f = 40$  GHz the attenuation constant of the TEM mode propagating in a PPW with copper plates reaches the value of 7 Np/m. 176

- Figure 5.11  $X_s$  vs.  $f$  for a homogenized PRS constituted by a periodic ( $p = \lambda_0/10$ ) array of double-layered interleaved metallic square patches. The value of the surface impedance is calculated for different values of the distance between the patches ranging from  $g = 200 \mu\text{m}$  to  $g = 50 \mu\text{m}$ , which is the maximum tolerance for PCB technology. 177
- Figure 5.12 Illustration of the millimeter-wave Bessel-beam launcher under consideration. The blue arrows show the outward and inward Hankel waves excited by a central coaxial probe. The constructive interference of these cylindrical waves creates the Bessel beam profile. 179
- Figure 5.13 (a) Normalized phase constant and (b) normalized attenuation constant vs. frequency  $f$  up to 100 GHz for the first three TM of a LRW as in Fig. 5.3. The solid and dashed lines denote the dispersion curves for the proper and improper modes, respectively. The blue and red curves represent the dispersion curves for the real and complex modes, respectively. Hence surface-wave (SW) modes are shown by black solid lines, whereas the leaky-wave (LW) modes are shown by grey dashed lines. In these plots, it is assumed that  $X_s = -25 \Omega$ ,  $\epsilon_r = 2.17$ ,  $h = 3.175 \text{ mm}$  [153]. 183
- Figure 5.14 Dispersion curves (SW and LW in blue solid and red dashed lines, respectively) for the design of the higher-order launcher prototype. The operating points are given by the intersections of the fast leaky-wave modes and the hyperbolic curves given by the Bessel zeros (black dashed lines). Once the operating point is chosen, the operating bandwidth (highlighted gray region) is fixed by the closest intersections of either the fast leaky-wave or the surface-wave modes. The parameters used in Fig. 5.13 are also assumed here. 184
- Figure 5.15 Geometrical interpretation of the problem in Fig. 5.14. The blue dot represents the operating point given by the intersection between  $q = 5$  and  $n = 1$  dispersion curves. The green dots represent the operating points given by the intersection between  $n = 1$ , and  $q = 4, 6$  dispersion curves. Once  $a'$  is found, it can be used to calculate both  $f_{\text{inf}}^{\text{LW}1}$  and  $f_{\text{sup}}^{\text{LW}1}$ , thanks to the symmetry of the problem. 185

- Figure 5.16 Approximation of the tangent function  $\tan(k_{z1}h)$  vs.  $h$  with  $(k_{z1}h - n\pi)$  for  $n = 0, 1, 2$  when  $k_{z1} = k_0\sqrt{\varepsilon_r - \hat{k}_\rho^2}$  with  $\hat{k}_\rho = 0.8$ . As expected, at  $h = 3.175$  mm the approximation is very good, leading to percentage error of 0.3%. 187
- Figure 5.17 (a) Geometry of the COMSOL model of the prototype. The size of the evaluation box is set slightly larger than necessary in order to avoid spurious reflections from the PML boundary conditions. (b) Boundary conditions setting of the COMSOL model of the prototype. 187
- Figure 5.18 Contour plot of the electric field  $|E_z|$  along the  $\rho z$ -plane for the mm-wave launcher under analysis at (a)  $f = 39.7$  GHz, (b)  $f = 37.3$  GHz, and (c)  $f = 40.3$  GHz. 188
- Figure 5.19 1-D profile of the normalized electric field  $|E_z|$  at  $f = 39.7$  GHz, for the proposed launcher (parameters as in Fig. 5.13), for various distances  $z = \lambda/2, \lambda, 3\lambda/2, 2\lambda$  from the aperture. 188
- Figure 5.20 Prototype of the mm-wave leaky-mode Bessel-beam launcher. The feeding probe can be recognized at the center of the structure. 189
- Figure 5.21 Schematic of the coaxial probe transition used for matching the mm-wave launcher. 189
- Figure 5.22 HFSS unit-cell model for the impedance synthesis of the capacitive sheet. The respect of the homogenization limit  $p \ll \lambda_0 p$  [50] allows for describing the fields with only the fundamental  $n = 0$  Floquet harmonic, and hence only an equivalent transmission-line is required to model the structure. 190
- Figure 5.23 Some pictures of the Near-Field Test Range at IETR, Rennes, France. Courtesy of Ioannis Iliopoulos [285]. Note that the antenna under test (AUT) shown in the picture on the left is not our actual prototype which was not mounted on the mast. These pictures are reported just to show the measurement setup. 191
- Figure 5.24 (a) Measured reflection coefficient ( $|S_{11}|$  in dB) and (b) reflection phase ( $\angle S_{11}$ ) of the prototype in the frequency range  $37 \div 40$  GHz. The black dashed lines highlight the frequency range for which the return loss is under  $-10$  dB. 191
- Figure 5.25 Measured intensity of  $E_z$  along the  $xy$  plane at  $f = 38.3$  GHz at  $z = 0.5\lambda_0, 0.75\lambda_0, \lambda_0, 1.5\lambda_0, 2\lambda_0, 2.5\lambda_0$  from the impedance surface, where  $\lambda_0$  equal to 7.5 mm. 192

- Figure 5.26 Measured intensity of  $E_z$  along the  $xy$  plane at  $z = \lambda$  at  $f = 38.0$  GHz, 38.3 GHz, 38.6 GHz, 38.9 GHz, 39.2 GHz, 39.5 GHz. 192
- Figure 5.27 Comparison between measurements (solid gray lines), simulations (dashed blue lines), and numerical results (red dashed lines). (a)-(c) Normalized  $E_z$  vs.  $\rho$  at  $f = 38.3$  GHz at  $z = 0.5\lambda_0, 0.75\lambda_0, \lambda_0$ . (d)-(f) Normalized  $E_z$  vs.  $\rho$  at  $z = \lambda$  at  $f = 38.0$  GHz, 38.8 GHz, 39.5 GHz. 193
- Figure 5.28 Measured intensity of  $E_z$  along the  $xz$  plane at  $f = 38.0$  GHz, 38.3 GHz, 38.6 GHz, 38.9 GHz, 39.2 GHz, 39.5 GHz. 193
- Figure 5.29 Measured HPBW vs.  $f$  in the range 38 GHz to 39.5 GHz at different distances  $z = 0.5\lambda_0, 0.75\lambda_0, \lambda_0, 1.5\lambda_0, 2\lambda_0, 2.5\lambda_0$ . The color shades from blue to cyan as  $z$  increases from  $0.5\lambda$  to  $2.5\lambda$ . At  $z = \lambda$  the HPBW shows a remarkable stability with respect to the frequency. 194
- Figure 6.1 Definition of a *metric of confinement* for an X-wave. A pulse characterized by a transverse spot width  $S_\rho$  and a longitudinal spot width  $S_z$  is launched through a finite radiating aperture of diameter  $d_{\text{ap}} = 2\rho_{\text{ap}}$ . Since the main constituents of an X-wave, i.e., Bessel beams, maintain their spot widths up to the non-diffractive range  $z_{\text{ndr}}$ , an X-wave will be properly defined over an area on the  $\rho z$  plane which is limited along  $\rho$  by the aperture diameter and along  $z$  by the nondiffractive range. If most of the energy of the pulse is contained in this region, we can actually state that the considered X-wave is *efficiently confined*. 199
- Figure 6.2 Normalized  $\chi_t^U(\rho)$  vs.  $\rho$  for  $f_0 = 60$  GHz,  $\theta_0 = 11^\circ$  and (a)  $\Delta\omega/\omega_0 = 0.05$  (b)  $\Delta\omega/\omega_0 = 0.2$ . Comparison between the numerical integration of Eq. (6.12) (red circles), the exact integral of Eq. (6.12) (green solid curves), and the approximation given by Eq. (6.15) (blue dashed curves). As the fractional bandwidth  $\Delta\omega/\omega_0$  increases, the approximation is less accurate on the tails, but the width of the main beam is always well approximated. 203

- Figure 6.3 Weak confinement  $C_{\rho,z}^{(w)}$  vs.  $\rho_{\text{ap}}/\lambda_0$  and  $\theta$ . The yellow hyperbola represents the boundary between the region of efficient (in white) and non-efficient confinement (in black) for ideal UXWs, when fractional bandwidths of (a)  $\overline{\Delta\omega} = 0.01$ , (b)  $\overline{\Delta\omega} = 0.05$ , (c)  $\overline{\Delta\omega} = 0.1$ , and (d)  $\overline{\Delta\omega} = 0.2$  are considered. The region of efficient confinement increases for larger fractional bandwidths. In any case, this region corresponds to electrically large apertures with small axi-con angles. 205
- Figure 6.4 The yellow and white hyperbola represents the boundaries between the region of efficient (in white) and non-efficient confinement (in black)  $\overline{\Delta\omega} = 0.01$  and  $\overline{\Delta\omega} = 0.2$ , respectively. The transition region is limited by the two hyperbola. 206
- Figure 6.5  $C_{\rho,z}^{(w)}$  vs.  $\rho_{\text{ap}}/\lambda_0$  and  $\theta_0$  for (a) FBW = 1% and (d) FBW = 20%. The purple dot  $p_1$  represents an X-wave with  $m = 8$  and  $\theta = 10^\circ$ . The yellow dot  $p_2$  represents an X-wave with  $m = 1$  and  $\theta = 10^\circ$ . The blue dot  $p_3$  represents an X-wave with  $m = 25$  and  $\theta = 20^\circ$ . An X-wave in  $p_1$  is generated for (b) FBW = 1% and (c) FBW = 20%, whereas X-waves in (e)  $p_2$  and (f)  $p_3$  are both generated for FBW = 20%. In (b-c) and (e-f), the intensity of the X-wave is reported over a  $\rho z$  plane limited by  $\rho_{\text{ap}}$  along  $\rho$  and  $z_{\text{ndr}}$  along  $z$ . From this representation, if  $S_\rho$  and  $S_z$  fit in the plot, then the X-wave is confined over the respective axis. Note that, the  $\rho$ -axis is normalized to  $\rho_{\text{ap}}$  while the  $z$ -axis is normalized to  $z_{\text{ndr}}$ . 206
- Figure 6.6 Strong confinement  $C_{\rho,z}^{(s)}$  vs.  $\rho_{\text{ap}}/\lambda_0$  and  $\theta$ . The yellow curves represent the boundaries between the region of efficient (in white) and non-efficient confinement (in black) for ideal UXWs, when fractional bandwidths of (a)  $\overline{\Delta\omega} = 0.01$ , (b)  $\overline{\Delta\omega} = 0.05$ , (c)  $\overline{\Delta\omega} = 0.1$ , and (d)  $\overline{\Delta\omega} = 0.2$  are considered. The region of efficient confinement increases for larger fractional bandwidths as for  $C_{\rho,z}^{(w)}$ . However, the efficient region is considerably narrower due to the more strict criterion applied by the strong metric  $C_{\rho,z}^{(s)}$  with respect to the weak metric  $C_{\rho,z}^{(w)}$ . 207

- Figure 6.7 Upper-left and lower-left corner:  $C_{\rho,z}^{(w)}$  and  $C_{\rho,z}^{(s)}$  vs.  $\rho_{\text{ap}}$  and  $\theta$  for  $\text{FBW} = 20\%$ . Upper-right and lower-right corner: 3-D view of the normalized  $|\chi(\rho, z)|^2$  vs.  $\rho$  and  $z$  with parameters as in  $p_1$  and  $p_2$ , respectively (viz.,  $m = 10$  and  $\theta_0 = 60^\circ$  for  $p_1$ , and  $m = 10$  and  $\theta_0 = 30^\circ$  for  $p_2$ ). 208
- Figure 6.8 Comparison between numerical integrations (red circles) and approximations (Eqs. (6.29) and (6.17) in green solid lines and Eqs. 6.18 and 6.19 in blue dashed lines) of (a)-(b) transverse profiles and (c)-(d) longitudinal profiles for a dispersive X-wave in fractional bandwidths (a)-(c)  $\text{FBW} = 5\%$  and (b)-(d)  $\text{FBW} = 20\%$  centered around  $f_0 = 60$  GHz. The resulting profiles have been obtained assuming  $k_{z0} = 0.2k_0$ ,  $k_{z1} = 0.55 \cdot 10^{-12}$ , and  $k_{z2} = 0$ . Results are reported over an aperture plane of  $\rho_{\text{ap}} = 15\lambda_0$  and  $z_{\text{ndr}}$  calculated at  $f_0$ . Note that  $\rho' = k_{\rho 0}\rho$  and  $z' = k_{z0}\overline{\Delta\omega}z/2$ . 211
- Figure 6.9 (a) Prospective view of an RLSA. (b) Brillouin diagram  $f$  vs.  $k_z$  for the structure in Fig. 6.9.  $k_z$  (green curve) is given by Eq. 6.33 through the relation of separability. The second-order Taylor approximation (blue circles) accurately describe the wavenumber dispersion curve. The slope of  $k_z$  is lower than the light line (black line), so that  $c_0 > v_z > 0$ . 212
- Figure 6.10 2-D normalized intensities for ideal (first column: (a) and (d)), dispersive (second column: (b) and (e)), and dispersive-finite (third column: (c) and (f)) UXWs, when the pulse has reached half the propagating distance of  $z_{\text{dof}}^{(c)}$ . The numerical results are shown for  $\overline{\Delta\omega} = 0.05$  (first row: (a-c)), and  $\overline{\Delta\omega} = 0.2$  (second row: (d-f)). 215
- Figure 6.11 Evolution of the (a) transverse and (b) longitudinal HPBW vs.  $t$ . The ideal (red curves), dispersive (green curves), and the dispersive-finite case (blue curves) are represented for  $\overline{\Delta\omega} = 0.2$ . The  $x$ -axis on the top is obtained by scaling the temporal axis with the theoretical group velocity  $v_z \simeq 0.84c_0$ . 216
- Figure 6.12 Evolution of the normalized intensity vs. time  $t$ . The ideal (red solid line), dispersive (green dashed line), and the dispersive-finite case (blue circles) are represented for  $\overline{\Delta\omega} = 0.2$ . 217

- Figure 6.13 3-D view of the normalized intensities of a dispersive-finite UXW, generated with a fractional bandwidth  $\overline{\Delta\omega} = 0.2$ . The time evolution is numerically reproduced for 9 different time frames, ordered from left to right and from top to bottom. 218
- Figure 6.14 Schematic view of the generation of localized twisted pulses from a radiating aperture on the  $xy$  plane. The intersection of the shadow boundaries (dotted black lines) defines the nondiffractive range ( $z_{\text{ndr}} = \rho_{\text{ap}} \cot \theta$ ). Dashed red lines define the envelope of the confined region whose section slowly increases beyond the nondiffractive range due to the limited spatio-temporal dispersion of the pulse. In the numerical examples of 6.3.4 the transverse distributions are observed at the reference plane for different time instants. 221
- Figure 6.15 Normalized amplitude distribution of  $E_z$  vs.  $x, y$  at  $f = 12.5$  GHz with  $k_\rho = 0.4k_0$  of the near field radiated over the transverse (i.e.,  $xy$ ) plane at  $z = z_{\text{ndr}}/2$ . (a-c) Contour plot of  $E_z$  radiated at  $z = z_{\text{ndr}}/2$  by a standing-wave aperture distribution (Eqs. (6.40)-(6.41)) and (d-f) by an inward traveling-wave aperture distribution (Eqs. (6.42)-(6.43)) for  $n = 1, 3, 5$  (looking from left to right) over a radiating aperture with radius  $\rho_{\text{ap}} = 10\lambda$ . 222
- Figure 6.16 Phase distribution at  $f = 12.5$  GHz with  $k_\rho = 0.4k_0$  of the  $E_z$  near field obtained by radiating a first-order inward traveling-wave distribution over the transverse (i.e.,  $xy$ ) plane at  $z = z_{\text{ndr}}/2$ . The correspondent normalized amplitude distribution is given in Fig. 6.15(d). 223
- Figure 6.17 Comparison between (a)-(b) nondispersive and (c)-(d) dispersive case. The norm of  $\chi_E$  is reported over the  $xz$  plane. The  $x$ -axis is normalized to  $\lambda_0$ , whereas the  $z$ -axis is normalized to  $z_{\text{ndr}}^{(c)}$ . The contour plot of  $\|\chi_E\|$  has been reported for two time instants: (a), (c)  $t_i = 0.8$  ns and (b), (d)  $t_f = 2.4$  ns. 225
- Figure 6.18 Screen-shots of (a)  $\chi_\rho$ , (b)  $\chi_\phi$ , (c)  $\chi_z$ , and (d)  $\|\chi_E\|$  at  $t_1 = 0.8$  ns,  $t_2 = 1.3$  ns over the  $xy$  plane (both axes are normalized to  $\lambda$ ). Note that the colorscale for (d) and (h) is different since  $\|\chi_E\| > 0$ . 226

Figure B.1 (a) CST unit-cell model of a GSS antenna. In green and blue the substrate and the superstrate, respectively. The transparency of the materials has been set in order to make visible the monolayer graphene within the substrate. The probe for evaluating the tangential magnetic field  $H_y$  at the ground plane is represented with a blue arrow. (b) Phase-shift walls have been implemented to emulate an infinitely transverse uniform structure by means of a periodic unit cell. 231

## LIST OF TABLES

Table 2.1	MAPE for HTF, HETF, MHTF, MHTEF, MHTMEF and spline approximations. 40
Table 2.2	Values of the fitting parameters for HTF, HETF, MHTF, MHTEF, and MHTMEF functions. 42
Table 2.3	Values of $N_O$ to have the exact beamwidthth evaluation. 48
Table 2.4	Evaluation of OBW, eBW and APE in the range $5^\circ \leq \theta_0 \leq 90^\circ$ for $e_r = 90\%$ and antenna lengths $L = 10\lambda$ and $L = 20\lambda$ . 50
Table 2.5	Variation of $N_O$ in the range $5^\circ \leq \theta_0 \leq 90^\circ$ and for $e_r = 50\% \div 99.9994\%$ antenna lengths $L = 10^2\lambda, 10^4\lambda, 10^6\lambda$ . 50
Table 2.6	Values of $\tau$ for different antenna efficiencies $e_r$ . 55
Table 2.7	Values of $\Delta b_{\max}$ for different antenna efficiencies $e_r$ . 58
Table 2.8	Figures of Merit (FoM), namely $\Delta\theta_h$ and SLL, for different values of $\Delta b$ and different antenna efficiencies $e_r$ , for $L = 10\lambda$ . 60
Table 2.9	Fitting parameters for $\Delta\theta_h$ and SLL. 65
Table 2.10	Values of the fitting coefficients for $w_1(r)$ and $w_2(r)$ . 75
Table 2.11	Values of the fitting coefficients for $w_1(r)$ , $w_2(r)$ and $w_3(r)$ . 77
Table 3.1	HPBW on H(E)-planes for different bias-scanned pointing angles of GSS and GPW antennas at fixed frequency. 113



Table 3.2	HPBW on both H(E)-planes for different frequency-scanned pointing angles of GSS, GPW (at fixed $\mu_c = 1 \text{ eV}$ ), and SS antennas. 113
Table 3.3	Comparison of efficiency $\eta$ , directivity at broadside $D_0$ and reconfigurability $\Delta\theta$ (scanning angular range) for GPW and GSS antennas, for different quality ( $\tau$ ) of the graphene sheet. 116
Table 3.4	Comparison of directivity and reconfigurability for GSS antennas with different efficiencies and for different quality ( $\tau$ ) of the graphene sheet. 117
Table 3.5	Relevant parameters for the design of the proposed THz FPC-LWAs based on NLC. 132
Table 3.6	Radiating performance in terms of beam reconfigurability ( $\theta_p^M$ ), directivity ( $D_0$ ) and beamwidth ( $\Delta\theta$ ), for all layouts. 134
Table 3.7	Performance of Layout 2 and 4 in lossless and lossy case. 137



## ABSTRACT

In recent years, microwave, millimeter-wave, and THz applications such as medical and security imaging, wireless power transfer, and near-field focusing, just to mention but a few, have gained much attention in the area of ICT due to their potentially high social impact. On one hand, the need of highly-directive THz sensors with tunable radiating features in the far-field region has recently boosted the research activity in the design of flexible, low-cost and low-profile devices. On the other hand, it is of paramount importance to focus energy in the near-field region, and thus the generation of limited-diffraction waves in the microwave and millimeter-wave regime is a topic of recent increasing interest.

In this context, leaky-wave theory is an elegant and extremely useful formalism which allows for describing in a common fashion guiding and radiating phenomena in both the near field and the far field, spanning frequencies from microwaves to optics passing through THz.

In this PhD thesis we aim to exploit the intrinsic versatility of the leaky-wave approach to design advanced radiating systems for controlling the far-field radiating features at THz frequencies and for focusing electromagnetic radiation in the near field at millimeter waves. Specifically, the use of relatively new materials such as *graphene* and *liquid crystals* has been considered for the design of leaky-wave based radiators, achieving very promising results in terms of reconfigurability, efficiency, and radiating capabilities. In this context, an original theoretical analysis has provided new general formulas for the evaluation of the radiating features (e.g., half-power beamwidth, sidelobe level, etc.) of leaky-wave antennas. Indeed, the current formulations are based on several simplifying hypotheses which do not allow for an accurate evaluation of the beamwidth in different situations.

In addition to the intriguing reconfigurable capabilities offered by leaky waves in far-field applications, interesting focusing capabilities can be obtained in the near field. In particular, it is shown that leaky waves can profitably be used to generate limited-diffraction Bessel beams by means of narrow-band radiators in the microwave range. Also, the use of higher-order leaky-wave modes allows for achieving almost the same performance in the millimeter-wave range, where previous designs were subjected to severe fabrication issues. Even more interestingly, the limited-diffractive character of Bessel beams can also be used to generate limited-diffraction pulses as superpositions of monochromatic Bessel beams over a considerable fractional bandwidth. In this context, a novel theoretical framework has been developed to understand the practical limitations to efficiently generate limited-diffraction, limited-dispersion pulses, such as X-waves, in

the microwave/millimeter-wave range. As a result of this investigation, a class of wideband radiators has been thoroughly analyzed, showing promising capabilities for the generation of both zeroth-order and higher-order X-waves. The latter may pave the way for the first localized transmission of orbital angular momentum in the microwave range.

*Knowing not grieving remembers a thousand savage and lonely streets.*

— William Faulkner (“*Light in August*”)

## ACKNOWLEDGMENTS

Three long years of PhD have passed since I have decided to dedicate my life to this wonderful path called *scientific research*. This experience has been alternately scattered by hard and nice moments. However, I cannot forget the wonderful people that I had the luck to meet along this path, and that have individually contributed to enrich either my knowledge with their experience, or my life with their presence.

This part of the PhD thesis is dedicated to them, so I can thank them all one by one (each one in their native language, to the best of my knowledge!):

Grazie *Guido Valerio*. Sei la prima persona che ho incontrato nel mio cammino scientifico: dalla tesi di triennale (che forse ricordi a malapena!), a quella più significativa di magistrale, per poi proseguire nei primi anni di PhD. Sarebbe facile dire che avrei gradito collaborare ancor di più, ma preferisco ritenermi già immensamente fortunato per averti conosciuto nel momento più delicato della mia formazione scientifica. Grazie ancora e... *Viva le analisi dispersive!*

Grazie *Alessandro Galli*. È particolarmente difficile condensare in poche parole quanto la sua presenza sia stata importante per fare di me lo studente di PhD che sono oggi. Dal primo giorno in cui rimasi ‘affascinato’ dai riferimenti artistici all’elettromagnetismo, a oggi in cui tra una ricerca e l’altra ci sfugge un commento al cinema, alla letteratura, all’arte in genere che tanto ci appassiona. Perché entrambi sappiamo che, per quanto sia grande la scienza, la vita è davvero piccola senza la magia dell’arte. Grazie ancora per aver *illuminato* questo mio cammino.

Grazie *Mauro Ettore*. Sei stato la prima persona ‘di scienza’ che ho incontrato fuori dall’Italia, nella mia prima esperienza all’estero. Ho sempre apprezzato la tua sincerità a fronte di qualche differenza di vedute. Alcune cose hanno funzionato altre meno, ma dal nostro confronto e dalla nostra collaborazione sono nati grandi cose. Non scorderò mai l’emozione nel vedere le misure del nostro lanciatore... Credo che ci siano poche cose che ripaghino il lavoro di un ricercatore più del vedere la conferma di una *teoria* da parte di un *esperimento*. Grazie.

Grazie *Paolo Burghignoli*. Per un ex-studente di Matematica, che si rammarica tuttora di non aver avuto la forza di completare quel percorso, non poteva esserci miglior fortuna che incontrare te. Mi sono imbattuto in tanti ingegneri e matematici e posso dire che, per distacco, rappresenti il miglior

*ingegnere-matematico* mai conosciuto! Grazie per farmi sentire scientificamente *a casa* quando lavoriamo.

Grazie *Paolo Baccarelli*. Mi considero estremamente fortunato nell'aver collaborato con te in questi tre anni. La cosa che ho più ammirato in te, è la passione nel trasmettere le tue conoscenze. Certi aspetti della teoria *leaky* mi sono oggi così chiari grazie all'accuratezza delle tue spiegazioni. Grazie per avermi fatto fatto acquisire *padronanza* di certe tematiche.

Thank you *David R. Jackson*. After spending four months in Houston, I have understood the reason why Guido defined it *human-unfriendly!* It is even more true that I do not think it does exist in the world any other place where one can hope to learn something about leaky waves, because of you. Since the very first day I was really impressed by your intuition about physical phenomena. However, what I will really miss is our *Running Wednesdays/Saturdays*. Thank you for always treating me as a *friend* rather than as a student.

Grazie *Germana Peggion*. Quante probabilità ci sono di conoscere una 'stravagante' matematica/oceanografa in una base NATO a La Spezia? Non voglio saperlo, ma credo che la vita sia preziosa soprattutto perché ci regala questi eventi inaspettati. Avere guadagnato la tua amicizia prima ancora della tua stima è motivo di grande orgoglio per me. Grazie a te, ho apprezzato i ponti 'non-euclidei' di New Orleans (che sono paralleli ai fiumi), ammirato i quadri fatti con la sabbia di tua sorella Gabriella, visto la casa natale di uno dei miei scrittori preferiti (i.e., William Faulkner), e persino conosciuto il fantasma di casa tua. Insomma nella classifica dell'originalità vinci a mani basse! Grazie.

Grazie *Caterina Dominianni*. Se oggi la mia sensibilità artistica, in particolare quella rivolta alla letteratura, si è sviluppata in un certo modo, lo devo in parte a Lei. Mi ha fatto conoscere dei paradisi letterari nei quali mi sono rifugiato e in cui continuo a rifugiarmi tuttora. Poche persone mi hanno saputo fare un regalo più bello. Grazie.

Grazie *Costanza Parisella*. A distanza di vent'anni resta la persona a cui mi sento più grato per quello che mi ha insegnato. La curiosità scientifica e la poetica sono le luci che lei ha acceso in me, e che tuttora svolgono il duplice compito di scaldare il mio cuore e al tempo stesso indicarmi la strada da percorrere. Grazie per aver acceso quelle luci.

Grazie *Maurizio Fascetti*. Se in questo laboratorio non ci siamo ancora abituati al tuo pensionamento, un motivo ci sarà! Ricordo sempre con piacere le lunghe chiacchierate sui *massimi sistemi*, così come custodisco gelosamente le *perle di saggezza* che parsimoniosamente hai dispensato. Grazie davvero.

Merci *Noëlle Le Ber*. Vous étiez pour moi, ma première enseignante de français, mon soutien spirituel dans mon séjour en France, et ma 'mère' d'adoption. Existe-t-il un moyen pour vous remercier pour tout ça? Je ne crois pas, mais j'espère très fortement que la vie pourra un jour vous récompenser de votre gentillesse. Merci du fond du coeur.

Grazie *Federica Polverari*. Tra tutti i compagni di Dottorato, l'unica che mi sento di poter chiamare un'amica prima di una collega. La gita a Los Angeles è stata bellissima, ma ciò che mi porterò sempre dietro sono le nostre chiacchierate mattutine ai piedi del DIET. Indimenticabili!

Gracias *Darwin Joel Blanco Montero*. Nunca les voy a olvidar los "burpees" en frente al *Diapason*, las carreras al Parc des Gayeulles, y el nuestro intercambio de proverbios. Tu eres mi mejor amigo que yo he tenido fuera del Italia. ¡Mucha suerte!

Grazie *Santi Concetto Pavone*. Ti lamenti sempre che non rendo giusto merito alla nostra amicizia, eccoti servito! Abbiamo avuto occasione di 'insultarci' a vicenda per sei lunghi mesi, ma alla fine sono proprio gli insulti a cementare le amicizie non trovi!? Abbiamo condiviso tanto nei nostri mesi 'rennesi', persino una Twingo viola... Ricordi? *Bonjour!* Tu sai! ;-) Grazie compare.

Grazie *Martina Porfiri*. A volte conoscere una persona che riesce a sorridere e a reagire nonostante tutto, ci permette di vedere le cose sotto una nuova luce. Ci siamo supportati a vicenda per sopportare, tra le tante cose, il peso schiacciante della burocrazia francese. Grazie per le migliori pause pranzo nel soggiorno romano!

Grazie *Giulia Bacchini*. Se c'è una persona tra i miei amici con cui condivido i maggiori interessi scientifici/artistici/socio-psicologici/culturali quella sei tu. Da ogni manciata di ore trascorse insieme sono uscito con nuove idee, nuove cose da indagare, nuovi territori da esplorare. Grazie per avermi sempre supportato nelle scelte che ho fatto.

Grazie *Leonardo Millefiori*. Voglio bene a tutte le persone con cui ho trascorso gli anni universitari, ma se ce n'è una che considero un amico vero quella sei tu. Ho sempre avuto l'impressione che fossimo quasi complementari nello studio, ma con le *giuste* intersezioni. Se mi resta un rammarico è il non aver ancora unito le nostre forze per un progetto a più lungo termine: sono sicuro che ne uscirebbe una gran cosa. Ma chissà... mai dire mai! Grazie.

Grazie *David William Caruso*. Quando ci siamo conosciuti (sul campo di calcetto) la prima cosa che ho pensato è stata: "nella mia vita manca un amico così, sarebbe grandioso averlo come amico...". Che dire, a distanza di poco meno di 10 anni posso dire che avevo ragione. Mancava un amico così, e che spettacolo essere amici! Ti voglio bene come a un fratello (e sappiamo entrambi che significa per noi). Io la tesi di Dottorato l'ho scritta, e tu l'Auditorium l'hai preso. Io non sono ancora sazio e tu...? Grazie per aver creduto nelle mie capacità come io nel tuo talento musicale.

Grazie *Emanuele Gatti*. Mio *fratello adottivo*, l'unico che, assieme a Claudia, conosce il vero Walter. L'unico che, assieme a David, mi ha tenuto con i piedi per terra (soprattutto sul pallone da calcio) impedendomi (grazie!) di essere risucchiato dal mondo degli ingegneri *nerd*. Sei l'amico più importante e di più lunga data e anche se di questa tesi non te ne frega niente, non posso

non ringraziarti per essermi stato sempre vicino. Grande Luis Nazario da Lima! Grazie.

Grazie *Fabio Fuscaldo*. A volte la vita si mette sfortunatamente 'di traverso' all'amore e non fa andare le cose come vorremmo. Tuttavia, certi amori riescono a spingersi oltre la vita. Ti ho sempre portato con me, trovando in te la forza per superare i momenti difficili. È per questo che, seppur qualcosa di più grande può averla fermata, in ogni mia azione degna d'essere vissuta sento scorrere forte in me la tua vita. Grazie Frate'.

Grazie *Andrea Fuscaldo*. A volte (ma non troppo spesso) le cose vanno come avremmo sempre sognato. È il caso di un amore fraterno che negli anni ha assunto sembianze diverse, ma senza mai smettere di crescere. Siamo un po' il giorno e la notte, ma paradossalmente non abbiamo mai sentito il bisogno di dover litigare (come, al contrario, tutti i fratelli ho scoperto fanno...). Sei la certezza più grande che ho, e ricordo come fosse ieri il giorno che sei andato via di casa. Per un po' mi sono sentito perso. Grazie Fratello'.

Grazie *Grazia Monaco*. Mi hai insegnato che la sofferenza è il prezzo che pagano gli animi sensibili, un prezzo irrisorio al cospetto della magnificenza con la quale le emozioni gli si rivelano. Mi hai insegnato tutto quello di cui avevo bisogno col tuo solo esempio. Non c'è mai stato bisogno di parole (al contrario mio). Grazie Ma'.

Grazie *Alfredo Fuscaldo*. Mi hai insegnato che il talento è nulla senza il sacrificio, e che la fortuna vera passa attraverso di esso. Ancor di più, mi hai insegnato a diffidare della fortuna improvvisa, e a gustare il sapore delle cose guadagnate attraverso il sacrificio. In una parola mi hai insegnato a stare al mondo, e questo è l'insegnamento più grande di cui avevo bisogno, che nessuno all'infuori di te sarebbe mai stato in grado di darmi. Grazie Pa'.

Grazie *Claudia Masuri*. A volte l'amore si mette fortunatamente 'di traverso' alla vita impedendoci di commettere degli errori. Non solo, ma è grazie all'amore che, incoscientemente, ci si avvia su dei percorsi che forse prima non avremmo intrapreso. Sei l'unica persona nella vita che mi ha permesso di non dovermi *vergognare* di nulla, e quella che con più forza mi ha supportato nelle scelte difficili. Sei la dimostrazione grande che la vera forza non è una risorsa appariscente, ma ben celata, nell'ombra. Grazie Amore, senza te mi sarei perso (vedi Bartlebooth nell'Epigrafe più avanti)...

And finally I want to acknowledge a list of people who also deserve to be acknowledged, but I rather prefer to put in a sort of a *collective acknowledgment*:

Grazie alla famiglia del mio amore: Francesco Masuri, Giuseppina Scanu, Roberta Masuri e Giampiero Fortezza per avermi sempre supportato in questa scelta e non avermi mai fatto mancare il loro affetto e calore durante le mie visite sull'isola.



Grazie a mia cognata Ramona D'Ottavio e alla piccola Irene Fuscaldo-D'Ottavio per aver portato tanta gioia e leggerezza nella mia famiglia. Ne avevamo tanto bisogno.

Grazie alle mie cugine Assunta Danese e Angela Danese e alle loro rispettive stupende famiglie. Mi avete sempre fatto sentire 'importante' per quello che faccio, ma a me sembra tutto così piccolo di fronte al vostro spessore umano. Grazie per il vostro grande affetto.

Grazie al gruppo di La Spezia, in particolare Paolo Braca e Gemine Vivone, per l'opportunità concessa e la fiducia riposta. In nessun altro posto mi sono sentito così ben integrato in un gruppo in così breve tempo.

Grazie alla *famiglia* Corpea: Marco Marciano, Enrico Picone, Antonietta Orsini, Francesco Marciano, Angelo Cittadini. *Mens sana, in corpore sano*, mai fu detta frase più vera. Senza lo sport, mi sarei perso. Quella che io chiamo *la filosofia del sudore* credo sia l'insegnamento più grande che abbia ricevuto nella vita. Grazie per avermelo fatto capire.

Thanks to several PhD students as me that I have met during conferences and during my stay abroad: Francesco Foglia Manzillo, Ioannis Iliopoulos, Bastian, and Cher Cheikh Diallo from IETR, Murilo Seko, Krishna Kota, Sohini Sengupta, Xinyu Liu from ECE at UH, Simone Zuffanelli met at APS16 in Puerto Rico, Fabrizio Silvestri and David González-Ovejero met at EuCAP16 in Davos, Giuseppe Labate and Alice Benini met at the ESoA in Zagreb. Each of you has in some way left in me a very positive record. And I strongly feel that some nice *souvenirs* is what we really need to ensure us a pleasant old age.

Grazie ai compagni di Università: Matteo Coppi, Cristiano Montori, Fabrizio De Prosperis, Italo Palmacci e Costanza Scozzafava. Avete sempre creduto in me dandomi la fiducia necessaria per arrivare fino a qui. Studiando insieme credo che abbiamo imparato tutti più di quanto avremmo ottenuto singolarmente, peccato non essere riusciti a farlo più a lungo.

Grazie ai compagni di dottorato conosciuti qui al DIET: Davide Comite, Luca Amicucci, Roberta Anniballe, Laura Farina, Emanuela Miozzi, Fabio Fascetti, Marianna Biscarini, Luigi Mereu, Maura Casciola, Silvia Tofani, Marta Tecla Falconi. Rimango sempre dell'idea che è troppo difficile andare *collettivamente* d'accordo, ma posso dire che per me è stato molto facile trovarmi *individualmente* molto bene con ognuno di voi.

Grazie ai tesisti che ho avuto la fortuna di seguire: Francesca Moratti, Alessandro Boesso e Andrea Gilardi. In tre anni di dottorato, se dovessi dire qual è stata la cosa più bella direi l'opportunità di trasmettere qualche frammento del mio piccolo sapere a qualcuno. Tuttavia non è facile trovare ancora persone disposte a imparare attraverso il dialogo. Grazie per avermelo permesso.

Thanks to all the artists who strongly influenced the perception of my life (in order of their 'appearance' in my life in their respective category, i.e., in order, *Literature, Music, Cinema*): Eugenio Montale, Friedrich Wilhelm Nietzsche, Hermann Hesse, Heinrich Böll, Franz Kafka, Italo Calvino, Jorge Luis

Borges, Georges Perec, William Faulkner; Subsonica, R.E.M., Pink Floyd, Radiohead, Franco Battiato, Django Reinhardt, Chet Baker, Claude Debussy, Explosions in the Sky; François Truffaut, Stanley Kubrick, Darren Aronofsky, Federico Fellini, Lars von Trier, Richard Linklater, Paul Thomas Anderson, Eric Rohmer, and Krzysztof Kiesłowski.

*Rome, January, 2017*

Walter Fuscaldo

## EPIGRAPH

Il y a des livres qui ont la force de changer la perception de nôtre vie. *La Vie mode d'emploi* c'est l'un de ceux qui ont changé la mienne.

— Georges Perec (*“La Vie mode d'emploi”, chap. XXVI, Bartlebooth, 1*)

*Imaginons un homme dont la fortune n'aurait d'égale que l'indifférence à ce que la fortune permet généralement, et dont le désir serait, beaucoup plus orgueilleusement, de saisir, de décrire, d'épuiser, non la totalité du monde - projet que son seul énoncé suffit à ruiner - mais un fragment constitué de celui-ci: face à l'inextricable incohérence du monde, il s'agira alors d'accomplir jusqu'au bout un programme, restreint sans doute, mais entier, intact, irréductible.*

*Bartlebooth, en d'autres termes, décida un jour que sa vie tout entière serait organisée autour d'un projet unique dont la nécessité arbitraire n'aurait d'autre fin qu'elle-même. [...] Elle se développa dans les mois, dans les années qui suivirent, s'articulant autour de trois principes directeurs:*

*Le premier fut d'ordre moral: il ne s'agirait pas d'un exploit, d'un record, ni d'un pic à gravir, ni d'un fond à atteindre. Ce que ferait Bartlebooth ne serait ni spectaculaire ni héroïque; ce serait simplement, discrètement, un projet, difficile certes, mais non irréalisable, maîtrisé d'un bout à l'autre et qui, en retour, gouvernerait dans tous ses détails la vie de celui qui s'y consacrerait.*

*Le second fut d'ordre logique: excluant tout recours au hasard, l'entreprise ferait fonctionner le temps et l'espace comme des coordonnées abstraites où viendraient s'inscrire avec une récurrence inéluctable des événements identiques se produisant inexorablement dans leur lieu, à leur date.*

*Le troisième, enfin, fut d'ordre esthétique : inutile, sa gratuité étant l'unique garantie de sa rigueur, le projet se détruirait lui-même au fur et à mesure qu'il s'accomplirait; sa perfection serait circulaire : une succession d'événements qui, en s'enchaînant, s'annuleraient: parti de rien, Bartlebooth reviendrait au rien, au travers des transformations précises d'objets finis.*

*Ainsi s'organisa concrètement un programme que l'on peut énoncer succinctement ainsi: Pendant dix ans, de 1925 à 1935, Bartlebooth s'initierait à l'art de l'aquarelle.*

*Pendant vingt ans, de 1935 à 1955, il parcourrait le monde, peignant, à raison d'une aquarelle tous les quinze jours, cinq cents marines de même format (65 X 50, ou raisin) représentant des ports de mer. Chaque fois qu'une de ces marines serait achevée, elle serait envoyée à un artiste spécialisé (Gaspard Winckler) qui la collerait sur une mince plaque de bois et la découperait en un puzzle de sept cent cinquante pièces.*

*Pendant vingt ans, de 1955 à 1975, Bartlebooth, revenu en France, reconstituerait, dans l'ordre, les puzzles ainsi préparés, à raison, de nouveau, d'un puzzle tous les quinze jours. A mesure que les puzzles seraient réassemblés, les marines seraient “retexturées” de manière à ce qu'on puisse les décoller de leur support, transportées à l'endroit même où - vingt ans auparavant - elles avaient été peintes, et plongées dans une solution détersive d'où ne ressortirait qu'une feuille de papier Whatman, intacte et vierge.*

*Aucune trace, ainsi, ne resterait de cette opération qui aurait, pendant cinquante ans, entièrement mobilisé son auteur.*



*A Fabio*



# INTRODUCTION

This PhD thesis deals with two extremely interesting physical phenomena: *leaky waves* and *nondiffracting waves*. This ‘apparent’ distinction has initially suggested to split this thesis in two parts, the first one dealing with reconfigurable leaky-wave antennas for far-field THz applications, and the second one dealing with the design of near-field focusing devices. However, this apparent distinction will slowly disappear throughout the thesis, unveiling the strong connection between these physical phenomena. The greatest evidence of this concept will naturally emerge in Chapter 5, where the use of leaky waves allows for producing a monochromatic nondiffracting wave, namely a *Bessel beam*.

It should be stressed that, under the frame of the cotutelle agreement, the first part and the second part of this thesis have been mainly developed during the stay of the Author in University of Rome “Sapienza” under the supervision of Prof. A. Galli, and in University of Rennes 1 under the supervision of Dr. Mauro Ettore, respectively.

Both parts of the thesis are divided in three chapters. The first chapter of each part is a useful review of the state of the art and of the fundamental concepts underlying the topics covered in each part. The following chapters of each part illustrate the original investigations developed in their respective contexts.

The thesis is outlined as follows:

**CHAPTER 1** In this Chapter, a review of leaky-wave theory is presented.

Starting from the fundamental physics underlying leaky waves, the design methods, and the radiating properties of conventional leaky-wave antennas are discussed through the analysis of several well-known examples. The content of this Chapter will serve to understand the possibilities and limitations offered by conventional leaky-wave antenna design, thus motivating the study of more advanced techniques and devices. The two last ones will be the object of Chapter 2 and 3, respectively.

**CHAPTER 2** In this Chapter, a novel theoretical framework is laid down to characterize the radiating properties of 1-D unidirectional and bidirectional leaky-wave antennas even in the endfire case. Starting from the original formulation early proposed by Oliner in the ‘60s, and by progressively removing all simplifying hypotheses, a more general and accurate formulation is obtained. Therefore, more accurate and reliable formulas are rigorously derived, also showing that Oliner’s results are approximate limiting cases of this more general formulation.

This study is a result of a fruitful collaboration with Prof. David R. Jackson, gained at University of Houston during the last four months of this PhD.

**CHAPTER 3** In this Chapter, the design of several reconfigurable leaky-wave antennas in the THz range is presented. By exploiting the tunable features of relatively new materials such as *graphene* and *liquid crystals* (LC), it is shown that is possible to design either graphene- or LC-based leaky-wave antennas with fixed-frequency electronical scanning of the far-field pattern. The performance of both devices is thoroughly discussed in terms of directivity, efficiency, and pattern reconfigurability by means of ad-hoc customized numerical techniques. Also, the impact of technological issues inherent to either graphene synthesis, or multistacked LC-based cells assembly is rigorously assessed, showing how it affects the overall performance of the proposed THz devices. Possible workarounds are suggested throughout the Chapter.

**CHAPTER 4** In this Chapter, a review of the first experiments about the generation of nondiffracting waves is presented. A unified mathematical framework is first developed to analyze in a common fashion monochromatic (beams), and polychromatic (pulses) nondiffracting solutions. A specific focus is devoted to cylindrical solutions, i.e. *Bessel beams* and *X-shaped pulses*, respectively. Most of the current mathematical formulations are based on some simplifying hypotheses that no longer hold in the microwave regime. Hence, a rigorous application of a full-wave analysis is needed for a correct description of the microwave/millimeter-wave devices discussed in Chapter 5 and 6.

**CHAPTER 5** In this Chapter, the analysis, design, prototyping, and measurements of microwave and millimeter-wave Bessel-beam launchers are presented. As will be shown, the design of a microwave Bessel beam launcher is based on the excitation of a pair of resonant leaky modes. Such a design does not allow for frequency-scaling the device at millimeter waves. Thus, a novel design based on higher-order leaky modes is here presented. Full-wave simulations and measurements corroborate the accuracy and the validity of the analysis.

**CHAPTER 6** In this Chapter, the possibility to generate X-waves at microwaves is discussed. The fundamental limitations inherent to the efficient generation of such waves are addressed under the frame of an original theoretical framework. Relevant figures of merit are introduced to evaluate and predict the focusing properties of X-waves through finite aperture in the microwave regime. Rigorous theoretical and numerical results show the efficient generation of zeroth-order and higher-order X-waves. These promising results may pave the way for the first localized transmission of energy and orbital angular momentum at microwaves.



Part I

RECONFIGURABLE LEAKY-WAVE ANTENNAS  
FOR THZ FAR-FIELD APPLICATIONS



# 1

## CONVENTIONAL LEAKY-WAVE ANTENNAS

### 1.1 INTRODUCTION

In many sectors of physics, such as acoustics, electromagnetics and optics, where the transmission of energy is generally described by wave propagation, the damping of waves is frequently associated to a mechanism of losses in dissipative systems. In electromagnetics, these losses are commonly attributed to the dissipation of energy in passive media due to ohmic, dielectric, or radiation losses. In particular, when an open region characterized by a nondissipative medium is considered, (e.g., air-filled open waveguides) the nature of losses is attributed to radiation. The resulting damped oscillations belong to the category of *radio-active states* in quantum mechanics, *damped resonances* in acoustics, and *leaky waves* in electromagnetics.

Despite its rather intuitive interpretation, the concept of *energy leakage* to explain radiating phenomena has been mainly developed only at the end of the first half of the last century thanks to the pioneering work of N. Marcuvitz [1]. Since then, many engineers applied this concept to design radiating systems by suitably opening closed waveguides in order to enhance radiation. However, it was only in the '60s, thanks to the seminal papers of T. Tamir and A. A. Oliner [2], [3] that the so-called *leaky-wave theory* was rigorously set from a mathematical and a physical point of view. The elegant theory exposed in those papers furnished the tools for designing leaky-wave based radiating systems in an extremely simple and systematic way; a worthwhile aspect in that era of limited computational resources.

Nowadays, *leaky-wave antennas* as well as *leaky-wave theory*, are commonly recognized as active and promising research areas in both physics and engineering communities. On one hand, *leaky-wave theory* is used to explain and interpret different physical phenomena such as *Cherenkov radiation* [4], *Wood's anomalies* [5], and *enhanced transmission* [6], [7]. On the other hand, *leaky-wave antennas* still represent some of the most promising advanced radiating systems in microwave engineering.

In Section 1.2, we briefly review the fundamentals of leaky-wave physics, as well as the most important theoretical aspects underlying the design of *conventional* leaky-wave antennas (LWAs). This Section 1.2 will allow us to introduce the well-known classification among the different types of LWAs. In this context, in Sections 1.3 and 1.4 we specifically focus on the class of 1-D and 2-D LWAs, respectively. There, the specific radiation properties characterizing both types of LWAs will be thoroughly reviewed.

The recent advances in the theoretical formulations for *conventional* 1-D and 2-D LWAs will be the object of Chapter 2, whereas the most recent investigations on *unconventional* 2-D LWAs will be the object of Chapter 3.

## 1.2 LEAKY-WAVE THEORY

In this Section 1.2 we discuss the fundamentals of *leaky-wave physics*. Starting from a rigorous mathematical standpoint, the nature of leaky waves will be clearly revealed in 1.2.1 as a direct consequence of the *continuum spectrum* possessed by the solutions of the wave equation in *unbounded media*. In 1.2.2 the physical significance of leaky waves will be intuitively explained with the aid of a ‘ray-interpretation’ of the radiating problem. Section 1.2.3 will set the leaky-wave phenomena in a rigorous mathematical framework. Then, in 1.2.4 a convenient technique (viz. the *transverse resonance technique* [8]) to analyze leaky-wave solutions in waveguiding problems will be thoroughly discussed by means of two canonical examples: the parallel-plate waveguide and the grounded dielectric slab. Finally, a possible classification among the different leaky-wave antennas is suggested in 1.2.5.

### 1.2.1 Nature of waves

Time-harmonic<sup>1</sup> source-free solutions of the scalar wave equation  $\nabla^2 f + k^2 f = 0$  (where  $k$  is the propagation constant) are usually distinguished between those which exist in *closed regions* and those which exist in *open regions*. With regard to the electromagnetic problem, so elegantly and concisely expressed by Maxwell’s equations, we will consider regions of infinite transverse extent along the  $z$ -axis, invariant with respect to the  $y$ -axis, and in case bounded along the vertical  $x$ -axis (see Fig. 1.1). As a result of these assumptions the separation relation  $k_x^2 + k_y^2 + k_z^2 = k_0^2$  where  $k_0$  is the vacuum wavenumber and  $k_i$  with  $i = \{x, y, z\}$  are the wavenumbers along the  $i$ -axis, takes the simplified form

$$k_x^2 + k_z^2 = k_0^2, \quad (1.1)$$

since  $k_y = 0$  due to the invariance along the  $y$ -axis ( $\partial/\partial y = 0$ ). Moreover, due to the infinite extent along the  $z$ -axis, any solution  $f(x, z)$  of the problem will take the form  $f(x, z) = m(x)e^{-jk_z z} = m(x)e^{-\alpha_z z}e^{-j\beta_z z}$ , where  $m(x)$  is a modal function, and  $\alpha_z$  (related to amplitude variations) and  $\beta_z$  (related to phase variations) are the imaginary and real parts of the generally complex longitudinal wavenumber  $k_z = \beta_z - j\alpha_z$ .

In closed regions (see Fig. 1.1(a)), the transverse wavenumber is real  $k_x \in \mathbb{R}$  and belongs to a *discrete orthogonal complete* set of eigenvalues. These solutions are known as *guided waves* and their superposition can provide a *complete* description of any field<sup>2</sup>. In addition, *evanescent waves* may ex-

<sup>1</sup> A time-dependence  $e^{j\omega t}$  is tacitly assumed throughout all the PhD thesis. The imaginary unit is  $i = -j$  according to the convention of the engineering community different from the physics community.

<sup>2</sup> More precisely, in lossless closed regions *guided waves* ( $\Re\{k_z\} \neq 0$ ) are described by purely real  $k_z \in \mathbb{R}$  longitudinal wavenumbers, otherwise an imaginary part accounts for losses in the medium.

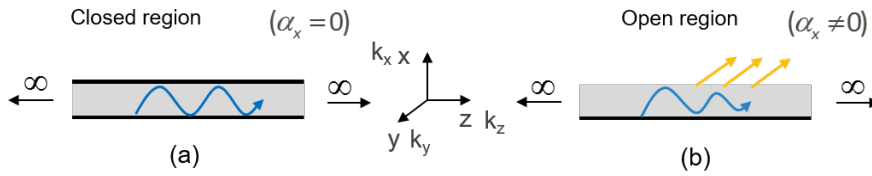


Figure 1.1.: (a) A closed and (b) an open region with respect to the vertical  $x$ -axis. In the electric/magnetic case the boundaries would represent *perfect electric/magnetic conductor* (PEC/PMC) walls.

ist whose propagating wavenumber is purely imaginary  $k_z = -j\alpha_z$ , thus they neither propagate nor contribute to the description of the field. The formulation of electromagnetic problems in closed regions is at the root of *waveguiding phenomena* [9].

In open regions (see Fig. 1.1(b)), a discrete spectrum might exist but a *continuum spectrum* must be added to guarantee the completeness of the set of solutions. The discrete spectrum is characterized by complex transverse wavenumbers  $k_x = \beta_x - j\alpha_x$  that still belong to a discrete set. In particular, those eigenvalues for which  $\beta_z > k_0 \in \mathbb{R}$  and  $\alpha_x > 0$  have a physical meaning, since they satisfy the *Sommerfeld radiation boundary condition* at infinity. These *modal solutions* (or, equivalently *proper waves*) are called *surface waves* since their eigenvalues describe waves which propagate along the interface and exponentially decay away from it.

Conversely, the continuum spectrum is characterized by both complex wavenumbers  $k_x$  and  $k_z$  which both belong to an infinite set. Such solutions are generally called *spatial waves*. However, in the presence of a continuum spectrum, *nonmodal solutions* (or, equivalently *improper waves*) may exist, which are characterized by a negative attenuation constant  $\alpha_x < 0$  and thus they do not satisfy the Sommerfeld condition at infinity. A representation of the field in terms of nonmodal solutions is called *nonspectral representation*, and its physical significance will be investigated in the next Subsection.

### 1.2.2 Physical significance of leaky waves

At a first glance, nonmodal solutions in open regions might seem to have no physical meaning because they would describe an infinite field at infinity. However, it is possible to prove that when the structure is excited by a finite source these solutions describe fields that are exponentially growing only in a limited wedge-shaped region close to the interface [10]–[15], and then abruptly decay after the so-called *shadow boundary* (see Fig. 1.2(a)) given by the equation  $x = z \tan \theta_0$  ( $\theta_0$  being the angle measured from the vertical  $x$ -axis). Hence, these solutions, known as *leaky waves*, provide a physical description of the field that, in the near field, is dominant with respect to other solutions when  $|\beta_z| < k_0$  (see next Subsection). The imaginary part  $\alpha_z > 0$  will account only for radiation losses in lossless regions, otherwise it

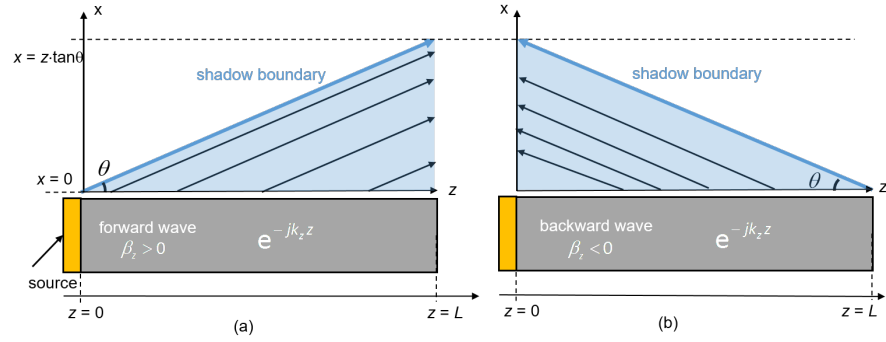


**Figure 1.2.:** Ray interpretation of the physical significance of (a) a *forward* and (b) a *backward* leaky wave in a waveguiding structure of finite extent. Within a wedge-shaped region (highlighted in light blue) limited by the shadow boundary, the leaky-wave field dominates the near-field region. It is worth noting the capability of backward leaky waves to focus radiation in the near field.

will take into account losses for both radiation and dielectric/ohmic losses in the medium.

Considerable physical insight on the problem is gained if one takes a look at the separation relation (see Eq. (1.1)). By splitting the imaginary and real parts of Eq. (1.1), the following relation is found:

$$\beta_z \alpha_z = -\beta_x \alpha_x. \quad (1.2)$$

If we generally assume a *forward wave*  $\beta_z > 0$ , several possibilities are found as conveniently summarized by the scheme in Fig. 1.3. It is worth noting here that two kind of *complex waves* may exist: those characterized by  $\alpha_z < 0$ , and those characterized by  $\alpha_z > 0$ . The former will never have physical meaning since they describe fields that exponentially increase as they propagate along the  $z$ -axis. The latter may have physical meaning despite their nonmodal character. In fact, those with  $\beta_x < 0$  only exist in lossy media, and they describe waves whose power density flows inside the medium to compensate for ohmic or dielectric losses. Conversely, those with  $\beta_x > 0$  may exist in lossless media, and they describe waves whose power density radiates outside the medium. When  $\beta_z < k_0$  these waves are called *fast leaky waves* (since when  $\beta_z < k_0$ , then  $v_z \triangleq \omega/\beta_z > \omega/k_0 = c_0$ ), and their presence in an open region is at the root of *radiating phenomena*<sup>3</sup>. In the following paragraph the same conclusions will be obtained under the frame of a rigorous mathematical viewpoint.

As a final remark, we should note the completely different behavior of *backward leaky waves*. As is seen from Fig. 1.2(b), the field of a *fast leaky wave* is always *proper*, since it would always describe an exponential decay in

<sup>3</sup> Actually, according to Oliner's viewpoint [2], the term leaky wave should be used to distinguish complex waves which describe radiation losses, from those complex waves which describe medium losses [2]. Since proper complex waves may exist in lossless media due to anisotropic [16] or dispersive [17] media, the term leaky wave accounts for both proper and improper waves, being the distinction purely formal [2].

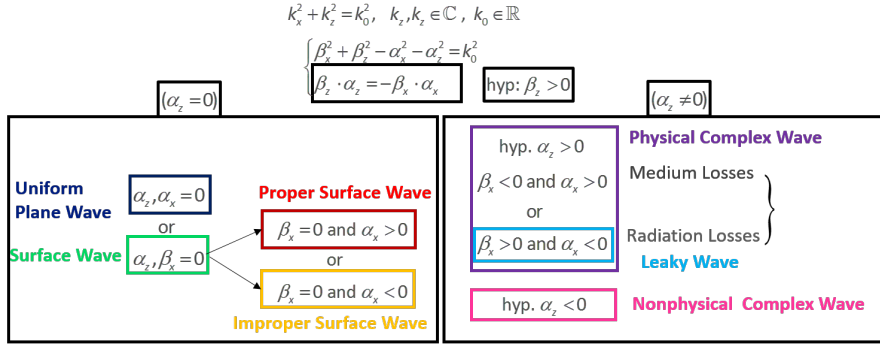


Figure 1.3.: Classification of forward waves in open regions with respect to their propagating features. When  $\alpha_z = 0$  two kinds of waves exist: uniform plane waves  $\alpha_x = 0$ , and surface waves  $\alpha_x \neq 0$ . Surface waves might be proper or improper, depending on the sign of  $\alpha_x$ . When  $\alpha_z \neq 0$ , physical leaky waves exist only when  $\alpha_z > 0$ . Even more interestingly, in order to describe a radiation mechanism  $\beta_x > 0$ , a forward leaky wave must be improper.

the vertical direction. This can also be inferred from the scheme of Fig. 1.3 under the hypothesis  $\beta_z < 0$ <sup>4</sup>. However, the most important consequence of the nature of *backward leaky waves* is that they describe fields with near-field focusing features as clearly shown in Fig. 1.2(b). This will have important consequences that will be carefully analyzed from Chapter 4 to 6.

### 1.2.3 Mathematical significance of leaky waves

In the previous Subsection we have discussed the physical significance of leaky waves in the frame of ray-optics interpretation. On this ground, it has emerged that leaky waves may be physically significant if they are *fast* waves, while they are not likely to be physically significant if they are *slow* waves. However, it is possible to prove the physical significance of leaky waves under the frame of a rigorous mathematical theory by analyzing a guiding structure that is excited by a finite source. Thus, to understand the mathematical significance of leaky waves, we consider the case of a grounded dielectric slab (GDS) covered with a *lossy* partially reflecting sheet (PRS). This choice is motivated by the fact that, throughout this work, we frequently analyze radiating devices that are in some way ascribable to those structures.

As is known [10]–[15], these structures support leaky-wave (LW) modes that evolve from the well-known surface-wave (SW) modes that exist on the structure, as the frequency is lowered. In Fig. 1.4(a), the normalized phase constant ( $\hat{\beta}_z = \beta_z/k_0$ ) is reported as a function of the frequency. As is seen, as long as  $f > f_c$  (where  $f_c; \hat{\beta}_z(f_c) = 1$  is the SW cutoff frequency), the mode is a slow wave with  $\hat{\beta}_z \geq 1$  (solid black line). As the frequency is lowered below  $f_c$ , the surface-wave mode becomes an *improper real* SW mode (dashed black line), and  $\beta_z > k_0$  increases with frequency until a

<sup>4</sup> In fact, for  $\beta_z < 0$  one would find the following two conditions  $\beta_x > 0, \alpha_x > 0, \beta_x < 0, \alpha_x < 0$



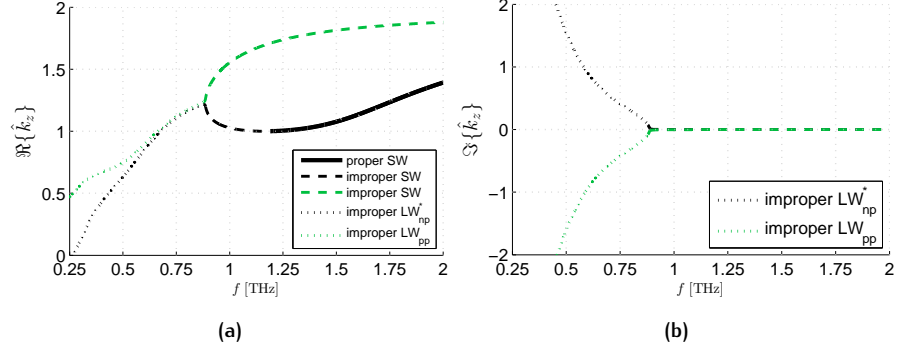


**Figure 1.4.:** (a) Real  $\Re\{k_z\}$  part and (b) imaginary  $\Im\{k_z\}$  part of  $k_z$  vs.  $f$  for a SW mode (black solid line) evolving in a LW mode (dotted green line), after ‘crossing’ the *spectral gap* (improper real SW are there represented with green and black dashed lines) in a typical GDS covered with a PRS. The nonphysical LW solution (which is the complex conjugate of the potentially physical one) is represented in dotted black line.

*splitting point* frequency  $f_{sp}$  is encountered. At this point, the improper real SW mode merges with another improper real SW mode (dashed green line) that is never physical, decreases with frequency, and does not evolve from a proper SW mode.

As the frequency is further lowered, the two improper SW modes coalesce into two complex modes (dotted green and black lines). This happens at a frequency  $f_0 < f_{sp}$  for which  $\beta_z = k_0$ . The frequency region  $f_0 < f < f_c$  is usually referred to as the *spectral-gap region* [18], a term coined by A. A. Oliner. The first solution is the *leaky-wave* solution, and is characterized by a negative imaginary part (see Fig. 1.4(b)), while the second solution is always regarded as being nonphysical, since its wavenumber corresponds to a mode that grows exponentially in the direction of propagation  $z$ . Note that, in an ideal *lossless* PRS this solution would be the complex conjugate of the leaky-wave one. Here, the presence of the losses in the PRS is considered because it generally describes the behavior of a graphene sheet as we will further discuss in 3.2.3.

As the frequency is further lowered, the phase constant of the LW mode will typically continue to decrease. For a sufficiently low frequency  $\beta_z \leq k_0$  LW mode is then said to have entered into the *physical* region. However, for  $f > f_{sp}$  the imaginary part of both the improper LWs usually increases in modulus as  $f$  decreases (see Fig. 1.4(b)). In Fig. 1.5, the behavior of  $k_z$  is differently represented on the complex  $k_z$ -plane, which shows the trajectory of the modes represented in Fig. 1.4. Also shown are the usual *Sommerfeld branch cuts* for the wavenumber that emanates from the *branch points* at  $k_z = \pm k_0$ <sup>5</sup>. The SW mode originally ‘living’ on the *top sheet* (i.e., defined by the proper choice  $\Im\{k_x\} < 0$  of  $k_z$ ) falls on the *bottom sheet* (i.e., defined by the improper choice  $\Im\{k_x\} > 0$  of  $k_z$ ) of the *two-sheeted Riemann surface*

<sup>5</sup> It is worth noting that the branch points  $k_z = \pm k_0$  are placed infinitesimally above the real  $k_z$ -axis (the medium is assumed to have small losses) so that  $P$  does not cross any branch cuts.

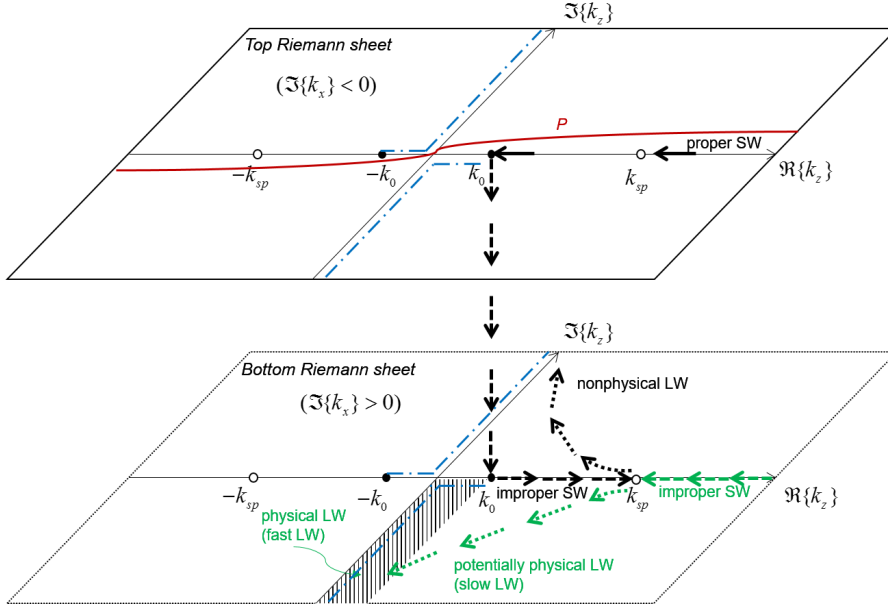


**Figure 1.5.:** The top and bottom sheets (i.e.,  $k_z$ -planes) of the *two-sheeted Riemann surface* for  $k_x$ . The Sommerfeld branch cuts are represented in blue dashed-dotted lines. Color styles and line styles are the same of Fig. 1.4. The arrow indicates the direction for which the frequency is decreasing. A path of integration, labeled as  $P$ , is also shown in red solid line on the top Riemann sheet.

for  $k_x$  when the branch point  $k_z = k_0$  is first encountered. The two real improper SW waves merge at the splitting point  $k_{sp} = k_z(f_{sp})$  and then leave the real axis in opposite vertical directions as previously described.

Further insight may be gained by considering the problem of an infinite electric line source located at the interface between the PRS and air. The exact electric field in the region  $x > 0$  may be written in the form [2], [19]

$$E_x(x, z) = \frac{1}{2\pi} \int_{-\infty}^{+\infty} f(k_x) e^{-jk_x x} e^{-jk_z z} dk_z, \quad (1.3)$$

where  $f(k_x)$  is an amplitude function which depends on the input impedance specified at the interface and on the source location. The field as expressed in Eq. (1.3) is the *spectral longitudinal representation* of modes in the form  $e^{-jk_z z}$  propagating along the vertical  $x$ -axis. The path  $P$  of integration stays on the top Riemann sheet and is performed along the entire real  $k_z$  axis (see Fig. 1.5). To solve Eq. (1.3), it is convenient to recast the problem in terms of the *transverse spectral representation* and then evaluate the integral with the aid of the *steepest-descent method* for the asymptotic evaluation of the radiation integrals [20]. Hence, the original path  $P$  is first deformed into the path  $P'$  along a semicircle at infinity (in the bottom half  $k_z$ -plane to account for physical contributions, i.e.,  $\Im\{k_z\} < 0$ ) and properly detours around the Sommerfeld branch cuts and the poles of the  $f(k_x)$  on the real axis (see Fig. 1.6). Since the path at infinity contributes nothing to the inte-

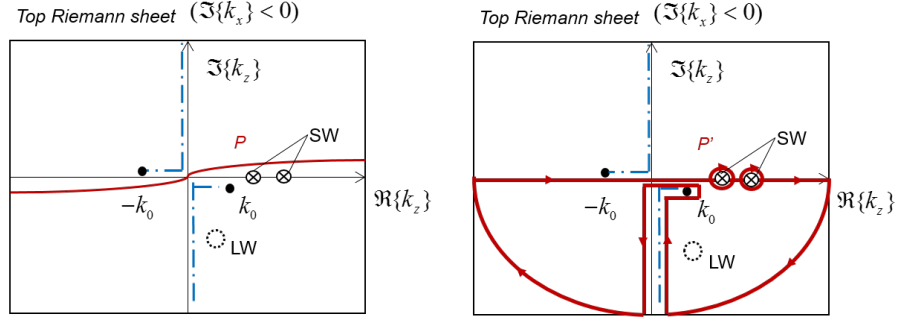


Figure 1.6.: The deformation of the path  $P$  into  $P'$  (solid red lines). The LW poles are represented with dotted circles since they lie on the bottom Riemann sheet and thus they are not captured during the path deformation.

gral due to *Jordan's Lemma* [21], by *Cauchy's theorem* [22], Eq. (1.3) is recast as:

$$E_x(x, z) = \frac{1}{2\pi} \int_{-\infty}^{+\infty} f(k_x) e^{-jk_x x} e^{-jk_z z} \frac{dk_z}{dk_x} dk_x + 2\pi j \sum \text{Res}(f(k_x)), \quad (1.4)$$

where the first term (*continuum spectrum*) accounts for the integration along the branch cuts<sup>6</sup>, whereas the second term (*discrete spectrum*)<sup>7</sup> accounts for the residue contributions (due to the possible presence of singularities in  $f(k_x)$ , e.g., SW modes, that are eventually captured during the path deformation over the top Riemann sheet.

However, this mathematical point of view does not allow to understand the physical significance of leaky waves. Indeed, LW poles will never be captured by the path of integration since they 'live' on the opposite (bottom) sheet. Nevertheless, if the LW poles are *close* to the real-axis (i.e.,  $\alpha_z \simeq 0$ ) their presence may strongly influence the evaluation of the integral. To this purpose, the *steepest-descent representation* is customarily employed. Briefly, it consists in the transformation expressed by the following two equations:

$$\begin{aligned} k_x &= k_0 \cos \phi, \\ k_z &= k_0 \sin \phi, \end{aligned} \quad (1.5)$$

where  $\phi = \phi_r + j\phi_j$  is the complex plane in which the integration is performed. The transformation described by Eq. (1.5) maps the entire two-sheeted Riemann surface into a strip of the  $\phi$ -plane as shown in Fig. (1.7). It is very straightforward to show that the original path  $P$  is now described by  $\phi_r = \pm\pi/2$  for  $\phi_j \geq 0$ . Remarkably, in the  $\phi$ -plane there are no branch cuts and the path  $P$  is deformed into the so-called *steepest descent path* (SDP) [20] (see Fig. 1.7). According to this transformation, if one expresses Eq. (1.4) in cylindrical coordinates  $x = \rho \cos \theta$  and  $z = \rho \sin \theta$  (where  $\theta$  is the obser-

<sup>6</sup> We recall here that Sommerfeld branch cuts are defined by Eq. ( $\Im\{k_x\} = 0$ ), thus the integration is over the entire real  $k_x$  axis, i.e.,  $-\infty < \Re\{k_x\} < +\infty$

<sup>7</sup> It is worth noting that the discrete spectrum appears only in the transverse spectral representation. The longitudinal one involves a continuum spectrum only. The former has therefore the advantage of exhibiting explicitly the proper modes supported by the structure

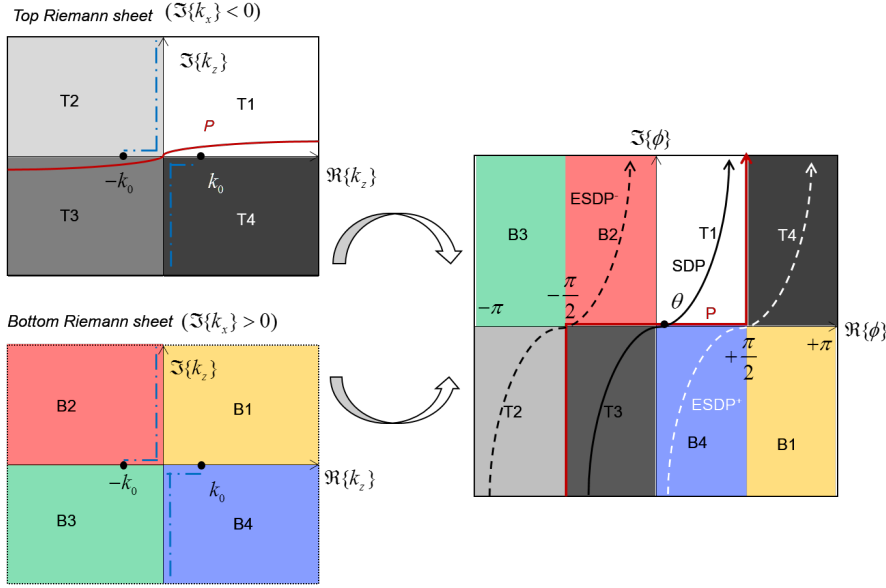


**Figure 1.7.:** Steepest descent  $\phi$ -plane. The eight quadrants (from T1 to T4 for the top sheet and from B1 to B4 for the bottom sheet) constituting the two sheets are mapped in a single strip onto the  $\phi$ -plane. The original path  $P$  (red solid line) is deformed into the SDP (black solid line) for any angle of observation  $\theta$ . The *extreme* SDPs (ESDPs) are obtained for  $\theta = \pm\pi/2$ , and are reported in black and white dashed line for the positive one (ESDP<sup>+</sup>) and the negative one (ESDP<sup>-</sup>), respectively. Only the poles which lie within ESDP<sup>+</sup> and ESDP<sup>-</sup> may contribute to the radiated field.

vation angle, measured from the vertical  $x$ -axis), the electric field is then represented by:

$$E_x(\rho, \theta) = \frac{1}{2\pi} \int_{\text{SDP}} f(\phi) e^{-jk_0\rho \cos(\phi-\theta)} d\phi, \quad (1.6)$$

where the SDP passes through the saddle point  $\phi = \phi_r = \theta$  and is defined by [20]:

$$\cos(\phi_r - \theta) \cosh(\phi_j) = 1. \quad (1.7)$$

If the pole lies to the left of the SDP, then the total field consists of the integration along the SDP plus the residue contribution from the pole. If the pole is to the right of the SDP, there is no residue contribution to the field. If one denotes as ESDP<sup>+</sup> and ESDP<sup>-</sup> the *extreme* SDP obtained for  $\phi = \pm\pi/2$ , respectively, it is clear that only the poles which lie within ESDP<sup>+</sup> and ESDP<sup>-</sup> may contribute to the radiated field. This finally motivates the physical significance of LWs in the *fast-wave region*, i.e.,  $|\beta_z| < k_0$  (note that  $\beta_z = \pm k_0$  for  $\phi_r = \pm\pi/2$  through Eq.(1.5)). The final asymptotic form of the radiation integral can be then written in the following form:

$$E_x(\rho, \theta) \sim \sqrt{\frac{2\pi}{k_0\rho}} F(\theta) e^{-j(k_0\rho - \pi/4)} - j2\pi \sum_i \text{Res} \left[ F(\phi_{p,i}) e^{-jk_0 \cos(\phi_{p,i} - \theta)} \right] H(\theta - \phi_{p,i}), \quad (1.8)$$

where  $\phi_{p,i}$  are the loci of the relevant poles, whereas  $H(\cdot)$  is the Heaviside step function. The first term is usually regarded as the *space-wave* term<sup>8</sup>.

This result shows that the asymptotic evaluation of the field is discontinuous across the angle  $\theta = \phi_p$ . For  $\theta > \phi_p$  (within the shadow boundary region shown in Fig. 1.2) the total field contains a leaky-wave contribution, and this becomes the dominant field as  $k_0\rho \rightarrow \infty$  due to the  $1/\sqrt{\rho}$  decay of the *space-wave* term. For  $\theta < \phi_p$  (beyond the shadow boundary region shown in Fig. 1.2) the total field does not contain a leaky-wave contribution, and the total field is equal to the space-wave field and has the usual form of a cylindrical wave, decaying as  $1/\sqrt{\rho}$ .

Moreover it is worth noting that for a LW mode with  $\alpha_z \simeq 0$  the LW pole is very *close* to the SDP and thus the corresponding leaky-wave field is a dominant one on the aperture (interface) out to a considerable distance, beyond which the field level is very small. This is consistent with the far-field radiation pattern which comes from a Fourier transform of the aperture field<sup>9</sup>. In fact, as long as  $\alpha_z \rightarrow 0$  the leaky-wave aperture field is almost constant giving rise to a *peaked* far-field distribution and viceversa.

#### 1.2.4 The transverse resonance technique

In the previous paragraphs we have reviewed the physical and mathematical significance of the different eigenvalues of the wave equation in both open and closed regions. Here, we want to show a convenient procedure to determine these eigenvalues in waveguiding problems.

A ‘standard’ procedure consists of expressing a general solution of Maxwell’s equations in any homogeneous region of the domain of interest and then applying the boundary conditions. A nontrivial solution is then found by enforcing the determinant of the coefficients to 0. The complex roots of the resulting determinantal equation, which is called *dispersion equation*, are the sought eigenvalues. This procedure allows for expressing any solution of the problem with its eigenvalue (a *mode* of the waveguide) and the associated eigenfunction (the *modal field*)<sup>10</sup>. However, this procedure can be lengthy, especially if different media are present in the domain of interest. If one is interested only in the determination of the eigenvalues (and not in the determination of the eigenmodes), the *transverse resonance technique* [8] may represent a valuable tool.

Indeed, it is well known [1] that the eigenvalues of a waveguide problem correspond to pole singularities of an appropriate characteristic Green’s function in the  $k_x$  complex plane, which represents the voltage (or current) in a transmission line along one of the transverse directions of the waveguide.

<sup>8</sup> Actually, for  $\theta \simeq \pm\pi/2$  the space-wave term takes the following form:  $F''(\pm\pi/2) \frac{e^{-j(k_0|z|-3\pi/4)}}{\sqrt{2\pi|k_0z|^3}}$ .

<sup>9</sup> This is also consistent with the previous discussion based on the *closeness* of the pole to the path of integration  $P$  on the top Riemann sheet.

<sup>10</sup> The modal field is unique up to a scale factor which is determined as long as the excitation is fixed.

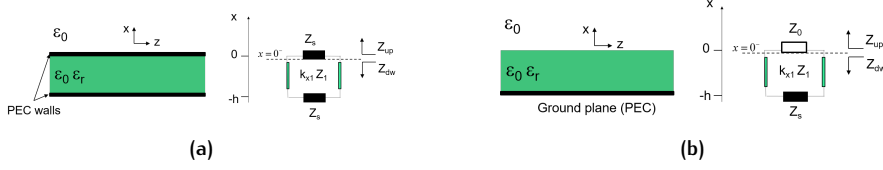


Figure 1.8.: 2-D section and TEN model of (a) a PPW and (b) a GDS.

uide [2], [3], [20]. Within this network formalism, the pole singularities correspond to resonances of the transverse equivalent network (TEN) model, which can be conveniently calculated using analytical methods.

As a proof-of-concept we apply the *transverse resonance technique* (TRT) at two well-known waveguiding problems: the parallel-plate waveguide (PPW) and the GDS. The reason for the choice of these two specific examples is motivated by the fact that they represent two limiting cases of a *conventional* LWA characterized by a GDS covered with a PRS. If the PRS is almost transparent to radiation (e.g., a small metallic patch printed on a dielectric) the modes of the structure might be seen as perturbations of those of a GDS, otherwise if the PRS is almost opaque to radiation (e.g., a small slot etched on a metallic sheet) they might be seen as perturbations of those of a PPW. This formal analogy will be extremely helpful in the analysis of the graphene-based LWAs described in Chapter 3.

### Parallel-plate waveguide

In Fig. 1.8(a) the 2-D section of a dielectric-filled PPW (a dielectric of relative permittivity  $\epsilon_r$  is considered) is reported together with its TEN model. A transmission-line segment with characteristic impedance  $Z_1$  and transverse wavenumber  $k_{x1} = \sqrt{k_0^2 \epsilon_r - k_z^2}$  is terminated at both ends with a surface impedance  $Z_s = 0$ . The application of the TRT to the TEN model consists of equating to 0 the sum between the input impedance looking downward  $Z_{dw}$  and the one looking upward  $Z_{up}$  at an arbitrary cross-section:

$$Z_{dw} + Z_{up} = 0. \quad (1.9)$$

In this example, a convenient choice of the cross-section is represented by  $x = 0^-$  so that  $Z_{up} = Z_s = 0$  and  $Z_{dw} = +jZ_1 \tan(k_{x1}h)$ , and the zeros of the *dispersion equation* are easily found equal to  $k_{xm} = m\pi/h$  with  $m \in \mathbb{Z}$  where  $m$  is the vertical modal order. As expected, the  $k_x$  eigenvalues of a closed region belong to a discrete set.

By means of the separation relation (see Eq. (1.1)), one finds a closed-form expression for the normalized wavenumber  $\hat{k}_z = k_z/k_0$  (from now on,

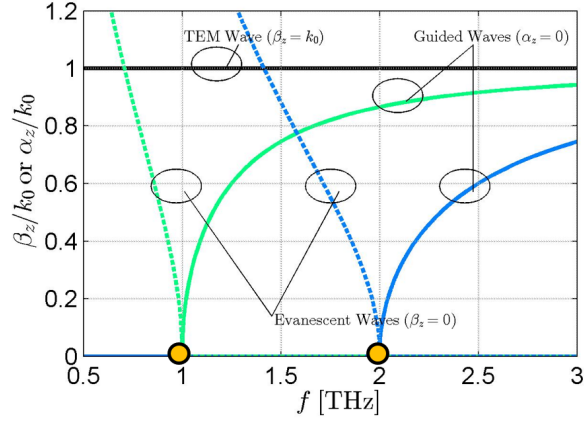


**Figure 1.9.:** Dispersion diagram  $\hat{k}_z$  vs.  $f$  of a PPW. Dispersion curves are found for  $\varepsilon_r = 1$  and  $h = \lambda_0/2$  where  $\lambda_0 = 300 \mu\text{m}$ . Evanescent modes  $k_z = -j\alpha_z$  in dashed lines and guided modes  $k_z = \beta_z \in \mathbb{R}$  in solid lines. Since the structure is not simply-connected, a TEM mode (black solid line) propagating from DC frequency is obtained for  $m = 0$  (green lines are for  $m = 1$  and blue lines are for  $m = 2$ , TE-TM modes, respectively). Yellow dots indicates the cutoff frequencies  $f_c^{(m)}$ .

we refer with a  $(\hat{\cdot})$  to wavenumbers normalized to  $k_0$ ) as a function of the frequency  $f$ :

$$\hat{k}_z = \pm \sqrt{1 - \hat{k}_{xm}^2} = \pm \sqrt{1 - \left(\frac{mc_0}{2hf}\right)^2} = \hat{\beta}_z - j\hat{\alpha}_z. \quad (1.10)$$

As is clear from Eq. (1.10), *guided modes* are obtained for  $\hat{k}_{xm} > 1$ , whereas *evanescent modes* are obtained for  $\hat{k}_{xm} < 1$ . The frequencies  $f_c^{(m)}$  for which  $\hat{k}_{xm} = 1$  are called *cutoff frequencies* and are equal to  $f_c^{(m)} = mc_0/2h$ . All these aspects can be alternatively inferred by looking at the *dispersion diagram* reported in Fig. 1.9 as  $\hat{k}_z$  vs.  $f$ .

We recall here that, for a PPW, transverse-electric (TE) and transverse-magnetic (TM) modes with respect to the  $xz$  plane are degenerate modes, in the sense that they are different eigenmodes sharing the same eigenvalue. Hence, the dispersion diagram of Fig. 1.9 is equal for both polarizations, except for the presence of a transverse-electromagnetic (TEM) mode which originates only from TM modes.

It is worth noting the explicit dependence between the propagating wavenumber  $k_z$  and the frequency  $f$  in Eq. (1.10). As a matter of fact, the dependence between  $k_z$  and  $f$  is often expressed by an implicit function, so that the eigenvalues of the dispersion equation are required to be found by numerical means. In this sense, the search of the modes of a GDS provides a valuable example.

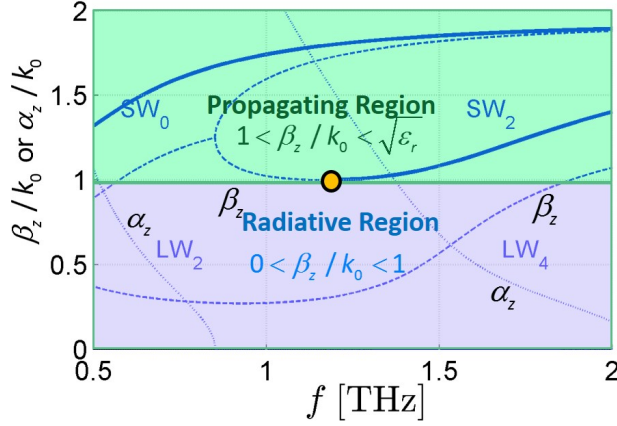


Figure 1.10.: Dispersion diagram  $\hat{k}_z$  vs.  $f$  of a GDS. Dispersion curves are found for  $\epsilon_r = 2.17$  and  $h = \lambda_0/2$  where  $\lambda_0 = 300\mu\text{m}$ . The light line  $k_z = k_0$  sets the boundary between the *radiating region* (just below, highlighted in blue) where *leaky waves* ( $\hat{\beta}_z$  in dashed blue lines and  $\hat{\alpha}_z$  in dotted blue lines) may describe radiation, and *propagating region* (just above, highlighted in green) where *surface waves* ( $\hat{\beta}_z$  in solid blue lines) may describe surface propagation.

#### Grounded dielectric slab

In Fig. 1.8(b) the 2-D section of a grounded dielectric slab GDS (a dielectric of relative permittivity  $\epsilon_r$  is considered) is reported together with its TEN model. A transmission-line segment with characteristic impedance  $Z_1$  and transverse wavenumber  $k_{x1} = \sqrt{k_0^2\epsilon_r - k_z^2}$  is terminated at the bottom by  $Z_s = 0$  and at the top by the air characteristic impedance  $Z_0$ . The application of the TRT to the TEN model provides the following dispersion equation:

$$Z_0 + jZ_1 \tan(k_{x1}h) = 0. \quad (1.11)$$

For conciseness's sake, we limit our attention to TM modes, so that  $Z_0 = \eta_0\hat{k}_{x0}$  and  $Z_1 = \hat{k}_{x1}\eta_0/\epsilon_r$  where  $\eta_0 = 377 \Omega$  is the vacuum impedance and  $\hat{k}_{x0} = \sqrt{1 - \hat{k}_z^2}$ , and Eq. (1.11) can be recast as:

$$\sqrt{1 - \hat{k}_z} + j \frac{\sqrt{\epsilon_r - \hat{k}_z}}{\epsilon_r} \tan(k_0 \sqrt{\epsilon_r - \hat{k}_z} h) = 0, \quad (1.12)$$

which is in the form  $g(\hat{k}_z, f) = 0$  where  $g$  is a function of the two variables  $\hat{k}_z$  and  $f$ . *Dini's Theorem* (also known as *Implicit Function Theorem*), guarantees the existence of an implicit function  $\hat{k}_z(f)$  which locally maps the zeros of  $g$  in a way that  $g(\hat{k}_z(f), f) = 0$ . However, the theorem does not have a constructive proof, so a numerical method is usually needed to find such a mapping. For searching the modes of a GDS it is convenient to use a *Padé*-based root-finding algorithm [23], that is an exponentially convergent procedure that allows for an efficient computation of the complex propagation wavenumbers for layered structures.



Since one of the key aspects of the algorithm lies in a correct choice of the initial points, some insights about the location of the zeros can be gained by computing the cutoff frequencies  $f_c^{\text{SW}}$  of the surface wave modes. Evaluating Eq. (1.12) in the limit for  $\hat{k}_z \rightarrow 1$ , it is found:

$$f_m^{(\text{SW})} = \frac{mc_0}{2h\sqrt{\epsilon_r - 1}}. \quad (1.13)$$

From these initial points (i.e.,  $\hat{k}_z = 1$  for  $f = f_m^{(\text{SW})}$ ), it is easy to track both *surface-wave* modes (by enforcing  $\alpha_{x0} > 0$ <sup>11</sup>) which exist above the *light line* (i.e.,  $\hat{k}_z = 1$ ), and *leaky-wave* modes (by enforcing  $\alpha_{x0} < 0$ ) which exist below the light line, as shown in Fig. 1.10. According to this definition, it is manifest that *leaky-wave* modes can also be interpreted as analytical continuation in the complex  $k_z$ -plane of *surface-wave* modes. Specifically, they can also be ‘labeled’ with the same vertical modal order  $m$  of the surface waves. Interestingly, a *quasi-cutoff* (or *leaky-cutoff*) frequency for leaky modes can be defined in the limit for  $\hat{k}_z \rightarrow 0$  of Eq. (1.12):

$$f_m^{(\text{LW})} = \frac{c_0}{2\pi h\sqrt{\epsilon_r}} [\arctan(j\sqrt{\epsilon_r}) + m\pi].. \quad (1.14)$$

Eq. (1.14) might appear meaningless since it would provide complex-valued frequencies. This is a direct consequence of the fact that leaky modes in a GDS will never reach the *leaky cutoff* condition. A different situation is encountered when the GDS is loaded with graphene as we will see in Chapter 3.

In the next paragraph a widely-accepted [10]–[15] classification of LWAs is provided to introduce the main features of those discussed in Sections 1.3 and 1.4.

### 1.2.5 Classification of leaky-wave antennas

Leaky-wave antennas are typically classified depending on the geometry and the operating principle. With respect to the geometry, LWAs are classified in *one-dimensional* (1-D) or *two-dimensional* (2-D) LWAs, depending on whether the guiding structure is mainly 1-D or 2-D. With respect to the operating principle they are classified in *uniform*, *quasi-uniform*, or *periodic*. According to the abovementioned distinctions, the following class of LWAs are identified.

#### 1-D Uniform LWAs

One-dimensional *uniform* leaky-wave antennas are 1-D LWAs whose cross-section remains constant along the direction of propagation, usually the longitudinal  $z$ -axis. A typical example would be the case of a rectangular

<sup>11</sup> Note that, whereas the corresponding choice for the square root that defines the wavenumber in the slab  $k_{x1}$  is immaterial (because the dispersion equations are even functions of  $k_{x1}$ ), the two determinations of  $k_{x0}$  provide different dispersion equations.

waveguide with a longitudinal slit to allow power to gradually leak out the waveguide. Even though in 1-D uniform LWAs the cross-section should not change with respect to the  $z$ -axis, sometimes the slot is gradually tapered to improve certain radiating features. In any case, radiation is described only by the fundamental mode, which is a *fast leaky wave*.

When fed at one end, the main beam can be scanned in the forward quadrant ( $z > 0$ ), from nearly broadside to nearly endfire. The radiation at exactly broadside and endfire from a 1-D LWAs presents some intrinsic physical issues as we will readily show in Section 1.3.

### 1-D Periodic LWAs

One-dimensional *periodic* leaky-wave antennas are 1-D LWAs whose guiding structure has been periodically modulated along the longitudinal  $z$ -axis. Due to the periodic modulation, the guided wave is represented by an infinite number of *space harmonics* (*Floquet modes*), with longitudinal wavenumbers  $k_{zn} = k_{z0} + 2\pi n/p$  where  $k_{z0}$  is the wavenumber of the *fundamental Floquet mode*,  $n$  is the harmonic order, and  $p$  is the period. Although the fundamental (i.e.,  $n = 0$ ) Floquet mode is usually a slow wave ( $k_{z0} > k_0$ ) (and thus it does not radiate), the structure is typically designed so that the  $n = -1$  harmonic is fast ( $k_z > k_0$ ) and thus it radiates.

One of the main advantages of 1-D periodic LWAs with respect to 1-D uniform LWAs is that the main beam can scan from the backward to the forward quadrant, despite radiation is generally not good through broadside. As is known [10]–[15], the antenna performance generally degrades when the main beam approaches broadside, due to the presence of an open stopband of the periodic structure<sup>12</sup>.

### 1-D Quasi-Uniform LWAs

One-dimensional *quasi-uniform* structures are also characterized by a periodic modulation of their geometry along the longitudinal  $z$ -axis. However, in this case, the fundamental mode is a fast leaky wave, as for 1-D uniform LWAs. The reason why it is called *quasi-uniform* is because the period is electrically small (i.e.  $p \ll \lambda$ ) such that radiation comes only from the fundamental mode, and not from any of the higher-order ( $n \neq 0$ ) space harmonics. As a consequence, the radiation properties of this type of antennas are more similar to those of 1-D uniform LWAs than those of 1-D periodic LWAs.

### 2-D Uniform LWAs

Two-dimensional *uniform* leaky-wave antennas are partially-open waveguiding structures, which are able to support a *cylindrical leaky wave* that

<sup>12</sup> The issue of poor broadside radiation in periodic LWAs has been intensively investigated in the literature. The interested reader can find a recent survey in [10].

radially propagates outward from the source. This type of LWAs can produce a directive pencil beam at broadside or a conical beam with the cone axis along the vertical  $x$ -axis.

Most of 2-D LWAs are characterized by uniform or quasi-uniform waveguiding structures, and thus radiation is usually described by the fundamental leaky mode, which is a fast wave. The most known example of 2-D LWAs is a GDS covered with a PRS.

An interesting aspect of *uniform* and *quasi-uniform* LWAs (either of 1-D or 2-D type) is that they can conveniently be modeled with homogenized effective materials or surface impedances. For this reason, in the following Sections 1.3 and 1.4 we will limit the discussion to these types of antennas.

### 1.3 1-D LEAKY-WAVE ANTENNAS

In this Section we limit our attention to 1-D *uniform* LWAs, since all the theoretical framework developed in Chapter 2 applies for these two classes of 1-D LWAs. In 1.3.1 we introduce the first two historical examples of uniform and quasi-uniform 1-D LWAs. Since both types of antennas scan only in the forward quadrant, their radiating properties belong to the class of 1-D *unidirectional* LWAs. Finally, in 1.3.3 the radiating properties of 1-D *bidirectional* LWAs are discussed as a first step towards the study of 2-D LWAs which will be the object of the next Section 1.4. The theoretical content of 1.3.2 and 1.3.3 will lay the groundwork for a novel theoretical framework which will be thoroughly discussed in Chapter 2.

#### 1.3.1 Historical examples of 1-D LWAS

The long history of 1-D uniform LWAs started back to the '40s when W. W. Hansen [24] first introduce the *slitted rectangular waveguide*. As is shown in Fig. 1.11(a) the antenna consists of a rectangular waveguide with a longitudinal uniform slot cut along the propagating  $z$ -axis. The waveguide operating with its fundamental  $TE_{10}$ , continuously leaks energy from the slot. However, a rigorous explanation of the mechanism of radiation in terms of leaky waves appeared only later after the antennas were introduced, thanks to the works of L. O. Goldstone and A. A. Oliner [26], [27].

Starting from the '50s various types of 1-D LWAs were proposed, but most of them were still based on the introduction of long uniform slits into waveguides to achieve radiation. Since these slits were originally placed in positions where they strongly perturb the surface current distribution of the closed waveguides, the *leakage rate* (measured by the attenuation constant  $\alpha_z$  of the relevant leaky mode) of these antennas was usually high, thus producing beams with poor directivity. This phenomenon can be explained if one thinks at the typical aperture-field distribution of a *leaky-wave antenna* (see

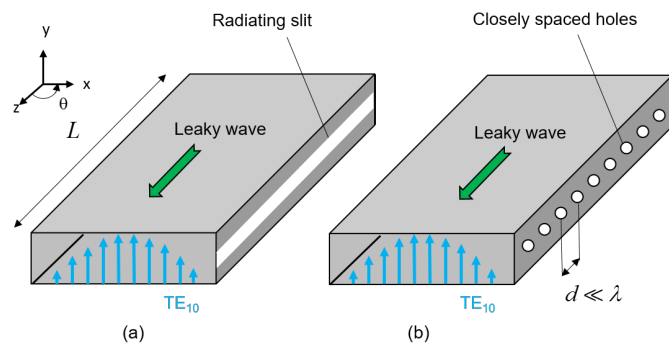


Figure 1.11.: Two well-known examples of 1-D LWAs. (a) An example of 1-D uniform LWA: the *slitted rectangular waveguide* [24]. (b) An example of 1-D quasi-uniform LWA: the *holey waveguide* [25].

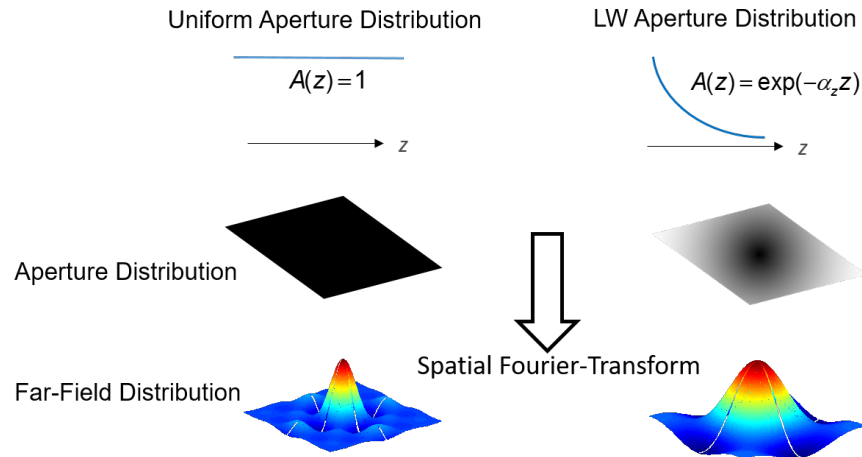


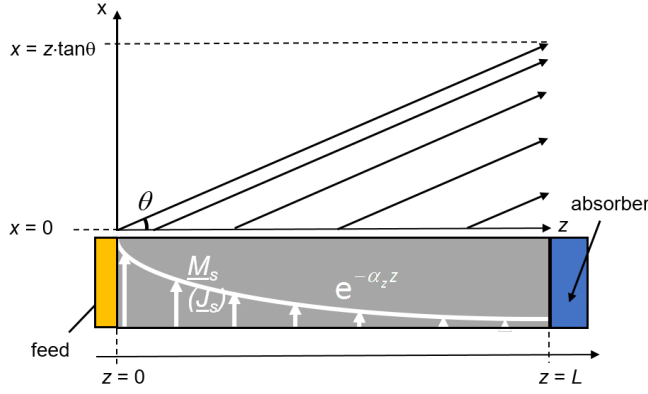
Figure 1.12.: Comparison between the far-field distributions of a uniform aperture distribution and a leaky aperture distribution. The directivity of LWAs increases as long as the leakage rate  $\alpha_z$  is low.

Fig. 1.12). At a first approximation, the aperture field distribution of a LWA is characterized by an exponential behavior of the type  $e^{-\alpha_z z} e^{-j\beta_z z}$ . Since, from Kirchhoff-Huygens principle [28] we know that the far-field distribution can be seen as a spatial Fourier-Transform of the aperture distribution, it is clear that *peaked* distributions in the far field can be achieved as long as the aperture distribution is uniform, i.e., with low level of the leakage rate  $\alpha_z$  (see Fig. 1.12).

One method for reducing the leakage rate in 1-D LWAs was proposed by J. N. Hines and J. R. Upson [25], in which the long slit was replaced by a series of closely spaced holes, thereby avoiding cutting the current lines. This structure was called *holey waveguide* and it was the first example of a 1-D quasi-uniform LWA. As is shown in Fig. 1.11(b), the holes are closely spaced (i.e., in the sense that the distance between adjacent elements was less than the operating wavelength), so that they act in a quasi-uniform manner.

A more general approach was suggested years later by W. Rotman and A. A. Oliner [29], who recognized that some open guiding structure did not radiate due to the symmetry of the current distribution. Only the introduction of some asymmetry in the design would allow for radiating power in a leaky-wave fashion. This new approach has led them to the successful measurements of the so-called *asymmetrical trough waveguide antenna* [29].

In general, 1-D LWAs became very popular in the microwave community during the '60s thanks to their ease of fabrication and design, structural simplicity, and cost-effectiveness, especially when compared to electrically long arrays of discrete elements that are expensive, and more difficult to implement [30]. Recently, 1-D LWAs are living a sort of *Renaissance* mainly thanks to the advent of metamaterials [31]. The recent interest in 1-D LWAs is expressed by the considerable amount of recent publications on the topic



**Figure 1.13.:** 2-D section of a unidirectional LWA with an equivalent magnetic (electric) surface current that models an aperture field with the typical exponentially-decaying distribution of forward leaky waves. An absorber is usually put at the end of the structure to avoid back-reflection from the forward leaky wave.

(e.g., see [10], [15] and Refs. therein). In particular, a growing interest has been stimulated by 1-D LWAs being able to scan through broadside [32]–[35], and by 1-D LWAs that either exhibit beam reconfigurability at a fixed frequency [36]–[40], or exhibit fixed-beam over a wide frequency range [41]–[44].

In any case, the radiating properties of 1-D uniform LWAs are the same regardless its constituent parameters. However, a distinction should be made between 1-D *unidirectional* and *bidirectional* LWAs, since their radiating features are considerably different as we will see in the next paragraphs.

### 1.3.2 Radiating properties of 1-D unidirectional LWAs

The radiating features of a 1-D unidirectional LWA as the one depicted in Fig. 1.13 are characterized by a forward leaky-wave which propagates in a single direction (the  $z$ -axis) from the feed (at  $z = 0$ ) to the end of the structure ( $z = L$ ). As we said in the previous paragraph, the far-field distribution of a 1-D LWA can easily be calculated by taking advantage of the Kirchhoff-Huygen's formula [28], i.e., calculating the spatial Fourier transform of the aperture distribution over a uniform aperture. For a forward leaky wave the tangential electric-field distribution  $E_y(0, z)$  given by an equivalent magnetic surface current  $M_s = e^{-jk_z z}$  (which can model, e.g., a longitudinal slit along the aperture) is equal to  $E_y(0, z) = e^{-jk_z z}$ . Its Fourier-Transform over the aperture plane is given by

$$\begin{aligned} \text{AF}(\theta) &= \int_{-\infty}^{\infty} E_y(0, z) e^{jk'_z z} dz = \int_{-L/2}^{L/2} e^{-j(k_z - k'_z)z} dz \quad k'_z = k_0 \cos \theta \\ &= jL e^{-j(k_z - k_0 \cos \theta)L/2} \text{sinc} \left[ \frac{L}{2} (k_z - k_0 \cos \theta) \right], \end{aligned} \quad (1.15)$$

where  $\theta$  is the angle measured from the  $z$ -axis and  $L$  is the length of the antenna. The expression in Eq. 1.15 is usually denoted as Array Factor (AF) in analogy with 1-D arrays, which can be thought of as a discrete version of the continuous leaky-wave aperture, in which the attenuation constant  $\alpha_z$  has been set to zero.

Taking only the modulus of this expression, and normalizing with respect to the maximum<sup>13</sup>, we get the expression:

$$R(\theta) = \frac{|\text{FF}(\theta)|}{\max\{|\text{FF}(\theta)|\}} = \text{sinc} \left[ \frac{L}{2}(k_z - k_0 \cos \theta) \right]. \quad (1.16)$$

For electrically long apertures (i.e.,  $L/\lambda_0 \gg 1$ , where  $\lambda$  is the operating wavelength)  $L \rightarrow \infty$  and the AF takes the following simplified expression:

$$\text{AF}(\theta) = \frac{-j}{k_z - k_0 \cos \theta}, \quad (1.17)$$

which reveals that the far-field pattern has a conical shape, with a maximum at some angle  $\theta_0$  from the  $z$ -axis which is given by:

$$\theta_0 = \arccos \frac{\beta_z}{k_0}, \quad (1.18)$$

whereas the HPBW, defined by the angle difference (in radians) between the two  $-3$  dB points, is given approximately by

$$\text{HPBW} = 2 \frac{\alpha_z}{k_0} \csc \theta_0, \quad (1.19)$$

which assumes an infinite aperture. Conversely, for finite apertures, A. A. Oliner [13] found the following formula:

$$\text{HPBW} = \frac{N_O}{(L/\lambda_0)} \csc \theta_0, \quad (1.20)$$

where  $N_O$  is an amplitude factor which depends on both  $\alpha_z$  and  $L$ . According to Oliner [12], [13], for constant-aperture distribution ( $\alpha_z = 0$ )  $N_O \simeq 0.88$ ; for sharply peaked distributions ( $\alpha_z \gg 0$ )  $N_O \simeq 1.25$  or more; for a LWA with a radiating efficiency  $e_r = 1 - \exp(-4\alpha_z L) = 90\%$ ,  $N_O \simeq 0.91$ . As a middle-of-the-range result, Oliner suggested  $N_O = 1$ .

Unfortunately, in the current literature there are neither more general nor more precise formulas for the calculation of the HPBW of a 1-D unidirectional LWAs for arbitrary values of efficiency and lengths of the antenna. Another evident problem of both Eqs. (1.19) and (1.20) is their singular behavior at endfire ( $\theta_0 = 0$ ). This would pose unavoidable issues for the beamwidth evaluation of endfire LWAs [45]–[47].

To this purpose, an original theoretical framework is developed in Chapter 2 in order to derive a general formula for the HPBW of 1-D unidirectional

<sup>13</sup> Actually, for this first normalization we have tacitly assumed that the argument of the  $\text{sinc}(\cdot)$  function is real, i.e.,  $\alpha_z \simeq 0$ . In Chapter 2, the radiated power will be renormalized to the actual maximum.

tional LWAs. The new formula is of general validity and comprises the old formulas originally derived by A. A. Oliner as limiting cases.

Similar considerations hold for bidirectional 1-D LWAs as we will readily see in the next paragraph.

### 1.3.3 Radiating properties of 1-D bidirectional LWAs

The radiating features of a *bidirectional* LWA are determined by a leaky mode which propagate equally in both the positive and negative  $z$ -axis, from a feed at  $z = 0$  to both ends of the structure at  $z = \pm L/2$ . Assuming the same magnetic current source as in the previous paragraph, the AF is now given by:

$$\text{AF} = \int_{-L/2}^{L/2} e^{-jk_z|z|} e^{-jk_0 \sin \theta z} dz, \quad (1.21)$$

where  $\theta$  is now the angle measured from the vertical  $x$ -axis to the longitudinal axis  $z$  (thus  $\theta = 0^\circ$  would correspond to broadside). We can profitably split the integral in two parts:

$$\text{AF} = \int_0^{L/2} e^{-jz(k_z+k_0 \sin \theta)} dz + \int_0^{L/2} e^{-jz(k_z-k_0 \sin \theta)} dz, \quad (1.22)$$

and conveniently define the following *dummy* variables:

$$\begin{cases} w^+ = k_z + k_0 \sin \theta, & w^- = k_z - k_0 \sin \theta \\ w^+ + w^- = 2k_z, & w^+ w^- = k_z^2 - k_0^2 \sin^2 \theta. \end{cases} \quad (1.23)$$

This allows to express Eq. (1.22) as

$$\text{AF} = \int_0^{L/2} e^{-jzw^+} dz + \int_0^{L/2} e^{-jzw^-} dz. \quad (1.24)$$

These simple integrals are known in closed form and yields:

$$\text{AF} = j \frac{w^- e^{-jw^+ L/2} + w^+ e^{-jw^- L/2} - w^+}{w^+ w^-}. \quad (1.25)$$

By means of (1.23) we get an explicit expression in terms of  $k_z$ ,  $k_0$ ,  $L$  and  $\theta$ :

$$\text{AF} = j \frac{(k_z - k_0 \sin \theta) e^{-j(k_z+k_0 \sin \theta) \frac{L}{2}} + (k_z + k_0 \sin \theta) e^{-j(k_z-k_0 \sin \theta) \frac{L}{2}} - 2k_z}{k_z^2 - k_0^2 \sin^2 \theta}. \quad (1.26)$$

A 1-D bidirectional LWA would normally produce a pair of conical beams at  $\theta = \pm \theta_0$ . Hence, as  $\theta \rightarrow 0$  the two beams approach each other and merge into a single beam, which has a maximum at broadside (see Fig. 1.14). As a result, a broadside beam can be produced by a 1-D LWA, differently from 1-D unidirectional LWA.



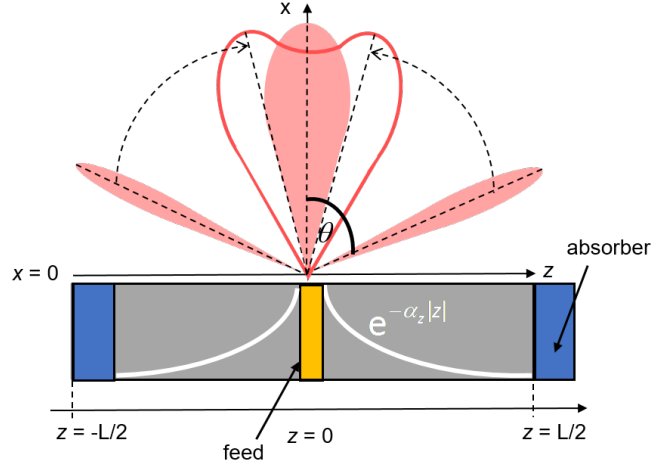


Figure 1.14.: 2-D section of a bidirectional LWA centrally-fed by a coaxial cable. When the two beams approaches each other, they merge in a single beam which points exactly at broadside.

Again, for  $L \rightarrow \infty$  the AF takes the following simplified expression:

$$\text{AF}(\theta) = \frac{-2jk_z}{k_z^2 - k_0^2 \sin^2 \theta'} \quad (1.27)$$

which reveals that pointing angle is given by the following approximate formula:

$$\theta_0 \simeq \arcsin \sqrt{\left(\frac{\beta_z}{k_0}\right)^2 - \left(\frac{\alpha_z}{k_0}\right)^2}, \quad (1.28)$$

that for  $\alpha_z/k_0 \ll 1$  is the same result of 1-D unidirectional LWAs (see Eq. (1.18)).

The derivation of the formulas for the HPBW are lengthy and are postponed to the next Chapter 2 where they will also be generalized as for the unidirectional case. However, it is worth to recall that, in the bidirectional case, the HPBW formulas for scanned beams (i.e., when  $\beta_z \gg \alpha_z$ ) are the same of the unidirectional case, whereas, at broadside (i.e., when  $\beta_z \leq \alpha_z$ ) they substantially differ. In fact, when  $\beta_z < \alpha_z$  [48]:

$$\text{HPBW} = 2\sqrt{(\hat{\beta}^2 - \hat{\alpha}^2) \pm \sqrt{2(\hat{\beta}^4 + \hat{\alpha}^4)}}, \quad (1.29)$$

Even more interestingly, when  $\beta_z = \alpha_z$  (known as the *splitting condition*<sup>14</sup>) the radiated power density is maximized [14], [48]. When  $\beta = \alpha$ , the HPBW is given by:

$$\text{HPBW} = 2\sqrt{2}\frac{\alpha_z}{k_0}. \quad (1.30)$$

In Chapter 2, we also provide a rigorous demonstration of these formulas which will result as limiting cases of more general ones.

<sup>14</sup> In fact, for  $\beta > \alpha$  a single beam *splits* into two beams pointing off broadside.

## 1.4 2-D LEAKY-WAVE ANTENNAS

In this Section we discuss the properties of 2-D LWAs because all the structures introduced in Chapter 3 fall into this category. In a specular way to the previous Section 1.3 we first review in 1.4.1 some significant historical examples of 2-D LWAs. In 1.4.2 the radiating properties of 2-D LWAs are briefly summarized, emphasizing similarities and differences with 1-D LWAs. In particular, the design rules for two specific types of 2-D LWAs will be discussed in 1.4.3 due to their wide usage in Chapter 3. Finally, in 1.4.4 the intrinsic limitations inherent to radiation from *conventional* LWAs are pointed out, thus motivating the need for the investigation of *unconventional* LWAs. This last part will be the object of Chapter 3.

### 1.4.1 Historical examples of 2-D LWAS

The first historical evidence of the concept of a 2-D LWA is dated back to the '50s when G. von Trentini [49] originally proposes a periodic PRS over a ground plane to achieve directive pencil beams at broadside (see Fig. 1.15). Inspired by the *Fabry-Perot* concept, he interpreted the radiation phenomenon in terms of multiple reflections between the ground plane and the PRS, and then derived an expression for the resonance condition that yields maximum radiated power at broadside. For this reason, this specific type of 2-D LWAs are also called *Fabry-Perot Cavity* (FPC) LWAs. In this derivation, he assumes that the PRS consisted of an array of closely spaced parallel conducting wires oriented parallel to the electric field. Since the period  $p$  of the unit-cell is electrically small ( $p \ll \lambda_0$ ), the PRS acts

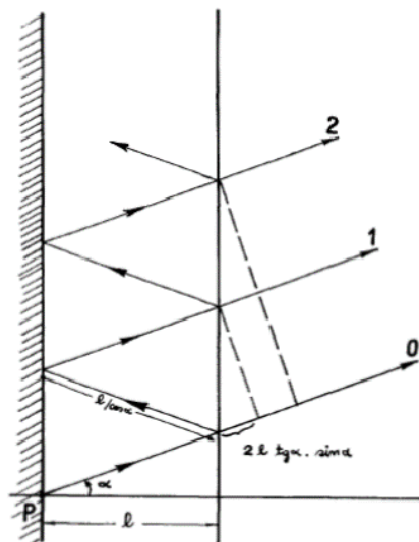
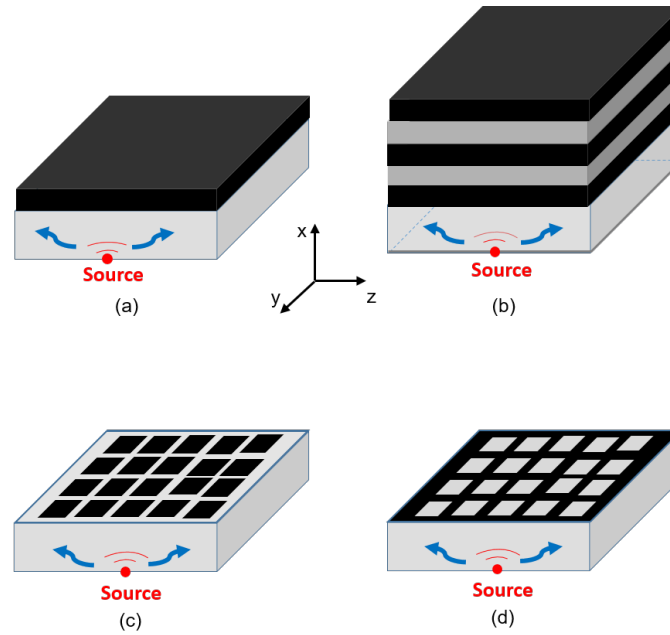


Figure 1.15.: The original ray explanation proposed by von Trentini in [49] for FPC-like antennas. At that time, these kind of antennas were not recognized as 2-D LWAs.



**Figure 1.16.:** Several examples of different types of PRS. The PRS consists of a single (a) dielectric layer, (b) a multistack of alternating dielectric layers, (c) a 2-D periodic array of metallic patches, and (d) its complementary version, i.e., slots in a thin metal plate.

as a quasi-uniform reflective surface, where the reflection coefficient of the fundamental PPW mode determines the characteristics of the antenna. An alternative way to interpret this phenomenon was later suggested by S. A. Tretyakov [50], who first introduced the concept of *homogenized impedances* for the modeling of PRS characterized by sub-resonant elements ( $p \ll \lambda_0$  and  $d \ll p$  where  $d$  is the edge-to-edge distance between adjacent elements). A concept that, years later, was successively borrowed by C. L. Holloway et al. to develop the well-known *generalized sheet transition conditions* (GSTCs) for the characterization of *metasurfaces* [51].

The pioneering work of G. von Trentini laid the foundation for further work in the area 2-D LWAs, despite it was not appreciated at the time that this type of structure was actually a 2-D quasi-uniform LWA. Nowadays, the different types of existing 2-D LWAs mainly consist of a GDS that is covered with a PRS on top of the dielectric layer (the dielectric layer may also be air). However, the PRS can take various forms, such as a stack of one or more dielectric layers, or a metal screen consisting of a periodic array of slots or patches (see Fig. 1.16). Interestingly, S. A. Tretyakov and his research group developed very useful homogenization formulas for such PRS and more sophisticated topologies [50], [52], [53].

Several examples of such structures have been investigated half a century later by A. P. Feresidis and J. C. Vardaxoglou [54]. Following von Trentini ray theory analysis and assuming the structure to have infinite extent, they note that the antenna would have greater bandwidth if the phase of its PRS were to linearly increase with frequency. They therefore investigated PRSs loaded

with several different elements, such as crossed dipoles, patches, rings, and square loops. They found that dipoles, or square or circular patches (or their complementary structures), particularly when the elements are densely packed ( $d \ll p$ ), produced slowly variation of the beam with frequency.

Investigations of a uniform 2-D LWA consisting of a dielectric superstrate layer over a substrate layer were conducted by N. G. Alexópoulos and D. R. Jackson in the '80s [55], [56], although this structure was also not initially recognized as a LWA. It was only in the late '80s and early '90s [57], [58] that A. A. Oliner suggested to his colleagues a leaky-wave interpretation of the gain enhancement effect.

#### 1.4.2 Radiating properties of 2-D LWAs

One of the main differences between this type of structures and 1-D LWAs is that the leaky mode is a cylindrical wave, which propagates outward radially from the source along the interface. The leaky wave then furnishes a large aperture that in turn produces a narrow radiation beam. A vertical electric or magnetic dipole (VED or VMD) source launches only a TM or TE (with respect to the vertical  $x$ -axis) leaky wave respectively, which has no  $\phi$  variation. This results in an omnidirectional conical beam [58], but not a broadside beam (the pattern will always have a null at broadside). A horizontal electric or magnetic dipole (HED or HMD) source launches a pair of leaky waves, one TM and one TE. The TM leaky wave determines the E-plane pattern, while the TE leaky wave determines the H-plane pattern [58]. For a broadside beam these two leaky waves have very nearly the same phase and attenuation constants, and hence an omnidirectional *pencil* beam is created.

A rigorous description of radiation from cylindrical leaky waves can be found in [58]. Here, we will limit to give some of the most interesting results of that investigation. In particular, it was found that the pointing angle in a 2-D LWA is still given by Eq. (1.18), although, for this kind of antennas (as for 1-D bidirectional LWAs), it is usually preferable to express the pointing angle  $\theta_0$  as measured from the vertical  $x$ -axis, so that Eq. (1.18) reads:

$$\theta_0 = \arcsin \frac{\beta_z}{k_0}. \quad (1.31)$$

The reason for this change of notation is due to the fact that 2-D LWAs are usually designed to achieve maximum directivity at broadside, i.e.,  $\theta = 0$  in this new notation. However, when  $\hat{a}_z$  is not small enough, the pointing angle is generally given by Eq. (1.28).

Conversely, the beamwidth formulas for 2-D LWAs are very similar to those of 1-D bidirectional LWAs. However, a distinction should be made between the case of VED (VMD) sources and HED (HMD) sources. In the first case, an omnidirectional beam is obtained with a HPBW given by

Eq. (1.19)<sup>15</sup>. In the second case, since the beam is no longer azimuthally independent, we should distinguish the beamwidth with respect to the E- and the H- plane. In particular, for scanned beam  $\beta_z \gg \alpha_z$  it is found that [58]

$$\begin{aligned} \text{HPBW}_E &= 2 \frac{\alpha_z^{\text{TM}}}{k_0} \sec \theta_0, \\ \text{HPBW}_H &= 2 \frac{\alpha_z^{\text{TE}}}{k_0} \sec \theta_0, \end{aligned} \quad (1.32)$$

whereas at broadside  $\beta_z \simeq \alpha_z$ :

$$\begin{aligned} \text{HPBW}_E &= 2\sqrt{2} \frac{\alpha_z^{\text{TM}}}{k_0}, \\ \text{HPBW}_H &= 2\sqrt{2} \frac{\alpha_z^{\text{TE}}}{k_0}. \end{aligned} \quad (1.33)$$

From Eqs. 1.32 and Eqs. 1.33 it is manifest the similarity with bidirectional LWAs. It is also clear that, as the wavenumbers of the two leaky waves begin to differ, the beamwidths become different in the principal planes. This typically happens as the scan angle increases.

#### 1.4.3 Design rules for dielectric-based 2-D LWAs

In all PRS-based 2-D LWAs, the PRS is used to create a leaky PPW region, and the leaky waves are leaky (radiating) versions of the PPW modes that would be excited by the source in an ideal PPW, which results if the PRS is replaced by a PEC wall. This point of view allows for a simple design formula for the thickness of the dielectric layer in order to obtain a beam at a desired angle  $\theta_0$  (either a broadside or a conical beam).

For  $m$ -th order TM and TE PPW modes the radial wavenumber of an ideal PPW waveguide would be  $\beta_z = \beta_z^{\text{TM}} = \beta_z^{\text{TE}} = \sqrt{k_0^2 \varepsilon_r - \left(\frac{m\pi}{h_1}\right)^2}$  (see Eq. (1.10)), where  $h_1$  is the thickness of the dielectric substrate and  $\varepsilon_{r1}$  its relative permittivity.

Using Eq. (1.31) one finds the following design rule

$$h_1 = \frac{m\lambda_0}{2\sqrt{\varepsilon_{r1} - \sin^2 \theta_0}}. \quad (1.34)$$

On the other hand, the location of the source usually has little effect on the pattern shape, since this is dictated by the leaky-wave phase and attenuation constants. The phase constant is primarily determined by the thickness of the dielectric layer, while the attenuation constant is primarily determined by the properties of the PRS. However, a HMD and a VED sources maximize the peak power density when they are placed on the ground plane, while a

<sup>15</sup> Note that  $\theta_0$  should be changed according to the new definition.

VMD and a HED sources do so when they are placed in the middle of the layer.

Other interesting design rules are found when the PRS under consideration is represented by a cover layer made of a denser dielectric material with respect to the substrate, as depicted in Fig. 1.11(a). This kind of structures, commonly known as *substrate-superstrate* (SS) LWAs, have been extensively studied by N. G. Alexópoulos and D. R. Jackson [55], [56]. In those works [55], [56], they showed that the PRS (represented by the superstrate) would act as a perfectly reflecting layer, when the thickness  $h_2$  of the superstrate (the *cover* layer) is chosen so that it is an odd multiple of one-quarter of a wavelength in the vertical direction. This corresponds to the condition

$$h_2 = \frac{(2m - 1)\lambda}{4\sqrt{\epsilon_{r2} - \sin^2 \theta_0}}. \quad (1.35)$$

It is clear that Eqs. (1.34) and (1.35) reveal that the design rules for optimizing radiation at broadside ( $\theta_0 = 0$ ) with the fundamental ( $m = 1$ ) TE, TM leaky modes, suggest to choose thickness of a half- and of a quarter-wavelength in their respective media for the substrate and the superstrate, respectively. On the other hand, the use of higher-order modes allows for thicker layers; a choice that may be beneficial in millimeter-wave design as we will see in Chapter 5.

Another distinctive feature of SS-LWAs is that the directivity increases as the permittivity of the superstrate layer increases relative to that of the substrate layer, since the superstrate PRS then acts as a more reflective surface.

To conclude, a different way to increase directivity was proposed in [59]. There, the single superstrate is replaced by a periodic array of such superstrates, as shown in Fig. 1.11(b). In this structure the PRS consists of a stack of multiple alternating layers of high permittivity and low permittivity, whose thicknesses are chosen according to Eq. (1.35). As is shown in [59], the directivity increases geometrically with the number of superstrate layers, and thus very directive beams may be obtained using modest values of superstrate permittivity, provided that several superstrate layers are used.

As a last remark, it is worth noting that the multistack of alternating layers can be interpreted as a *distributed Bragg reflector* (DBR) meaning that it is a periodic *electronic bandgap* (EBG) structure operating in a stopband. From this point of view the substrate acts as a defect in the periodic EBG structure [60]. More interestingly, a leaky-wave explanation of the phenomenon is provided in [61].

#### 1.4.4 Motivation for the study of unconventional 2-D LWAs

As is manifest from Eqs. (1.31), (1.32) and (1.33) the beam angle and the beamwidth are frequency sensitive. Indeed, the frequency-scanning behavior is a distinctive feature common to all LWAs. Unfortunately, in most

of microwave applications this is an undesirable effect since the antenna radiating performance should not change within a small fractional bandwidth centered around the operating frequency. Conversely, it would be extremely beneficial for *satcom applications* to dynamically change certain radiating properties, such as the pointing angle, at a fixed frequency. This would allow for avoiding the heavy antenna rotating mechanism that is still needed to scan the beam in airborne systems as pointed out in [62].

This fundamental aspect has recently boosted the scientific community in the search of tunable materials which allow for dynamically change the properties of the PRS in order to achieve beam-steering capability at a fixed frequency. Over the years a lot of solutions have been proposed, comprising active impedances [36], [63], [64], ferroelectric and ferromagnetic materials [62], [65], [66], just to name but a few. In Chapter 3 we will focus on the extremely intriguing possibilities offered by tunable materials such as liquid crystals and more recently by graphene.

## 1.5 CONCLUSION

In this Chapter we have reviewed the fundamental aspects of leaky-wave theory. Leaky-wave antennas have been classified in four different categories depending on the geometry and the operating principle. In particular, it is seen that 1-D uniform and quasi-uniform leaky-wave antennas can be treated with the same formalism. Almost the same conclusion holds for 1-D bidirectional and 2-D leaky-wave antennas. This aspect would be particularly useful for the analysis proposed in Chapter 2.

Furthermore, a rather useful technique, viz. the *Transverse Resonance Technique* has been applied for the analysis of two canonical problems: the parallel-plate waveguide and the grounded dielectric slab. These two examples will result to be limiting cases of the graphene-based leaky-wave antennas described in Chapter 3.



# 2

## FORMULAS FOR LEAKY-WAVE ANTENNAS

### 2.1 INTRODUCTION

In the previous Chapter 1, we have reviewed the general properties of different classes of LWAs, spanning from 1-D uniform LWAs to 2-D quasi-uniform LWAs passing through 1-D periodic LWAs. In this Chapter 2, we specifically deal with the radiating properties of 1-D *uniform* or *quasi-uniform* LWAs.

As is known, the relevant radiating properties such as the radiation efficiency, the pointing angle, and the half-power beamwidth (HPBW), have always been theoretically predicted by means of the old *Oliner formulas* provided in Eqs. (1.18), (1.19), and (1.20). These formulas relate the pointing angle and the HPBW to the phase and the attenuation constants of the relevant leaky-mode responsible for radiation [10]–[14]. However, some limitations exist on the validity of this HPBW formula. In particular, it is seen that:

- i) there is a singularity when the pointing angle (measured from the axis of propagation) is equal to zero, and hence the formula loses accuracy as the beam approaches endfire;
- ii) the formula is accurate only when the HPBW is small with respect to the pointing angle;
- iii) it is not clear how the amplitude factor  $N_O$  that appears in Eq. (1.20) varies with the radiation efficiency [11]–[13].

Recently, several efforts have been made for evaluating the fundamental properties of 2-D *uniform* LWAs as well as for 1-D uniform *bidirectional* LWAs [48] and 1-D *periodic* LWAs [34]. However, the current literature still lacks a thorough derivation of Oliner formulas for 1-D *unidirectional* LWAs, as well as an improvement of his original results to overcome the limitations mentioned above. Such an improvement would allow for extending the evaluation of HPBW in 1-D LWAs to more general cases, such as radiation near and at endfire, structures with finite apertures, and cases of large beamwidth.

To this purpose, here we derive for the first time analytical formulas for the HPBW of 1-D LWAs that can be applied in the most general cases. Remarkably, no assumptions will be made on the pointing angle or the HPBW, and the antenna aperture will be arbitrarily large or small. Moreover, a clear

explanation of Oliner formula will directly emerge from this analysis, under the small beamwidth assumption.

The Chapter is organized as follows. In Section 2.2, a general formula for the HPBW of a 1-D unidirectional LWA is found. The only assumption made in this derivation would regard the range of the leaky-wave phase constant that is limited to  $0 \leq \beta_z < k_0$ . This means that the beam angle can be anything from broadside down to *near* endfire. In fact, the theoretical framework needed for evaluating the radiating features of *endfire* LWAs deserves a separate analysis that will be the object of Section 2.3. There, we will only assume that the beam angle points at endfire, although the leaky-wave phase constant can take values beyond the *ordinary* endfire condition  $\beta_z > k_0$ . Finally, in Section 2.4 new general formulas are proposed for the evaluation of the beamwidth of 1-D bidirectional LWAs. This would also represent the first step towards the development of a forthcoming theoretical framework able to provide new general formulas for 2-D LWAs.

## 2.2 FORMULAS FOR 1-D UNIDIRECTIONAL LEAKY-WAVE ANTENNAS

In this Section we aim to find an expression for the beamwidth of 1-D unidirectional LWAs which accounts for both the attenuation constant and the length of the aperture. First, in 2.2.1 a theoretical framework is laid down to derive a simple transcendental equation which implicitly defines the HPBW as a function of the leakage rate, the length of the antenna, and the pointing angle for 1-D LWAs with a beam pointing anywhere from broadside to near endfire. A simpler formula is also proposed which is accurate as long as the beamwidth is smaller than the pointing angle. It will be shown that Oliner formula results as a limiting case of this approximate expression.

However, the beamwidth formula relies on the solution of the aforementioned transcendental equation in order to obtain a parameter that appears in the formula. Hence, in 2.2.2 a fitting procedure is used to find an approximate but very accurate analytical expression for the solution of the transcendental equation derived in 2.2.1. Different interpolating functions are adopted and compared each other. Among them a suitable function is then used to derive a final formula for the beamwidth that is completely in closed form, and is very general. Numerical results are shown in 2.2.3 to corroborate the validity of the proposed approach. In 2.2.4 the limitations of the old formula early proposed by Oliner in the '60s [10]–[12], [14] are shown for different situations where the formula is not supposed to have a good accuracy. Finally, in 2.2.5 the theoretical framework developed in 2.2.1 is extended to the endfire case. This would serve as a preliminary step towards the analysis proposed in the next Section 2.3.

### 2.2.1 Analytical framework

In 1.3.2 we have seen that the radiation pattern of a 1-D unidirectional LWA is expressed by Eq. (1.16), that we report here for convenience:

$$R(\theta) = \text{sinc} \left[ \frac{L}{2} (k_z - k_0 \cos \theta) \right]. \quad (2.1)$$

where  $L$  is the length of the antenna,  $k_z = \beta - j\alpha$  is the complex longitudinal wavenumber,  $k_0$  is the vacuum wavenumber, and  $\theta$  is the angle measured from the longitudinal  $z$ -axis to the vertical  $x$ -axis (see Fig. 1.2).

The aim of this analysis, is to find an accurate formula for the evaluation of the HPBW in terms of  $L$ ,  $\beta$ ,  $\alpha$ , and the pointing angle  $\theta_0$ . To this purpose, we first expand the  $\text{sinc}(\cdot)$  function and then express  $k_z$  in terms of its real and imaginary part:

$$R(\theta) = \frac{\sin \left\{ \frac{L}{2} [(\beta - k_0 \cos \theta) - j\alpha] \right\}}{\frac{L}{2} [(\beta - k_0 \cos \theta) - j\alpha]}. \quad (2.2)$$

For convenience we define the following normalized variables:

$$\begin{cases} b & \triangleq \beta L/2, \\ l & \triangleq k_0 L/2, \\ a & \triangleq \alpha L/2, \\ t(\theta) & \triangleq b - l \cos \theta, \end{cases} \quad (2.3)$$

so that, the power distribution  $P(\theta) = |R(\theta)|^2$ , given by the modulus squared of Eq. (2.2) can be rewritten with a more compact notation as follows:

$$P(\theta) = \frac{\sin^2 t(\theta) \cosh^2 a + \cos^2 t(\theta) \sinh^2 a}{t^2(\theta) + a^2}, \quad (2.4)$$

Using the fundamental trigonometric identities (viz.,  $\cos^2 x + \sin^2 x = 1$  and  $\cosh^2 x - \sinh^2 x = 1$ , respectively) we can further simplify our expression:

$$\begin{aligned} P(t) &= \frac{\sin^2 t(\theta) [1 + \sinh^2 a] + \cos^2 t(\theta) \sinh^2 a}{t^2(\theta) + a^2} \\ &= \frac{\sinh^2 a [\cos^2 t(\theta) + \sin^2 t(\theta)] + \sin^2 t(\theta)}{t^2(\theta) + a^2} \\ &= \frac{\sin^2 t(\theta) + \sinh^2 a}{t^2(\theta) + a^2}. \end{aligned} \quad (2.5)$$

Since we are interested in evaluating the HPBW, it is more convenient to have an expression for the normalized power distribution  $\bar{P}(\theta) = P(\theta)/P(\theta_0)$  where the pointing angle  $\theta_0$  is given by Eq. (1.18) which is equivalent to

$$b = l \cos \theta_0, \quad (2.6)$$

through Eq. (2.3). Equation (1.18) and in turn Eq. (2.6) are usually regarded as being approximate. However, it can be shown that this formula for the pointing angle is actually exact as long as  $\beta \leq k_0$  (see the Appendix A for a proof of this). Using Eq. (2.6) we get

$$P(\theta_0) = \sinh^2 a / a^2, \quad (2.7)$$

and thus  $\bar{P}(\theta)$  is equal to

$$\bar{P}(\theta) = \frac{1 + \sin^2 t(\theta) / \sinh^2 a}{1 + t(\theta)^2 / a^2}. \quad (2.8)$$

At this stage, we can find an expression for the HPBW. In mathematical terms, we are seeking for

$$\Delta\theta_h; \quad P(\theta_0 + \Delta\theta_h) = \frac{1}{2}P(\theta_0), \quad (2.9)$$

where  $\Delta\theta_h$  is the *single-sided* HPBW. From Eqs. (2.8) and (2.9) it is possible to get an equation

$$\frac{1 + \sin^2[t(\theta_0 + \Delta\theta_h)] / \sinh^2 a}{1 + [t(\theta_0 + \Delta\theta_h)]^2 / a^2} = \frac{1}{2}, \quad (2.10)$$

that relates  $b, l, a$  and  $\Delta\theta_h$ . It is now convenient to define the variable  $t_h$  as

$$t_h \triangleq t(\theta_0 + \Delta\theta_h) = b - l \cos(\theta_0 + \Delta\theta_h), \quad (2.11)$$

so that Eq. (2.10) can easily be recast as

$$\left(\frac{t_h}{a}\right)^2 - 2\left(\frac{\sin t_h}{\sinh a}\right)^2 - 1 = 0. \quad (2.12)$$

The left-hand side of Eq. (2.12) is a function of two variables  $f(a, t_h)$  whose roots, as stated by *Dini's Theorem* (see Section 1.2.4) define an implicit function  $t_h(a)$ . The search for an approximate explicit function will be given in the next Subsection 2.2.2. Once such an expression is found, it is straightforward to find a closed-form expression for  $\Delta\theta_h$  in terms of  $b, l$ , and  $a$ . In particular, rearranging the terms of Eq. (2.11) yields

$$\Delta\theta_h = \arccos\left(\frac{b - t_h(a)}{l}\right) - \theta_0, \quad (2.13)$$

which is the sought general formula<sup>1</sup> for the HPBW of 1-D unidirectional LWAs, obtained without any restricting assumption. This formula is exact and makes no approximations.

When  $\Delta\theta_h \ll \theta_0$  (i.e., the HPBW is much less than the pointing angle) it is possible to find an approximate expression by rearranging the terms of Eq. (2.11),

$$\begin{aligned} t_h &= b - l \cos \theta_0 \cos \Delta\theta_h - l \sin \theta_0 \sin \Delta\theta_h \\ \lim_{\Delta\theta_h \rightarrow 0} t_h &= b - l \cos \theta_0 + l \sin \theta_0 \Delta\theta_h, \end{aligned}$$

and using Eq. (2.6):

$$\Delta\theta_h \simeq \frac{t_h(a) \csc \theta_0}{l}, \quad (2.14)$$

which is very similar to the original expressions proposed by Oliner, i.e., Eqs. (1.19) and (1.20). Indeed, it can easily be shown that when  $t_h(a)$  is evaluated for the limiting case of an infinitely long antenna ( $L \rightarrow \infty$  and in turn  $a \rightarrow \infty$ ), Eq. (2.14) gives the same result of Eq. (1.19) (we note here that  $\text{HPBW} = 2\Delta\theta_h$ ):

$$\lim_{a \rightarrow \infty} \Delta\theta_h \simeq \frac{\alpha}{k_0} \csc \theta_0. \quad (2.15)$$

<sup>1</sup> We note here that  $b, a$ , and  $l$  are directly related to  $\beta, \alpha$ , and  $L$  through Eq. (2.3).

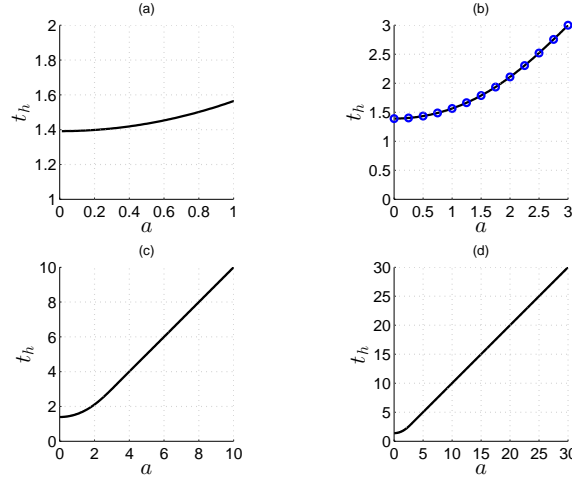


**Figure 2.1.:**  $t_h$  vs.  $a$  calculated numerically (black solid lines). The behavior of  $t_h$  has been reported for (a)  $0 \leq a \leq 1$ , (b)  $0 \leq a \leq 3$ , (c)  $0 \leq a \leq 10$ , and (d)  $0 \leq a \leq 30$ . In (b)  $t_h$  has been fit with a cubic spline curve (blue circles).

Conversely, when  $t_h(a)$  is evaluated for the limiting case of a constant (i.e., non-attenuated) aperture distribution ( $a \rightarrow 0$ ), Eq. (2.14) gives the same result of Eq. (1.20) (we note here that  $L/\lambda = l/\pi$ , and  $N_O = 0.88$  for  $a \rightarrow 0$ ):

$$\lim_{a \rightarrow 0} \Delta\theta_h \simeq \frac{0.88}{2l/\pi} \csc \theta_0. \quad (2.16)$$

As a matter of fact, when  $a \rightarrow \infty$  Eq. (2.12) reduces to  $t_h = a$  and thus Eq. (2.14) corresponds to Eq. (2.15), whereas when  $a \rightarrow 0$  Eq. (2.12) reduces to  $t_h = \sqrt{2} \sin t_h$ . This equation can be solved straightforwardly with an easy fixed-point iteration method. After few steps the root search converges to the value  $t_h \simeq 1.3915 \simeq 0.886\pi/2$  and thus Eq. (2.14) corresponds to Eq. (2.16) with good accuracy. A detailed explanation of Oliner results is postponed to Section 2.2.4.

Since the function  $t_h(a)$  plays a key-role in both Eqs. (2.13) and (2.14), the following Subsection 2.2.2 is devoted to the search of an approximate explicit form for  $t_h(a)$  by means of a fitting procedure to describe the roots defined by Eq. (2.12).

## 2.2.2 Fitting procedure

In the previous paragraph we have seen that for large arguments of  $a$   $t_h(a)$  is almost linear with  $a$  ( $t_h \simeq a$ ), whereas for small arguments of  $a$ ,  $t_h(a)$  is almost constant ( $t_h(a) \simeq 1.3915$ ). However, for arbitrary values of  $a$  Eq. (2.12) needs to be solved. The numerical solution (a simple secant method has been used) gives the curve reported in Fig. 2.1 for different ranges of  $a$ . As can be seen, the curve is an almost perfectly linear function for large values of  $a$ , whereas it is almost constant for small values of  $a$ , as previously predicted. However, it could be interesting to find an approximate closed-

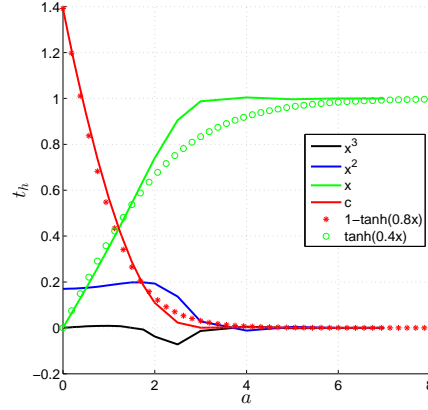


Figure 2.2.: Evolution of the third-order polynomial coefficients of the spline interpolation.

form expression which could fit this unknown function for intermediate values of  $a$ .

From now on, the analysis of Eq. (2.12) will be limited to the restricted range of  $a \in \{0, 3\}$ . This choice is motivated by the following consideration. As is known [11], the radiation efficiency of LWAs is given by the simple expression:

$$e_r = 1 - e^{-2\alpha L} = 1 - e^{-4a}. \quad (2.17)$$

Practical LWAs would not reach efficiencies higher than 95%. Hence, we can safely limit our discussion to values of  $a$  comprised in the range  $a \in \{0, 3\}$  at which corresponds, through Eq. (2.17), the following range of efficiencies  $e_r[\%] \in \{0, 99.9994\}$ . In this new light, we can try to fit the zeros of Eq. (2.12).

In order to find a suitable fitting function, we have fit the data with different types of interpolating functions. As a first trial, we have fit the data with a *cubic spline* interpolation curve over an extended range  $0 \leq a \leq 8$  (see Fig. 2.1). Since the cubic spline is a piecewise cubic polynomial of the form  $a_3x^3 + a_2x^2 + a_1x + a_0$ , the evolution of the coefficients for each segment has been reported in Fig. 2.2 to gain more insights about the behavior of this function. In fact, a thorough analysis of Fig. 2.2 would allow for understanding which polynomial term is dominant in each region, and also what kind of function would suitably describe this behavior. We recall here that the spline approximation, being a piecewise polynomial, does not allow for a simple closed-form expression.

In particular, Fig. 2.2 revealed us that the quadratic and the cubic terms are almost negligible with respect to the constant and the linear ones<sup>2</sup>. Moreover, the constant term seems to be *deactivated* by a sigmoid function

<sup>2</sup> Actually, the quadratic term is not negligible at all. However, the aim of the fitting is to take an expression as simple as possible, thus, we neglect the effect of this term. Nevertheless, it is possible to take it into account (with a consequent higher complexity in the final expression) using a sigmoid function like those used for the linear and the constant term. This analysis goes beyond the scope of our analysis, and thus has been omitted.

whose behavior resembles that of a *complementary hyperbolic tangent* function  $1 - \tanh(\cdot)$ , whereas the linear term is *activated* by a sigmoid function whose behavior resembles that of a *hyperbolic tangent* function  $\tanh(\cdot)$  (see Fig. 2.2). As a result, the following relevant interpolating functions have been considered:

- a) The *hyperbolic tangent function* (HTF) fitting with one degree of freedom:  $f(x) = d + x \tanh(p_1 x)$ .
- b) The *hyperbolic tangent exponential function* (HTEF) fitting with two degrees of freedom:  $f(x) = d + x \tanh^{q_2}(p_2 x)$ .
- c) The *mixed hyperbolic tangent function* (MHTF) fitting with two degrees of freedom:  $f(x) = d(1 - \tanh(q_3 x)) + x \tanh(p_3 x)$ .
- d) The *mixed hyperbolic tangent exponential function* (MHTEF) fitting with three degrees of freedom:  $f(x) = d(1 - \tanh(q_4 x)) + x \tanh^{r_4}(p_4 x)$ .
- e) The *mixed hyperbolic tangent exponential function* (MHTMEF) fitting with four degrees of freedom:  $f(x) = d(1 - \tanh(q_5 x))^{s_5} + x \tanh^{r_5}(p_5 x)$ .

where  $p_1$  and  $q_1$ , and  $p_2, q_2, r_2$  and  $s_2$  are the fitting parameters, whereas  $d = 1.3915$  is found through the spline interpolation when  $a \rightarrow 0$  (see Fig. 2.2) and coincides with the value previously obtained for the numerical solution of Eq. (2.12) in the limit  $a \rightarrow 0$ .

As can be seen, the HTF takes into account the activation of the linear term by means of a sigmoid function ( $\tanh(\cdot)$ ), whereas the MHTF takes into account also the deactivation of the constant term by means of a complementary sigmoid function ( $1 - \tanh(\cdot)$ ). This would allow for catching the asymptotic behavior of  $t_h(a)$ . The HTEF and MHTEF, MHTMEF, simply add further degrees of freedom to the HTF and the MHTF functions, respectively.

Relevant results have been reported in Figs. 2.3, 2.4 and Table 2.1. In particular, in Fig. 2.4(a) the behavior of the approximations for large arguments ( $80 \leq a \leq 100$ ) has been reported to check the asymptotic behavior of the fitting functions. As can be seen, even if they all predict the correct asymptotic behavior (dashed green lines and solid blue lines are overlapped as well as the yellow circles and solid cyan lines) with sufficient accuracy, only the MHTF exactly approaches the oblique asymptote given by  $t_h \simeq a$ .

The values of the fitting parameters (see Table 2.2) have been found after refining the interpolation formulas in 25 equispaced points in the considered range, using a weighted least squares (WLS) method [67]. The exact value

Table 2.1.: MAPE for HTF, HTEF, MHTF, MHTEF, MHTMEF and spline approximations.

function	HTF	HTEF	MHTF	MHTEF	MHTMEF	spline
MAPE [%]	0.84	0.19	0.48	0.075	0.074	$< 10^{-5}$



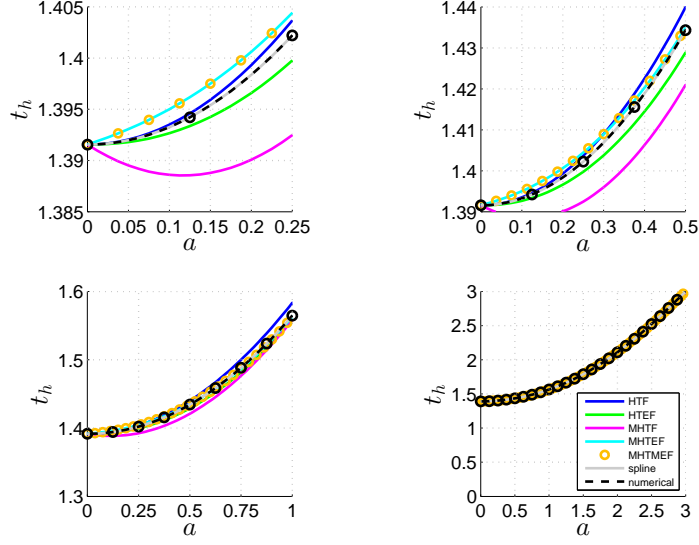


Figure 2.3.: Comparison of data fitting of  $t_h$  vs.  $a$  by means of different fitting functions in the range  $0 \leq a \leq 0.25$  (top-left corner),  $0 \leq a \leq 0.5$  (top-right corner),  $0 \leq a \leq 1$  (bottom-right corner), and  $0 \leq a \leq 3$  (bottom-left corner).

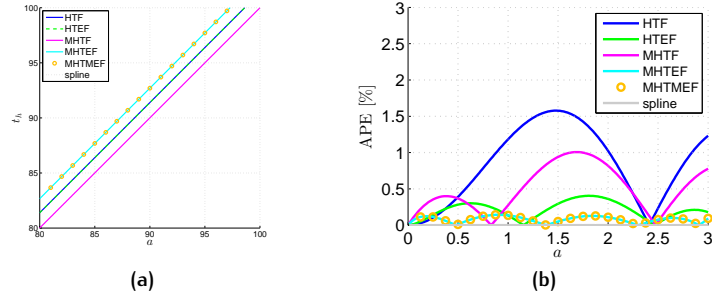


Figure 2.4.: (a) Asymptotic behavior of  $t_h$  vs.  $a$  for the various fitting functions in the range  $0 \leq a \leq 3$ . (b) Absolute percent error (APE) vs.  $a$  of the various fitting functions in the range  $0 \leq a \leq 3$ .

of the fitting parameters will depend on the weighting function used in the WLS method, and the values suggested in Table 2.2 have been found after some numerical experimentations.

Hence, in the next paragraphs we will show results for: *i*) MHTMEF which shows the lowest mean absolute percent error (MAPE  $\simeq 0.07\%$ ), and *ii*) MHTF which catches the correct asymptotic behavior and shows a moderate MAPE  $\simeq 0.48\%$  (see Table 2.1).

For readability purposes, we refer to MHTF and MHTMEF with the acronyms  $F_1$  and  $F_2$ , respectively.

$$F_1 : t_h(a) = d(1 - \tanh(q_1 a)) + a \tanh(p_1 a), \quad (2.18)$$

$$F_2 : t_h(a) = d(1 - \tanh(q_2 a))^{s_2} + a \tanh^{t_2}(p_2 a), \quad (2.19)$$

**Table 2.2.:** Values of the fitting parameters for HTF, HTEF, MHTF, MHTEF, and MHTMEF functions.

function	$p_i$	$q_i$	$r_i$	$s_i$
HTF	0.194	none	none	none
HTEF	0.220	1.159	none	none
MHTF	0.208	0.021	none	none
MHTEF	0.229	-0.020	1.301	none
MHTMEF	0.227	-0.015	1.301	1.320

With regard to the beamwidth formula, we choose the  $F_1$  because of its simplicity. In fact, using Table 2.2, the explicit expression for  $t_h(a)$  becomes:

$$t_h(a) = 1.3915(1 - \tanh(0.021a)) + a \tanh(0.21a). \quad (2.20)$$

Thus, Eq. (2.13) combined with Eq. (2.20) defines the sought general formula for the evaluation of the beamwidth in terms of the leakage rate, the length of the antenna, and the pointing angle. Therefore, the final formula for the single-sided beamwidth takes the following form:

$$\Delta\theta_h = \arccos\left(\frac{b - 1.3915[1 - \tanh(0.021a)]}{l} - \frac{a \tanh(0.21a)}{l}\right) - \theta_0. \quad (2.21)$$

### 2.2.3 Numerical results

The following acronyms will be adopted throughout this Section: eBW (exact beamwidth) and aBW (approximate beamwidth) refer to the use of Eqs. (2.13) and (2.14), respectively, when the exact value of  $t_h$  is used (found from Eq. (2.12)). The term eF<sub>*i*</sub>BW,  $i \in \{1, 2\}$  (exact fit beamwidth) refers to the approximate analytical formulas for  $\Delta\theta_h$  obtained by means of either  $F_1$  (for  $i = 1$ ) or  $F_2$  (for  $i = 2$ ) for the approximation of  $t_h$  in Eq. (2.13).

Numerical results are shown for comparing the performance of eBW equation with aBW equation for  $l = 2\pi, 10\pi, 20\pi$ , and  $100\pi$ . This would correspond, through the well-known relation  $k_0 = 2\pi/\lambda$  and definitions of Eq. (2.3), to antenna lengths of  $L = 2\lambda, 10\lambda, 20\lambda$ , and  $100\lambda$ . In particular, the single-sided beamwidth  $\Delta\theta_h$  is reported as a function of the efficiency  $e_r$  (note that  $e_r$  is related to  $a$  through Eq. (2.17)) for different pointing angles  $\theta_0 = 5^\circ, 15^\circ, 45^\circ, 90^\circ$  in Fig. 2.5, and as a function of the pointing angle  $\theta_0$  for different efficiencies  $e_r = 50\%, 75\%, 90\%, 99\%$  in Fig. 2.6.

It is worth to stress here that the aBW equation coincides with Oliner's formula in the limit of large  $e_r$ . Therefore, the comparison between aBW and eBW should reveal the need of a new formula for the correct prediction of the beamwidth when  $\theta_0$  is close to endfire, especially for large values of  $e_r$  and small values of  $L$ . Note also that the comparison between aBW

and eBW does not introduce any error from the fitting formulas  $F_1$  and  $F_2$ , proposed in Eqs. (2.18) and (2.19).

As expected,  $\Delta\theta_h$  decreases as  $L$  and  $\theta_0$  increase. In Fig. 2.5, it is also evident that  $\Delta\theta_h$  slowly increases when  $e_r$  increases as long as  $e_r < 90\%$  and provided that  $\theta_0$  is not too small, whereas in Fig. 2.6 the divergence of the aBW formula when  $\theta_0$  approaches endfire ( $\theta_0 = 0$ ) is clearly shown. In Fig. 2.5 the aBW (in circles) is in practice overlapped with the eBW (solid line) only for broadside (in blue) and  $\theta_0 = 45^\circ$  (in green). Furthermore, in Fig. 2.6 it is noticed that the agreement between the eBW and the aBW formulas improves as  $\theta_0$  increases.

This behavior can be further highlighted by evaluating the absolute percent error (APE) defined as  $100 \cdot |aBW - eBW| / |eBW|$ . For the sake of completeness, in Figs. 2.7 and 2.8, the APE is reported for the same cases in Figs. 2.5 and 2.6. The agreement is good as long as  $\theta_0 > \theta_m(L)$ , where  $\theta_m$  is the minimum angle for which an ‘acceptable’ agreement between the aBW and the eBW (APE is less than 5%) is guaranteed. It is seen that  $\theta_m$  is approximately equal to  $\theta_m = 65^\circ, 35^\circ, 25^\circ, 10^\circ$  for  $L = 2\lambda, 10\lambda, 20\lambda, 100\lambda$ , respectively, for all the efficiencies (see the dashed black lines).

A different way to represent this result is reported in Fig. 2.9 where the APE between aBW and eBW has been plotted as a contour plot of a two-valued function of  $e_r$  and  $\theta_0$  for  $L = 2\lambda, 10\lambda, 20\lambda$ , and  $100\lambda$ . This representation clearly reveals that the APE is almost constant with respect to the efficiency (except for very high efficiencies), but highly depends on  $\theta_0$ , abruptly increasing as the pointing angle exceeds  $\theta_m(L)$ . Finally, the APE defined as  $100 \cdot |eF_1BW - eBW| / |eBW|$  has been reported in Figs. 2.10(a)

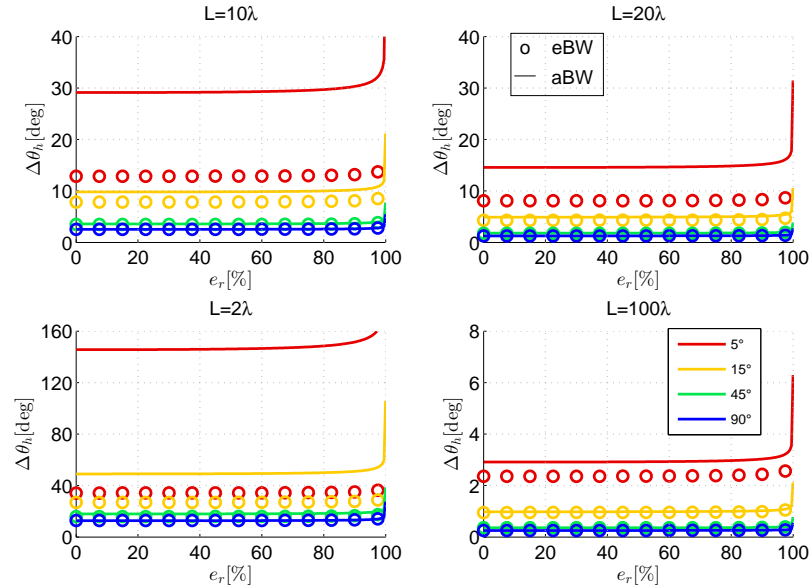


**Figure 2.5.:**  $\Delta\theta_h$  vs.  $e_r$  for  $\theta_0 = 5^\circ, 15^\circ, 45^\circ, 90^\circ$  (in order in red, yellow, green, blue) Comparison between aBW (in solid lines) and eBW (in circles) results for the evaluation of  $\Delta\theta_h$  for  $L = 10\lambda$  (top-left corner),  $L = 20\lambda$  (top-right corner),  $L = 2\lambda$  (bottom-left corner),  $L = 100\lambda$  (bottom-right corner).

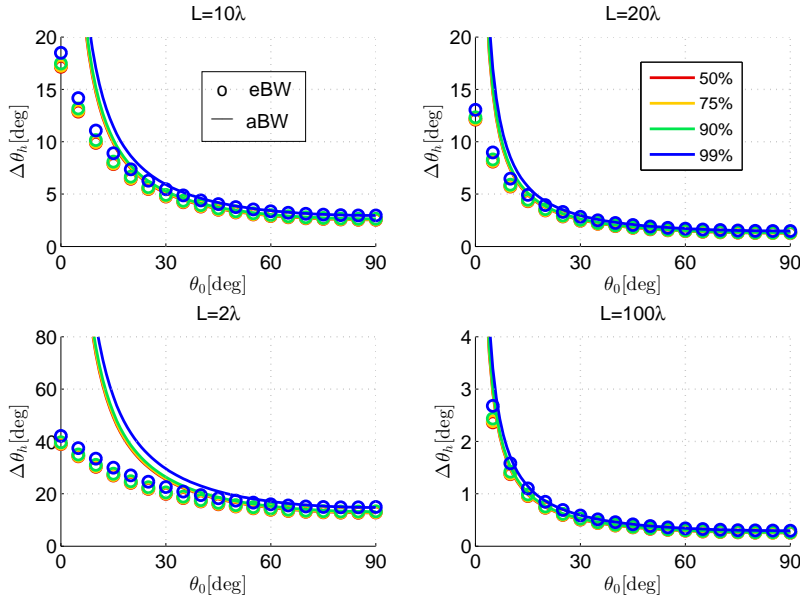


Figure 2.6.:  $\Delta\theta_h$  vs.  $\theta_0$  for  $e_r = 50\%, 75\%, 90\%, 99\%$  (in order in red, yellow, green, blue). Comparison between aBW (in solid lines) and eBW (in circles) results for the evaluation of  $\Delta\theta_h$  for  $L = 10\lambda$  (top-left corner),  $L = 20\lambda$  (top-right corner),  $L = 2\lambda$  (bottom-left corner),  $L = 100\lambda$  (bottom-right corner).

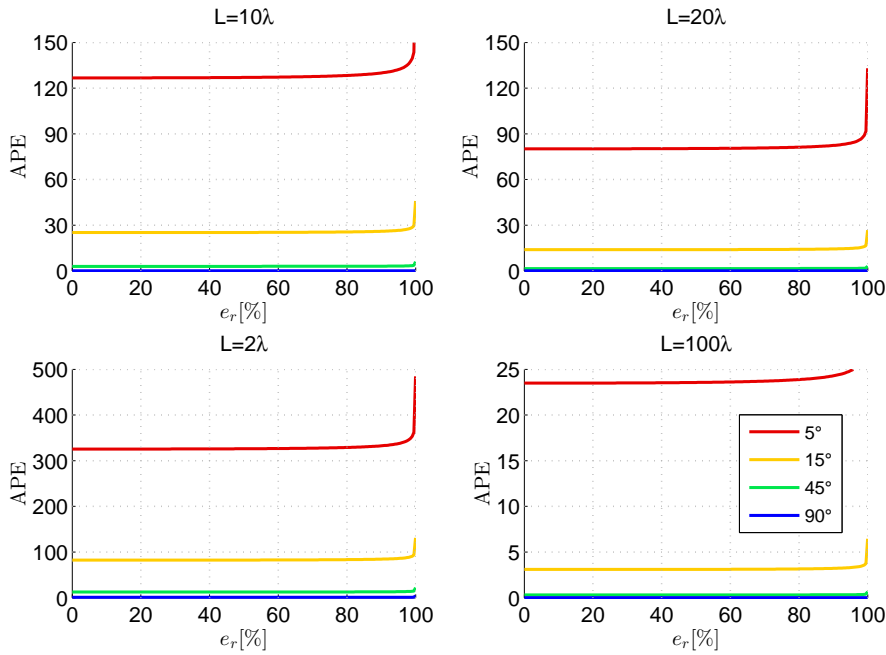


Figure 2.7.: APE (calculated as  $100 \cdot |aBW - eBW| / |eBW|$ ) vs.  $e_r$  for  $\theta_0 = 5^\circ, 15^\circ, 45^\circ, 90^\circ$  (in order in red, yellow, green, blue) for  $L = 10\lambda$  (top-left corner),  $L = 20\lambda$  (top-right corner),  $L = 2\lambda$  (bottom-left corner),  $L = 100\lambda$  (bottom-right corner).

and (b) for  $L = 10\lambda$  in order to assess the accuracy of both the  $F_1$  and  $F_2$  formulas. (Only one result is shown since the accuracy of the fitting procedure is almost independent on  $L$ .) As shown, both the  $F_1$  and  $F_2$  results exhibit a

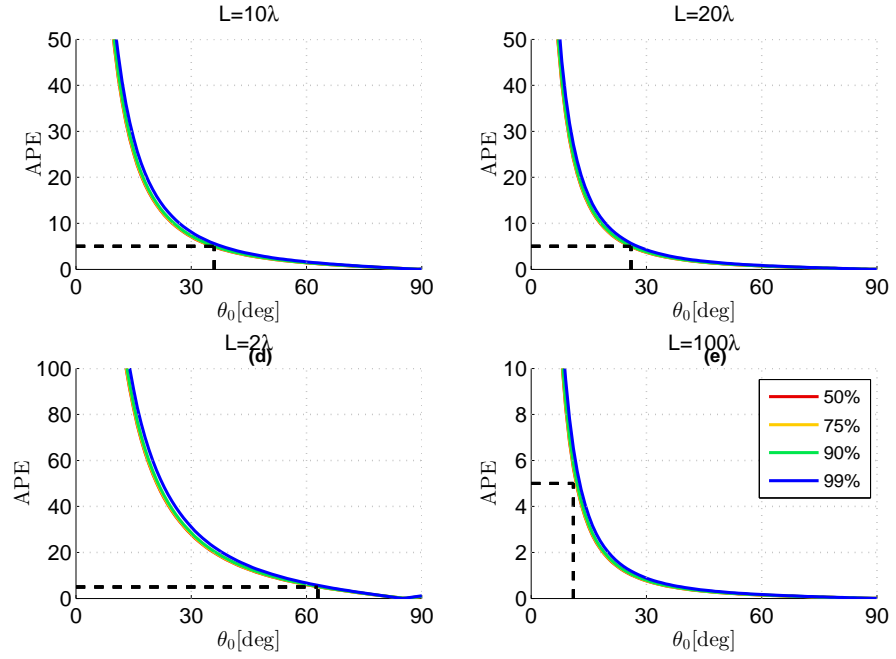


Figure 2.8.: APE vs.  $\theta_0$  for  $e_r = 50\%$ ,  $75\%$ ,  $90\%$ ,  $99\%$  (in order in red, yellow, green, blue) for  $L = 10\lambda$  (top-left corner),  $L = 20\lambda$  (top-right corner),  $L = 2\lambda$  (bottom-left corner),  $L = 100\lambda$  (bottom-right corner). In black dashed lines the location of  $\theta_m$  defined as the minimum  $\theta_0$  for which the APE is less than 5%.

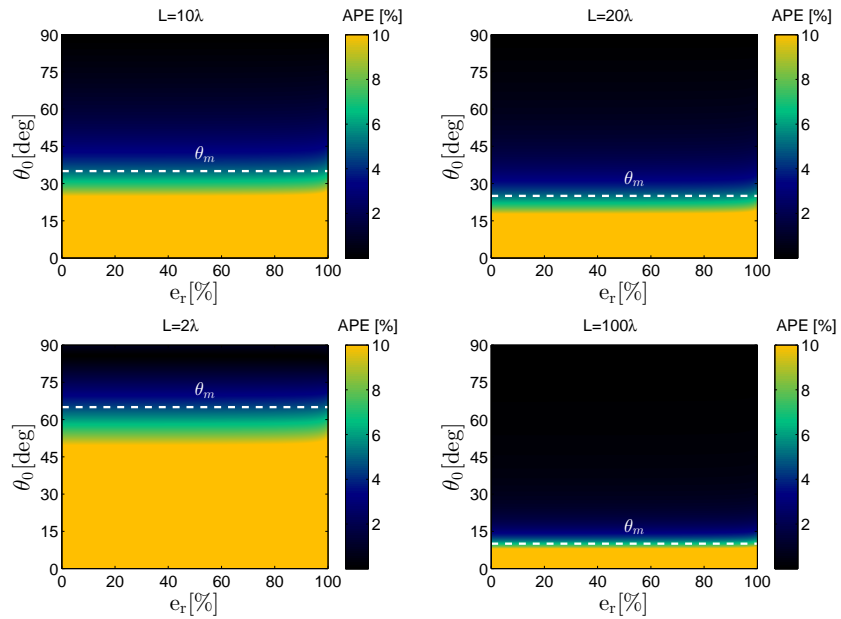


Figure 2.9.: APE (calculated as  $100 \cdot |aBW - eBW| / |eBW|$ ) vs.  $\theta_0$  and  $e_r$ . White dashed lines highlight the boundaries set by  $\theta_m$ .

maximum APE usually lower than  $0.5\%$  and  $0.1\%$ , respectively (see also the considerations on the error in 2.2.2). Figure 2.10(a) shows that the accuracy of both  $F_1$  and  $F_2$  slightly depends on  $\theta_0$ , being the APE a slowly-increasing

function of  $\theta_0$ . Interestingly, the dependence on  $e_r$  is quite different for the  $F_1$  and  $F_2$  as revealed by Fig. 2.10(b). In particular, both  $F_1$  and  $F_2$  exhibit multiple local maxima and minima with respect to  $e_r$ . However, the global maximum for  $F_1$  is lower than 0.8% and is attained for  $e_r = 99.9994\%$  which is already an unfeasible value for any 1-D LWA. Note that the APE of the  $F_1$  result does not diverge for  $e_r \rightarrow 100\%$  as might appear from the plot with the scale shown, since its asymptotic behavior is correct as shown in 2.2.2 (see Fig. 2.4(a)).

It is also worth to remark that the location of the maxima and minima for the  $F_1$  and the  $F_2$  function merely depends on the choice of the weights in the WLS method [67] used for retrieving the fitting parameters. However, for any choice of the weights the resulting MAPE would be almost the same. Here, our choice has led to an acceptable trade-off among the location of the maximum APE and the value of the MAPE. Nevertheless, an optimum choice of the weights in order to minimize the variance of the APE with respect to  $e_r$  is worth of being investigated, but it is beyond the scope of this PhD thesis.

For the sake of completeness, in Fig. 2.11 the APE between e $F_1$ BW and eBW for  $L = 2\lambda, 10\lambda, 20\lambda,$  and  $100\lambda$  has been reported as has been done in Fig. 2.9 for the APE between aBW and eBW. Figure 2.11 confirms that the antenna length  $L$  has a negligible effect on the fitting procedure. Also, it is noted that, except for  $e_r \rightarrow 100\%$ , in the region of worst approximation (around  $65\% < e_r < 85\%$ ) the APE never exceeds 0.4%.

As a final comment, it is noted that the improvement of the accuracy given by the  $F_2$  formula is paid at the expense of a more complicated expression for  $\Delta\theta_h$ . Thus, for applications in which an accuracy of the order of 0.5% for the beamwidth evaluation is acceptable, the  $F_1$  function is a good choice.

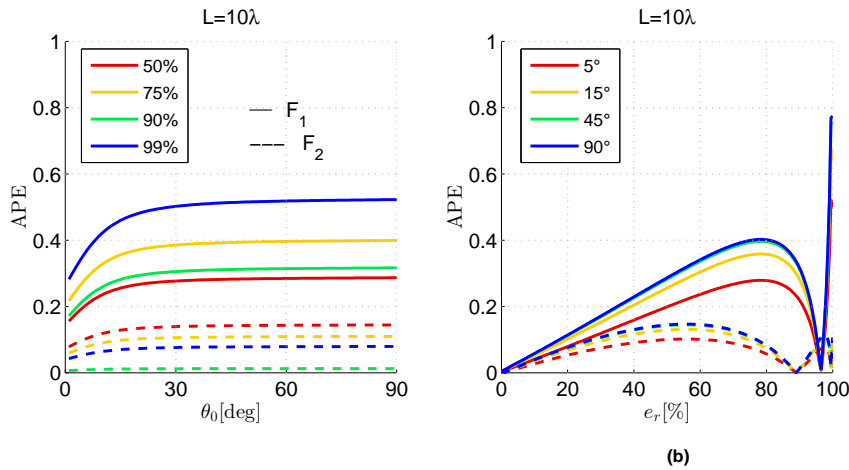


Figure 2.10.: (a) APE (calculated as  $100 \cdot |eF_1BW - eBW| / |eBW|$ ) vs.  $\theta_0$  for  $e_r = 50\%, 75\%, 90\%, 99\%$  (in order in red, yellow, green, blue) and (b) APE vs.  $e_r$  for  $\theta_0 = 5^\circ, 15^\circ, 45^\circ, 90^\circ$  (in order in red, yellow, green, blue). The e $F_1$ BW is calculated using either the  $F_1$  (solid lines) or the  $F_2$  (dashed lines) formulas. Results are shown only for  $L = 10\lambda$ .

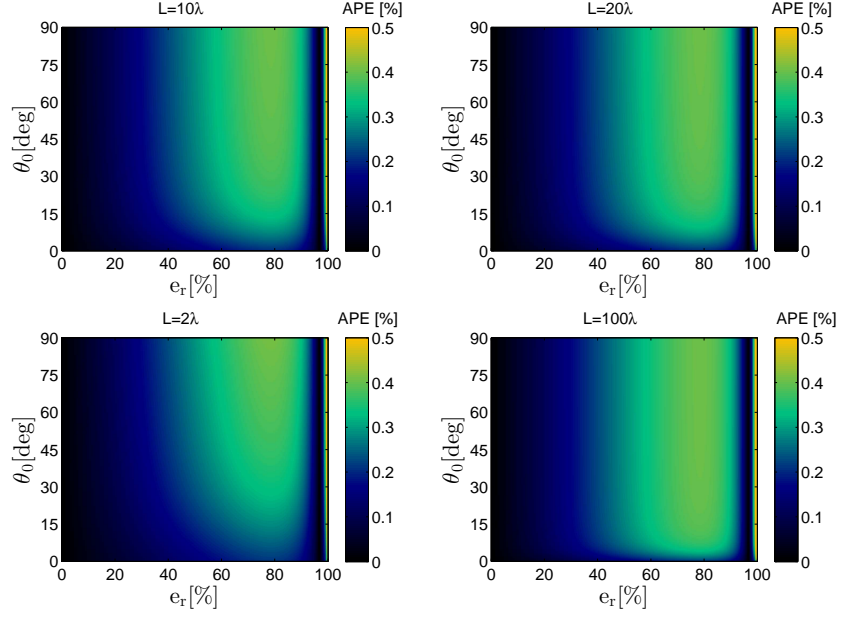


Figure 2.11.: APE (calculated as  $100 \cdot |eBW - eF_1BW|/|eBW|$ ) vs.  $\theta_0$  and  $e_r$ .

#### 2.2.4 Comparison with Oliner's formula

In this paragraph, we aim to compare our results with those obtained by Oliner (see 1.3.2). There, the beamwidth HPBW was estimated with Eq. (1.20) that we report here for convenience (from now on referred as Oliner Beamwidth or OBW):

$$\text{HPBW} = \frac{N_O}{(L/\lambda) \sin \theta_0}, \quad (2.22)$$

where  $N_O$  is a factor that, according to Oliner, depends on both  $a$  and  $l$ . Note that there is still no demonstration about the nature of the values assumed by  $N_O$ . Here, we will prove how such values can easily be determined through Eq. (2.14). We start by expressing Eq. (2.22) in the following manner:

$$\Delta\theta_h = \frac{\pi N_O}{2l \sin \theta_0}, \quad (2.23)$$

so that  $N_O$ :

$$N_O = \frac{2\Delta\theta_h l \sin \theta_0}{\pi} \simeq 2 \frac{t_h}{\pi}. \quad (2.24)$$

Now, for a constant aperture distribution we can simply consider the expression of  $t_h$  for small arguments ( $a \rightarrow 0$ , and in turn  $e_r \rightarrow 0$ ) which is given by Eq. (2.15) and yields  $t_h = 1.3915$  at which corresponds  $N_O = 0.886$  that is in very good agreement with the value suggested by Oliner (viz., 0.88 see 1.3.2). For a leaky-wave distribution such that  $e_r = 0.9$  we have (through Eq. (2.17))  $a = 4 \ln(1/1 - e_r) \simeq 0.5756$ . If we put this value in one of our fitting functions, e.g.  $F_1$ , we get  $t_h \simeq 1.456$  at which corresponds  $N_O = 0.927$  that is again in good agreement with the value suggested by Oliner (viz., 0.91 see

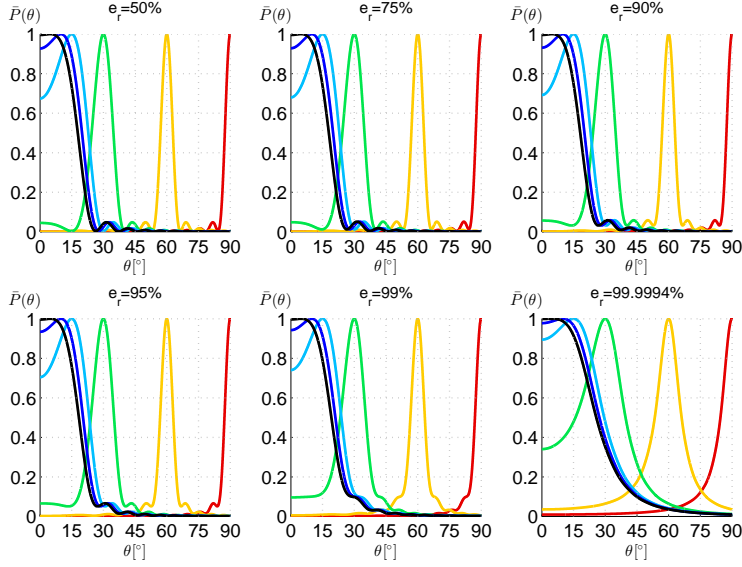


Figure 2.12.:  $\bar{P}(\theta)$  vs.  $\theta$  (in linear scale) for different values of  $\theta_0$  and  $e_r$ .

1.3.2). However, these empirical values (obtained for  $L = 10\lambda$ ) are accurate as long as we are not approaching endfire. Also, Oliner chose  $N_O = 1$  as a middle-of-the-range result [13], probably considering efficiencies up to 99.99%. In fact, it will readily be shown that, when higher efficiencies are considered, the factor  $N_O$  should be further increased. To this purpose, in Table 2.3 we have reported the value of  $N_O$  given by Eq. (2.24) when  $\Delta\theta_h$  is given by the eF<sub>1</sub>BW for  $e_r \in \{50\%, 75\%, 90\%, 95\%, 99\%, 99.9994\}$  and  $\theta_0 \in \{90^\circ, 60^\circ, 30^\circ, 15^\circ, 10^\circ, 5^\circ\}$  for  $L = 10\lambda^3$ .

Also, in Fig. 2.12 the corresponding radiation patterns for the cases analyzed in Table 2.3 have been reported for verifying the consistency of the results. As is seen, when the pointing angle approaches endfire ( $\theta_0 = 0$ ), the standard definition of beamwidth loses sense, since the left side of the mainlobe may not go down  $-3$  dB. In this case, the double-sided beamwidth (HPBW) is no longer given by the double of the single-sided beamwidth ( $\Delta\theta_h$ ). Actually, in this case a general definition of HPBW still lacks. One

<sup>3</sup> Note that for  $\theta_0 = 0$ , Eq. (2.24) becomes meaningless.

Table 2.3.: Values of  $N_O$  to have the exact beamwidthth evaluation.

$e_r$ [%] \ $\theta_0$ [°]	90	60	30	15	10	5
50	0.8899	0.8771	0.8308	0.7102	0.5997	0.3918
75	0.9010	0.8879	0.8405	0.7176	0.6053	0.3949
90	0.9269	0.9131	0.8632	0.7348	0.6184	0.4022
95	0.9550	0.9404	0.8876	0.7532	0.6324	0.4099
99	1.0474	1.0298	0.9674	0.8126	0.6775	0.4348
99.9994	1.8933	1.8376	1.6600	1.2990	1.0359	0.6274



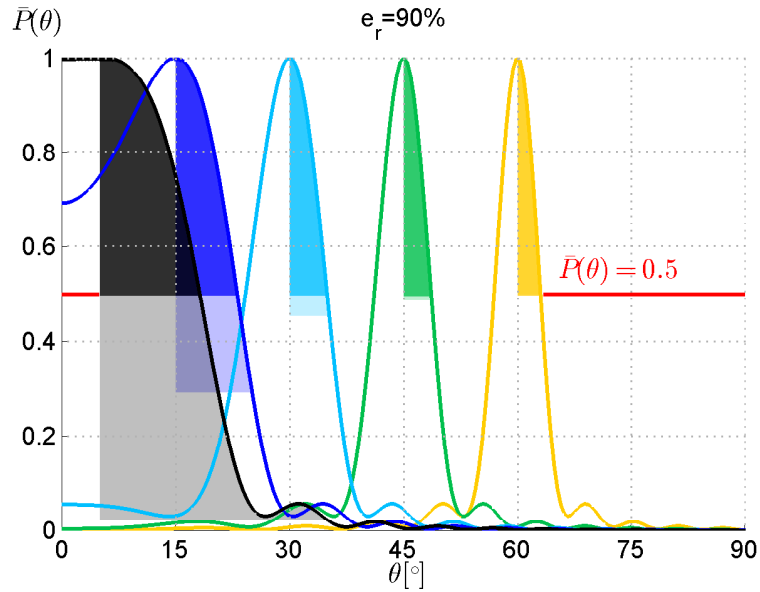


Figure 2.13:  $\bar{P}(\theta)$  vs.  $\theta$  (in linear scale) for different values of  $\theta_0$  when  $e_r = 90\%$ . Lighter colored region represent the estimation of the single-sided beamwidth when using Oliner's formula. The red solid line is reported for helping the reader to find the half-power value value.

possibility is to calculate the value of the normalized power distribution at endfire ( $\bar{P}(0)$ ); if this value is less than 0.5 we can still use  $\text{HPBW} = 2\Delta\theta_h$  as a very good estimation of the double-sided beamwidth, otherwise we can take  $\text{HPBW} = \theta_0 + \Delta\theta_h$  as a reasonable estimation of the beamwidth<sup>4</sup>. In other words:

$$\text{HPBW} = \begin{cases} 2\Delta\theta_h & \text{if } \bar{P}(0) < 1/2 \\ \theta_0 + \Delta\theta_h & \text{elsewhere,} \end{cases} \quad (2.25)$$

where  $\bar{P}(0)$  can simply be evaluated once  $b$ ,  $a$ , and  $l$  are known:

$$\bar{P}(0) = \frac{\sin^2(b-l) + \sinh^2 a}{(b-l)^2 + a^2}. \quad (2.26)$$

However, the definition of a single-sided beamwidth  $\Delta\theta_h$  as the one defined by the eF<sub>1</sub>BW (Eq. 2.21) still holds. This result has been highlighted in Fig. 2.13 for  $\theta_0 \in \{60^\circ, 45^\circ, 30^\circ, 15^\circ, 5^\circ\}$  when  $e_r = 90\%$  and  $L = 10\lambda$ . In this case, we know that according to Oliner,  $N_O = 0.91$ . Hence, we have calculated  $\Delta\theta_h$  using the OBW formula for  $N_O = 0.91$  (see lightly colored areas in Fig. 2.13) and compared with the eBW prediction (see fully colored areas in Fig. 2.13). As we expected, the accuracy of the OBW formula breaks down as  $\theta_0$  approaches to endfire, whereas the eF<sub>1</sub>BW always predicts the correct  $\Delta\theta_h$ .

<sup>4</sup> Note that, in practical cases, beyond the endfire there would be the ground plane.

**Table 2.4.:** Evaluation of OBW, eBW and APE in the range  $5^\circ \leq \theta_0 \leq 90^\circ$  for  $e_r = 90\%$  and antenna lengths  $L = 10\lambda$  and  $L = 20\lambda$ .

L	Method	$\theta_p [^\circ]$					
		90	60	30	15	10	5
10 $\lambda$	OBW [°]	2.61	3.01	5.21	10.07	15.01	29.91
	eBW [°]	2.64	3.01	4.92	8.09	10.16	13.18
	APE [%]	1.34	0.15	5.91	24.36	47.70	126.99
20 $\lambda$	OBW [°]	1.30	1.50	2.61	5.04	7.51	14.96
	eBW [°]	1.32	1.51	2.54	4.46	5.90	8.31
	APE [%]	1.31	0.56	2.46	12.92	27.30	80.00

This result is quantitatively summarized in Table 2.4, where the single-sided beamwidth has been calculated with the same parameters of Fig. 2.13 but for two practical antenna lengths (namely,  $L = 10\lambda$  and  $L = 20\lambda$ ) when  $e_r = 90\%$ . The APE between the two formulas has been calculated as  $APE = 100 \cdot |\text{OBW} - \text{eBW}| / |\text{eBW}|$ . As expected the OBW formula is quite accurate near broadside, but fails as  $\theta_0$  approaches endfire. This is because the Oliner formula is consistent with the narrow beamwidth approximation of Eq. (2.14), and, as already demonstrated, this approximation loses accuracy as we approach endfire.

Finally, in Table 2.5 the factor  $N_O$  has been calculated again for  $e_r \in \{50\%, 75\%, 90\%, 95\%, 99\%, 99.9994\%\}$  and  $\theta_0 \in \{90^\circ, 5^\circ\}$  through Eq. (2.24) with  $\Delta\theta_h$  given by the eF<sub>1</sub>BW for  $L = 10^2\lambda, 10^4\lambda, 10^6\lambda$ . Even if these antenna lengths are unfeasible, the results clearly show how the Oliner's formula is correct in the asymptotic limit of an infinite aperture. As is clearly shown from the values of the last two columns of Table 2.4,  $N_O$  no longer depends on the pointing angle as soon as  $L > 10^6\lambda$ . Also, looking at the third row of Table 2.5, it may be inferred that the value of 0.91 that Oliner obtained for  $e_r = 90\%$  was found as a middle-of-the-range result for antenna lengths of the order of  $10^3\lambda$ . In that case, not shown here for brevity, one would obtain a variation of  $N_O$  in the range  $0.9266 \div 0.9001$  whose mean value is 0.9134.

**Table 2.5.:** Variation of  $N_O$  in the range  $5^\circ \leq \theta_0 \leq 90^\circ$  and for  $e_r = 50\% \div 99.9994\%$  antenna lengths  $L = 10^2\lambda, 10^4\lambda, 10^6\lambda$ .

$e_r [\%]$ \ $\theta_0 [^\circ]$	$L = 10^2\lambda$		$L = 10^4\lambda$		$L = 10^6\lambda$	
	90	5	90	5	90	5
50	0.8896	0.7199	0.8896	0.8870	0.8896	0.8896
75	0.9007	0.7274	0.9007	0.8980	0.9007	0.9007
90	0.9266	0.7449	0.9266	0.9238	0.9266	0.9266
95	0.9547	0.7637	0.9546	0.9517	0.9546	0.9546
99	1.0469	0.8244	1.0469	1.0433	1.0469	1.0468
99.9994	1.8905	1.3204	1.8904	1.7859	1.8904	1.8789

## 2.2.5 Beamwidth evaluation at endfire

In this last paragraph we exclusively deal with the endfire case since it is known [45], [68] that, when  $\theta_0 = 0$ , the relation  $\beta = k_0 \cos \theta_0 = k_0$  does not allow for maximizing directivity at endfire. Hence, at endfire, cases for which  $\beta > k_0$  deserve a separate analysis. Here, starting from Eq. (2.5), that is rather general, we conveniently express  $\theta = \theta_0 + \Delta\theta_h$  so that in the endfire case ( $\theta_0 = 0$ ) Eq. (2.5) can simply be recast as follows:

$$P(\theta) = \frac{\sin^2[b - l \cos(\Delta\theta_h)] + \sinh^2 a}{[b - l \cos(\Delta\theta_h)]^2 + a^2}. \quad (2.27)$$

From here, it is useful to define the following variables:

$$\begin{cases} t_d \triangleq b - l \cos \Delta\theta, \\ t_h \triangleq b - l \cos \Delta\theta_h, \\ t_0 \triangleq b - l, \end{cases} \quad (2.28)$$

so that Eq. (2.27) takes the compact form

$$P(\theta) = \frac{\sin^2 t_d + \sinh^2 a}{t_d^2 + a^2}, \quad (2.29)$$

and according to the definition of beamwidth  $\Delta\theta_h$  (see Eq. (2.3)) and Eq. (2.28), we can then write:

$$P(\Delta\theta_h) = \frac{\sin^2 t_h + \sinh^2 a}{t_h^2 + a^2} = \frac{1}{2}P(0). \quad (2.30)$$

Differently from the analysis of the previous paragraph, as long as we assume that  $\beta \neq k_0$  the calculation for  $P(0)$ <sup>5</sup> is different from the one given in Eq. (2.7) and assume the more general form:

$$P(0) = \frac{\sin^2 t_0 + \sinh^2 a}{t_0^2 + a^2}. \quad (2.31)$$

Thus, using Eq. (2.31) in Eq. (2.30) yields:

$$\begin{aligned} 2 \frac{\sin^2 t_h + \sinh^2 a}{t_h^2 + a^2} &= \frac{\sin^2 t + \sinh^2 a}{t^2 + a^2} \\ 2 \left( \frac{\sin^2 t_h}{\sinh^2 a} + 1 \right) &= \left( \frac{t_h^2}{a^2} + 1 \right) \left( \frac{a^2}{\sinh^2 a} \right) \left( \frac{\sin^2 t + \sinh^2 a}{t^2 + a^2} \right). \end{aligned} \quad (2.32)$$

<sup>5</sup> Note that the discussion given in the Appendix ensures that even if  $\beta \neq k_0$  the pointing angle is always given by the relation  $\beta = k_0$

For convenience we now define a new variable  $\zeta(a, t_0)$ , function of both  $a$  and  $t_0$  (for readability purposes we will omit the dependencies using the symbol  $\zeta := \zeta(a, t_0)$ ):

$$\zeta = \left( \frac{a^2}{\sinh^2 a} \right) \left( \frac{\sin^2 t_0 + \sinh^2 a}{t_0^2 + a^2} \right). \quad (2.33)$$

Then Eq. (2.32) can be rewritten with a more compact notation as follows:

$$\begin{aligned} 2 \left( \frac{\sin^2 t_h}{\sinh^2 a} + 1 \right) &= \left( \frac{t_h^2}{a^2} + 1 \right) \zeta \\ 2 \frac{\sin^2 t_h}{\sinh^2 a} + 2 &= \zeta \frac{t_h^2}{a^2} + \zeta \\ \zeta \frac{t_h^2}{a^2} - 2 \frac{\sin^2 t_h}{\sinh^2 a} - 1 - (1 - \zeta) &= 0. \end{aligned} \quad (2.34)$$

The very interesting aspect of Eq. (2.34) in the current form is that can easily be connected to Eq. (2.12) in the limit  $\zeta \rightarrow 1$ ; thus Eq. (2.34) can be seen as a perturbation of Eq. (2.12) through the function  $\zeta(a, t_0)$ . Also, it is worth noting that for small argument of  $t$ , Eq. (2.33) takes the more compact form:

$$\lim_{t \rightarrow 0} \zeta = \frac{1 + (t \operatorname{csch} a)^2}{1 + (t/a)^2}. \quad (2.35)$$

Equation (2.34) together with Eq. (2.33) define the most general solution to the problem of the beamwidth evaluation in 1-D unidirectional LWAs even at endfire when  $\beta > k_0$  is used to improve endfire directivity. However, the roots of Eq. (2.34) now depend not only on  $a$  but also on  $t_0$ , which does not lead to a simple approximate analytic formula as the one proposed in Eq. (2.20). In the next Section 2.3 we will specifically deal with the radiating features of endfire LWAs.

## 2.3 FORMULAS FOR 1-D ENDFIRE LEAKY-WAVE ANTENNAS

In this Section, the radiating performance of 1-D endfire LWAs is discussed in terms of single-sided beamwidth<sup>6</sup> and sidelobe level (SLL). Specific interest is devoted to those endfire LWAs whose phase constant is given by the *Hansen-Woodyard condition* [68] for maximizing directivity at endfire. Therefore, in 2.3.1 the *original* Hansen-Woodyard that applies for endfire antennas arrays is reviewed. Then, a modified version that applies for 1-D endfire LWAs [45] is briefly outlined.

On this basis, in 2.3.2, a limitation on the maximum value of the phase constant is first derived as a function of the radiation efficiency. Although the beamwidth becomes increasingly narrow as the phase constant increases in the region  $\beta > k_0$ , the SLL also increases, and eventually a point is reached at which the level of the first sidelobe equals that of the main beam. As for *grating lobes* in antenna arrays, when these multiple maxima appear, the antenna radiates the field in one or more unintended directions. As a consequence, a definition beam angle, or equivalently pointing angle, is not unique, and in turn the beamwidth is no longer well-defined.

In 2.3.3 numerical results show the beamwidth and sidelobe level for different phase constants and efficiencies, and a tradeoff is established based on the maximum SLL that can be accepted. A suitable objective function is defined in 2.3.4 to handle this tradeoff. In addition, as has been done in Section 2.2 for 1-D unidirectional LWAs, approximate closed-form expressions are reported in 2.3.5, which express the beamwidth and sidelobe level as functions of the phase constant and efficiency. These formulas are accurate for the practical range of radiation efficiencies normally encountered, where the efficiency  $e_r$  (due to a load termination) is less than 95%. The nature of the beam changes when the aperture becomes very large, corresponding to very high radiation efficiencies.

To this purpose, in Section 2.3.6, a separate analysis for the case of an infinite aperture is discussed. A separate formula, which is exact, is derived for the beamwidth in the infinite aperture case, when the beam is scanned to or beyond ordinary endfire. In this case there are no sidelobes, and the beamwidth is only a function of the phase and attenuation constants. This result is appropriate for cases where the radiation efficiency is very high and there are thus no sidelobes in the pattern.

### 2.3.1 The modified Hansen-Woodyard condition for 1-D LWAs

It is well known that for continuous antenna arrays, as well as for 1-D LWAs, the pointing angle  $\theta_0$  and the phase constant  $\beta$  are related through  $\beta = k_0 \cos \theta_0$ , where  $k_0$  is the wavenumber in vacuum. As a matter of fact,

<sup>6</sup> Note that, at endfire, a definition of double-sided beamwidth would not be well-posed.

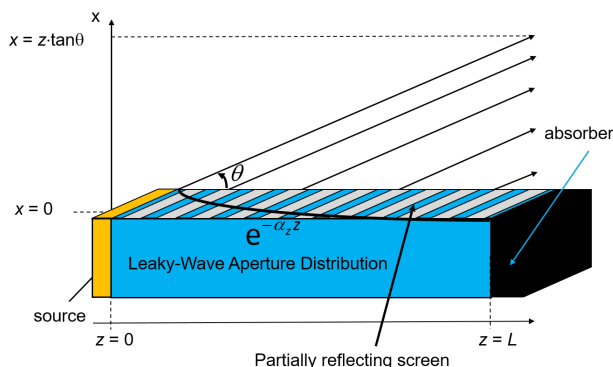


**Figure 2.14.:** An example of a 1-D LWA. A leaky mode is excited at the source location  $z = 0$ . The metallic top wall of a rectangular waveguide is replaced by a partially reflecting screen to allow the propagating mode to leak out along the  $z$ -axis. The antenna is terminated with a matched load at  $z = L$ .

this relation is exact as long as  $\beta \leq k_0$ . When  $\beta \geq k_0$  the beam points at endfire ( $\theta_0 = 0$ ). Interestingly, W. W. Hansen and J. R. Woodyard have shown that a particular value of  $\beta$  allows for improving directivity at endfire [68]. In particular, they found that the optimum condition for maximizing directivity at endfire is given by the so-called *Hansen-Woodyard condition* (HW condition) [68]

$$\beta = k_0 + \frac{2.94}{L}, \quad (2.36)$$

where  $L$  is the length of the antenna (see Fig. 2.14). Since  $\beta = k_0$  (i.e.,  $\theta_0 = 0$ ) corresponds to the *ordinary endfire condition* (OE condition), it is seen that the phase shift ( $\Delta\beta$ ) given by

$$\Delta\beta = \frac{2.94}{L}, \quad (2.37)$$

represents the *perturbation* of the OE condition to achieve maximum directivity at endfire for antenna arrays.

This condition applies only for antenna arrays with a constant aperture distribution. However, it has recently been demonstrated [45] that a modified version of Eq. (2.37) can suitably be applied to endfire 1-D LWAs (see Fig. 2.14 for an example), which are equivalent to antenna arrays with an exponentially-decaying aperture distribution of the form  $\exp(-jk_z z)$  where  $k_z = \beta - j\alpha$  is the complex longitudinal wavenumber, and  $\alpha$  is the attenuation constant (or *leakage constant*). This new condition is known as *modified Hansen-Woodyard condition* (mHW condition) and it states that

$$\Delta\beta = \frac{\tau}{L}, \quad (2.38)$$

where  $\tau$  is a parameter that depends on the *radiation efficiency*  $e_r$  of the antenna due to load termination [45]. In Table 2.6 some relevant values of  $\tau$  have been reported for several different efficiencies  $e_r$  when a 1-D LWA

**Table 2.6.:** Values of  $\tau$  for different antenna efficiencies  $e_r$ .

$e_r$ [%]	0	70	90	95
$\tau$	2.93	2.82	2.62	2.50

of length  $L = 20\lambda$  (at which correspond  $l = 20\pi$ ) is considered<sup>7</sup>. As is shown, as long as  $e_r$  increases (and hence the aperture is no longer uniform as assumed in [68]), the difference between  $\tau$  and the value predicted by the Hansen-Woodyard condition gets greater.

The above condition gives the phase constant necessary for achieving the maximum directivity from a 1-D LWA. This does not imply however a minimum beamwidth. In the next paragraphs we explore the beamwidth properties of a 1-D LWA when the beam is scanned beyond ordinary endfire ( $\beta > k_0$ ) showing that beamwidths smaller than in the Hansen-Woodyard condition are possible, but at the expense of an increased sidelobe level (SLL). To this purpose, we first mathematically prove that a maximum value of  $\beta$  exists beyond which the beamwidth is no longer well defined. In particular, when  $\beta > \beta_{\max}$  the first sidelobe reaches the same amplitude of the main beam, thus it is no longer possible to define a unique single-sided beamwidth.

### 2.3.2 Analytical investigation about the limitations on the choice of an optimum phase constant

In this paragraph we show the existing limitations on the choice of a value of  $\beta$  such that the beamwidth is minimized. In particular, it is shown that in order to have a well-defined single-sided beamwidth, then  $k_0 \leq \beta \leq \beta_{\max}$ .

The maximum value of the phase constant  $\beta_{\max}$  is defined as that which causes the level of the first sidelobe to equal that of the main beam<sup>8</sup>.

Our discussion starts from Eq. (2.5), that we rewrite here in the following form:

$$P(\theta) = \frac{\sin^2[b - l \cos(\theta)] + \sinh^2 a}{[b - l \cos(\theta)]^2 + a^2}. \quad (2.39)$$

To simplify our discussion, we start from the particular case of a constant (i.e. non-attenuated) aperture distribution  $a = 0$  (and in turn  $e_r = 0$ ), i.e.:

$$P(\theta) = \frac{\sin^2[b - l \cos(\theta)]}{[b - l \cos(\theta)]^2}. \quad (2.40)$$

<sup>7</sup> Actually, the length of the antenna  $L$  should not affect the results.

<sup>8</sup> Note that the pattern calculation is based solely on the traveling-wave field on the aperture, and ignores any non-ideal effects such as diffraction from edges, radiation from discontinuities, etc..

In this case, the radiated power at endfire is

$$P(0) = \frac{\sin^2(b-l)}{(b-l)^2}. \quad (2.41)$$

When the OE condition holds (i.e.,  $\beta = k_0$ ),  $b = l$  and in turn  $P(0) = 1$  so that the normalized radiated power  $\bar{P}(\theta) = P(\theta)/P(0)$  will exhibit a single absolute maximum at endfire, whereas the second local maximum (commonly known as the *first sidelobe*) attains the value of  $\zeta = 0.0472$  (corresponding to  $-13.26$  dB). In order to find the location of the first sidelobe  $\theta_{\text{SL}}$ , it is more convenient to define the variable

$$y \triangleq b - l \cos \theta, \quad (2.42)$$

so that Eq. (2.39) can easily be recast as follows:

$$P(\theta) = \frac{\sin^2 y}{y^2}, \quad (2.43)$$

and  $y_{\text{SL}} = b - l \cos(\theta_{\text{SL}})$  is given by the first non-trivial root of:

$$y_{\text{SL}} \cos y_{\text{SL}} = \sin y_{\text{SL}}, \quad (2.44)$$

which is obtained by differentiating with respect to  $y$  Eq. (2.43) and setting it to 0. The application of a simple root-finding algorithm gives the value  $y_{\text{SL}} = 1.43\pi$  (slightly less than  $3\pi/2$ ). When  $b = l$ , from Eq. (2.43),  $y_{\text{SL}} = l[1 - \cos(\theta_{\text{SL}})]$ , then:

$$\theta_{\text{SL}} = \arccos\left(1 - \frac{y_{\text{SL}}}{l}\right), \quad (2.45)$$

that for  $l = 10\pi$  gives  $\theta_{\text{SL}} \simeq 31^\circ$  as shown in Fig. 2.15 (see red dashed line).

However, when the mHW condition applies, or more generally when the beam is scanned beyond OE,  $\beta > k_0$  and in turn  $b > l$ . In this case, it is convenient to define a *perturbation*  $\Delta b$  from  $b = l$  such that  $b = l + \Delta b$ . The perturbation  $\Delta b$  is related to the parameter  $\tau$  in Eq. (2.38) as  $\Delta b = \tau/2$ . The normalized radiated power is then given by Eq. (2.43) with

$$y \triangleq l + \Delta b - l \cos \theta. \quad (2.46)$$

The pattern as a function of  $y$  is shifted by  $\Delta b$  with respect to the pattern obtained when the OE condition applies, i.e., for  $b = l$ . Thus, there exists a particular value  $\Delta b_{\text{max}}$  such that  $P(0) = \zeta$ . In this case, the intensity of the normalized radiated power  $\bar{P}(\theta) = P(\theta)/P(0)$  would be the same for  $\theta = 0$  and for a value  $\theta = \theta_{\text{SL}}$  that depends on  $\Delta b_{\text{max}}$ . Now, having  $\bar{P}(\theta)$  two main lobes, the definition of beamwidth and pointing angle  $\theta_0$  are no longer well-posed. Clearly, it is not practical to scan beyond this point.



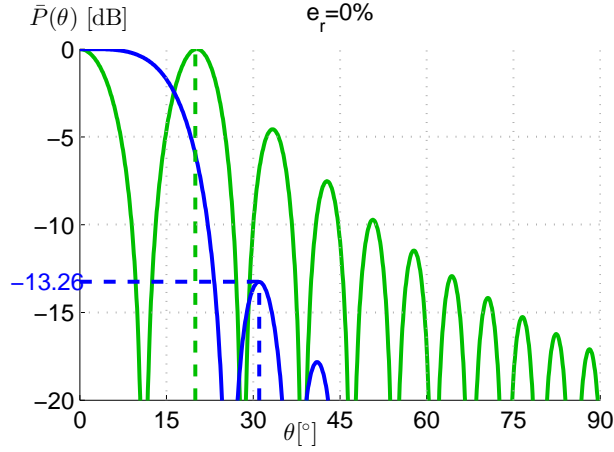


**Figure 2.15:**  $\bar{P}(\theta)$  vs.  $\theta$  (in dB scale) for  $e_r = 0\%$ ,  $l = 10\pi$ ,  $b = l$  (solid blue line) and  $b = l + \Delta b_{\max}$  (solid green line), respectively. The first sidelobe for  $b = l$  occurs around  $\theta_{\text{SL}} \simeq 31^\circ$  (dashed blue lines). When  $b = l + \Delta b_{\max}$  the first sidelobe (dashed green line) reaches the same intensity of the main lobe.

In order to find  $\theta_{\text{SL}}$  we first evaluate  $\Delta b_{\max}$ . Hence, from Eq. (2.46) evaluated at  $\theta = 0$ ,  $\Delta b_{\max}$  is given by the first root of the following equation:

$$\begin{aligned} \frac{\sin^2 \Delta b_{\max}}{\Delta b_{\max}^2} - \zeta &= 0 \\ \Rightarrow \sin^2 \Delta b_{\max} &= \zeta \Delta b_{\max}^2, \end{aligned} \quad (2.47)$$

which gives  $\Delta b_{\max} = 0.813\pi \simeq 2.5541$ . Then, from Eq. (2.46)  $\theta_{\text{SL}}$  is given by:

$$\theta_{\text{SL}} = \arccos \left( 1 - \frac{y_{\text{SL}} - \Delta b_{\max}}{l} \right), \quad (2.48)$$

where  $y_{\text{SL}}$  is still given by  $y_{\text{SL}}$  in Eq. (2.44) since they define the roots of the same equation. Clearly, for  $\Delta b_{\max} = 0$  Eq. (2.48) reduces to Eq. (2.45), being the latter a limiting case of the former. Finally, the correctness of Eq. (2.48) has been assessed for  $l = 10\pi$ ,  $\theta_{\text{SL}} \simeq 20^\circ$  as shown in Fig. 2.15 (see blue dashed line).

This analysis can be extended to the complex case, i.e., when  $a \neq 0$  and in turn  $e_r \neq 0$ . In this case, when  $\Delta b = 0$ ,  $P(0) = \sinh^2 a / a^2 \neq 1$  and  $\zeta \neq 0.0472$ . More precisely, the sidelobe level  $\zeta$  depends now on  $a$ , being  $\zeta(a)|_{a=0} = \zeta(0) = 0.0472$  its limiting case. This would be the only difference with respect to the case  $e_r = 0$ . Once  $\zeta$  is replaced with  $\zeta(a)$  the search of  $\Delta b_{\max}$  when  $e_r \neq 0$  follows as above, but leads to a more general equation:

$$\sin^2 \Delta b_{\max} + \sinh^2 a = \zeta(a)(\Delta b_{\max}^2 + a^2), \quad (2.49)$$

whose roots will give a different  $\Delta b_{\max}$  for each value of  $a$  and in turn of  $e_r$ . This is clearly shown in Table 2.7 where the values of  $\Delta b_{\max}$  as a function

**Table 2.7.:** Values of  $\Delta b_{\max}$  for different antenna efficiencies  $e_r$ .

$e_r$ [%]	0	50	75	90	95	99
$\Delta b_{\max}$	2.5541	2.5698	2.6232	2.7552	2.9185	6.2298

of  $e_r$  has been reported for  $e_r \in \{0, 0.5, 0.75, 0.90, 0.95, 0.99\}$ . Note that, for  $a \rightarrow 0$ , Eq. (2.49) reduces to Eq. (2.47), since  $\zeta(0) = \zeta$ .

Another useful validation of our analytical results is given in Fig. (2.16), where the normalized power distributions for  $b = l$  (solid blue lines) and for  $b = l + \Delta b_{\max}$  (dashed grey lines) have been reported for the same values of  $e_r$  used in Table 2.7, considering  $L = 10\lambda$  ( $l = 10\pi$ ). Though the results reported in Table 2.7 do not depend on  $l$ , the patterns obviously depend on  $l$ , being more directive as  $l$  increases.

As is clearly shown, the *ordinary* endfire patterns (the one with  $b = l$ ) exhibit one main lobe, whereas their *shifted* versions (those with  $b = l + \Delta b_{\max}$ ) exhibit two main lobes with the same intensity, thus leading to an ambiguous definition of beamwidth and  $\theta_0$ . Interestingly, when  $e_r = 99\%$  the first sidelobe is incorporated by the main lobe and is seen as a turning point rather than a maximum. As a consequence, the first sidelobe is revealed farther with respect to the previous cases, thus justifying the higher value achieved by  $\Delta b_{\max}$  in Table 2.7.

It is worth here to remark that our analysis allows for predicting the pointing angle of the second peak, the beamwidth of the main peak, and the sidelobe level (SLL) when  $k_0 \leq \beta \leq \beta_{\max}$  by means of simple and fast nu-

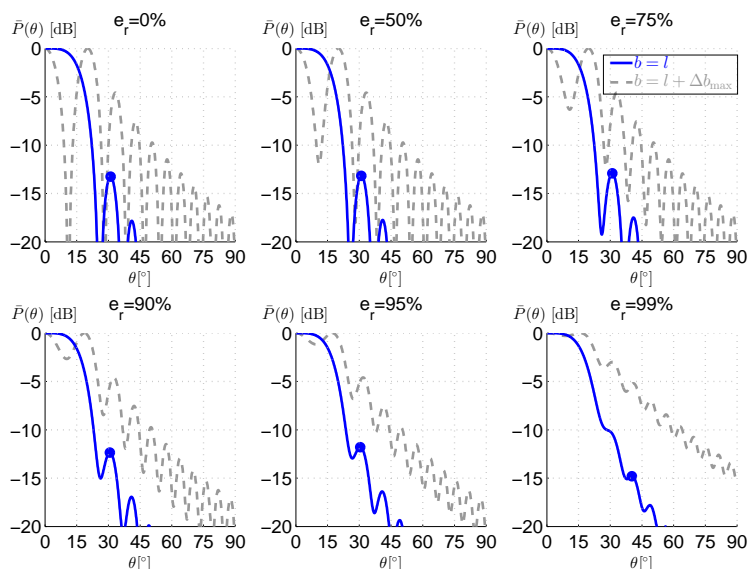


**Figure 2.16.:**  $\bar{P}(\theta)$  vs.  $\theta$  (in dB scale) for  $e_r \in \{0\%, 50\%, 75\%, 90\%, 95\%, 99\%\}$ ,  $l = 10\pi$ ,  $b = l$  (solid blue line) and  $b = l + \Delta b_{\max}$  (dashed grey line), respectively.

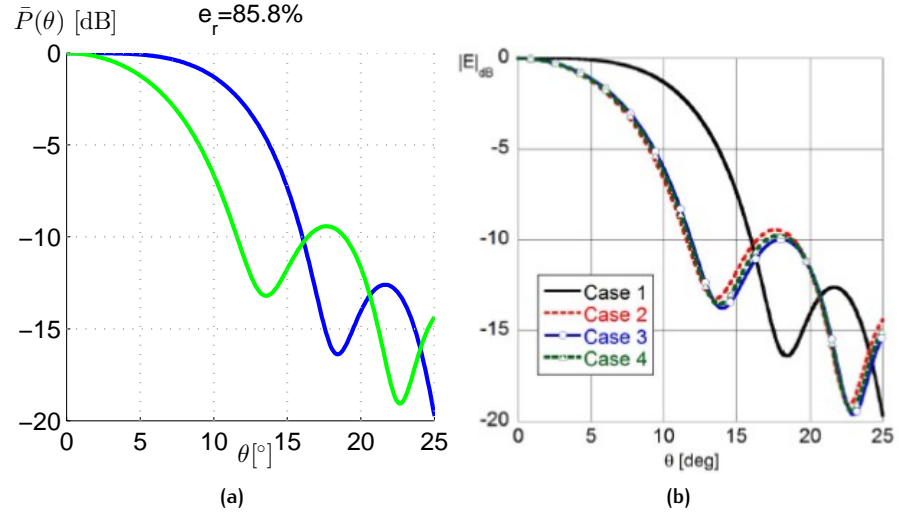


**Figure 2.17.:** (a)  $\bar{P}(\theta)$  vs.  $\theta$  for  $e_r = 85.8\%$ ,  $l = 20\pi$ , when  $\Delta b = 0$  (blue line) and  $\Delta b = 1.47$  (green line). (b) Fig. 4 of Reference [45] reported here for convenience. Case 1 and Case 2 perfectly match the blue and green curves, respectively.

merical methods<sup>9</sup>. Note also that the definition of  $\Delta b$  is equivalent to the one of  $\tau/2$  provided in [45], which is independent of the antenna length  $L$ . As expected, the value of  $\tau/2$  provided in [45] for maximizing directivity at endfire are always less than  $\Delta b_{\max}$ . Some relevant examples will be shown in the next Subsection 2.3.3.

### 2.3.3 Beamwidth and SLL evaluation for endfire 1-D LWAs

In this paragraph the beamwidth and the SLL of 1D-LWAs radiating at endfire are evaluated for the relevant case of an antenna with length  $L = 10\lambda$  for  $e_r \in \{0.1, 0.5, 0.75, 0.90, 0.95, 0.99\}$  when different values of  $\Delta b$  are applied.

First, in order to have a thorough comparison with available results which can be found in literature, the normalized radiation patterns have been reported in Fig. 2.17 for  $\Delta b = 0$  (OE condition) and for  $\Delta b = 1.47$  (HW condition) when  $L = 20\lambda$  and  $e_r = 85.8\%$  as has been done in Fig. 4 in [45]. As is shown, there is a perfect agreement between our pattern and Case 1 and Case 2 of [45]. Specifically, the SLL is  $-12.64$  dB<sup>10</sup> for the OE condition and  $-9.56$  dB for the HW condition, whereas the beamwidth is  $12.24^\circ$  and  $7.42^\circ$ , respectively. Thus, the improvement in terms of directivity and beamwidth given by the HW condition is paid at the expense of a worst SLL.

Now that we have assessed our theoretical framework through the comparison with literature results, we can extend our investigation to more relevant examples. In order to limit our analysis only to meaningful cases we have decided to use values of  $\Delta b < \min_{e_r}\{\Delta b_{\max}\} = 2.5541$ . In particular,

<sup>9</sup> We note here that  $\beta_{\max}$  is related to  $\Delta b_{\max}$  through  $\beta_{\max} = k_0 + 2\Delta b_{\max}/L$   
<sup>10</sup> Note that the SLL is  $-13.26$  dB only when  $e_r = 0\%$

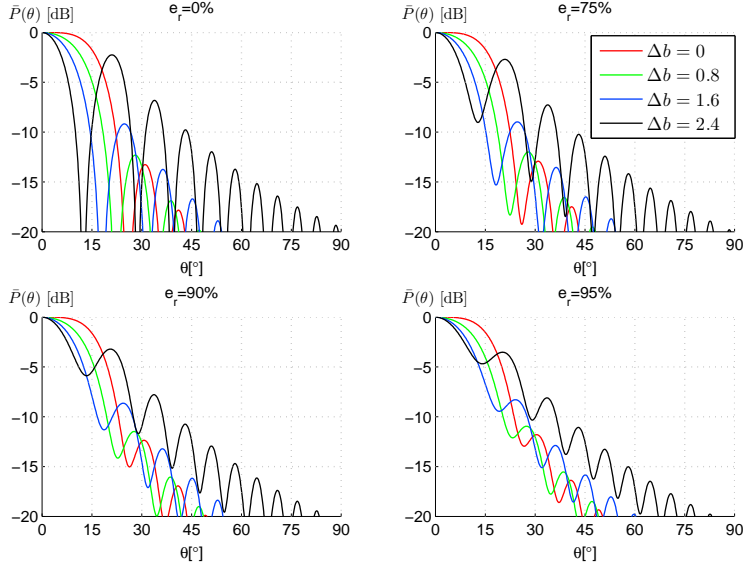


Figure 2.18.:  $\bar{P}(\theta)$  vs.  $\theta$  for  $e_r \in \{0\%, 75\%, 90\%, 95\%\}$ ,  $l = 10\pi$ ,  $\Delta b = 0$  (red line),  $\Delta b = 0.8$  (green line),  $\Delta b = 1.6$  (blue line), and  $\Delta b = 2.4$  (black line) respectively.

in Fig. 2.18 the normalized radiation patterns are shown for  $L = 10\lambda$  when  $\Delta b_{\max} = 0, 0.8, 1.6, 2.4$ .

The related figures of merit, viz.,  $\Delta\theta_h$  and SLL, have been reported in Table 2.8. As is seen, as  $\Delta b$  increases the beamwidth gets narrower, but the SLL gets higher, achieving unacceptable values for  $\Delta b = 2.4$ . This behavior is more pronounced for lower efficiencies, but generally both the SLL and the beamwidth increase as the efficiency increases.

As we previously pointed out in Section 2.3.1, the results of Table 2.8 corroborate our initial guess about the existence of a tradeoff between the minimum beamwidth that we can achieve by increasing  $\Delta b$  and the maximum

Table 2.8.: Figures of Merit (FoM), namely  $\Delta\theta_h$  and SLL, for different values of  $\Delta b$  and different antenna efficiencies  $e_r$ , for  $L = 10\lambda$ .

$\Delta b$	FoM	$e_r$ [%]			
		0	75	90	95
0	$\Delta\theta_h$ [°]	17.12	17.24	17.47	17.70
	SLL [dB]	-13.26	-12.92	-12.36	-11.80
0.8	$\Delta\theta_h$ [°]	12.77	12.94	13.23	13.54
	SLL [dB]	-12.31	-12.00	-11.48	-10.95
1.6	$\Delta\theta_h$ [°]	9.49	9.75	10.19	10.67
	SLL [dB]	-9.17	-8.98	-8.64	-8.29
2.4	$\Delta\theta_h$ [°]	6.44	7.16	8.33	9.51
	SLL [dB]	-2.25	-2.70	-3.21	-3.52

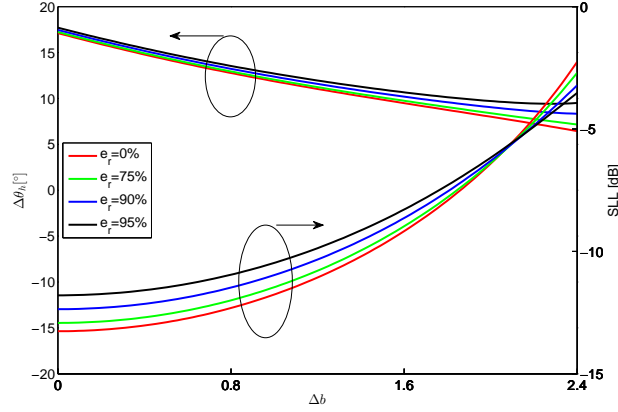


Figure 2.19.:  $\Delta\theta_h$  and SLL vs.  $b$  for  $e_r \in \{0\%, 50\%, 75\%, 90\%, 95\%\}$ ,  $L = 10\lambda$ .

SLL that we can accept. To this purpose, in the following Subsection 2.3.4 an extended analysis about the performance of an endfire 1-D LWA will be reported by expressing the beamwidth and the SLL as functions of  $\Delta b$  and  $e_r$  for an antenna length of  $L = 10\lambda$ . Finally a suitable objective function will be defined in order to find a *quasi-optimum* design for endfire 1-D LWAs, taking into account the beamwidth and the SLL as relevant figures of merit.

#### 2.3.4 Definition of a suitable objective function for taking into account the $\Delta\theta_h$ vs. SLL tradeoff

Here we aim to extend the analysis developed in the previous Subsection 2.3.3, showing some relevant FoM of endfire 1-D LWAs, namely the beamwidth and the SLL, as a function of  $\Delta b$  when  $L = 10\lambda$  and  $e_r \in \{0, 0.75, 0.90, 0.95\}$ . Results are shown in a unified plot in Fig. 2.19. Two major points should be stressed:

- i) The behavior of  $\Delta\theta_h$  vs.  $\Delta b$  looks similar to the one reported in [45] for  $2kLF(u, v)$  vs.  $u$ , where  $F(u, v)$  is a useful FoM inversely proportional to the directivity  $D_0$  and  $u$  and  $v$  are convenient variables equivalent to our  $\Delta b$  and  $a$ , respectively. This is exactly what we expect from theory, since the beamwidth is also inversely proportional to directivity through the approximated relation  $D_0 \simeq 4\pi/2\Delta\theta_h$  [11], and  $u$  is directly proportional to  $b$ .
- ii) As pointed out in Subsection 2.3.3, for higher values of  $\Delta b$  the beamwidth decreases whereas the SLL increases.

As regards point ii), a tradeoff is dictated by the beamwidth and the SLL. Thus, an optimization procedure for the design of endfire 1-D LWAs should take into account such a tradeoff. To this purpose, we suggest the definition of the following objective function, obtained as a convex combination of  $\Delta\theta_h$  and SLL:

$$g(\Delta b) = w \cdot \widetilde{\text{SLL}}(\Delta b) + (1 - w) \cdot \widetilde{\Delta\theta_h}(\Delta b), \quad (2.50)$$

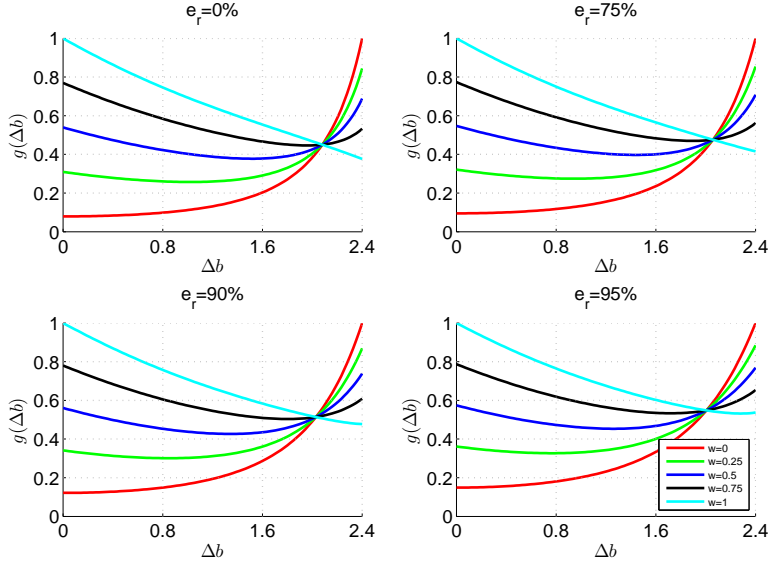


Figure 2.20.: The optimizing function vs.  $\Delta b$  for  $e_r \in \{0\%, 75\%, 90\%, 95\%, 99\%\}$ , and for  $w = 0, 0.25, 0.5, 0.75, 1$  when  $L = 10\lambda$ . Obviously, the extreme cases  $w = 0$  and  $w = 1$  would lead to the same  $b$  which minimizes the beamwidth and the SLL, respectively.

where  $0 \leq w \leq 1$  is a weight coefficient, and the tilde ( $\tilde{\cdot}$ ) identifies the normalization to the maximum for both the FoM. Once the efficiency  $e_r$  and the antenna length  $L$  are fixed, the minimization of  $g(\Delta b)$  would lead to a quasi-optimum design in terms of  $\Delta\theta_h$  and SLL subjected to the weight  $w$  assigned by the antenna designer. In fact, the minimization of  $g(\cdot)$  leads to the minimization of both  $\Delta\theta_h$  and SLL.

In Fig. 2.20,  $g(\Delta b)$  has been reported for  $e_r \in \{0, 0.75, 0.90, 0.95\}$ , and for  $w = 0, 0.25, 0.5, 0.75, 1$  when  $L = 10\lambda$ . On one hand, the extreme cases  $w = 0$  and  $w = 1$  would lead to the same  $\Delta b$  which minimizes the  $\Delta\theta_h$  and the SLL, respectively. On the other hand, the intermediate choices lead to intermediate conditions which would better match the constraints required to the antenna designer. However, the results reported so far have been obtained considering an antenna length of  $L = 10\lambda$ . In the next paragraph, a different approach is proposed to extend the results to any antenna length. Even more interestingly, a general approximate closed formula is derived to evaluate both  $\Delta\theta_h$  and SLL of endfire LWAs.

### 2.3.5 Approximate formulas for the beamwidth and the sidelobe level

To extend the results to any antenna length, we define a normalized beamwidth as  $\bar{\Delta\theta}_h = \Delta\theta_h \sqrt{0.5L/\lambda}$ . This is a convenient normalization for *endfire* 1-D LWAs, since the beamwidth varies as the square root of the antenna length, instead of varying with the antenna length (see Eq. (1.20)) as it does for 1-D LWAs scanned to an angle  $\theta_0 > 0$  [69]. With this normalization, results are shown in a unified plot in Fig. 2.19 where the normalized

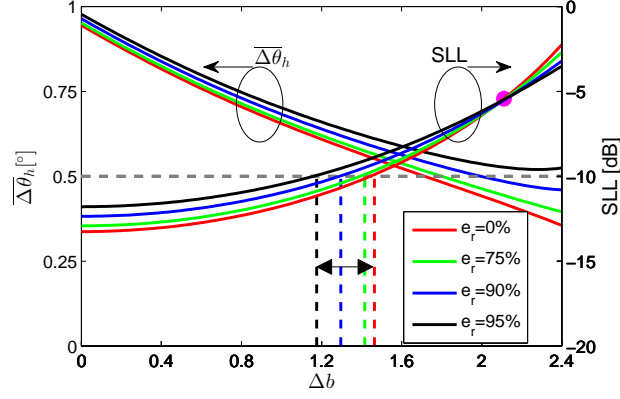


Figure 2.21.:  $\overline{\Delta\theta}_h$  and SLL vs.  $\Delta b$  for  $e_r = 0\%$ ,  $75\%$ ,  $90\%$ ,  $95\%$ . The magenta dot indicates the value of  $\Delta b$  for which the SLL improves as  $e_r$  increases.

beamwidth  $\overline{\Delta\theta}_h$  and the SLL have been reported as functions of  $\Delta b$  in the range  $0 \leq \Delta b \leq 2.4$ , for  $e_r = 0, 0.75, 0.90, 0.95$ . An inspection of Fig. 2.19 reveals two major points. First, it is seen that for practical cases (i.e., for  $e_r < 95\%$ ) and when  $1.2 < \Delta b < 1.4$ , it is possible to narrow the beamwidth and simultaneously not exceed the value of  $-10$  dB for the SLL (which is a reasonable threshold value). Note that this range of values for  $\Delta b$  is almost the same suggested in [45] for maximizing the directivity at endfire, since the mHW condition results in a SLL of roughly  $-10$  dB [45]. This is an alternative criterion to handle the  $\Delta\theta_h$  vs. SLL *tradeoff* with respect to the one proposed in 2.3.4 through the objective function  $g(\cdot)$  (see Eq. (2.50)). Second, there exists a specific value of  $\Delta b \simeq 2.1$  beyond which the SLL decreases rather than increases as the efficiency gets higher (see the magenta dot in Fig. 2.19). This motivates the opposite trend previously noticed in the last row of Table 2.8.

From Fig. 2.21 it appears that a 2<sup>nd</sup>-order polynomial interpolation for both  $\overline{\Delta\theta}_h$  and SLL as functions of  $\Delta b$  may provide sufficiently accurate results. However, such an interpolation should also take into account the dependence on  $e_r$  and in turn on  $a$ . This would suggest to search for a family of  $a$ -parametric fitting functions of  $\overline{\Delta\theta}_h(\Delta b; a)$  and  $SLL(\Delta b; a)$  which both belong to the same class of functions with respect to  $\Delta b$ . For any value of  $a$  this class of functions would be characterized by a different set of parameters which depends only on  $a$ . It would then be possible to fit the parameters as functions of  $\Delta b$  and  $a$ . This would result in two final parametric formulas  $\overline{\Delta\theta}_h(\Delta b; a)$  and  $SLL(\Delta b; a)$ :

$$\overline{\Delta\theta}_h(\Delta b; a) = v_0(a) + v_1(a)\Delta b + v_2(a)\Delta b^2 \quad (2.51)$$

$$SLL(\Delta b; a) = w_0(a) + w_1(a)\Delta b + w_2(a)\Delta b^2, \quad (2.52)$$

where now the fitting parameters  $v_i(a) = v_{i,0} + v_{i,1}a$  and  $w_i(a) = w_{i,0} + w_{i,1}a$  for  $i = \{0, 1, 2\}$  both depends on  $a$ . In this way, we have obtained our

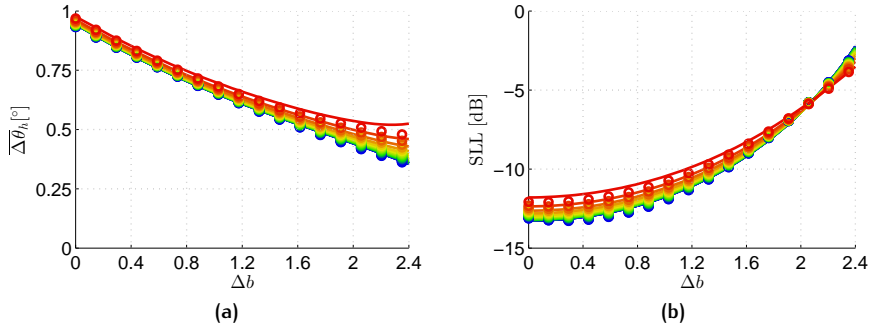


Figure 2.22.: (a)  $\overline{\Delta\theta}_h$  and (b) SLL vs.  $\Delta b$  in the range  $0 \leq \Delta b \leq 2.4$ . A family of  $a$ -parametric curves (solid lines) shading from blue to red is generated for  $a$  going from 0 to 0.8. Fitting curves are reported in circles in both figures.

desired  $a$ -parametric functions which belongs to the same class of functions with respect to  $a$ . These first results have been reported in Fig. 2.22(a) and (b) for  $\overline{\Delta\theta}_h$  and SLL, respectively, where  $a$  has been varied from 0 to 0.8, thus covering efficiencies up to 95%. Also the behavior of the coefficients  $v_{i,j}(a)$  and  $w_{i,j}(a)$  has been reported in Fig. 2.23(a) and (b), respectively. As is clear, a first-order polynomial expression for the coefficients would be sufficient to accurately interpolate such functions, as corroborated by the remarkable agreement between the fit curves (circles) and the original ones (solid lines) (see Fig. 2.22). A slight disagreement is observed for increasing values of  $a$  (see red lines in Fig. 2.22)<sup>11</sup>, but can be mitigated by increasing the order of the interpolating polynomials. Here, we decided to still use the first-order approximation to reduce the complexity of the final formula. Thus, the final interpolating functions are represented by Eqs. (2.51) and (2.52) with parametric coefficients in Table 2.9.

Remarkably, the proposed Eqs. (2.51) and (2.52), with parameters as in Table 2.9, provide a useful tool for evaluating the beamwidth and SLL for

<sup>11</sup> Such an effect is due to the nonlinear behavior of  $\overline{\Delta\theta}_h$  vs.  $\Delta b$  for  $e_r = 0.95$  as is evident from Fig. 2.21 (see the solid black line).

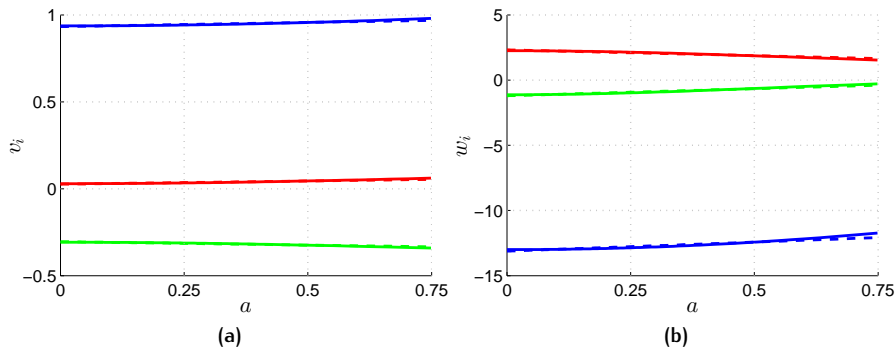


Figure 2.23.: (a)  $v_i$  and (b)  $w_i$  vs  $a$  for  $i = 0, 1, 2$  (in order blue, green, and red solid lines) and their linear interpolations (dashed lines).



Table 2.9.: Fitting parameters for  $\Delta\theta_h$  and SLL.

$i$	0		1		2	
$j$	0	1	0	1	0	1
$v_{i,j}$	0.933	0.048	-0.304	-0.039	0.026	0.036
$w_{i,j}$	-13.12	1.39	-1.20	1.08	2.312	-0.89

endfire 1-D LWAs of any length and for efficiencies up to  $e_r = 95\%$ , with a MAPE on the order of 1% for each formula (the APE as a function of  $a$  and  $\Delta b$  is not reported here for the sake of conciseness). A discussion about the behavior of endfire 1-D LWAs with  $e_r > 95\%$  is given in the next paragraph.

### 2.3.6 Investigation for extremely-efficient endfire leaky-wave antennas

As a last investigation, we focused our attention on the evaluation of the  $\Delta b_{\max}$  parameter for extremely efficient 1-D LWAs, i.e.,  $e_r > 99\%$ . Results are shown in Fig. 2.24 for an antenna length of  $L = 10\lambda$  for four different values of radiation efficiency, namely  $e_r \in \{99\%, 99.5\%, 99.95\%, 100\%\}$ . Note that with  $e_r = 100\%$  is meant an asymptotic value of the efficiency that approaches 100% up to value whose difference between 100% is less than  $10^{-10}$ . As is seen, for an extremely efficient 1-D LWA the definition of a  $\Delta b_{\max}$  is immaterial. Indeed, as can be inferred from general theory, as long as the efficiency gets higher, the sidelobe level tends to decrease and the pattern assumes almost a *uniform* distribution without any sidelobes. As

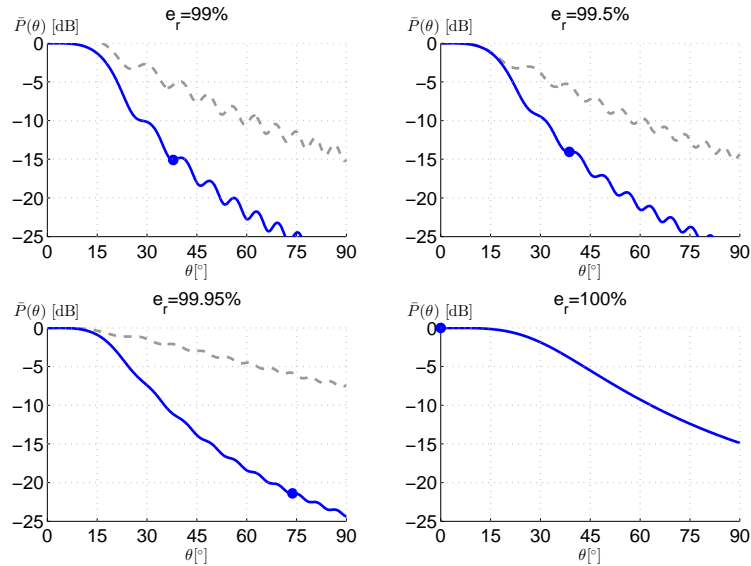


Figure 2.24.:  $\bar{P}(\theta)$  vs.  $\theta$  (in dB scale) for  $L = 10\lambda$  for  $e_r \in \{99\%, 99.5\%, 99.9\%, 99.95\%, 99.99\%, 100\%\}$ ,  $b = l$  (blue line) and  $b = l + \Delta b_{\max}$  (grey line), respectively. A blue dot highlights the location of the first sidelobe encountered from the main lobe for  $b = l$ .

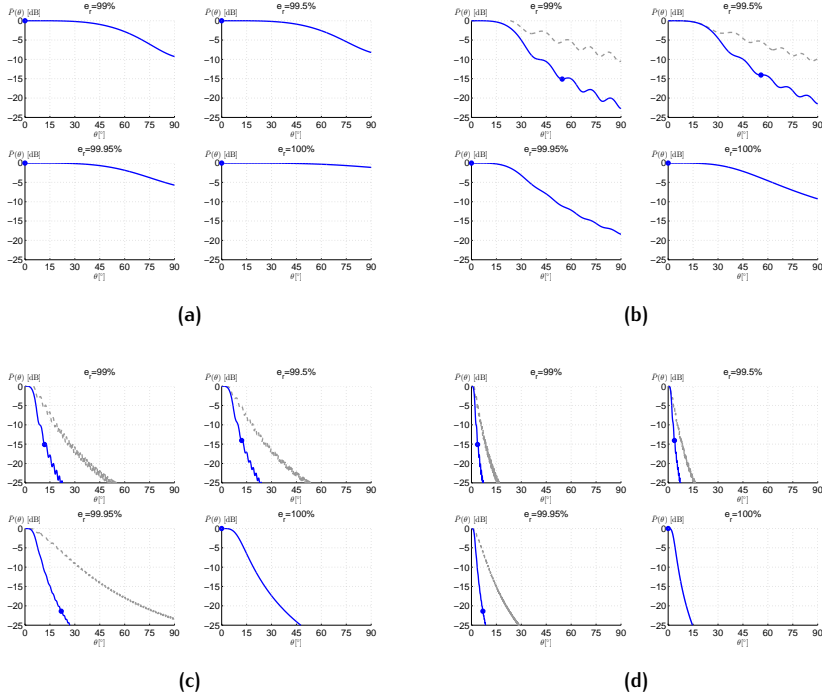


Figure 2.25.:  $\bar{P}(\theta)$  vs.  $\theta$  (in dB scale) for (a)  $L = 1\lambda$ , (b)  $L = 5\lambda$ , (c)  $L = 100\lambda$ , (d)  $L = 1000\lambda$  for  $e_r \in \{99\%, 99.5\%, 99.95\%, 100\%\}$ ,  $b = l$  (blue line) and  $b = l + \Delta b_{\max}$  (grey line), respectively. A blue dot highlights the location of the first sidelobe encountered from the main lobe for  $b = l$ .

a consequence, the definition of  $\Delta b_{\max}$  is no longer useful for neither the design nor the optimization of these particular class of endfire 1-D LWAs.

Moreover, similar results have been reported in Fig. 2.25 for different antenna lengths, namely  $L = 1\lambda, 5\lambda, 100\lambda, 1000\lambda$ , to highlight the effect of  $L$  in the beamwidth. On one hand, for extremely short antennas (see Figs. 2.25(a) and (b)) the radiation patterns show a unique big main lobe without exhibiting any sidelobes. On the other hand, for extremely long antennas, the beamwidth gets narrower and narrower, approaching to 0. Some insights on this last behavior can be gained if we look at the expression for the beamwidth under the hypothesis  $L \rightarrow \infty$ . For convenience, we report here Eqs. (2.30) and (2.33) obtained in 2.2.5:

$$\zeta \frac{(b - l \cos \Delta\theta_h)^2}{a^2} - 2 \frac{\sin^2(b - l \cos \Delta\theta_h)}{\sinh^2 a} - 1 - (1 - \zeta) = 0, \quad (2.53)$$

where:

$$\zeta = \left[ \frac{a^2}{\sinh^2 a} \right] \left[ \frac{\sin^2(b - l) + \sinh^2 a}{(b - l)^2 + a^2} \right]. \quad (2.54)$$

Hence, if  $L \rightarrow \infty$ , then  $a, b$ , and  $l$  go to infinity. Since  $|\sin(\cdot)| \leq 1$  then:

$$\zeta \simeq \frac{a^2}{(b - l)^2 + a^2}, \quad (2.55)$$

and

$$\frac{(b - l \cos \Delta\theta_h)^2}{(b - l)^2 + a^2} - 2 + \frac{a^2}{(b - l)^2 + a^2} = 0 \quad (2.56)$$

$$\Rightarrow \frac{(b - l)^2 + a^2}{(b - l \cos \Delta\theta_h)^2 + a^2} = \frac{1}{2} \quad (2.57)$$

and with simple algebraic manipulations we get:

$$l^2 \cos^2 \Delta\theta_h - 2bl \cos \Delta\theta_h - (b^2 + 2l^2 - 4bl + a^2) = 0. \quad (2.58)$$

From here, it is straightforward to get a simple analytic closed formula for  $\Delta\theta_h$  as a function of  $b$ ,  $a$ , and  $l$ . In fact, if we define  $x = \cos \Delta\theta_h$ , we get a quadratic equation whose roots are given by:

$$x = \frac{b}{l} \pm \frac{1}{l} \sqrt{2(b - l)^2 + a^2}, \quad (2.59)$$

so that

$$\Delta\theta_h = \arccos \left( \frac{b}{l} \pm \frac{1}{l} \sqrt{2(b - l)^2 + a^2} \right), \quad (2.60)$$

which is the sought formula for the beamwidth for endfire extremely long 1-D LWAs. However, a suitable definition of the following variables:

$$\begin{cases} \Delta b &= b - l, \\ \Delta \hat{\beta} &= \Delta b / l, \\ \hat{\beta} &= b / l, \\ \hat{\alpha} &= a / l, \end{cases} \quad (2.61)$$

allows us to recast Eq. (2.60) as follows:

$$\Delta\theta_h = \arccos \left( 1 + \Delta \hat{\beta} \pm \sqrt{2\Delta \hat{\beta}^2 + \hat{\alpha}^2} \right). \quad (2.62)$$

Note that, since the domain of the  $\arccos(\cdot)$  is limited between  $-1$  and  $1$ , we must choose the negative determination of the square root, so our final formula would be:

$$\Delta\theta_h = \arccos \left( 1 + \Delta \hat{\beta} - \sqrt{2\Delta \hat{\beta}^2 + \hat{\alpha}^2} \right), \quad (2.63)$$

which has some reminiscences of Eq. (1.29) (see Section 2.4), i.e., the beamwidth formula for a broadside beam ( $\beta < \alpha$ ) of 1-D bidirectional LWAs. Radiation from this class of antennas will be the object of the next Section 2.4.

Note also that, when the attenuation constant is zero, the beamwidth depends solely on the phase constant. In this case, after some manipulation Eq. (2.63) implies that the beamwidth is proportional to  $\Delta \hat{\beta}$ . Conversely,

when  $\hat{\alpha} \neq 0$  and  $\beta = k_0$ , the beamwidth is proportional to  $\hat{\alpha}$ . In particular, for a given value of  $\hat{\alpha}$ , the narrowest beam is obtained by maximizing<sup>12</sup> the term in parentheses with respect to  $\Delta\hat{\beta}$ :

$$\begin{aligned} \frac{\partial}{\partial \Delta\hat{\beta}} \left( 1 + \Delta\hat{\beta} - \sqrt{2\Delta\hat{\beta}^2 + \hat{\alpha}^2} \right) &= 0 \\ 1 - \frac{2\Delta\hat{\beta}}{\sqrt{2\Delta\hat{\beta}^2 + \hat{\alpha}^2}} &= 0. \end{aligned} \quad (2.64)$$

After some manipulations the following condition is found:

$$\Delta\hat{\beta} = \frac{\hat{\alpha}}{\sqrt{2}}, \quad (2.65)$$

with a corresponding minimum beamwidth of:

$$\Delta\theta_h^{(\min)} = \arccos \left( 1 - \hat{\alpha} / \sqrt{2} \right). \quad (2.66)$$

Since there are no sidelobes in the infinite aperture case, this condition will also maximize<sup>13</sup> the directivity. On the other hand, for a given value of  $\Delta\hat{\beta}$ , the beamwidth continuously decreases as  $\hat{\alpha}$  decreases.

<sup>12</sup> Recall that the condition  $\Delta\theta_h = 0^\circ$  is obtained when  $\arg \arccos(\cdot) = 1$  which corresponds to the condition  $\Delta\hat{\beta}^2 = -\hat{\alpha}^2/2$  that is never possible.

<sup>13</sup> A study of the sign of Eq. (2.64) confirms that Eq. (2.65) is actually a maximum.

## 2.4 FORMULAS FOR 1-D BIDIRECTIONAL LEAKY-WAVE ANTENNAS

In the previous Sections 2.2 and 2.3, we have found new approximate closed-form expressions for evaluating the beamwidth of 1-D unidirectional LWAs. Differently from previous existing formulations [10]–[14] based on certain simplifying hypotheses regarding the antenna length and the beam size, the new formulas are rather general.

However, the endfire case has been analyzed in Section 2.3 aside from conventional 1-D unidirectional LWAs. This is because radiation at endfire involves several aspects that cannot be addressed with the same theoretical framework developed in Section 2.2. Such a consideration is even more true for 1-D bidirectional LWAs whose underlying physics is substantially different from that of 1-D unidirectional LWAs, being more similar to that of 2-D LWAs.

In this Section, we aim to find an expression for the bidirectional case. In 2.4.1 we first derive closed-form expressions for the infinite aperture case. The same theoretical framework is then used in 2.4.2 to derive approximate formulas for the beamwidth which account also for the finiteness of the aperture. Since for scanned beams the beamwidth of a finite aperture is still well approximated by the formulas derived in Section 2.2, the beamwidth formula is derived only for broadside beams. Interestingly, the phase constant  $\beta$  can be anything from 0 to  $\alpha$  (note that  $\beta = \alpha$  is the *splitting condition* [48]).

The results of this Section 2.4 represents a first significant step towards the characterization of the radiating features of 2-D LWAs when the finiteness of the aperture is taken into account.

### 2.4.1 Beamwidth formulas for uniform and infinite apertures

The first step for the evaluation of the beamwidth of 2-D LWAs should be the analysis of 1-D *bidirectional* LWAs. In fact, the physics underlying 1-D bidirectional LWAs and 2-D LWAs is formally the same. However, 1-D bidirectional LWAs are easier to be analyzed due to the simpler expression that describes the resulting radiation pattern. Here, we start our analysis considering Eq. (1.26) that is reported here for convenience:

$$\text{AF} = j \frac{(k_z - k_0 \sin \theta) e^{-j(k_z + k_0 \sin \theta)L/2} + (k_z + k_0 \sin \theta) e^{-j(k_z - k_0 \sin \theta)L/2} - 2k_z}{k_z^2 - k_0^2 \sin^2 \theta}, \quad (2.67)$$

where  $\theta$  is the angle, measured from the vertical  $x$ -axis to the longitudinal  $z$ -axis. It is worth noting that this definition of  $\theta$  is the complementary of the definition provided in the previous Sections 2.2 and 2.3 for 1-D unidi-

rectional LWAs. This choice is motivated by the fact that 1-D bidirectional LWAs, as well as 2-D LWAs, are mainly designed for operating at broadside that with this definition of  $\theta$  would correspond to  $\theta = 0^\circ$ . Other convenient definitions of variables are the following:

$$\begin{cases} p = k_z L/2 = \beta L/2 - j\alpha L/2 = b - ja, \\ l = k_0 L/2, \\ t = l \sin \theta, \end{cases} \quad (2.68)$$

which allow for expressing Eq. (2.67) as:

$$\text{AF} = -j \frac{L}{2} \frac{(p-t)e^{-j(p+t)} + (p+t)e^{-j(p-t)} - 2p}{p^2 - t^2}, \quad (2.69)$$

or even simpler

$$\text{AF} = j \left[ \frac{L}{t^2 - p^2} \right] \left[ p - e^{-jp} (p \cos t + jt \sin t) \right], \quad (2.70)$$

so that the power distribution  $P(\theta) = |\text{AF}|^2$  reads:

$$P(\theta) = \frac{L^2}{|t^2 - p^2|^2} \left| p - e^{-jp} (p \cos t + jt \sin t) \right|^2. \quad (2.71)$$

Since we are interested in LWAs radiating at broadside, it would be useful to normalize the power distribution to the power radiated at broadside ( $\theta = 0^\circ$ ) that is equal to

$$P(0) = \frac{L^2}{|p|^2} \left| 1 - e^{-jp} \right|^2 \quad (2.72)$$

or

$$P(0) = \frac{4L^2}{|p|^2} |\sin(p/2)|^2 e^{-a}, \quad p \in \mathbb{C}. \quad (2.73)$$

Hence, the normalized power distribution  $\bar{P}(\theta) = P(\theta)/P(0)$  yields:

$$\bar{P}(\theta) = \frac{|p|^2}{|p^2 - t^2|^2} \frac{\left| p - e^{-jp} (p \cos t + jt \sin t) \right|^2 e^a}{4 |\sin(p/2)|^2}. \quad (2.74)$$

By means of Eq. (2.74) the one-sided half-power beamwidth  $\Delta\theta_h$  can easily be found solving the roots of the following equation:

$$\bar{P}(\Delta\theta_h) = \frac{|p|^2}{|p^2 - t_h^2|^2} \frac{\left| p - e^{-jp} (p \cos t_h + jt_h \sin t_h) \right|^2 e^a}{4 |\sin(p/2)|^2} = \frac{1}{2}, \quad (2.75)$$

where  $t_h = l \sin(\Delta\theta_h)$ . It is worth here to stress that we will always assume that  $\Delta\theta_h$  is small enough to assume  $t_h \simeq l\Delta\theta_h$ . Moreover, since we are evaluating the normalized radiation pattern at broadside it is assumed that

$b \leq a$ . However we will distinguish between cases for which  $b = a$  and those for which  $b \neq a$ .

*Evaluation of the beamwidth when  $b = a$*

It is well known that when  $b = a$  (and in turn  $p = (1 - j)a$ ) the radiated power density at broadside is maximized [48]. To prove the correctness of Eq. (2.75), let us check the expressions in the limit for  $a \rightarrow 0$  (which would correspond to uniform apertures) and for  $a \rightarrow \infty$  (which would correspond to infinitely large apertures). Hence, for  $a \rightarrow 0$ :

$$\lim_{a \rightarrow 0} \bar{P}(\Delta\theta_h) \stackrel{p \rightarrow 0, \sin x \simeq x}{=} \frac{|p|^2}{|t_h^2|^2} \frac{|t_h^2| |\sin^2 t_h|}{4|p/2|^2} = \frac{1}{2}$$

$$t_h^2 = 2 \sin^2 t_h, \quad (2.76)$$

which is the same result given by Eq. (2.12) for  $a \rightarrow 0$  that gives  $t_h = 1.3915$  (see 2.2.1) and thus

$$\Delta\theta_h = \frac{1.3915}{l} \simeq \frac{0.44}{L/\lambda}. \quad (2.77)$$

Conversely, for  $a \rightarrow \infty$  we get:

$$\lim_{a \rightarrow \infty} \bar{P}(\Delta\theta_h) = \frac{|p|^4}{|p^2 - t_h^2|^2} \frac{e^a}{4|\sin(p/2)|^2} = \frac{1}{2}. \quad (2.78)$$

Note that:

$$\lim_{a \rightarrow \infty} \sin(p/2) = \frac{e^{j(1-j)a/2} - e^{-j(1-j)a/2}}{2}$$

$$\lim_{a \rightarrow \infty} |\sin(p/2)|^2 = \frac{e^a}{4}, \quad (2.79)$$

so that

$$\lim_{a \rightarrow \infty} \bar{P}(\Delta\theta_h) = \frac{|p|^4}{|p^2 - t_h^2|^2} = \frac{1}{2}, \quad (2.80)$$

but since  $p = (1 - j)a$  we have:

$$|p| = \sqrt{2}a,$$

$$p^2 = -2ja^2, \quad (2.81)$$

and Eq. (2.78) simplifies as:

$$\lim_{a \rightarrow \infty} \bar{P}(\Delta\theta_h) = \frac{4a^4}{t_h^4 + 4a^4} = \frac{1}{2}, \quad (2.82)$$

and finally

$$t_h = \sqrt{2}a, \quad (2.83)$$

which gives

$$\Delta\theta_h = \sqrt{2} \frac{a}{l} = \sqrt{2} \frac{\alpha}{k_0}, \quad (2.84)$$

according to the result found in literature for 2-D LWAs [11].

*Evaluation of the beamwidth when  $b \neq a$*

Now that the consistency of Eq. (2.74) has been assessed, the second step consists of considering the possibility to extend the results even when  $b \neq a$ . However, since we are interested in broadside radiation (for scanned beams, the beamwidth of 1-D bidirectional LWAs is the same as 1-D unidirectional LWAs provided that  $\alpha \ll k_0$ ) we would consider  $b \leq a$ . Here, it is useful to define the ratio

$$r = \frac{b}{a} < 1, \quad (2.85)$$

so that we can express  $p$  as  $p = a(r - j)$ . With this new definition, it is quite obvious that the result for the limit  $a \rightarrow 0$  would remain the same as for  $b = a$ . Conversely, for  $a \rightarrow \infty$ , Eq. (2.81) now reads:

$$\begin{aligned} |p| &= a\sqrt{r^2 + 1} \\ p^2 &= a^2(r^2 - 1 - 2jr). \end{aligned} \quad (2.86)$$

As a consequence Eq. (2.80) can easily be recast as:

$$\begin{aligned} 2|p|^4 &= |p^2 - t_h^2|^2 \\ 2a^4(r^2 + 1)^2 &= |r^2a^2 - a^2 - t_h^2 - 2ja^2r|^2. \end{aligned} \quad (2.87)$$

After some algebra we get the following quadratic equation for  $\phi_h = t_h^2$ :

$$\phi_h^2 - 2a^2(r^2 - 1)\phi_h - a^4(r^4 + 2r^2 + 1), \quad (2.88)$$

whose roots give:

$$\phi_h = a^2 \left[ (r^2 - 1) \pm \sqrt{2(r^4 + 1)} \right], \quad (2.89)$$



and consequently

$$t_h = a \sqrt{(r^2 - 1) \pm \sqrt{2(r^4 + 1)}}. \quad (2.90)$$

The substitution of  $r = b/a$  and the choice of the positive determination of the square root (which corresponds to consider the right-side of the beamwidth with respect to the pointing angle) yields

$$t_h = \sqrt{(b^2 - a^2) + \sqrt{2(b^4 + a^4)}}, \quad (2.91)$$

from which we get the sought expression for  $\Delta\theta_h$ :

$$\Delta\theta_h = \sqrt{(\hat{\beta}^2 - \hat{\alpha}^2) \pm \sqrt{2(\hat{\beta}^4 + \hat{\alpha}^4)}}, \quad (2.92)$$

which is the well-known expression for the beamwidth of 2-D LWAs in the limit of infinite aperture (see Eq. (1.29)).

#### 2.4.2 Beamwidth formulas for finite apertures

In the previous paragraph 2.4.1 it has been proven that, in the asymptotic limit of infinite apertures, the beamwidth formulas for 1-D bidirectional LWAs coincide with those of 2-D LWAs. In this Section, we aim to extend the previous results for finite LWAs. This would require to numerically solve Eq. (2.75). However, it is in authors' belief that, under certain conditions, it should be possible to find a fitting procedure (as has already been done in 2.2.2 and 2.3.5), for obtaining an approximate analytic formula for the evaluation of the beamwidth of 1-D bidirectional LWAs which takes into account the finiteness of the aperture. Starting from Eq. (2.75), simple algebra lead us to the following transcendental equation:

$$2|p|^2 \left| p - e^{jp} (p \cos t_h + jt_h \sin t_h) \right|^2 - \left| p^2 - t_h^2 \right| \left| 1 - e^{-jp} \right|^2 = 0, \quad (2.93)$$

where  $p = r(a - j)$  and  $t_h = l \sin \Delta\theta_h$ . As is clear, Eq. (2.93) defines a function  $f(a, r, l, \Delta\theta_h) = 0$  of the two variables,  $a$  and  $\Delta\theta_h$ , and the two parameters  $l$  and  $r$ . Again, as has already been pointed out, *Dini's Theorem* guarantees the existence of an implicit function  $\Delta\theta_h(a; r, l)$  such that  $f(\Delta\theta_h(a; r, l), a) = 0$  where  $l$  and  $r$  are parameters. Hence, a suitable fitting procedure onto the roots of Eq. (2.93) should give us the sought expression. It is worth here to remark that, in order to reduce the space of the parameters, we will actually search for an implicit function  $t_h(a; r)$  for any fixed  $l$ . In such a way, the function will no longer depends on  $l$  and the beamwidth  $\Delta\theta_h$  will easily be expressed in terms of  $t_h(a; r)$  through:

$$\Delta\theta_h(a; r, l) = \arcsin \left( \frac{t_h(a; r)}{l} \right). \quad (2.94)$$

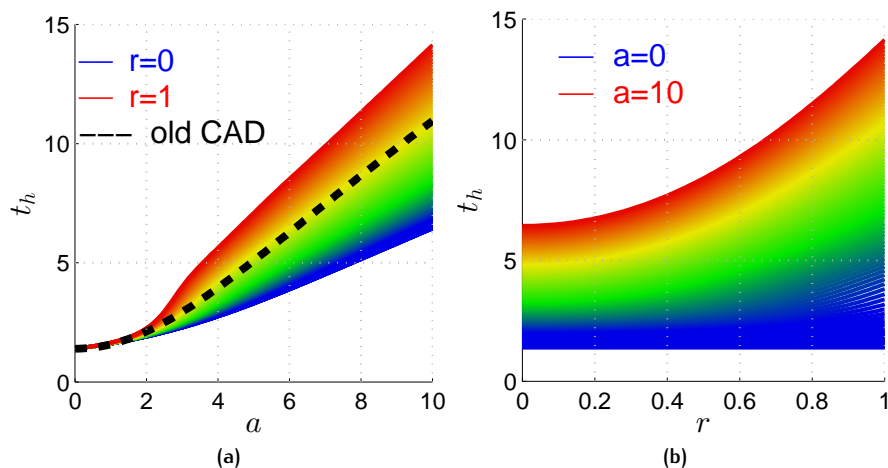


Figure 2.26.: (a)  $t_h$  vs.  $a$ . A family of curves shading from blue to red is generated for  $r$  going from 0 to 1. The black solid line represent the result obtained through Eq. (2.12). (b)  $t_h$  vs.  $r$ . A family of curves shading from blue to red are generated for  $a$  going from 0 to 10.

In Fig. 2.26 the behavior of  $t_h$  as a function of  $a$  (see Fig. 2.26(a)) and  $r$  (see Fig. 2.26(b)) has been reported for parametric variations of  $r$  and  $a$ , respectively. Note that  $r$  has been limited to the range  $0 \leq r \leq 1$  since we are interested only in broadside radiation, whereas the range of  $a$  widely covers any practical efficiency for LWAs. As is seen, the parameter  $r$  strongly affects the behavior of  $t_h(a)$  (see Fig. 2.26(a)), so that it would not be possible to find a unique fitting function for  $t_h(a)$ . However, the behavior of  $t_h(r)$  (see Fig. 2.26(b)) seems to be much simpler than  $t_h(a)$ . This fact would suggest to search for a family of  $r$ -parametric fitting functions of  $t_h(a; r)$  which belong to the same class of functions with respect to  $a$ . This is the same kind of problem encountered in 2.3.5.

As a first guess, due to the similarity with the old fitting formula provided in 2.2.2 (see black dashed line in Fig. 2.27(a)) we used the following interpolating function:

$$t_h(a; r) = 1.3915 + w_1(r)a \tanh(w_2(r)a), \quad (2.95)$$

where now the coefficients  $w_1$  and  $w_2$  both depends on  $r$ <sup>14</sup>. In this way, we have obtained our desired  $r$ -parametric functions. These first results have been reported in Fig. 2.27(a). Also the behavior of the coefficients  $w_1(r)$  and  $w_2(r)$  has been reported in Fig. 2.27(b). As is clear, a second-order polynomial function would be sufficient to accurately interpolate such functions, as corroborated by the remarkable agreement between the fit curves (dashed

<sup>14</sup> Note that Eq (2.95) is basically the HTF function described in 2.2.2.

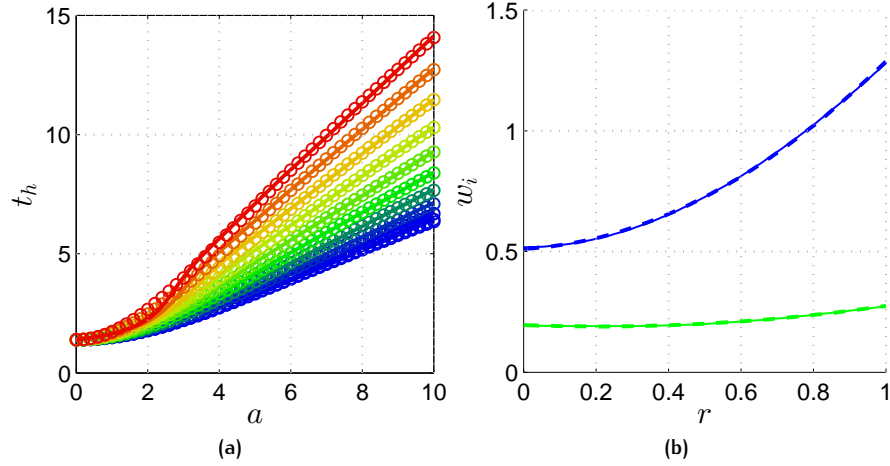


**Figure 2.27.:** (a)  $t_h$  vs.  $a$ . A family of curves (solid lines) shading from blue to red is generated for  $r$  going from 0 to 1. The fitting curves are reported in circles. (b)  $w_1$  vs.  $r$  (blue solid line) and  $w_2$  vs.  $r$  (green solid line). The corresponding interpolations are reported in dashed lines.

lines) and the original ones (solid lines). The final interpolating function would thus be represented by Eq. (2.95) with *parametric* coefficients:

$$\begin{aligned} w_1(r) &= w_{1,1} + w_{1,2}r + w_{1,3}r^2, \\ w_2(r) &= w_{2,1} + w_{2,2}r + w_{2,3}r^2, \end{aligned} \quad (2.96)$$

where the coefficients  $w_{ij}$  for  $i = 1, 2$  and  $j = 1, 2, 3$  have been reported in Table 2.10. Finally, the resulting interpolation has been reported in Fig. 2.28. As can be seen, the second fitting procedure introduce negligible error with respect to the previous one that shows a good accuracy except for the range  $a \in \{1.5, 2.5\}$ .

This is clearly seen in Fig. 2.29 where the APE is reported before (see left panel of Fig. 2.29) and after (see right panel of Fig. 2.29) the fitting of the coefficients. In both cases, the region that is less accurate (APE  $\simeq 18\%$ ) corresponds to  $a \in \{1.5, 2.5\}$ , whereas the MAPE is around 2%

A thorough inspection of Fig. 2.26(a) convinced us that a more suitable class of interpolating functions would be the following one:

$$t_h(a; r) = 1.3915 + 0.25a(1 - \tanh a) + w_1(r)a \tanh[w_2(r)(a - w_3(r))]. \quad (2.97)$$

**Table 2.10.:** Values of the fitting coefficients for  $w_1(r)$  and  $w_2(r)$ .

$w_{i,j}$	$j = 1$	$j = 2$	$j = 3$
i=1	0.511	0.084	0.693
i=2	0.195	-0.056	0.135

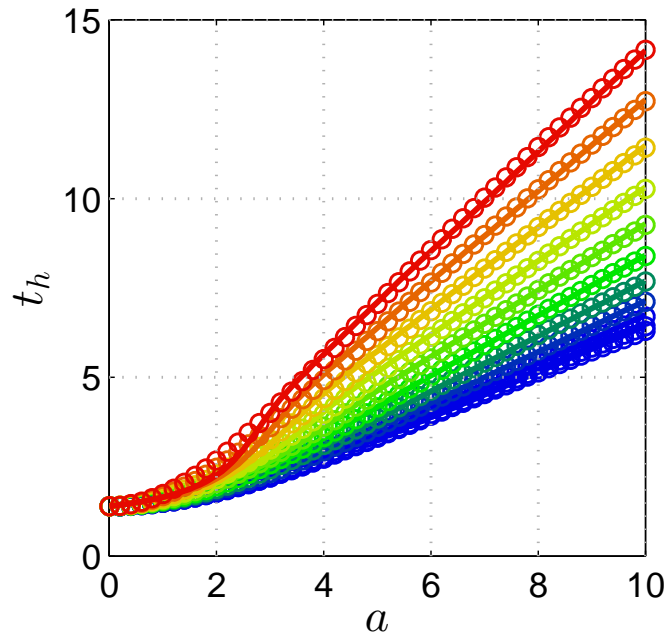


Figure 2.28.:  $t_h$  vs.  $a$ . A family of curves (solid lines) shading from blue to red is generated for  $r$  going from 0 to 1. The fitting curves are reported in circles.

The reason why we came to this conclusion is because  $t_h(a; r)$  seems to be characterized by two linear functions with different slopes that are smoothly joint at a certain point within the *delicate* region  $a \in \{1.5, 2.5\}$  which depends on  $r$ . As a consequence the first complementary hyperbolic tangent is used to reduce the effect of the first linear function, whereas the second hyperbolic tangent is used to enhance the second linear function. In particular  $w_1$  is used for tuning the *slope*,  $w_2$  is used for tuning the *hardness* of the enhancement, and  $w_3$  is used for tuning the *locus of the joint* between the linear functions.

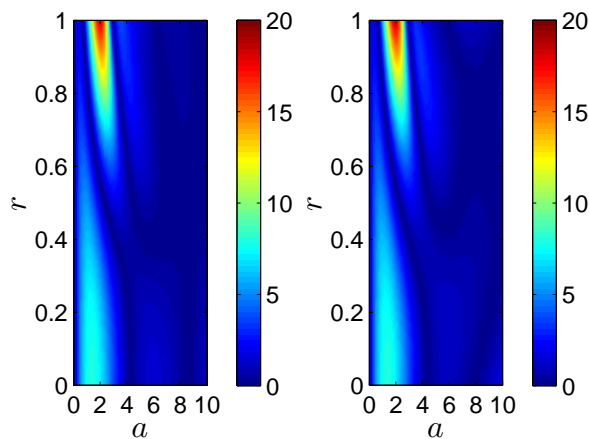
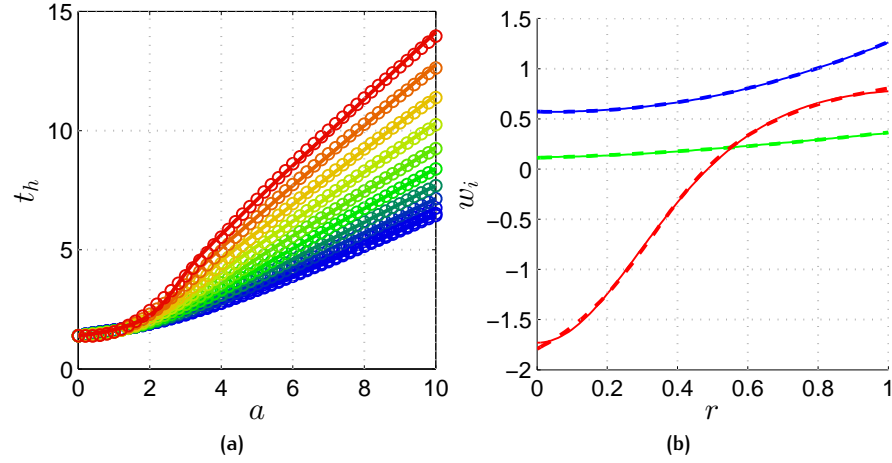


Figure 2.29.: Contour plot of APE vs.  $a$  and  $r$ . Left panel: APE is calculated after the first fitting procedure (see Fig. 2.27). Right panel: APE is calculated after the second (last) fitting procedure (see Fig. 2.28).



**Figure 2.30.:** (a)  $t_h$  vs.  $a$ . A family of curves (solid lines) shading from blue to red is generated for  $r$  going from 0 to 1. The fitting curves are reported in circles. (b)  $w_1$  vs.  $r$  (blue solid line),  $w_2$  vs.  $r$  (green solid line), and  $w_3$  (red solid line). The corresponding interpolations are reported in dashed lines.

These first results have been reported in Fig. 2.30(a). Also the behavior of the coefficients  $w_1(r)$  and  $w_2(r)$  has been reported in Fig. 2.30(b). As is clear, a second-order polynomial function would be sufficient to accurately interpolate only  $w_1$  and  $w_2$ . For  $w_3$  we used an  $\arctan(\cdot)$  function. This choice gave very accurate results, as corroborated by the remarkable agreement between the fit curves (dashed lines) and the ideal ones (solid lines). The final interpolating function would be thus represented by Eq. (2.95) with *parametric* coefficients:

$$\begin{aligned}
 w_1(r) &= w_{1,1} + w_{1,2}r + w_{1,3}r^2, \\
 w_2(r) &= w_{2,1} + w_{2,2}r + w_{2,3}r^2, \\
 w_3(r) &= w_{3,1} + w_{3,2}r \arctan(w_{3,3}r + w_{3,4}), \quad (2.98)
 \end{aligned}$$

where the coefficients  $w_{ij}$  for  $i = 1, 2, 3$  and  $j = 1, 2, 3, 4$  have been reported in Table 2.11.

Again, the resulting interpolation has been reported in Fig. 2.31. As can be seen, the second fitting procedure introduce negligible error with respect to the previous one that shows a good accuracy except for the range  $1.5 \leq a \leq 2.5$ .

**Table 2.11.:** Values of the fitting coefficients for  $w_1(r)$ ,  $w_2(r)$  and  $w_3(r)$ .

$w_{i,j}$	$j = 1$	$j = 2$	$j = 3$	$j = 4$
$i=1$	0.572	-0.072	0.767	0
$i=2$	0.111	0.104	0.149	0
$i=3$	-0.676	1.248	3.989	-1.3

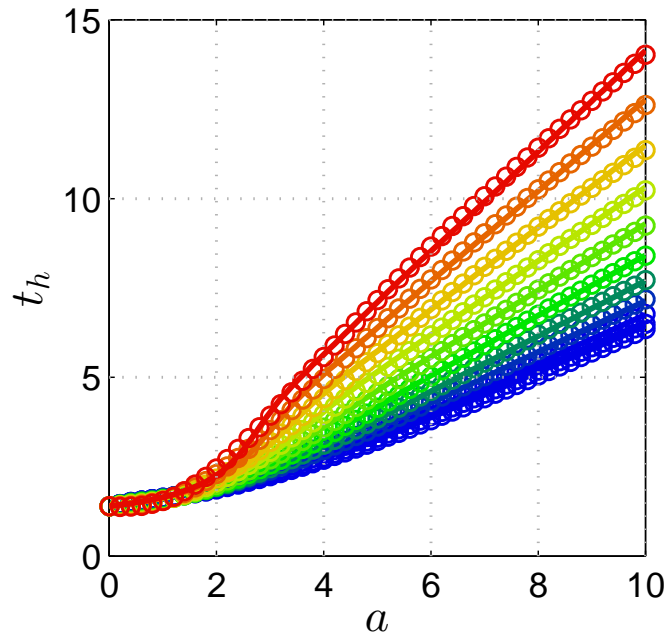


Figure 2.31.:  $t_h$  vs.  $a$ . A family of curves (solid lines) shading from blue to red is generated for  $r$  going from 0 to 1. The fitting curves are reported in circles.

This is clearly seen in Fig. 2.32 where the APE is reported before (see left panel of Fig. 2.32) and after the fitting of the coefficients (see right panel of Fig. 2.32). In both cases, the region that is less accurate (APE  $\simeq 8.8\%$ ) corresponds to  $a \in \{1.5, 2.5\}$ , whereas the MAPE is around 0.9%.

As a final remark, it should be stressed that the considerable improvement in terms of APE of the last interpolation (the APE is reduced of about a half) is paid only at the expense of the complexity of the expression.

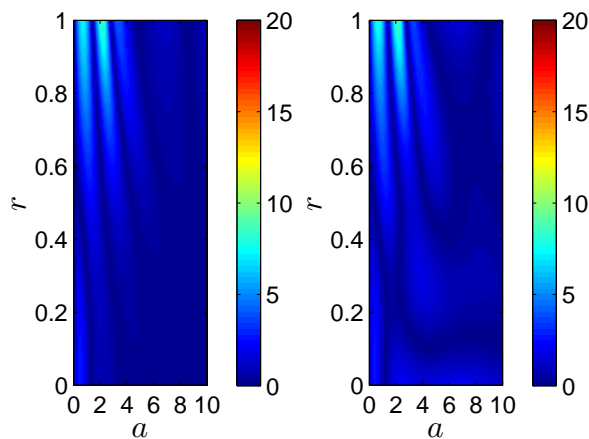


Figure 2.32.: Contour plot of APE vs.  $a$  and  $r$ . Left panel: APE is calculated after the first fitting procedure (see Fig. 2.30). Right panel: APE is calculated after the second (last) fitting procedure (see Fig. 2.31).

The final formula for the single-sided beamwidth of 1-D bidirectional LWAs is then:

$$\Delta\theta_h(a; r, l) = \arcsin \left( \frac{1.3915 + 0.25a(1 - \tanh a) + w_1(r)a \tanh[w_2(r)(a - w_3(r))]}{l} \right),$$

with

$$\begin{cases} w_1(r) = 0.572 - 0.072r + 0.767r^2, \\ w_2(r) = 0.111 + 0.104r + 0.149r^2, \\ w_3(r) = -0.676 + 1.248r \arctan(3.989r - 1.3). \end{cases}$$

(2.99)

## 2.5 CONCLUSION

In this Chapter a general formula for the evaluation of the beamwidth of 1-D unidirectional LWAs which accounts for both the attenuation constant and the length of the aperture, has been presented. Previous formulas can now be derived as a special case of the new general formula that is accurate for any combination of phase constant, attenuation constant, and aperture length. This means that the beam can be pointed to any angle in space, down to where endfire is first encountered. However, when the beam is scanned beyond ordinary endfire, these new formulas no longer hold.

The radiating features of endfire leaky-wave antennas are then described with a different formulation. Simple approximate formulas (exact closed-form expressions are found in the infinite aperture case) for the beamwidth and sidelobe level are found, which account for both the antenna length and the radiation efficiency. In fact, as the phase constant increases and the beam scans beyond ordinary endfire, the beamwidth continuously decreases as the phase constant increases, but the sidelobe level also correspondingly increases. A tradeoff between beamwidth and sidelobe level is then established.

Finally, a more accurate beamwidth formula is found for 1-D bidirectional leaky-wave antennas. In this case, the beamwidth of scanned beams is equal to the one of 1-D unidirectional LWAs, whereas it substantially differs at broadside. As a consequence an approximate formula (an exact one is again derived in the infinite aperture case) is derived only for broadside beams taking into account the dependence of both the phase constant and the efficiency. This analysis represents a significant step towards the development of more accurate formulas for the evaluation of the beamwidth in 2-D leaky-wave antennas.



# 3

## RECONFIGURABLE LEAKY-WAVE ANTENNAS

### 3.1 INTRODUCTION

In the last decade, the concept of Transformation Optics (TO), introduced for the first time in 2006 by J. B. Pendry [70] (for which he won the Kavli Prize in Nanoscience in 2014), has strongly boosted the research activity in metamaterials [31]. Their use has been promoted in [70] for practically achieving a considerable control of the electromagnetic fields. In principle, the uncommon features exhibited by metamaterials would allow for the realization of intriguing applications such as *electromagnetic cloaking* [71] and *metasurfing*, i.e., addressing electromagnetic waves on metasurfaces [72], as well as reconfigurable LWAs [73].

Although different designs of metasurfaces exist in the microwave range [72], [74], [75], only few implementations have been proposed in the terahertz (THz) range [76], [77], i.e., that part of the spectrum that nominally goes from 300 GHz to 3 THz [78]. In recent years, a lot of efforts (see, e.g., [79], [80] and Refs. therein) have been made in order to close as much as possible the well-known *THz gap* [81], [82] by designing efficient THz sources and sensors. These elements leverage components from both microwaves and optics [83], [84]. As a result, there is still a high demand of efficient sensors, especially for medical and security applications [78], [85]. Such an interest is motivated by the various applications offered by THz radiation in several interdisciplinary fields, such as molecular spectroscopy, astrophysics, security screening, high-resolution imaging, drug detection, THz free-space communication [86]–[88].

In the last years, we have witnessed the exponential development of efficient optical and terahertz (THz) devices by means of cutting-edge materials such as *black phosphorous* [89], *molybdenum disulphide* MoS<sub>2</sub> [90], *graphene* [91], and *liquid crystals* [92], [93]. In this Chapter we specifically deal with the opportunities offered by graphene and liquid crystals. In fact, the possibility to dynamically tune both the electronic and the optical properties of these materials through the application of a control voltage has allowed for the design of reconfigurable THz devices. On one hand, it has recently been demonstrated that LCs can profitably be used for the realization of THz composite free-space materials [94]–[98] as well as guided-wave THz phase shifters [99]–[102]. On the other hand, recent works have considered the use of a graphene sheet as a frequency selective surface for the design of reconfigurable radiating elements [103]–[116]. However, in the current literature,

very few works have considered the possibility of designing reconfigurable THz LWAs by employing either liquid crystals or graphene sheets.

In Section 3.2, we thoroughly analyze the radiating properties of graphene-based LWAs based on *ordinary* (i.e. non-plasmonic) leaky waves in the THz range. In Section 3.3, the design of a THz Fabry-Perot Cavity (FPC) LWA based on liquid crystals is discussed from both a theoretical point of view and a technological perspective. It is worth noting that the proposed structures can be seen as advanced versions of the *unconventional* 2-D LWAs previously mentioned in 1.4.4.

### 3.2 GRAPHENE-BASED LEAKY-WAVE ANTENNAS

The pioneering experiments on graphene led by A. K. Geim and K. S. Novoselov [117] have paved the way to the application of this promising material in a multitude of scenarios including integrated technologies, especially at THz frequencies. In this frequency range, graphene shows interesting properties, because its surface conductivity (which completely characterizes its electromagnetic properties, due to the mono-atomic layer structure) becomes mostly reactive [118], [119] and hence can support plasmonic propagation [120]. Moreover, surface plasmon polariton (SPP) waves supported by graphene may have a guided wavelength much shorter than the wavelength of plane waves in free space, thus resulting in a tight transverse confinement of the SPP field [121], [122], especially if compared to SPP propagation along ordinary metal surfaces. However, the most intriguing feature of graphene is perhaps the possibility of dynamically tuning its conductivity through the application of an electrostatic bias field, which lays the ground for the development of reconfigurable THz devices.

Despite all these excellent properties, graphene was initially considered mainly as an alternative to post-silicon transistors [123] rather than as a material for antennas and other passive devices. Specifically in antenna applications, graphene was first employed as a parasitic layer of a THz dipole antenna array radiating around 1 THz [124]. Also, the propagation of SPPs along an infinite graphene sheet was theoretically derived [118], [119], [125], and the first study on graphene used as an actual antenna radiator was presented in [106]. There, it was shown that graphene allows for the realization of miniaturized resonant and reconfigurable THz antennas with good efficiency, compared to the small electrical size, and good direct matching, as required by most of the present THz communication and sensing devices. Over the years [103]–[116], other works have further investigated the possibilities of graphene in antenna design.

Most of these works [103]–[111] consider the radiation mechanism through the excitation of a transverse-magnetic (TM) SPP. Interestingly, in [103], [104] a sheet of graphene is sinusoidally modulated by applying a DC bias to a polysilicon layer located beneath it, in order to control its surface reactance; this allows for coupling the SPP with the  $n = -1$  harmonic which is in the *fast-wave region* and thus radiates as a leaky-wave mode. Such *plasmonic* leaky waves allows for achieving the beam-steering capability at a fixed frequency. However, the well-known relatively high losses experienced by SPPs over graphene limit the efficiencies of these LWAs to values on the order of 20% [103]–[106]. To the author's best knowledge, only recently [113] a *non-plasmonic* graphene-based LWA has been proposed. There, a patterned graphene sheet is used to enhance the tunability of a high-impedance surface that acts as a ground plane in a 2-D LWA. However, the directivity of the proposed antenna is rather low [113].

As a matter of fact, it has recently been shown [126], [127] that fundamental limits exist on the efficiency of any reconfigurable graphene antenna. However, we note that the fundamental role of the graphene losses in affecting the performance of such kind of radiators, in terms of theoretical radiation efficiency, directivity, and pattern reconfigurability has not been yet properly analyzed in detail. Most importantly, a thorough investigation of dissipation losses and radiation efficiencies of THz graphene antennas based both on plasmonic and non-plasmonic field configurations has never been considered in the literature. Only very recently [128], the aspect of radiative losses in the class of composite right/left-handed (CRLH) leaky-wave graphene devices has gained specific attention, especially in connection with the graphene quality.

In this Section, we focus our investigation on FPC-LWAs, whose radiation mechanism is based on the excitation of *ordinary* (i.e., non-plasmonic) leaky waves which exhibit a sinusoidal transverse modal profile [114], [115], and compare them with those of graphene antennas based on the excitation of SPPs either in bound or leaky propagation regimes [103], [104], [106]. The ultimate goal is to assess the true limitations of these devices and ascertain the benefits of designing graphene THz antennas whose radiation mechanism is based on non-plasmonic leaky waves.

The Section is organized as follows. In 3.2.1 the electronic and physical properties of graphene are briefly reviewed. In particular, the validity of Kubo formula [129], [130] is compared with more sophisticated models which take into account the spatially-dispersive nature of graphene. A specific focus is devoted to the impact of graphene quality in graphene ohmic losses. In 3.2.2 the role of plasmonic losses in graphene-based structures is rigorously discussed, showing how it affects the performance of graphene THz antennas based on SPPs. This motivates the employment of non-plasmonic leaky-waves in 2-D LWAs.

In 3.2.3 and 3.2.4 we present a thorough dispersive, modal, and radiative analysis of two novel graphene-based 2-D LWAs: the *Graphene Planar Waveguide* (GPW) [114] and the *Graphene Substrate-Superstrate* (GSS) antenna [115]. The non-negligible ohmic losses of graphene in the THz range are shown here to determine a design trade-off between efficiency, directivity, and angular reconfigurability of the radiation pattern. With particular reference to radiation efficiency, the substrate-superstrate configuration (e.g., [115]) is shown to provide additional desirable degrees of freedom with respect to other solutions [103], [104], [106], [114].

In 3.2.5 some preliminary results are reported, considering the possibility to use patterned graphene metasurfaces [113], [131], and thus add further degrees of freedom in the antenna slab. Specifically, a *Graphene-Strip Grating* (GSG) antenna has been considered as a perturbation of the GPW. Finally, in 3.2.6 considerations about the technological implementation of the proposed devices are carefully addressed, taking into account all the limitations imposed by THz technology and graphene synthesis as well.

### 3.2.1 Graphene properties

Graphene, a one-atom thick layer of carbon atoms arranged in a honeycomb lattice, has been the subject of intense research in the last few years, after the production of the first isolated flakes in 2004 [132], because of its exceptional electronic transport properties [117], [133]. Graphene has a triangular unit cell with a basis of two atoms with lattice constant  $a = 1.42 \text{ \AA}$  (see Fig. 3.1(a)) and is a zero-bandgap material, with electron wavefunctions exhibiting pseudospin and linear dispersion around the chemical potential at the corners ( $K$  points) of the first Brillouin zone (see Fig. 3.1(b)). Consequently, the linear dispersion of the energy allows for evaluating the Fermi velocity as  $v_F = \hbar^{-1} \partial \mathcal{E} / \partial \mathbf{k}$  where the energy is given by  $\mathcal{E} = (3\hbar t a / 2) |\mathbf{k}|$  in the tight-binding model approximation [91], [134], [135], and where  $t$  is the first nearest-neighbor tight-binding parameter. As a result, charge carriers act as mass-less, chiral relativistic Dirac fermions with a constant Fermi velocity  $v_F = 3at/2 \simeq 10^6 \text{ m/s}$  at low energies.

On one hand, this produces a number of unusual features, typically observed only in the context of quantum electrodynamics. On the other hand, the resulting low electron effective mass and long scattering lengths lead to very high carrier mobilities, with room-temperature values having orders of magnitude as high as  $200\,000 \text{ cm}^2 \text{ V}^{-1} \text{ s}^{-1}$  [136]. Graphene is thus emerging as a very attractive candidate for the realization of nanoelectronic circuits [91], such as optoelectronic RF mixers [137], fast-switching transistors [138] just to mention but a few.

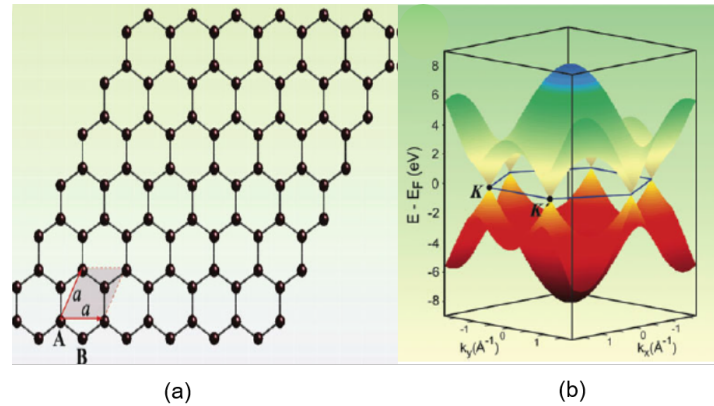


Figure 3.1.: (a) The hexagonal lattice of a graphene monolayer. The unit cell of graphene with lattice constant  $a$  has two carbon atoms per unit cell, A and B. (b) Electronic dispersion (energy vs.  $k_x$  and  $k_y$ ) obtained in the frame of the *tight-binding model* [91]. Note the conical shape (linear dispersion) of the diagram in proximity of the  $K$  points of the first Brillouin zone of graphene. Around the  $K$  points the Fermi velocity. The figure is a concession of [91].

### Graphene conductivity: Kubo formalism

The theory of graphene opens to a lot of other exceptional and unique thermal, electrical, physical, and mechanical properties, whose discussion goes beyond the scope of this PhD thesis. From an antenna engineering point of view, one extremely interesting aspect of graphene theory is that, due to its infinitesimal thickness, a graphene monolayer is adequately treated as a metasurface whose homogenized surface conductivity (neglecting nonlocal effects [139], [140]) can be derived in scalar form by means of the Kubo formalism [129], [130]. In this frame, graphene conductivity  $\sigma = \sigma_{\text{intra}} + \sigma_{\text{inter}}$  is described by its *intra*band  $\sigma_{\text{intra}}$  and *inter*band  $\sigma_{\text{inter}}$  contributions given by the following expressions:

$$\sigma_{\text{intra}} = \frac{2q_e^2 k_B T}{\pi \hbar^2 (\tau^{-1} + j\omega)} \ln \left[ 2 \cosh \left( \frac{\mu_c}{2k_B T} \right) \right], \quad (3.1)$$

$$\sigma_{\text{inter}} = -j \frac{q_e^2}{4\pi \hbar} \ln \left( \frac{2|\mu_c| - (\omega - j\tau^{-1}\hbar)}{|\mu_c| - (\omega + j\tau^{-1}\hbar)} \right), \quad \text{hyp.: } k_B T \ll |\mu_c|, \hbar\omega, \quad (3.2)$$

where  $\omega = 2\pi f$  is the angular frequency (assumed throughout the paper),  $-q_e$  is the electron charge,  $k_B$  is the Boltzmann constant, and  $\hbar$  is the reduced Planck constant,  $\tau$  is the *relaxation time* (related to the *scattering rate*  $\Gamma$  through  $\Gamma = 1/(2\tau)$ ),  $\mu_c$  is the chemical potential (which is equivalent to the Fermi level  $E_F$ ).

Clearly,  $\sigma$  is strongly affected by the values of  $\mu_c$  which is in turn related to the electrostatic bias  $E_0$ . In fact, if one considers a graphene sheet embedded in a medium of relative permittivity  $\epsilon_r$ , the normal component of the displacement vector field  $D_n = \epsilon_0 \epsilon_r E = \rho_s$  should be equal to the surface charge (on either side of the graphene sheet) which is given by  $\rho_s = n_s q_e / 2$ . Due to the *ambipolar electric field-effect* [117], the 2-D surface-charge density  $n_s$  takes contributions from both negative and positive charge carriers, i.e., *electrons* and *holes*, respectively. As a consequence  $n_s = |n - p|$ , where  $n$  and  $p$  are the electron and hole carrier densities, respectively, whose expressions are [141]:

$$n = \frac{2}{\pi} \left( \frac{k_B T}{\hbar v_F} \right)^2 \mathfrak{J}_1(+\mu_c), \quad (3.3)$$

$$p = \frac{2}{\pi} \left( \frac{k_B T}{\hbar v_F} \right)^2 \mathfrak{J}_1(-\mu_c), \quad (3.4)$$

with

$$\mathfrak{J}_1(\mu_c) = \frac{1}{(k_B T)^2} \int_0^\infty \mathcal{E} (1 + \exp[(\mathcal{E} - \mu_c)/(k_B T)])^{-1} d\mathcal{E}. \quad (3.5)$$

Combining Eqs. (3.3) and (3.4) in  $n_s$  we finally have:

$$n_s = \frac{2}{\pi \hbar^2 v_F^2} \int_0^\infty \mathcal{E} [f_d(\mathcal{E}) - f_d(\mathcal{E} + 2\mu_c)] d\mathcal{E}, \quad (3.6)$$

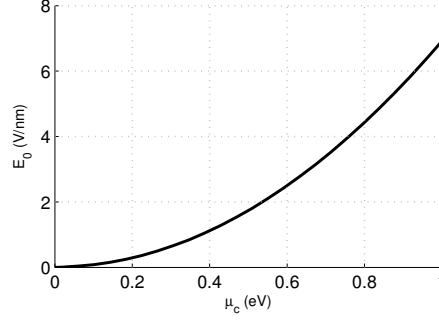


Figure 3.2.:  $E_0$  vs.  $\mu_c$  in the range  $0 \leq \mu_c \leq 1$  eV, obtained from 3.8, for  $\epsilon_r = 1$  (air).

where  $f_D(\mathcal{E})$  is the *Fermi-Dirac distribution*:

$$f_D(\mathcal{E}) = (1 + \exp[(\mathcal{E} - \mu_c)/(k_B T)])^{-1}. \quad (3.7)$$

With these definitions at hand,  $E_0$  is expressed as a function of the chemical potential  $\mu_c$  through the following integral equation:

$$E_0 = \frac{q_e}{\pi \epsilon_0 \epsilon_r \hbar^2 v_F^2} \int_0^\infty \mathcal{E} [f_d(\mathcal{E}) - f_d(\mathcal{E} + 2\mu_c)] d\mathcal{E}. \quad (3.8)$$

Hence,  $E_0$  can be directly obtained for a given chemical potential  $\mu_c$ , by numerically solving the integral on the right-hand side of Eq. (3.8) [119]. The relation  $E_0$  vs.  $\mu_c$  has been reported in Fig. (3.2) in the range  $0 \leq \mu_c \leq 1$  eV for a suspended graphene sheet (i.e.,  $\epsilon_r = 1$ ). As is shown, the maximum absolute value of the chemical potential that can be obtained with electrostatic field on the order of several V/nm (typically used in experiments<sup>1</sup>) is around 1 eV. It should be noted that such an electrostatic field is rather high and is generally above the voltage breakdown of most of common dielectric materials [143]. This aspect will be further exacerbated in 3.2.6.

In the context of antenna engineering the *ambipolar electric-field effect* is one of the most exceptional aspects of graphene theory, since it reveals that the application of a bias voltage allows for changing the conductivity of graphene even at fixed frequency, thus opening the possibility of designing reconfigurable LWAs.

#### *Graphene conductivity: non-local model*

As is known [119], in the low THz band and for sufficiently low values of the longitudinal wavenumber  $k_z$ , spatial-dispersion effects can generally be neglected. When such hypotheses are not fulfilled (e.g., extremely confined SPP for which  $k_z \gg k_0$ ), a non-local spatially dispersive conductivity model [139] has to be taken into account. As is shown in [139], [140], graphene conductivity is generally described by a non-local dyadic conductivity of

<sup>1</sup> In recent experiments, bias voltages  $V_b$  on the order of 100 V have been applied across a grounded dielectric slab covered with a graphene sheet [142]. In that case, a slab of quartz ( $\epsilon_r = 3.8$ ) of thickness  $t = 300 \mu\text{m}$  was considered. Thus, for typical bias voltages in the range of 0 – 100 V,  $E_0 = V_g/t$  would be in the range 0 – 1 V/nm.

graphene which, in spectral domain and polar coordinates, assumes the following form:

$$\underline{\underline{\sigma}} = \begin{bmatrix} \sigma_\rho & 0 \\ 0 & \sigma_\phi \end{bmatrix}, \quad (3.9)$$

where  $\sigma_\rho$  and  $\sigma_\phi$  are functions of the radial wavenumber  $k_\rho$  only (hence graphene is isotropic) and are given by

$$\sigma_\rho = \frac{v_F}{2\pi\gamma_D(1-\chi) + v_F\chi} \sigma_\phi, \quad (3.10)$$

$$\sigma_\phi = \gamma \frac{2\pi\alpha}{v_F^2 k_\rho^2} (1-\chi), \quad (3.11)$$

where

$$\gamma = \frac{jq_c^2 k_B T}{\pi^2 \hbar^2} \ln \left\{ 2 \left[ 1 + \cosh \left( \frac{\mu_c}{k_B T} \right) \right] \right\}, \quad \gamma_D = -j \frac{v_F}{2\pi\omega\tau},$$

$$\chi = \sqrt{1 - \frac{v_F^2 k_\rho^2}{\alpha^2}}, \quad \alpha = \omega + j\tau^{-1}. \quad (3.12)$$

In Figs. 3.3(a) and (b), the expressions of  $\sigma_\rho$  and  $\sigma_\phi$  have been calculated in the range  $0.3 \leq f \leq 3$  THz for an unbiased graphene sheet ( $\mu_c = 0$ ) when  $k_\rho = k_0$  and  $k_\rho = 200k_0$ , respectively, and compared with the expression of  $\sigma$  given by Kubo formula (see Eqs. (3.1) and (3.2)). As expected, a non-negligible difference is seen only for very high values of  $k_\rho$  for which the values of  $\sigma_\rho$  and  $\sigma_\phi$  start to differ. In any case,  $\sigma$  (given by Kubo formula) is always an underestimation of both  $\sigma_\rho$  and  $\sigma_\phi$ .

The non-local model may result useful, for particularly accurate simulations of graphene, as well as dispersion analysis of extremely confined ( $k_\rho \gg k_0$ ) SPP propagating along graphene sheets. Some results will be shown further in this Section.

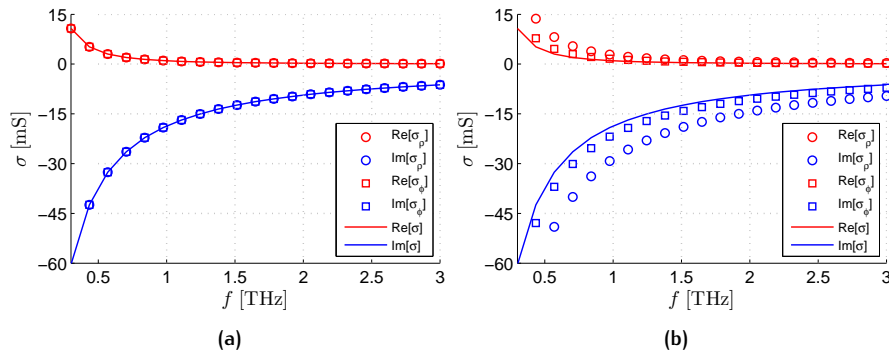
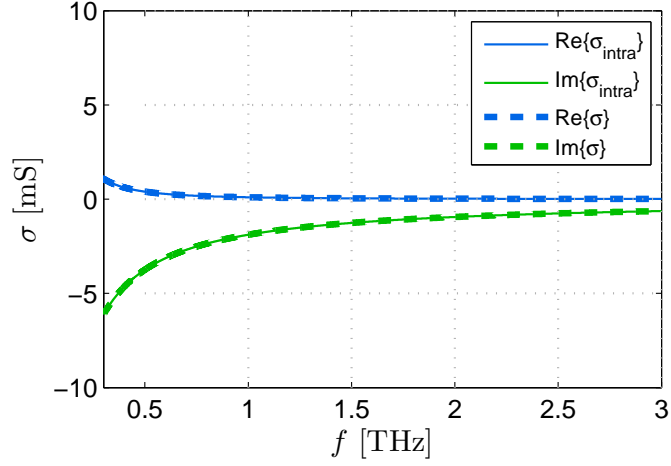


Figure 3.3.: Real part (in red) and imaginary part (in blue) of the graphene surface conductivity as a function of the frequency. Comparison between the expressions of the non-local model, i.e.,  $\sigma_\rho$  (circles) and  $\sigma_\phi$  (in squares), and the Kubo formula  $\sigma$  (solid line). Results are shown for  $\mu_c = 0$  eV and (a)  $k_\rho = k_0$ , (b)  $k_\rho = 200k_0$ .





**Figure 3.4.:** Comparison between  $\sigma = \sigma_{\text{intra}} + \sigma_{\text{inter}}$  (solid lines) and  $\sigma_{\text{intra}}$  (dashed lines) in the low THz range  $0.3 \leq f \leq 3$  THz for  $\mu_c = 0.1$  eV and  $\tau = 3$  ps. The agreement remains good for reasonable values of  $\mu_c$  and  $\tau$ .

#### Graphene conductivity: analysis of Kubo model

In the low THz range, i.e., for  $0.3 \leq f \leq 1$  [THz] and at room temperature, i.e.,  $T = 300$  K  $\sigma_{\text{intra}} \gg \sigma_{\text{inter}}$  [118], [119], thus  $\sigma \simeq \sigma_{\text{intra}}$  (see Fig. 3.4). This means that  $\sigma$  is sufficiently well described by a Drude-like expression, by retaining only the intraband contributions, thus expressing  $\sigma$  as a complex-valued scalar function of the chemical potential  $\mu_c$ , the frequency  $f$ , and the relaxation time  $\tau$ . Since in this Chapter we always fulfill the hypothesis of low THz and room temperature, from now on we will always assume  $\sigma := \sigma_{\text{intra}}$  so that:

$$\sigma = \sigma_R - j\sigma_J = \frac{2q_e^2 k_B T}{(\tau^{-1} + j\omega)\pi\hbar^2} \ln \left[ \cosh \left( \frac{\mu_c}{2k_B T} \right) \right], \quad (3.13)$$

where  $\sigma_R$  and  $-\sigma_J$  expressed in Siemens  $S$  are the conductance and the susceptance of graphene equivalent admittance, respectively. The behavior of both  $\sigma_R$  and  $\sigma_J$  as functions of the frequency  $f$  and the chemical potential  $\mu_c$  in the range  $|\mu_c| < 1$  eV at  $f = 1$  THz, and in the range  $0.3 < f < 3$  THz for  $\mu_c$  ranging from 0 to 1 eV are reported in Fig. 3.5. In all these results,  $\tau$  has always be assumed equal to 3 ps. However,  $\tau$  is never known *a priori* since it mainly depends on the quality of the graphene sample; in the current literature various values in the range 0.01 – 10 ps have been assumed [112].

It is worth here to stress that, despite the existence of sophisticated models [144], [145] which account for the impact of phonon-scattering, grain boundaries and impurities, etc. on graphene quality (either represented by its charge carrier mobility  $\mu$ , or represented by its relaxation time  $\tau$ ), the latter strongly varies sample by sample, depending also on the adopted synthesis technique [146]. Thus, a thorough analysis of graphene conductivity

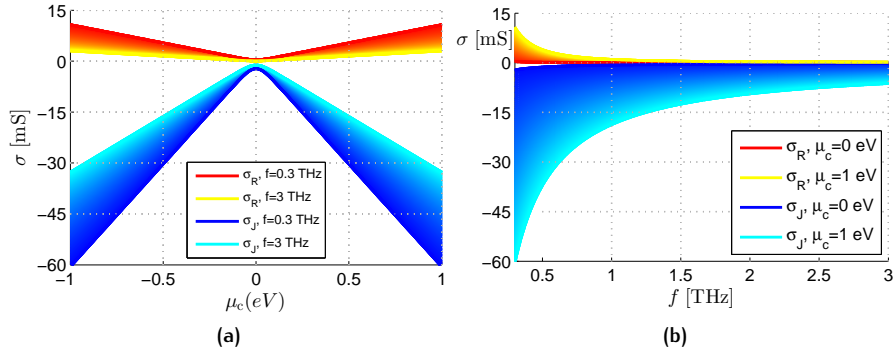


**Figure 3.5.:** (a) Graphene surface conductivity vs. chemical potential in the range  $-1$  to  $1$  eV at the frequency for frequency raising from  $0.3$  THz to  $3$  THz (colors shade from blue to cyan for  $\sigma_J$  and from red to yellow for  $\sigma_R$ , respectively). (b) Graphene surface conductivity vs. frequency in the band  $0.3$ - $3$  THz for chemical potential raising from  $0$  to  $1$  eV (colors shade from blue to cyan for  $\sigma_J$  and from red to yellow for  $\sigma_R$ , respectively).

should take into account the variability of the relaxation time within a suitable range of values provided by experimental data. The interested reader can refer to the recent detailed survey proposed in [147].

In this frame, in order to make our analysis as general as possible, we have considered values of  $\tau$  ranging from  $0$  ps to  $3$  ps (which is the highest value of  $\tau$  that one can hope for pristine graphene [119]), rather than limit our study to one specific value. Clearly, when the frequency  $f$  is fixed,  $\sigma$  depends only on  $\mu_c$  and  $\tau$ . In Fig. 3.6 the values of  $\sigma_R$  (in colors) and  $\sigma_J$  (in black and white), at  $f = 1$  THz, have been reported as functions of  $\tau$  and  $\mu_c$ . As it can be expected, the resistive part of graphene conductivity ( $\sigma_R$ ) increases as  $\mu_c$  increases and  $\tau$  decreases (note that the graphene quality is worse for lower values of  $\tau$ ), whereas its reactive part ( $\sigma_J$ ) increases as  $\tau$  and  $\mu_c$  both increase. This behavior was already commented in [114], where it

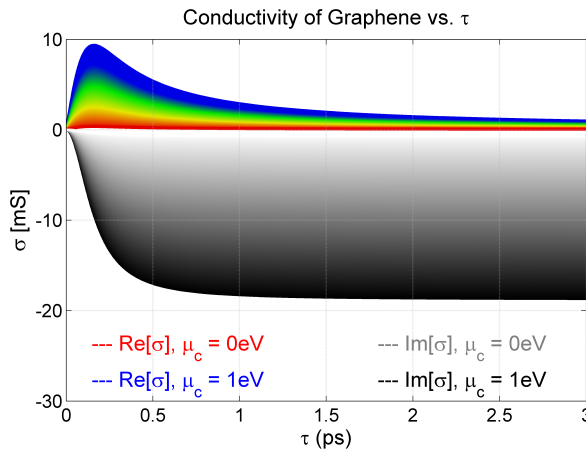


**Figure 3.6.:** (a) Graphene  $\text{Re}[\sigma]$  and  $\text{Im}[\sigma]$  vs.  $\tau$  at  $f = 1$  THz for  $\mu_c$  ranging from  $0$  eV to  $1$  eV.  $\text{Re}[\sigma]$  and  $\text{Im}[\sigma]$  curves gradually shade from red to blue and from gray to black, respectively, as  $\mu_c$  increases from  $0$  eV to  $1$  eV.

was emphasized that, for high values of  $\mu_c$ ,  $\sigma$  becomes mostly reactive, so that graphene can be switched from a bad to a good conductor when  $\mu_c$  is raised in the range 0 eV to 1 eV. However, from Fig. 3.6 we now notice that also the ohmic losses increase for high values of  $\mu_c$ . Hence, biased graphene, even if of good quality (high values of  $\tau$ ), behaves as a good conductor with non-negligible ohmic losses in the considered THz range.

In the next Subsection, this behavior is more deeply discussed in connection with the dissipation losses of an SPP expressed by the normalized attenuation constant  $\hat{\alpha}_{\text{SPP}}$  of the normalized SPP wavenumber  $\hat{k}_{\text{SPP}} = \hat{\beta}_{\text{SPP}} - j\hat{\alpha}_{\text{SPP}} = k_{\text{SPP}}/k_0$  ( $k_0$  being the wavenumber in vacuum). In the next, wavenumbers normalized to  $k_0$  will always be identified with a hat ( $\hat{\cdot}$ ).

### 3.2.2 Graphene plasmonics

As is known [121], an SPP-wave supported by a graphene sheet is characterized by a phase constant much larger than the free-space wavenumber, thus resulting in a transversely evanescent and thus highly-confined surface wave. Both the propagation wavenumber  $\hat{k}_{\text{SPP}}$  and the modal configuration of the SPP directly depend on  $\sigma$ . For the simplest case of a conducting graphene sheet suspended in vacuum (this is also a good approximation for a graphene sheet in air above a ground plane at a distance greater than half the wavelength in the substrate [104]),  $\hat{k}_{\text{SPP}}$  can be calculated in closed form [120], [121]. In this case the normalized plasmonic wavenumber  $\hat{k}_{\text{SPP}}$  reads:

$$\hat{k}_{\text{SPP}} = \sqrt{1 - \frac{4}{(\sigma\zeta_0)^2}}, \quad (3.14)$$

where  $\zeta_0 \simeq 377 \Omega$  is the characteristic impedance of vacuum.

In particular, with the aid of some algebraic manipulations, it is possible to derive an exact formula for the dissipation losses, expressed by  $\hat{\alpha}_{\text{SPP}}$  as a function of  $\sigma_R$  and  $\sigma_J$ :

$$\begin{aligned} \hat{\beta}_{\text{SPP}} &= \left[ \sigma_R \cos\left(\frac{1}{2} \arctan \frac{\Pi}{\Delta}\right) - \sigma_J \sin\left(\frac{1}{2} \arctan \frac{\Pi}{\Delta}\right) \right] \frac{(\Delta^2 + \Pi^2)^{\frac{1}{4}}}{\sigma_R^2 + \sigma_J^2}, \quad (3.15) \\ \hat{\alpha}_{\text{SPP}} &= - \left[ \sigma_J \cos\left(\frac{1}{2} \arctan \frac{\Pi}{\Delta}\right) + \sigma_R \sin\left(\frac{1}{2} \arctan \frac{\Pi}{\Delta}\right) \right] \frac{(\Delta^2 + \Pi^2)^{\frac{1}{4}}}{\sigma_R^2 + \sigma_J^2}, \quad (3.16) \end{aligned}$$

where  $\Delta = \sigma_R^2 - \sigma_J^2 - 4/\zeta_0^2$  and  $\Pi = -2\sigma_R\sigma_J$ .

#### Graphene plasmonic losses

In Fig. 3.7, the value of  $\hat{\alpha}_{\text{SPP}}$ , calculated using Eq. (3.16), is represented as a greyscale map in the complex-conductivity plane for approximately the same range of values achieved by  $\sigma_R$  and  $\sigma_J$  in Fig. 3.6. Furthermore, the

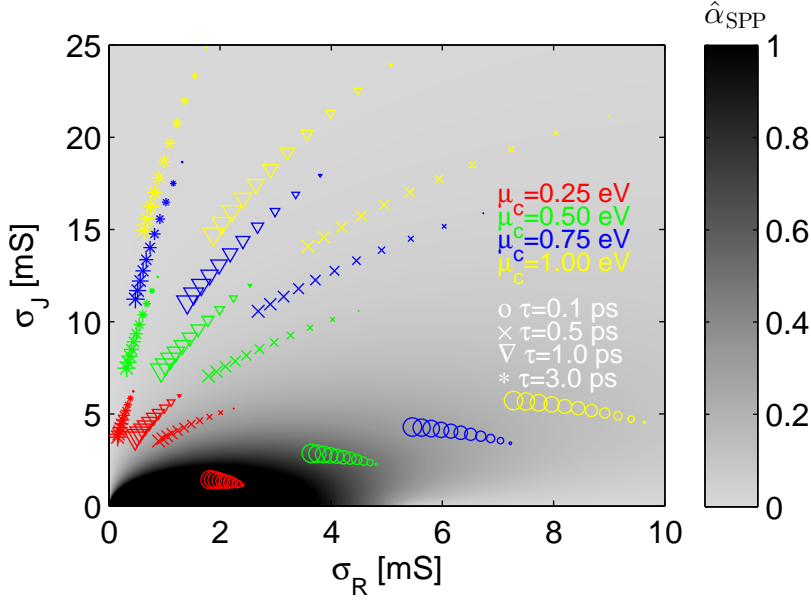


Figure 3.7.: Intensity of plasmonic dissipation losses  $\hat{\alpha}_{SPP}$  in the range  $[0, 1]$  in the  $\sigma$  complex plane. The dynamic range of  $\hat{\alpha}_{SPP}$  has been saturated to values greater than 1 for readability purposes. The paths followed by the graphene surface conductivity in the complex plane have been reported for values of  $f$  ranging from 0.75 THz to 1.25 THz (size of the symbols increases),  $\tau$  ranging from 0.1 ps to 3 ps (symbols change shape in the following order:  $\circ$ ,  $\times$ ,  $\nabla$ ,  $*$ ) and  $\mu_c$  ranging from 0.25 eV to 1 eV (color of the symbol change in the following order: red, green, blue, and yellow). The black region represents the area characterized by the highest dissipation losses and is attained by graphene samples with both lower  $\mu_c$  and  $\tau$ .

paths followed by the complex-valued surface conductivity of graphene in the complex-conductivity plane, when frequency ranges from 0.75 THz (the smallest size of the symbols) to 1.25 THz (the largest size of the symbols) are represented for values of  $\mu_c$  from 0.25 eV to 1 eV (using different colors) and for values of  $\tau$  from 0.1 ps to 3 ps (using different symbols). Note that  $\tau = 0.1$  ps is a typical value for graphene on  $\text{SiO}_2$  substrate [128].

Since the black region in Fig. 3.7 represents the values of the complex-conductivity leading to the highest dissipation losses, it is manifest that:

- i) When frequency increases from 0.75 THz to 1.25 THz (following each colored symbol from its smallest size to the biggest one), the graphene surface conductivity moves to the region of highest dissipation losses, for any chemical potential (color) or relaxation time (symbol), i.e., for any biasing status or graphene quality. It is also evident that the variation of  $\sigma$  with frequency increases by increasing  $\mu_c$ .
- ii) When  $\mu_c$  increases (following the color style of each symbol of any size in the following order: red, green, blue, and yellow), the graphene surface conductivity moves from the region of highest dissipation losses to regions of lowest ones, approximately following a radial line with

respect to the origin of the complex-conductivity plane. The slope of this line depends on the value of  $\tau$  and  $f$ .

- iii) When  $\tau$  increases (following the symbol style of each color of any size in the following order:  $\circ, \times, \nabla, *$ ) the graphene surface conductivity moves from the region of highest dissipation losses to regions of lowest ones, approximately following an arc of circumference centered at the origin and whose radius depends on the value of  $\mu_c$  and  $f$ .

The operating conditions of most graphene THz antennas based on SPPs found in the literature [103], [104], [106] are such that  $\tau \simeq 1$  ps and  $\mu_c \simeq 0.5$  eV at frequency of  $f \simeq 1$  THz. From Fig. 3.7, this choice would lead to  $\hat{\alpha}_{\text{SPP}} \simeq 0.1$  in agreement with the values found in [104]<sup>2</sup>. The resulting dissipation losses are the most important limiting factor for the radiation efficiency  $\eta$  of graphene THz antennas based on SPPs, which are typically lower than 20% [103], [104], [106]. A similar result has recently been emphasized in [148] in connection with the use of silver patches in optical nanoantennas.

#### *Plasmonic figures of merit*

So far, we have considered the quantity  $\hat{\alpha}_{\text{SPP}} = \alpha_{\text{SPP}}/k_0 = \alpha_{\text{SPP}}\lambda_0/2\pi$  as a figure of merit (FoM) for the dissipation losses of the SPP since we are dealing with antenna applications, where the relevant dimensions are typically related to the free-space wavelength  $\lambda_0$ . However, a measure of the *quality* of surface plasmons in waveguiding structures (such as, e.g., nano-interconnects, nano-resonators, Bragg gratings etc.) is given by different FoM. In [149], three figures of merit have been proposed as benefit-to-cost ratios (where the benefit is represented by confinement and the cost is the attenuation). Specifically, we focus on the  $M_2$  and the  $M_3$  FoM which are defined as:

$$M_2 = (\hat{\beta}_{\text{SPP}} - 1) / \hat{\alpha}_{\text{SPP}}, \quad (3.17)$$

$$M_3 = \hat{\beta}_{\text{SPP}} / (2\pi\hat{\alpha}_{\text{SPP}}), \quad (3.18)$$

$M_2$  gives a direct measure of the confinement of an SPP for 1-D and 2-D structures, whereas  $M_3$  is strictly related to the quality factor  $Q$  [149]. In Figs. 3.8(a) and (b),  $M_2$  and  $M_3$  are reported, respectively, as functions of  $\sigma_R$  and  $\sigma_I$  for an SPP propagating along a conductive sheet. As is seen, both  $M_2$  and  $M_3$  considerably improve for rather low values of  $\sigma_R$  and sufficiently high values of  $\sigma_I$ . This clearly emphasizes that the use of SPP along

<sup>2</sup> In [104], the propagation of an SPP along a graphene sheet (with parameters  $\tau = 1$  ps and  $\mu_c = 0.436$  eV) over a quartz (SiO<sub>2</sub>) substrate ( $\epsilon_{\text{rs}} = 3.8$ ) at  $f = 2$  THz was considered. From Fig. 3.6 we get  $\sigma_R \simeq 3$  mS and  $\sigma_I \simeq 7$  mS at  $f = 1$  THz, which gives rise through Eq. (3.16) to  $\hat{\alpha}_{\text{SPP}} \simeq 0.08$  (see Fig. 3.7). According to [107],  $\alpha_{\text{SPP}}$  linearly depends on  $f$  and on a scaling factor  $S = (\epsilon_{\text{rs}} + 1)/2$ . As a result,  $\hat{\alpha}_{\text{SPP}}$  does not depend on  $f$ , but it should be scaled by a factor  $S = 2.4$  (since we are considering a half-space of air), which gives  $\hat{\alpha}_{\text{SPP}} \simeq 0.2$ , as is found in [104], thus corroborating the validity of our analysis.

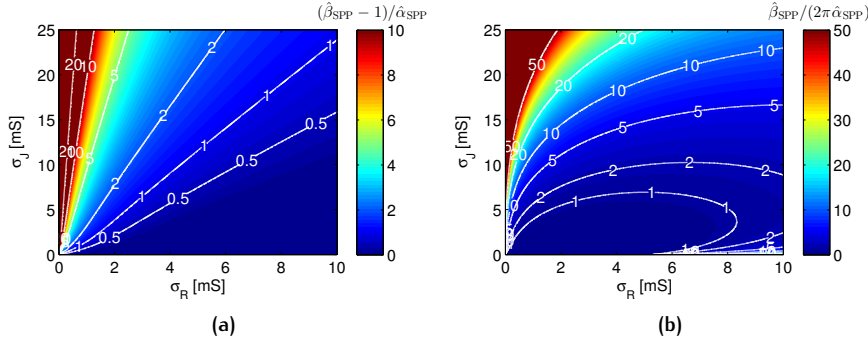


**Figure 3.8.:** SPP figures of merit: (a)  $M_2 = (\hat{\beta}_{\text{SPP}} - 1)/\hat{\alpha}_{\text{SPP}}$  and (b)  $M_3 = \hat{\beta}_{\text{SPP}}/(2\pi\hat{\alpha}_{\text{SPP}})$  vs.  $\sigma_R$  and  $\sigma_J$  in the dynamic range shown in Fig. 3.5(a). The former (Fig. 3.8(a)) gives a measure of the confinement of a suspended SPP for 1-D and 2-D waveguide structures. The latter (Fig. 3.8(b)) is strictly connected to the quality factor  $Q$  [149].

graphene sheets is of potential interest for future applications only for sufficiently high values of  $\tau$  and  $\mu_c$ , for which graphene shows a relatively high  $\sigma_J$  and a moderate  $\sigma_R$  (see Fig. 3.6). As a final remark, it is worth here to note that Eqs. (3.15) and (3.16), allow for deriving closed-form analytical expressions for the evaluation of both  $M_2$  and  $M_3$ . Hence, Eqs. (3.15) and (3.16) as well as Figs. 3.6 and 3.7, may provide a useful tool for the design of plasmonic-based devices either for antenna applications or for guided-wave structures. (Note that Fig. 3.7 is specifically related to graphene plasmonic losses, but Eq. (3.16) can be used for any metasurface whose surface admittance  $\sigma$  is known).

#### Leaky-waves vs. surface plasmons

As is seen, dissipation losses in SPP-based THz antennas may lead to very low efficiencies. To overcome these limitations, we consider now the propagation of the *ordinary*, non-plasmonic, fundamental TE-TM<sup>3</sup> leaky mode pair inside a GPW [114]. (A thorough dispersive and modal analysis of the GPW is postponed to Subsection 3.2.3).

Considerable physical insight can be gained by evaluating and comparing the modal field configuration for both the fundamental TM leaky mode and the SPP mode supported by a GPW; these have been computed by means of a standard field-matching procedure [150] and are shown in Fig. 3.9(b) for the GPW structure described in Fig. 3.9(a) (parameters are:  $\mu_c = 1$  eV,  $f = 0.92$  THz,  $h = 77$   $\mu\text{m}$ , and  $\epsilon_r = 3.8$ ). On one hand, the SPP modal configuration is highly confined in proximity of the graphene sheet where the electric field is maximum. This means that the graphene surface conductivity strongly affects the modal fields and in turn radiation (we recall that we are considering a *biased* graphene sheet at 1 eV); at the same time, graphene ohmic losses impact more so that the efficiency is lower. On the other hand,

<sup>3</sup> Throughout the Chapter we will refer with the acronyms TE (TM) to transverse electric (magnetic) fields with respect to the  $xz$ -plane (see Fig. 3.9).

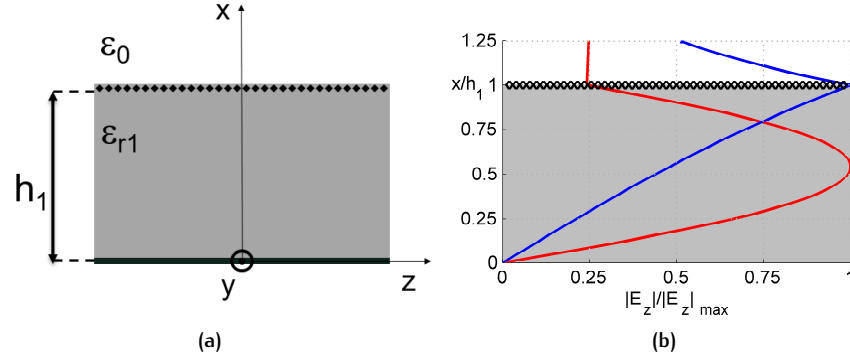


**Figure 3.9.:** (a) 2-D sketch of the GPW structure ( $\epsilon_{r1} = 3.8$ ). The biasing scheme is not reported. (b) Normalized field configurations of the tangential component of the electric field  $E_z$  at  $f = 0.92$  THz for the fundamental TM leaky mode (red line) and the SPP (blue line) in a GPW antenna. Grey and white regions represent the substrate and the air, respectively, whereas the black diamonds stand for the graphene sheet. The  $x$ -axis is normalized to the height of the substrate  $h_1$ .

the LW mode configuration resembles the one of the fundamental TM mode of a parallel-plate waveguide (PPW), i.e., an ordinary mode with sinusoidal transverse variation and a maximum on the middle plane of the antenna cavity. As a consequence, the variation of the graphene surface conductivity may have a reduced impact on the radiating features. At the same time the graphene ohmic losses impact less and in turn efficiency should be significantly higher. Such considerations motivate the use of antennas based on *ordinary* leaky waves rather than those based on SPPs (either in guided or leaky regimes), for designing efficient reconfigurable graphene-based THz antennas.

### 3.2.3 Graphene planar waveguide

The structure of the GPW considered here is shown in Fig. 3.10 along with the relevant transverse equivalent network (TEN) [9], [151]. It consists of a dielectric-filled PPW where the lower plate is assumed first a perfectly electric conducting (PEC) plane, whereas the upper plate is a graphene plane that acts as a partially reflecting sheet (PRS) in order to allow for radiation and exhibit reconfigurability properties (see Section 1.4). An extremely-thin moderately-conductive polymer films, e.g., PEDOT:PSS [99], [152], is used as a gate electrode to control graphene conductivity, but it is safely neglected in the equivalent transmission-line model due to its extremely thin profile and moderate losses [104], [153]. In this idealized structure we have assumed several simplifying hypotheses. In particular, we have considered a two-dimensional structure independent of  $y$  and laterally infinite, in which the ground plane is treated as an ideal conductor characterized by an infinite value of the conductivity and the substrate has no dielectric losses. More accurate models will be treated at the end of this Subsection 3.2.3, where

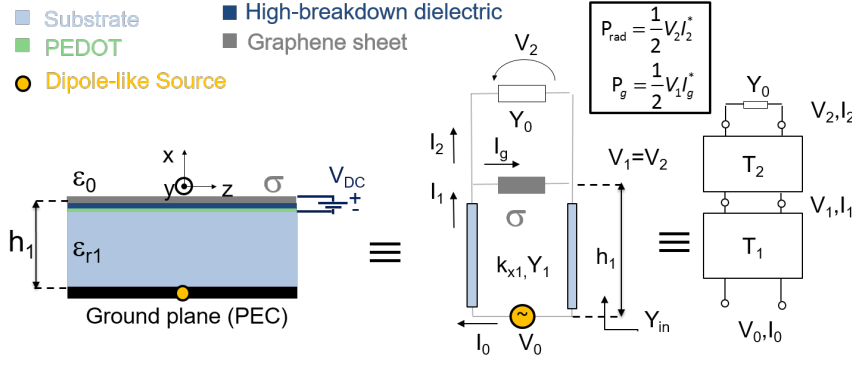


Figure 3.10.: 2-D sketch, TEN model, and ABCD-matrix representation of a GPW antenna.

it will be shown that the introduction of either realistic losses or non-local conductivity models (see 3.2.1) do not significantly affect the results of our analysis.

### Dispersion analysis

The dispersion equation for modes propagating along the considered GPW is obtained by enforcing the condition of resonance on the relevant transverse equivalent network (TEN) model (see Fig. 3.10), where the equivalent admittances in air  $Y_0$  and inside the slab  $Y_1$  for TE and TM modes have the following expressions:

$$Y_0^{\text{TM}} = \frac{\omega \epsilon_0}{k_{x0}}, \quad Y_1^{\text{TM}} = \frac{\omega \epsilon_0 \epsilon_{r1}}{k_{x1}}, \quad (3.19)$$

$$Y_0^{\text{TE}} = \frac{k_{x0}}{\omega \mu_0}, \quad Y_1^{\text{TE}} = \frac{k_{x1}}{\omega \mu_0}, \quad (3.20)$$

where  $k_{x0} = \sqrt{k_0^2 - k_z^2}$  and  $k_{x1} = \sqrt{k_0^2 \epsilon_{r1} - k_z^2}$  are the transverse wavenumbers in air and in the dielectric, respectively, and  $k_z = \beta_z - j\alpha_z$  is the complex longitudinal wavenumber, with  $\beta_z$  and  $\alpha_z$  the relevant phase and attenuation (or leakage) constants, respectively.

The resulting dispersion equation for TE modes is

$$\sqrt{1 - \hat{k}_z^2} + \sigma \zeta_0 - j\sqrt{\epsilon_{r1} - \hat{k}_z^2} \cot\left(k_0 h_1 \sqrt{\epsilon_{r1} - \hat{k}_z^2}\right) = 0, \quad (3.21)$$

whereas for TM modes is

$$\left(\sqrt{1 - \hat{k}_z^2}\right)^{-1} + \sigma \zeta_0 - j\epsilon_{r1} \left(\sqrt{\epsilon_{r1} - \hat{k}_z^2}\right)^{-1} \cot\left(k_0 h_1 \sqrt{\epsilon_{r1} - \hat{k}_z^2}\right) = 0, \quad (3.22)$$

where  $h_1$  is the thickness of the slab. In Figs. 3.11(a)-(b) and (c)-(d) Eqs. (3.21) and (3.22) have been solved (see 1.2.4), respectively, in the range 0.25 – 2 THz and for different bias conditions, searching for both surface-wave (SW) and leaky-wave (LW) modes. The waveguide is assumed to



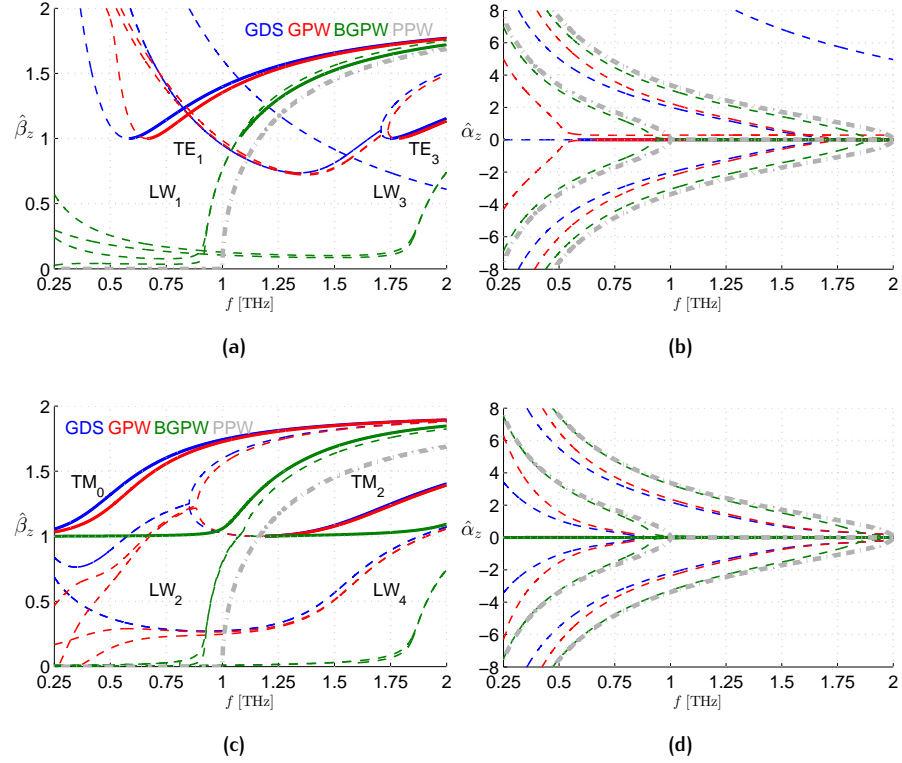


**Figure 3.11.:** Dispersion curves of SWs and LWs within the band 0.25 – 2 THz for a GDS (blue lines), a GPW (red lines), a BGPW (green lines), and a PPW (gray lines). In dashed lines improper waves, in solid lines proper waves. In (a)  $\hat{\beta}_z$ , in (b)  $\hat{\alpha}_z$  for TE modes, and in (c)  $\hat{\beta}_z$ , in (d)  $\hat{\alpha}_z$  for TM modes.

be filled with a dielectric medium with  $\varepsilon_{r1} = 3.8$  (quartz) and thickness  $h_1 = (\lambda/2\sqrt{\varepsilon_{r1}}) \simeq 77 \mu\text{m}$  at  $f = 1 \text{ THz}$ . The obtained dispersion behaviors are then compared with those of an *equivalent* grounded dielectric slab (GDS), where the graphene sheet has been removed, and with those of an *equivalent* PPW, where the graphene sheet has been substituted by a perfectly conducting metal plate.

Since graphene at low THz frequencies and for low values of  $\mu_c$  is almost *transparent* to radiation (its reactance  $|\sigma_J| \simeq \sigma_R$  being rather low, see Fig. 3.5), the *unbiased* GPW (henceforth referred to as GPW) can be seen as a perturbation of the GDS. Conversely, for sufficiently high values of  $\mu_c$  graphene is almost *opaque* to radiation (its reactance  $|\sigma_J| \gg \sigma_R$  being rather high, see Fig. 3.5), and thus the *biased* GPW (henceforth referred as BGPW) can be seen as a perturbation of a PPW. Results shown in Fig. 3.11 confirm how the dispersion curves of the GPW are only slightly different from those of the GDS. As can be seen, in both the TE and TM cases the propagating modes exhibit the well-known transition regions between bound and leaky regimes typical of dielectric-based open guiding structures [154], [155]. Unfortunately, LWs of the GPW are not suitable for efficient radiation here,

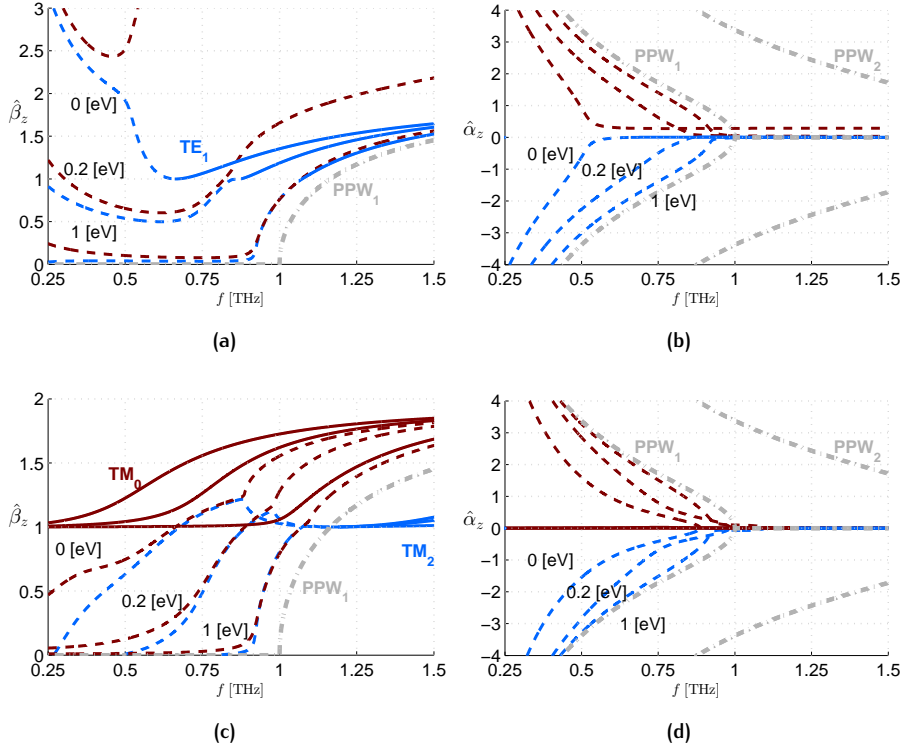


Figure 3.12.: Dispersion curves of SWs and LWs within the band 0.25 – 1.5 THz for three different values of the chemical potential. In dashed red line improper leaky poles, in dashed blue line improper non-physical poles, in solid red line SWs for the fundamental TM mode and in solid blue line the remaining SWs. In (a)  $\hat{\beta}_z$ , in (b)  $\hat{\alpha}_z$  for TE modes, and in (c)  $\hat{\beta}_z$ , in (d)  $\hat{\alpha}_z$  for TM modes.

because they exhibit a very high leakage rate [2] especially at low frequency, where the *splitting condition* ( $\hat{\beta}_z = \hat{\alpha}_z$ ) is met (see Section 1.3).

On the other hand, the LW modes of the BGPW are shifted closer to the PPW ones, thus exhibiting a moderate leakage rate at the splitting condition. This is a direct consequence of the behavior of  $\sigma$  as a function of the chemical potential. Indeed, we have previously seen that for low level of  $\mu_c$  graphene is almost *transparent* to radiation, getting more *opaque* for increasing values of  $\mu_c$ . Hence, it is worth to inspect the behavior of the complex modes supported by the GPW for intermediate values of  $\mu_c$ .

To this purpose, the dispersion curves of TE and TM fundamental modes for three different values of  $\mu_c = 0, 0.2, 1$  eV are shown in Fig. 3.12 in order to describe in more detail the nature of improper and proper complex solutions in lossy GPW and to highlight the effect of increasing the bias. As concerns improper leaky modes, we note that the introduction of a (lossy) graphene sheet causes the generation of an improper complex pair of solutions<sup>4</sup>, the leaky-wave solution, i.e., with  $\alpha_x < 0$  and  $\alpha_z > 0$  (see red dashed lines in Fig. 3.12), and one with no physical meaning, i.e.,  $\alpha_x < 0$  and  $\alpha_z < 0$

<sup>4</sup> As it happens for a GDS covered with a lossy PRS (here represented by a graphene sheet), as already commented in 1.2.3.

(see blue dashed lines in Fig. 3.12). The leaky-wave solution is *physical* when  $0 < \hat{\beta}_z < 1$  and can hence contribute to radiation, if properly excited (see 1.2.3). We remind that the leaky-wave solution corresponds to a pole of the Green's function of the waveguide: the LW is physical when the pole is captured by the relevant steepest-descent path (SDP) [2]. Furthermore, as concerns the nonphysical improper complex solution, by increasing frequency it becomes proper complex and reaches the cutoff condition of the corresponding surface waves (see blue solid lines in Fig. 3.12(a), or red solid lines in Fig. 3.12(c)). This kind of evolution of the complex wavenumbers below cutoff is common to all the SW higher-order modes in both TE and TM cases, as already extensively commented in 1.2.3.

Finally, specific attention is devoted to the behavior of the fundamental TE improper complex solution of the GPW (the TE<sub>1</sub> mode) as  $\mu_c$  increases. As is well known, for the fundamental TE mode of the GDS (blue dashed line in Fig. 3.11), there exists only a real improper pole below cutoff (whereas for the high-order modes a complex pair exists). However, we observe in Fig. 3.12(a) that as  $\mu_c$  increases up to 1 eV the fundamental TE improper complex solution with  $\alpha_z < 0$  gradually joins that with  $\alpha_z > 0$  (a solution that never exists in a GDS and that is of no interest in a GPW). Furthermore, the latter becomes a fast (and physical) leaky mode in the frequency range 0.5 – 0.75 THz.

The main results introduced by the application of the bias are better shown in Fig. 3.13 where the dispersion curves for the fundamental TE and TM LWs have been reported in (a) for three significant values of the chemical potential as frequency varies from 0.75 to 1.1 THz, and in (b) for a fixed frequency ( $f = 0.92$  THz) as chemical potential varies from 0.2 to 1 eV. We recall here that the pointing angle  $\theta_p$  and the half-power beamwidth  $\Delta\theta$  of a 2-D LWA are simply related to the normalized LW wavenumber  $\hat{k}_z = \hat{\beta}_z - j\hat{\alpha}_z$ , through Eqs. (1.28) and (1.32)-(1.33), respectively. Considering now Fig. 3.13(a), it is clear that the radiative behavior over frequency associated with the fundamental LWs improves for higher values of  $\mu_c$  since the leakage rate reaches lower values for both the TE and TM cases. Considering Fig. 3.13(b), we remark that the frequency of  $f = 0.92$  THz corresponds to the *splitting condition* for both TE and TM LWs when a bias of 1 eV is applied (as can be seen by inspection of Fig. 3.13(a)). Here, the beam scanning over chemical potential follows an optimal quasi-linear behavior for both TE and TM modes, thus corroborating once more the tunable features of such kind of LW radiation.

As concerns plasmonic propagation, it is worth mentioning that in the TM case a SPP mode propagates in both the GPW and the BGPW, as it always occurs between a dielectric (with relative permittivity  $\epsilon_r$ ), non-absorbing half space with  $\text{Re}[\epsilon_r] > 0$  and an adjacent conducting interface with  $\text{Re}[\epsilon_r] < 0$  [120]. The dispersion curves of this mode are shown in Fig. 3.14 for the GPW with a chemical potential that varies almost continuously from 0 to 1 eV.

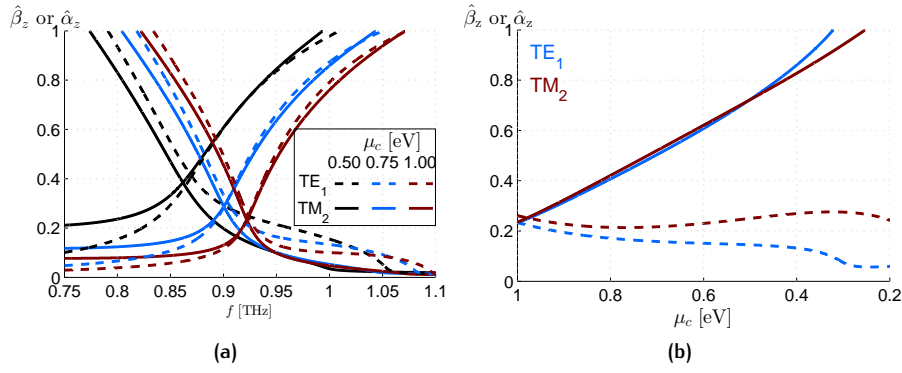


Figure 3.13.: Dispersion curves of the TE<sub>1</sub>, TM<sub>2</sub> fundamental LWs (a) within the band 0.75 – 1.1 THz for  $\mu_c = 0.5, 0.75, 1$  eV, and (b) within the range  $0.2 \leq \mu_c \leq 1$  eV for  $f = 0.92$  THz. In (a)  $\hat{\beta}_z$  and  $\hat{\alpha}_z$  are both represented in dashed lines for the TE<sub>1</sub> mode and in solid lines for the TM<sub>2</sub>. In (b)  $\hat{\beta}_z$  and  $\hat{\alpha}_z$  are represented in solid lines and dashed lines, respectively, for both modes.

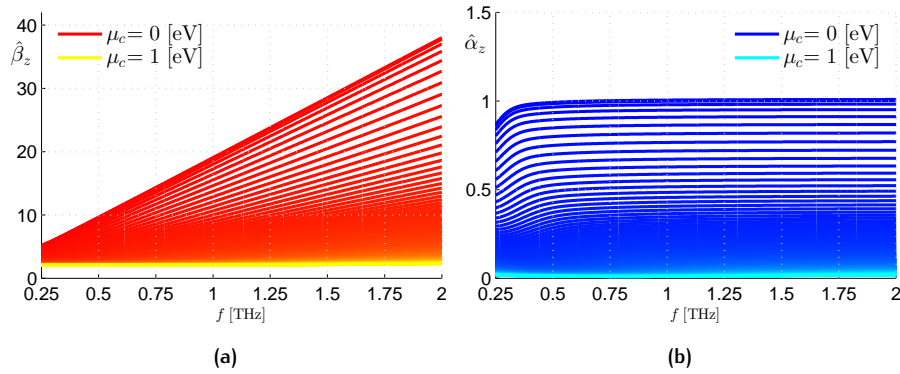
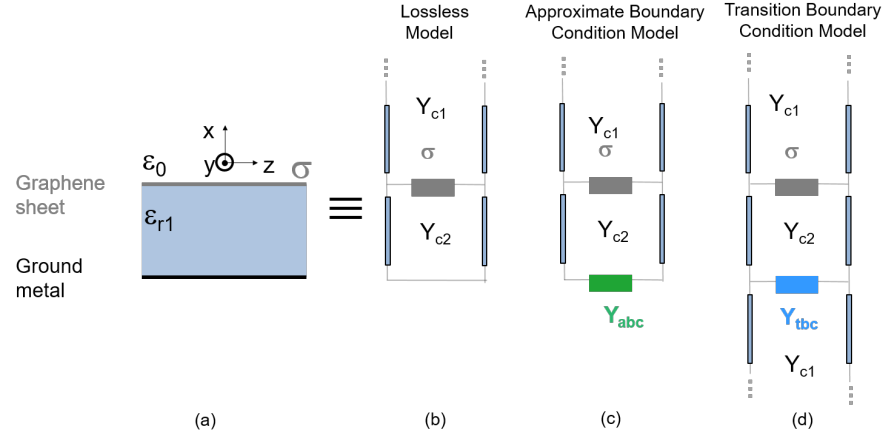


Figure 3.14.: Dispersion curves of (a)  $\hat{\beta}_z$ , (b)  $\hat{\alpha}_z$  for the plasmonic mode SPP. Lines become brighter (red to yellow, and blue to cyan) as  $\mu_c$  increases from 0 to 1 eV. Note that as  $\mu_c$  approaches 1 eV the SPP mode approaches the PPW TEM mode.

### Loss effects

A remark about ohmic and dielectric losses at THz frequencies is useful. In fact, in all the results shown above, the effects of losses have been always neglected in both the dielectric substrate and the metalization. We have then computed the dispersion curves of the fundamental LWs considering a more realistic model of quartz, with a complex permittivity characterized by a real part  $\text{Re}[\epsilon_{r1}] = 3.852$  and a loss tangent  $\tan \delta = 0.0141$  at  $f = 1$  THz [156]. On the other hand, ohmic losses have also taken into account for a metalization of gold (see Fig. 3.15(a)) using two different models. The first model is related to the approximate *Leontovich* boundary condition [157], assuming a thick layer of gold with respect to the skin depth (see Fig. 3.15(c)). The equivalent admittance is then given by the formula



**Figure 3.15.:** (a) 2-D section of the structure and its transverse equivalent networks: (b) using the lossless model, (c) using the approximate Leontovich boundary condition, and (d) using the transition boundary condition.

$$Y_{abc} = \frac{1}{1+j} \sqrt{\frac{\sigma_m}{\pi\mu_0 f}}, \quad (3.23)$$

where  $\sigma_m \simeq 44 [\mu\Omega\text{m}]^{-1}$  is the bulk conductivity of gold at 1 THz [158]. This value is used in place of the short circuit of the TEN model of Fig. 3.15(b). The second model does not assume a metal thickness  $t$  much larger than the skin depth; however, since in any case  $t \ll \lambda$ , the metal layer can be modeled through a *transition* boundary condition (see Fig. 3.15(c)). The admittance is given by the formula

$$Y_{tbc} = \sigma_m t, \quad (3.24)$$

where  $t = 150$  nm is the thickness of the layer, and  $\sigma_m \simeq 30 [\mu\Omega\text{m}]^{-1}$  is now a thin-film conductivity which is accordingly reduced of a factor 0.69 [158]. Since the skin depth of gold at  $f = 1$  THz,  $\delta_{\text{gold}} \simeq 127.4$  nm is slightly

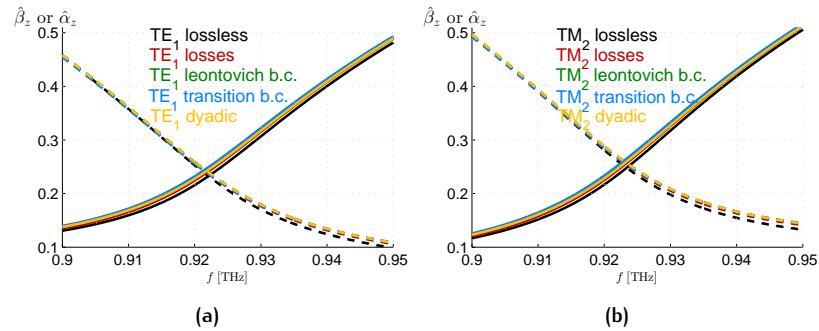


**Figure 3.16.:** Effects of the introduction of losses and spatial dispersion in the curves of the fundamental LWs in the band 0.9 – 0.95 THz for (a) TE and (b) TM modes. The red and green-blue lines consider the effect of dielectric losses and ohmic losses, respectively. The yellow ones consider the effect of a spatially dispersive model in addition to dielectric and ohmic losses.

shorter than the thickness of the layer, the short circuit represented in Fig. 3.15(b) is now replaced by an equivalent admittance given by Eq. (3.24) connected to a semi-infinite transmission line of Fig. 3.23(d). In Figs. 3.16(a) and 3.16(b) it is clearly shown that the effect of losses is quite negligible in both TE and TM cases, and hence the ideal model previously investigated can be considered as a good approximation of more realistic conditions.

#### *Effects of spatial dispersion*

Furthermore, a spatially dispersive conductivity model of biased graphene (see Section 3.2.1) has been considered in order to assess the accuracy of Kubo formula. The longitudinal ( $\sigma_\rho$ ) conductivity (Eq. (3.10)) affects TM fields, whereas the transverse ( $\sigma_\phi$ ) one (Eq. (3.11)) affects TE fields ( $E_\phi$  is the only non-null electric field component of a TE mode with respect to the  $xz$ -plane). Therefore the value of  $\sigma$  in the Eqs. (3.21), (3.22) is respectively replaced by  $\sigma_\phi$  and  $\sigma_\rho$ , where we have used  $k_\rho = k_z$ . The resulting dispersion curves are shown in Figs. 3.16(a) and Fig. 3.16(b) where they are compared with those obtained by using the Kubo formula for both the lossless and lossy case. As it can be seen, spatial dispersion has a negligible impact on the modal properties of the leaky modes (physical leaky waves are characterized by  $\beta_z < k_0$  and  $\alpha_z \leq \beta_z$ , hence  $|k_z|$  is of the order of  $k_0$  and therefore spatial dispersion can be ignored [140]). As a consequence, the beam scanning over frequency and over chemical potential is almost the same, thus confirming the effectiveness of Kubo formula for a first qualitative description of the radiating properties of this kind of structures. In the light of these results, throughout this Section 3.2 (if not differently stated) we will always assume *i*) a graphene scalar conductivity model as described in Eq. (3.13), *ii*) ideal lossless dielectric layers, and *iii*) a perfectly conducting ground plane.

#### *Radiative analysis*

Finally, the far-field expressions of the GPW are calculated using the TEN model (see Fig. 3.10), and with the aid of the reciprocity theorem [114], [160], considering a horizontal magnetic dipole (HMD) directed along the  $y$ -axis (see Fig. 3.17(a)) as a source. As has been discussed in Section 1.4, for scanned beams the TE leaky mode primarily determines the radiation features in the H-plane ( $xy$ -plane), whereas the TM leaky mode determines those in the E-plane ( $xz$ -plane). For broadside patterns, both TE and TM leaky modes are required for achieving a directive (pencil) beam [48], [57], [58]. After some calculations it is found that on the H-plane (TE leaky mode) the far-field expression  $F(\theta)$  reads:

$$F(\theta) = -j \frac{k_0}{4\pi} \cos \theta \frac{2Y_{sc}^{TE} \cos(k_{x1}h_s) \sec(k_{x1}h_1)}{(\sigma + Y_0^{TE} + Y_{sc}^{TE})}, \quad (3.25)$$

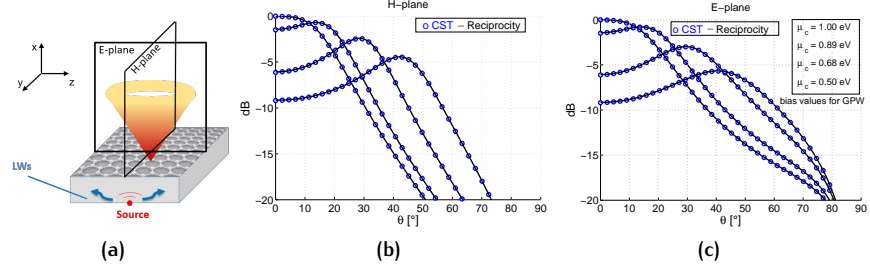


**Figure 3.17.:** (a) Illustrative example of the typical scannable conical beam-scanning feature of a GPW antenna. In (b) and (c), the radiation patterns normalized to the overall maximum (achieved at broadside) vs. elevation angle  $\theta$  for the GPW antenna represented in (a), are reported for the H-plane and E-plane, respectively. Analytical results are plotted in black solid lines, whereas full-wave results obtained with the tool CST Microwave Studio [159] are given by blue circles. The scanning behavior at a fixed frequency ( $f_c = 0.922$ ) is shown for beam maxima at  $\theta_p = 0^\circ, 15^\circ, 30^\circ, 45^\circ$ . The corresponding chemical potentials are reported in the legend.

where  $Y_{sc}^m = -jY_1^m \cot(k_{x1}h_1)$  with  $m \in \{\text{TE}, \text{TM}\}$  (depending on the polarization) is the short-circuit admittance seen from the graphene-slab interface ( $x = h_1^-$ ), and  $h_s$  is the distance of the source with respect to the ground plane. The expression for the E-plane pattern can be obtained by suppressing in Eq. (3.25) the factor  $\cos \theta$  and replacing the TE admittances with the TM ones:

$$F(\theta) = -j \frac{k_0}{4\pi} \frac{2Y_{sc}^{\text{TM}} \cos(k_{x1}h_s) \sec(k_{x1}h_1)}{(\sigma + Y_0^{\text{TM}} + Y_{sc}^{\text{TM}})}. \quad (3.26)$$

In the present form it is easy to recognize that the denominator of the Green's functions in Eqs. (3.25)-(3.26) correspond to the dispersion equations defined in Eqs. (3.21)-(3.22), whose zeros (and in turn the poles of Eqs. (3.25)-(3.26)) represent the *resonant frequencies* of the system [1], [20]. We also note that the intensity of the radiation pattern over both planes is maximized when the source is placed on the ground plane  $h_s = 0$ . This location is quite convenient, since a HMD source can be used to model a slot etched in the ground plane and back-illuminated by a coherent THz source as a quantum cascade laser (QCL) or a photomixer [83].

The results of our TEN approach (i.e., Eqs. (3.25)-(3.26) have been fully validated for different values of  $\mu_c$  (and corresponding pointing angles) by means of the electromagnetic CAD tool CST Microwave Studio [159] (details on the relevant implementation are provided in Appendix B): the agreement between our approach and CAD is remarkable (see Figs. 3.17(b) and (c) for the H- and E-plane, respectively).

As expected, the pointing angle is reached at almost the same bias over both planes (see Fig. 3.17(b)-(c), since both the phase and the attenuation constants are equally affected. It is worth here to notice that the equalization of the TM, TE leaky-wave phase constants allows for both frequency- and



bias-scanning (as can also be inferred from Figs. 3.13(a) and (b), respectively) for a considerable range of the elevation angle with a nearly circular conical scanned beam [114], [161].

### Power analysis

Nevertheless, it is important to evaluate the theoretical radiation efficiency in terms of the ratio  $\eta = P_{\text{rad}} / (P_{\text{rad}} + P_{\text{g}} + P_{\text{L}})$  where  $P_{\text{rad}}$  is the power radiated in space,  $P_{\text{g}}$  is the power dissipated along the graphene sheet, and  $P_{\text{L}}$  is the power dissipated at the antenna termination [10], [162]. As is typical [11], these structures are assumed to be electrically large in the transverse plane so that  $P_{\text{L}}$  is negligible, thus  $\eta$  reduces to  $\eta = P_{\text{rad}} / (P_{\text{rad}} + P_{\text{g}})$ . (Note that practical dimensions of such antennas are on the order of several hundreds of  $\mu\text{m}$  as shown in [104], [114]).

The quantities  $P_{\text{rad}}$  and  $P_{\text{g}}$  have been evaluated using the TEN model and the ABCD-matrix representation [157] as in Fig. 3.10, where the ABCD parameters of the transmission matrices  $T_1$  and  $T_2$  are given by:

$$T_1 = \begin{bmatrix} A_1 & B_1 \\ C_1 & D_1 \end{bmatrix} = \begin{bmatrix} \cos(k_{x1}x_0) & jY_1 \sin(k_{x1}h_1) \\ j(Y_1)^{-1} \sin(k_{x1}h_1) & \cos(k_{x1}h_1) \end{bmatrix}, \quad (3.27)$$

$$T_2 = \begin{bmatrix} A_2 & B_2 \\ C_2 & D_2 \end{bmatrix} = \begin{bmatrix} 1 & 0 \\ \sigma & 1 \end{bmatrix}. \quad (3.28)$$

with  $m \in \{\text{TE}, \text{TM}\}$ .

When power density is maximized at broadside, i.e., when the splitting condition  $\hat{\beta}_z \simeq \hat{\alpha}_z$  is met (this would happen at  $f = 0.92$  THz with  $\hat{\alpha}_z \simeq 0.24$ , for the TM mode when  $\mu_c = 1$  eV), one would obtain  $\eta \simeq 70\%$  which is quite above any graphene THz LWA based on *plasmonic* leaky waves [103]–[106], thus motivating the use of *ordinary* leaky wave in the design of THz graphene-based LWAs. This improved efficiency is paid at the expense of a just slightly reduced reconfigurability, as can be seen by comparing the dynamic range of  $\mu_c$  that is needed to scan an angular range of  $45^\circ$  (from Fig. 3.17 it is seen that  $\mu_c$  scans a range from 1 eV to 0.5 eV) with the one reported in [104] (there,  $\mu_c$  scans a range from 1 eV to 0.6 eV).

A concluding remark on the performance of the GPW antenna concerns the obtained directivity. As is seen in Figs. 3.17(b) and (c), the HPBW is rather large on both planes, thus directivity is rather low. This is mainly due to the relatively high values attained by the normalized attenuation constant  $\hat{\alpha}_z$  (see Eqs. (1.32)–(1.33)). To improve directivity, an innovative GSS antenna has recently been proposed in [115]. In the following Subsection, we present the dispersive, radiative, and power analysis of such a novel antenna, and compare its performance with respect to the GPW.



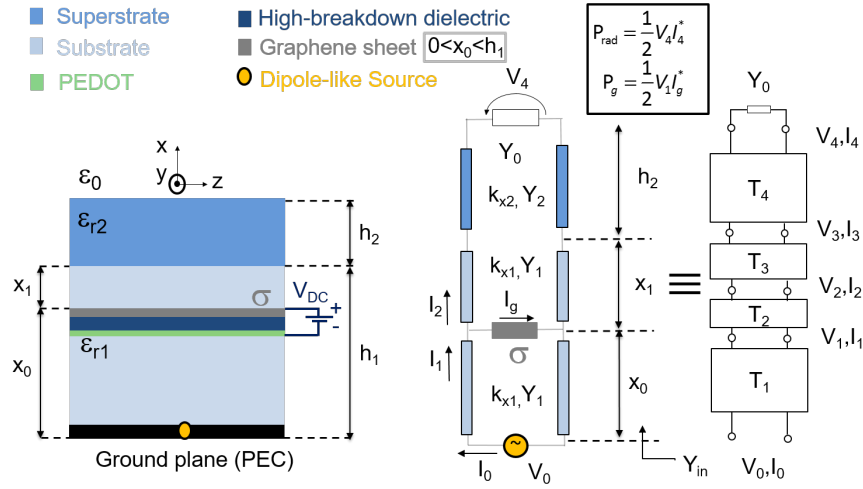


Figure 3.18.: 2-D sketch, TEN model, and ABCD-matrix representation of a GSS antenna.

### 3.2.4 Graphene substrate-superstrate antenna

The GSS structure proposed here basically consists of a GDS (relative permittivity  $\epsilon_{r1}$ , thickness  $h_1$ ) covered with a high-permittivity dielectric superstrate (relative permittivity  $\epsilon_{r2}$ , thickness  $h_2$ ) and hosting a graphene sheet located at  $x = x_0$ , with  $0 < x_0 \leq h_1$  (see Fig. 3.18 for the details).

The GSS can be thought as a perturbation of a substrate-superstrate (SS) antenna. As seen in Section 1.4, in a conventional SS antenna it is possible to maximize the gain at a given pointing angle  $\theta_p$  (measured from broadside) and for an operating frequency  $f_0$  when the layer thicknesses are chosen according to Eqs. (1.34)-(1.35) for the fundamental ( $m = 1$ ) TE-TM leaky-mode pair, i.e., as  $h_1 = (\lambda_1/2)/\sqrt{1 - \sin^2 \theta_p / \epsilon_{r1}}$ ,  $h_2 = (\lambda_2/4)/\sqrt{1 - \sin^2 \theta_p / \epsilon_{r2}}$ , where  $\lambda_{1,2}$  are the wavelengths inside the dielectric layers. Under these conditions the antenna acts as a Fabry-Perot cavity where the superstrate has the role of a PRS; a dominant TE/TM leaky mode pair can be shown to exist in the modal spectrum of the structure, whose attenuation constant can be made very small (and hence the antenna very directive) by selecting layers with a high dielectric contrast (i.e., with  $\epsilon_{r2}/\epsilon_{r1} \gg 1$ ) [57].

However, the introduction of a graphene monolayer inside the substrate poses the question to find an *optimum* location (in terms of maximization of directivity at broadside) in which to locate the graphene sheet to efficiently perturb the SS structure. Clearly, when  $x_0 = h_1$ <sup>5</sup>, the interaction between the electric field and graphene is expected to be low, whereas when  $x_0 = h_1/2$  the interaction is expected to be high as is manifest from Fig. 3.9. However, it is not clear if the position of maximum interaction would provide the maximization of directivity at broadside. To this purpose, a rigorous numerical analysis is presented here to find such an optimum position. It should be

5 In this case, the GSS is equivalent to the GPW except for the introduction of the *cover* layer (i.e., the superstrate).

noted that, in the innovative solution presented here, the introduction of a tunable element (as it is graphene) in the cavity of a SS antenna would allow for achieving fixed-frequency directive beam scanning, a feature that is never possible in a conventional SS configuration. We note that this distinctive feature is highly desirable in Multiple Input Multiple Output (MIMO) THz communications and in security and safety applications as well

As for the GPW, a standard TEN model has been used for the modal analysis of this structure (see Fig. 3.18), with transmission-line wavenumbers  $k_{x,i} = \sqrt{\varepsilon_{r,i}k_0^2 - k_z^2}$  and characteristic admittances  $Y_i^{\text{TE}} = k_{x,i}/\omega\mu_0$ ,  $Y_i^{\text{TM}} = \omega\varepsilon_0\varepsilon_{r,i}/k_{x,i}$  (indices  $i = 0, 1, 2$  refer to air region, substrate, and superstrate, respectively). Assuming that the graphene layer is located inside the substrate, the dispersion equation for both TE and TM modes reads:

$$\sigma - jY_1^m \cot(k_{x1}x_0) + Y_{\text{in}1}^m = 0, \quad (3.29)$$

where  $m = \{\text{TE}, \text{TM}\}$ ;  $x_1 = h_1 - x_0$  is the distance of the graphene sheet from the substrate-superstrate interface;  $Y_{\text{in}1}^m$  is the input admittance at  $x = x_0^+$  looking upwards, given by

$$Y_{\text{in}1}^m = Y_1^m \frac{Y_{\text{in}2}^m \cos(k_{x1}x_1) + jY_1^m \sin(k_{x1}x_1)}{Y_1^m \cos(k_{x1}x_1) + jY_{\text{in}2}^m \sin(k_{x1}x_1)}, \quad (3.30)$$

in terms of the input admittance  $Y_{\text{in}2}^m$  at  $x = h_1$  looking upwards:

$$Y_{\text{in}2}^m = Y_2^m \frac{Y_0^m \cos(k_{x2}h_2) + jY_2^m \sin(k_{x2}h_2)}{Y_2^m \cos(k_{x2}h_2) + jY_0^m \sin(k_{x2}h_2)}. \quad (3.31)$$

The same TEN can also be used to calculate the far field of a GSS excited by a HMD source according to reciprocity theorem, as has been done for the GPW.

### Design method

Ideally, the graphene sheet should be placed at a suitable position where it is capable of *i*) significantly affecting the normalized LW phase constant  $\hat{\beta}_z$ , in order to produce useful beam-angle reconfigurability; *ii*) minimizing the normalized LW attenuation constant  $\hat{\alpha}_z$ , in order also to improve the antenna directivity. Since the horizontal electric field of the dominant leaky modes has a null on the ground plane ( $x = 0$ ) and a minimum at the substrate-superstrate interface ( $x = h_1$ ), these two locations give rise to zero or negligible graphene/SS interaction, respectively; an optimal position  $x_0$  is thus expected to exist in-between ( $0 < x_0 < h_1$ ). Such optimum position has rigorously been determined here with a numerical analysis, by deriving the complex roots  $k_z$  from Eq. 3.29 as a function of frequency for any given  $x_0$  and searching for a minimum value of the normalized attenuation constant  $\hat{\alpha}_z$  at the cutoff frequency  $f_c$  where the TM mode radiates at broadside, i.e., where  $\hat{\beta}_z \simeq \hat{\alpha}_z$  [48] (note that, by increasing frequency above cutoff, the LW

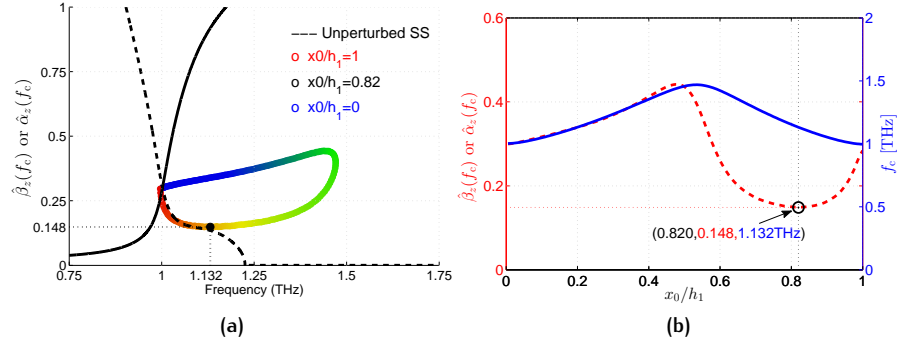


**Figure 3.19:** (a) The dispersion curve ( $\hat{\beta}_z$  and  $\hat{\alpha}_z$  vs.  $f$  in black solid and dashed lines, respectively) of the fundamental TM leaky mode of the unperturbed SS is reported in the frequency range  $0.75 \leq f \leq 1.25$  THz. On the same plot the values of the splitting condition ( $\hat{\beta}_z = \hat{\alpha}_z$ ) are shown for different positions of the graphene sheet starting from the interface  $x_0/h_1 = 1$  to the ground plane  $x_0/h_1 = 0$ . The color of the dots shades from red to blue as the graphene sheet moves from  $x_0/h_1 = 1$  to  $x_0/h_1 = 0$ . An optimum position is found at  $f = 1.132$  THz for  $x_0/h_1 = 0.82$  (black dot). Note that the frequency  $f_c$  at which splitting condition occurs ranges approximately from 1 THz to 1.5 THz. (b) Cutoff frequency  $f_c$  (blue solid line) and relevant value of  $\hat{\beta}_z(f_c) = \hat{\alpha}_z(f_c)$  (red dashed line) as a function of the normalized distance  $x_0/h_1$  of the graphene sheet from the ground plane, for the fundamental TM mode in the GSS structure.

attenuation constant typically decreases). We note here that in 2D-LWAs the directivity is straightforwardly related to the normalized attenuation constant  $\hat{\alpha}_z$ . In particular, for directive antennas the half-power beamwidth  $\Delta\theta_{\text{BW}}$  is given by  $\Delta\theta_{\text{BW}} \simeq 2\hat{\alpha}_z / \cos\theta$  for  $\theta \neq 0$  and  $\Delta\theta_{\text{BW}} \simeq 2\sqrt{2}\hat{\alpha}_z$  for  $\theta = 0$  (see Section 1.3). Thus, the directivity at broadside ( $\theta = 0$ ) can be approximated by the following formula  $D_0 \simeq 4\pi / \Delta\theta_{\text{BW}}^2 \simeq 0.5\pi / \hat{\alpha}_z^2$ .

For all the numerical results presented here (if not differently stated), a quartz (SiO<sub>2</sub>) substrate ( $\epsilon_{r1} = 3.8$ ) of thickness  $h_1 = 77 \mu\text{m}$  and a hafnium-oxide (HfO<sub>2</sub>) superstrate ( $\epsilon_{r2} = 25$ ) of thickness  $h_2 = 15 \mu\text{m}$  are considered, loaded with a graphene sheet biased with a chemical potential  $\mu_c = 1$  eV (a value for which graphene behaves as a good conductor at low THz frequencies [114]).

In Fig. 3.19(a), we have reported the dispersion curve of the fundamental TM leaky mode of the unperturbed SS and the splitting condition<sup>6</sup> for the GSS when the graphene sheet position  $x_0$  ranges from  $h_1$  (red dot) to 0 (blue dot). As expected the TM dispersion curves of the leaky modes of the GSS for  $x_0 = h_1$  are very similar to those of the unperturbed SS. More interestingly, it is seen that a position  $x_0$  exists for which  $\hat{\alpha}_z$  is actually minimized. This can be easier inferred from Fig. 3.19(b), where the cutoff frequency  $f_c$  and the relevant value of  $\hat{\beta}_z(f_c) = \hat{\alpha}_z(f_c)$  are reported for the same conditions of Fig. 3.19(a). As is shown,  $\hat{\beta}_z \simeq \hat{\alpha}_z$  attains a minimum value of about 0.148 when  $x_0 = 0.82h_1$  at  $f_c = 1.132$  THz. Moreover, as the graphene sheet

<sup>6</sup> For readability purposes we do not have reported the dispersion curves for any value of  $x_0 = h_1$ , but *only* the splitting condition.

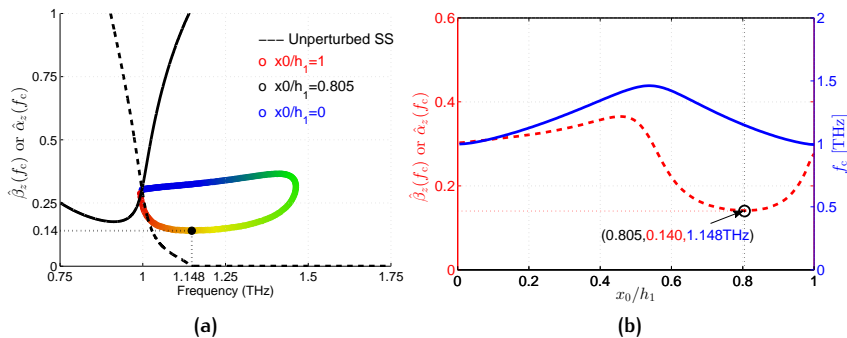


Figure 3.20.: (a) The dispersion curve ( $\hat{\beta}_z$  and  $\hat{\alpha}_z$  vs.  $f$  in black solid and dashed lines, respectively) of the fundamental TE leaky mode of the unperturbed SS is reported in the frequency range  $0.75 \leq f \leq 1.25$  THz. An optimum position is found at  $f = 1.148$  THz for  $x_0/h_1 = 0.805$  (black dot). Note that the frequency  $f_c$  at which splitting condition occurs ranges approximately from 1 THz to 1.5 THz. (b) Cutoff frequency  $f_c$  (blue solid line) and relevant value of  $\hat{\beta}_z(f_c) = \hat{\alpha}_z(f_c)$  (red dashed line) as a function of the normalized distance  $x_0/h_1$  of the graphene sheet from the ground plane, for the fundamental TM mode in the GSS structure.

is moved towards the middle of the substrate, the cutoff frequency is shifted upwards with a maximum in the position  $x_0 = 0.5h_1$ , where the horizontal electric field is maximum and hence the graphene sheet strongly perturbs the structure.

For the fundamental TE leaky mode very similar results are found (see Fig. 3.20(a)-(b)). Specifically, the minimum condition ( $\hat{\beta}_z \simeq \hat{\alpha}_z \simeq 0.140$ ) is now reached when  $x_0 = 0.805h_1$  at  $f_c = 1.148$  THz. However, the region of *minimum*  $\hat{\alpha}_z$  is rather flat, so that the *optimum* condition for the antenna directivity at broadside for a given polarization would be a *quasi-optimum* condition for the other polarization. In the following, we will ‘arbitrarily’ consider an optimized GSS with respect to the TM polarization.

It is seen that, when graphene is placed at an optimum location  $x_0 = x_{\text{opt}}$ , the SS is efficiently perturbed, since the layered structure formed by the graphene sheet, by the portion of substrate of height  $x_1$ , and by the superstrate behaves as a highly reflective surface. As a consequence, the TE and TM fundamental LWs of the modified structure have lower leakage constants if compared to those of an equivalent unperturbed SS (attained at  $x_0 = 0$  in Fig. 3.19), or to those of an equivalent GPW [114], as we expressly see from the radiative analysis. It is worth here to remark that the position of graphene has been chosen in order to minimize radiation losses at broadside (cutoff condition), thus we can even more expect that this minimization still works for greater pointing angles [57].

It is worth noting that these optimum values generally depend on the SS dielectric contrast  $d_{1,2} = \epsilon_{r2}/\epsilon_{r1}$ . Thus, the particular values of  $x_{\text{opt}} = 0.82h_1$  and  $f_{\text{opt}} = 1.132$  THz for the fundamental TM mode, are related to the choice  $d_{1,2} \simeq 6$  made in this work. However, in Fig. 3.21 it is shown

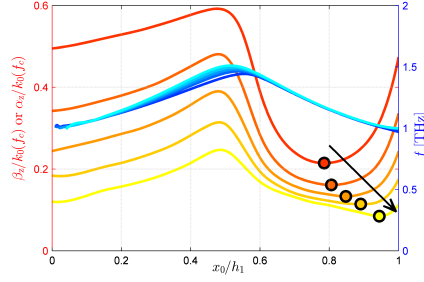


**Figure 3.21.:** Cutoff frequency  $f_c$  (blue to cyan solid lines) and relevant value of  $\hat{\beta}_z(f_c) = \hat{\alpha}_z(f_c)$  (red to yellow solid lines) as a function of the distance of the graphene sheet from the ground plane  $x_0$  normalized to the substrate thickness  $h_1$ , for the fundamental TM leaky mode in the GSS. Similar results are found for the fundamental TE leaky mode. As the dielectric contrast spans the following values  $d_{1,2} = 2, 5, 10, 20, 50$ , the curves shade from blue to cyan and from red to yellow for values of  $f_c$  and of  $\hat{\alpha}_z(f_c)$ , respectively.

that, when different dielectric contrasts are considered, this minimum condition still exists but is less pronounced and achieved for graphene positions shifted towards the interface between the layers, as  $d_{1,2}$  increases. This is exactly what we expect from theory, since, for a higher  $d_{1,2}$ , *cover* effects [163] dominate over *graphene* effects. Generally,  $x_{\text{opt}}$  and  $f_{\text{opt}}$  are nonlinear monotonic limited increasing and decreasing functions of  $d_{1,2} \in (1, \infty)$ , respectively. Consequently, it is convenient to place graphene in a position where it weakly interacts with the tangential electric fields (we recall here that in a standard SS antenna the tangential electric field has a minimum at the interface between the layers).

In the next paragraph the GSS with the graphene placed in the optimum location previously described (i.e., for  $d_{1,2} \simeq 6$ ) will be further investigated. Particularly, the possibility to obtain beam-scanning over bias at a fixed frequency will be addressed.

### Dispersion analysis

We will focus here on the interesting dispersion and radiation behaviors of the fundamental LWs (TE<sub>1</sub> and TM<sub>2</sub>) of the optimized GSS, i.e., with the graphene sheet located at the optimum position  $x_0 = 0.82h_1$  and the frequency fixed at the cutoff value  $f_c = 1.132$  THz for the fundamental TM leaky mode, as the chemical potential is decreased from the starting value of 1 eV to 0 eV (unbiased graphene).

In Fig. 3.22, the normalized phase  $\hat{\beta}_z$  and attenuation  $\hat{\alpha}_z$  constants of the fundamental TE and TM LWs are plotted as a function of the chemical potential  $\mu_c$  for the optimized GSS configuration (solid lines) and compared with those of an equivalent GPW configuration [114] (dashed lines), i.e., when the superstrate cover is removed from the GSS and the graphene sheet is replaced at the interface with the air (in this configuration the frequency is fixed at  $f_c = 0.92$  THz corresponding to the cutoff frequency of the fun-

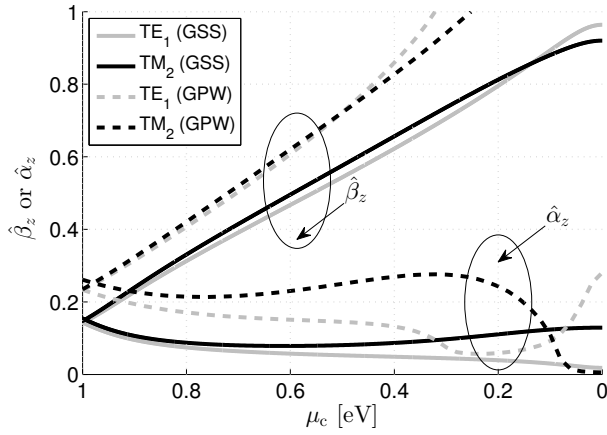


**Figure 3.22.:** Normalized phase constants and attenuation constants of the fundamental TM (in black) and TE (in grey) leaky modes of a GPW (dashed lines) with parameters as in [114] (i.e., with graphene placed at the interface between the air and a dielectric layer at a fixed frequency  $f_c = 0.92$  THz) and of the proposed GSS (solid lines) with parameters as in Fig. 3.19, with graphene placed at the optimum position  $x_0 = 0.82h_1$  at a fixed frequency  $f_c = 1.132$  THz, as a function of the chemical potential in the range  $1 > \mu_c > 0$  eV.

damental TM leaky mode supported by the GPW, as shown in [114]). As can be seen, both the TE and TM leaky modes of the GSS show two very interesting features: *i*) the phase constants follow an optimal quasi-linear behavior over the whole  $\mu_c$  bias range, i.e., from 1 eV to 0 eV, *ii*) the attenuation constants exhibit a mild variation, remaining consistently under the value of  $\hat{\alpha}_z \simeq 0.15$ , considerably smaller than those in the GPW case (see Fig. 3.22). The former feature, related to  $\hat{\beta}_z$ , enables for having a finer linear tuning sensitivity over a considerable range of chemical potentials, namely from 1 eV to 0 eV, thus allowing an accurate control of the beam-scanning process. As a matter of fact, the  $\hat{\beta}_z$  of the GSS fundamental leaky modes ranges from 0.15 to 1 over a bias that ranges from 1 eV to 0 eV, whereas for the GPW fundamental leaky modes it ranges from 0.25 to 1 over a bias that ranges from 1 eV to 0.35 eV. The latter feature, related to  $\hat{\alpha}_z$ , enables for having a desirable quasi-constant narrow beamwidth over the whole scanning region. Notably, the superstrate cover is beneficial in order to achieve lower leakage rates, thus strongly improving directivity. Indeed, the normalized attenuation constant of a GSS never exceeds the value of 0.15, whereas for a GPW the attenuation constant of the TM fundamental leaky mode can attain values above 0.3.

Even more interestingly, the almost perfect equalization of the TE and TM LW phase constants (essentially related to the fact that the equivalent admittance  $\sigma$  of the graphene sheet is the same for both polarizations) implies that the pointing angle is almost the same for both modes when bias is fixed. By exciting the antenna with a pair of simple sources (e.g., electric and magnetic dipoles) it is then possible to achieve dual or reconfigurable polarizations.

As we can expect from [114], both modes follow an optimal quasi-linear behavior. Furthermore, the fundamental leaky modes of the GSS have a finer tuning sensitivity and lower leakage-rates with respect to previous designs [114], thus justifying the higher complexity of the structure.

### Radiative analysis

As has been done for the GPW, the far-field expression of the magnetic field radiated on the H-plane for a GSS, considering a HMD source directed along the  $y$ -axis, is found:

$$F(\theta) = \frac{-jk_0}{4\pi} \cos \theta \frac{2Y_{\text{in}3}^{\text{TE}}}{(Y_{\text{in}3}^{\text{TE}} + Y_0^{\text{TE}})} \cdot \frac{Y_{\text{sc}2}^{\text{TE}}}{(Y_{\text{sc}2}^{\text{TE}} + \sigma)} \cdot \frac{\cos(k_{x1}h_s)}{\cos(k_{x1}h_1)} M, \quad (3.32)$$

with

$$\begin{aligned} Y_{\text{sc}2}^{\text{TE}} &= -jY_1^{\text{TE}} \cot(k_{x1}\xi h_1), \quad \xi = x_0/h_1, \\ Y_{\text{in}3}^{\text{TE}} &= Y_2^{\text{TE}} \frac{Y_{\text{in}2}^{\text{TE}} \cos(k_{x2}h_2) + jY_2^{\text{TE}} \sin(k_{x2}h_2)}{Y_2^{\text{TE}} \cos(k_{x2}h_2) + jY_{\text{in}2}^{\text{TE}} \sin(k_{x2}h_2)}, \\ Y_{\text{in}2}^{\text{TE}} &= Y_1^{\text{TE}} \frac{Y_{\text{in}1}^{\text{TE}} \cos(k_{x1}(1-\xi)h_1) + jY_1^{\text{TE}} \sin(k_{x1}(1-\xi)h_1)}{Y_1^{\text{TE}} \cos(k_{x1}(1-\xi)h_1) + jY_{\text{in}1}^{\text{TE}} \sin(k_{x1}(1-\xi)h_1)}, \\ Y_{\text{in}1}^{\text{TE}} &= \sigma + Y_{\text{cc}}^{\text{TE}}, \\ M &= \cos(k_{x1}h_1) + j\sigma Y_1^{\text{TE}} \sin(k_{x1}h_1) - \frac{j \sin(k_{x1}h_1) + \sigma Y_1^{\text{TE}} \cos(k_{x1}h_1)}{Y_1^{\text{TE}} Y_{\text{in}3}^{\text{TE}}}. \end{aligned} \quad (3.33)$$

It is straightforward to verify that for  $\xi = 1$  (i.e., when the graphene sheet is placed at the substrate-superstrate interface) and  $h_2 = 0$  (i.e., without the superstrate), Eq. (3.32) coincides with Eq. (3.25). (The expression for the E-plane can be obtained as previously described).

Both full-wave simulations (CST) and analytical results for the radiation patterns (see Figs. 3.23(b)-(c)) confirm that the optimized GSS shows substantially improved directivities with respect to GPW solutions (see Figs. 3.17(b)-(c)) for all the considered pointing angles ( $\theta_p = 0^\circ, 15^\circ, 30^\circ, 45^\circ$ ). Note that the obtained directivities of both the GPW and GSS are comparable with those obtained for the graphene-based SPP antennas proposed in [104], [107]. The beam-scanning behavior is obtained at a fixed frequency by just lowering the bias voltage (the relation between the chemical potential and the bias voltage is expressed by Eq. (3.8)) to decrease the graphene chemical potential from 1 eV to 0.3 eV for the GSS and from 1 eV to 0.5 eV for the GPW, corresponding to initial and final pointing angles on H-plane  $\theta_p = 0^\circ$  and  $\theta_p = 45^\circ$ , respectively. For further angles the radiation patterns start to widen on both planes, as predicted from the dispersion analysis shown in Fig. 3.22. Moreover, the radiation patterns have a quasi-constant beamwidth over the considered angular range from  $0^\circ$  to  $45^\circ$ , as can be predicted by looking at the slowly-varying leakage rates shown in Fig. 3.22.



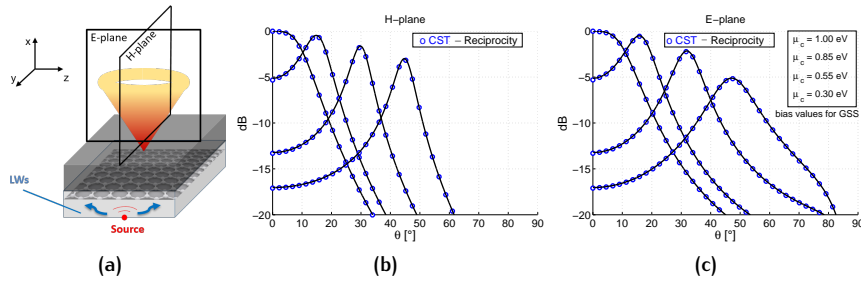


Figure 3.23.: (a) Illustrative example of the typical conical beam-scanning feature of a GSS antenna. In (b) and (c), the radiation patterns normalized to the overall maximum (achieved at broadside) vs. elevation angle  $\theta$  for the GSS antenna represented in (a), are reported for the H-plane and E-plane, respectively. Analytical results are plotted in black solid lines, whereas full-wave results obtained with the tool CST Microwave Studio [159] are given by blue circles. The scanning behavior at a fixed frequency ( $f_c = 1.132$  THz) is shown for beam maxima at  $\theta = 0^\circ, 15^\circ, 30^\circ, 45^\circ$ . The corresponding chemical potentials are reported in the legend.

Finally, quantitative comparisons between the beam features of the GSS and of the equivalent GPW and SS are presented either graphically in Fig. 3.24 for the H-plane, or tabularly for both planes in Table 3.1 and Table 3.2 (note that all the reported values have been rounded to the second decimal place). As is manifest from Fig. 3.24, the GSS patterns are rather narrower than those of the GPW for any pointing angle. This aspect is also corroborated by the numerical results of Table 3.1 where bias-scanning process at fixed frequency is considered, and the HPBW on both H-plane and E-plane of the GSS is compared to that of a GPW for pointing angles and

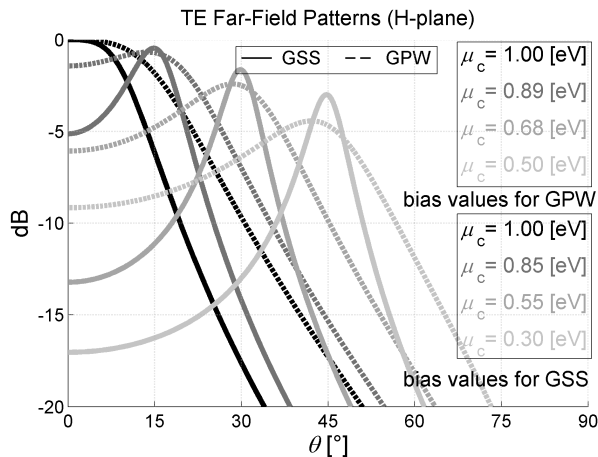


Figure 3.24.: H-plane radiation patterns, normalized to the overall maximum (achieved at broadside), vs. elevation angle  $\theta$  for a GSS antenna (solid lines) with parameters as in Fig. 3.22 and for an equivalent GPW (dashed lines), excited by a HMD placed on the ground plane. The scanning behavior at a fixed frequency ( $f_c = 1.132$  THz for the GSS and  $f_c = 0.92$  THz for the GPW) is shown for four theoretical pointing angles  $\theta_p = \sin^{-1}(\beta_z^2 - \alpha_z^2)^{1/2} = 0^\circ, 15^\circ, 30^\circ, 45^\circ$ . The chemical potentials for the GPW and the GSS are reported in the legend.



**Table 3.1.:** HPBW on H(E)-planes for different bias-scanned pointing angles of GSS and GPW antennas at fixed frequency.

HPBW [°] on H(E)-plane at $\mu_c$ [eV]		
$\theta_p$ [°]	GSS	GPW
0	22.46(24.19) at 1.00	35.55(39.03) at 1.00
15	8.87(10.46) at 0.85	21.33(25.85) at 0.89
30	6.80(10.50) at 0.55	18.36(27.95) at 0.68
45	6.75(16.75) at 0.30	20.20(35.27) at 0.50

**Table 3.2.:** HPBW on both H(E)-planes for different frequency-scanned pointing angles of GSS, GPW (at fixed  $\mu_c = 1$  eV), and SS antennas.

HPBW [°] on H(E)-plane at $f$ [THz]			
$\theta_p$ [°]	GSS	GPW	SS
0	22.46(24.19) at 1.14	35.55(39.03) at 0.92	44.62(45.15) at 1.00
15	7.80(9.13) at 1.15	18.37(22.34) at 0.93	28.84(35.30) at 1.01
30	4.36(6.27) at 1.18	11.02(16.45) at 0.95	16.61(24.53) at 1.03
45	3.17(7.02) at 1.22	8.10(17.30) at 0.99	11.22(24.21) at 1.06

related chemical potentials according to the values reported in Eq. (3.24). These results highlight that the introduction of a cover superstrate in a GPW can significantly improve the directivity over the whole considered angular range. From these results, however, it is not manifest whether the introduction of graphene is beneficial in an equivalent conventional SS configuration. It is worth noting here that in a conventional SS LWA (i.e., without graphene) the beam scanning property can be achieved only by changing the frequency. A comparison similar to the one shown in Table 3.1 is then reported in Table 3.2 for the GSS, for an equivalent GPW, and for an equivalent SS (equal to the GSS without the graphene sheet) when a frequency-scanning process is considered (for the graphene-based devices the chemical potential has been fixed at  $\mu_c = 1$  eV). From this last comparison, it is noticeable that the GSS configuration exhibits a significantly higher directivity with respect to both SS and GPW configurations, thus corroborating the interest in such GSS reconfigurable THz LWAs.

### Power analysis

As for the GPW antenna, it is important to evaluate the theoretical radiation efficiency  $\eta$  of the GSS antenna. Following the same procedure outlined in the previous subsection,  $P_g$  and  $P_{\text{rad}}$  have been evaluated using the TEN

model and the ABCD-matrix representation as in Fig. 3.18, where the ABCD parameters of the transmission matrices  $T_1$ ,  $T_2$ ,  $T_3$ , and  $T_4$  are given by:

$$T_1 = \begin{bmatrix} A_1 & B_1 \\ C_1 & D_1 \end{bmatrix} = \begin{bmatrix} \cos(k_{x1}x_0) & jY_1 \sin(k_{x1}x_0) \\ j(Y_1)^{-1} \sin(k_{x1}x_0) & \cos(k_{x1}x_0) \end{bmatrix}, \quad (3.34)$$

$$T_2 = \begin{bmatrix} A_2 & B_2 \\ C_2 & D_2 \end{bmatrix} = \begin{bmatrix} 1 & 0 \\ \sigma & 1 \end{bmatrix}, \quad (3.35)$$

$$T_3 = \begin{bmatrix} A_3 & B_3 \\ C_3 & D_3 \end{bmatrix} = \begin{bmatrix} \cos(k_{x1}x_1) & jY_1 \sin(k_{x1}x_1) \\ j(Y_1)^{-1} \sin(k_{x1}x_1) & \cos(k_{x1}x_1) \end{bmatrix}, \quad (3.36)$$

$$T_4 = \begin{bmatrix} A_4 & B_4 \\ C_4 & D_4 \end{bmatrix} = \begin{bmatrix} \cos(k_{x2}x_2) & jY_2 \sin(k_{x2}x_2) \\ j(Y_2)^{-1} \sin(k_{x2}x_2) & \cos(k_{x2}x_2) \end{bmatrix}. \quad (3.37)$$

In [115] it has been shown that the directivity at broadside is a non-linear function of the graphene position  $x_0$ . As it can be inferred from the expressions of the ABCD parameters,  $\eta$  is also a non-linear function of the graphene position  $x_0$ , thus in Fig. 3.25(a) the values of the efficiency  $\eta$  (red line) and of the directivity at broadside normalized to its maximum  $\bar{D}_0 = D_0/D_{\max}$  ( $D_{\max}$  being the maximum value of  $D_0$  with respect to  $x_0$ ) have been reported for graphene positions ranging from the ground plane ( $x_0 = 0$ ) to the substrate-superstrate interface ( $x_0 = h_1$ ). As is shown, the maximum directivity does not correspond to a maximum of the efficiency, thus the *optimal* position for the directivity, i.e.,  $x_0 = 0.82h_1$ , does not lead to the best configuration in terms of efficiency.

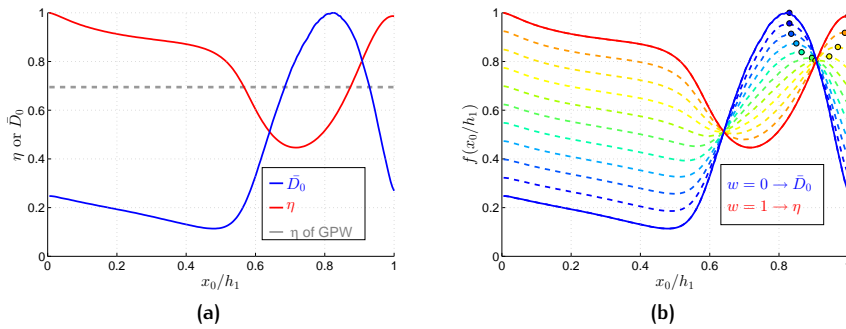


**Figure 3.25.:** (a) Efficiency  $\eta$  vs. graphene positions in the substrate  $x_0/h_1$  (red lines), and directivity at broadside normalized to its maximum  $\bar{D}_0$  (blue lines). Both  $\eta$  and  $\bar{D}_0$  have been calculated at the corresponding cutoff frequency for each graphene position  $x_0/h_1$ . The grey dashed line, representing the efficiency of an equivalent GPW antenna, has been reported for comparison. (b) The function  $f$  vs.  $x_0/h_1$  of Eq. (3.38) for different values of  $w$ . Color of the lines shades from blue to red as  $w$  ranges from 0 to 1. Colored dots highlight the positions of the maxima of  $f$  as  $w$  ranges from 0 (blue dot) to 1 (red dot). Maxima are located closer to the interface as the efficiency is weighted more than the directivity.

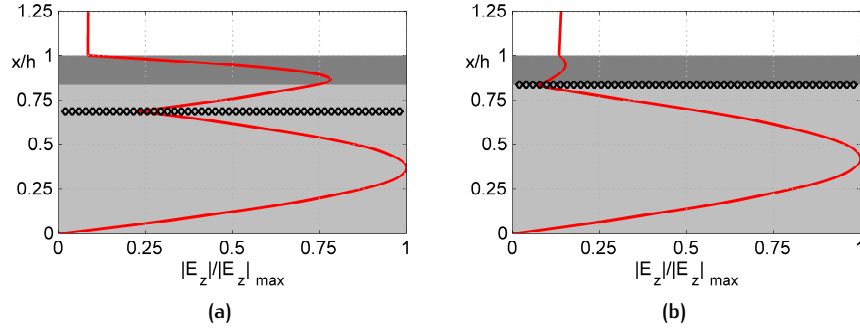


**Figure 3.26.**: Field configurations of the tangential component of the electric field  $E_z$  for the fundamental TM leaky mode (red line) in a GSS antenna (a) at  $f = 1.13$  THz when graphene is placed at  $x_0 = 0.82h_1$  and (b) at  $f = 1.00$  THz when graphene is placed at the interface  $x_0 = h_1$ . Light grey, dark grey, and white regions represent the substrate, the superstrate, and the air, respectively, whereas the black diamonds stand for the graphene sheet. The  $x$ -axis is normalized to the height of the overall structure  $h = h_1 + h_2$ .

In order to take into account both the directivity and the radiation efficiency in the design process of such LWAs, we have therefore defined a suitable function:

$$f(x_0/h_1) = w(\eta(x_0/h_1)) + (1 - w)\bar{D}_0(x_0/h_1) \quad (3.38)$$

where  $w \in [0, 1] \subset \mathbb{R}$  is an arbitrary parameter which represents the weight given to the efficiency. Note that  $f(x_0/h_1)$  is a convex combination of  $\eta(x_0/h_1)$  and  $\bar{D}_0(x_0/h_1)$ , thus maximizing this function would lead to maximizing the efficiency for  $w \rightarrow 1$  or to maximizing the directivity at broadside for  $w \rightarrow 0$ . In Fig. 3.25(b) the function  $f(x_0/h_1)$  is represented for intermediate values of  $w$  between 0 and 1. The curves shade from blue to red as  $w$  increases from 0 to 1. As is seen, the maximum condition (small colored dots in Fig. 3.25(b)) shifts toward positions  $x_0$  in the proximity of the substrate-superstrate interface (positions too close to the ground plane have not been considered for practical considerations) when  $w$  increases; in fact, the efficiency of the GSS antenna is improved when the electric field weakly interacts with the graphene sheet.

This physical explanation is also corroborated by the modal configuration of the tangential component of the electric field  $E_z$  of the fundamental TM leaky mode in a GSS reported in Fig. 3.26. As is shown, the intensity of the electric field at the graphene position is stronger when graphene is placed at  $x_0 = 0.82h_1$  (see Fig. 3.26(a)) than when graphene is placed at  $x_0 = h_1$  (see Fig. 3.26(b)). Consequently, the position  $x_0 = 0.9h_1$  (see Fig. 3.25(b)) would lead to both efficiencies  $\eta$  and normalized directivities at broadside  $\bar{D}_0$  almost equal to 80%, thus representing a very good trade-off for the antenna design. It is worth noting that this position is correctly predicted by the maximum condition of Eq. (3.38) when  $w = 0.5$  (see small green

**Table 3.3.:** Comparison of efficiency  $\eta$ , directivity at broadside  $D_0$  and reconfigurability  $\Delta\theta$  (scanning angular range) for GPW and GSS antennas, for different quality ( $\tau$ ) of the graphene sheet.

	$\tau$ [ps]	$x_0/h_1$	$f_c$ [THz]	$D_0$ [dB]	$\eta$ [%]	$\Delta\theta$ [°]
GPW	3.0	1.000	0.923	14.07	70	90
	1.0	1.000	0.926	12.11	43	90(*)
	0.5	1.000	0.928	10.34	29	90(*)
GSS	3.0	0.820	1.132	18.56	55	70
	1.0	0.910	1.045	16.16	60	37
	0.5	0.940	1.024	14.84	63	28

dot in Fig. 3.25(b)), i.e., when the same weight is given to  $\eta$  and  $\bar{D}_0$  in the maximization of Eq. (3.38).

Finally, calculations of efficiency and directivity have also been performed considering  $\tau = 0.5$  ps and  $\tau = 1$  ps in order to show the significant impact of the graphene quality on the performance of both GPW and GSS antennas. The choice of these particular values of  $\tau$  is motivated by the fact that  $\tau = 1$  ps is the value used in [103], [104], [106], whereas  $\tau = 0.5$  ps seems to be the best value one can hope to achieve for a graphene flake at room temperature when deposited on impurity-free substrates like SiO<sub>2</sub> [76], [147]. A comparison of the values of efficiency,  $\eta$ , of directivity  $D_0$  in dB, and of reconfigurability, given in terms of the angular range  $\Delta\theta$  that can be scanned with a bias variation of 1 eV, is reported in Table 3.3 for three different values of  $\tau$ , namely 0.5 ps, 1 ps and 3 ps, for both the GPW and the GSS antennas, when in the latter  $x_0/h_1$  is chosen to maximize directivity at broadside.

As is shown, the directivity  $D_0$  and the reconfigurability  $\Delta\theta$  of both GPW and GSS antennas worsen as the quality of graphene (i.e.,  $\tau$ ) decreases. However, the efficiency of the GSS antenna counterintuitively improves as  $\tau$  decreases. This behavior can readily be explained by noting the different positions assumed by the graphene sheet inside the substrate. As it can be seen, when  $\tau$  decreases, the position which leads the GSS antenna to the configuration that exhibits the maximum directivity at broadside shifts toward the interface where the interaction with the tangential electric field is weaker and thus the efficiency becomes higher. Conversely, the reconfigurability is considerably reduced, as confirmed by the abrupt decrease of  $\Delta\theta$  as  $\tau$  decreases as well. This is mainly due to the fact that, for lower values of  $\tau$ , graphene ohmic losses are no longer negligible and thus a weaker interaction is preferred for maximizing the directivity, but at the expense of a reduced reconfigurability. Note that the asterisk (\*) for  $\Delta\theta = 90^\circ$  for GPW antennas with  $\tau = 0.5$  ps and  $\tau = 1$  ps means that the whole angular range (from broadside  $\theta_p = 0^\circ$  to endfire  $\theta_p = 90^\circ$ ) is reached for a larger bias range, thus leading to a reduced performance in terms of reconfigurability.

**Table 3.4.:** Comparison of directivity and reconfigurability for GSS antennas with different efficiencies and for different quality ( $\tau$ ) of the graphene sheet.

	$\tau$ [ps]	$x_0/h_1$	$f_c$ [THz]	$D_0$ [dB]	$\Delta\theta$ [°]
GSS ( $\eta = 75\%$ )	3.0	0.890	1.062	17.93	44
	1	0.940	1.023	15.73	28
	0.5	0.955	1.015	14.69	25
GSS ( $\eta = 90\%$ )	3.0	0.940	1.023	16.48	28
	1.0	0.970	1.007	14.61	21
	0.5	0.980	1.003	13.93	18

Finally, we have calculated the performance of the GSS antenna when graphene is no longer placed in the position which maximizes directivity at broadside, but in positions that would lead to fixed efficiencies  $\eta = 75\%$  and  $\eta = 90\%$ , respectively. It is worth here to stress that these results are in good agreement with the theoretical limits established in [126] for the efficiency of reconfigurable graphene antennas. Indeed, the theoretical efficiency of a GSS would be upper-bounded by  $\eta_{\max} \lesssim 95\%$ , as can be inferred looking at the values on the bisector of Fig. 2 in [127] for  $\gamma_{\max} = 30$  (the minimum value of  $\gamma_{\max}$  for  $0.5 < \tau < 3$  ps and  $f = 1$  THz, when one considers the maximum achievable angular range, i.e.,  $\mu_c = 1$  eV and 0 eV is still greater than 70, according to Eq. (10) in [127]). We should also mention that the results of [126], [127] are based on a far-field representation through spherical waves that holds for antennas with finite dimensions [164], in contrast with our initial assumption of transversely-infinite size. However, any practical 2-D LWA is laterally truncated at a suitable radial distance (which depends on both the desired radiation efficiency and the leakage rate, such that the antenna performance is negligibly different from that obtained in the ideal infinite case [114]).

Results are shown in Table 3.4. As expected, a higher efficiency is paid at the expense of a reduced reconfigurability for the aforementioned reasons. In particular, when standard graphene ( $\tau = 0.5$  ps) is considered, an extremely efficient GSS antenna ( $\eta = 90\%$ ) would exhibit poor reconfigurable properties, scanning angular regions being limited to an angular sector of only  $18^\circ$ . A similar conclusion holds also for LWAs based on SPP as has been stressed in [128] for the graphene CRLH metamaterial waveguides, whose performance is severely affected by the graphene quality. However, our last results emphasize even more the better design flexibility of GSS with respect to GPW antennas, and especially with respect to their counterparts based on SPPs.

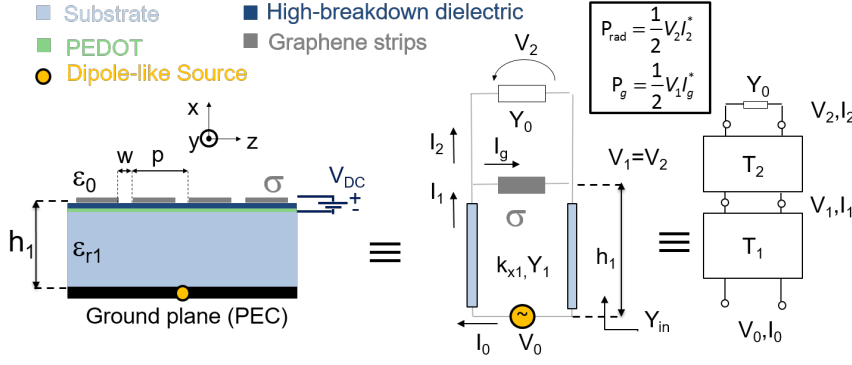


Figure 3.27.: 2-D section of the GSG antenna and its TEN model.

### 3.2.5 Graphene strip grating antennas

The GSG proposed finally here is a reconfigurable leaky-wave antenna based on a patterned graphene metasurface as the one depicted in Fig. 3.27. The structure is equal to the GPW [114], except for the patterning of the graphene sheet. Specifically, we have considered a dense array of infinitely-long graphene strips aligned along the  $y$ -axis. The proposed grating is characterized by a subwavelength period  $p = \lambda/5$  and a very small gap between the strips  $w = p/10 = \lambda/50$  at the design frequency  $f = 1$  THz (which corresponds to  $\lambda \simeq 300 \mu\text{m}$ ). Under these conditions, the patterned graphene sheet can accurately be described by a single homogenized surface impedance [50], [52], [53]. Note that, under these hypotheses, the proposed GSG is considerably different from those proposed in [131], where the period of the grating is comparable with the wavelength, and hence a single impedance would not suffice for the description of the properties of the surface [52].

For an imperfect conductor, or more generally for an arbitrary 2-D material characterized by a complex surface conductivity as graphene, the following expressions for the homogenized TE and TM impedances hold [50], [53]:

$$Z_s^{\text{TM}} = \frac{p}{\sigma(p-w)} - j \frac{\zeta_{\text{eff}}}{2\alpha}, \quad (3.39)$$

$$Z_s^{\text{TE}} = \frac{p}{\sigma(p-w)} - j \frac{\zeta_{\text{eff}}}{2\alpha(1 - (k_z/k_{\text{eff}})^2/2)}, \quad (3.40)$$

with

$$\alpha = (k_{\text{eff}} p / \pi) \ln \csc \left( \frac{\pi w}{2p} \right),$$

where  $k_{\text{eff}} = k_0 \sqrt{\epsilon_{\text{eff}}}$ ,  $\zeta_{\text{eff}} = \zeta_0 / \sqrt{\epsilon_{\text{eff}}}$ , and  $\epsilon_{\text{eff}} = (\epsilon_{r1} + 1)/2$ .

Following the same procedure outlined in [114], [165], the dispersion curves of the GSG are readily obtained using Eqs. (3.39)-(3.40) to describe the sheet impedance. Results are shown in Fig. 3.28 where the dispersion curves of the fundamental TE (see Figs. 3.28(a) and (c)) and TM (see

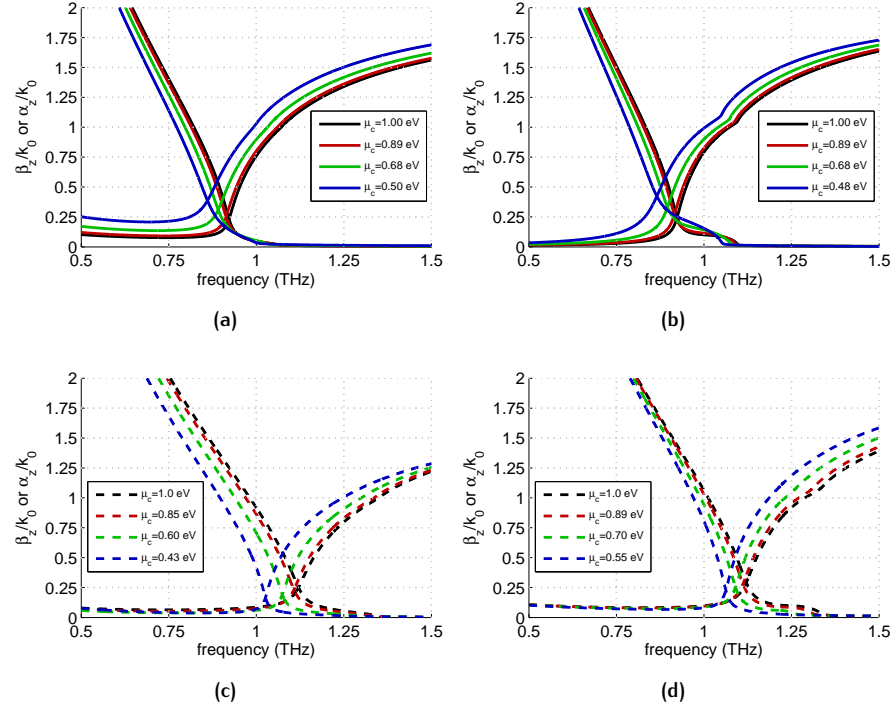


**Figure 3.28.**: Dispersion diagrams of  $\hat{\beta}_z$  and  $\hat{\alpha}_z$  vs.  $f$  for (a)-(c) TE and (b)-(d) TM fundamental leaky modes of a (a)-(b) graphene-based planar single-slab antenna (solid lines) and a (c)-(d) graphene-strip grating antenna (dashed lines). The values of the chemical potentials  $\mu_c$  are reported in the legends.

Figs. 3.28(b) and (d) leaky modes of the GSG have been reported and compared with those of the GPW (see Figs. 3.28(a)-(b)) for four different values of the chemical potential  $\mu_c$ . The values of  $\mu_c$  have been selected in order to get the same theoretical pointing angles [48] analyzed for the GPW and the GSS antennas, i.e.,  $\theta_p = 0^\circ, 15^\circ, 30^\circ, 45^\circ$ , at the fixed frequencies of  $f \simeq 0.922$  THz for the first one and of  $f \simeq 1.12$  THz for the second one. As is shown, except for a frequency shift, the behaviors are similar, and hence comparable radiative performances are expected from the contribution of the relevant leaky modes.

To verify this, the radiation patterns (see Fig. 3.29) have been calculated analytically by taking into account only the contribution of the leaky mode, as described in [48]. As expected, the radiation patterns at broadside (black lines) of a GSG show a slightly larger beamwidth due to the small increase of the leakage rate, as can be inferred from the inspection of Figs. 3.28 and 3.29. However, as the bias is decreased from its maximum value  $\mu_c = 1$  eV (broadside condition), graphene ohmic losses increase as extensively commented in 3.2.1. As a consequence, in the GPW (see Figs. 3.28(a)-(b)), the leakage rates at the cutoff frequency  $f \simeq 0.922$  THz tend to remain almost the same (note that, in 2-D LWAs, as the phase constant increases beyond the cutoff frequency, the leakage rate usually decreases [48]), and in turn the corresponding half-power beamwidths are rather large over the

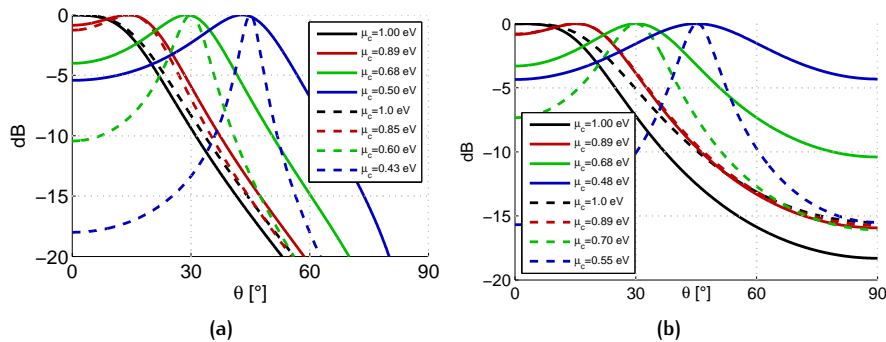


Figure 3.29.: Normalized radiation patterns  $P(\theta)/P_{\max}$  vs.  $\theta$  for (a) TE and (b) TM fundamental leaky mode of a GPW (blue lines) and a GSG (red lines).

considered scanning range (see solid lines in Figs. 3.29(a)-(b)). Conversely, in the GSG (see Figs. 3.28(c)-(d)) the leakage rates at the cutoff frequency  $f \simeq 1.12$  THz decrease as  $\mu_c$  decreases, and in turn the corresponding half-power beamwidths (see dashed lines in Figs. 3.29(a)-(b)) are narrower than those of the GPW (see solid lines in Figs. 3.29(a)-(b)) as the beam is scanned for a wider angle. This behavior has a simple physical explanation. As can be inferred from Eqs. (3.39)-(3.40), the dependence of  $\sigma$  on the homogenized impedance of the graphene-strip grating, is ‘weighted’ by the geometrical properties of the grating. As a consequence, any change in the graphene conductivity  $\sigma$  is reflected in a weaker effect whose intensity depends on the ‘filling-factor’  $w/p$ . The results shown here are thus a direct consequence of the choice  $w/p = 0.1$ .

As a final remark, the different equalization of the TE-TM modes in the case of a GSG is worth to be commented. As is seen, the values of the chemical potentials needed to obtain the same pointing angles are different over the H- and the E-plane, whereas they are almost the same for the GPW. This is a consequence of the different expression (see Eqs. (3.39)-(3.40)) of the equivalent impedance shown by the graphene-strip grating for the TE and the TM case. However, the GSG, is still quite attractive thanks to the additional degrees of freedom provided to antenna designers. In fact, the possibility to use a patterned graphene sheet, instead of a uniform unpatterned graphene sheet, allows for independently biasing each strip, thus permitting the realization of tunable LWAs with a tapered aperture distribution.

We finally note that the radiating features of the GSG have been preliminarily analyzed assuming a homogenized impedance for the GSG. In this context, full-wave simulations are even more required in order to assess the validity of the homogenization formulas in Eqs. (3.39)-(3.40) for conductive strips characterized by a finite complex conductivity as graphene.



### 3.2.6 Technological aspects

In this Subsection, we provide some information about the technological implementation of a GPW, a GSS, and a GSG. The proposed structures are depicted in Figs. 3.10, 3.18 and 3.27, respectively. The antenna feed excitation can be achieved through a finite-size slot etched in the ground plane whose dimensions along the  $y$ - and the  $z$ -axis are in the order of  $\lambda/5$  and  $\lambda/10$ , respectively. Then, a coherent THz source, such as a quantum cascade laser (QCL) beam, can be used to illuminate the slot in order to suitably excite the fundamental leaky modes.

The lateral dimensions of the structure are calculated following the design rules outlined in [114], in order to minimize diffraction from edges which would affect the shape of the radiation patterns, especially on the sidelobes. In particular, considering a circular substrate with radius  $\rho_{\text{ap}}$  and assuming, as is customary, that the relevant leaky modes have radiated 90% of their power before reaching the structure edges, it can readily be shown that

$$\frac{\rho_{\text{ap}}}{\lambda_0} \simeq \frac{0.18}{\hat{\alpha}_z}, \quad (3.41)$$

where  $\lambda_0$  is the free-space wavelength at  $f = 1$  THz. With reference to the case of the GPW, where  $\hat{\alpha}_z \simeq 0.2$ , this implies a substrate having linear dimensions of the order of  $500 \mu\text{m}$ , whereas for the case of a GSS, where  $\hat{\alpha}_z \simeq 0.15$ , they should be of the order of  $750 \mu\text{m}$ . The increased linear dimensions of a GSS with respect to a GPW are due to the reduced value of the leakage rate provided by the *cover effect* of the superstrate [115]. However, such dimensions, and even higher, are within the state of the art for the production of high-quality graphene sheets as pointed out by many recent works [166]–[171]. As is known, the chemical vapor deposition (CVD) method allows for the synthesis of high-quality large-area graphene films grown on copper foils. Even more interestingly, it has recently been shown that a new, simple and effective method based on CVD [171] allows for the production of several square centimeters of strictly monolayer graphene sheet, thus paving the way for the mass production of monolayer graphene in industry.

Once the graphene film is produced, it can be transferred onto a back-metalized  $\text{SiO}_2$  substrate (already comprising the polysilicon layer) as described in [169]. In the case of a GSS, a double-layered slab consisting of a layer of  $\text{SiO}_2$  and a layer of  $\text{HfO}_2$  is then stacked on top of the graphene sheet.

With regard to the GSG, the only difference would consist in the transfer process of the graphene sheet from the copper foil to an imprinted poly-methyl-methacrylate (PMMA), as well described in [172]. It is worth here to stress that this technique [172] preserves the quality of the CVD grown graphene, and offers the possibility to transfer of the GSG onto the silicon oxide substrate.

The tunable features of graphene are then exploited by varying the DC voltage between the graphene sheet and the polysilicon layer, used here as a gate electrode (the interested reader can find further details on the realization of different biasing schemes in [173]). With regard to this last aspect, some limitations exist due to the high electrostatic field requested to achieve significant values of chemical potentials. As shown in 3.2.1, an integral equation relates the chemical potential  $\mu_c$  to the electrostatic field  $E_0$ . In Fig. 3.2, it is seen that a variation of  $\mu_c$  in the range 0 eV to 1 eV requires electrostatic fields of several V/nm. However, the voltage breakdown of the dielectric filling the capacitor constituted by the graphene layer and the conductive polymer layer is rarely taken into account in the literature. Indeed, by means of the approximate formula [142], [174]:

$$E_0 \simeq \frac{q_e}{\epsilon_0 \epsilon_r} \frac{1}{\pi} \left( \frac{\mu_c}{\hbar v_F} \right)^2, \quad (3.42)$$

where  $v_F \simeq 10^6$  m/s is the Fermi velocity in graphene, it is easy to find that the maximum chemical potential  $\mu_{c,\max}$  that can be achieved for a certain material is given by the formula:

$$\mu_{c,\max} = \hbar v_F \sqrt{\frac{\pi \epsilon_0 \epsilon_r E_{\text{bd}}}{q_e}}, \quad (3.43)$$

where  $E_{\text{bd}}$  represents the voltage breakdown of a given dielectric material. If one uses  $E_{\text{bd}}$  of SiO<sub>2</sub> ( $\epsilon_r = 3.8$ ,  $E_{\text{bd}} = 1.5$  V/nm) which is one of the materials with the highest  $E_{\text{bd}}$  [143], it comes out that the maximum chemical potential that can be achieved is only 0.436 eV. However, since  $\mu_{c,\max}$  depends not only on  $E_{\text{bd}}$  but also on  $\epsilon_r$ , an accurate analysis of Table I in [143] revealed us that the choice of HfO<sub>2</sub> ( $\epsilon_r = 25$  and  $E_{\text{bd}} = 0.67$  V/nm), TiO<sub>2</sub> ( $\epsilon_r = 95$  and  $E_{\text{bd}} = 0.25$  V/nm), and Al<sub>2</sub>O<sub>3</sub> ( $\epsilon_r = 9$  and  $E_{\text{bd}} = 1.38$  V/nm) lead to values of  $\mu_{c,\max}$  equal to 1.12 eV, 1.33 eV, and 0.92 eV respectively. It is worth here noting that, even if both HfO<sub>2</sub>, TiO<sub>2</sub>, and Al<sub>2</sub>O<sub>3</sub> are characterized by a non-negligible loss tangent in the THz range [175], [176], the extremely thin layer that is needed in our design would result in a negligible impact on the performance of the antenna. It should also be noted that these materials (viz., HfO<sub>2</sub>, TiO<sub>2</sub> and Al<sub>2</sub>O<sub>3</sub>) provide minimal degradation of epitaxial graphene structural properties when integrated with thin dielectric layers [177]. In particular, it is seen that Al<sub>2</sub>O<sub>3</sub> is only mildly affected by surface-optical phonon-scattering with respect to other high-permittivity materials [144].

On the other hand, it has been shown that high-permittivity materials are subject to phonon scattering which reduce the mobility of graphene [144]. A good choice is represented by Alumina (Al<sub>2</sub>O<sub>3</sub>).

Furthermore, very recently new techniques involving ion gel gate dielectrics [174], [178] seem to provide an innovative solution in order to bias

graphene up to 1 eV avoiding the problems posed by the voltage breakdown of the most common dielectric materials.

As a final comment, since in our design the minimum value of the chemical potential for scanning the beam at  $45^\circ$  is of the order of 0.30 eV [115], a suitable solution in order to avoid the use of  $\text{TiO}_2$  and  $\text{HfO}_2$  could be represented by the possibility of chemically pre-doping graphene. Note also that chemical doping seems to scarcely affect the mobility of carriers in graphene [117].

## 3.3 FABRY-PEROT CAVITIES BASED ON LIQUID CRYSTALS

### 3.3.1 Introduction

In the previous Section we have exhaustively seen the exceptional features of graphene LWAs. Several designs, namely, the Graphene Planar Waveguide (GPW), the Graphene Substrate-Superstrate (GSS), and the Graphene Strip Grating (GSG) antennas have been promoted as promising candidates for the development of novel efficient reconfigurable 2-D LWAs in the THz range.

However, the technological implementation and the measurements of the proposed devices in the THz range is a delicate task. As is seen (see 3.2.6), the graphene synthesis as well as the realization of the biasing scheme, may present some issues. The former, usually impact on graphene quality causing the degradation of the radiation performance, as recently pointed out in [173]. The latter may restrict the range of tunability of the proposed devices due to the high required levels of the electrostatic field, which may cause the voltage breakdown of the dielectric materials.

In this context, in the present Section we will consider nematic liquid crystals (NLCs) as an alternative tunable element to graphene, for the design of THz reconfigurable 2-D LWAs. As is known [92], [93], the application of a low driving voltage allows for tuning the dielectric properties of LCs. As a consequence, the phase constant of the LW modes responsible for radiation is affected, determining the beam steering capability at fixed frequency. We then propose an innovative configuration of electronically scanning THz Fabry-Perot cavity (FPC) LWAs based on NLCs.

In 3.3.2 we briefly describe the general physical properties of LCs with particular emphasis on NLCs. In 3.3.3 a simplified electromagnetic model for NLCs is derived to characterize its dielectric properties. The dynamic range exhibited by its permittivity tensor is shown for a considerably wide range of bias voltages. Thus, inspired by tunable filters using LCs in a FPC [179], [180], several designs of FPC-LWAs based on NLCs are developed in 3.3.4 using the electromagnetic model derived in the previous Subsection. Dispersive and radiative analyses are presented for different configurations, characterized by different choices of the thicknesses and the number of the layers, assuming lossless models. On the basis of such an analysis, two specific designs are validated through full-wave simulations for both the lossless and the lossy case. Results clearly reveal the advantages and disadvantages of their implementation in both ideal and realistic scenarios.

### 3.3.2 Liquid crystals

Nematic liquid crystals (NLCs) are the most widely studied and used liquid crystals (LCs). As is known [92], in addition to the solid crystalline and liquid phases, LCs exhibit intermediate phases (*mesophases*) where they flow like liquids (thus requiring hydrodynamical theories for their complete description), yet possess some physical properties characteristic of solids (thus requiring the *elastic continuum theory* for their complete description). As a function of temperature, or depending on the constituents, concentration, substituents, and so on, LCs exist in many so-called mesophases: *nematic*, *cholesteric*, *smectic*, and *ferroelectric* [92].

As a matter of fact, among all liquid crystals mesophases, NLCs best exemplify the dual nature of liquid crystals—fluidity and crystalline structure. Generally speaking, we can divide liquid crystalline phases into two distinctly different types: the ordered and the disordered. For the ordered phase, LCs behave much more as solids. However, even in the ordered phase, LCs still possess many properties typical of liquids. Liquid crystals in the disordered or isotropic phase behave very much like ordinary fluids of anisotropic molecules. There is, however, one important difference, which makes them attractive for electromagnetic applications: near the isotropic *nematic phase transition temperature*, the LC molecules become highly susceptible to external fields, and their responses tend to slow down considerably [92].

In particular, it is known that [92], [93], when no bias is applied, the optical axis of the LC molecules is aligned along the horizontal axis (*unbiased state*), whereas, when a sufficiently large driving voltage (typically an alternating voltage in the few kHz range to prevent electrochemical degradation) is applied across the LC, the optical axis is fully tilted along the vertical axis (*biased state*) [181] (see Fig. 3.30). While the maximum achievable tuning range can be inferred from the knowledge of these two limiting states, the voltage-dependent tunable properties of LCs require a rigorous study of the

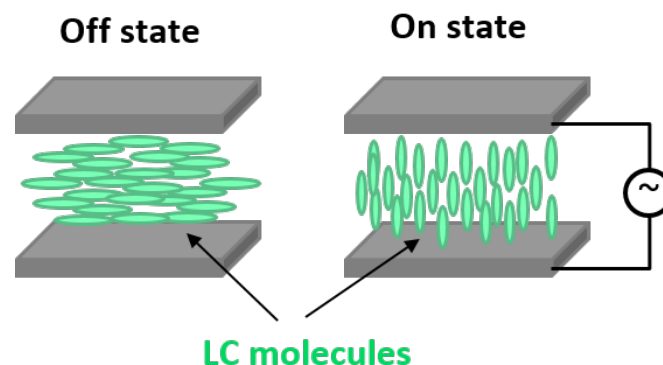


Figure 3.30.: Representation of NLC molecules twisting in a LC cell. The optical axis of the NLC switches under the effect of an applied bias voltage.

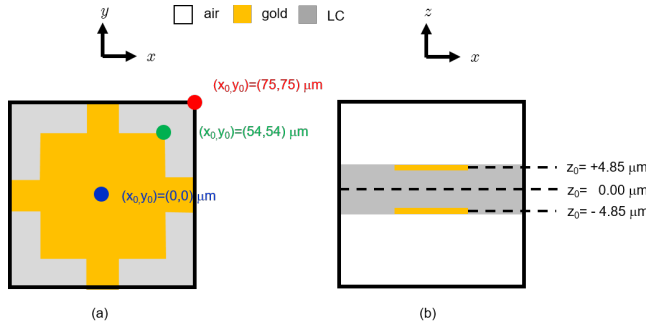


Figure 3.31.: 2-D section (a) on the  $xy$ -plane and (b) on the  $xz$ -plane of the THz fishnet MM. Further details on the unit-cell are available in [96].

LC dynamics. This task can be performed by employing the  $Q$ -tensor formulation, an advanced numerical tool for the accurate studies of the LC orientation in confined geometries [96].

In the next Subsection, we will show the results of such an analysis in relation to a novel tunable THz fishnet metamaterial (MM) based on thin NLC layers. These results will serve us to develop a simplified electromagnetic model of LCs to be used in the analysis of some original FPC-LWAs based on NLCs.

### 3.3.3 Electromagnetic model for nematic liquid crystals

Among the different kind of NLCs, we consider here the nematic mixture 1825 because of its high birefringence at THz frequencies [96]. The dielectric properties of such a material are described by a complex permittivity tensor:

$$\underline{\underline{\epsilon}} = \epsilon_0 \begin{bmatrix} \epsilon_{xx} & \epsilon_{xy} & \epsilon_{xz} \\ \epsilon_{yx} & \epsilon_{yy} & \epsilon_{yz} \\ \epsilon_{zx} & \epsilon_{zy} & \epsilon_{zz} \end{bmatrix}, \quad (3.44)$$

where  $\epsilon_{ij} \in \mathbb{C}$  for  $i, j \in \{x, y, z\}$  are the cartesian components of the relative permittivity. In general  $\epsilon_{ij} \neq \epsilon_{kl}$  for any pair  $\{i, j\} \neq \{k, l\}$  with  $i, j, k, l \in \{x, y, z\}$ , due to the anisotropic nature of the NLC. The analysis of the  $Q$ -tensor in [96] provided us the values of the relative permittivity components for different values of the electrostatic field when the LC layer is biased through the THz fishnet MM reported in Fig. 3.31. In Fig. 3.32, the real parts<sup>7</sup> of the diagonal components, i.e.,  $\epsilon_{ii}$ , are reported for bias voltages  $V_b$  going from 0 V (*unbiased* state) to  $V_\infty = 7$  V (*biased* state), as contour plots over the  $xy$ -plane for  $z = 0$  (see Fig. 3.31(b)). In Fig. 3.33, the same plots are reported for the off-diagonal components, i.e.,  $\epsilon_{ij}$  for  $i \neq j$ <sup>8</sup>. As is seen, the optical axis of the NLC tilts in the  $xz$ -plane exhibiting a negligible rotation

<sup>7</sup> Imaginary parts are not reported for brevity. Their behavior is qualitatively similar to those of the real parts but on a different scale, the imaginary parts changing from approximately 0.08 to 0.05.

<sup>8</sup> Only three components are reported due to the *Hermitian* symmetry of  $\underline{\underline{\epsilon}}$ , viz.,  $\epsilon_{ij} = \epsilon_{ji}^*$ .

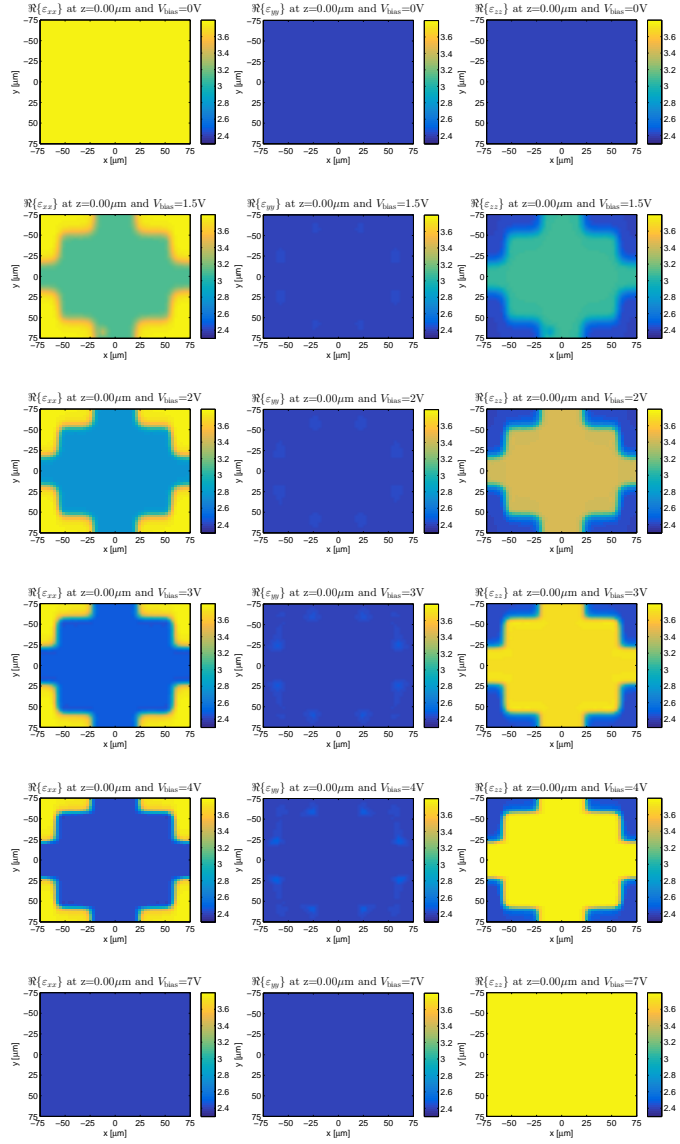


Figure 3.32.: Real part of the diagonal terms  $\varepsilon_{ii}(x, y, z = 0)$  vs.  $xy$ -plane of the relative permittivity tensor for  $V_{\text{bias}} = 0 - 7$  [V]. First column ( $i = x$ ), second column ( $i = y$ ), and third column ( $i = z$ ). Starting from the first row the driving voltage takes the following values:  $\{0, 1.5, 2, 3, 4, 7\}$  [V].

over both the  $yz$ - and the  $xy$ -plane. Thus, at a first approximation<sup>9</sup>, the NLC can be locally modeled as a *uniaxial* crystal whose complex permittivity tensor is given by:

$$\underline{\underline{\varepsilon}}(0) = \varepsilon_0 \begin{bmatrix} \varepsilon_o & 0 & 0 \\ 0 & \varepsilon_o & 0 \\ 0 & 0 & \varepsilon_e \end{bmatrix}, \quad \underline{\underline{\varepsilon}}(V_\infty) = \varepsilon_0 \begin{bmatrix} \varepsilon_e & 0 & 0 \\ 0 & \varepsilon_o & 0 \\ 0 & 0 & \varepsilon_o \end{bmatrix}, \quad (3.45)$$

<sup>9</sup> A more accurate model should take into account the non-zero values of the  $\varepsilon_{xz}$  and  $\varepsilon_{zx}$  components.

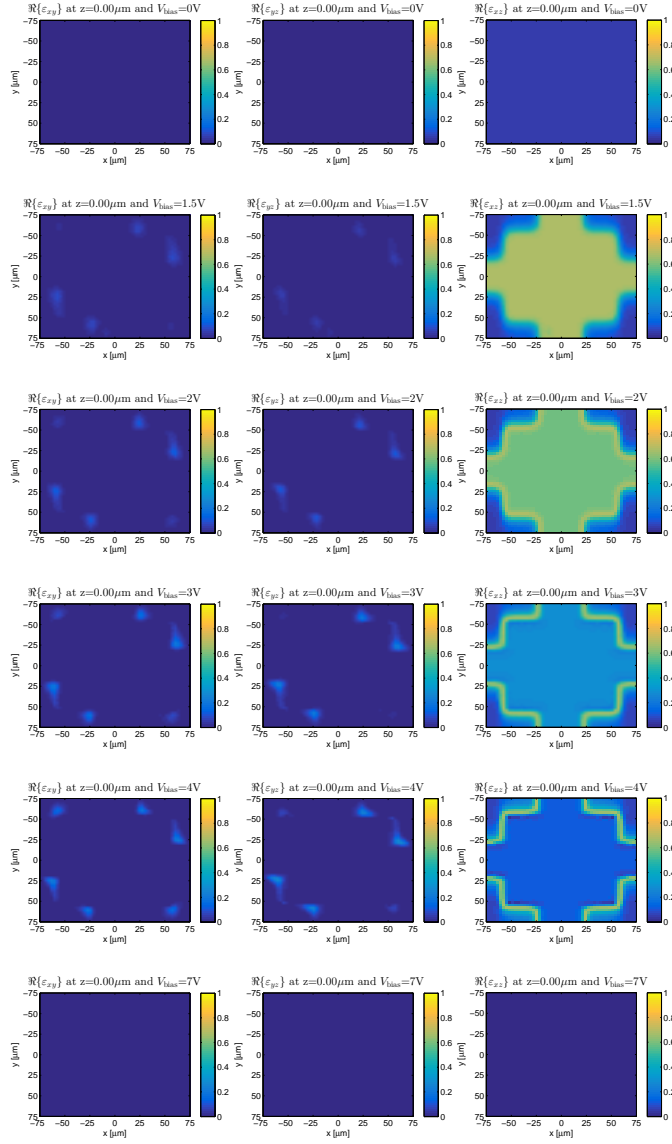


Figure 3.33.: Real part of the off-diagonal terms  $\epsilon_{ij}(x, y, z = 0)$  vs.  $xy$ -plane of the relative permittivity tensor for  $V_{\text{bias}} = 0 - 7$  [V]. First column ( $i = x, j = y$ ), second column ( $i = y, j = z$ ), and third column ( $i = x, j = z$ ). Starting from the first row the driving voltage takes the following values:  $\{0, 1.5, 2, 3, 4, 7\}$  [V].

where  $\epsilon_o \simeq 2.42$  and  $\epsilon_e \simeq 3.76$  are the ordinary and the extraordinary relative permittivities of the NLC in the THz range [96], respectively.

It is worth noting here that the assumption of uniaxial crystal for the NLC layer allows for easily describing its behavior with a relatively simple equivalent circuit model [182]. On the contrary, when the off-diagonal components are non-negligible, more complicated equivalent networks are needed [182]. However, the analysis of such cases go well beyond the scope of this PhD thesis.

To fully characterize the voltage dependence of the NLC, we have also evaluated the longitudinal  $z$  variation of the diagonal components of the



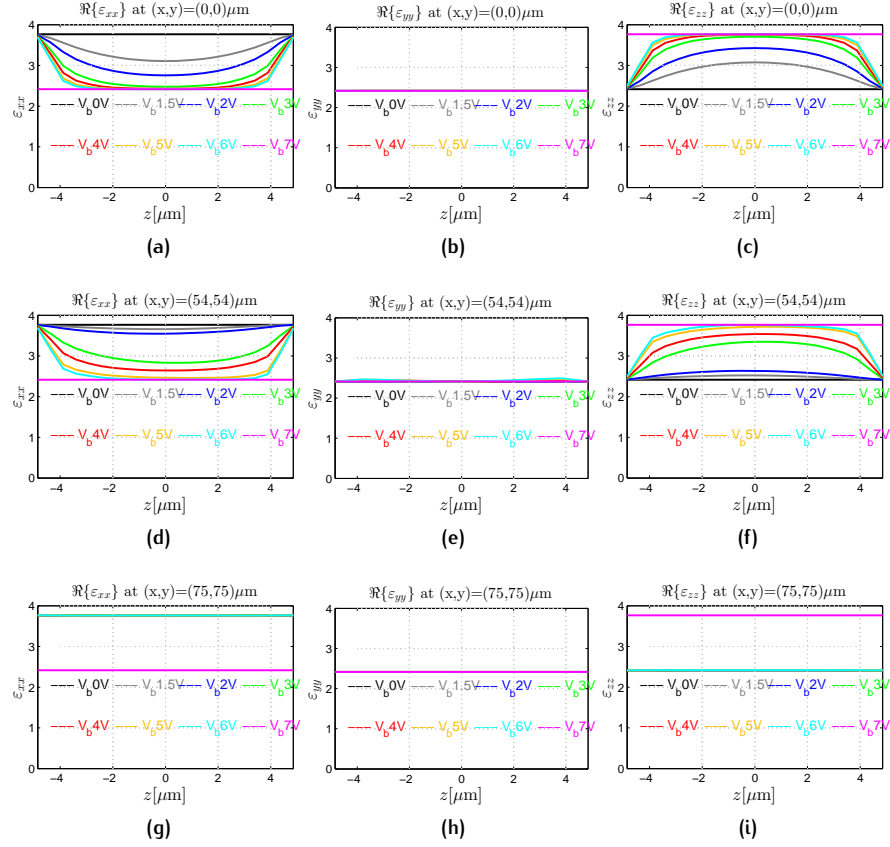


**Figure 3.34.:** Real part of the diagonal terms  $\varepsilon_{ii}(x = x_0, y = y_0, z)$  vs.  $z$  for  $V_{\text{bias}} = 0 - 7$  [V]. First column ( $i = x$ ), second column ( $i = y$ ), and third column ( $i = z$ ). Starting from the first row the  $(x_0, y_0)$  position takes the following values:  $(0, 0)$   $\mu\text{m}$ ,  $(54, 54)$   $\mu\text{m}$ , and  $(75, 75)$   $\mu\text{m}$ .

relative permittivity in three different locations over the  $xy$ -plane, for  $-4.85 \leq z \leq 4.85$   $\mu\text{m}$  (see Figs. 3.31(a)-(b)). Results are shown in Figs. 3.34 and 3.35 for the real and imaginary parts of  $\varepsilon_{ii}$ , respectively. As is seen, the variation is quite uniform even at the edge of the fishnet  $((x_0, y_0) = (54, 54)$   $\mu\text{m})$ , whereas no variation is seen outside the fishnet  $((x_0, y_0) = (75, 75)$   $\mu\text{m})$  where there is no applied electric field. However,  $\varepsilon_{xx}$   $\varepsilon_{zz}$  exhibit a specular nonlinear variation as the bias changes from 0 V to 7 V. Conversely,  $\varepsilon_{yy}$  does not depend on  $V_b$ . This would allow for further simplifying our NLC model in the following way:

$$\underline{\underline{\varepsilon}}(V_b) = \varepsilon_0 \begin{bmatrix} \varepsilon_{xx}(V_b) & 0 & 0 \\ 0 & \varepsilon_{yy} & 0 \\ 0 & 0 & \varepsilon_{zz}(V_b) \end{bmatrix}. \quad (3.46)$$

In the following Subsection, we will model the NLC layers with the complex permittivity tensor described in Eq. (3.46). Although the voltage dependence of the dielectric tensor distribution [181], [183] can routinely be computed, for sake of brevity, we study only averaged values along the normal to the layers and the two limiting cases (i.e., *unbiased* and *biased* states)

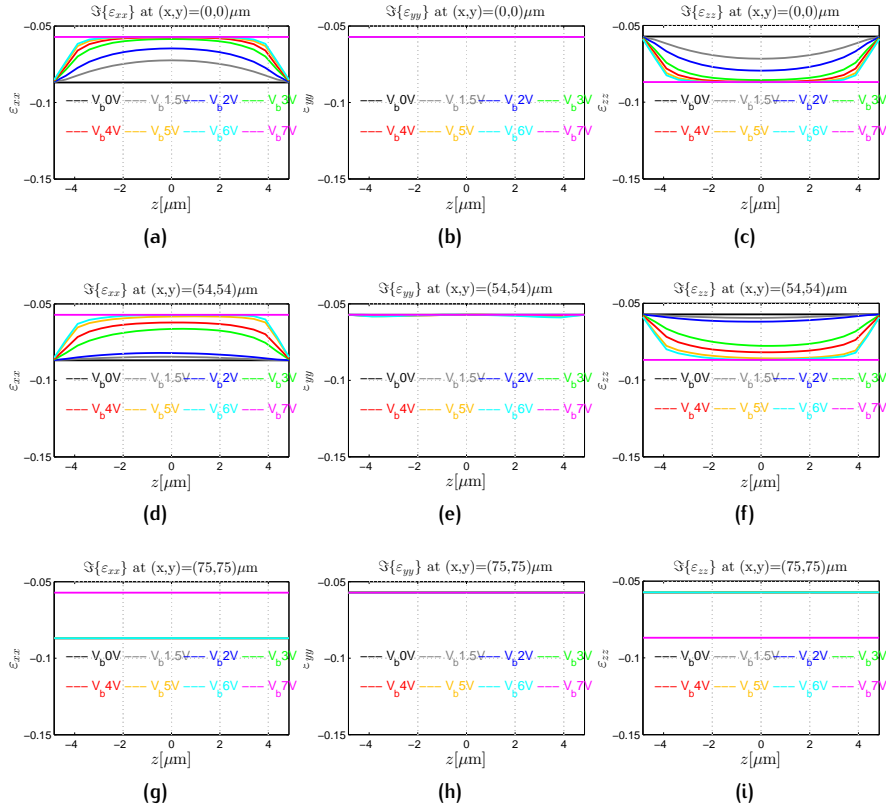


**Figure 3.35:** Imaginary part of the diagonal terms  $\varepsilon_{ii}(x = x_0, y = y_0, z)$  vs.  $z$  for  $V_{\text{bias}} = 0 - 7$  [V]. First column ( $i = x$ ), second column ( $i = y$ ), and third column ( $i = z$ ). Starting from the first row the  $(x_0, y_0)$  position takes the following values:  $(0, 0)$   $\mu\text{m}$ ,  $(54, 54)$   $\mu\text{m}$ , and  $(75, 75)$   $\mu\text{m}$ .

to clarify the concept and investigate the maximum tunability range of the proposed devices.

### 3.3.4 Tunable THz Fabry-Perot cavity leaky-wave antenna based on NLCs

In this Subsection we employ the complex permittivity model of Eq. (3.46) to evaluate the performance of different FPC-LWAs based on NLCs.

The proposed device (see Fig. 3.36) consists of a multistack of alternating layers of a high-permittivity dielectric (a thin layer of alumina  $\text{Al}_2\text{O}_3$ ) and of NLCs, placed above a GDS. The choice of Zeonor (a THz low-loss polymer which exhibits a moderate loss tangent  $\tan \delta_1 = 0.006$  [184]) for the substrate layer has been motivated by the index matching between its relative permittivity  $\varepsilon_{r1} = 2.3$  and the ordinary relative permittivity  $\varepsilon_o = 2.42$  of the NLC layer in the THz range [96], [185], as required to properly enhance the resonance condition in a FPC [61]. Note that the low absorption of the polymer introduces negligible losses overall.

As we have seen in 1.4.3, the alternation of high- and low-permittivity layers, with thicknesses fixed at odd multiples of a quarter wavelength in their respective media, allows for obtaining a narrow radiated beam at broadside

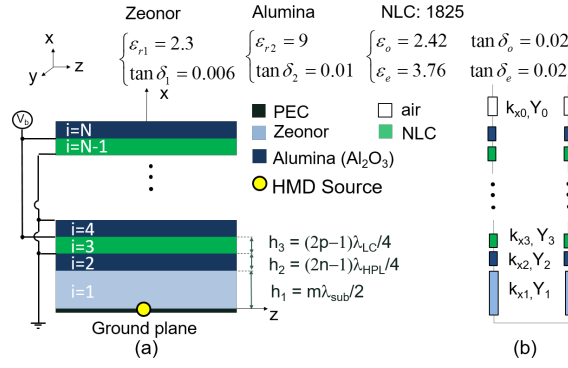


**Figure 3.36:** 2-D section view of the proposed device and its equivalent transmission-line representation. The NLC layers are biased through a pair of extremely-thin moderately-conductive polymer films (not reported in the picture), e.g., PEDOT:PSS [99], whose absorption is neglected here.

[61]. In the proposed device, the innovating feature is represented by the possibility of exploiting the tunable properties of the NLC [96], here representing the low-permittivity layer. In particular, the application of a common control signal to the NLC layers allows for changing their dielectric properties, thus achieving beam steering capability at a fixed frequency.

A customized circuit model (see Fig. 3.36(b)) has been developed for the dispersion analysis of such a structure, taking into account the anisotropy of the NLC layers through the simplified model describe in Eq. (3.46). Hence, when no bias is applied ( $V_b = 0$  V), the LC molecules are aligned along the horizontal  $z$ -axis (Fig. 3.36)<sup>10</sup>, i.e.,  $\epsilon_{zz}(0) = \epsilon_e$ , promoted by a few tens nm-thin alignment layer, which does not affect the electromagnetic properties of the device. When a sufficiently large driving voltage ( $V_\infty$ ) is applied across the LC layers, as shown in Fig. 3.36(a), the LC molecules reorient along the vertical  $x$ -axis, i.e.,  $\epsilon_{zz}(V_\infty) = \epsilon_e$ , thus providing the maximum reconfigurability [183].

As a consequence, with reference to the transverse transmission line of Fig. 3.36(b), the characteristic admittances and the normal wavenumbers of the NLC layers for both the TE and the TM polarizations (with respect to the  $xz$ -plane) are functions of  $V_b$ . Their expression are given by,

$$Y_0^{\text{TE}} = \frac{k_x}{\omega\mu_0}, \quad k_x^{\text{TE}} = \sqrt{(k_0 n_{yy})^2 - k_z^2}, \quad (3.47)$$

$$Y_0^{\text{TM}} = \frac{\omega\epsilon_0\epsilon_{zz}^2(V_b)}{k_x}, \quad k_x^{\text{TM}} = \sqrt{\frac{\epsilon_{zz}(V_b)}{\epsilon_{xx}(V_b)}k_0^2\epsilon_{xx}(V_b) - k_z^2}, \quad (3.48)$$

Since  $\epsilon_{yy}$  is the only component of the NLC which does not depend on  $V_b$ , only the TM leaky modes will be affected by the application of the bias, thus

<sup>10</sup> Note that, in the current coordinate reference frame, the  $x$ - and  $z$ -axis have been inverted with respect to the previous Subsection 3.3.3

**Table 3.5.:** Relevant parameters for the design of the proposed THz FPC-LWAs based on NLC.

Layout	$N$	$h_1[\mu\text{m}]$	$h_2[\mu\text{m}]$	$h_3[\mu\text{m}]$	$f_0[\text{THz}]$
1	4	167	127	82	0.59
2	8	167	127	82	0.56
3	6	100	75	145	1.00
4	4	188	127	82	0.56

the following discussion will be limited to the study of the fundamental TM leaky mode<sup>11</sup>.

As is customary for the analysis of LWAs, the dispersion equation relating the free-space wavenumber  $k_0$  and the complex longitudinal wavenumber  $k_z = \beta_z - j\alpha_z$  of the TM modes is readily obtained equating to 0 the input admittances looking upwards  $Y_{\text{up}}$  and downwards  $Y_{\text{dw}}$  at an arbitrary cross section (here we have chosen  $x = h_1$ ):

$$Y_{\text{up}} + Y_{\text{dw}} = 0, \quad (3.49)$$

where

$$Y_{\text{dw}} = -jY_0^{\text{TM}} \cot(k_{x,0}h_0), \quad (3.50)$$

$$Y_{\text{up}} = Y_{\text{in},i}, \quad (3.51)$$

with

$$Y_{\text{in},i} = Y_i^{\text{TM}} \frac{Y_{\text{in},i+1} \cos(k_{x,i}h_i) + Y_i^{\text{TM}} \sin(k_{x,i}h_i)}{Y_i^{\text{TM}} \cos(k_{x,i}h_i) + Y_{\text{in},i+1} \sin(k_{x,i}h_i)}, \quad \text{for } i = 1, 2, \dots, N, \quad (3.52)$$

where  $Y_i^{\text{TM}}$ ,  $k_{x,i}$ ,  $\varepsilon_{r,i}$ , and  $h_i$  are the characteristic admittances, transverse wavenumbers, relative permittivities, and thicknesses of the  $i$ -th layer ( $i = 0$  indicates the slab), respectively, and  $Y_{\text{in},i}$  are the input admittances looking upwards at the beginning of the  $i$ -th layer (note that  $Y_{\text{in},i}$  are calculated recursively from  $Y_{\text{in},N+1}$ , that is equal to the characteristic admittance of air).

To give a proof-of-concept, we have first obtained the dispersion curves for an *ideal* layout (Layout 1) described in the first row of Table 3.5, considering  $N = 4$  lossless dielectric layers (the impact of the dielectric losses in the performance of the antenna will be carefully analyzed further on). The thicknesses of the materials are given by the design rules in Fig. 3.36(a), where the wavelengths in the media are given by  $\lambda_{\text{LC}} = \lambda_0 / \sqrt{\varepsilon_o}$ ,  $\lambda_{\text{HPL}} = \lambda_0 / \sqrt{\varepsilon_{r2}}$  and  $\lambda_{\text{sub}} = \lambda_0 / \sqrt{\varepsilon_{r1}}$ , being  $\lambda_0 = c_0 / f_0$  the vacuum wavelength,  $c_0$  the velocity of light in vacuum, and  $f_0$  the design frequency. In this specific design, the choice of  $f_0 = 0.59$  THz is dictated by the thickness of commercially

<sup>11</sup> Note that the assumption of uniaxial crystal allows for decoupling the TM fields from the TE fields. This is not generally true when an anisotropic layer is at the interface with another medium, since in the most general case, more complicated networks are needed to describe its behavior [182].

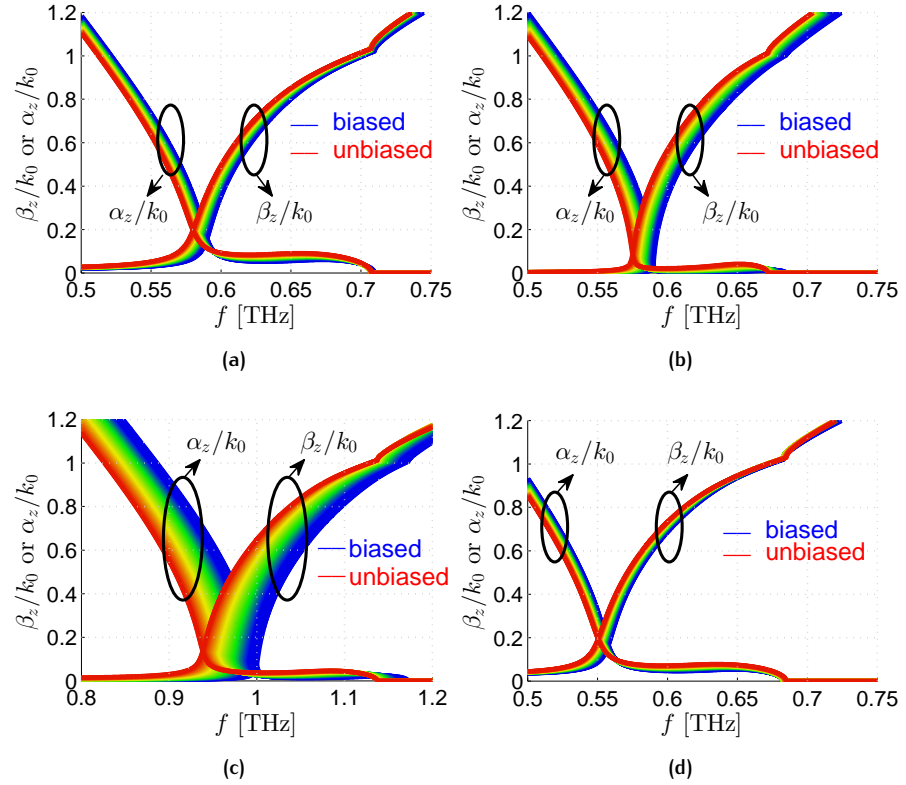


**Figure 3.37.:** Dispersion curves ( $\hat{\beta}_z$  and  $\hat{\alpha}_z$  vs.  $f$ ) of the fundamental TM leaky mode for (a) Layouts 1, (b) 2, (c) 3, and (d) 4 (see Table 3.5) when the NLC layer is biased at  $V_\infty$  (blue lines) and when is unbiased 0 V (red lines). Colors gradually shades from blue to red as  $V_b$  decreases from  $V_\infty$  to 0 V.

available alumina thin layers ( $127 \mu\text{m}$ ) which exhibits a relative permittivity  $\varepsilon_{r2} = 9$  and a loss tangent of about  $\tan \delta_2 \simeq 0.01$  (not considered in this preliminary analysis) at 0.59 THz [186]. The choice  $m = 1$ ,  $n = 2$ , and  $p = 1$  corresponds to the design of Layout 1 (see Table 3.5). We note that for higher values of  $m$ ,  $n$ , and  $p$  higher-order modes appear with a consequential degradation of the antenna performance.

In Fig. 3.37(a) the dispersion curves of the fundamental TM leaky mode have been calculated in the range 0.50 – 0.75 THz. The color of the curves gradually shades from red to blue when the bias  $V_b$  is changed from 0 (*unbiased* state) to a threshold voltage  $V_\infty$  (*biased* state), which can be accurately calculated through the method described in [181], [183]. For the proposed LC cell, values below 20 V are sufficient to practically cover almost the whole switching range. In this simplified analysis, the relative permittivities are assumed to linearly vary with  $V_b$ . Thus, while the *unbiased* and *biased* states are always correctly predicted, the dynamic variation of  $\hat{\beta}_z$  and  $\hat{\alpha}_z$  for intermediate values of  $V_b$  could significantly change once the voltage-dependence of  $\underline{\underline{\varepsilon}}$  is computed.

As expected, when  $V_b = V_\infty$  (blue curve) the splitting condition  $\hat{\beta}_z \simeq \hat{\alpha}_z$  is achieved for  $f_{\text{op}} = 0.59$  THz, i.e., when the operating frequency  $f_{\text{op}}$  is equal

**Table 3.6.:** Radiating performance in terms of beam reconfigurability ( $\theta_p^M$ ), directivity ( $D_0$ ) and beamwidth ( $\Delta\theta$ ), for all layouts.

Layout	$f_{\text{op}}$ [THz]	$\hat{\beta}_z^M$	$\theta_p^M$ [°]	$\hat{\alpha}_z^{(c)}$	$D_0$ [dB]	$\Delta\theta$ [°]
1	0.59	0.37	22	0.16	17.87	26
2	0.59	0.44	26	0.05	27.98	8
3	1.00	0.65	40	0.08	23.90	13
4	0.56	0.34	20	0.17	17.35	34

to the design frequency  $f_0$ . Even more interestingly, once the frequency is fixed, e.g., at  $f_{\text{op}}$ , it is possible to change the value of the normalized phase constant  $\hat{\beta}_z$ , such that  $\hat{\beta}_z > \hat{\alpha}_z$  by simply lowering the bias voltage, whereas the value of the normalized attenuation constant  $\hat{\alpha}_z$  remains almost the same. As a consequence, the dispersion diagram of Fig. 3.37(a) reveals the possibility to steer the beam with a quasi-constant beamwidth at a fixed frequency through bias voltage. The relevant radiating features have been reported in the first row of Table 3.6. The maximum pointing angle  $\theta_p^M$ , and the HPBW at broadside  $\Delta\theta$  have been evaluated through Eqs. (1.28) and (1.32)-(1.33), respectively, whereas the directivity at broadside is approximated by the formula  $D_0 = 4\pi/\Delta\theta^2$ .

As is shown in Table 3.6, we expect that Layout 1 would allow for dynamically scanning the beam from broadside to  $22^\circ$  as the voltage is decreased from its limit value  $V_\infty$ . However, the HPBW remains relatively high ( $\Delta\theta \simeq 26^\circ$ ) during the scanning of the beam, due to the relatively high leakage rates ( $\hat{\alpha}_z^{(c)} \simeq 0.16$ ). It is worth noting that the HPBW at broadside is greater than the maximum pointing angle. This means that during the steering of the beam the radiated power density never decreases below  $-3\text{dB}$  within the scanned angular range.

Possible workarounds for improving either the scanning range or the beamwidth are the use of an increasing number of layers or of a thicker NLC layer as proposed in Layouts 2 and 3, respectively (see Table 3.5). As expected, in Layout 2 (see Fig. 3.37(b)), the attenuation constant is considerably reduced whereas the range of tunability is almost the same. Conversely, in Layout 3 (see Fig. 3.37(c)), the attenuation constant is just slightly reduced, but a wider range of tunability is achieved with respect to Layout 1. Note that, in Layout 3, the operating frequency has been raised to  $f_0 = 1$  THz and the thickness of alumina thin layer has been reduced to  $75 \mu\text{m}$ [187]. This has been made possible by designing the FPC-LWA with a higher-order LW mode ( $m = 1$ ,  $n = 2$ , and  $p = 2$ ). Unfortunately, the assembly of Layout 2 and Layout 3 is not practical for the technological implementation of such devices. Therefore, in Layout 4, we have considered the same configuration of Layout 1 and further modified the thickness of the Zeonor substrate according to the closest available commercial value, i.e.,  $h_{\text{sub}} = 188 \mu\text{m}$ , thus simplifying the fabrication of the device. As it can be expected, the only

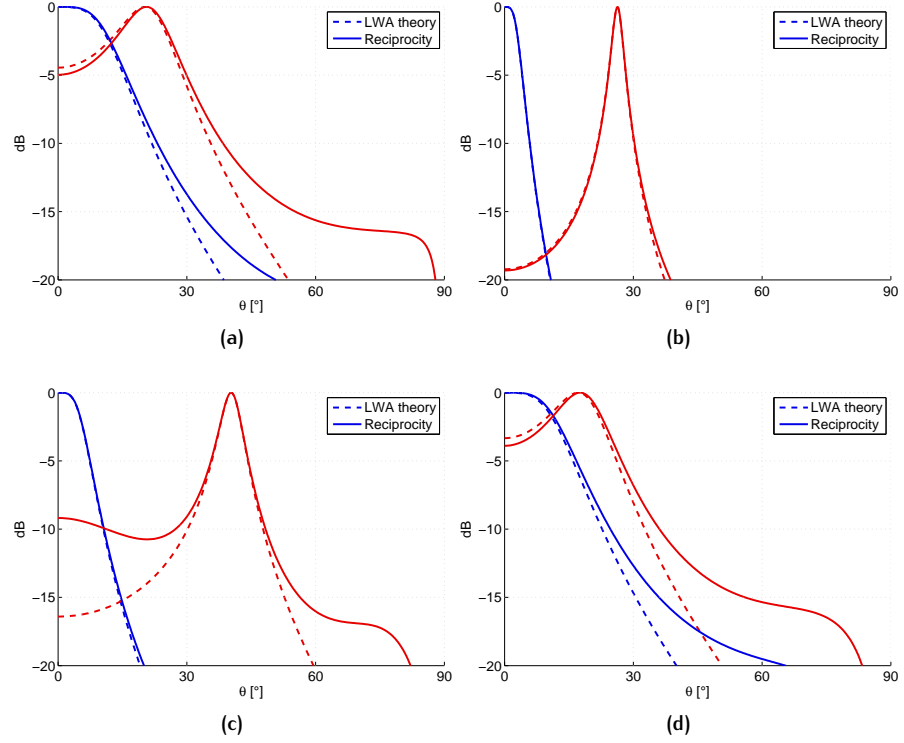


**Figure 3.38:** Radiation patterns predicted considering only the LW pole contribution (dashed lines) and by means of reciprocity theorem (solid lines) for (a) Layouts 1, (b) 2, (c) 3, and (d) 4 (see Table 3.5) when the beam points at broadside (blue lines) and when is steered at the maximum pointing angle (red lines).

noticeable differences between Layout 1 and 4 are the frequency shift of  $f_0$  from 0.59 to 0.56 THz, and a reduced range of tunability.

On the basis of the previous dispersion analysis, the radiating patterns on the E-plane of all the proposed Layouts (see Table 3.5) have been evaluated considering a HMD excitation placed on the ground plane. Two methods have been used: *i) LWA theory*, i.e., taking into account only the contribution of the relevant leaky mode and using Eq. (1.27)<sup>12</sup>; *ii) Reciprocity*, i.e., by means of a rigorous application of the reciprocity theorem. Specifically, an in-house MATLAB code has been developed to derive the relevant 1-D Green's functions of the TEN model shown in Fig. 3.36(b), using the ABCD-matrix formalism [157]. Then the reciprocity theorem is invoked to calculate the E-plane far-field radiation patterns excited by a HMD source.

Results have been reported in Figs. 3.38(a)-(d) for all the layouts, considering radiation at broadside (*biased* status) and at the maximum pointing angle (*unbiased* status). In Figs. 3.38(a), (b), and (d) a very good agreement is seen between *LWA theory* and *Reciprocity*. However, in Fig. 3.38(c) it is noted that the LWA theory does not allow for an accurate evaluation. This is probably due to the presence of a higher-order LW mode (we recall here

<sup>12</sup> For E-plane patterns excited by a HMD source Eq. (1.27) should be multiplied by a factor  $\cos \theta$ .

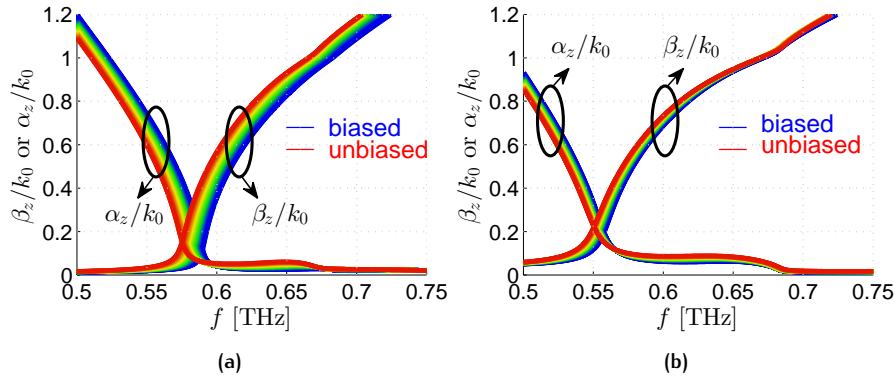


Figure 3.39.: Dispersion curves ( $\hat{\beta}_z$  and  $\hat{\alpha}_z$  vs.  $f$ ) of the fundamental TM leaky mode for (a) Layout 2 and (b) Layout 4 (see Table 3.5) in the lossy case, when the NLC layer is biased at  $V_\infty$  (blue lines) and when is unbiased 0 V (red lines). Colors gradually shades from blue to red as  $V_b$  decreases from  $V_\infty$  to 0 V.

that Layout 3 is a higher-order design) which increases the sidelobe level, as correctly predicted using reciprocity.

The relevant radiating features are listed in Table 3.6 to give the reader a concise description of the radiating performance of any Layout. As is seen from both Fig. 3.38 and Table 3.6, Layouts 2 and 3 allow for considerably improving the performance in terms of directivity (and consequently the beamwidth) and reconfigurability, respectively. On one hand, the increased size of the LC layers in Layout 3 determines an increased range of tunability, which is paid at the expense of a pattern *degradation*. On the other hand, the higher number of additional cover layers in Layout 2, determines an increased directivity, which is paid at the expense of a higher complexity of the structure.

As a matter of fact, any realistic implementation of a FPC-LWA based on NLC should take into account several aspects: *i*) the non-negligible dielectric losses which affect the dielectric layers in the THz regime, *ii*) the assembly of any additional NLC layer which entails the introduction of a couple of electrodes with a consequent increase of the ohmic losses, *iii*) the available commercial thickness of the substrate (Zeonor layer).

Consequently, we have selected Layout 2 (the best performance in terms of directivity) and Layout 4 (the easiest to fabricate) to investigate the dispersion properties of the fundamental TM LW modes in the lossy case. We have then evaluated the dispersion curves of the relevant TM leaky mode in the same range of frequencies taking into account all the dielectric losses of the layers (see Table 3.7). Note that the PEDOT:PSS electrodes can safely be neglected due to the moderate values of the conductance required to apply a few KHz control voltage, and consequent moderate conductivity and extremely thin profile [99]. Consequently, the values of the efficiencies  $\eta$  reported in Table 3.6 take into account only the dielectric losses of the layers.



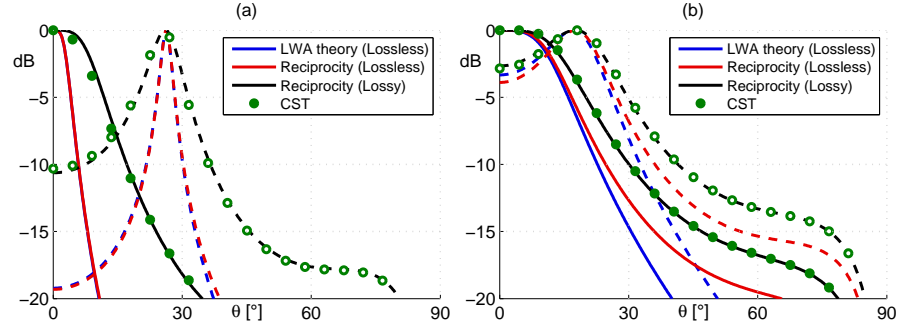


**Figure 3.40:** Radiation patterns for (a) Layout 2 and (b) Layout 4 for radiation at broadside (solid) and at the maximum pointing angle (dashed). The radiation patterns have been calculated by means of reciprocity theorem in both the lossless (in red) and the lossy (in black) case, and then compared with those given by means of LWA theory (blue). Full-wave simulations with CST are also reported for the lossy case for radiation at broadside (filled green circles) and at the maximum pointing angle (empty green circles).

As is shown in Fig. 3.39, the introduction of dielectric losses are responsible for increasing the value of  $\hat{\alpha}_z$ , causing a deterioration of the performance in terms of both the HPBW and the directivity (compare the performance of lossless and lossy cases of both Layout 2 and Layout 4 in Table 3.7). Finally, full-wave simulations performed by using CST Microwave Studio together with reciprocity [148] have been reported only for Layouts 2 and 4 in this lossy case. We recall here that the simulation setup is the same as the one used for evaluating the performance of the GPW and the GSS in 3.2 (details are given in Appendix B). For both layouts, it is manifest that a rigorous application of the reciprocity theorem helps to easily get an accurate evaluation of the radiating performance of the proposed antennas, as corroborated by the remarkable agreement between our MATLAB in-house code and full-wave simulations (see Figs. 3.40(a) and (b)). Furthermore, the introduction of dielectric losses in the models has a detrimental effect in terms of the directive features of the pattern, considerably widening the beamwidth. This is especially true for Layout 2, as clearly shown in Table 3.7. Indeed, the attenuation constants  $\alpha_z$ , which mainly governs the directivity and is proportional to  $\Delta\theta$ , indiscriminately accounts for both radiation and dielectric losses. Consequently, as dielectric losses increase, the beamwidth increases as well.

**Table 3.7.:** Performance of Layout 2 and 4 in lossless and lossy case.

Layout	$f_{\text{op}}[\text{THz}]$	$\hat{\beta}_z^{\text{M}}$	$\theta_p^{\text{M}}[^\circ]$	$\hat{\alpha}_z^{(c)}$	$D_0$ [dB]	$\Delta\theta$ [°]	$\eta$ [%]
2 Lossless	0.59	0.44	26	0.05	27.98	8	100
2 Lossy	0.59	0.44	26	0.13	19.26	21	40
4 Lossless	0.56	0.34	20	0.17	17.35	34	100
4 Lossy	0.56	0.34	20	0.21	15.52	27	80

On the other hand, the overall dielectric losses in Layout 4 play only a minor effect in the deterioration of the pattern when compared to Layout 2 (due to the increased overall thickness of lossy layers, and the negligible losses of the dielectric polymer). As a matter of fact, the introduction of losses considerably affects the performance in Layout 2, causing a 60% loss of efficiency  $\eta$  (see Table 3.7), whereas it has only a moderate impact (20% loss of  $\eta$ ) in the performance of Layout 4 (see Table 3.7).

### 3.4 CONCLUSION

In this Chapter we have discussed the radiating performance of two class of reconfigurable THz antennas based on leaky waves. Graphene and liquid crystals have been considered as tunable materials, to be included in a leaky-wave antenna design for achieving pattern reconfiguration at a fixed frequency in the THz range. In both cases the application of a driving voltage allows for varying the electronic properties of the material, thus allowing the dynamic control of certain radiating properties.

To this purpose, we first discussed graphene surface conductivity as a function of several relevant parameters comparing different theoretical models. The intraband contributions of Kubo formula are shown to adequately describe graphene in the proposed analysis. Using this model, plasmonic losses in graphene have been discussed to motivate the study of graphene radiators whose mechanism of radiation is based on the propagation of non-plasmonic leaky modes. Two class of graphene antennas have been considered in detail taking into account the impact of graphene quality on the overall performance. As a result of this investigation, a trade-off is shown to exist between the maximum efficiency, the maximum directivity, and the maximum reconfigurability. However, both designs have shown superior performance with respect to their plasmonic counterparts. In particular, one of the proposed devices has shown attractive design flexibility considering the typical antenna constraints.

Finally, the electromagnetic properties of liquid crystals have been briefly discussed to justify the adoption of a simplified model for the description of its permittivity tensor. The liquid crystal material is then treated as a uniaxial crystal, whose optical axis can be switched from the horizontal to the vertical axis by the simple application of a low-driving voltage. Specifically, different multi-stacked Fabry-Perot cavity-like configurations have been considered for the design of a reconfigurable THz radiator. The benefits and drawbacks of ideal designs against those of more practical configurations have been carefully addressed. It is seen that ideal designs show excellent radiating features, but are not easy to fabricate, whereas practical designs show a considerably reduced performance, but are very straightforward to fabricate. The results of the investigations proposed in this Chapter may be pivotal for the future designs of reconfigurable and efficient THz leaky-wave antennas.



Part II

GENERATION OF NONDIFFRACTING BEAMS  
AND PULSES FOR NEAR-FIELD APPLICATIONS  
AT MILLIMETER WAVES



# 4

## NONDIFFRACTING WAVES

### 4.1 INTRODUCTION

Since remote times, humankind observed that the propagation of any wave (light, sound, etc.) is commonly adversely affected by diffraction and dispersion phenomena, that is by spatial and temporal broadening of the beams as they propagate. According to Huygens' wave theory (XVII century), such effects generally occur in any kind of wave propagation (electromagnetics, acoustics, etc.). As a consequence, diffraction limits all the applications in which is required to maintain a spatial transverse confinement of a beam over a considerable distance, such as free-space communications, medical imaging, radiometry, and so on.

With the multiplication of modern applications of the electromagnetic fields, the generation of limited-diffraction and limited-dispersion electromagnetic waves has increasingly attracted physics and engineering communities. Over the years and over the world, many groups of researchers employed their efforts to develop more and more advanced techniques able to reduce the undesired effects of diffraction, or even better to find diffraction-free solutions of the wave-equation. Nowadays, we know that such solutions, the so-called *nondiffracting waves* (or *localized waves* as well), theoretically exist but are not physically realizable since they possess infinite energy. However, it has been shown that it is possible to theoretically construct and experimentally reproduce a finite version of these solutions by accepting a limitation on the maximum achievable distance in which the resulting fields do not undergo diffraction [188], [189].

Since localized waves comprise a large family of diffraction-limited solutions to the wave equation, in Section 4.2 we intend to study such solutions within a unified mathematical framework. Afterwards, we will separately investigate monochromatic (i.e., nondiffracting beams) and polychromatic (i.e., nondiffracting pulses) solutions. In fact, even if both phenomena (viz., nondiffracting beams and pulses) belong to the same sector of physics, their physical properties are quite different one another. The sense of this distinction will become clearer in Section 4.3 and Section 4.4, where we comprehensively review the different features of two specific monochromatic and polychromatic solutions, namely *Bessel beams* and *X-waves*, respectively. Finally, the most relevant technologies and systems for the generation of Bessel beams and X-waves are briefly presented in the context of near-field focusing applications spanning from the microwave to the optical regime. Specifically, our analysis will be devoted to the millimeter-wave range where

the simultaneous high demand for near-field focusing systems and the current lack of compact-size, low-cost, low-profile devices motivate the increasing interest in this research area. This last part would be the object of Chapters 5 and 6.



## 4.2 MATHEMATICAL FRAMEWORK

Our analysis starts from considering the expression of the homogeneous wave equation in a cylindrical reference frame  $(\rho, \phi, z)$ :

$$\left( \frac{\partial^2}{\partial \rho^2} + \frac{1}{\rho} \frac{\partial}{\partial \rho} + \frac{1}{\rho^2} \frac{\partial^2}{\partial \phi^2} + \frac{\partial^2}{\partial z^2} - \frac{1}{c_0^2} \frac{\partial^2}{\partial t^2} \right) \psi(\rho, \phi, z, t) = 0, \quad (4.1)$$

where  $c_0$  is the light velocity in vacuum. For the sake of simplicity, let us consider axially-symmetric solutions ( $\partial/\partial\phi = 0$ )<sup>1</sup>:

$$\left( \frac{\partial^2}{\partial \rho^2} + \frac{1}{\rho} \frac{\partial}{\partial \rho} + \frac{\partial^2}{\partial z^2} - \frac{1}{c_0^2} \frac{\partial^2}{\partial t^2} \right) \psi(\rho, z, t) = 0. \quad (4.2)$$

A general solution  $\psi(\rho, z, t)$  to the wave equation can be expressed by means of the spectral representation [20] (also known as *Fourier method*), i.e., in terms of a Hankel transform with respect to the variable  $\rho$ , and two Fourier transforms with respect to the variables  $z$  and  $t$ :

$$\psi(\rho, z, t) = \int_0^{+\infty} \int_{-\infty}^{+\infty} \int_{-\infty}^{+\infty} k_\rho J_0(k_\rho \rho) e^{-jk_z z} e^{j\omega t} \tilde{\psi}(k_\rho, k_z, \omega) dk_\rho dk_z d\omega, \quad (4.3)$$

where  $k_\rho$  and  $k_z$  are the radial and longitudinal wavenumbers,  $\omega$  is the angular frequency, and  $\tilde{\psi}(k_\rho, k_z, \omega)$  is the generalized transform of  $\psi(\rho, z, t)$ <sup>2</sup>. This general expression implies the fulfillment of the dispersion relation  $k_0^2 = k_z^2 + k_\rho^2$ , where  $k_0 = \omega/c_0$  is the vacuum wavenumber. By using this relation, we can elide the dependence on  $k_z$  from the previous integral. In this way, any solutions to the wave equation can be recast as follows:

$$\psi(\rho, z, t) = \int_0^{+\infty} \int_{-k_0}^{+k_0} k_\rho J_0(k_\rho \rho) e^{-jk_z z} e^{j\omega t} S(k_\rho, \omega) dk_\rho d\omega, \quad (4.4)$$

where  $S(k_\rho, \omega)$  is an arbitrary spectral function. With this expression at hand, we investigate how the choice of the spectral function affects the type of solutions. A specific attention will be devoted to those spectra that give rise to *localized, nondiffracting* solutions.

### Gaussian beam

Gaussian beams are well-known solutions of the paraxial Helmholtz equation, whose popularity is due to their application in laser technology [190]. Here, we want to show how such a beam can also be expressed with the

<sup>1</sup> The most general case for which  $\partial/\partial\phi \neq 0$  will be envisaged in Section 6.3.

<sup>2</sup> Note that the end-points of the  $\omega$ -integral in Eq. (4.3) are limited to the real positive spectral content since  $\psi(\rho, z, t)$  is defined as the analytic signal of  $\tilde{\psi}(\rho, z, \omega)$ , viz.  $\psi(\rho, z, t) \triangleq \mathfrak{F}^{-1}\{\psi(\rho, z, \omega) \cdot H(\omega)\}$ , where  $\mathfrak{F}^{-1}(\cdot)$  represents the inverse Fourier transform and  $H(\cdot)$  is the Heaviside step function defined as  $H(\omega) = 1$  for  $\omega \geq 0$  and 0 elsewhere.

general formulation expressed by Eq. (4.3). It is worth here to recall that the word *beam* refers to a monochromatic solution of the wave equation, and thus its frequency spectrum is represented by a Dirac function of the frequency variable  $\omega$  centered around a single frequency  $\omega_0$  (i.e.,  $\delta(\omega - \omega_0)$ ). In particular, for a Gaussian beam the frequency spectrum is decoupled from the spectral function of the angular variable  $k_\rho$  which is represented by a Gaussian function. Thus the overall spectral function is given by:

$$S(k_\rho, \omega) = 2a^2 e^{-a^2 k_\rho^2} \delta(\omega - \omega_0), \quad (4.5)$$

where  $a > 0$  is a constant which is inversely related to the variance of a Gaussian distribution. As is known, this beam suffers diffraction spreading doubling its beamwidth after having traveled a distance commonly referred as the diffraction length and calculated as  $z_{\text{dif}} = \pi \sqrt{3} w_0^2 / \lambda_0$  where  $w_0 = 2a$  is the initial waist of the beam [191]. A quick glance to this formula reveals the diffractive character of Gaussian beams. Indeed, it is easy to check that a Gaussian beam with an initial waist comparable with its wavelength will double its transverse spot size after having traveled just few wavelengths. For this reason we are not interested in such kind of solutions.

### Gaussian pulse

The Gaussian pulse is obtained from the Gaussian beam, simply by superposing them at different frequencies. As a result, the spectral function is the same of a Gaussian beam except for having replaced the Dirac function with a normalized Gaussian function:

$$S(k_\rho, \omega) = 2\pi^{-1/2} \left( a^2 e^{-a^2 k_\rho^2} \right) \left( b e^{-b^2 (\omega - \omega_0)^2} \right), \quad (4.6)$$

where  $a, b > 0$ . This solution also suffers diffraction spreading (the diffractive distance is the same as for a Gaussian beam) and hence it is of no interest for our purposes. It should be noted that for Gaussian beams and pulses (that are both *diffracting* solutions), the spectral function  $S(k_\rho, \omega)$  has been decoupled as the product of two terms  $S(k_\rho, \omega) = R(k_\rho)F(\omega)$  which separately depends on  $\omega$  and  $k_\rho$ . It will readily be shown that the coupling of  $\omega$  and  $k_\rho$  [192] plays a key-role in the determination of the nondiffractive properties of localized solutions.

### Bessel beam

In the previous examples, we have presented spectral functions in which we can always split the two-variable spectral function  $S(k_\rho, \omega)$  into two independent functions of  $\omega$  and  $k_\rho$ . However, only by imposing a linear coupling between  $\omega$  and  $k_\rho$  it is possible to obtain a localized solution [192]. This is

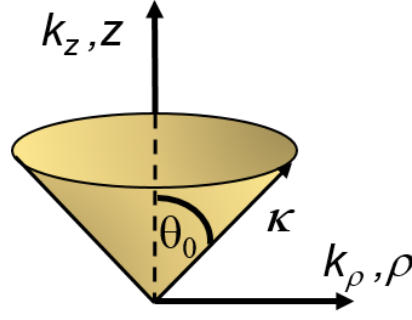


Figure 4.1.: Wavevectors  $\kappa = k_\rho \hat{\rho}_0 + k_z \hat{z}_0$  lying on the surface of a cone with axicon angle  $\theta_0$ .

the reason why the previous examples are not diffraction-free beams. With this in mind, let us consider the following spectral function

$$S(k_\rho, \omega) = \frac{\delta(k_\rho - k_0 \sin \theta_0)}{k_\rho} \delta(\omega - \omega_0), \quad (4.7)$$

which implies that  $k_\rho = k_0 \sin \theta_0 = (\omega/c_0) \sin \theta_0$  with  $0 \leq \theta_0 \leq \pi/2$  where  $\theta_0$  is the *axicon angle*. Such a description reveals us that a Bessel beam can be thought as a superposition of plane waves with wavenumbers lying on the surface of a cone of angle  $2\theta_0$  (see Fig. 4.1). Even more interestingly, the linear coupling between  $\omega$  and  $k_\rho$  together with the dispersion relation also implies that  $k_z = (\omega/c_0) \cos \theta_0$ . This is also a linear coupling of the type  $\omega = V k_z + b$  where  $b$  and  $V$  are arbitrary constants, as needed for obtaining an ideal localized wave [192]. Another way to get the same result has been suggested in [193] where it has been shown that a nondiffracting field must have a spatial-frequency spectrum located on an annulus of the spatial frequency  $k_\rho$ .

Using Eq. (4.7) in Eq.(4.4) we get the Bessel beam solution:

$$\psi(\rho, z, t) = J_0(k_0 \sin \theta_0 \rho) e^{-jk_0 \cos \theta_0 z} e^{j\omega_0 t}. \quad (4.8)$$

This ideal solution is a diffraction-free beam according to Durnin's definition [188], i.e., in the sense that the transverse intensity distribution is independent of the propagating distance  $z$ , or, mathematically speaking,  $\psi(\rho, \phi, z \geq 0, t) = \psi(\rho, \phi, z = 0, t)$  [188], [194]. Unfortunately, such an ideal solution is not physically realizable since it carries infinite energy. However, it is always possible to generate truncated Bessel beams which possess finite energy at the expense of a limitation in the maximum achievable nondiffractive distance. The *nondiffractive range* (also referred as *depth of focus*) of a truncated Bessel beam is given by the following simple equation [188], [189]:

$$z_{\text{ndr}} = \rho_{\text{ap}} \cot(\theta_0), \quad (4.9)$$

where  $\rho_{\text{ap}}$  is the aperture radius. Differently from the diffraction length  $z_{\text{dif}}$  of Gaussian beams, the nondiffractive range  $z_{\text{ndr}}$  does not represent

the distance at which the Bessel beam doubles its beamwidth, but rather the distance within which the field can accurately be described by an ideal Bessel function (i.e.,  $J_0(k_\rho \rho) e^{-jk_z z}$ ). Afterwards, the Bessel beam intensity abruptly decreases as a consequence of the aperture truncation. It is worth to stress the fact truncated Bessel beams, even if they cannot rigorously be considered free diffraction beams, they resist diffraction for a distance much larger than a Gaussian beam as has been shown in [188], [191]. The interested reader can find a rigorous comparison of the advantages and disadvantages provided by Bessel beams and Gaussian beams in [194], [195].

### X-shaped pulses

Let us consider the previous spectral function and replace the Dirac function  $\delta(\omega - \omega_0)$  with a more general frequency spectrum  $F(\omega)$ :

$$S(k_\rho, \omega) = \frac{\delta(k_\rho - k_0 \sin \theta_0)}{k_\rho} F(\omega). \quad (4.10)$$

Again, using Eq. (4.10) in Eq.(4.4) we get a family of nondiffracting solutions called *X-shaped pulses*

$$\psi(\rho, z, t) = \int_0^\infty F(\omega) J_0(k_0 \sin \theta_0 \rho) e^{-jk_0 \cos \theta_0 z} e^{j\omega t} d\omega. \quad (4.11)$$

In principle, any choice of a well-behaved function for  $F(\omega)$  would lead to a nondiffracting pulse. The *ordinary X-wave* is one of the simplest X-shaped pulse<sup>3</sup> and is obtained by choosing:

$$F(\omega) = \frac{a}{V} e^{-\frac{a}{V}\omega}, \quad (4.12)$$

where  $a > 0$  is an arbitrary positive constant, and  $V = c_0 / \cos \theta_0$  is the phase velocity. It should be stressed that for an ideal X-wave, there is no cone dispersion with frequency (i.e.,  $\theta(\omega) = \theta_0$ ), thus the group velocity  $v_g$  coincides with the phase velocity. Note that the spectrum in Eq. (4.12) is suitable only for low frequencies (the frequency spectrum actually behaves as a low-pass filter). However, by means of the generalized bidirectional decomposition [196], it has been shown [192] that a suitable choice of the spectral function allows for getting solutions shifted to higher frequencies. In particular, by multiplying  $F(\omega)$  for a factor  $(0.5\omega/V + 0.5k_z)^m$  it is possible to *bump* the solutions in correspondence of the frequency  $\omega = mV/a$  [192].

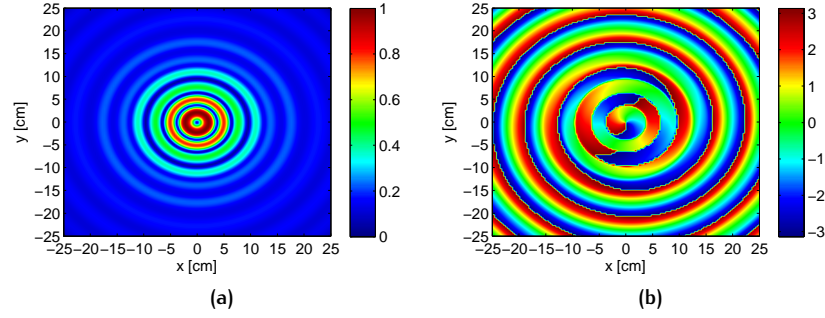


**Figure 4.2.:** (a) Modulus and (b) phase of a higher-order Bessel beam of order  $n = 1$  generated by an aperture of 25 cm at 12.5 GHz. The phase follows the typical spiral path, whereas the modulus exhibits a central dark spot.

### Higher-order localized waves

In Eq. (4.4) we have assumed to deal with axially-symmetric solutions, i.e., with  $\partial/\partial\phi = 0$ , and thus the azimuthal order is  $n = 0$ . However, in the most general case,  $n \neq 0$  and the general solution of the wave equation takes the following form:

$$\psi(\rho, \phi, z, t) = \int_0^{+\infty} \int_{-k_0}^{+k_0} k_\rho J_n(k_\rho \rho) e^{jn\phi} e^{-jk_z z} e^{j\omega t} S(k_\rho, \omega) dk_\rho d\omega. \quad (4.13)$$

Once the  $k_\rho$ - $\omega$  coupling is enforced as in Eqs. (4.7) or (4.10) a *higher-order Bessel beam* or a *higher-order X-wave* solution is readily obtained. Such solutions have arisen a great interest in several branches of physics (see [191], [197] and references therein). In particular, the first-order Bessel beam is of main interest because the intensity vanishes at the center of the beam. This so-called *dark-beam* with a small and well-defined dark central spot has applications, for example, in precision alignment [198]. Note that Bessel beams of any non-null order exhibit a nearly dark central spot whose intensity fades gradually away from the  $z$ -axis as the order  $n$  of the beam increases.

Another intriguing property of higher-order Bessel beam is inherent to the azimuthal phase variation. Indeed, for  $n \neq 0$  the phase of a Bessel beam exhibits a peculiar spiral path that creates a *twisted* wavefront (see Fig. 4.2(a) and (b)). Such a particular feature gave them the name of *vortex beams* [199]. This has important physical implications, because the eigenvalue of the  $z$ -component of the orbital angular momentum OAM operator  $L_z = j\partial/\partial\phi$  is exactly  $n$  [200]. This means that a higher-order nondiffracting wave (either a Bessel beam or an X-wave) carries OAM; a feature that is of interest in different areas of applied physics [201], especially in the context of optical trapping and micro-manipulation of multiple particles [202]–[205].

<sup>3</sup> Note that throughout the following Chapters we always refer with the term *X-wave* to any *X-shaped pulse*, regardless of the frequency spectrum that has been used. This kind of *synecdoche* is also widely used in the current literature.

Obviously, it is possible to generate polychromatic higher-order nondiffracting solutions, the so-called *higher-order X-waves* [191] or *twisted pulses* [206]. Such solutions have recently been proposed in optics for applications in ultrafast photonics and OAM-based free-space quantum communications, to name but a few [207]. However, in the microwave range, such twisted pulses have never been proposed. This would be the object of the last part of Chapter 6.

### Superluminal localized waves

One of the most discussed features possessed by nondiffracting waves is *superluminality*, i.e., the property for which an electromagnetic wave seemingly travels faster than light. This property, has initially arisen a lot of confusion and debates [208]–[211] among physicists because the existence of a superluminal wave violates the principle of causality and thus it is not consistent with the frame of the *Special Relativity* [212], [213].

This problem was first noted in 1914 by A. Sommerfeld and L. Brillouin when, by examining the transmission of a truncated sinusoid through an absorbing and dispersive media, they found the *precursors*: pulses whose leading edge travels exactly at  $c$  (where  $c$  is the light velocity in the medium) but not exceed it. However the precursors were troubling because their group velocity exceeds the speed of light [214]. As a matter of fact, in 1970 C. G. B. Garrett and D. E. McCumber [215] analytically estimate that a Gaussian pulse can travel in a linear anomalous dispersive medium with a group velocity  $v_g > c$ .

According to Sommerfeld [216] this would not create any *causality dilemma* for the following three reasons:

- a) The information is from the leading edge and  $v_g$  does not measure its velocity.
- b) In case of passive media the energy of the emerging pulse never exceeds the one of the pulse traveling in vacuum.
- c) The front's velocity is always limited to the precursor's velocity that never exceeds  $c$ .

On one hand, group velocity  $v_g = \partial\omega/\partial k$ , and energy velocity  $v_e = \Pi/(w_e + w_m)$  where  $\Pi$  is the Poynting vector and  $w_e$  and  $w_m$  are the electric and magnetic energy density, respectively, are well-defined quantities. On the other hand, the information velocity  $v_i$  depends on the level of noise of a system. Hence, to investigate superluminal propagation of information (or lack thereof), one may consider any pulse shape as long as a noise model is incorporated [212]. With this clarification at hand, it was proven that using the principles of information theory is strictly impossible to transfer *useful* (i.e., a detectable signal in terms of signal-to-noise ratio) superluminal information if the principle of causality applies [212]. Hence,

we can conclude that the condition  $v_g > c$  does not imply the violation of causality.

One way to look at this is to note that any pulse is composed of different frequency components. At the pulse's peak these frequency components are all in phase; after the pulse's transmission through a medium the relative phases between them are modified, so that a coherent superposition of these components give rise to a shifted peak in the output pulse, causing the pulse to appear traveling at a speed different from  $c$ . Therefore, an advance of the pulse of the peak results in a sufficiently strong anomalous dispersion medium, where the phases of the different frequency components of a pulse become aligned at the exit surface of the medium earlier than even in the case of the same pulse propagating through the same distance in vacuum [217].

This implies that the peak of a pulse can emerge from a medium at an instant even earlier than the instant at which the peak of the pulse enters the medium. This particular behavior is sometimes referred as *superluminal wave propagation* [213]. In this sense, nondiffracting waves may exhibit superluminal properties, without any violation of causality.

However, here we will not deal with the superluminal behavior of nondiffracting waves but rather on their focusing properties. Specifically, in the next Sections the different nondiffracting properties of both Bessel beams and X-waves will be summarized, as well as their possible generation from microwaves to optics. A brief review of the technologies and potential applications which involves Bessel beam and X-wave generation will be briefly outlined. A specific attention will be devoted to millimeter-wave devices.

## 4.3 BESSEL BEAMS

### 4.3.1 History, definition and properties

The word *beam* refers to a monochromatic solution to the wave equation, with a transverse localization of its field. It was known back to 1941 [218] that a Bessel function could ideally represent a monochromatic solution to the wave equation whose transverse profile was concentrated around the axis of propagation and did not suffer diffraction. Such a solution, known as Bessel beam, has not attracted the attention it deserved since it was endowed with infinite energy and hence, from a theoretical point of view, it was no longer different from a plane-wave<sup>4</sup>. In fact, the intensity distribution of a zeroth-order Bessel beam decays as  $\rho^{-1}$  (see Fig. 4.3), and thus it is not square integrable [188].

Only in 1987, J. Durnin et al. [188], [189] brought justice to Bessel beams, showing that it was possible to generate a truncated Bessel beam from a finite transverse aperture and hence, the beam was now endowed with finite energy. In their experiment, they showed that the field does not undergo diffractive spreading along a considerable distance, instead of an infinite one as predicted for an ideal Bessel beam. In fact, from the experiment emerged that a Bessel beam was actually reproducible at the expense of a limitation in the depth of field. More precisely, a well-defined propagating distance exists within which the Bessel-beam profile is preserved. With the aid of geometrical optics, J. Durnin predicted that for a finite aperture with radius  $\rho_{\text{ap}}$  the *nondiffractive range* of a Bessel beam characterized by an axicon angle  $\theta_0$  is given by Eq. (4.9). As we previously said, beyond the nondiffractive range, the on-axis intensity of the main-lobe rapidly decays

<sup>4</sup> Plane waves are also diffraction-free mode solutions of the Helmholtz equation. They differ from Bessel beams because they have not confined transverse profiles with narrow beam radii [189]

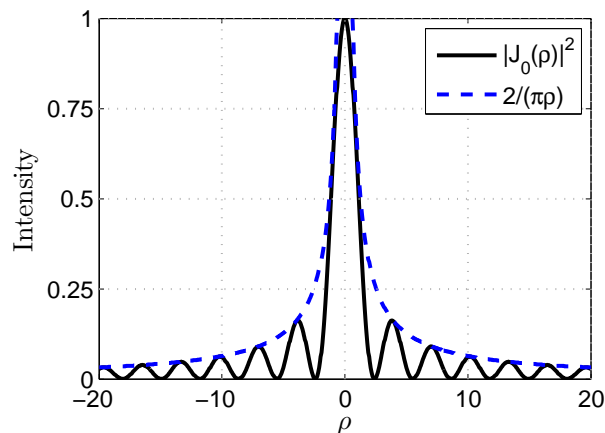
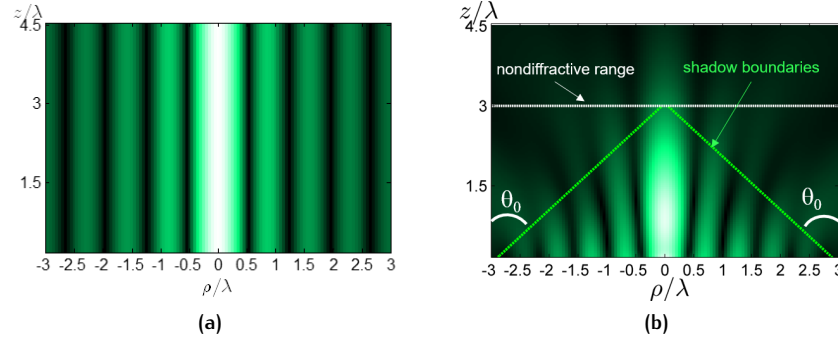


Figure 4.3.: Intensity distribution of a zeroth-order Bessel function of the first kind (black solid line) and its envelope (blue dashed line) decaying as  $\rho^{-1}$ .





**Figure 4.4.:** Contour-plot of a zeroth-order Bessel beam generated by an (a) infinite aperture and (b) a finite aperture of radius  $\rho_{\text{ap}} = 3\lambda$  and with an axicon angle  $\theta_0 = 45^\circ$ .

and the Bessel-beam behavior is no longer appreciable<sup>5</sup>. This behavior is clearly shown in Fig. 4.4 where the generation of an ideal Bessel beam (see Fig. 4.4(a)) is compared with the generation of a truncated Bessel beam (see Fig. 4.4(b)) from a finite aperture of radius  $\rho_{\text{ap}} = 3\lambda$  and with an axicon angle  $\theta_0 = 45^\circ$ . As predicted by geometrical optics (GO) [220], the Bessel beam profile generated from a finite aperture corresponds to the ideal one within a triangular region whose boundaries, the so-called *shadow boundaries*, are defined by the axicon angle  $\theta_0$ .

Even though the transverse intensity profile of a Bessel beam is sharply peaked, the amount of energy in each ring (i.e., between two consecutive zeros of the Bessel function) is approximately equal to that contained in the central maximum. This would have posed some problems from the perspective of power efficiency (e.g., a Bessel beam profile which exhibits five nulls over the aperture would carry less than 20% of the total energy in its main lobe). Indeed, the more rings the beam has the lower the energy in the central core.

Nevertheless, J. Durnin et al. [194] showed that, even if each lobe (i.e., the area between two successive nulls) of a Bessel beam carries approximately the same energy as the central spot, the power transport efficiency of a Bessel beam was comparable with that of a Gaussian beam which contains 50% of its total energy within its half-power beamwidth. They also showed that the depth of field of a Bessel beam could be made far larger than that of a Gaussian but at the expense of power in the central core. This result, can easily be inferred from Eq. (4.14). In fact, from the coupling expressed by Eq. (4.7) we know that  $k_\rho = k_0 \sin \theta$  and  $k_z = k_0 \cos \theta_0$  and hence Eq. (4.9) can be recast as

$$z_{\text{ndr}} = \rho_{\text{ap}} k_z / k_\rho, \quad (4.14)$$

so that  $z_{\text{ndr}} \propto k_\rho^{-1}$ . Moreover, the null-to-null beamwidth  $\text{NNBW} = 2\rho_{\text{NN}}$  of a zeroth-order Bessel function of the first kind is given by the following

<sup>5</sup> We note here that its most outer lobe will diverge first, followed by the second most outer one and so on up to the main lobe which will diverge last [219]. Hence, beyond the nondiffractive range, none of the lobes will be clearly distinguishable.

relation  $k_\rho \rho_{\text{NN}} = j_{0,1}$  where  $j_{0,1} = 2.4048$  is the first null of the  $J_0(\cdot)$  function. As a consequence,

$$\text{NNBW} \simeq 4.81/k_\rho, \quad (4.15)$$

so that  $\text{NNBW} \propto k_\rho^{-1}$ . From Eqs. (4.14) and (4.15) it is manifest that a trade-off is dictated between the narrowest NNBW and the maximum non-diffractive range that one can hope to achieve for a given  $k_\rho$  and in turn a given axicon angle  $\theta_0$ .

Another remarkable feature of Bessel beams is the *self-healing* (or *self-reconstruction*) property [191], [197], which is the capability for a beam to reconstruct itself after a certain distance when an obstacle is placed along the axis of propagation. This outstanding property gets a physical and clear explanation from the plane waves decomposition of a Bessel beam (a different explanation in terms of conical waves is reported in [221]). As we have already emphasized, the Bessel beam can be thought as a set of plane waves with wavenumbers lying on the surface of a cone, (thus sharing the same *axicon angle*). In fact, if we place an object in the center of a beam of light, this will typically project a shadow for only a few wavelengths. In general, the length of a shadow region produced by an object of diameter  $D$  would be of the order  $D^2/\lambda$  [222]. In the case of a Bessel beam, the waves that create the beam are able to move past the obstruction, casting a shadow into the beam, but ultimately reforming the intensity of the profile beyond the obstruction [204], at a distance

$$z_{\min} = \frac{r_o}{2 \cos \theta_0}, \quad (4.16)$$

where  $r_o$  is the radius of the obstacle placed at the center of the beam. Experimental results confirmed the self-healing property, showing that an initial intensity pattern following a zeroth-order Bessel distribution is clearly recovered in shape and contrast after the distance  $z_{\min}$  [197].

It is worth noting that such remarkable properties are exhibited in the near-field. In the far-field range, the Bessel beam is expanding linearly with distance  $z$  as a spherically outgoing wave modulated by Bessel-like angular functions. In these regions the beams will exhibit properties of normal beams, i.e., the central spot radius greatly exceeds  $\lambda$ , shadows are produced in a normal manner, etc. [222].

#### 4.3.2 Potential applications

From J. Durnin's work a lot of interesting applications of nondiffracting beams have been investigated in several sectors of physics and engineering. As pointed out by R. M. Herman and T. A. Wiggins in [222] the main properties of zeroth-order Bessel beams that can make them quite attractive for practical use are:

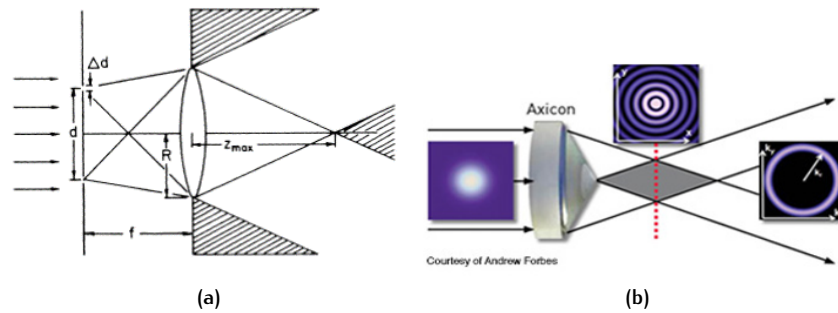


**Figure 4.5.:** (a) A sketch of the experimental setup used by J. Durnin for the first generation of a Bessel beam in optics [189]. (b) A sketch of the experimental setup for generation of a Bessel beam through an axicon lens as presented in [223]. The axicon element allows for converting a Gaussian beam within a rhomboidal region located in the near field. The dashed red line is located at  $z = z_{\text{ndr}}/2$ . In the far-field, the Fourier-Transform of the aperture field gives rise to the expected annulus shape.

- i) The existence of a narrow central range with a transverse size comparable or even smaller than the operating wavelength<sup>6</sup>.
- ii) The quasi-invariant transverse intensity distribution with respect to the propagating axis  $z$ , over an extensive range.
- iii) The self-healing character, which means the absence of significant shadows within the near field.

Property *i*) implies uses in investigating the position, size, or motion of small objects, as well as in applications demanding high pointing accuracy. Property *ii*) implies a usefulness in applications requiring great depths of field. Property *iii*) implies uses in applications where it is required to illuminate many collinear objects without making them shadowing by one another.

Hence, some specific applications might be nonlinear optical applications (thanks to the large length-to-central-beam-size ratio), photolithography, alignment of optical components, micropositioning for optical data storage, wireless power transfer, covert communications, near field probing, chip-to-chip communications, medical imaging, security screening, and so on.

### 4.3.3 Realizations

Over the time, a lot of techniques have been implemented for the generation of Bessel beams, especially in the optical regime. The first realization dates back to the 1987, when J. Durnin [189] proposed an annular slit (a diffracting ring) of radius  $\rho_{\text{ap}}$  backilluminated by a plane wave and placed at the focal distance  $z_f$  of a converging lens to form the beam, as shown in Fig. 4.5(a). A simple geometrical argument reveals that the axicon angle of such a system can be estimated to be  $\theta_0 = \arctan \frac{\rho_{\text{ap}}}{z_f}$ .

<sup>6</sup> J. Durnin has shown that the center of the beam has a minimum diameter of  $0.75\lambda$ .

This experimental setup results from the application of *Fourier Optics*, since the spatial spectrum of a Bessel beam (i.e., its Fourier Transform in the  $k_\rho$ -domain) consists of a single ring (annulus) in the spectral domain [224]. However, this experimental setup suffers from very low efficiency, since most of the incoming power is blocked by the diaphragm.

To this purpose, *conical lenses* [225], [226], commonly known as *axicons*, were proposed [227], [228] to overcome this issue. An axicon is a conical lens with a flat entrance surface which is commonly used to convert a Gaussian beam in a Bessel beam (see Fig. 4.5(b)). The resulting Bessel beam distribution behind the lens can be interpreted as the constructive interference of the plane waves coming from the surface of the cone, which share the same axicon angle  $\theta_0$  (whose name origins from this device) and hence define a Bessel beam<sup>7</sup>.

Other efficient methods have been suggested in the literature such as aberrating lens [222], computer-generated holograms [229], Fabry-Perot cavities [230], distributed Bragg reflectors [81], concentric circular piezo-electric rings [231] etc.. However, most of these techniques are suitable for acoustics or optics applications, where the vectorial nature of electromagnetic fields is fairly neglected. Conversely, in the microwave range, where a full-wave analysis is usually recommended, very few implementations have been proposed [232]–[234]. In these works [232]–[234], the scalar-wave approximation has been generally adopted limiting its range of applicability to devices with an aperture size much larger than the wavelength of operation  $\rho_{\text{ap}} \gg \lambda$ , and for small transverse wavenumbers  $k_\rho \ll k_0$  [224], [235]. As a consequence of Eq. (4.15), the resulting Bessel beams were characterized by beamwidths much larger than the operating wavelength. However, it is of paramount importance for near-field focusing applications, to generate Bessel beams with narrow beamwidths. In such conditions, a full-wave analysis is needed.

To this purpose, different rigorous vector analyses of the generation of Bessel beams by finite apertures have been suggested in [224], [236]–[238], which avoid the paraxial approximation of earlier works [188], [239]. These vector approaches paved the way for the first microwave realizations of Bessel beams with arbitrary small transverse wavenumber  $k_\rho \ll k_0$ . Such realizations include circular array of antennas [219], radial-line slot-array antennas (RLSA) [220], [240]–[242], near-field plates [243], metasurfaces [244], [245], flanged metallic circular waveguides [246], and leaky radial waveguides [153], [224], [235]. Among the abovementioned devices, those in [224], [235], represent some of the most compact-size low-cost, low-profile *Bessel-beam launchers* in the microwave range. However, their scalability to the millimeter-wave frequency range poses some technological issues due to the extremely-thin substrates that they would require to operate with the fundamental mode. To this purpose, in [153] it has recently been proposed a leaky radial waveguide operating with a higher-order leaky mode. Since,

<sup>7</sup> The interested reader can find a rigorous explanation in terms of path integrals in [222].

in this second part of the thesis we mainly deal with the generation of non-diffracting waves in the millimeter-wave range the leaky-radial waveguide originally proposed in [224] at microwaves, and its modified version suitable for the millimeter-wave regime [153] will be the object of the next Chapter 5.

## 4.4 X-WAVES

### 4.4.1 History, definition and properties

The word *pulse* commonly refers to a perturbation of a system with a very short duration. According to Heisenberg's principle, from a high localization in time follows a broadening in the frequency spectrum associated with the pulse. As a consequence, an ideal pulse is usually seen as the counterpart of an ideal beam which has a punctual localization in frequency but requires an infinite time duration. However, if on one hand the non-monochromatic spectrum of a pulse allows for a wider class of solutions to the wave equation, on the other hand it has been harder to find such solutions.

All started in 1983, with the pioneering work of J. N. Brittingham [247]. For the first time a mathematical formulation for packet-like solutions of Maxwell's equations were introduced. In this work, the solutions were found in a heuristical way and then rigorously proven to be three-dimensional nondispersive electromagnetic pulses [248], i.e., packet-like solutions which maintain both their shape invariant during propagation. He gave the name of Focus Wave Modes (FWM) to such kind of pulses. It is worth noting that in literature such solutions are also referred as *splash pulses* [249], *slingshot pulses* [250], *undistorted progressive pulses* [251], and *complex source wave-fields* [252], [253], even if they represent only different classes of the wider family of nondiffracting pulses; a useful and clarifying comparative table is reported in [234].

Then, in 1985, R. W. Ziolkowski showed that this FWM solution was a space-time version of a Gaussian-beam [249], especially when the latter is thought to be equivalent to a spherical wave centered at a stationary complex location [253], [254]. Consequently, the FWM is clearly a moving Gaussian beam with complex source location that moves parallel to real  $z$ -axis, where  $z$  is the axis of propagation. As for ideal Bessel beams, these solutions had infinite energy [248], [249] and thus they were nonphysical.

In particular, A. Sezginer gave a formal proof, for the nonexistence of an electromagnetic mode in vacuum, which has finite energy, and which retains the superluminal, nondispersive, and nondiffractive properties of a FWM [248] for an infinite distance. However, he showed how to construct finite-energy luminal pulses, which propagate with constant speed and approximately without deformation for a certain (long) depth of field.

Subsequently (1989), a simple theoretical method known as *bidirectional decomposition* allowed for constructing a new series of nondiffracting luminal pulses [196], [250], [255], [256]. Another elegant and comprehensive theoretical framework for a unified treatment of different nondiffracting solutions of the wave equation was then (1996) proposed by J. Fagerholm et al. in terms of an angular-spectrum representation [198].

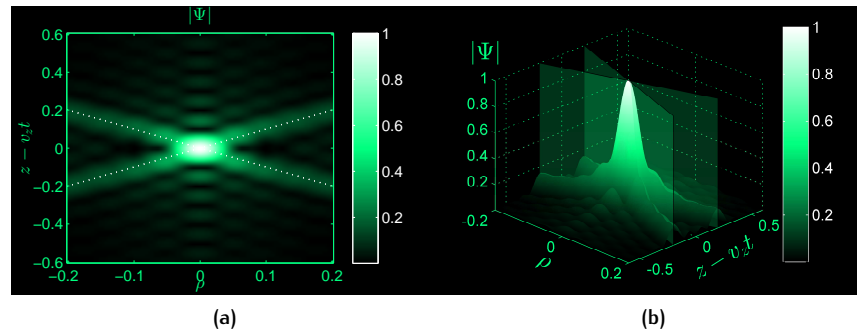


**Figure 4.6.:** (a) 2-D and (b) 3-D plot of the normalized amplitude of an X-wave as a function of  $\rho$  and  $z - v_z t$  where  $v_z$  is the group velocity of the wave. Since for an ideal X-wave cone dispersion is neglected, the group velocity  $v_z$  coincides with the phase velocity  $v_{\text{ph}} = c / \cos \theta_0$ . As a consequence the variable  $z - v_z t$  gives a measure of the spatio-temporal confinement of the pulse. In this example, we have considered a wide uniform frequency spectrum and an axicon angle  $\theta_0 = 45^\circ$ . The X-shape of the pulse follows the inclination dictated by the axicon angle, as emphasized by the boundaries in both figures.

Other methods to get exact finite-energy nondiffracting pulses were also proposed [257] to show that their superluminal versions (i.e., nondiffracting pulses characterized by a group velocity which exceeds that of the light in the medium) are supported by Maxwell's equations in vacuum, thus without requiring any anomalous dispersion phenomena in the propagating medium [258].

Nevertheless, in the abovementioned mathematical constructions the superluminality of FWMs played a central role, whereas the focusing properties of such pulses were not sufficiently emphasized. Fortunately, Durnin [188] suggested that it was possible to generate nondiffracting electromagnetic pulses with a simple linear superposition of Bessel beams sharing the same axicon angle over a certain frequency range. Such a polychromatic version of Bessel beams is now commonly recognized as *X-wave*. It is easy to understand that an X-wave, once thought as a frequency superposition of Bessel beams, inherits the self-healing property and the nondiffractive character of Bessel beams.

With regard to the focusing properties, it should be noted that the increase of the spectral content of an X-wave with respect to a Bessel beam is reflected in a higher time localization of the pulse. Since the pulse is supposed to travel along the longitudinal direction, this would result in a longitudinal localization of the pulse (see Fig. 4.6). In fact, while a Bessel beam solution is ideally characterized by a Bessel-like transverse distribution and a flat longitudinal distribution (as a result of the monochromatic character of the Bessel beam<sup>8</sup>), the X-wave solution is characterized by the same transverse distribution, but a limited longitudinal distribution (as a consequence of

<sup>8</sup> We recall here that the Fourier-Transform of a Dirac function is a constant function.

the polychromatic character of the Bessel beam<sup>9</sup>). A thorough discussion of these properties is postponed to Chapter 6.

#### 4.4.2 Potential applications

As we have already said, the high-confinement of X-waves in both the transverse and the longitudinal axis is a result of the frequency-modulation of Bessel beams. This would suggest their application to a lot of millimeter-wave applications such as medical imaging, wireless power transfer, radiometry, etc., where the focusing capabilities of a device are of paramount importance.

The exponential growth in these research areas, has driven researchers in developing more sophisticated techniques for producing spatially and temporally localized field profiles. In the context of localized waves, perhaps the most intriguing perspectives were opened by the work of M. Zamboni-Rached et al. [192], where different localized fields with finite total energies and arbitrary frequency spectra were proposed. Just to mention but a few, they showed how it was possible to produce different localized solutions, by simply superimposing an infinite sets of X-waves (which gives rise at the so-called X-wave Transform [191], [259]) with their energy concentrated more and more in a spot corresponding to the vertex region.

However, the frequency-modulation of Bessel beams is not the only way to manipulate Bessel beams in order to obtain more interesting properties. In a recent contribution [260], it has been shown that a suitable superposition of Bessel beams all endowed with the same frequency, but different longitudinal wave numbers gives rise to a stationary localized wave field with high transverse localization, and whose longitudinal intensity pattern can assume any desired shape within a chosen interval. Since the intensity envelope associated to this field remains static, these solutions of the wave equation are known as *frozen waves*.

Since this field is generated by a superposition of beams at fixed frequency, but with different wave numbers, this technique is also referred as *angular modulation*. A detailed analysis of such *frozen waves* as well as their applicability in modern applications goes beyond the scope of this thesis. (The interested reader can find in [261] a theoretical work which deals with the generation of frozen waves through finite apertures, whereas its experimental generation in optics is reported in [262]).

Here, specifically in Chapter 6, we will mainly deal with the efficient generation of X-waves, i.e., *frequency-modulated* Bessel-beams in the millimeter-wave range.

---

<sup>9</sup> If each frequency component has the same weight (i.e., a uniform frequency spectrum), the longitudinal distribution will follow a cardinal sine function, as an effect of the Fourier Transform.



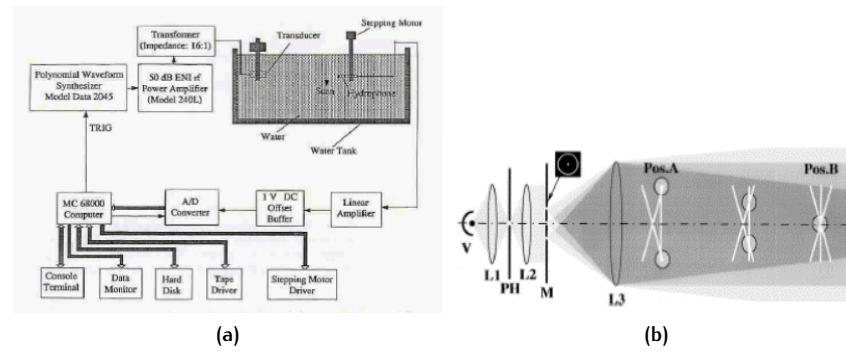


**Figure 4.7.:** (a) A sketch of the experimental setup used by Lu and Greenleaf for the first generation of X-waves in acoustics [264]. (b) A sketch of the experimental setup for the first measurement of the 3-D field distribution of X-waves in optics [265]. Except for a system of converging lenses and a pinhole, the mechanism of generation was equal to the one originally proposed by Durnin [189] for the Bessel beam generation.

#### 4.4.3 Realizations

At the end of the '80s, the main issue related to the practical generation of nondiffracting pulses was represented by the launchability of pulses derived from the fundamental Gaussian pulses. This topic was further exacerbated by E. Heyman, B. Z. Steinberg, and L. B. Felsen [252]. In 1987, they introduced the Complex Source Pulses (CSP) [252] which differ from FWM in having a bidirectional spectra, i.e. both forward and backward components. Thus, they were not a true-source excited field since they were described by the sum of both causal and anticausal Green's functions. Fortunately, in 1989, further studies revealed that localized-wave solutions could be designed by means of causal components only and, moreover, they could be generated from finite apertures [250].

Once the launchability of FWM was proven, it remained to understand how to launch these kind of waves from finite apertures. The answer came from acoustics in 1992, when J. Y. Lu and J. F. Greenleaf designed an experimental ultrasound setup [263] for the generation X-wave [264], a special kind of localized solutions of the wave equation. In that experiment [263], a discrete array of 10 transducers (see Fig. 4.7(a)) was proposed. A polynomial waveform synthesizer was used to generate 10 broadband X-wave drive functions for the 10 transducer elements which were excited following specific time patterns. The acoustic waves were successfully measured in water in a plane along the axis of the transducer with a calibrated hydrophone. The measured RF signals produced by the 10 transducer elements were summed, in order to obtain the sought X-wave signal by means of the frequency modulation.

The difficulties with meeting the requirement of ultrawideband spectral content in the case of light field, have obstructed the study of X-waves in optics. As a consequence, the first evidence of optical X-wave generation came only in 1997 thanks to the experiments performed by P. Saari and

K. Reivelt [265] who reported the first measurements of the whole three-dimensional distribution of the field of optical X waves in free space (the first experimental evidence of X waves aimed only to demonstrate the suppression of temporal spread of ultrashort pulses in dispersive media and it was performed by H. Sönajalg and P. Saari in 1996 [266]). In that experiment [265], an annular slit similar to the one used by Durnin [189] for generating truncated Bessel beams was used (see Fig. 4.7(b)). The original part of the experiment was related to the method for recording the fields which was based on a field cross-correlation technique. In fact, a simple CCD camera would have required a temporal resolution in the subfemtosecond range to measure such pulses.

These promising results won the initial common scepticism that floated around the generation of localized waves. However, if the requirement of ultrawideband spectral content obstructed the study of X-waves in optics, this is even more true in the microwave range, where most of radiators have fractional bandwidth optimistically limited to values of 10%-20%. Moreover, in the previous experiments the *cone dispersion*, i.e., the frequency dependence of the axicon angle, has always been fairly neglected. Such an assumption no longer holds at microwaves where longitudinal and radial wavenumbers commonly show a non-linear frequency dispersion (even in the vacuum), thus affecting the axicon angle dispersion. In fact, if we define the normalized longitudinal and radial wavenumbers  $\hat{k}_z = k_z/k_0$  and  $\hat{k}_\rho = k_\rho/k_0$ , it is manifest from the definition of the axicon angle

$$\theta(\omega) = \arctan \frac{k_\rho(\omega)}{k_z(\omega)} = \arctan \frac{\hat{k}_\rho(\omega)}{\hat{k}_z(\omega)}, \quad (4.17)$$

that one needs to enforce normalized wavenumbers constant with respect to frequency, to prevent cone dispersion. A condition that, at microwaves, is never met, except for guided, non-radiating, transverse electromagnetic (TEM) modes. Hence, neglecting dispersion in such polychromatic solutions as X-waves is not possible for an accurate analysis. Moreover, despite the large amount of different theoretical formulations [192], [234], [249], [263], [267], only few works [266], [268] have taken into account cone dispersion on a theoretical basis. Such an effect, it is supposed to have a non-negligible impact in the focusing features of X-waves. As a matter of fact, there is still lack of an experimental evidence of X-waves in the microwave range, except for a “controversial” experiment done by D. Mugnai and A. Ranfagni in 2000, aimed to the observation of the superluminal properties of such waves rather than their remarkable properties of both spatial and temporal confinement<sup>10</sup>.

<sup>10</sup> There, the experimental setup, consisting of a circular slit fed by a horn antenna placed in the focal plane of a circular mirror, and of a second horn antenna placed at a variable distance along the propagating axis, measured the velocity of propagation of a microwave signal carried by X-waves. Unfortunately, no measurements have been provided of the 3-D field distribution of the field. Thus, there was no experimental proof of the effective X-wave generation.

To this purpose, in Chapter 6 we will present an original framework for the evaluation of the nondiffractive features of X-wave even when wavenumber dispersion is taken into account. With this new criterion at hand, we will propose a realistic wideband millimeter-wave radiator which looks particularly promising for the first experimental evidence of X-waves in the millimeter-wave range.

## 4.5 CONCLUSION

In this Chapter we have reviewed the mathematical framework needed to understand the properties of nondiffracting beams and pulses. Two particular solutions, i.e., Bessel beams and X-waves, have been discussed in detail, emphasizing their focusing properties and their nondiffracting/self-healing character as well. These features are shown to be extremely useful for a lot of millimeter-wave applications, thus motivating the increasing interest in this class of solutions.

Afterwards, we have outlined the significant 'milestones' in the field of Bessel beams and X-waves generation, from a historical point of view. The first experiments in acoustics and optics have been reviewed to introduce the first realizations at microwaves and millimeter waves. It has been shown that, while monochromatic Bessel beams have been already generated at microwaves, efficient generation in the millimeter-wave range are rather scarce. This motivates the investigations of Chapter 5. Even more interestingly, there is still a lack of evidence of X-waves at microwaves. This is mainly due to the non-negligible wavenumber dispersion which commonly affects microwave wideband radiators. In this sense, the analysis developed in Chapter 6 clearly reveal perspectives and limitations in the context of X-waves microwave generation.

# 5

## BESSEL-BEAM LAUNCHERS

### 5.1 INTRODUCTION

In the previous Chapter 4, we have reported a thorough review of the state of the art inherent to the generation of nondiffracting waves from microwave frequencies to optical frequencies. In this Chapter 5, we specifically deal with the generation of Bessel beams in the microwave and millimeter-wave range. As we have already emphasized, the interest in this specific range of frequencies is motivated by the increasingly high demand of focusing devices in modern applications suited for millimeter waves.

Among the different Bessel beam launchers proposed to date, here we want to focus our attention on a specific one: the *leaky radial waveguide*. The reason for this choice is twofold. On one hand, the leaky radial waveguide represents one of the most performing prototype thanks to its cost-effectiveness, structural simplicity, and easiness of fabrication. On the other hand, the leaky-wave radiation mechanism typical of such devices allow us to make a strong connection between *leaky waves* and *nondiffracting waves*, i.e., between the first and the second part of this PhD thesis, respectively.

Chapter 5 is organized in two Sections. In Section 5.2, we introduce the leaky-radial waveguide by reviewing the main features of a prototype operating in the microwave-range [224], [235]. After a rigorous description of the device on a theoretical basis, we will review some relevant numerical and measurement results to assess the capabilities of this device. Finally, it will be shown, how unfeasible it would be the application of a simple frequency scaling of this microwave design to millimeter-waves. Such a result motivated the need a different approach suitable for millimeter-wave frequencies. The result of this investigation will be the object of Section 5.3.

In Section 5.3, an original and different theoretical analysis of the leaky radial waveguide is proposed to deal with a suitable millimeter-wave design. Such a study will furnish extremely useful analytical formulas for the design of leaky-radial waveguides at millimeter waves. Numerical and full-wave analyses will validate the theoretical results. Finally, the fabrication and the measurement of the proposed millimeter-wave prototype will be reported and accurately described. For completeness, the performance of this device within its operating bandwidth will be carefully addressed for its potential use as an X-wave launcher. These devices would be the object of Chapter 6.

## 5.2 MICROWAVE BESSEL-BEAM LAUNCHERS

In this Section a microwave Bessel beam launcher based on a *leaky radial waveguide* (LRW) is presented. The leaky radial waveguide under consideration (see Fig. 5.1) is basically a dielectric-filled metallic parallel-plate waveguide in which the upper plate has been replaced by a partially reflecting sheet (PRS). This structure belongs to the class of 2-D leaky-wave antennas (LWAs) described in Chapter 1. The main difference with respect to 2-D LWAs is the presence of a circular metallic rim which transversely limits the structure. As a consequence, the considered LRW is not designed to let their excited leaky modes radiate most of the power before they have reached the edge of the structure. On the contrary, the presence of a metallic wall at a suitable radial position enforces the presence of a pair of *inward* and *backward* leaky waves which gives rise to a *resonant* leaky mode. The resonance has a central role for the creation of the Bessel beam. This aspect will readily be clarified in 5.2.1 where we will rigorously review the theoretical framework underlying the design principles of the LRW. Then, in 5.2.2 and 5.2.3 numerical and experimental results will be provided to validate the concept. Finally, in 5.2.4 we will frequency scale the design at millimeter waves. The failure of this approach will motivate the need of a new design principle described in Section 5.3.

It is also worth here to emphasize the strong connection between *leaky waves* and *nondiffracting waves*. Indeed, for this class of devices (viz., LRWs) *leaky waves* are responsible for the radiation of a *monochromatic nondiffracting wave*, such as a Bessel beam. This aspect is extremely important since it bridges the two main parts of this thesis, i.e., the first one focused on *leaky waves* and the second one focused on *nondiffracting waves*.

### 5.2.1 Theoretical analysis

As is known, zeroth-order Bessel beams emerge as axially-symmetric solutions of the scalar wave equation when expressed in a cylindrical reference frame [164], [218], [269]. In the microwave range, the scalar theory is not sufficient to describe Bessel beams of arbitrary beam size, since the paraxial approximation holds only when  $k_\rho \ll k_0$  [224], [235], [236]. To account for the vector wave nature of Bessel beams, one should use Maxwell's equations. A very convenient method, is to use the vector potentials  $\mathbf{A}$  and  $\mathbf{F}$ . In fact, the translational invariance of the LRW with respect to the  $z$ -axis, allows to decouple the electromagnetic problem, searching independently for an electromagnetic field which is transverse-electric (TE) or transverse-magnetic (TM) with respect to the axis of symmetry (viz., the  $z$ -axis). Thus, the only  $z$ -component of the vector potential  $A_z(F_z)$  is required to describe a TM(TE) electromagnetic field. The vectorial formulation is then reconducted to the resolution of a scalar problem through the use of the vector potentials. As is

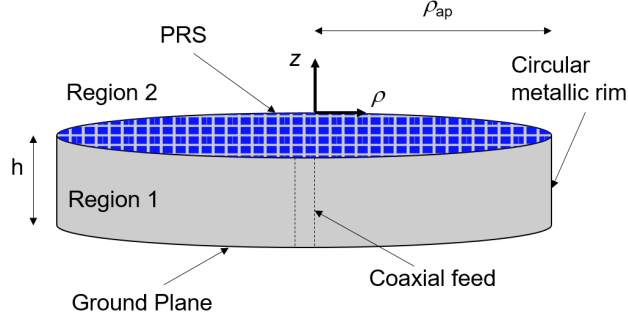


**Figure 5.1.:** Geometrical view of a leaky-wave radial waveguide of thickness  $h$ . A metallic rim is placed at  $\rho = \rho_{ap}$ . The PRS is represented by a square lattice of metallic patches.

customary [164], [269], all the electric and magnetic fields components are finally derived from  $A_z$  and  $F_z$ .

Here, we are interested in generating a zeroth-order Bessel beam over the longitudinal component of the electric field  $E_z = J_0(k_\rho \rho) e^{-jk_z z}$ . In the following paragraph we will derive the required boundary conditions to enforce such a field distribution over the aperture of a LRW, starting from the general solutions provided by the vector potentials. The interested reader can find the field derivation for vector Bessel beams of any order and any polarization in [237].

#### Field Derivation

We start from considering the LRW as shown in Fig. 5.1. Since we are searching for solutions with  $E_z = J_0(k_\rho \rho) e^{-jk_z z} \neq 0$  we only consider TM electromagnetic fields. Thus, the  $z$ -component of the magnetic vector potential  $A_z$  is enough to derive all the fields components. As is known [164], [269], the longitudinal component of the vector magnetic potential satisfies the homogeneous Helmholtz equation in cylindrical coordinates:

$$\frac{\partial^2 A_z}{\partial \rho^2} + \frac{1}{\rho} \frac{\partial A_z}{\partial \rho} + \frac{1}{\rho^2} \frac{\partial^2 A_z}{\partial \phi^2} + \frac{\partial^2 A_z}{\partial z^2} + k^2 A_z = 0. \quad (5.1)$$

A generic solution of Eq. (5.1) is expressed as the product of three independent functions of the three variables  $\rho$ ,  $\phi$ , and  $z$ , whose expressions are given by linear combinations of Hankel functions (for the radial dependence) and exponentials (for both the azimuthal and longitudinal dependence) [164], [269]. Without loss of generality, inside this cylindrical waveguide (Region 1 in Fig. 5.1)  $A_z$  can be expressed as [164], [224], [269]:

$$A_z = \cos(k_z z) e^{jn\phi} \left[ A_1 H_n^{(1)}(k_\rho \rho) + A_2 H_n^{(2)}(k_\rho \rho) \right], \quad (5.2)$$

where  $k_z$  and  $k_\rho$  are the longitudinal wavenumber and the radial wavenumber, respectively, related through the *separation equation*  $k^2 = k_z^2 + k_\rho^2$ ,  $H_n^{(1)}(\cdot)$  and  $H_n^{(2)}(\cdot)$  are the  $n$ th-order Hankel functions of the first and sec-

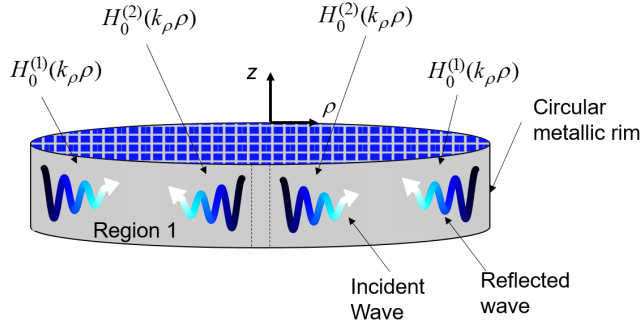


Figure 5.2.: The mechanism of generation of a Bessel beam through the superposition of an inward Hankel wave and an outward Hankel wave. An outward Hankel wave is generated at the center by a coaxial feed and is then reflected back by the circular metallic rim to create an inward Hankel wave. If the circular rim is placed in one of the zeros of the Bessel function and the incident wave is slowly-attenuated, the two Hankel waves constructively interfere each other and create the Bessel beam.

ond order, respectively. The coefficients  $A_1$  and  $A_2$  will be determined once the boundary conditions and excitation will be stipulated. Note that circular functions (i.e.,  $\cos(\cdot)$  and  $\sin(\cdot)$ ) have been chosen for the longitudinal dependence due to the confinement of the fields inside the waveguide.

From here, it is straightforward to calculate the field components as [164], [269]:

$$E_\rho = -j\frac{\eta}{k}\frac{\partial^2 A_z}{\partial\rho\partial z} \quad H_\rho = \frac{1}{\rho}\frac{\partial A_z}{\partial\phi}, \quad (5.3)$$

$$E_\phi = -j\frac{\eta}{k}\frac{1}{\rho}\frac{\partial^2 A_z}{\partial\phi\partial z} \quad H_\phi = -\frac{\partial A_z}{\partial\rho}, \quad (5.4)$$

$$E_z = j\frac{\eta}{k}\left(\frac{\partial^2}{\partial z^2} + k^2\right)A_z \quad H_z = 0, \quad (5.5)$$

where  $\eta$  is the characteristic impedance of Region 1. Note that for an azimuthally-invariant field ( $\partial/\partial\phi = 0$ ),  $n = 0$  and Eq. (5.2) reduces to

$$A_z = \cos(k_z z) \left[ A_1 H_0^{(1)}(k_\rho \rho) + A_2 H_0^{(2)}(k_\rho \rho) \right], \quad (5.6)$$

so that  $E_\phi = H_\rho = H_z = 0$  and the only non-null components of the field are:

$$E_\rho = -j\frac{\eta k_z k_\rho}{k} \sin(k_z z) [A_1 H_1^{(1)}(k_\rho \rho) + A_2 H_1^{(2)}(k_\rho \rho)], \quad (5.7)$$

$$E_z = -j\frac{\eta k_\rho^2}{k} \cos(k_z z) [A_1 H_0^{(1)}(k_\rho \rho) + A_2 H_0^{(2)}(k_\rho \rho)], \quad (5.8)$$

$$H_\phi = k_\rho \cos(k_z z) [A_1 H_1^{(1)}(k_\rho \rho) + A_2 H_1^{(2)}(k_\rho \rho)]. \quad (5.9)$$

As is manifest from Eq. (5.8), the  $E_z$  field component is expressed as the superposition of an outward ( $H_n^{(2)}$ ) and an inward ( $H_n^{(1)}$ ) cylindrical wave (see Fig. 5.2). As originally suggested in [239], [270], the  $E_z$  field component would assume the desired  $J_0$  profile when  $A_1 = A_2$ . The required boundary



condition to get  $A_1 \simeq A_2$  can be achieved by placing a circular metallic rim at a distance  $\rho = \rho_{ap}$ , which corresponds to one of the zeros of the Bessel function  $J_0(k_\rho \rho_{ap})$ . As a matter of fact, once an outgoing cylindrical wave  $H_0^{(2)}(k_\rho \rho)$  is excited from the center of the waveguide (see the coaxial feed in Fig. 5.1) the presence of a metallic wall at  $\rho = \rho_{ap}$  would produce a reflected wave  $H_0^{(1)}(k_\rho \rho)$  with almost the same coefficient of the incident one, if this incident wave has not been strongly attenuated (due to any kind of losses, e.g., radiation, ohmic, dielectric losses). It immediately follows that the required equations to establish the condition  $A_1 \simeq A_2$  are [153], [224], [235]

$$\beta_\rho \rho_{ap} = j_{0n}, \quad n \in \mathbb{N}, \quad (5.10)$$

$$\alpha_\rho \rho_{ap} \ll 1, \quad (5.11)$$

where  $j_{0n}$  represents the  $n$ -th zero of the zeroth-order Bessel function [271]. The first one of the two equations requires that the inward and outward waves constructively interfere each other two create the Bessel beam<sup>1</sup>. The second one requires that the waves are slowly attenuated so that  $A_1 \simeq A_2$ . Note that, if one takes the formal analogy between traveling cylindrical waves ( $H_0^{(1),(2)}(k_\rho \rho)$ ) and traveling plane waves ( $e^{\pm jk_\rho \rho}$ ), such conditions are equal to those required to plane waves to obtain a stationary cosine-like solution (which is the analogue of a  $J_0$  function in cylindrical problems [269]). Note also that in conventional 2-D leaky-wave antennas as those seen in Chapter 1, the structure is usually designed to be long in terms of wavelengths so that the excited forward leaky mode has already radiated most of the power when it has reached the end of the structure. In such a way, no backward waves are expected and diffraction from the edges is prevented. Here, the structure is resonant in the radial direction and the presence of a reflected wave is crucial to establish the desired Bessel beam profile. The fulfillment of Eqs. (5.10)-(5.11) allows us to rewrite Eqs. (5.7)-(5.9) as

$$E_\rho = A_1 \frac{-j\eta k_z k_\rho}{k} \sin(k_z z) J_1(k_\rho \rho), \quad (5.12)$$

$$E_z = A_1 \frac{-j\eta k_\rho^2}{k} \cos(k_z z) J_0(k_\rho \rho), \quad (5.13)$$

$$H_\phi = A_1 k_\rho \cos(k_z z) J_1(k_\rho \rho), \quad (5.14)$$

which uniquely describe the fields inside the waveguide, unless for an arbitrary constant amplitude factor  $A_1$  stipulated by the excitation (see [224] for further details). We note here, that  $E_z$  takes a cosinusoidal dependence along  $z$  instead of the desired exponential one. This is due to having correctly selected circular functions to describe the auxiliary potential  $A_z$  inside the waveguide. However, the fields just above the aperture should be described by a magnetic vector potential of the type

<sup>1</sup> If one takes in mind the asymptotic behavior of Hankel functions for large arguments [272], this would correspond to require that the waves are out of phase at  $\rho = \rho_{ap}$  [224].

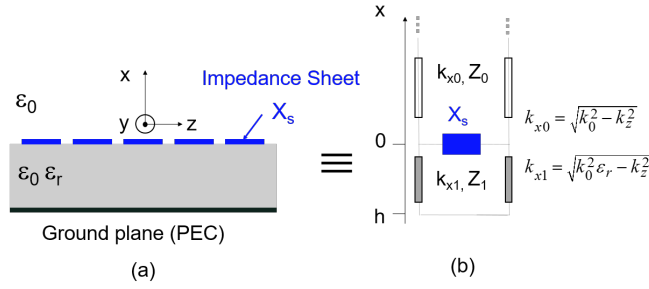


Figure 5.3.: (a) 2-D section of the LRW and its (b) transverse equivalent network (TEN) model.

$A_z = e^{-jk_z z} e^{jn\phi} \left[ A_1 H_n^{(1)}(k_\rho \rho) + A_2 H_n^{(2)}(k_\rho \rho) \right]$ , thus obtaining the required *propagating* Bessel beam profile, whose intensity is invariant with respect to the  $z$ -axis and up to the nondiffractive range.

The field derivation hitherto developed furnishes the required boundary conditions to get a Bessel-beam profile over the longitudinal component  $E_z$  of the electric field. Nevertheless, no insights have been given about the modes supported by this structure. To this purpose, in the next paragraph, an equivalent circuit-model as those presented in Chapter 3 for graphene-based and LC-based LWAs will be derived in order to gain some physical insights.

#### Equivalent Circuit Model

Taking advantage of the axial symmetry, we consider an arbitrary  $\phi$ -cut of the LRW to develop an equivalent circuit model (Fig. 5.3(b)) for the 2-D section depicted in Fig. 5.3(a). As we have exhaustively described in Chapter 3 the application of the *transverse resonance technique* (TRT) to the *transverse equivalent network* (TEN) model, furnishes the sought dispersion equation of the LRW:

$$Y_0 + Y_s - jY_1 \cot(k_{z1}h) = 0, \quad (5.15)$$

where  $k_{z1} = \sqrt{k_0^2 \epsilon_r - k_\rho^2}$ , is the longitudinal wavenumber in the slab,  $\epsilon_r$  is the permittivity of the dielectric filling the LRW,  $Y_0$  and  $Y_1$  are the characteristic admittances in vacuum and in the dielectric medium, and  $Y_s$  is the surface admittance of the impedance sheet. Since we are only dealing with TM electromagnetic fields, the impedance sheet is described by a purely capacitive surface impedance  $Z_s = jX_s$  with  $X_s < 0$  [28], [224], whereas  $Y_0 = k_0/(\eta_0 k_z)$  and  $Y_1 = k_0 \epsilon_r/(\eta_0 k_{z1})$ , where  $k_z = \sqrt{k_0^2 - k_\rho^2}$  and  $\eta_0$  is the vacuum impedance, so that Eq. (5.15) can be recast as:

$$\frac{k_0}{\sqrt{k_0^2 - k_\rho^2}} - j \frac{\eta_0}{X_s} - j \frac{k_0 \epsilon_r}{\sqrt{k_0^2 \epsilon_r - k_\rho^2}} \cot(k_{z1}h) = 0. \quad (5.16)$$

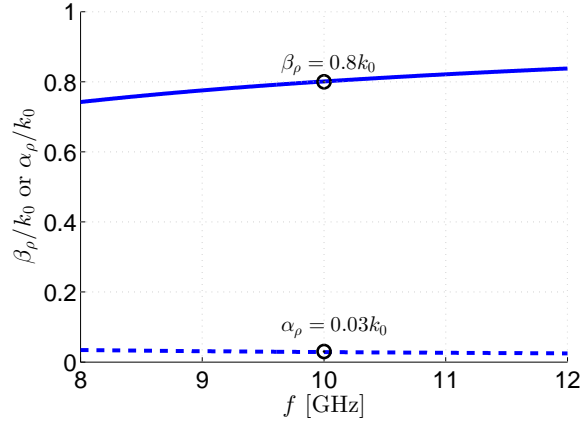


**Figure 5.4.:**  $\beta_\rho/k_0$  vs. frequency ( $f$ ). The intersections between the transverse (solid blue lines) and the radial (black dashed lines) resonances define the operating points.

As we have already seen, the roots of the dispersion equation are the complex modes (either of SWs or LWs) supported by the LRW. Furthermore, from the equation above, it is easy to check that the *surface-wave* (SW) cutoff frequency (i.e.,  $f_c^{\text{SW}}$  such that  $k_\rho(f_c^{\text{SW}}) = k_0$  and in turn  $k_z(f_c^{\text{SW}}) = 0$ ) of the first higher-order SW mode is given by the expression [153]:

$$f_{c1}^{\text{SW}} = \frac{c_0}{2h\sqrt{\varepsilon_r - 1}}, \quad (5.17)$$

so that  $h$  and  $\varepsilon_r$  should be chosen small enough to guarantee monomodal propagation at a given frequency. In the next Subsection 5.2.2, Eq. (5.16) is solved for a given set of parameters to give a proof-of-concept. Then, some numerical results obtained in [224], [235] are reported to demonstrate how the theoretical methods developed up to now can be applied for the design of a realistic device.

### 5.2.2 Numerical results

In order to get the dispersion curves of the modes supported by the LRW, one needs to numerically solve the dispersion equation for  $k_\rho$ . To accomplish this task the values of  $X_s$ ,  $h$ , and  $\varepsilon_r$  are needed. To give a proof-of-concept, let us suppose to know these values; for the following choice  $\varepsilon_r = 1$ ,  $Z_s = -j28.47 \Omega$ , and  $h = 1 \text{ mm}$  [235], in the frequency range  $8 < f < 12 \text{ GHz}$  we are evidently in monomodal regime, hence only the fundamental TM leaky mode is expected to be in the radiative region  $k_\rho/k_0 < 1$  (of course, a TM surface wave is always propagating with a radial wavenumber along the light line  $k_\rho = k_0$ ), as is shown in Fig. 5.4. Such a result suggests that once the fundamental TM leaky mode is excited (e.g., exciting the cavity with a centrally-fed coaxial probe) at the central frequency  $f_0 = 10 \text{ GHz}$ , a Bessel beam with a spectral content defined by

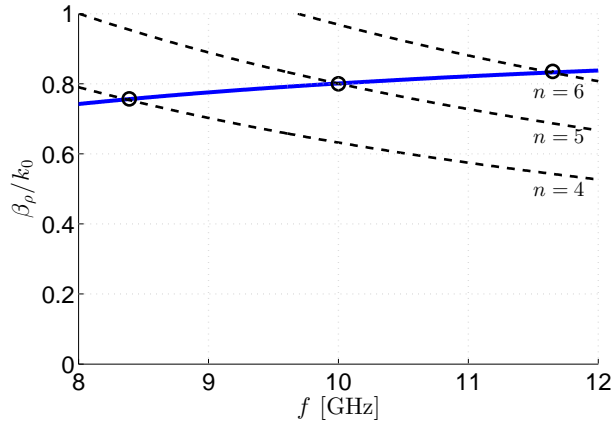


Figure 5.5.:  $\beta_\rho^{(n)}/k_0$  vs.  $f$ . The intersections between the transverse (solid blue lines) and the radial (black dashed lines) resonances define the operating points of the launcher. The radial resonance are reported only for  $4 \leq n \leq 6$ .

$k_\rho = (0.8 - j0.03)k_0$  would be radiated by the LRW, provided that Eqs. (5.10)-(5.11) are satisfied.

On one hand, Eq. (5.11) simply requires that  $\rho_{\text{ap}} \ll 1/(0.03k_0) \simeq 159$  mm. A practical criterion to size the rim radius is to require that the field amplitude at  $\rho = \rho_{\text{ap}}$  is greater than half its value at  $\rho = 0$  that is

$$e^{-\alpha_\rho \rho_{\text{ap}}} > 1/2 \quad \rightarrow \quad \rho_{\text{ap}} < \frac{\ln 2}{\alpha_\rho} \simeq 111 \text{ mm}, \quad (5.18)$$

which fixes a strict upper-bound to the rim radius.

On the other hand, a close look at Eq. (5.11) reveals that, once  $\rho_{\text{ap}} = 89$  mm is fixed, a family of  $n$  dispersion curves are given by the fulfillment of this radial resonance. Indeed, Eq. (5.11) can conveniently be recast as:

$$\frac{\beta_\rho^{(n)}}{k_0} = \frac{j_{0,n}}{\rho_{\text{ap}} k_0}. \quad (5.19)$$

If one plots this family of  $n$  curves over the dispersion diagram of the fundamental LW mode (see Fig. 5.5), one finds a set of operating frequencies established by the intersections between the transverse resonances (roots of Eq. (5.15)) and the radial resonances (roots of Eq. (5.19)) of the LRW. The dark circles of Fig. 5.5) represent the operating points of the launcher, i.e., the frequencies at which a Bessel beams with  $n$  zeros is correctly realized over the aperture. The nondiffractive range ( $z_{\text{ndr}}$ ) and the null-to-null beamwidth (NNBW) of such beam can easily be calculated through Eqs. (4.14) and (4.15), respectively.

This result has been validated through the computation of the radiated fields by the leaky radial waveguide as described in the Appendix of [224]: taking advantage of the equivalence theorem and the *method of image charges* [163], [164], [269], [273], the equivalent surface currents over the aperture

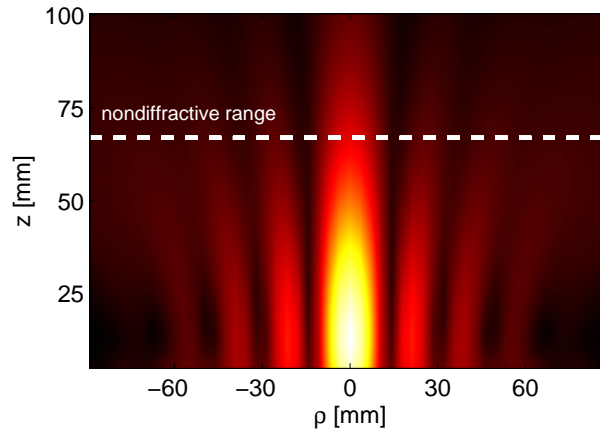


**Figure 5.6.:** Contour plot of the electric field  $|E_z|$  along the  $\rho z$ -plane for the proposed LRW at the operating frequency  $f = 10$  GHz. The five nulls are clearly distinguishable, as expected from theory.

are evaluated and then the radiated near field is derived through numerical integration of the scalar free-space Green's function [164].

As is shown in Fig. 5.6, the Bessel-beam profile is correctly radiated over the longitudinal component of the electric field  $E_z$  at  $f = 10$  GHz. The theoretical nondiffractive distance  $z_{\text{ndr}} \simeq 67$  mm (see dashed white line in Fig. 5.6) correctly identifies the longitudinal distance beyond which the main beam starts to spread out. In the next Subsection 5.2.3, some experimental results from [235] are reported for a microwave Bessel-beam launcher with almost the same electrical and geometrical features of the one described in this Subsection 5.2.2.

### 5.2.3 Experimental results

The Bessel beam launcher described in the previous paragraph 5.2.2 has been realized and measured in 2012 by M. Ettore, S. M. Rudolph, and A. Grbic [235]. The PRS was realized by printing a periodic lattice of square patches on both sides of a thin dielectric substrate. Full-wave simulations performed with HFSS [274] provided the value of the patch size

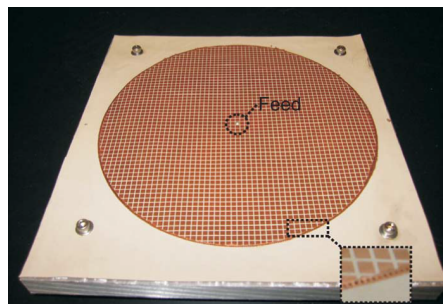


**Figure 5.7.:** Final prototype. The array of vias comprising the outer metallic rim is shown in the inset. Courtesy of Mauro Ettore [235].

$l_s = 2.32$  mm needed to obtain the required impedance sheet boundary of  $Z_s = -j28.76 \Omega$  at  $f_0$ . Note that the periodicity of the patch elements was set to  $\lambda_0/10$  (where  $\lambda_0$  is the operating wavelength at  $f_0$ ) to respect the homogenization limit (i.e.,  $p \ll \lambda$ ) [50], [52], so that the PRS was accurately described by a single homogenized surface impedance.

The final prototype was then fabricated using PCB technology (see Fig. 5.7) and measured in the frequency range from 8 GHz to 12 GHz at the University of Michigan. More details about the fabrication process and the measurements can be found in [235]. For convenience, we report here just few experimental results of [235] to assess the validity of the theoretical approach proposed so far.

As is seen in Fig. 5.8(a) HFSS simulations (at  $f = 9.92$  GHz) and measurements (at  $f = 9.6$  GHz)<sup>2</sup> of the normalized  $E_z$  component of the electric field at different  $\phi$ -planes for  $z = 0.75\lambda_0$  show a remarkable agreement. For

<sup>2</sup> The frequency shift is attributed to tolerances inherent to the milling and etching fabrication processes [235].

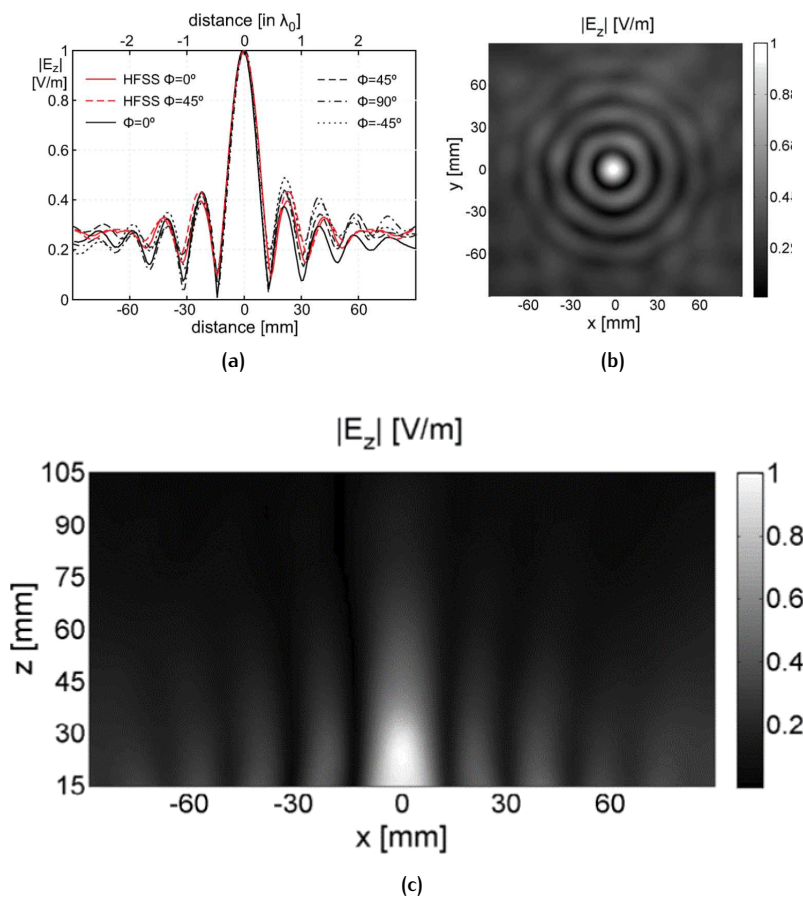


Figure 5.8.: Normalized component  $E_z$  of the electric field. (a) Comparison between measured and simulated results at  $z = 0.75\lambda_0$  for different  $\phi$ -cuts. (b) 2D field distribution over the  $xy$ -plane at  $f = 9.6$  GHz at  $z = 0.75\lambda_0$ . (c) 2D field distribution over the  $xz$ -plane at  $f = 9.6$  GHz at  $y = 0$ . Courtesy of Mauro Ettore [235].

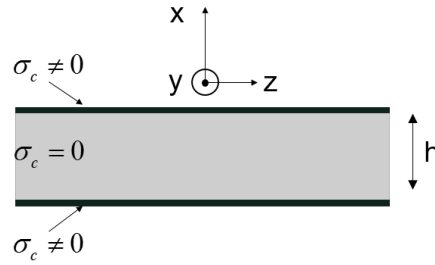


Figure 5.9.: 2-D section of a PPW with lossy metallic plates.

completeness, the two-dimensional representation of  $E_z$  along the  $xy$ -plane (at  $z = 0.75\lambda_0$ ) and the  $xz$ -plane (at  $y = 0$ ) are reported in Figs. 5.8(b) and 5.8(c), clearly showing the distinctive ring-shaped profile of a zeroth-order Bessel beam.

#### 5.2.4 Millimeter-wave design

In [224] are reported very convenient design formulas to get the values of the surface impedance and the thickness of the cavity in order to obtain a given  $k_\rho$  (which in turn determine the focusing features of the Bessel beam, i.e., the null-to-null beamwidth and the nondiffractive range). However, if one tries to use these formulas to design a similar Bessel beam launcher in the millimeter-wave range, these equations would provide unpractical values, such as *i*) extremely thin substrates and *ii*) quite low values of the impedance. Regarding to *i*), the small thickness of the substrate may pose severe issues in terms of attenuation due to ohmic losses. Indeed, considering the case of a parallel-plate waveguide (PPW) whose plates (separated by a distance  $h$ ) are characterized by a finite conductivity  $\sigma_c$  (see Fig. 5.9), the attenuation constant due to ohmic losses of the TEM mode propagating inside the waveguide is given by [157]:

$$\alpha_c = \frac{1}{h} \sqrt{\frac{f}{c\eta_0\sigma_c}}. \quad (5.20)$$

It is clear from Eq. (5.20) and Fig. 5.10 that  $\alpha_c$  increases as  $f$  increases and  $h$  decreases, thus highlighting the unavoidable difficulties of an efficient design of a low-profile (i.e.,  $h \ll \lambda_0$ ) Bessel-beam launcher at millimeter waves. Regarding to *ii*), a very low value of the surface impedance may pose significant problems for the impedance synthesis through an array of square patches. As is known, a PRS constituted by an array of square patches has a capacitive behavior [50], [52]. This means that, in order to get a very low value of impedance, the equivalent capacitance of the sheet must increase, and in turn the distance between the patches might be very small. Unfortunately, the tolerances of PCB technology do not allow to etch the metallic

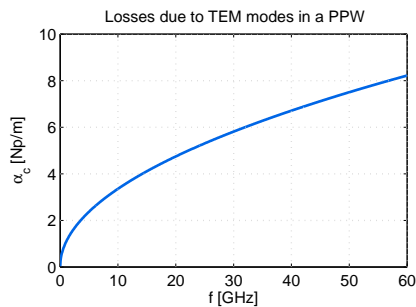


**Figure 5.10:**  $\alpha_c$  vs. frequency ( $f$ ). At  $f = 40$  GHz the attenuation constant of the TEM mode propagating in a PPW with copper plates reaches the value of 7 Np/m.

patches with edge-to-edge distances smaller than  $50 \mu\text{m}$ , putting a lower-bound to the minimum achievable values for such a PRS.

Just to give a practical example, let re-design the Bessel-beam launcher described in the previous paragraph [224] at  $f = 40$  GHz by simply frequency scaling. As a small difference with the previous design, let us consider a dielectric of permittivity  $\epsilon_r = 2.17$  (which is a common value for the permittivity of Teflon in the microwave range [157]) filling the LRW. This choice is motivated by our intention to extend the current design based on the fundamental LW mode to higher-order modes<sup>3</sup>. Under these conditions, the application of Eqs. (37)-(38) in the Appendix of [224] for  $k_\rho = 0.8 - j0.03$ ,  $\epsilon_r = 2.17$  and  $f = 40$  GHz gives the following values for the impedance sheet  $Z_s$  and the substrate thickness  $h$ :

$$Z_s = -j7 \Omega, \quad (5.21)$$

$$h = 30 \mu\text{m}. \quad (5.22)$$

On one hand, the value of  $h = 30 \mu\text{m}$  leads to very high losses, as can be inferred by evaluating Eq. (5.20) for a TEM mode in a PPW made of copper ( $\sigma_c \simeq 59.6 \text{MS/m}$ ) at  $f = 40$  GHz (see Fig. 5.9). On the other hand, the minimum value of the surface impedance achievable with an array of double-layered interleaved square patches at 40 GHz with periodicity  $p = \lambda_0/10$  is  $Z_s \simeq -25 \Omega$ . These results have been obtained by a parametric HFSS simulation in which we have tried different designs by changing the gap  $g$  between the patches up to the PCB tolerance of  $50 \mu\text{m}$  (see Fig. 5.11).

From this numerical example, we have concluded that a simple frequency-scaling law of a Bessel beam launcher is not possible at millimeter waves. A potential work-around is represented by the possibility to use a thicker substrate with the consequent excitation of higher-order leaky-wave modes. However, if one properly designs the structure, it is still possible to find a frequency range where the *modal coupling* between the propagating modes is prevented, and the generation of Bessel beam possible.

<sup>3</sup> Eq. (5.17) reveals that for air-filled PPW higher-order SWs never propagate. Note that LW modes can be thought as analytical continuations in the complex plane of the corresponding SW modes.



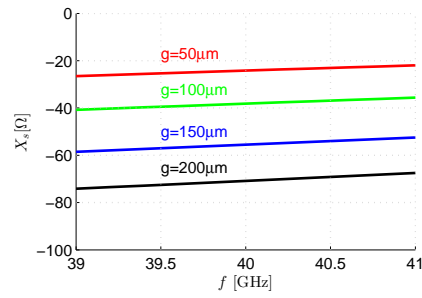


**Figure 5.11.:**  $X_s$  vs.  $f$  for a homogenized PRS constituted by a periodic ( $p = \lambda_0/10$ ) array of double-layered interleaved metallic square patches. The value of the surface impedance is calculated for different values of the distance between the patches ranging from  $g = 200 \mu\text{m}$  to  $g = 50 \mu\text{m}$ , which is the maximum tolerance for PCB technology.

Such an investigation requires a thorough modal analysis and a completely new approach for establishing the design rules of the LRW. As a matter of fact, the current ones [224], [235] assume that only the fundamental leaky mode is propagating inside the waveguide. To this purpose, in the following Section 5.3 the analysis, design, prototyping and measurement of a millimeter-wave Bessel-beam launcher working at 40 GHz with the first higher-order TM leaky mode is carefully discussed.

### 5.3 MILLIMETER-WAVE BESSEL-BEAM LAUNCHERS

In 5.2.1, Eq. (5.17) revealed us that for  $\epsilon_r \neq 1$  the single-mode operation of the launcher in [224] and [235] restricts the separation between the PRS and ground plane of the LRW to thicknesses much smaller than the operating wavelength  $h \ll \lambda_0$ . Moreover, it has been seen in 5.2.4 that the application of the frequency-scaling law to design the structure in the millimeter-wave range would require extremely thin waveguides (e.g., a thickness of the dielectric substrate equal to  $30 \mu\text{m}$  at  $f = 40 \text{ GHz}$ ) and PRS with patterning below the default tolerance of PCB technology ( $\sim 50 \mu\text{m}$ ) leading to restrictively high ohmic losses [157] and practical mechanical problems.

For all these reasons, here we propose a millimeter-wave Bessel-beam launcher whose radiation mechanism is based on higher-order TM leaky modes rather than the fundamental ones [224], [235]. The proposed structure is a dielectric-filled LRW covered with a capacitive sheet (see Fig. 5.12 [206]). In contrast to the previous designs [224], [235], larger separation distances (on the order of half the wavelength at the operating frequency of 40 GHz) are considered between the ground plane and the PRS. In addition, the dielectric filling the LRW is no longer a foam<sup>4</sup>, but a Teflon dielectric material ( $\epsilon_r \simeq 2.1$ ) [157]. The launcher can then support *higher-order leaky waves* and possibly *surface waves*. A completely novel design approach is thus proposed based on dispersion analysis. Suitable closed-form equations are derived for calculating the design parameters that ensure the generation of propagating Bessel beams at the desired operating point (which is defined by the value of  $\hat{k}_\rho$  at the operating frequency  $f_0$ ).

The use of higher-order modes requires a frequency range where the presence of lower-order modes and possible surface waves does not affect the pattern of the generated Bessel beam. A bandwidth of operation of the proposed structure where the simultaneous presence of *lower-order* and *higher-order leaky waves*, as well as *surface waves* can be avoided is then analytically derived and verified by full-wave simulations with COMSOL Multiphysics [276].

The proposed concept and design relations are experimentally validated with a prototype operating at 38.3 GHz, which is fabricated using a standard Printed Circuit Board (PCB) fabrication process. Measurements of the vertical electric field demonstrate that, within the considered band (38-39.5 GHz), the generated Bessel beam presents a stable spot size. These results are discussed in connection to the generation of polychromatic localized waves since they are basically combination of propagating Bessel beams in a defined frequency range [191], [197], [263]. This would be the object of the last Chapter 6.

<sup>4</sup> In [235] a Rohacell foam substrate has been used [275].

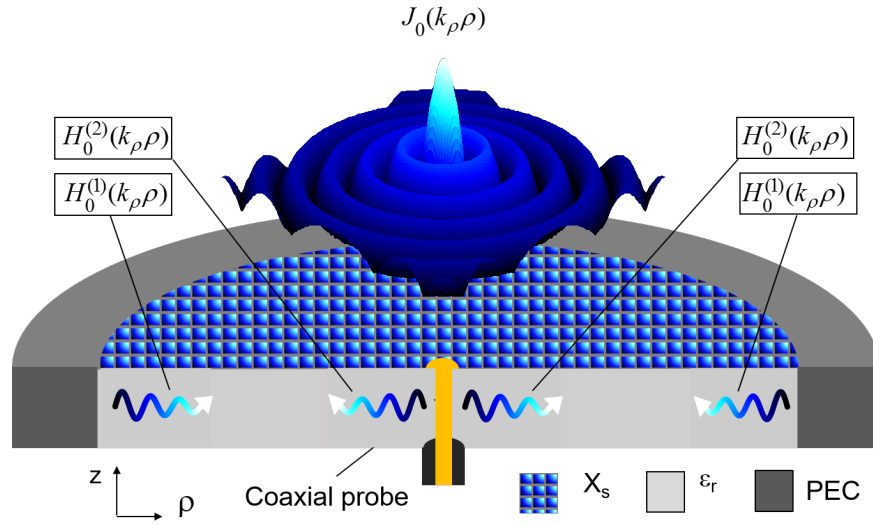


**Figure 5.12:** Illustration of the millimeter-wave Bessel-beam launcher under consideration. The blue arrows show the outward and inward Hankel waves excited by a central coaxial probe. The constructive interference of these cylindrical waves creates the Bessel beam profile.

This Section 5.3 is organized as follows. In 5.3.1, a modal analysis is outlined and used to derive design equations for the launcher operating with higher-order modes. The maximum achievable bandwidth of the device is also provided. In 5.3.2 the proposed equations are applied to design a millimeter-wave Bessel-beam launcher working at 38.3 GHz. The proposed design is validated through full-wave simulations to assess the consistency of this novel theoretical approach. In 5.3.4 the prototype is reported, and measurement results are shown validating the design. Finally, in 5.3.5, we discuss the features of this device are in view of its use as an X-wave launcher.

### 5.3.1 Design of the structure

In order to investigate the modal properties of the waves supported by the structure in Fig. 5.12, we solve the dispersion equation of the radial waveguide for TM modes [224], [151], as has been done in 5.2.2. In the general case of a dielectric-filled leaky radial waveguide the dispersion equation can be expressed by means of the standard transverse resonance technique [8], [277] as

$$Y_0 + Y_s - jY_1 \cot(k_{z1}h) = 0, \quad (5.23)$$

where  $Y_1 = \omega\epsilon_0\epsilon_r/k_{z1}$ ,  $Y_0 = \omega\epsilon_0/k_z$  are the characteristic admittances in the dielectric and in the air, respectively and  $Y_s$  is the sheet admittance;  $k_{z1} = \sqrt{k_0^2\epsilon_r - k_\rho^2}$  and  $k_z = \sqrt{k_0^2 - k_\rho^2}$  are the longitudinal wavenumbers

in the dielectric and in the air, respectively, which are generally complex quantities ( $k_z = \beta_z - j\alpha_z$ ,  $k_{z1} = \beta_{z1} - j\alpha_{z1}$ ).

The values of  $Y_s$  and  $h$  can be found through Eq.(5.23) once the transverse  $k_\rho$  or the longitudinal  $k_z$  propagation constants of the required Bessel beam are fixed, together with the operating frequency  $f_0$ , and the dielectric constant  $\epsilon_r$ . This procedure has been already used in [224] to get the sought design rules of a microwave Bessel-beam launcher working with the fundamental leaky mode. However, those equations (viz., Eqs. (37)-(38) in the Appendix of [224]) were derived under the assumption of  $k_{z1}h \ll 1$ , which implies  $h \ll \lambda_0$ . Here, the higher-order mode operation requires that  $h \simeq \lambda_0$ . As a consequence, the previous design equations no longer hold. To this purpose, in the first paragraph, more general equations are derived which allow for designing Bessel beam launchers of almost arbitrary thicknesses and working with leaky modes of any order.

In the second paragraph, the knowledge of these values of  $Y_s$  and  $h$  will allow us for solving the dispersion equation for all the modes (either *surface waves* or *leaky waves*) supported by the structure. As expected, when the dispersion equation is solved with the values of  $Y_s$  and  $h$  found through the new expressions derived in the first paragraph, they give rise to the previously fixed  $k_\rho$  at the operating frequency  $f_0$ . These modal and dispersion analyses will reveal us the range of frequency in which the modal coupling is prevented.

Finally, in the third paragraph, we will show that it is possible to establish *a priori* the *maximal available bandwidth* of the structure, i.e., the range of frequency in which the simultaneous presence of more than one relevant mode (i.e., which may contribute to radiation if properly excited) is avoided. Approximate closed-form expressions are found in a heuristic way.

### Design rules

When thicker substrates are considered we can no longer assume that  $k_{z1}h \ll 1$ . However, for higher-mode operation  $h \simeq \lambda_0/2$  is usually assumed, so that  $k_{z1}h \simeq \pi$ . Under this hypothesis, the argument of the cotangent function in Eq. (5.23) is close to a multiple  $n = 0, 1, 2, \dots$  of  $\pi$ , and hence the cotangent function in (5.23) can be approximated by the first term of its *Laurent Series expansion* close to  $n\pi$ ,

$$Y_0 + Y_s - \frac{jY_1}{k_{z1}h - n\pi} = 0. \quad (5.24)$$

Furthermore, assuming that the impedance sheet is lossless  $Y_s = -jX_s^{-1}$ , the approximate dispersion equation (5.24) becomes

$$\frac{1}{\hat{k}_z} - j\frac{\eta_0}{X_s} - \frac{j\epsilon_r}{\hat{k}_{z1}} \left( \frac{1}{k_0\hat{k}_{z1}h - n\pi} \right) = 0, \quad (5.25)$$

where  $(\hat{\cdot})$  refers to the usual normalization with respect to the vacuum wavenumber  $k_0$ , whereas  $n$  is related to the modal longitudinal (i.e., along  $z$ ) integer index. Following the same procedure outlined in [224], we can rearrange the terms in (5.25) and solve for  $X_s$ ,

$$X_s = -\frac{\hat{k}_{z1}}{\hat{k}_z \epsilon_r} (jX_s + \eta_0 \hat{k}_z) (k_0 \hat{k}_{z1} h - n\pi). \quad (5.26)$$

After some algebraic manipulations, a quadratic equation in  $h$  is obtained,

$$a_2 h^2 + a_1 h + a_0 = 0, \quad (5.27)$$

where

$$\begin{aligned} a_2 &= k_0^2 [2\hat{\alpha}_{z1} \hat{\beta}_{z1} w_1 - (\hat{\beta}_{z1}^2 - \hat{\alpha}_{z1}^2) z_1], \\ a_1 &= k_0 \{ 2\epsilon_r \hat{\alpha}_{z1} \hat{\beta}_{z1} (\hat{\beta}_z^2 + \hat{\alpha}_z^2) \\ &\quad - n\pi [2\hat{\alpha}_{z1} \hat{\beta}_{z1} w_2 + \hat{\alpha}_{z1} w_1 - z_2 (\hat{\beta}_{z1}^2 - \hat{\alpha}_{z1}^2) - z_1 \hat{\beta}_{z1}] \}, \\ a_0 &= -n\pi [\epsilon_r \hat{\alpha}_{z1} (\hat{\beta}_z^2 + \hat{\alpha}_z^2) + n\pi (\hat{\beta}_{z1} z_2 - \hat{\alpha}_{z1} w_2)], \end{aligned} \quad (5.28)$$

with:

$$\begin{aligned} w_1 &= (-\hat{\alpha}_z \hat{\alpha}_{z1}^2 + \hat{\alpha}_z \hat{\beta}_{z1}^2 - 2\hat{\alpha}_{z1} \hat{\beta}_{z1} \hat{\beta}_z), \\ w_2 &= (\hat{\beta}_{z1} \hat{\alpha}_z - \hat{\beta}_z \hat{\alpha}_{z1}), \\ z_1 &= (\hat{\beta}_z \hat{\beta}_{z1}^2 - \hat{\beta}_z \hat{\alpha}_{z1}^2 + 2\hat{\alpha}_{z1} \hat{\alpha}_z \hat{\beta}_{z1}), \\ z_2 &= (\hat{\beta}_{z1} \hat{\beta}_z + \hat{\alpha}_{z1} \hat{\alpha}_z). \end{aligned} \quad (5.29)$$

Finally, by solving (5.26) and (5.27) we get:

$$h = \frac{-a_1 \pm \sqrt{a_1^2 - 4a_2 a_0}}{2a_2}, \quad (5.30)$$

$$X_s = -\frac{\eta_0 \hat{\alpha}_{z1} (2k_0 h \hat{\beta}_{z1} - n\pi) (\hat{\beta}_z^2 + \hat{\alpha}_z^2)}{k_0 h z_1 - n\pi z_2}. \quad (5.31)$$

It is easy to verify that for  $n = 0$  and  $\epsilon_r = 1$  these results coincide with those presented in [224] for the lowest-order leaky-mode launcher. However, in contrast to earlier works [219], [224], higher-order leaky-wave Bessel-beam launchers can generate nondiffractive radiation for either inductive ( $X_s > 0$ ) or capacitive ( $X_s < 0$ ) (see Eqs. (5.30) and (5.31)) and corresponding substrate heights. As an example, for the first  $n = 1$  higher-order leaky mode with  $\hat{k}_\rho = 0.8 - j0.03$  at  $f = 40$  GHz, Eqs. (5.30) and (5.31) give the following two possibilities: *a*) an inductive impedance  $X_s = 47.3\Omega$  with a thickness  $h = 2.82$  mm, or *b*) a capacitive impedance  $X_s = -53.3\Omega$  with a thickness  $h = 3.25$  mm. This gives designers an additional degree of freedom during the design process. It is worth here to emphasize that only free-standing inductive surface impedances cannot support TM leaky waves [28]. In this case, the presence of a ground plane adds a capacitive effect

to the equivalent impedance at the interface, and hence a TM leaky wave can actually be supported by an inductive surface impedance, as correctly revealed by Eqs. (5.30) and (5.31).

### Dispersion and modal analysis

The modes supported by the LRW are computed by numerically solving Eq. (5.23) [23]. The values of  $X_s = -25 \Omega$  and  $h = 3.175$  mm are derived using Eqs. (5.30), and (5.31) for a tangential wavenumber  $k_\rho = (0.8 - j0.007)k_0$  at  $f \simeq 40$  GHz and  $\epsilon_r = 2.17$ . A rigorous application of Eqs. (5.30), and (5.31), would give  $X_s = -24.57 \Omega$  and  $h = 3.139$  mm (or, for the inductive case  $X_s = 22.97 \Omega$  and  $h = 2.928$  mm). Here, we have used slightly different values for taking into account the commercial availability of PTFE substrates [278] whose nearest available thickness is 3.175 mm.

However, for a wide range of parameters the dispersion diagrams of the structure are qualitatively very similar. For convenience, we have decided to present the numerical results related to the choice of parameters that have been used for the realized prototype described in 5.3.2 and 5.3.3. Hence, this paragraph does not only give a description of the dispersive and modal properties of a generic millimeter-wave Bessel-beam launcher, but also furnishes the theoretically expected dispersive analysis of the proposed prototype developed in paragraphs 5.3.2 and 5.3.3.

In Figs. 5.13(a) and 5.13(b) the normalized phase constant  $\beta_\rho/k_0$  and attenuation constant  $\alpha_\rho/k_0$  as functions of the frequency  $f$  are reported for all the complex modes (either proper  $\alpha_z > 0$  or improper  $\alpha_z < 0$  [2], [3]) supported by the structure. Specifically, three leaky-wave (LW) modes are observed. Note that, in the limit of  $k_\rho \rightarrow 0$ , Eq. (5.23) gives an approximate expression for the LW cutoff frequencies ( $\hat{\beta}_\rho \simeq \hat{\alpha}_\rho \ll 1$ ):

$$f_n^{\text{LW}} \simeq \frac{c}{2\pi h \sqrt{\epsilon_r}} \cot^{-1} \left( \frac{-\eta_0}{X_s \epsilon_r} \right) + \frac{nc}{2h \sqrt{\epsilon_r}}. \quad (5.32)$$

The phase constant  $\beta_\rho$  of each leaky-wave mode above cutoff varies in the range approximately from 0 to  $k_0$ . As is typical (see 1.2.3), slightly after  $\beta_\rho > k_0$ , the two conjugate leaky poles coalesce (the physical one with  $\alpha_\rho > 0$  and the non-physical one with  $\alpha_\rho$ , not reported here for readability purposes of Fig 5.13(a)) in the so-called *splitting-point* (also known as *fold singular point* [279] in the frame of *Morse critical points theory* [280], [281]) and afterwards give rise to a couple of purely real improper (nonphysical) poles. Specifically, one real improper pole (with a  $\beta_\rho$  greater than  $k_0$ ) has a decreasing  $\beta_\rho$  with respect to the frequency, until it reaches the value  $\beta_\rho = k_0$ . At this point, the real improper mode becomes a real proper pole, i.e. a physical surface wave guided at the interface, whose  $\beta_\rho$  tends to the asymptotic value of  $k_0 \sqrt{\epsilon_r}$  [151], [154], [162], [163]. The cutoff frequency of this surface-wave (SW) mode can be determined by replacing  $\beta_\rho$  with  $k_0$  in the dispersive equation.

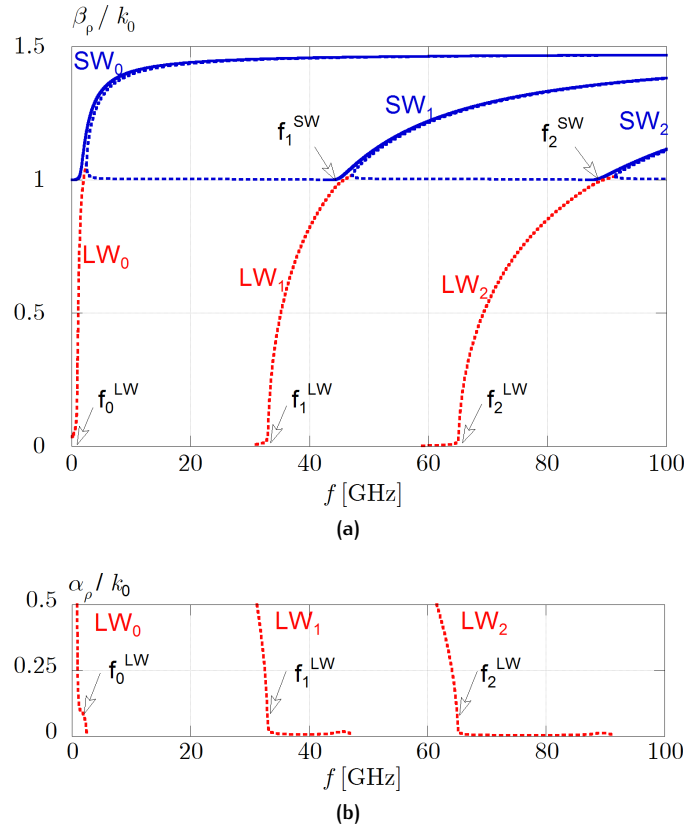


**Figure 5.13:** (a) Normalized phase constant and (b) normalized attenuation constant vs. frequency  $f$  up to 100 GHz for the first three TM of a LRW as in Fig. 5.3. The solid and dashed lines denote the dispersion curves for the proper and improper modes, respectively. The blue and red curves represent the dispersion curves for the real and complex modes, respectively. Hence surface-wave (SW) modes are shown by black solid lines, whereas the leaky-wave (LW) modes are shown by grey dashed lines. In these plots, it is assumed that  $X_s = -25 \Omega$ ,  $\epsilon_r = 2.17$ ,  $h = 3.175$  mm [153].

We note here that a zeroth-order surface wave propagates from DC frequency, since

$$f_n^{\text{SW}} \simeq \frac{nc}{2h\sqrt{\epsilon_r - 1}}, \quad (5.33)$$

whereas the expression for the first-order  $n = 1$  SW cutoff frequency coincides with Eq. (5.17) in 5.2.1.

It is also worth noting that the condition expressed by Eq. (5.11) which requires the weak attenuation of the relevant leaky modes that is necessary to efficiently combine the incident and the reflected cylindrical waves composing the Bessel beam, is satisfied by any leaky mode only for frequencies  $f > f_n^{\text{LW}}$  (see Fig. 5.13(b)).

Moreover, it is known [2], [3] that slow improper waves (i.e., waves with  $\beta_\rho \geq k_0$  and  $\alpha_z < 0$ ) do not actually contribute to the aperture field, but conversely the excitation of proper surface waves can deteriorate the profile of the generated Bessel beam. As a consequence, the proper definition

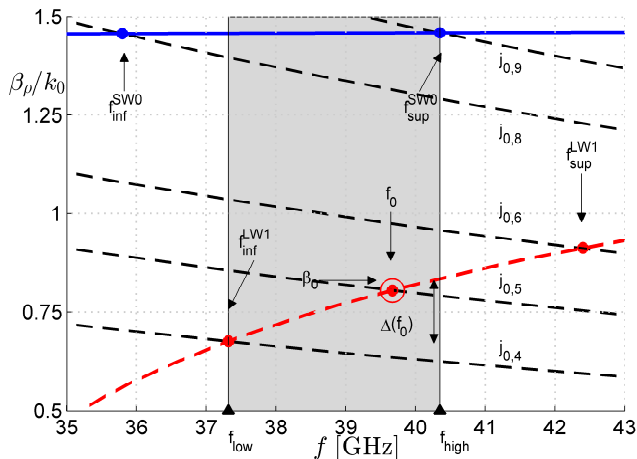


Figure 5.14.: Dispersion curves (SW and LW in blue solid and red dashed lines, respectively) for the design of the higher-order launcher prototype. The operating points are given by the intersections of the fast leaky-wave modes and the hyperbolic curves given by the Bessel zeros (black dashed lines). Once the operating point is chosen, the operating bandwidth (highlighted gray region) is fixed by the closest intersections of either the fast leaky-wave or the surface-wave modes. The parameters used in Fig. 5.13 are also assumed here.

of a frequency band where a single-mode leaky-wave propagation can be obtained, is of fundamental importance.

#### Determination of the maximal available bandwidth

As has been noted in Section 5.2, the resonance needed to produce a Bessel beam as a superposition of two Hankel waves of inward and outward type, is obtained by placing a circular metallic rim at a radial distance  $\rho_{ap}$  corresponding to a null of the required zeroth-order Bessel function, i.e.

$$\frac{\beta_\rho^{(q)}}{k_0} = \frac{j_{0,q}}{\rho_{ap}k_0}, \quad q = 1, 2, \dots \quad (5.34)$$

where  $j_{0,q}$  is the  $q$ -th zero of  $J_0$ . As we have seen in paragraph 5.2.2, the above relation is represented by  $q$  hyperbolic curves (dashed lines in Fig. 5.14). The intersections with the first higher-order ( $n = 1$ ) leaky-wave ( $LW_1$ ) and zeroth-order ( $n = 0$ ) surface-wave ( $SW_0$ ) phase constants (see also Fig. 5.13(a)) identify a grid of resonant modes of the radial waveguide with a metallic rim, as shown in Fig. 5.14 for  $\rho_{ap} = 22.3$  mm. Since improper slow waves do not contribute to radiation, the two improper branches emerging after the SW cutoffs (see blue dashed lines in Fig. 5.13(a)) are not reported in Fig. 5.14. Indeed, their presence would not affect the determination of the *maximal available bandwidth* as has been previously defined (see the end of the first paragraph in 5.3.1).

The intersection of the desired radial resonance (here  $q = 5$ ) with the required leaky-wave mode (here  $n = 1$ ) defines the operating frequency  $f_0$  of



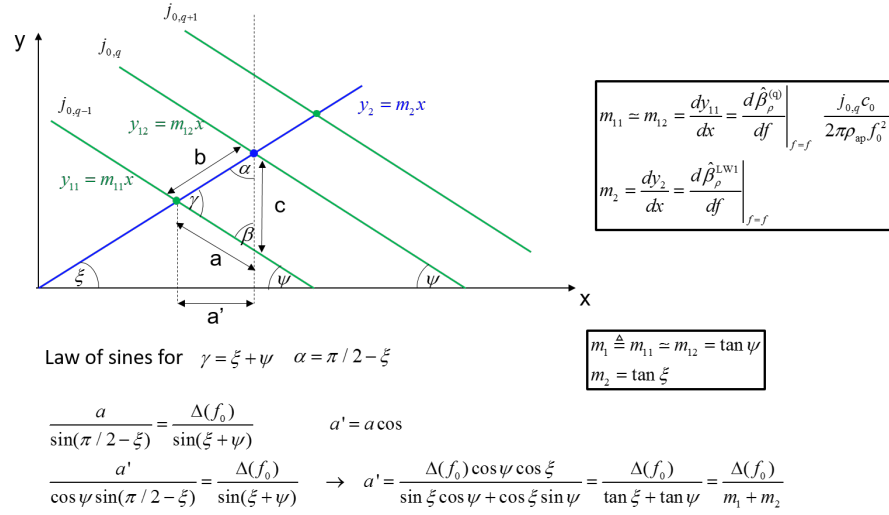


**Figure 5.15.:** Geometrical interpretation of the problem in Fig. 5.14. The blue dot represents the operating point given by the intersection between  $q = 5$  and  $n = 1$  dispersion curves. The green dots represent the operating points given by the intersection between  $n = 1$ , and  $q = 4, 6$  dispersion curves. Once  $a'$  is found, it can be used to calculate both  $f_{\text{inf}}^{\text{LW1}}$  and  $f_{\text{sup}}^{\text{LW1}}$ , thanks to the symmetry of the problem.

the Bessel-beam launcher, and the operating phase constant  $\hat{\beta}_0 = \hat{\beta}(f_0)$ . In addition, we can define the *maximal available bandwidth*  $B_{\text{av}}$  for single-mode operation as the smallest frequency range containing  $f_0$  and delimited at its ends by adjacent intersections with the adjacent resonant modes. It should be stressed that this *maximal available bandwidth* should not be confused with the *practical bandwidth* of the launcher, which will likely be narrower and limited by the input impedance match and the frequency dependence of the artificial surface.

As is manifest from Fig. 5.14, the lower bound of  $B_{\text{av}}$  is given by  $f_{\text{low}} = \max\{f_{\text{inf}}^{\text{SW0}}, f_{\text{inf}}^{\text{LW1}}\}$ , whereas the upper bound is given by  $f_{\text{high}} = \min\{f_{\text{sup}}^{\text{SW0}}, f_{\text{sup}}^{\text{LW1}}\}$ . These four frequencies can be expressed through approximate analytical expressions, by taking advantage of the geometrical interpretation of Fig. 5.15. In fact by exploiting the asymptotic periodicity of the zeros of the Bessel functions [271], i.e.

$$j_{0,q+1} - j_{0,q} \simeq \pi, \quad (5.35)$$

from Eq. (5.34) the vertical distance  $\Delta(f)$  between two consecutive hyperbolas at a given frequency  $f$  is given by

$$\Delta(f) = \frac{j_{0,q+1}}{\rho_{ap} k_0} - \frac{j_{0,q}}{\rho_{ap} k_0} \simeq \frac{c_0}{2\rho_{ap} f}. \quad (5.36)$$

By assuming a nearly linear leaky-wave phase constant between  $f_{\text{inf}}^{\text{LW1}}$  and  $f_{\text{sup}}^{\text{LW1}}$ , we get (see Fig. 5.15)

$$f_{\text{inf,sup}}^{\text{LW1}} = f_0 \pm \frac{\Delta(f_0)}{m_1 + m_2}, \quad (5.37)$$

where

$$m_1 = \left. \frac{d\hat{\beta}_\rho^{\text{LW1}}(f)}{df} \right|_{f_0}, \quad m_2 = \frac{j_{0,q}c_0}{2\pi\rho_{\text{ap}}f_0^2}. \quad (5.38)$$

Moreover, if the fundamental surface-wave phase constant is close to the asymptotic value  $\hat{\beta}_\rho^{\text{SW0}} \simeq \sqrt{\varepsilon_r}$ , we have

$$f_{\text{inf}}^{\text{SW0}} = \frac{j_{0,r}c_0}{2\pi\rho_{\text{ap}}}, \quad f_{\text{sup}}^{\text{SW0}} = \frac{j_{0,r+1}c_0}{2\pi\rho_{\text{ap}}}, \quad (5.39)$$

where

$$r = \left\lfloor \frac{\rho_{\text{ap}}k_0\delta\beta^{\text{SW0}}(f_0)}{\pi} \right\rfloor, \quad (5.40)$$

$\delta\beta^{\text{SW0}}(f_0) = \sqrt{\varepsilon_r} - \hat{\beta}_0$  being the phase difference between the leaky wave and the fundamental surface wave at the operating frequency  $f_0$ , and  $\lfloor \cdot \rfloor$  is the floor function.

In the next Section 5.3.2, the theoretical analysis developed so far will be validated through full-wave simulations. The performance of the prototype designed with the equations provided in the first paragraph of 5.3.1 will be investigated within the theoretical maximal available bandwidth, namely from 37.3 GHz to 40.3 GHz. This frequency domain analysis will allow us to assess the formulas for the maximum available bandwidth analytically derived above.

### 5.3.2 Numerical validation

In order to validate the results of the previous paragraph, a Bessel beam with  $k_\rho = (0.8 - j0.007)k_0$  around the operating frequency of  $f_0 = 39.7$  GHz has been designed with  $h$ ,  $X_s$  given by Eqs. (5.30) and (5.31), respectively, fixing the radial ( $q$ ) and vertical ( $n$ ) order of the resonances to  $q = 5$  (i.e., the fifth zero of the  $J_0$ ), and  $n = 1$  (viz., the first higher-order LW mode). This choice has led to the following set of parameters:

$$\begin{aligned} \rho_{\text{ap}} &= 22.3 \text{ mm}, \\ h &= 3.175 \text{ mm}, \\ X_s &= -25 \Omega, \end{aligned} \quad (5.41)$$

where we have considered a dielectric substrate with a permittivity  $\varepsilon_r = 2.17$  as in Section 5.3.1. These values lead to the desired operating point with a relative accuracy of 0.3% (see Fig. 5.16), in agreement with the small-argument first-order approximation of the cotangent function made in 5.3.1.

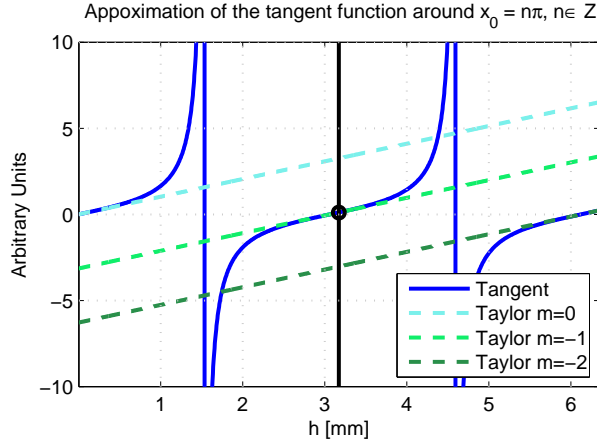


**Figure 5.16.:** Approximation of the tangent function  $\tan(k_{z1}h)$  vs.  $h$  with  $(k_{z1}h - n\pi)$  for  $n = 0, 1, 2$  when  $k_{z1} = k_0\sqrt{\epsilon_r - \hat{k}_\rho^2}$  with  $\hat{k}_\rho = 0.8$ . As expected, at  $h = 3.175$  mm the approximation is very good, leading to percentage error of 0.3%.

Note also that for  $\rho_{ap} = 22.3$  mm we get  $\alpha_\rho \rho_{ap} \simeq 0.13 \ll 1$  as required by Eq. (5.11).

The dispersion diagram of the structure in the range of interest was already shown in Fig. 5.14. As we have calculated in the third paragraph of 5.3.1 the single-mode propagation is obtained between  $f_{low} = 37.3$  GHz and  $f_{high} = 40.3$  GHz, respectively.

This operating bandwidth has been numerically validated using COMSOL Multiphysics [276]. Specifically, a 2-D section of the structure has been simulated enforcing an axial symmetry along the  $z$ -axis and a transition boundary condition (TBC) over the aperture to model the presence of the impedance sheet (see Fig. 5.17(a) and (b)). As is shown in Fig. 5.18(a), at the central frequency  $f_0 = 39.7$  GHz, the contour plot of the longitudinal  $E_z$  electric field component, takes the expected zeroth-order Bessel over the aperture plane and up to the nondiffractive range, equal to  $16.4$  mm  $\simeq 2.2\lambda_0$

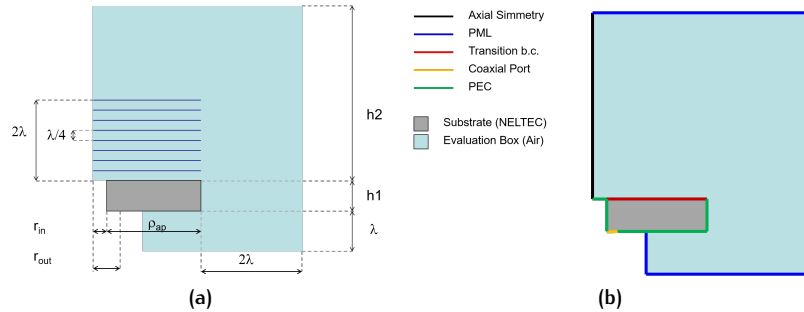


**Figure 5.17.:** (a) Geometry of the COMSOL model of the prototype. The size of the evaluation box is set slightly larger than necessary in order to avoid spurious reflections from the PML boundary conditions. (b) Boundary conditions setting of the COMSOL model of the prototype.

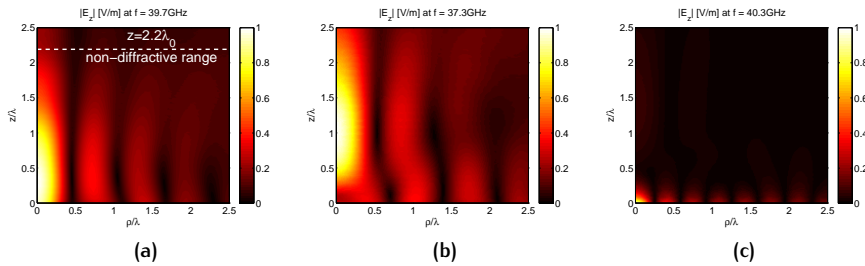


Figure 5.18.: Contour plot of the electric field  $|E_z|$  along the  $\rho z$ -plane for the mm-wave launcher under analysis at (a)  $f = 39.7$  GHz, (b)  $f = 37.3$  GHz, and (c)  $f = 40.3$  GHz.

( $\lambda_0 = 7.5$  mm, at  $f_0 = 40$  GHz), where the sidelobes are no longer clearly distinct, and the main beam starts to widen.

The behavior of  $E_z$  along the  $\rho z$ -plane at both the lower  $f_{\text{low}}$  and higher  $f_{\text{high}}$  limits of the maximal available bandwidth, is also shown in Figs. 5.18(b) and 5.18(c), respectively, in order to validate the closed-form expressions (5.37) and (5.39) for the bandwidth.

At the lower limit  $f_{\text{low}} = 37.3$  GHz, the radiated  $E_z$  field has a larger beamwidth (see Fig. 5.18(b)). This is due to the smaller transverse propagation constant of the leaky-wave mode which intersects the hyperbolic curve corresponding to  $q = 4$ . At the upper end,  $f_{\text{high}} = 40.3$  GHz, the  $E_z$  radiated field is perturbed by the excitation of a surface wave, and hence no useful focused beam is generated (see Fig. 5.18(c)). However, within the maximal available bandwidth 37.3 – 40.3 GHz, a Bessel beam with a stable spot size can be observed, as confirmed in the following Subsection by experimental tests.

To conclude this Subsection, the 1-D profiles of  $E_z$  along  $\rho$  at different distances  $z$  from the radiating apertures are shown in Fig. 5.19. Note that, as the distance from the aperture increases, the sidelobes present a higher

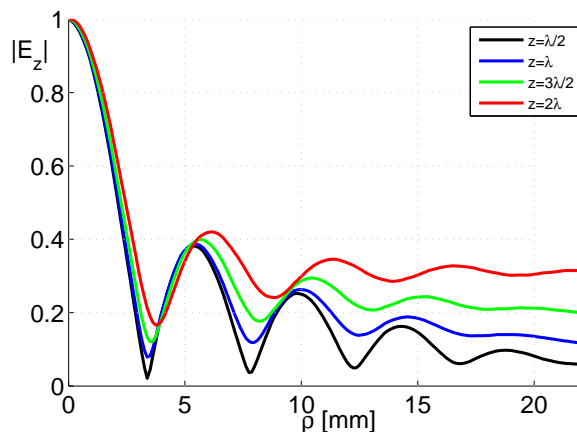


Figure 5.19.: 1-D profile of the normalized electric field  $|E_z|$  at  $f = 39.7$  GHz, for the proposed launcher (parameters as in Fig. 5.13), for various distances  $z = \lambda/2, \lambda, 3\lambda/2, 2\lambda$  from the aperture.

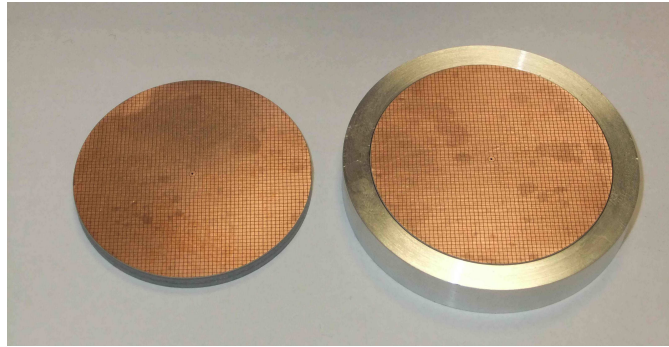


Figure 5.20.: Prototype of the mm-wave leaky-mode Bessel-beam launcher. The feeding probe can be recognized at the center of the structure.

level, whereas the alternation of maxima and minima is progressively less pronounced.

### 5.3.3 Prototype

The Bessel-beam launcher designed in the previous Subsection 5.3.2 has been manufactured (see Fig. 5.20) using a PCB process at IETR, Rennes, France. The LRW consists of a substrate with permittivity  $\epsilon_r = 2.17$  (Neltec NY9217 [278]) and height  $h = 3.175$  mm. The sheet impedance ( $X_s \simeq -25 \Omega$ ) is realized by etching a two-dimensional array of interleaved squared metallic patches [235] (see Fig. 5.21) with a periodicity  $p = 750 \mu\text{m}$  ( $\lambda_0/10$  at  $f_0 = 40$  GHz) and a border distance  $d = 50 \mu\text{m}$  on a double-side patterned substrate of permittivity  $\epsilon_r = 6.15$  (Rogers Duroid 6006) and height  $h_{\text{FSS}} = 0.127$  mm. The patch size has been tuned on HFSS [274] to get the required impedance value  $Z_s = -j25 \Omega$  at the operating frequency  $f_0 = 40$  GHz. Basically, a unit-cell is excited with a Floquet mode impinging with a normal incidence on the patch. The Y-parameters are then re-

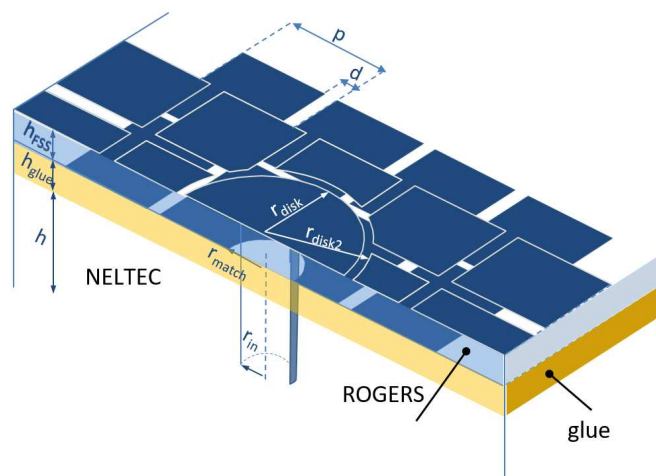
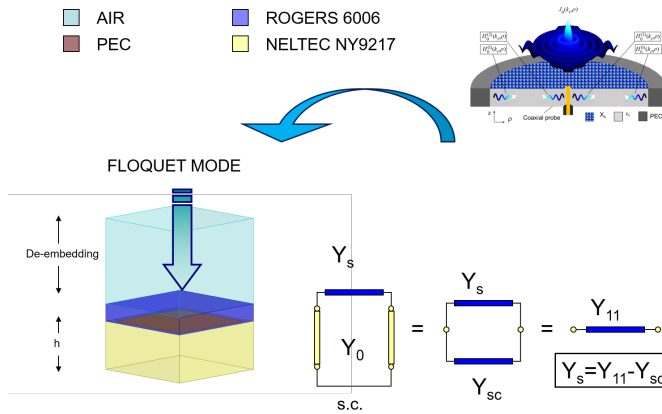


Figure 5.21.: Schematic of the coaxial probe transition used for matching the mm-wave launcher.



**Figure 5.22.:** HFSS unit-cell model for the impedance synthesis of the capacitive sheet. The respect of the homogenization limit  $p \ll \lambda_0 p$  [50] allows for describing the fields with only the fundamental  $n = 0$  Floquet harmonic, and hence only an equivalent transmission-line is required to model the structure.

trieved from the simulation, and the surface impedance is extracted using a simple equivalent transmission-line model [52], [282] (see Fig. 5.22). The impedance sheet has been glued to the NELTEC substrate using an adhesive layer Taconic fastRise FR – 27 – 0030 – 25 [283] with permittivity  $\epsilon_r = 2.78$  and thickness  $h_{\text{glue}} = 86 \mu\text{m}$ .

A commercial connector (SRI Connector Gage 85131100080 [284]) has been used to feed the structure from the back side of the launcher. The geometry of the impedance surface has been modified close to the inner probe of the coaxial connector (see Fig. 5.21) to improve the  $S_{11}$ . In fact, the radius of the metallic disk  $r_{\text{disk1}}$  and its distance from the adjacent patches are critical parameters for the impedance matching (further details can be found in [153]). The stacked structure is enclosed with a circular metallic rim of aluminum with radius  $\rho_{\text{ap}}$ . The final prototype is shown in Fig. 5.20.

### 5.3.4 Measurements

The measurements have been performed in the *Near-Field Test Range* at the IETR, Rennes, France. The prototype has been measured in the frequency range 38 – 39.5 GHz with a frequency step of 100 MHz, and compared with full-wave results of the complete structure performed in HFSS. The S-parameters have been calculated by connecting the measuring probe and the prototype to the Vector Network Analyzer (VNA). For the near-field measurements, the measuring probe has been connected to an  $xyz$  translation stage (see Fig. 5.23) to sample the longitudinal component of the electric field  $E_z$  over a scanning area of 45 mm  $\times$  45 mm with a step of 0.75 mm at six different  $z$ -planes starting from 3.75 mm ( $\lambda_0/2$ ) up to 18 mm ( $5\lambda_0/2$ ), in order to verify the Bessel beam generation. The measuring probe is made of a semi-rigid coaxial cable (UT-85) with the inner conductor extending

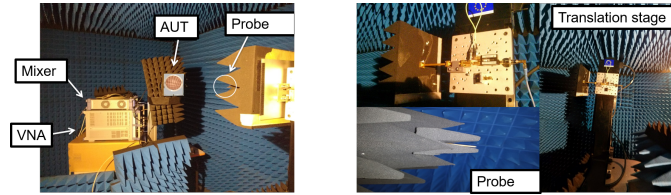


**Figure 5.23.:** Some pictures of the Near-Field Test Range at IETR, Rennes, France. Courtesy of Ioannis Iliopoulos [285]. Note that the antenna under test (AUT) shown in the picture on the left is not our actual prototype which was not mounted on the mast. These pictures are reported just to show the measurement setup.

0.75 mm ( $\lambda_0/10$  at  $f_0 = 40$  GHz) beyond the outer conductor and dielectric. In addition, the  $E_z$  component has been also measured along the  $xz$ -plane ( $\phi = 0^\circ$ ) in order to highlight the overall nondiffractive behavior of the generated Bessel beam within the expected nondiffractive range.

Through measurements, a minimum in the amplitude of the reflection coefficient (which also corresponds to the zero-crossing point of the reflection phase) of the prototype was found at a frequency of  $f_m = 38.3$  GHz as shown in Fig. 5.24(a)-(b). Around this frequency, the measured  $|S_{11}|$  shows a  $-10$  dB fractional bandwidth of approximately 3.7%. It is noted that  $f_m$  is shifted of 2.5% relative to the expected operating frequency  $f_0$ . This frequency shift may be attributed to fabrication tolerances (the interested reader can find more details in [153]).

Contour plots of the measured  $E_z$  component of the electric field above the aperture are shown in Figs. 5.25(a)-(f) at various distances ( $z = 0.5 \lambda_0, 0.75 \lambda_0, \lambda_0, 1.5 \lambda_0, 2 \lambda_0, 2.5 \lambda_0$ , where  $\lambda_0$  is equal to 7.5 mm) from the radiating aperture at the operating frequency 38.3 GHz. An azimuthally symmetric Bessel beam is clearly shown. In particular, it is possible to distinguish the five dark rings corresponding to the five nulls of the Bessel function.

A frequency sweep in the operating frequency range 38 – 39.5 GHz with a frequency step of 300 MHz, of the same contour plots at a fixed distance

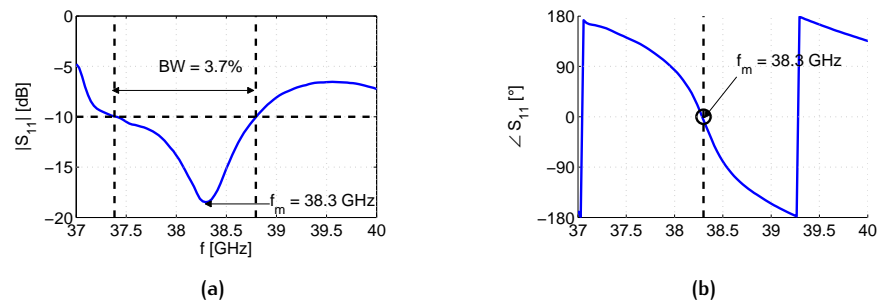


**Figure 5.24.:** (a) Measured reflection coefficient ( $|S_{11}|$  in dB) and (b) reflection phase ( $\angle S_{11}$ ) of the prototype in the frequency range 37 ÷ 40 GHz. The black dashed lines highlight the frequency range for which the return loss is under  $-10$  dB.



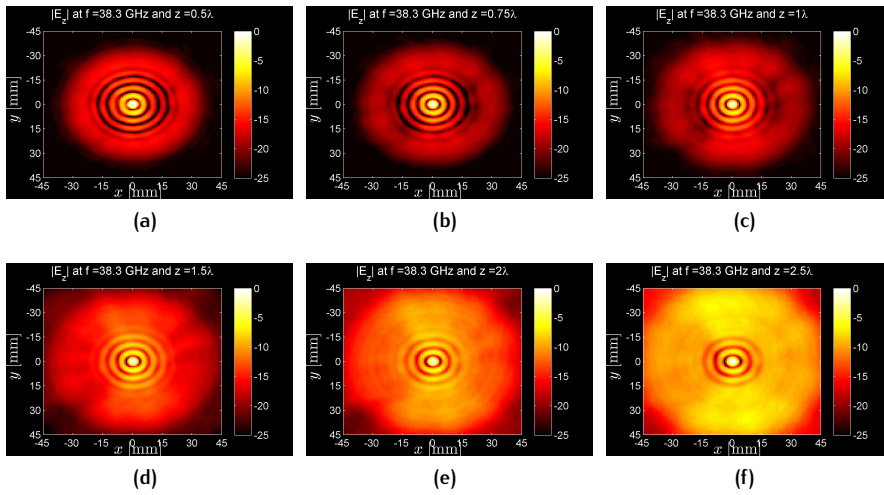


Figure 5.25.: Measured intensity of  $E_z$  along the  $xy$  plane at  $f = 38.3$  GHz at  $z = 0.5\lambda_0, 0.75\lambda_0, \lambda_0, 1.5\lambda_0, 2\lambda_0, 2.5\lambda_0$  from the impedance surface, where  $\lambda_0$  equal to 7.5 mm.

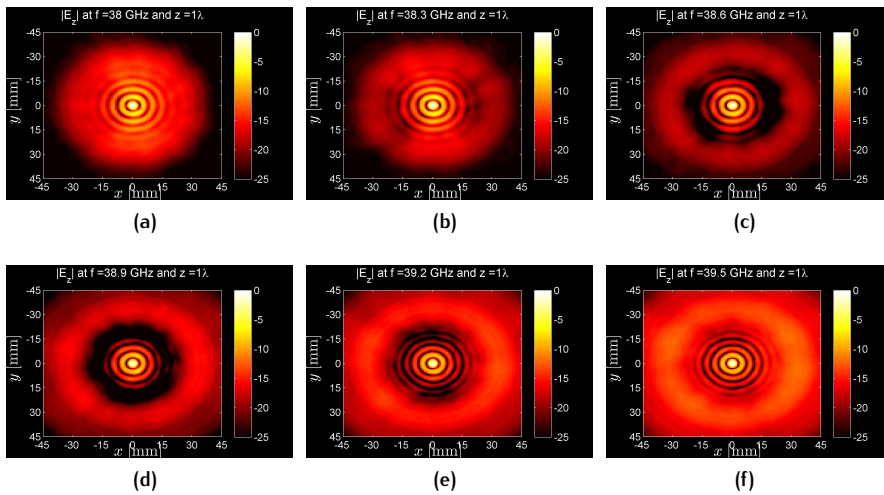
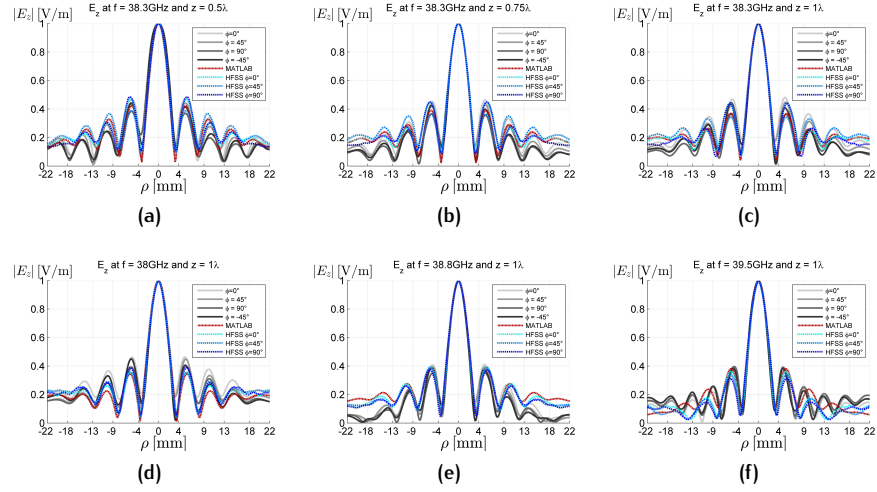


Figure 5.26.: Measured intensity of  $E_z$  along the  $xy$  plane at  $z = \lambda$  at  $f = 38.0$  GHz, 38.3 GHz, 38.6 GHz, 38.9 GHz, 39.2 GHz, 39.5 GHz.

$z = \lambda$  is reported in Figs. 5.26(a)-(f). A comparison with HFSS simulations and numerical results (MATLAB) has also been reported in Figs. (5.27)(a)-(c) at different distances  $z = 0.5\lambda_0, 0.75\lambda_0, \lambda$  at  $f = 38.3$  GHz, and in Figs. (5.27)(d)-(f) at different frequencies  $f = 38$  GHz, 38.8 GHz, 39.5 GHz at  $z = \lambda$ .

Finally, Fig. 5.28 provides the measured  $E_z$  field component along the  $xz$ -plane (almost the same results have been obtained along the  $xy$ -plane, due to the good azimuthal symmetry shown by the measurements) at  $f = 38.0$ GHz, 38.3 GHz, 38.6 GHz, 38.9 GHz, 39.2 GHz, 39.5 GHz. As expected, the spot size represented here by the Half-Power Beamwidth (HPBW) and the Bessel-beam profile are preserved along the axis of propagation up to the nondiffractive range (marked with a white dotted line).





**Figure 5.27:** Comparison between measurements (solid gray lines), simulations (dashed blue lines), and numerical results (red dashed lines). (a)-(c) Normalized  $E_z$  vs.  $\rho$  at  $f = 38.3$  GHz at  $z = 0.5\lambda_0$ ,  $0.75\lambda_0$ ,  $\lambda_0$ . (d)-(f) Normalized  $E_z$  vs.  $\rho$  at  $z = \lambda$  at  $f = 38.0$  GHz,  $38.8$  GHz,  $39.5$  GHz.

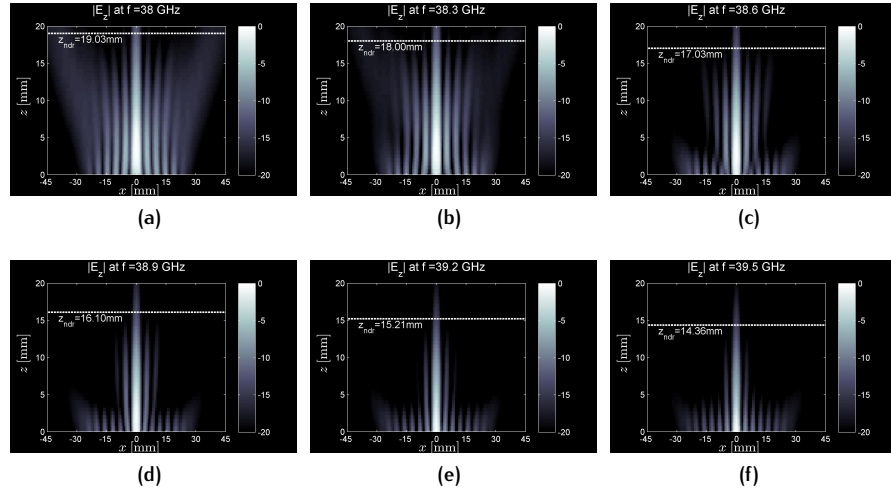


**Figure 5.28:** Measured intensity of  $E_z$  along the  $xz$  plane at  $f = 38.0$  GHz,  $38.3$  GHz,  $38.6$  GHz,  $38.9$  GHz,  $39.2$  GHz,  $39.5$  GHz.

Above this distance, diffraction prevails, and the beam starts to widen. Note that the nondiffractive range decreases with frequency according to the correspondent increase of  $\hat{k}_\rho$ , as expressed by Eq. (4.14).

The stability of the HPBW (see Fig. 5.29) is also maintained with respect to the frequency variation. This result has been validated through measurements (comparison with full-wave simulations is available for  $z = \lambda$  in [153]) for different distances  $z$  from the aperture plane. As predicted by Eq. (4.15), due to the dispersive behavior of  $\beta_\rho$ , the measured HPBW decrease monotonically slowly with frequency, within the measured frequency

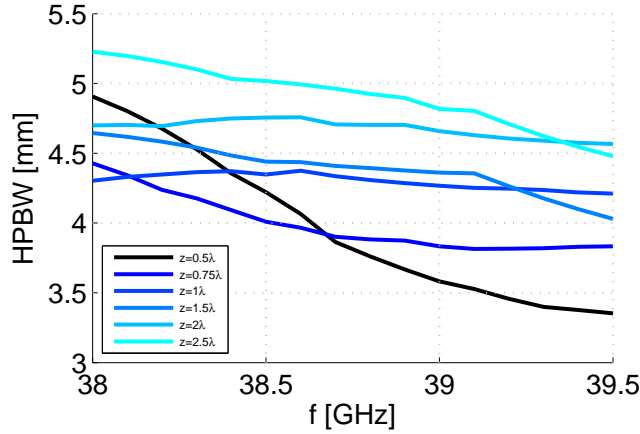


Figure 5.29.: Measured HPBW vs.  $f$  in the range 38 GHz to 39.5 GHz at different distances  $z = 0.5\lambda_0, 0.75\lambda_0, \lambda_0, 1.5\lambda_0, 2\lambda_0, 2.5\lambda_0$ . The color shades from blue to cyan as  $z$  increases from  $0.5\lambda$  to  $2.5\lambda$ . At  $z = \lambda$  the HPBW shows a remarkable stability with respect to the frequency.

range (38 – 39.5 GHz). Moreover, the measured HPBW remains quasi-stable at  $z = \lambda$  with a variation coefficient (CV):

$$CV = \frac{\sigma_{\text{HPBW}}}{\overline{\text{HPBW}}} \simeq 1.1\%, \quad (5.42)$$

being  $\sigma_{\text{HPBW}} \simeq 50 \mu\text{m}$  the standard deviation of the measured HPBW, and  $\overline{\text{HPBW}} \simeq 4.3 \text{ mm}$  its mean value. Note that, as the distance from the aperture increases, the average value of the HPBW increases because the main beam starts to widen as long as it approaches the nondiffractive range.

### 5.3.5 Use of a LRW as an X-wave launcher

These promising results, i.e., the generation of zeroth-order Bessel beams with a fixed spot size over a certain bandwidth, have suggested the investigation of the possibility to generate polychromatic nondiffracting solutions, i.e. X-waves, with this prototype. However, an intrinsic limitation has revealed us the unfeasibility of the project for any kind of Bessel-beam launcher generated with *forward* leaky waves. In fact, if one looks at the dispersion behavior of the leaky mode responsible for radiation (in this case the first higher-order mode, but the concept holds also for the fundamental mode), it is easy to check that the radial phase constant  $\beta_\rho$  monotonically increases with frequency around the operating point. This means that the longitudinal phase constant  $\beta_z$  will decrease with frequency (due to the separation equation  $k_z = \sqrt{k_0^2 - k_\rho^2}$ ). Furthermore, the group velocity along  $z$  is given by:

$$v_z = \left( \frac{\partial \beta_z}{\partial \omega} \right)^{-1} = \left( \frac{\partial \hat{\beta}_z}{\partial \omega} k_0 + \frac{1}{c_0} \hat{\beta}_z \right)^{-1} = c_0 \left( \frac{\partial \hat{\beta}_z}{\partial \omega} \omega + \hat{\beta}_z \right)^{-1}, \quad (5.43)$$

thus the condition required for having  $v_z > 0$  is:

$$\omega \frac{\partial \hat{\beta}_z}{\partial \omega} + \hat{\beta}_z > 0. \quad (5.44)$$

Since  $0 < \hat{\beta}_z < 1$  and  $\partial \hat{\beta}_z / \partial \omega < 0$ , if we define  $s = -|\partial \hat{\beta}_z / \partial \omega|$  the absolute value of the frequency slope of  $\hat{\beta}_z$ , the relation above is equal to:

$$s < \frac{\hat{\beta}_z}{\omega}. \quad (5.45)$$

It is easy to verify that, for the required forward leaky mode, one would obtain  $s > \hat{\beta}_z / \omega$  in a small bandwidth centered around the operating frequency (e.g.,  $s \simeq 10^{-10}$  at  $\omega_0 \simeq 10^{11}$  with  $\hat{\beta}_z \simeq 0.5$ , then  $s > \omega / \hat{\beta}_z$ ), thus describing a pulse which is propagating towards the aperture. Obviously, there would not be any pulse propagation away from the aperture, thus making impossible the generation of any pulse (especially a nondiffracting pulse such as an X-wave) from such a device.

Therefore, in order to investigate the possibility to generate nondiffracting pulses, we have considered structures able to radiate waves with a positive longitudinal group velocity  $v_z > 0$ . In the next Chapter 6 we thoroughly discuss the properties of Radial Line Slot Array (RLSA) antennas [242], [286], whose radiation mechanism can be attributed to backward leaky waves [206]. As we will see, such devices can realistically pave the way for the first experimental generation of X-waves in the microwave/millimeter-wave range.

## 5.4 CONCLUSION

In this Chapter the analysis, design, and implementation of a microwave Bessel-beam launcher has been reviewed. The considered device is based on the excitation of lower-order leaky modes, thus not allowing for a convenient frequency-scaling at millimeter waves. In fact, the existing design rules would have led to impractically thin substrates and considerably high ohmic losses at millimeter waves. To reduce the consequent ohmic losses and fabrication issues, a higher-order design is then proposed. New design rules are derived in analytical form to prevent modal coupling. Measurement results of a prototype working around 40 GHz have confirmed the proposed analysis and design over a fractional bandwidth of about 4%. Within the operating bandwidth the Bessel beam has shown a remarkable quasi-constant beamwidth; a feature that is of paramount importance in near-field focusing applications.

Finally, the propagating features of forward leaky waves have been discussed in connection to their use for generating X-waves. As a result, it is shown that forward leaky waves as those excited by this prototype do not allow for the generation of a propagating X-wave. Conversely, limited-dispersion backward waves seem to be particularly amenable for these purposes, as we will readily see in the next (and also last) Chapter 6.

# 6

## X-WAVE LAUNCHERS

### 6.1 INTRODUCTION

In the previous Chapter 5, we have seen some experimental realizations of Bessel beam launchers in the microwave and the millimeter-wave frequency range. As pointed out in Chapter 4, the generation of Bessel beams over a considerable fractional bandwidth may open the possibility to realize polychromatic nondiffracting solutions, such as *X-waves*. Unfortunately, in 5.3.5 it has been shown that the LRWs proposed in Chapter 4 are not suitable for X-wave generation due to the specific dispersive character of the relevant leaky modes. However, a different class of wideband microwave radiators will be considered in this Chapter 6 to overcome these limitations.

Chapter 6 is organized in two Sections. In Section 6.2, we introduce the reader to the theoretical framework that is needed to understand the fundamental limitations upon the millimeter-wave generation of *zeroth-order X-waves*<sup>1</sup> with finite apertures. This will bring us to evaluate the impact of both the aperture truncation and wavenumber dispersion on the spatio-temporal features of the generated X-wave. Finally, a wideband radiator, namely a *Radial Line Slot Array* (RLSA) antenna [242], [286], [287] is briefly outlined and proposed as an X-wave launcher. Numerical results will validate the concept.

In Section 6.3, we investigate the possibility to generate *higher-order X-waves* (i.e., *localized twisted pulses* characterized by an azimuthal phase variation) in the microwave range through finite apertures. A numerical validation will clearly reveal the focusing capabilities of a wideband dispersive radiator. It is worth to note here that *higher-order X-waves* have never been carefully studied in the microwave range. Moreover, the *higher-order* character of such waves, may pave the way for the first localized transmission of *orbital angular momentum* (OAM) in the microwave range. A possibility that could open unprecedented scenarios in the context of *high data-rate wireless transmissions* and *spatial diversity* in Telecommunications.

---

<sup>1</sup> From now on we omit this prefix, so that X-waves will always be considered of zeroth-order if not differently specified.

## 6.2 GENERATION OF ZERO-ORDER X-WAVES THROUGH FINITE APERTURES

Among the different solutions within the class of polychromatic nondiffracting waves, here we focus our attention on the family of *X-shaped pulses* (see Chapter 4). In particular, we will consider ‘*spectrally-flat*’ *X-shaped pulses*, i.e., nondiffracting solutions whose spectral content is described by Eq. (4.10) weighted with a *uniform frequency spectrum*. This choice has been motivated by the fact that any realistic frequency spectrum has *most* of its spectral content concentrated in a limited bandwidth around a central frequency<sup>2</sup>. As a consequence, uniform frequency spectra allow for describing a wide class of high-frequency *X-shaped pulses*. For this reason, in the following we adopt the notation of *X-waves* (which, by definition, are described by an exponentially-decaying frequency spectrum) to refer to such pulses.

In this Section, the spatio-temporal properties of *band-limited, dispersive*, electromagnetic X-waves generated by millimeter-wave wideband radiators are discussed within a novel theoretical framework. In particular, in 6.2.1 the original concept of *metric of confinement* is introduced in order to evaluate the focusing properties of an X-wave. The definitions of *weak* and *strong* confinement will emerge as useful criteria to determine if the spatial confinement of an X-wave is *efficient* or not. These tools are then used in 6.2.2 to show that even an *ideal X-wave* (where *ideal* means a nondiffracting and nondispersive X-wave) must fulfill some precise requirements in terms of fractional bandwidth, aperture size, and axicon angle, to show an *efficient spatial confinement* along both the transverse and the longitudinal axes. Even more interestingly, in 6.2.3 we will show how, by progressively removing some simplifying hypotheses, it is still possible to generate a *limited-diffraction* and *limited-dispersion* X-wave. Finally, in 6.2.4 a wideband radiator, namely an RLSA antenna [242], [286], [287], is briefly introduced and then considered for the practical generation of such X-waves. In fact, the wideband capability of RLSA antennas together with their limited-dispersion properties [206] suggest their use as X-wave launchers. Numerical results based on the characteristics of a realistic device corroborate the theoretical results of 6.2.2 and 6.2.3. Specifically, the impact of the aperture size and wavenumber dispersion on the spatio-temporal features of the generated X-wave are thoroughly discussed.

These results demonstrate that a dispersive-finite X-wave (even if it can no longer be considered nondiffractive and nondispersive in the most rigorous sense) retains localization properties in both the transverse and the longitudinal axes over a finite distance and time duration related to the physical size and bandwidth of the generating device. These features may be of in-

<sup>2</sup> Despite a finite spectral extension does not constitute a true signal which, on the contrary, requires an infinite spectrum.

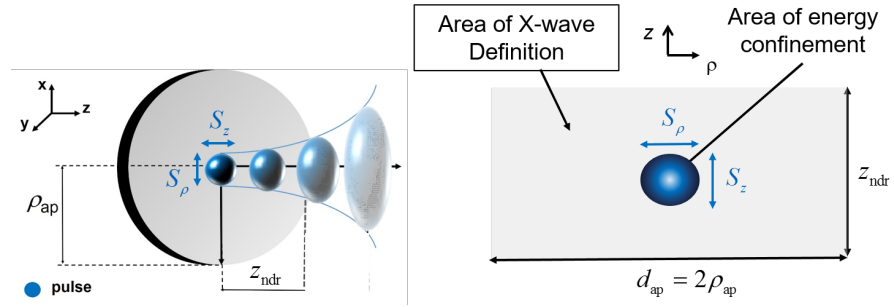


**Figure 6.1.:** Definition of a *metric of confinement* for an X-wave. A pulse characterized by a transverse spot width  $S_\rho$  and a longitudinal spot width  $S_z$  is launched through a finite radiating aperture of diameter  $d_{\text{ap}} = 2\rho_{\text{ap}}$ . Since the main constituents of an X-wave, i.e., Bessel beams, maintain their spot widths up to the nondiffractive range  $z_{\text{ndr}}$ , an X-wave will be properly defined over an area on the  $\rho z$  plane which is limited along  $\rho$  by the aperture diameter and along  $z$  by the nondiffractive range. If most of the energy of the pulse is contained in this region, we can actually state that the considered X-wave is *efficiently confined*.

terest in various applications at millimeters waves and optics, where the spatial confinement of electromagnetic pulses is of paramount importance.

### 6.2.1 Metric of confinement

In Section 4.3, we have thoroughly discussed the focusing features of Bessel beams providing a formula (viz., Eq. (4.15)) for evaluating the *transverse* spot width  $S_\rho$ , i.e., the null-to-null spatial length along the radial direction  $\rho$  (see Fig. 6.1). Since a Bessel beam is generated by a finite radiating aperture, its focusing performance may be evaluated by the *transverse confinement*  $C_\rho$ :

$$C_\rho \triangleq \frac{S_\rho}{d_{\text{ap}}}, \quad (6.1)$$

defined as the ratio between the transverse spot width  $S_\rho$  and the aperture size  $d_{\text{ap}}$ . An X-wave, as a spectral superposition of Bessel beams, retains almost the same transverse spatial distribution of a Bessel beam, so that  $C_\rho$  can be used to describe also the *transverse confinement* of an X-wave. However, an X-wave is also traveling along the longitudinal axis  $z$ , as is briefly sketched in Fig. 6.1. At this point, a question arises: given a longitudinal spot width  $S_z$ , how can we evaluate the focusing performance of an X-wave with respect to the longitudinal  $z$ -axis? The answer lies again in the focusing features of its main constituents. As a matter of fact, a truncated Bessel beam will retain its transverse spatial distribution within the nondiffractive range  $z_{\text{ndr}}$ . As a consequence, any definition of longitudinal spot width  $S_z$  is meaningless if not normalized to the nondiffractive range  $z_{\text{ndr}}$ . It immediately follows that the focusing performance of an X-wave may be evaluated

on the transverse axis by  $C_\rho$ , and on the longitudinal axis by the *longitudinal confinement*  $C_z$ :

$$C_z \triangleq \frac{S_z}{z_{\text{ndr}}}, \quad (6.2)$$

defined as the ratio between the longitudinal spot width  $S_z$  and the non-diffractive range  $z_{\text{ndr}}$ . As is clearly shown in Fig. 6.1, the spatial features of an ideal X-wave are *well defined* only within a  $\rho z$  plane limited by  $\rho_{\text{ap}}$  along the transverse axis, and  $z_{\text{ndr}}$ <sup>3</sup> along the longitudinal axis (see the ‘Area of X-wave definition’ in Fig. 6.1). Within the *area of X-wave definition*, we can say that an X-wave is *efficiently* confined along the  $\rho$ -axis *if and only if* the spot width along  $\rho$  ( $S_\rho$ ) is much smaller than the aperture size ( $d_{\text{ap}}$ ), i.e.,  $C_\rho < 1$ . Similarly, the confinement along the  $z$ -axis is effective if and only if the spot width along  $z$  ( $S_z$ ) is smaller than the nondiffractive range  $z_{\text{ndr}}$ , i.e.,  $C_z < 1$ .

From the discussion above, the concept of *efficient confinement* directly arises. Hence, a metric which is able to ‘capture’ the comprehensive confinement of an X-wave is needed. To this purpose, in the following two paragraphs we propose the concepts of *weak confinement* and *strong confinement*.

#### Weak Confinement

For some applications, the constraints on the confinement may be slightly relaxed since we could be interested in solutions that are not efficiently confined in one direction but extremely confined along the other one. From this viewpoint, a suitable definition of metric is given by the product of the ratios  $C_\rho = S_\rho/d_{\text{ap}}$  and  $C_z = S_z/z_{\text{ndr}}$ :

$$C_{\rho,z}^{(w)} = C_z \cdot C_\rho, \quad (6.3)$$

where  $C_{\rho,z}^{(w)}$  stands for *weak confinement*. From the definition above, we would say that an X-wave is *weakly confined* if and only if:

$$C_{\rho,z}^{(w)} < 1. \quad (6.4)$$

Obviously, for  $C_{\rho,z} = 1$  there will never be efficient confinement, since the transverse or the longitudinal spot widths would exceed the aperture size or the nondiffractive range, respectively.

#### Strong Confinement

For some other applications, the constraints on the confinement may be quite strict since we could be interested in solutions that are efficiently con-

<sup>3</sup> Indeed, beyond the nondiffractive range,  $S_\rho$  would no longer describe the actual spot width of the pulse.



finned in both directions. From this new viewpoint, a suitable definition of metric is given by the following<sup>4</sup>:

$$C_{\rho,z}^{(s)} = \begin{cases} 1 & \text{if } \max(C_\rho, C_z) > 1, \\ C_{\rho,z}^{(w)} & \text{elsewhere,} \end{cases} \quad (6.5)$$

where  $C_{\rho,z}^{(s)}$  stands for *strong confinement*. From the definition above, we would say that an X-wave is *strongly confined* if and only if:

$$C_{\rho,z}^{(s)} < 1. \quad (6.6)$$

In the following 6.2.2, both the transverse and the longitudinal profiles of an ideal X-wave are calculated in closed forms assuming *uniform frequency spectra*. This analysis allows for the evaluation of  $C_\rho$  and  $C_z$ , and in turn of the *confinement* features of ideal X-waves in the frame of both the *weak* and the *strong* metric of confinement.

It is worth noting that, for an ideal nondispersive X-wave, the phase velocity  $v_p$  does not change with frequency, and thus it coincides with the group velocity  $v_g$ . Since the propagation of an X-wave is along one dimension (viz., the z-axis), this means that the temporal axis  $t$  can be considered as a spatial coordinate through the product with  $v_p$ <sup>5</sup>. By duality, the longitudinal confinement properties of ideal X-waves give also a measure of the temporal spreading of the pulse, thus both the metrics defined above measure the spatio-temporal features of an ideal X-wave.

Finally, we should stress that the discussion on the confinement capabilities of X-waves in the present Subsection 6.2.1 is not related to any assumption on the chosen frequency spectrum. Conversely, the discussion of the following subsections holds only for uniform frequency spectra.

### 6.2.2 Ideal X-waves

In the representation of an ideal X-wave (see Section 4.2), some simplifying hypotheses are tacitly assumed:

- i) the aperture field is a nondiffractive Bessel beam over the entire frequency range and along an infinite propagating distance. This means that an infinite aperture, or infinite energy is required [188], [189];
- ii) the axicon angle  $\theta(\omega) = \theta_0$  does not change with frequency. This latter condition implies that no wavenumber dispersion is taken into account.

However, even under these simplifying hypotheses, it will readily be shown that is not always possible to efficiently confine an X-wave in the

<sup>4</sup> Which emulates the *boolean* operation  $C_\rho > 1$  OR  $C_z > 1$ .

<sup>5</sup> This is in agreement with the definition of *Minkowski's spacetime*.

sense expressed by the metrics  $C_{\rho,z}^{(w)}$  and  $C_{\rho,z}^{(s)}$  previously defined. The features of dispersive (i.e., removal of hypothesis *ii*) and dispersive-finite (i.e., removal of hypothesis *i* and *ii*) will be the objects of Subsections 6.2.3 and 6.2.4, respectively.

Note also that, though the spot-widths of ordinary X-waves have already been calculated in [263], it still lacks an insight about the confinement properties of X-waves in the current literature.

### Analytical description

The mathematical description of an X-wave has already been discussed in Chapter 4. Here, we report for convenience Eq. (4.11):

$$\psi(\rho, z, t) = \int_0^\infty F(\omega) J_0(k_0 \sin \theta_0 \rho) e^{-jk_0 \cos \theta_0 z} e^{j\omega t} d\omega. \quad (6.7)$$

We recall here that  $\psi(\rho, z, t)$  is defined as the *analytic signal* of  $\tilde{\psi}(\rho, z, \omega)$ , i.e.,

$$\psi(\rho, z, t) \triangleq \mathfrak{F}^{-1}\{\tilde{\psi}(\rho, z, \omega) \cdot H(\omega)\}, \quad (6.8)$$

where  $\mathfrak{F}^{-1}(\cdot)$  represent the inverse Fourier transform, and  $H(\cdot)$  is the most known *Heaviside step function*. This allows to discard the negative spectral content of an X-wave.

From now, we limit our study to *uniform frequency-spectrum X-waves* (UXWs)<sup>6</sup>, i.e., band-limited spectrally-flat X-waves described by Eq. (6.7) when  $F(\omega)$  is a uniform frequency spectrum centered around a carrier angular frequency  $\omega_0$  and zero outside a certain angular frequency band  $\Delta\omega$

$$F(\omega) = \Pi\left(\frac{\omega - \omega_0}{\Delta\omega}\right) = \begin{cases} 1 & |\omega - \omega_0| \leq \Delta\omega/2 \\ 0 & \text{elsewhere} \end{cases}, \quad (6.9)$$

where  $\Pi(x) = H(x + 1/2) - H(x - 1/2)$  is the *window function*.

For this choice of  $F(\omega)$ , the integral in Eq. (6.7) for a UXW reduces to:

$$\begin{aligned} \chi^U(\rho, z, t) &= \int_{\omega_0 - \Delta\omega/2}^{\omega_0 + \Delta\omega/2} J_0\left(\frac{\omega}{c_0} \sin \theta_0 \rho\right) \\ &\quad \times \exp\left[-j\frac{\omega}{c_0} \cos \theta_0 \left(z - \frac{c_0 t}{\cos \theta}\right)\right] d\omega \end{aligned} \quad (6.10)$$

$$= \int_{\omega_0 - \Delta\omega/2}^{\omega_0 + \Delta\omega/2} J_0\left(\frac{\omega}{u_\rho} \rho\right) \exp\left[-j\frac{\omega}{u_z} (z - u_z t)\right] d\omega, \quad (6.11)$$

where  $u_\rho = c_0 / \sin \theta_0$  and  $u_z = c_0 / \cos \theta_0$  are the radial and longitudinal phase velocities, respectively. The spatial confinement properties of an X-wave weighted with a uniform spectrum can easily be deter-

<sup>6</sup> For the interested reader, localized solutions characterized by different choices of frequency spectra as well as UXWs have been widely investigated in [192] with the aid of the bidirectional decomposition technique (see [196]).

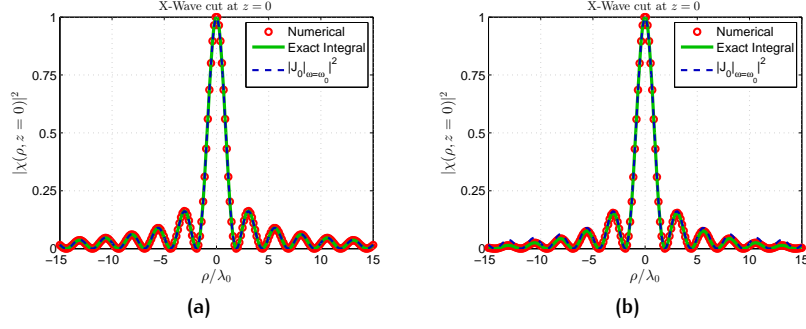


**Figure 6.2.:** Normalized  $\chi_t^U(\rho)$  vs.  $\rho$  for  $f_0 = 60$  GHz,  $\theta_0 = 11^\circ$  and (a)  $\Delta\omega/\omega_0 = 0.05$  (b)  $\Delta\omega/\omega_0 = 0.2$ . Comparison between the numerical integration of Eq. (6.12) (red circles), the exact integral of Eq. (6.12) (green solid curves), and the approximation given by Eq. (6.15) (blue dashed curves). As the fractional bandwidth  $\Delta\omega/\omega_0$  increases, the approximation is less accurate on the tails, but the width of the main beam is always well approximated.

mined by calculating the integral in Eq. (6.11) along both the  $z$ - and  $\rho$ -axis. Note that, the transverse ( $\chi_t^U(\rho, t) = |\chi^U(\rho, z = 0, t)|$ ) and longitudinal ( $\chi_1^U(z, t) = |\chi^U(\rho = 0, z, t)|$ ) profiles of the UXWs both depend on time  $t$ . However, since for ideal UXWs the nondispersive character of waves implies  $v_z(t) = u_z = c_0/\cos\theta_0$ , then  $\chi_t^U(\rho)$  and  $\chi_1^U(\xi)$  would depend on a single variable defined as  $\xi = z - u_z t$ . For the sake of simplicity we always assume  $t = 0$ , so that  $\xi = z$  and  $\chi_t^U(\rho)$  and  $\chi_1^U(z)$  are functions of a single spatial variable. Note that, by duality, if we assume  $z = 0$ , so that  $\xi = t$ , then  $\chi_1^U(t)$  would measure the temporal spreading of the pulse.

In particular, the transverse amplitude profile of a UXW is given by:

$$\chi_t^U(\rho) = |\chi(\rho, z = 0, t = 0)| = \left| \int_{\omega_m}^{\omega_M} J_0\left(\frac{\omega}{c_0} \sin\theta\rho\right) d\omega \right| = \left| \frac{xc_0}{2\rho \sin\theta} [\pi \mathbf{H}_0(x) J_1(x) + (2 - \pi \mathbf{H}_1(x)) J_0(x)]_{x_m}^{x_M} \right|, \quad (6.12)$$

where  $\mathbf{H}_0(\cdot)$  and  $\mathbf{H}_1(\cdot)$  are the Struve functions of zero and first order [272], respectively, and where

$$\omega_M = \omega_0 + \Delta\omega/2, \quad \omega_m = \omega_0 - \Delta\omega/2, \quad (6.13)$$

$$x_M = \frac{\omega_M \rho \sin\theta}{c}, \quad x_m = \frac{\omega_m \rho \sin\theta}{c}. \quad (6.14)$$

It can be shown that the expression in Eq. (6.12) is very well approximated by:

$$\chi_t^U(\rho) \simeq \Delta\omega \left| J_0\left(\frac{\omega_0 \sin\theta\rho}{c_0}\right) \right|, \quad (6.15)$$

for small arguments of  $J_0(\cdot)$  (see Fig. 6.2). Note that Eq. (6.15) simply represents the product of the integrand function in Eq. (6.12) evaluated at the

carrier frequency and the bandwidth, hence Eq. (6.15) can be interpreted as a result of the Mean Value Theorem [288]

Similarly, the longitudinal amplitude profile of a UXW is given by:

$$\chi_1^U(z) = |\chi(\rho = 0, z, t = 0)| = \left| \int_{\omega_m}^{\omega_M} \exp\left(-j\frac{z\omega}{c_0} \cos \theta\right) d\omega \right|. \quad (6.16)$$

The integration over  $\omega$  yields:

$$\chi_1^U(z) = \Delta\omega \left| \text{sinc}\left(\frac{z\Delta\omega \cos \theta}{2c_0}\right) \right|. \quad (6.17)$$

#### Conditions for the weak confinement of ideal X-waves

From Eqs. (6.15) and (6.17) it is possible to evaluate the spot size of the UXW. Here, we consider as spot size the null-to-null distance of the amplitude profile over both axes. The quantities  $S_\rho$  and  $S_z$  previously defined are then given by:

$$S_\rho = \frac{2j_{0,1}c_0}{\omega_0 \sin \theta'}, \quad (6.18)$$

$$S_z = \frac{4\pi c_0}{\Delta\omega \cos \theta'}, \quad (6.19)$$

where  $j_{0,1} = 2.4048$  identifies the first null of the  $J_0$  function. As stated in 6.2.1, a weak efficient spatial confinement takes place only when the constraint in Eq. (6.4) is respected.

Thus, using Eqs. (6.18), and (6.19) in Eq. (6.4), and expressing the aperture size  $\rho_{\text{ap}}$  in terms of the operating wavelength  $\lambda_0 = 2\pi c_0/\omega_0$ , yields:

$$C_{\rho,z}^{(w)} = \frac{j_{0,1}}{\underbrace{2\pi m \sin \theta}_{C_\rho}} \frac{2 \sin \theta}{\underbrace{m \Delta\omega \cos^2 \theta}_{C_z}} = \frac{j_{0,1}}{\pi m^2 \cos^2 \theta \overline{\Delta\omega}} < 1, \quad (6.20)$$

where  $m = \rho_{\text{ap}}/\lambda_0$  is the aperture radius in number of wavelengths and  $\overline{\Delta\omega} = \Delta\omega/\omega_0$  is the fractional bandwidth. Note that in Eq. (6.20) a ratio with respect to the aperture size has been considered, even if the fields are here computed by neglecting the finiteness of the aperture. However, Eq. (6.20) will allow for evaluating the impact of different parameters on the shape of the wave. This information will be useful even in the practical case of a finite aperture, discussed in 6.2.4.

In Fig. 6.3, the *weak confinement*  $C_{\rho,z}^{(w)}$  is expressed as a function of the electrical length  $m = \rho_{\text{ap}}/\lambda_0$  and the axicon angle  $\theta$ . The intensity of  $C_{\rho,z}^{(w)}$  goes from 0 (white) to 1 (black) <sup>7</sup>. The yellow hyperbola delimit a region of  $\theta, m$  values for which Eq. (6.20) is satisfied, for four different values of the fractional bandwidth:  $\overline{\Delta\omega} = 0.01, 0.05, 0.1, 0.2$  (Figs. 6.3(a)-(d)). As

<sup>7</sup> Note that, from the definition of  $C_{\rho,z}^{(w)}$  (Eq. (6.20)) values greater than 1 are possible, but they are here saturated to 1 for readability purposes.

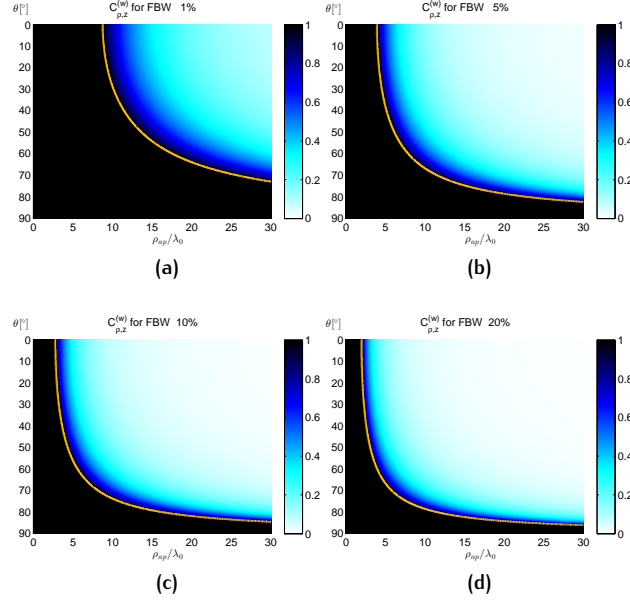


**Figure 6.3.:** Weak confinement  $C_{\rho,z}^{(w)}$  vs.  $\rho_{ap}/\lambda_0$  and  $\theta$ . The yellow hyperbola represents the boundary between the region of efficient (in white) and non-efficient confinement (in black) for ideal UXWs, when fractional bandwidths of (a)  $\overline{\Delta\omega} = 0.01$ , (b)  $\overline{\Delta\omega} = 0.05$ , (c)  $\overline{\Delta\omega} = 0.1$ , and (d)  $\overline{\Delta\omega} = 0.2$  are considered. The region of efficient confinement increases for larger fractional bandwidths. In any case, this region corresponds to electrically large apertures with small axicon angles.

clearly shown, the region of efficient confinement increases as the fractional bandwidth increases up to  $\overline{\Delta\omega} = 0.2$ . Note that for higher values of  $\overline{\Delta\omega}$  there are no significant changes with respect to Fig. 6.3(d).

Interestingly, from Fig. 6.3 it is easy to infer that electrically large apertures (high  $m$ ) and low axicon angles  $\theta$  are required to efficiently confine a pulse in a weak sense, even for ideal UXWs. Furthermore, it is clear from Eq. (6.20) that the fractional bandwidth  $\overline{\Delta\omega}$  controls the pulse confinement along the  $z$ -axis ( $C_z$ ) without affecting the confinement along the  $\rho$ -axis ( $C_\rho$ ). Conversely,  $\theta$  affects both  $C_\rho$  and  $C_z$ . In particular, as  $\theta$  increases, the pulse is more confined along  $\rho$  but spreads along  $z$ , and viceversa.

### Numerical examples

To give a proof-of-concept we have considered a small fractional bandwidth  $\overline{\Delta\omega} = 0.01$  and a large one  $\overline{\Delta\omega} = 0.2$ . In Fig. 6.4, we have overlapped the confinement boundary obtained for  $\overline{\Delta\omega} = 0.2$  over the contour plot of the weak confinement  $C_{\rho,z}^{(w)}$  obtained for  $\overline{\Delta\omega} = 0.01$ . As a result, in Fig. 6.4 a *transition region* is defined where a pulse would be efficiently confined in the weak sense for  $\overline{\Delta\omega} = 0.2$ , but inefficiently confined for  $\overline{\Delta\omega} = 0.01$ . These results have been validated through numerical simulations in Fig. 6.5. As is shown, if an X-wave is generated with parameters in  $p_1$  (see purple dot in Fig. 6.5(a)) the intensity distribution  $|\chi^U(\rho, z)|^2$  is not confined for

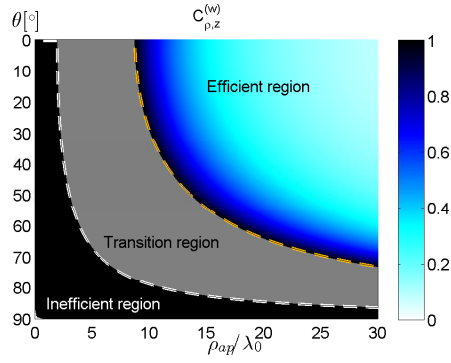


Figure 6.4.: The yellow and white hyperbola represents the boundaries between the region of efficient (in white) and non-efficient confinement (in black)  $\overline{\Delta\omega} = 0.01$  and  $\overline{\Delta\omega} = 0.2$ , respectively. The transition region is limited by the two hyperbola.

FBW =  $100 \cdot \overline{\Delta\omega} = 1\%$  because the longitudinal spot width does not go to zero within the nondiffractive range (see Fig. 6.5(b)). Conversely, for FBW = 20% the same X-wave would be confined as shown in Fig. 6.5(c). For completeness, numerical results for X-waves generated with parameters in  $p_2$  and  $p_3$  (see the yellow dot and the blue dot in Figs. 6.5(a) and (d), respectively) have been reported. As expected, the resulting X-wave is not efficiently confined for  $p_2$  even for a FBW = 20% (see Fig. 6.5(e)), whereas it is very well confined for  $p_3$  (see Fig. 6.5(f)).

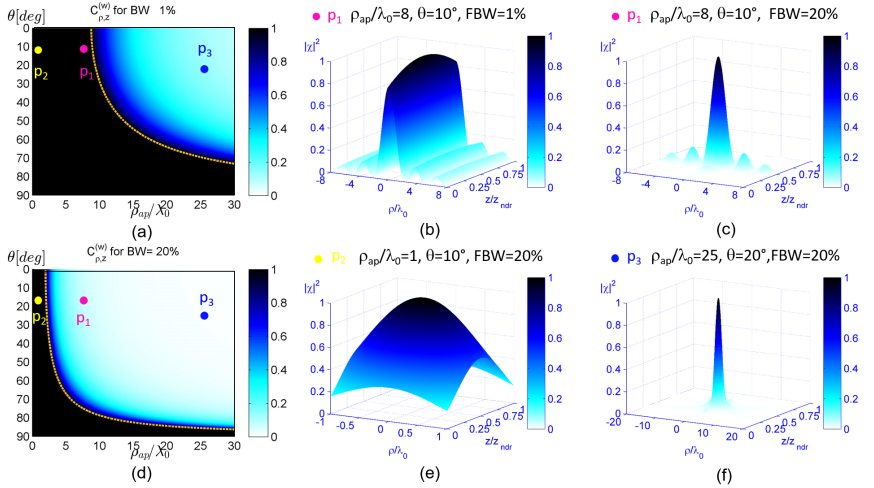
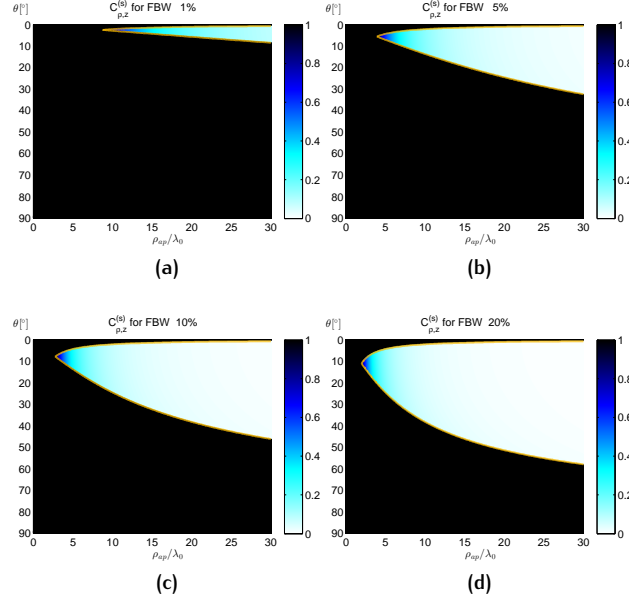


Figure 6.5.:  $C_{\rho,z}^{(w)}$  vs.  $\rho_{ap}/\lambda_0$  and  $\theta_0$  for (a) FBW = 1% and (d) FBW = 20%. The purple dot  $p_1$  represents an X-wave with  $m = 8$  and  $\theta = 10^\circ$ . The yellow dot  $p_2$  represents an X-wave with  $m = 1$  and  $\theta = 10^\circ$ . The blue dot  $p_3$  represents an X-wave with  $m = 25$  and  $\theta = 20^\circ$ . An X-wave in  $p_1$  is generated for (b) FBW = 1% and (c) FBW = 20%, whereas X-waves in (e)  $p_2$  and (f)  $p_3$  are both generated for FBW = 20%. In (b-c) and (e-f), the intensity of the X-wave is reported over a  $\rho z$  plane limited by  $\rho_{ap}$  along  $\rho$  and  $z_{ndr}$  along  $z$ . From this representation, if  $S_\rho$  and  $S_z$  fit in the plot, then the X-wave is confined over the respective axis. Note that, the  $\rho$ -axis is normalized to  $\rho_{ap}$  while the  $z$ -axis is normalized to  $z_{ndr}$ .



**Figure 6.6.:** Strong confinement  $C_{\rho,z}^{(s)}$  vs.  $\rho_{ap}/\lambda_0$  and  $\theta$ . The yellow curves represent the boundaries between the region of efficient (in white) and non-efficient confinement (in black) for ideal UXWs, when fractional bandwidths of (a)  $\Delta\bar{\omega} = 0.01$ , (b)  $\Delta\bar{\omega} = 0.05$ , (c)  $\Delta\bar{\omega} = 0.1$ , and (d)  $\Delta\bar{\omega} = 0.2$  are considered. The region of efficient confinement increases for larger fractional bandwidths as for  $C_{\rho,z}^{(w)}$ . However, the efficient region is considerably narrower due to the more strict criterion applied by the strong metric  $C_{\rho,z}^{(s)}$  with respect to the weak metric  $C_{\rho,z}^{(w)}$ .

Furthermore, the results hitherto obtained using the *weak confinement* expressed by  $C_{\rho,z}^{(w)}$  are compared with those obtained using the *strong confinement*. In fact, the results of Fig. 6.3 obtained for  $C_{\rho,z}^{(w)}$  are reported in Fig. 6.6 for  $C_{\rho,z}^{(s)}$ . As expected, the efficient region is considerably narrower due to the more strict criterion applied by the strong metric  $C_{\rho,z}^{(s)}$  with respect to the weak metric  $C_{\rho,z}^{(w)}$ .

Finally, the distinction between  $C_{\rho,z}^{(w)}$  and  $C_{\rho,z}^{(s)}$  has been highlighted by the numerical example of Fig. 6.7. As is seen, when an X-wave is generated with parameters as in  $p_1$  ( $m = 10$ ,  $\theta_0 = 60^\circ$ , and  $\Delta\bar{\omega} = 0.2$ ), the resulting pulse would be *weakly confined* but not *strongly confined* (see top-right panel); whereas when an X-wave is generated with parameters as in  $p_2$  ( $m = 10$ ,  $\theta_0 = 30^\circ$ , and  $\Delta\bar{\omega} = 0.2$ ), the resulting pulse is *strongly confined* (see bottom-right panel). Consistently to the definition of  $C_{\rho,z}^{(w)}$  and  $C_{\rho,z}^{(s)}$ , since  $p_1$  lies outside the region of *strong* confinement but within the region of *weak* confinement (see top-left and bottom-left panels of Fig. 6.7), the resulting X-wave is not confined along the longitudinal  $z$ -axis, but it is extremely confined along the transverse  $\rho$ -axis.

As a final remark, we provide here some useful analytical expressions. In fact, the yellow hyperbola which define the boundaries for  $C_{\rho,z}^{(w)}$  can be

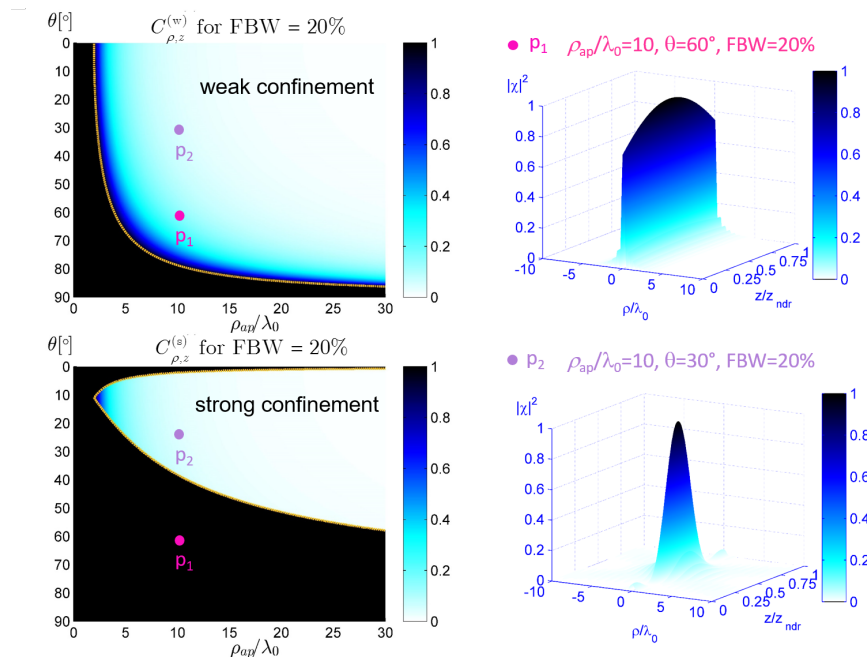


Figure 6.7.: Upper-left and lower-left corner:  $C_{\rho,z}^{(w)}$  and  $C_{\rho,z}^{(s)}$  vs.  $\rho_{ap}$  and  $\theta$  for FBW = 20%. Upper-right and lower-right corner: 3-D view of the normalized  $|\chi(\rho, z)|^2$  vs.  $\rho$  and  $z$  with parameters as in  $p_1$  and  $p_2$ , respectively (viz.,  $m = 10$  and  $\theta_0 = 60^\circ$  for  $p_1$ , and  $m = 10$  and  $\theta_0 = 30^\circ$  for  $p_2$ ).

calculated in closed-form, by setting Eq. (6.20) to 1. If one wants to express the hyperbole as a function of  $\theta$  one would obtain:

$$m_{\min}^{(w)} = \frac{1}{\cos \theta} \sqrt{\frac{j_{0,1}}{\pi \Delta \omega}}. \quad (6.21)$$

As is clearly expressed by the equation, as  $\overline{\Delta \omega}$  increases, the hyperbole is more pronounced, in agreement with the previous considerations. Note also that  $m_{\min}^{(w)}$  in Eq. (6.21) represents the minimum electrical aperture size  $m$  that the radiating device needs to be in order to achieve the weak confinement for any value of the axicon angle  $\theta$ . Obviously, this minimum aperture size increases for lower axicon angles.

Even the boundaries for  $C_{\rho,z}^{(w)}$  can be calculated in closed-form. In this case, one needs to set separately  $C_\rho$  and  $C_z$  in Eq. (6.20) to 1. As a result, one would obtain:

$$m_\rho^{(s)} = \frac{j_{0,1}}{2\pi \sin \theta}, \quad (6.22)$$

$$m_z^{(s)} = \frac{2 \tan \theta}{\overline{\Delta \omega} \cos \theta}, \quad (6.23)$$

so that the boundary is given by:

$$m_{\min}^{(s)} = \min_{\theta} \left\{ m_\rho^{(s)}, m_z^{(s)} \right\}. \quad (6.24)$$



From Eqs. (6.22) and (6.23) it is clear that  $\overline{\Delta\omega}$  only affects the longitudinal confinement, whereas  $\theta$  affects  $m_\rho^{(s)}$  and  $m_z^{(s)}$  with opposite trends. This aspect clearly emphasizes the importance of the fractional bandwidth  $\overline{\Delta\omega}$  which is the only independent parameter of an X-wave that allows to improve its overall confinement properties without negatively affects the confinement along the transverse direction as the axicon angle does.

In the following, we will use only the weak confinement. Specifically, Eq. (6.20) will be considered as an upper-bound limit for the weak confinement of both dispersive and dispersive-finite UXWs based on the ideal assumptions used for its derivation.

### 6.2.3 Dispersive X-waves

In the previous subsection we have assumed that the *axicon angle* does not change with frequency in the considered band  $\theta(\omega) = \theta_0$  for  $\omega \in \{\omega_0 - \Delta\omega/2, \omega_0 + \Delta\omega/2\}$ , and thus both the longitudinal and transverse wavenumbers, given by  $k_\rho = (\omega/c) \sin \theta_0$  and  $k_z = (\omega/c) \cos \theta_0$ , respectively, are also linear functions of frequency, as required for generating ideal localized waves (see Section 4.2). This assumption is widely assumed in optics and acoustics, thus motivating the reason why X-waves have been experimentally generated only in these range of frequencies [264], [265]

However, in most electromagnetic devices, especially for those with considerable fractional bandwidths, a non-linear relationship between  $k_z$ ,  $k_\rho$  and  $\omega$  is usually assumed, thus dispersion cannot be neglected [224], [241], [242].

Such a wavenumber dispersion should not be confused with the *anomalous dispersion* of nonlinear media (e.g. *Kerr media* [289]–[292]) that has already been exploited in relation with the spontaneous formation of X-waves [268], [289], [291], [293]. There, the frequency dispersion may be considered beneficial for the suppression of temporal broadening of pulses due to material dispersion [266], [268], [294]. Here, it is an undesirable phenomenon that has to be taken into account for a realistic analysis of pulse propagation and broadening.

Generally, the dependence of both longitudinal and transverse wavenumbers on  $\omega$  is not known in closed-form, but, for most cases (especially for narrow-band signals), it can be accurately described by a second-order Taylor series expansion [164]:

$$k_\rho = k_{\rho 0} + k_{\rho 1}(\omega - \omega_0) + \frac{1}{2}k_{\rho 2}(\omega - \omega_0)^2, \quad (6.25)$$

$$k_z = k_{z 0} + k_{z 1}(\omega - \omega_0) + \frac{1}{2}k_{z 2}(\omega - \omega_0)^2, \quad (6.26)$$

where  $\omega' = \omega - \omega_0$ , whereas  $k_{\rho 0}, k_{\rho 1}, k_{\rho 2}$  and  $k_{z 0}, k_{z 1}, k_{z 2}$  represent the coefficients of the second-order approximation for the transverse wavenum-

ber  $k_\rho$  and for the longitudinal wavenumber  $k_z$ , respectively. Note that,  $k_{z0}, k_{z1}, k_{z2}$  are also related to  $k_{\rho0}, k_{\rho1}, k_{\rho2}$  through the relation of separability  $k_\rho^2 + k_z^2 = k_0^2$ . After mathematical steps, one gets the sought relations

$$k_{z0} = \sqrt{k_0^2 - k_{\rho0}^2}, \quad (6.27a)$$

$$k_{z1} = (k_0 c^{-1} - k_{\rho0} k_{\rho1}) / k_{z0}, \quad (6.27b)$$

$$k_{z2} = (c^{-2} - k_{\rho1}^2 - k_{\rho0} k_{\rho2} - k_{z1}^2) / k_{z0}. \quad (6.27c)$$

Note that,  $k_{z0}, k_{z1}$ , and  $k_{z2}$  are related to the phase velocity  $u_z = \omega_0 / k_{z0}$ , the group velocity  $v_z = (\partial k_z / \partial \omega)|_{\omega=\omega_0}^{-1}$ , and the group velocity dispersion (GVD), respectively<sup>8</sup>.

As a consequence, the mathematical description of a dispersive UXW is approximated by

$$\begin{aligned} \chi^U(\rho, z, t) &= \int_{\omega_m}^{\omega_M} J_0 [k_\rho(\omega)\rho] \exp[-jk_z(\omega)z] \exp(j\omega t) d\omega \\ &\simeq \int_{-\Delta\omega/2}^{\Delta\omega/2} J_0 \left[ \left( k_{\rho0} + k_{\rho1}\omega' + \frac{1}{2}k_{\rho2}\omega'^2 \right) \rho \right] \\ &\quad \times \exp \left\{ -j \left[ \left( k_{z0} + k_{z1}\omega' + \frac{1}{2}k_{z2}\omega'^2 \right) z \right] \right\} \\ &\quad \times \exp [j(\omega' + \omega_0)t] d\omega', \end{aligned} \quad (6.28)$$

where  $\omega' = \omega - \omega_0$ . As a difference with respect to Eq. (6.11), the transport of the pulse is no longer rigid, hence both the transverse and longitudinal profiles depend on time. Moreover, the transverse profile  $\chi_t^U(\rho, t)$ , as a function of time, can only be calculated numerically. Nevertheless,  $\chi_t^U(\rho, t = 0)$  is still well approximated by Eq. (6.11) provided that  $\theta$  is now calculated at  $\omega_0$

$$\begin{aligned} \chi_t^U(\rho, t = 0) &\simeq \Delta\omega |J_0(k_{\rho0}\rho)| \\ &= \Delta\omega \left| J_0 \left( \frac{\omega_0 \sin \theta_0 \rho}{c} \right) \right|. \end{aligned} \quad (6.29)$$

Note that, for sufficiently low values of  $k_{\rho1}$ , Eq. (6.29) is a good approximation even for  $t > 0$ .

For the longitudinal amplitude profile, an analytical closed-form expression still exists and is given by

$$\begin{aligned} \chi_l^U(z, t) &\simeq \left| \operatorname{erf} \left[ \sqrt{\frac{jzk_{z2}}{2}} \left( \omega' + \frac{zk_{z1}k_{z2} - t}{zk_{z2}} \right) \right] \right|_{\omega'=-\Delta\omega/2}^{\omega'=\Delta\omega/2} \\ &\quad \times \left| \sqrt{\frac{\pi}{j2k_{z2}z}} \right|, \end{aligned} \quad (6.30)$$

<sup>8</sup> The interested reader can find an exhaustive analysis on this can be found in [268].

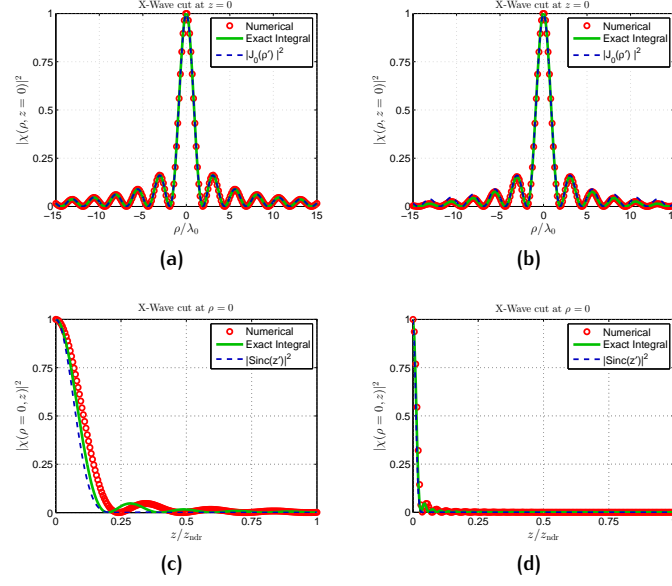


**Figure 6.8.:** Comparison between numerical integrations (red circles) and approximations (Eqs. (6.29) and (6.17) in green solid lines and Eqs. 6.18 and 6.19 in blue dashed lines) of (a)-(b) transverse profiles and (c)-(d) longitudinal profiles for a dispersive X-wave in fractional bandwidths (a)-(c) FBW = 5% and (b)-(d) FBW = 20% centered around  $f_0 = 60$  GHz. The resulting profiles have been obtained assuming  $k_{z0} = 0.2k_0$ ,  $k_{z1} = 0.55 \cdot 10^{-12}$ , and  $k_{z2} = 0$ . Results are reported over an aperture plane of  $\rho_{\text{ap}} = 15\lambda_0$  and  $z_{\text{ndr}}$  calculated at  $f_0$ . Note that  $\rho' = k_{\rho 0}\rho$  and  $z' = k_{z0}\Delta\omega z/2$ .

where  $\text{erf}(\cdot)$  is the error function [272]. Note that,  $k_{z2} = 0$  (i.e., when a first-order Taylor series expansion of  $k_z$  is assumed) is a removable singularity. Thus, as long as  $k_{z2} \rightarrow 0$ , Eq. (6.30) reduces to Eq. (6.17). It is possible to evaluate the spot size of a dispersive UXW in an approximate analytical form for Eq. (6.29) or numerical form for Eq. (6.30). In any case, both  $S_\rho$  and  $S_z$  are upper-bounded by Eqs. (6.18) and (6.19) (see Fig. 6.8), thus the weak confinement  $C_{\rho,z}^{(w)}$  given by Eq. (6.20) can still be used as a valid metric. In particular, for narrow fractional bandwidths ( $\overline{\Delta\omega} \lesssim 0.05$ ), the spot widths of a dispersive X-wave coincide with those of an ideal X-wave, and thus Eq. (6.20), as well as Eqs. (6.21) are still good approximations (see Fig. 6.8(a) and (c)). For wider fractional bandwidths ( $\overline{\Delta\omega} \gtrsim 0.2$ ),  $S_\rho$  remains unchanged with respect to the ideal case (as is clear by comparing Eqs. (6.29) and (6.15)), whereas  $S_z$  can only be calculated numerically and it is generally greater than the ideal one (see Fig. 6.8(b) and (d)). As a consequence, Eq. (6.20) should yield an underestimation of the actual pulse longitudinal size.

In the following Subsection a physical device is proposed to account for the finiteness of the structure. After a brief description of the radiating device, numerical results are presented under the frame of a rigorous theoretical formulation. Comments on the results will end Section 6.2.

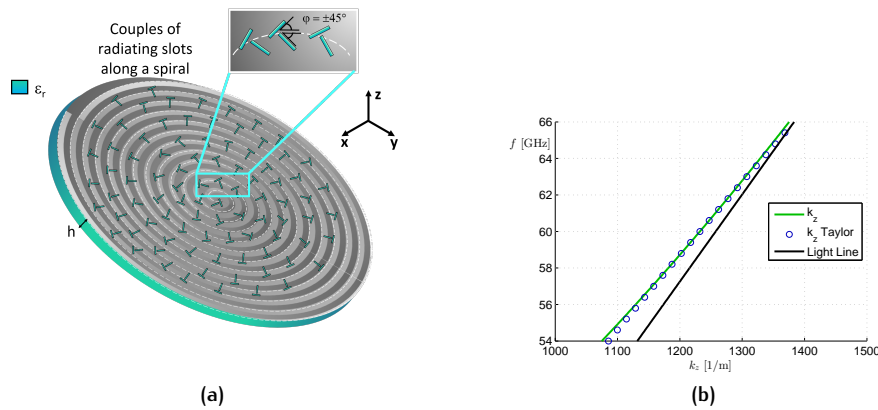


Figure 6.9.: (a) Prospective view of an RLSA. (b) Brillouin diagram  $f$  vs.  $k_z$  for the structure in Fig. 6.9.  $k_z$  (green curve) is given by Eq. 6.33 through the relation of separability. The second-order Taylor approximation (blue circles) accurately describe the wavenumber dispersion curve. The slope of  $k_z$  is lower than the light line (black line), so that  $c_0 > v_z > 0$ .

#### 6.2.4 Dispersive-finite X-waves

In Chapter 5 we have seen two specific structures for Bessel-beam generation at microwaves (see Section 5.2) and millimeter waves (see Section 5.3). Unfortunately, both devices use the combination of an inward and an outward Hankel wave to generate a Bessel beam profile. As a result, such Bessel-beam launchers are inherently narrow-band, thus providing poor localization of X-waves in the sense of both the weak and strong metrics. Moreover, in 5.3.5 we have seen that *forward* LWs as those used in Section 5.2 and Section 5.3, always provide  $v_z < 0$ , thus making impossible the description of an outward propagating X-wave. However, it has been recently shown [240] that Bessel beams can be efficiently generated through an inward traveling wave aperture distribution in a well-defined conical region centered around the axis of symmetry [220], [240], [295] (a rigorous mathematical explanation can be found in [240]). As a consequence of the non-resonant character of the aperture distribution, a radiating aperture able to support an inward Hankel wave may generate nondiffractive Bessel-like beams over a wide fractional bandwidth.

#### RLSA antennas

A class of microwave devices supporting such inward Hankel-wave distributions are RLSA antennas [242], [286], [287]. Basically, an RLSA is a dielectric-filled radial waveguide where the upper metallic plate is loaded with an array of radiating sub-resonant slots. The size and position of the slots are selected through an automatic-design procedure based on the *alternate projection method* [296]. Starting from a preliminary design, obtained by means of an approximate analytical model, the required aperture (*hologram*) is numerically refined by using an *ad-hoc* optimization tool [242], [286] (details on the synthesis procedure can be found in [286], [287]).

Briefly, according to *Bethe theory* [297], the radiation from a slot etched on a metallic plane is equivalent to the radiation of a pair of equivalent dipoles. In particular, for elongated slots [286], radiation can accurately be described only by an equivalent magnetic dipole  $\mathbf{M} = \underline{\underline{\alpha}}_m \cdot \mathbf{H}^{\text{inc}}$  parallel to the metallic plate and proportional to the incident magnetic field  $\mathbf{H}^{\text{inc}} = H^{\text{inc}} \hat{\mathbf{h}}_0$  through a dyadic polarizability  $\underline{\underline{\alpha}}_m$  [297]. For the fundamental  $\text{TM}_0^z$  mode of a radial waveguide (see Fig. 6.9(a)), the expression of the equivalent surface magnetic current distribution, takes the form [269]:

$$\mathbf{M} = j \underline{\underline{\alpha}}_m \cdot \hat{\mathbf{h}}_0 e^{j\phi} H_1^{(2)}(k_0 \sqrt{\varepsilon_r} \rho). \quad (6.31)$$

that is a first-order outward Hankel wave. Since, zeroth-order Hankel inward waves are necessary to generate Bessel beams (see [240]), the phase matching condition is enforced between the expression in Eq. (6.31) and the co-polar component of the desired surface magnetic current distribution  $\mathbf{M}_{\text{ap}} = H_0^{(1)}(k_\rho \rho) \hat{\mathbf{p}}_0$ , where  $\hat{\mathbf{p}}_0$  is an arbitrary polarization vector. By exploiting the asymptotic behavior of Hankel functions, the phase matching condition implies:

$$\begin{aligned} \frac{e^{j(\phi - k_0 \sqrt{\varepsilon_r} \rho)}}{\sqrt{\rho}} &\sim \frac{e^{jk_\rho \rho}}{\sqrt{\rho}} \\ \rightarrow \rho &= \frac{\phi}{k_\rho + k_0 \sqrt{\varepsilon_r}} \\ \rightarrow \rho &= \frac{\phi}{k_0 (\sin \theta_0 + \sqrt{\varepsilon_r})}, \end{aligned} \quad (6.32)$$

that is the equation of the spiral along which the slot pairs should be arranged. As frequency changes, Eq. (6.32) is still valid, but the equivalent magnetic current distributions becomes  $\mathbf{M} \sim \hat{\mathbf{p}}_0 e^{j(\phi - k_0(\omega) \sqrt{\varepsilon_r} \rho)} / \sqrt{\rho}$  and  $\mathbf{M}_{\text{ap}} \sim \hat{\mathbf{p}}_0 e^{jk_\rho(\omega) \rho} / \sqrt{\rho}$ . Consequently, from Eq. (6.32) follows an approximate dispersion equation for the RLSA given by:

$$\begin{aligned} \frac{e^{j(k_\rho(\omega_0) + k_0 \sqrt{\varepsilon_r} - k_0(\omega) \sqrt{\varepsilon_r}) \rho}}{\sqrt{\rho}} &\sim \frac{e^{jk_\rho(\omega) \rho}}{\sqrt{\rho}} \\ \rightarrow k_\rho(\omega) &= k_\rho(\omega_0) - \frac{\sqrt{\varepsilon_r}}{c_0} (\omega - \omega_0). \end{aligned} \quad (6.33)$$

A full-wave Method of Moments (MoM) analysis is needed to evaluate the field radiated by RLSA antennas [298], [299]. However, the knowledge of the dispersion relation allows for describing the near-field distribution of all the electromagnetic field components through the evaluation of the scalar potential  $A_z$  ( $F_z$ ) associated to the propagating TM (TE) mode (see Section 5.2).

### Theoretical formulation

In order to take into account the edge diffraction due to the finiteness of the radiating structure, the *dispersive-finite* UXW is calculated as

$$\chi^U(\rho, z, t) = \int_{\omega_m}^{\omega_M} E^{\text{rad}}(\rho, z) \exp(j\omega t) d\omega, \quad (6.34)$$

where  $E^{\text{rad}}$  is a proper scalar component of the total radiated electric field  $\mathbf{E}^{\text{rad}}$  which can be calculated e.g., as [163], [164]:

$$\mathbf{E}^{\text{rad}}(\mathbf{r}) = \frac{1}{4\pi} \int_{S'} (\mathbf{r} - \mathbf{r}') \times \mathbf{E}_t(\mathbf{r}') \frac{(1 + jkR)}{R^3} e^{-jkR} dS', \quad (6.35)$$

where  $\mathbf{r}$ , and  $\mathbf{r}'$  are the observation and source points, respectively,  $R = |\mathbf{r} - \mathbf{r}'|$  is the euclidean distance between the observation and source points,  $S'$  is the surface on which the electromagnetic sources are localized, and  $\mathbf{E}_t = \hat{\mathbf{n}} \times \mathbf{E} \times \hat{\mathbf{n}}$  is the tangential electric field component ( $\hat{\mathbf{n}}$  being the unit vector normal to the surface).

Note that Eq. (6.34) is the general form of Eq. (6.11) where  $E^{\text{rad}}$  replaces the ideal Bessel beam distribution. As we have previously discussed, the magnetic surface current distribution  $\mathbf{M}_{\text{ap}}$  is equal to a first-kind, zeroth-order Hankel inward wave so that the tangential electric field  $\mathbf{E}_t = \mathbf{M}_{\text{ap}} \times \hat{\mathbf{n}}$ , can be expressed as  $\mathbf{E}_t(\rho, \phi) = H_0^{(1)}(k_\rho(\omega_0)\rho) \hat{\mathbf{p}}_0 \times \hat{\mathbf{n}}_0$ , and  $k_\rho(\omega_0)$  is a design parameter.

The structure synthesizing such an aperture field distribution is shown in Fig. 6.9(a). It consists of a dielectric filled radial waveguide loaded with radiating slots operating at  $f_0 = 60$  GHz and with a finite radius of  $\rho_{\text{ap}} = 15\lambda_0 = 75$  mm, centrally fed by a coaxial probe. The dispersion equation of the RLSA (see Eq. (6.33) and its related Brillouin diagram Fig. 6.9(b)) has been obtained for  $\epsilon_r = 1.04$  and  $k_\rho(\omega_0) = 0.2k_0$ . This choice leads to an operating axicon angle  $\theta_0 \simeq 11^\circ$  with a nondiffractive range at  $f_0$  equal to  $z_{\text{ndr}}^{(c)} \simeq 367$  mm. It is worth mentioning that the design parameters of the proposed structure have been shown according to the results in Fig. 6.3 requiring an axicon angle smaller than  $50^\circ$  for a radiating aperture of  $15\lambda_0$ . Note also that such a wavenumber dispersion defines a *subluminal* ( $v_z < c_0$ ) *backward wave* [2] with  $v_z > 0$ , thus describing an outward propagating X-wave. Since  $v_z = 2\pi\partial f / \partial k_z$  from Fig. 6.9(b) it is readily obtained  $v_z \simeq 0.841c_0$

### Numerical results

The impact of the fractional bandwidth on the spatial features of an X-wave is here evaluated considering the ideal case (see 6.2.2), the dispersive case (see 6.2.3) and the dispersive-finite case. For convenience, we report here the different expressions for the numerical calculation of ideal, dispersive, and dispersive-finite X-waves:

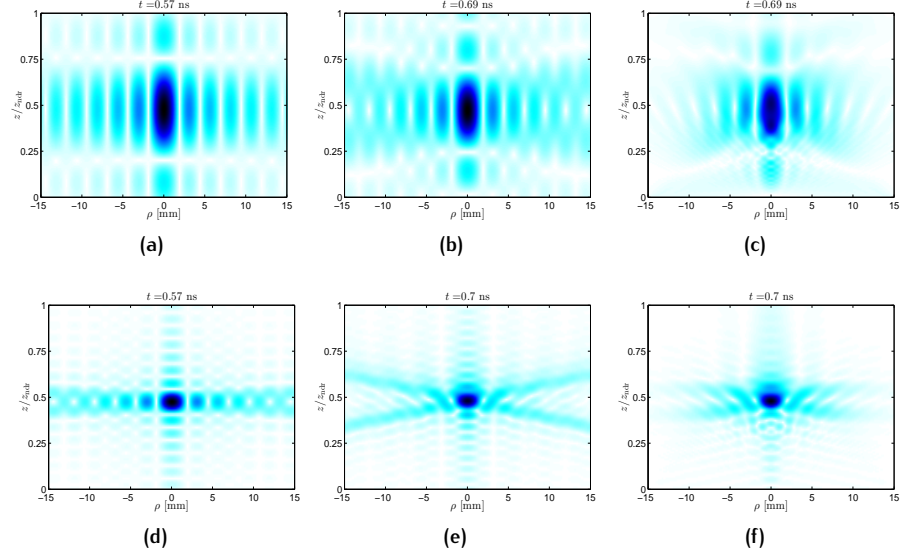


**Figure 6.10:** 2-D normalized intensities for ideal (first column: (a) and (d)), dispersive (second column: (b) and (e)), and dispersive-finite (third column: (c) and (f)) UXWs, when the pulse has reached half the propagating distance of  $z_{\text{dof}}^{(c)}$ . The numerical results are shown for  $\overline{\Delta\omega} = 0.05$  (first row: (a-c)), and  $\overline{\Delta\omega} = 0.2$  (second row: (d-f)).

$$\text{ideal :} \quad \int_{\omega_0 - \Delta\omega/2}^{\omega_0 + \Delta\omega/2} J_0(k_0 \sin \theta_0 \rho) e^{-k_0 \cos \theta_0 z} e^{j\omega t} d\omega \quad (6.36)$$

$$\text{dispersive :} \quad \int_{\omega_0 - \Delta\omega/2}^{\omega_0 + \Delta\omega/2} J_0(k_0 \sin \theta(\omega) \rho) e^{-k_0 \cos \theta(\omega) z} e^{j\omega t} d\omega \quad (6.37)$$

$$\text{dispersive-finite :} \quad \int_{\omega_0 - \Delta\omega/2}^{\omega_0 + \Delta\omega/2} E^{\text{rad}} e^{j\omega t} d\omega. \quad (6.38)$$

In Fig. 6.10 the 2-D maps of the normalized intensity (defined as  $|\chi^U(\rho, z, t)|^2$ ) of the pulse for the ideal (see Fig. 6.10(a-c)), the dispersive (see Fig. 6.10(b-e)), and the dispersive-finite (see Fig. 6.10(c-f)) cases, for a fractional bandwidth of  $\overline{\Delta\omega} = 0.05$  (see Fig. 6.10(a), (b), (c)), and  $\overline{\Delta\omega} = 0.2$  (see Fig. 6.10(d), (e), (f)). The field intensities are shown on a  $\rho z$ -plane limited on the  $\rho$ -axis by the aperture of the finite structure ( $\rho_{\text{ap}} = 15\lambda_0$ ,  $\lambda_0 = 5$  mm) and on the  $z$ -axis by the nondiffractive range achieved at the carrier frequency  $z_{\text{ndr}}^{(c)} = 367$  mm. Here it is worth to remark that the nondiffractive range is generally a function of the frequency (as is clear from Eqs. (4.14) and (6.33)) and thus its value varies within the bandwidth in both the dispersive and the dispersive-finite case. Conversely, in the ideal case, the pulse is assumed to be nondispersive and nondiffractive, thus the nondiffractive range is constant over all the frequency range. In the ideal case we have assumed  $k_\rho(\omega) = k_\rho(\omega_0)$  and thus  $\theta(\omega) = \theta_0$ .

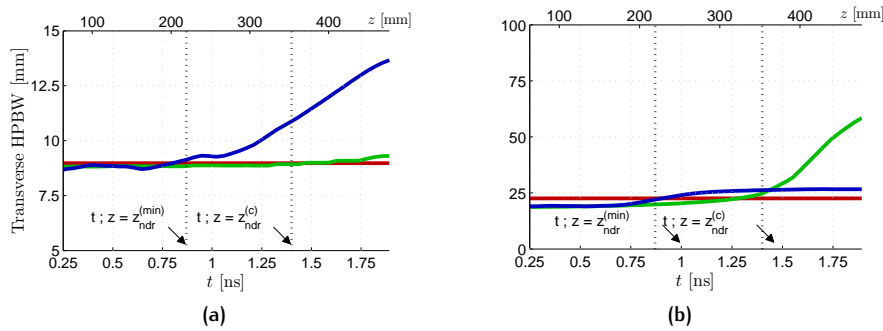


**Figure 6.11.:** Evolution of the (a) transverse and (b) longitudinal HPBW vs.  $t$ . The ideal (red curves), dispersive (green curves), and the dispersive-finite case (blue curves) are represented for  $\overline{\Delta\omega} = 0.2$ . The  $x$ -axis on the top is obtained by scaling the temporal axis with the theoretical group velocity  $v_z \simeq 0.84c_0$ .

As shown in Fig. 6.10, the pulse is depicted at a fixed time frame when its maximum has reached the distance  $z_p = z_{\text{dof}}^{(c)}/2 \simeq 183$  mm (the time evolution of the pulse is available as online supplemental material in [206]). For the ideal case (see first row of Fig. 6.10), the previous distance is reached for an instant of time  $t_p < z_p/c_0$  ( $t_p = 0.60$  ns,  $z_p/c_0 = 0.61$  ns), which means that the pulse is propagating superluminally, as expected for a nondispersive pulse whose phase velocity is greater than  $c_0$ . On the other hand, in both the dispersive and dispersive-finite case  $t_p > z_p/c_0$  ( $t_p = 0.73$  ns) and hence the pulse is obviously subluminal due to dispersion (as already seen in Fig. 6.9(b)). Note that, for the ideal case we get  $z_p/t_p \simeq 1.0194c_0$  m/s which is a good estimation of the theoretical phase velocity  $u_z = c_0/\cos(\theta_0) \simeq 1.0187c_0$  m/s, whereas for the dispersive (dispersive-finite) case we get  $z_p/t_p \simeq 0.8495c_0$  m/s which is also a good estimation of the theoretical group velocity  $v_z \simeq 0.8411$  ns as calculated from Fig. 6.9(b).

Figs. 6.10(a)-(f) clearly show the impact of the bandwidth in the  $z$ -confinement of the pulse: the greater is the fractional bandwidth, the narrower is the spot size along the  $z$ -axis. In particular, the pulse shape of an ideal UXW (Figs. 6.10(a) and (d)) does not depend on time, whereas for dispersive (Figs. 6.10(b) and (e)) and dispersive-finite (Figs. 6.10(c) and (f)) UXWs it is strongly time-dependent. This effect is highlighted in Fig. 6.11(a) and in Fig. 6.11(b), where the spot widths of the considered UXWs are reported for both the transverse and the longitudinal sections. Specifically, the half power beamwidth (HPBW) is calculated with respect to the absolute maximum at each time frame. Figs. 6.11(a) and (b) show the evolution of the spot size of ideal (red curves), dispersive (green curves), and dispersive-finite (blue curves) UXWs with respect to time  $t$  only for a fractional bandwidth  $\overline{\Delta\omega} = 0.2$ , for which the effects of the dispersion and of the truncation are more pronounced. The time evolution is limited in the range  $0.25$  ns  $< t < 1.8$  ns to avoid an initial transient time where the pulse still



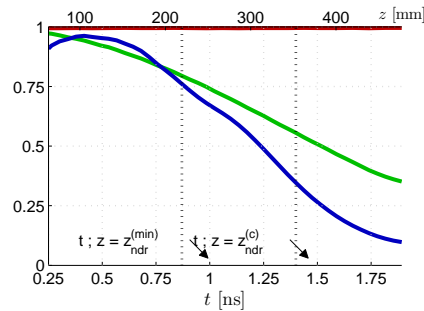


Figure 6.12.: Evolution of the normalized intensity vs. time  $t$ . The ideal (red solid line), dispersive (green dashed line), and the dispersive-finite case (blue circles) are represented for  $\overline{\Delta\omega} = 0.2$ .

travels through a region of reactive fields, and to limit the analysis at a time instant for which the pulse would have traveled beyond the nondiffractive range achieved at  $z_{\text{ndr}}^{(c)} = 367$  mm.

In details, in Fig. 6.11(a) it is seen that the transverse HPBW of the dispersive-finite UXW starts spreading at the time frame when the pulse has reached the minimum nondiffractive range  $z_{\text{ndr}}^{(\text{min})}$  of the constituent waves. We recall here that, due to the frequency dispersion described by Eq. (6.33),  $z_{\text{ndr}}^{(\text{min})}$  is achieved at the minimum frequency of 54 GHz for which  $\theta_0 \simeq 18^\circ$  and thus  $z_{\text{ndr}}^{(\text{min})} \simeq 222$  mm. Slightly after  $z_{\text{ndr}}^{(\text{min})}$ , the transverse spreading increases almost linearly with time. As expected, the ideal UXW maintains a constant transverse profile for all the time, whereas the dispersive UXW has a negligible spreading (less than 2 mm here) only at the end of the considered time propagation.

In Fig. 6.11(b) an opposite trend is noticeable. While the ideal UXW retains its longitudinal spot size as it propagates (due to the rigid transport inherent to all ideal nondispersive pulses), the dispersive UXW spreads along the longitudinal axis after a distance  $z_{\text{ndr}}^{(\text{min})}$  at which the spot size increases almost linearly with time. However, the dispersive-finite UXW only slightly spreads over the longitudinal direction. Such a different behavior for the transverse and the longitudinal spreading can be interpreted in terms of diffraction and dispersion phenomena (the interested reader can find a more detailed discussion in [206]).

In general, the beam spreading (either transverse or longitudinal) requires an attenuation of the field to grant energy conservation. To this purpose, in Fig. 6.12 the time evolution of the normalized intensities of ideal, dispersive, and dispersive-finite UXWs have been calculated for  $\overline{\Delta\omega} = 0.2$ . It is clear that the ideal UXW is a *soliton-like* solution in the sense that its normalized intensity is always constant. On the other hand, the normalized intensities of dispersive and dispersive-finite UXWs decrease with time as the pulse propagates. In the dispersive case, the attenuation is due to the different velocities of the various frequency components of the wavepacket and thus the intensity fades out even if the pulse is fed with infinite energy (edge diffraction is here neglected). In the dispersive-finite case, the intensity is

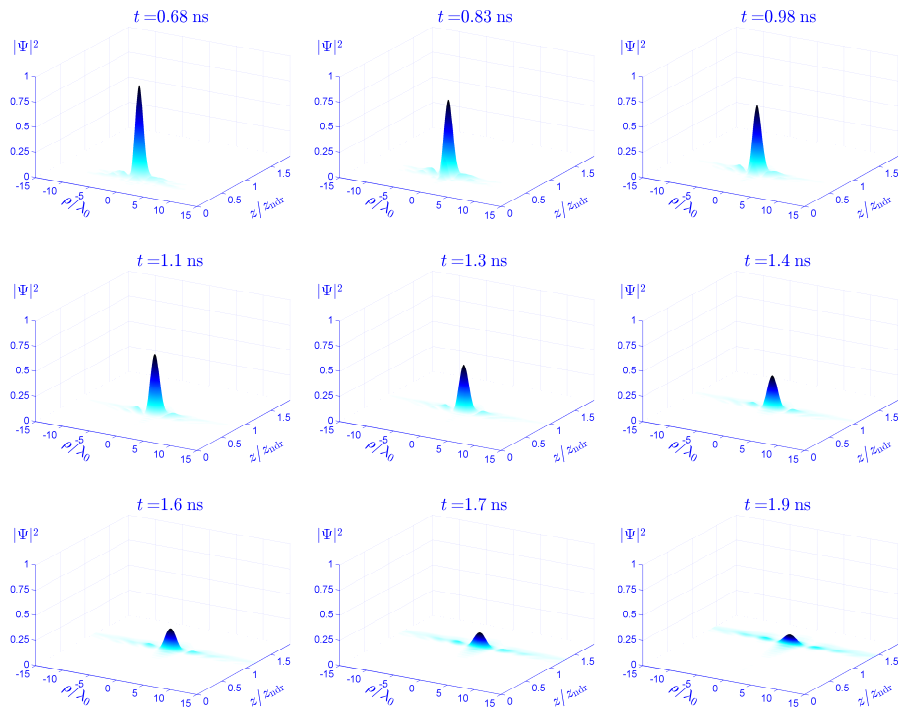


Figure 6.13.: 3-D view of the normalized intensities of a dispersive-finite UXW, generated with a fractional bandwidth  $\Delta\omega = 0.2$ . The time evolution is numerically reproduced for 9 different time frames, ordered from left to right and from top to bottom.

slightly attenuated (less than 25%) until the pulse reaches the  $z_{\text{ndr}}^{(\text{min})}$ . Beyond  $z_{\text{ndr}}^{(\text{min})}$  the intensity decreases rapidly and then slowly vanishes, as required for any physical system which is fed with finite energy (the dispersive-finite pulse is generated through a finite-size radiating aperture). It is worth noting that the strong fading of the pulse after  $z_{\text{ndr}}^{(\text{c})}$  further corroborates our first guess (see 6.2.1) to define a metric over the  $z$ -axis with respect to the nondiffractive range of an ideal X-wave as reference.

Finally, some relevant time frames of the pulse propagation of a dispersive-finite X-wave for a fractional bandwidth of 20% are reported in Fig. 6.13. It is manifest from this 3-D representation that as the time increases, the intensity of the pulse decreases in correspondence with the spreading of the main spot.

#### *Use of an RLSA as a higher-order X-wave launcher*

In this Section 6.2 we have analyzed both the focusing properties of ideal, dispersive, and dispersive-finite UXWs. Starting from an original definition of a metric which is able to describe the confinement of UXWs even in the presence of dispersion, the effect of the fractional bandwidth on the spatial features of UXWs generated from truncated radiating apertures has been thoroughly discussed. As a proof-of-concept a preliminary design of a radiating aperture of radius  $\rho_{\text{ap}} = 7.5$  cm fed by a 60-GHz signal with uniform

spectrum over a 20% fractional bandwidth around the carrier frequency has been considered. It has been shown through theoretical and numerical results that such a radiating aperture would be able to produce UXWs with an almost constant longitudinal HPBW of about 1 cm and a transverse HPBW of about 2.5 cm over a propagating distance of 20 cm. The proposed design may be synthesized with an RLSA antenna through the holographic principle. As a consequence, we strongly believe that RLSA antennas may also be considered for the generation of *higher-order X-waves*, being the holographic principle mainly based on the phase matching between the required aperture field distribution and the one supported by the radial waveguide.

It is worth here mentioning that the higher-order character implies a non-null orbital angular momentum (OAM), so that the generation of higher-order X-waves through RLSA antennas could pave the way for the first localized transmission of OAM at microwaves. Such a fascinating possibility will be theoretically and numerically investigated in the next Section 6.3

### 6.3 GENERATION OF HIGHER-ORDER X-WAVES CARRYING OAM THROUGH A FINITE APERTURE

In the previous Section 6.2 we have seen that the generation of zeroth-order X-waves requires electrically large apertures and low axicon angles over a possibly wide fractional bandwidth. Besides, we have seen that RLSA antennas are suitable radiating elements for the generation of a UXW.

In Chapter 4 we have seen different kind of localized solutions of the scalar-wave equation. Among them, *higher-order localized waves* (see Section 4.2) are characterized by an azimuthal phase variation. Such a feature is responsible of the OAM carrying typical of these kind of waves. As well established, OAM can profitably be used to micromanipulate small particles [300] or for the development of alternative techniques for accelerating them by using the so-called *accelerating beams* [205].

In this Section, we will focus our attention on *higher-order X-waves*, i.e., the polychromatic version of higher-order Bessel beams, commonly known as *vortex beams*. Indeed, *higher-order X-waves* allows for combining the non-diffractive character of X-waves with the OAM carrying of vortex beams, a possibility that has recently been explored by physicists in the optical range [207]. However, to the author's best knowledge, the generation of *twisted localized pulses* at microwaves is still lacking. The aim of this Section, is thus to provide a theoretical and numerical demonstration of the possibility to generate higher-order X-waves through microwave launchers.

To this purpose, in 6.3.1 we briefly review the synthesis method for the realization of an aperture distribution able to generate *higher-order* non-diffracting waves. With respect to Section 6.2, the inherent vectorial structure of Maxwell's equations is here rigorously considered to generalize the nondiffractive solution of the scalar wave-equation. In 6.3.2 the proposed method is used to generate a first-order Bessel-beam at a single frequency, in the microwave range. A first-order UXW is then obtained in 6.3.3 through a polychromatic spectral superposition of its monochromatic constituents, i.e., first-order Bessel beams, taking into account the wavenumber dispersion (as already done in Section 6.2 for zeroth-order UXWs). Finally, in 6.3.4 numerical results will be reported for all the radiated electric field components.

These results, together with those obtained in Section 6.2, demonstrate that a microwave wideband radiator as an RLSA antenna could generate X-waves of any order, if properly designed. Obviously, some technological aspects that go beyond the scope of this PhD thesis can limit the wideband capability, as well as the effectiveness of the synthesis procedure. However, the presented investigation may serve as a useful guideline for future experimental validations.

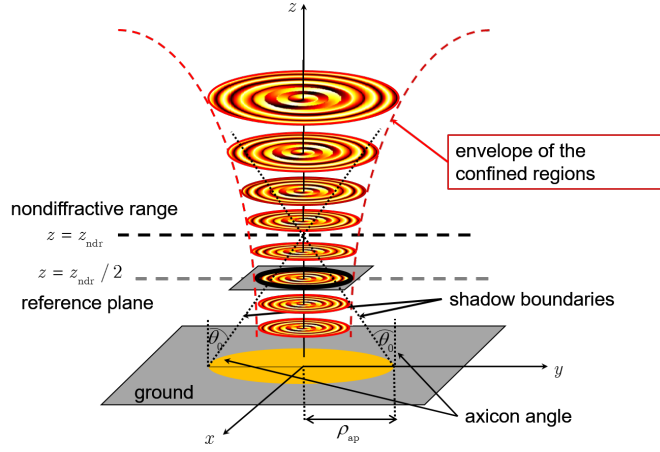


**Figure 6.14.:** Schematic view of the generation of localized twisted pulses from a radiating aperture on the  $xy$  plane. The intersection of the shadow boundaries (dotted black lines) defines the nondiffractive range ( $z_{\text{ndr}} = \rho_{\text{ap}} \cot \theta$ ). Dashed red lines define the envelope of the confined region whose section slowly increases beyond the nondiffractive range due to the limited spatio-temporal dispersion of the pulse. In the numerical examples of 6.3.4 the transverse distributions are observed at the reference plane for different time instants.

### 6.3.1 Analytical framework

A vectorial formulation of Maxwell's equations in a cylindrical reference frame (generally not axisymmetric  $\partial/\partial\phi \neq 0$ ) is adopted in this Subsection to find general expressions for Bessel beams of any order (note that the vectorial formulation for zeroth-order Bessel beams has been addressed in Section 5.2). Here, we want to develop a simple theoretical framework to derive the aperture distribution that is needed to radiate in the near field a  $n$ -th order  $\text{TM}^z$  Bessel beam over the longitudinal component  $E_z$ :

$$E_z = J_n(k_\rho \rho) e^{-jn\phi} e^{-jk_z z}. \quad (6.39)$$

As we have already seen in Section 5.2, since the wave is  $\text{TM}^{(z)}$  polarized, the  $E_z$  component can be used to derive the other components of the electric field (magnetic field components will be then cut out by the application of the *Equivalence Theorem* for aperture antenna radiation [164]). In fact, by means of Eqs. (5.3)-(5.5), the tangential components of the electric field read:

$$E_\rho = \frac{k_z}{jk_\rho} J'_n(k_\rho \rho) e^{-jn\phi} e^{-jk_z z}, \quad (6.40)$$

$$E_\phi = -\frac{nk_z}{k_\rho^2} \frac{J_n(k_\rho \rho)}{\rho} e^{-jn\phi} e^{-jk_z z}, \quad (6.41)$$

where first derivatives have been identified with a prime symbol  $(\cdot)'$ . The evaluation of Eqs. (6.40) and (6.41) at  $z = 0$  gives the equivalent tangential electric field distribution to be synthesized on the antenna aperture (see Fig. 6.14).

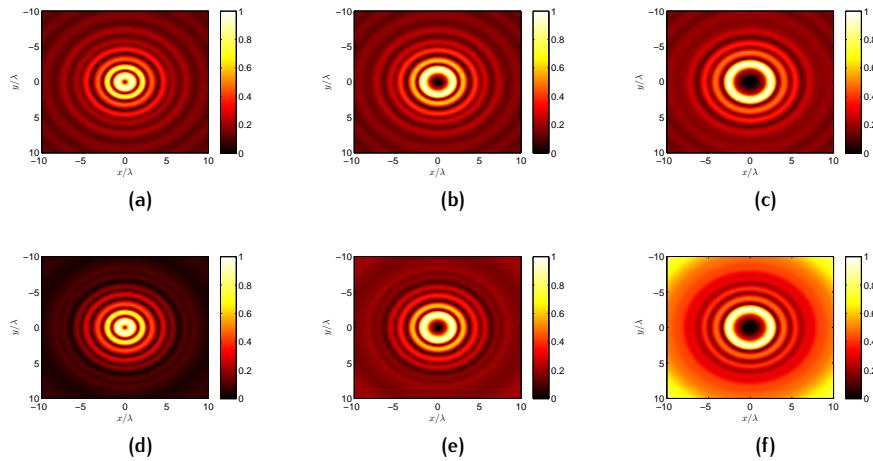


Figure 6.15.: Normalized amplitude distribution of  $E_z$  vs.  $x, y$  at  $f = 12.5$  GHz with  $k_\rho = 0.4k_0$  of the near field radiated over the transverse (i.e.,  $xy$ ) plane at  $z = z_{\text{ndr}}/2$ . (a-c) Contour plot of  $E_z$  radiated at  $z = z_{\text{ndr}}/2$  by a standing-wave aperture distribution (Eqs. (6.40)-(6.41)) and (d-f) by an inward traveling-wave aperture distribution (Eqs. (6.42)-(6.43)) for  $n = 1, 3, 5$  (looking from left to right) over a radiating aperture with radius  $\rho_{\text{ap}} = 10\lambda$ .

In Chapter 5 we have seen that standing-wave distributions, as those given by Eqs. (6.40) and (6.41), can be obtained by means of LRWs. However, we already know that the inherent narrow-band character of these resonant devices limits its use for the generation of monochromatic Bessel beams rather than their polychromatic version which this Section 6.3 is dedicated to. Nevertheless, in Section 6.2 we have seen that inward traveling distributions can be used to synthesize Bessel beams over a large fractional bandwidth.

Hence, in order to design a wideband launcher, we propose to synthesize an inward cylindrical traveling wave aperture distribution by replacing the  $J'_n, J_n$  functions in Eqs. (6.40)-(6.41) with the  $H_n^{(1)'}, H_n^{(1)}$ , respectively, hence obtaining

$$E_\rho(\rho, \phi, z = 0) = -j \frac{k_z}{k_\rho} H_n^{(1)'}(k_\rho \rho) e^{-jn\phi}, \quad (6.42)$$

$$E_\phi(\rho, \phi, z = 0) = -\frac{k_z}{k_\rho^2} \frac{H_n^{(1)}(k_\rho \rho)}{\rho} e^{-jn\phi}. \quad (6.43)$$

### 6.3.2 Monochromatic higher-order Bessel beams

The accuracy of this assumption for monochromatic fields, has been assessed through numerical evaluation of  $E_z$  assuming Bessel beams of different orders, as is shown in Fig. 6.15 (parameters are given in the caption of Fig. 6.15). As expected, an inward traveling distribution is able to correctly reproduce a higher-order Bessel beam over a limited portion of the transverse  $xy$ -plane which depends on the distance from the radiating aperture

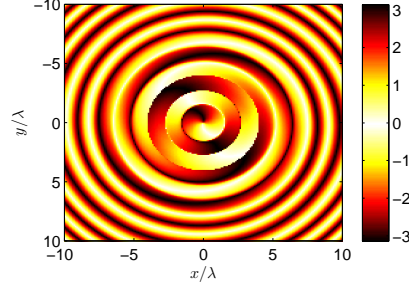


**Figure 6.16.:** Phase distribution at  $f = 12.5$  GHz with  $k_\rho = 0.4k_0$  of the  $E_z$  near field obtained by radiating a first-order inward traveling-wave distribution over the transverse (i.e.,  $xy$ ) plane at  $z = z_{\text{ndr}}/2$ . The correspondent normalized amplitude distribution is given in Fig. 6.15(d).

[240]. This region is maximized for  $z = z_{\text{ndr}}/2$  [240] at which the transverse distributions of Fig. 6.15 have been calculated. It is worth here to recall that, as for the case of zeroth-order Bessel beams [240], the unavoidable aperture truncation limits the nondiffractive behaviour up to  $z_{\text{ndr}}$ .

In the following, we restrict our analysis to first-order, i.e.,  $n = 1$ , Bessel beams and enforce a transverse electric field  $\mathbf{E}_t = E_\rho \mathbf{u}_\rho + E_\phi \mathbf{u}_\phi$  having a radial wavenumber  $k_\rho = 0.4k_0$  over a finite aperture having radius  $\rho_{\text{ap}} = 10\lambda$ , at the operating frequency  $f_0 = 12.5$  GHz. The total electromagnetic field  $\mathbf{E}_{\text{tot}}^{\text{rad}} = E_\rho^{\text{rad}} \hat{\mathbf{u}}_\rho + E_\phi^{\text{rad}} \hat{\mathbf{u}}_\phi + E_z^{\text{rad}} \hat{\mathbf{u}}_z$  radiated by this aperture is obtained as described in Section 6.2 for zeroth-order Bessel beams.

In Fig. 6.16, the phase of the resulting monochromatic Bessel beam has been reported for the longitudinal  $E_z$  component (the normalized amplitude was previously reported in Fig. 6.15(d)). As expected, the higher-order character of the solution implies the azimuthal phase variation. A vortex beam is then generated, which carries a non-null OAM. Such vortex beams will be the main constituents of the higher-order X-wave described in the next Subsection.

### 6.3.3 Polychromatic superposition of higher-order Bessel beams

Once a monochromatic higher-order Bessel beam is generated, an ideal higher-order UXW can be obtained by superposing monochromatic *vortex beams* over a certain frequency range, or, equivalently, taking the inverse Fourier Transform of Eq. (6.39):

$$\chi_z(\rho, \phi, z; t) = \int_{\omega_0 - \Delta\omega/2}^{\omega_0 + \Delta\omega/2} \underbrace{J_n(k_\rho(\omega)\rho) e^{jn\phi} e^{-jk_z(\omega)z}}_{E_z^{\text{rad}}} e^{j\omega t} d\omega, \quad (6.44)$$

where we have again considered a uniform frequency spectrum centered around  $\omega_0 = 2\pi f_0$  over a bandwidth  $\Delta\omega$ . Note that the wavenumber dispersion which commonly affect RLSA launchers has been properly taken

into account by considering the approximate dispersion equation, given by Eq. (6.33). For the considered design, the following expression is found:

$$k_\rho(\omega) = 0.4 \frac{\omega}{c_0} - \frac{\sqrt{\varepsilon_r}}{c_0} (\omega - \omega_0), \quad (6.45)$$

with  $\varepsilon_r = 1.04$  as in Section 6.2. We note here that, due to the wavenumber dispersion,  $z_{\text{ndr}}(f)$  varies with frequency. As in Section 6.2, we conveniently define  $z_{\text{ndr}}^{(c)} = z_{\text{ndr}}(f_0)$  as the nondiffractive range calculated at the central frequency  $f_0 = 12.5$  GHz.

According to Eq. (6.44), the time-domain representation of the longitudinal scalar component  $E_z$  is given by replacing the ideal  $n$ -th order Bessel solution with the values of  $E_z^{\text{rad}}$  and retaining the real part of  $\chi_z(\rho, \phi, z; t)$ . Note that  $E_z^{\text{rad}}$  is obtained through the application of Huygens' principle to the aperture field described by Eqs. (6.42)-(6.43) with  $k_\rho(\omega)$  given by Eq. (6.45)

Obviously, the time-domain representations of each electromagnetic scalar component can be obtained by replacing  $E_z$  in Eq. (6.44) with the respective scalar component so that:

$$\chi_\rho(\rho, \phi, z; t) = \Re \left[ \int_{\omega_0 - \Delta\omega/2}^{\omega_0 + \Delta\omega/2} E_\rho^{\text{rad}} e^{j\omega t} d\omega \right], \quad (6.46)$$

$$\chi_\phi(\rho, \phi, z; t) = \Re \left[ \int_{\omega_0 - \Delta\omega/2}^{\omega_0 + \Delta\omega/2} E_\phi^{\text{rad}} e^{j\omega t} d\omega \right], \quad (6.47)$$

$$\chi_z(\rho, \phi, z; t) = \Re \left[ \int_{\omega_0 - \Delta\omega/2}^{\omega_0 + \Delta\omega/2} E_z^{\text{rad}} e^{j\omega t} d\omega \right], \quad (6.48)$$

where each time-domain representation is an inverse Fourier-Transform of an electric field scalar component.

However, a detailed analysis of electromagnetic fields at microwaves requires a fully vectorial wave analysis. As a consequence, the scalar components in Eqs. (6.46)-(6.48) are replaced by the radiated electric field  $\mathbf{E}^{\text{rad}}$  leading to the vectorial expression of the localized electric pulse  $\chi_E(\rho, \phi, z; t) = \chi_\rho \hat{\mathbf{u}}_\rho + \chi_\phi \hat{\mathbf{u}}_\phi + \chi_z \hat{\mathbf{u}}_z$

$$\chi_E(\rho, \phi, z; t) = \Re \left[ \int_{-\omega_0 + \Delta\omega/2}^{\omega_0 + \Delta\omega/2} \mathbf{E}^{\text{rad}}(\rho, \phi, z; \omega) e^{j\omega t} d\omega \right]. \quad (6.49)$$

It is worth noting that each component of  $\chi_E(\rho, \phi, z; t)$  is a spectral superposition of vortex beams, as long as Eqs. (6.40)-(6.41) are correctly reproducing Eqs. (6.42)-(6.43). Hence, limited-diffraction *twisted* pulses are expected to be generated for each component of the electric pulse  $\chi_\rho$ ,  $\chi_\phi$ , and  $\chi_z$ , and over  $\|\chi_E\|$ , i.e., its norm in  $L^2$ . Note that, a fractional bandwidth  $\Delta\omega/\omega_0 = 0.2$  is assumed as in Section 6.2.



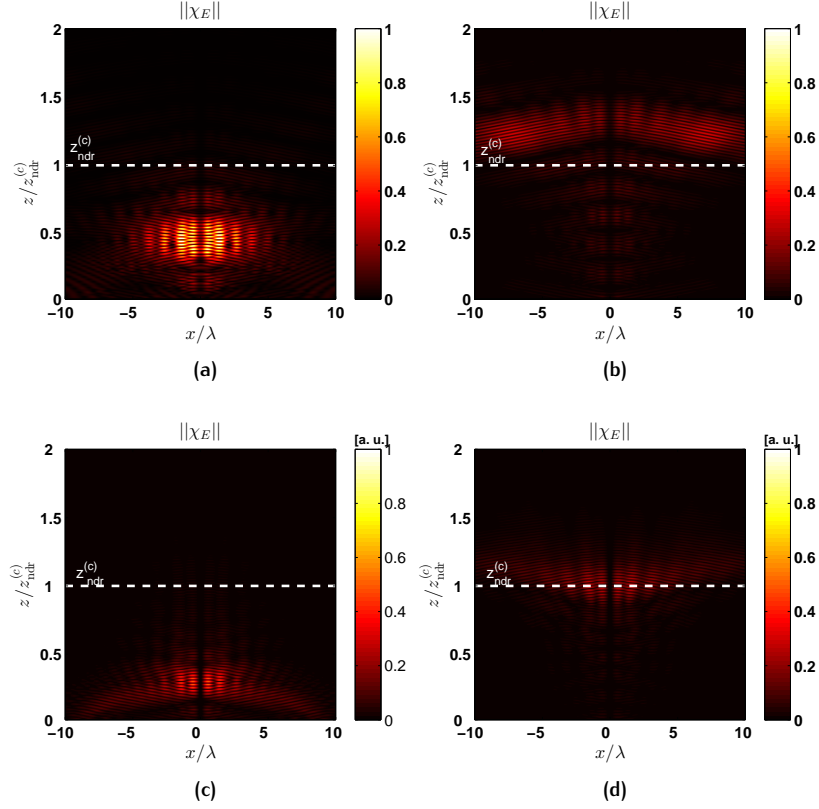


**Figure 6.17.:** Comparison between (a)-(b) nondispersive and (c)-(d) dispersive case. The norm of  $\chi_E$  is reported over the  $xz$  plane. The  $x$ -axis is normalized to  $\lambda_0$ , whereas the  $z$ -axis is normalized to  $z_{\text{ndr}}^{(c)}$ . The contour plot of  $\|\chi_E\|$  has been reported for two time instants: (a), (c)  $t_i = 0.8$  ns and (b), (d)  $t_f = 2.4$  ns.

### 6.3.4 Numerical results

To assess the effect of the wavenumber dispersion and the diffraction limit, in Fig. 6.17 the normalized electric field intensity of the *twisted pulse*  $\chi_E(\rho, \phi, z, t)$  has been reported at two time instants  $t_i$  and  $t_f$  (see the caption for the relevant details) corresponding to distances  $z = z_{\text{ndr}}^{(c)}/2$  and  $z = 1.25z_{\text{ndr}}^{(c)}$  for both the nondispersive (see Figs. 6.17(a) and (c)) and dispersive case (see Figs. 6.17(b) and (d)).

The spatio-temporal features for such higher-order UXWs are similar to those obtained in Section 6.2 for zeroth-order UXWs. In fact, as can be inferred from Fig. 6.17, while nondispersive UXWs are superluminal  $v_z > c_0$ , dispersive UXWs result subluminal  $v_z < c_0$ . Moreover, the spot size is slightly widened along the transverse direction (see Figs. 6.17(c) and (d)) without compromising the spatio-temporal localization of the pulse within the nondiffractive range.

Conversely, when the pulse is propagating beyond the nondiffractive range (see Figs. 6.17(b) and (d)), the central spot is not clearly visible either when dispersion is or is not taken into account. On one hand, the

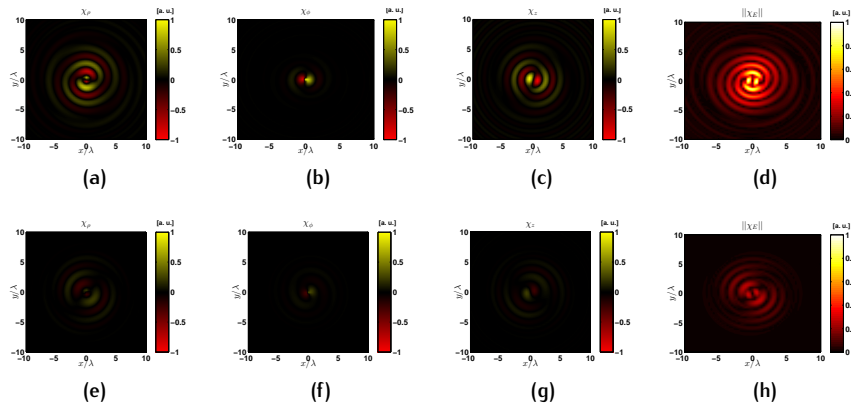


Figure 6.18.: Screen-shots of (a)  $\chi_\rho$ , (b)  $\chi_\phi$ , (c)  $\chi_z$ , and (d)  $\|\chi_E\|$  at  $t_1 = 0.8$  ns,  $t_2 = 1.3$  ns over the  $xy$  plane (both axes are normalized to  $\lambda$ ). Note that the colorscale for (d) and (h) is different since  $\|\chi_E\| > 0$ .

nondispersive twisted pulse has a group velocity  $v_z$  equal to the phase velocity  $u_z = \omega/k_z$  which is greater than the speed of light, thus exceeding the nondiffractive distance at  $t_f = 1.25z_{\text{ndr}} = 2.4$  ns. As a result, its spot size progressively grows up and in turn the intensity of the central spot abruptly vanishes for energy conservation. On the other hand, the dispersive pulse travels at a group velocity lower than the speed of light, thus reaching the nondiffractive distance without exceeding it. As a result, the central pulse is highly attenuated but it is still distinguishable (Note that similar results have been obtained for zeroth-order UXWs in Section 6.2). As a consequence, the nondiffractive range also represents the distance for which the OAM is effectively carried by the pulse.

Finally, numerical results for each component of the twisted pulse on a transverse plane have been reported in Fig. 6.18, where their spatial distributions have been evaluated at the reference plane  $z = z_{\text{ndr}}/2$  (refer to Fig. 6.14) for two distinct time instants. Note that  $t_1 = 0.8$  ns corresponds to the time instant at which the pulse is supposed to cross the reference plane. In fact, the intensities of the pulses in Figs. 6.18(a)-(d) is remarkably greater than those in Figs. 6.18(e)-(h), thus confirming the excellent space-time localization of the generated pulse. The peculiar rotating behavior as well as its nondiffractive nature are clearly visible. The former confirms the OAM carrying feature inherited by *vortex beams*, whereas the latter confirms the outstanding spatial confinement features typical of UXWs.

## 6.4 CONCLUSION

In this Chapter, we have analyzed both the spatial and the temporal properties of ideal and dispersive X-waves generated by a finite radiating aperture in the presence of dispersion at millimeter waves. In particular, we have first defined an efficiency of confinement for ideal X-waves. This analysis revealed that, even in the ideal case, large fractional bandwidths and electrically large apertures with low-axicon angles are required to efficiently generate such pulses. Moreover, we provided exact and approximated analytically closed-form relations for the calculation of the transverse and longitudinal profiles for both ideal and dispersive X-waves with a limited uniform spectrum. On this ground, the propagation of ideal, dispersive, and dispersive-finite X-waves has been considered and then compared for different values of the fractional bandwidth. As is seen, a radiating aperture of diameter 15 cm fed by a 60-GHz signal with uniform spectrum over the 54 – 66 GHz bandwidth is able to produce X-waves with an almost constant longitudinal spot-size of about 1 cm and a transverse spotsize of about 2.5 cm over a propagating distance of 20 cm.

The results obtained so far for zeroth-order X-waves have been then extended for the study of higher-order X-waves carrying orbital angular momentum at microwaves. Numerical results have shown that a wideband radiator, as an RLSA antenna, can efficiently generate such intriguing solutions, over each component of the electric field. This evidence may pave the way for the first localized transmission of OAM at microwaves. Such an outstanding possibility would open unprecedented scenarios in modern applications spanning from wireless communications to medical imaging.



# A

## A POSSIBLE PROOF ABOUT THE DEFINITION OF THE POINTING ANGLE IN LWAS

Here we wish to prove that Eq. (2.6) is exact from a mathematical point of view. As soon as we define  $P_0 = P(\theta_0)$ , we should prove that if Eq. (2.6) holds, then  $P_0$  (not  $P(\theta)$ ) is actually maximized. Hence, we are searching for the value of  $\beta^*$ ;  $P_0(\beta^*) = \max_{\beta} P_0(\beta)$ . More generally, we are searching for the maximum of the following function

$$f(z) = \frac{|\sin z|^2}{|z|^2}, \quad (\text{A.1})$$

where  $z = x + iy = \beta - k_0 \cos \theta_0 - j\alpha$ . For a real argument  $z = x$ , the  $\text{sinc}(\cdot)$  function is obviously maximum at  $x = 0$ , where it has a removable singularity and nothing remains to be proven. Thus, for a rigorous proof we just need to analytically extend this result. To do this, let us express  $f(z)$  in terms of its real and imaginary part as:

$$f(x, y) = \frac{\sin^2 x + \sinh^2 y}{x^2 + y^2}. \quad (\text{A.2})$$

Since we are searching the maximum of this function with respect to  $\beta$  and  $x$  is a function of  $\beta$  whose first derivative is 1, from the chain rule we have:

$$\frac{\partial f(x(\beta), y)}{\partial \beta} = \frac{\partial f}{\partial x} \frac{\partial x}{\partial \beta} = \frac{\partial f}{\partial x}. \quad (\text{A.3})$$

To search for  $\beta^*$  (or equivalently for  $x^*$ ) we then set Eq. (A.3) to 0:

$$\begin{aligned} \frac{\partial f}{\partial x^*} &= \frac{\partial}{\partial x^*} \left[ \frac{N(x^*)}{D(x^*)} \right] \rightarrow N'(x^*)D(x^*) = D'(x^*)N(x^*) \rightarrow \\ &2 \cos x^* (x^{*2} + y^2) = 2x^* \sin x^* \\ &\rightarrow x^* = 0 \rightarrow \boxed{\beta^* = k_0 \cos \theta_0} \end{aligned} \quad (\text{A.4})$$

This proves only that  $x^* = 0$  is a *local* maximum. Since, it does not exist an algorithm for computing the *global* maximum, we prove it by a heuristic argument:

$$f(x = 0, y) = \sinh^2 y / y^2 = N/D,$$

$$\text{we can then write } f(x, y) = \frac{N + \Delta N}{D + \Delta D},$$

$$\text{where } N = \sinh^2, D = y^2, \Delta N = \sin^2 x, \text{ and } \Delta D = x^2,$$

If  $x = 0$  is a global maximum, then

$$\frac{N}{D} > \frac{N + \Delta N}{D + \Delta D} \rightarrow N\Delta D > \Delta ND \rightarrow \frac{N}{D} > \frac{\Delta N}{\Delta D},$$

but for any values of  $x$ ,  $\Delta N/\Delta D < 1$  whereas  $N/D > 1$  for any values of  $y$ .

$$\text{Hence, } \frac{N}{D} > \frac{N + \Delta N}{D + \Delta D}$$

$$\rightarrow x^* = 0 \text{ is a global maximum. } \square$$

Hence, we have proven that  $\beta^* = k_0 \cos \theta_0$  is the value of  $\beta$  which maximizes  $P_0$ .

# B

## SIMULATION MODEL FOR THE FULL-WAVE ANALYSIS OF GRAPHENE-BASED LWAS

The calculation of radiation patterns based on the reciprocity theorem [113], [160] has been here validated through full-wave simulations of both GPW and GSS antennas with the aid of CST Microwave Studio [159] considering HMD sources. As is known [160], the far-field intensity at a given angle  $\theta$  is equal to the  $H_y$  field excited at the original source location by an incident plane wave impinging with the same angle of incidence  $\theta$  from a testing dipole source. This scenario can be modeled in CST [148], by exciting a unit cell of period  $p$  (see Fig. B.1(a)) with a waveguide port at a proper distance  $h_{\text{air}}$ . Note that both the GPW and the GSS antennas are electrically large in the transverse plane so that they could be assumed transversely infinite, and hence Floquet boundary conditions can be applied to the unit cell (see Fig. B.1(b)). The period of the unit cell and the distance of the waveguide port are here set equal to  $p = \lambda_{\text{op}}/4$  and  $h_{\text{air}} = \lambda_{\text{op}}/2$  ( $\lambda_{\text{op}}$  being the operating wavelength), in order to prevent the excitation of higher-order Floquet modes [282]. Finally, graphene has been modeled with the built-in 2-D model used by CST which implements the full-integral expression of Kubo formula [129]. The almost perfect agreement between our analytical results and full-wave simulations (see Figs. 3.17 and 3.23) confirms the validity of our approach, as well as the use of Eq. (3.13) for modelling the graphene surface conductivity. Note also that in our previous work [114], [116], we have used more sophisticated models taking into account both dielectric and ohmic losses, as well as the spatial dispersion of graphene [139], obtaining a very good agreement with the simplified model. It is worth to remind

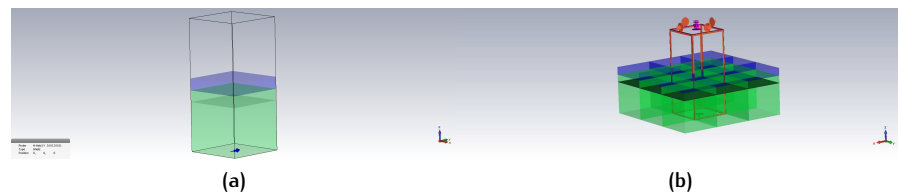


**Figure B.1.:** (a) CST unit-cell model of a GSS antenna. In green and blue the substrate and the superstrate, respectively. The transparency of the materials has been set in order to make visible the monolayer graphene within the substrate. The probe for evaluating the tangential magnetic field  $H_y$  at the ground plane is represented with a blue arrow. (b) Phase-shift walls have been implemented to emulate an infinitely transverse uniform structure by means of a periodic unit cell.

that, although spatial dispersion can safely be neglected for fast *ordinary* leaky waves, it can instead significantly affects the propagation features of extremely slow SPPs in the low-THz regime (see 3.2.1).



## BIBLIOGRAPHY

- [1] N. Marcuvitz, "On field representations in terms of leaky modes or eigenmodes", *IRE Trans. Antennas Propag.*, vol. 4, no. 3, pp. 192–194, 1956 (cit. on pp. 3, 13, 103).
- [2] T. Tamir and A. A. Oliner, "Guided complex waves. Part 1: Fields at an interface", *Proc. IEE*, vol. 110, no. 2, pp. 310–324, 1963 (cit. on pp. 3, 7, 10, 14, 98, 99, 182, 183, 214).
- [3] T. Tamir and A. A. Oliner, "Guided complex waves. Part 2: Relation to radiation patterns", *Proc. IEE*, vol. 110, no. 2, pp. 325–334, 1963 (cit. on pp. 3, 14, 182, 183).
- [4] I. Palocz and A. A. Oliner, "Leaky space-charge waves I: Čerenkov radiation", *Proc. IEEE*, vol. 53, no. 1, pp. 24–36, 1965 (cit. on p. 3).
- [5] A. Hessel and A. A. Oliner, "A new theory of Wood's anomalies on optical gratings", *Applied Optics*, vol. 4, no. 10, pp. 1275–1297, 1965 (cit. on p. 3).
- [6] A. A. Oliner and D. R. Jackson, "Leaky surface-plasmon theory for dramatically enhanced transmission through a subwavelength aperture, Part I: Basic features", in *IEEE Antennas Propag. Soc. Int. Symp., 2003.*, IEEE, vol. 2, 2003, pp. 1091–1094 (cit. on p. 3).
- [7] D. R. Jackson, T. Zhao, J. T. Williams, and A. A. Oliner, "Leaky surface-plasmon theory for dramatically enhanced transmission through a sub-wavelength aperture, Part II: Leaky-wave antenna model", in *IEEE Antennas Propag. Soc. Int. Symp., 2003.*, IEEE, vol. 2, 2003, pp. 1095–1098 (cit. on p. 3).
- [8] R. Sorrentino, "Transverse Resonance Technique", in *Numerical Techniques for Microwave and Millimeter-Wave Passive Structures*, T. Itoh, Ed., New York, NY, USA: John Wiley & Sons, 1989, ch. 11 (cit. on pp. 5, 13, 179).
- [9] N. Marcuvitz, *Waveguide Handbook*, 21. London, UK: IEE, 1951 (cit. on pp. 6, 95).
- [10] A. Galli, P. Baccarelli, and P. Burghignoli, "Leaky-Wave Antennas", in *The Wiley Encyclopedia of Electrical and Electronics Engineering*, J Webster, Ed., New York, NY, USA: John Wiley & Sons, 2016 (cit. on pp. 6, 8, 17, 18, 22, 33, 35, 69, 104).
- [11] D. R. Jackson and A. A. Oliner, "Leaky-Wave Antennas", in *Modern Antenna Handbook*, C. A. Balanis, Ed., New York, NY, USA: John Wiley & Sons, 2011, ch. 7 (cit. on pp. 6, 8, 17, 18, 33, 35, 39, 61, 69, 72, 104).

- [12] A. A. Oliner and D. R. Jackson, "Leaky-Wave Antennas", in *Antenna Engineering Handbook*, J. L. Volakis, Ed., New York, NY, USA: McGraw-Hill, 2007, ch. 11 (cit. on pp. 6, 8, 17, 18, 23, 33, 35, 69).
- [13] A. A. Oliner, "Leaky-Wave Antennas", in *Antenna Engineering Handbook*, R. C. Johnson, Ed., New York, NY, USA: McGraw-Hill, 1984, ch. 10 (cit. on pp. 6, 8, 17, 18, 23, 33, 48, 69).
- [14] D. R. Jackson, C. Caloz, and T. Itoh, "Leaky-Wave Antennas", in *Frontiers in Antennas: Next Generation Design & Engineering*, F Gross, Ed., New York, NY, USA: McGraw-Hill, 2011, ch. 9 (cit. on pp. 6, 8, 17, 18, 25, 33, 35, 69).
- [15] F. Monticone and A. Alù, "Leaky-wave theory, techniques, and applications: From microwaves to visible frequencies", *Proc. IEEE*, vol. 103, no. 5, pp. 793–821, 2015 (cit. on pp. 6, 8, 17, 18, 22).
- [16] C. T. Tai, "Evanescent modes in a partially filled gyromagnetic rectangular wave guide", *J. App. Phys.*, vol. 31, no. 1, pp. 220–221, 1960 (cit. on p. 7).
- [17] T. Tamir and A. A. Oliner, "The spectrum of electromagnetic waves guided by a plasma layer", *Proc. IEEE*, vol. 51, no. 2, pp. 317–332, 1963 (cit. on p. 7).
- [18] H. Shigesawa, M. Tsuji, and A. A. Oliner, "The nature of the spectral gap between bound and leaky solutions when dielectric loss is present in printed-circuit lines", *Radio Science*, vol. 28, no. 6, pp. 1235–1243, 1993 (cit. on p. 9).
- [19] W. C. Chew, *Waves and Fields in Inhomogeneous Media*. New York, NY, USA: IEEE Press, 1995, vol. 522 (cit. on p. 10).
- [20] L. B. Felsen and N. Marcuvitz, *Radiation and Scattering of Waves*. Hoboken, NJ, USA: John Wiley & Sons, 1994, vol. 31 (cit. on pp. 10–12, 14, 103, 145).
- [21] S. Lang, *Complex Analysis*. New York, NY, USA: Springer Science & Business Media, 2013, vol. 103 (cit. on p. 11).
- [22] W. Rudin, *Real and Complex Analysis*. New York, NY, USA: McGraw-Hill, 1986 (cit. on p. 11).
- [23] V. Galdi and I. M. Pinto, "A simple algorithm for accurate location of leaky-wave poles for grounded inhomogeneous dielectric slabs", *Microw. and Opt. Technol. Lett.*, vol. 24, no. 2, pp. 135–140, 2000 (cit. on pp. 16, 182).
- [24] W. W. Hansen, "Radiating electromagnetic waveguides", Patent No. 2.402.622, 1940 (cit. on p. 20).
- [25] J. N. Hines and J. R. Upson, "A wide aperture tapered-depth scanning antenna", *Ohio State Univ. Res. Found*, 1957, Report 667–7 (cit. on pp. 20, 21).

- [26] L. Goldstone and A. A. Oliner, "Leaky-wave antennas I: Rectangular waveguides", *IRE Trans. Antennas Propag.*, vol. 7, no. 4, pp. 307–319, 1959 (cit. on p. 20).
- [27] ———, "Leaky-wave antennas II: Circular waveguides", *IRE Trans. Antennas Propag.*, vol. 9, no. 3, pp. 280–290, 1961 (cit. on p. 20).
- [28] R. E. Collin and F. J. Zucker, *Antenna Theory*. New York, NY, USA: McGraw-Hill, 1969 (cit. on pp. 21, 22, 170, 181).
- [29] W. Rotman and A. A. Oliner, "Asymmetrical trough waveguide antennas", *IRE Trans. Antennas Propag.*, vol. 7, no. 2, pp. 153–162, 1959 (cit. on p. 21).
- [30] C. A. Balanis, *Antenna Theory: Analysis and Design*. Hoboken, NJ, USA: John Wiley & Sons, 2005 (cit. on p. 21).
- [31] N. Engheta and R. W. Ziolkowski, *Metamaterials: Physics and Engineering Explorations*. Hoboken, NJ, USA: John Wiley & Sons, 2006 (cit. on pp. 21, 81).
- [32] F. P. Casares-Miranda, C. Camacho-Peñalosa, and C. Caloz, "High-gain active composite right/left-handed leaky-wave antenna", *IEEE Trans. Antennas Propag.*, vol. 54, no. 8, pp. 2292–2300, 2006 (cit. on p. 22).
- [33] S. Paulotto, P. Baccarelli, F. Frezza, and D. R. Jackson, "A novel technique for open-stopband suppression in 1-d periodic printed leaky-wave antennas", *IEEE Trans. Antennas Propag.*, vol. 57, no. 7, pp. 1894–1906, 2009 (cit. on p. 22).
- [34] P. Burghignoli, G. Lovat, and D. R. Jackson, "Analysis and optimization of leaky-wave radiation at broadside from a class of 1-D periodic structures", *IEEE Trans. Antennas Propag.*, vol. 54, no. 9, pp. 2593–2604, 2006 (cit. on pp. 22, 33).
- [35] R. Guzmán-Quirós, J. L. Gomez-Tornero, A. R. Weily, and Y. J. Guo, "Electronic full-space scanning with 1-D Fabry–Pérot LWA using electromagnetic band-gap", *IEEE Antennas Wireless Propag. Lett.*, vol. 11, pp. 1426–1429, 2012 (cit. on p. 22).
- [36] D. K. Karmokar, K. P. Esselle, and S. G. Hay, "Fixed-frequency beam steering of microstrip leaky-wave antennas using binary switches", *IEEE Trans. Antennas Propag.*, vol. 64, no. 6, pp. 2146–2154, 2016 (cit. on pp. 22, 31).
- [37] R. Guzmán-Quirós, J. L. Gomez-Tornero, A. R. Weily, and Y. J. Guo, "Electronically steerable 1-D Fabry-Perot leaky-wave antenna employing a tunable high impedance surface", *IEEE Trans. Antennas Propag.*, vol. 60, no. 11, pp. 5046–5055, 2012 (cit. on p. 22).

- [38] M. Garcia-Vigueras, J. L. Gomez-Tornero, G. Goussetis, A. R. Weily, and Y. J. Guo, "1D-leaky wave antenna employing parallel-plate waveguide loaded with PRS and HIS", *IEEE Trans. Antennas Propag.*, vol. 59, no. 10, pp. 3687–3694, 2011 (cit. on p. 22).
- [39] —, "Efficient synthesis of 1-D Fabry–Perot antennas with low side-lobe levels", *IEEE Antennas Wireless Propag. Lett.*, vol. 11, pp. 869–872, 2012 (cit. on p. 22).
- [40] R. O. Ouedraogo, E. J. Rothwell, and B. J. Greetis, "A reconfigurable microstrip leaky-wave antenna with a broadly steerable beam", *IEEE Trans. Antennas Propag.*, vol. 59, no. 8, pp. 3080–3083, 2011 (cit. on p. 22).
- [41] A. Neto, S. Bruni, G. Gerini, and M. Sabbadini, "The leaky lens: A broad-band fixed-beam leaky-wave antenna", *IEEE Trans. Antennas Propag.*, vol. 53, no. 10, pp. 3240–3246, 2005 (cit. on p. 22).
- [42] S. Bruni, A. Neto, and F. Marliani, "The ultrawideband leaky lens antenna", *IEEE Trans. Antennas Propag.*, vol. 55, no. 10, pp. 2642–2653, 2007 (cit. on p. 22).
- [43] N. Yang, C. Caloz, and K. Wu, "Fixed-beam frequency-tunable phase-reversal coplanar stripline antenna array", *IEEE Trans. Antennas Propag.*, vol. 57, no. 3, pp. 671–681, 2009 (cit. on p. 22).
- [44] J. L. Gomez-Tornero, A. Martinez-Ros, A. Alvarez-Melcón, F. Mesa, and F. Medina, "Substrate integrated waveguide leaky-wave antenna with reduced beam squint", in *Eur. Microw. Conf. (EuMC 2013)*, IEEE, Nuremberg, Germany, 2013, pp. 491–494 (cit. on p. 22).
- [45] E. M. O'Connor, D. R. Jackson, and S. A. Long, "Extension of the hansen–woodyard condition for endfire leaky-wave antennas", *IEEE Antennas Wireless Propag. Lett.*, vol. 9, pp. 1201–1204, 2010 (cit. on pp. 23, 51, 53, 54, 59, 61, 63).
- [46] J. Liu, D. R. Jackson, and Y. Long, "Substrate integrated waveguide (SIW) leaky-wave antenna with transverse slots", *IEEE Trans. Antennas Propag.*, vol. 60, no. 1, pp. 20–29, 2012 (cit. on p. 23).
- [47] J. Liu, D. R. Jackson, Y. Li, C. Zhang, and Y. Long, "Investigations of SIW leaky-wave antenna for endfire-radiation with narrow beam and sidelobe suppression", *IEEE Trans. Antennas Propag.*, vol. 62, no. 9, pp. 4489–4497, 2014 (cit. on p. 23).
- [48] G. Lovat, P. Burghignoli, and D. R. Jackson, "Fundamental properties and optimization of broadside radiation from uniform leaky-wave antennas", *IEEE Trans. Antennas Propag.*, vol. 54, no. 5, pp. 1442–1452, 2006 (cit. on pp. 25, 33, 69, 71, 102, 106, 119).
- [49] G. V. Trentini, "Partially reflecting sheet arrays", *IRE Trans. Antennas Propag.*, vol. 4, no. 4, pp. 666–671, 1956 (cit. on p. 26).

- [50] S. Tretyakov, *Analytical Modeling in Applied Electromagnetics*. Norwood, MA, USA: Artech House, 2003 (cit. on pp. 27, 118, 174, 175, 190).
- [51] C. L. Holloway, E. F. Kuester, J. A. Gordon, J. O'Hara, J. Booth, and D. R. Smith, "An overview of the theory and applications of metasurfaces: The two-dimensional equivalents of metamaterials", *IEEE Antennas Propag. Magazine*, vol. 54, no. 2, pp. 10–35, 2012 (cit. on p. 27).
- [52] O. Luukkonen, C. Simovski, G. Granet, G. Goussetis, D. Lioubtchenko, A. V. Raisanen, and S. A. Tretyakov, "Simple and accurate analytical model of planar grids and high-impedance surfaces comprising metal strips or patches", *IEEE Trans. Antennas Propag.*, vol. 56, no. 6, pp. 1624–1632, 2008 (cit. on pp. 27, 118, 174, 175, 190).
- [53] A. B. Yakovlev, Y. R. Padooru, G. W. Hanson, A. Mafi, and S. Karbasi, "A generalized additional boundary condition for mushroom-type and bed-of-nails-type wire media", *IEEE Trans. Microw. Theory Tech.*, vol. 59, no. 3, pp. 527–532, 2011 (cit. on pp. 27, 118).
- [54] A. P. Feresidis and J. C. Vardaxoglou, "High gain planar antenna using optimised partially reflective surfaces", *IEE Proc. Microwaves, Antennas Propag.*, vol. 148, no. 6, pp. 345–350, 2001 (cit. on p. 27).
- [55] N. G. Alexopoulos and D. R. Jackson, "Fundamental superstrate (cover) effects on printed circuit antennas", *IEEE Trans. Antennas Propag.*, vol. 32, no. 8, pp. 807–816, 1984 (cit. on pp. 28, 30).
- [56] D. R. Jackson and N. G. Alexopoulos, "Gain enhancement methods for printed circuit antennas", *IEEE Trans. Antennas Propag.*, vol. 33, pp. 976–987, 1985 (cit. on pp. 28, 30).
- [57] D. R. Jackson and A. A. Oliner, "A leaky-wave analysis of the high-gain printed antenna configuration", *IEEE Trans. Antennas Propag.*, vol. 36, no. 7, pp. 905–910, 1988 (cit. on pp. 28, 102, 105, 108).
- [58] A. Ip and D. R. Jackson, "Radiation from cylindrical leaky waves", *IEEE Trans. Antennas Propag.*, vol. 38, no. 4, pp. 482–488, 1990 (cit. on pp. 28, 29, 102).
- [59] H. Yang and N. G. Alexopoulos, "Gain enhancement methods for printed circuit antennas through multiple superstrates", *IEEE Trans. Antennas Propag.*, vol. 35, no. 7, pp. 860–863, 1987 (cit. on p. 30).
- [60] M. Thevenot, C. Cheype, A. Reineix, and B. Jecko, "Directive photonic-bandgap antennas", *IEEE Trans. Microw. Th. Tech.*, vol. 47, no. 11, pp. 2115–2122, 1999 (cit. on p. 30).
- [61] D. R. Jackson, A. A. Oliner, and A. Ip, "Leaky-wave propagation and radiation for a narrow-beam multiple-layer dielectric structure", *IEEE Trans. Antennas Propag.*, vol. 41, no. 3, pp. 344–348, 1993 (cit. on pp. 30, 130, 131).

- [62] V. K. Varadan, V. V. Varadan, K. A. Jose, and J. F. Kelly, "Electronically steerable leaky wave antenna using a tunable ferroelectric material", *Smart Mater. Struct.*, vol. 3, no. 4, p. 470, 1994 (cit. on p. 31).
- [63] D. Sievenpiper, J. Schaffner, J. J. Lee, and S. Livingston, "A steerable leaky-wave antenna using a tunable impedance ground plane", *IEEE Antennas Wireless Propag. Lett.*, vol. 1, no. 1, pp. 179–182, 2002 (cit. on p. 31).
- [64] L.-Y. Ji, Y. J. Guo, P.-Y. Qin, S.-X. Gong, and R. Mittra, "A reconfigurable partially reflective surface (PRS) antenna for beam steering", *IEEE Trans. Antennas Propag.*, vol. 63, no. 6, pp. 2387–2395, 2015 (cit. on p. 31).
- [65] G. Lovat, P. Burghignoli, and S. Celozzi, "A tunable ferroelectric antenna for fixed-frequency scanning applications", *IEEE Antennas Wireless Propag. Lett.*, vol. 5, no. 1, pp. 353–356, 2006 (cit. on p. 31).
- [66] P. Baccarelli, C. Di Nallo, F. Frezza, A. Galli, and P. Lampariello, "Attractive features of leaky-wave antennas based on ferrite-loaded open waveguides", in *IEEE Antennas Propag. Soc. Int. Symp. (IEEE AP-S, 1997)*, IEEE, vol. 2, Montreal, Quebec, Canada, 1997, pp. 1442–1445 (cit. on p. 31).
- [67] T. Strutz, *Data Fitting and Uncertainty: A Practical Introduction to Weighted Least Squares and Beyond*. Wiesbaden, Germany: Vieweg and Teubner, 2010 (cit. on pp. 40, 46).
- [68] W. W. Hansen and J. R. Woodyard, "A new principle in directional antenna design", *Proc. IRE*, vol. 26, no. 3, pp. 333–345, 1938 (cit. on pp. 51, 53–55).
- [69] W. L. Stutzman and G. A. Thiele, *Antenna Theory and Design*. Hoboken, NJ, USA: John Wiley & Sons, 2012 (cit. on p. 62).
- [70] W. B. Williams and J. B. Pendry, "Generating Bessel beams by use of localized modes", *J. Opt. Soc. Am. A*, vol. 22, no. 5, pp. 992–997, 2005 (cit. on p. 81).
- [71] A. Alù and N. Engheta, "Achieving transparency with plasmonic and metamaterial coatings", *Phys. Rev. E*, vol. 72, no. 1, p. 016 623, 2005 (cit. on p. 81).
- [72] S. Maci, G. Minatti, M. Casaletti, and M. Bosiljevac, "Metasurfing: Addressing waves on impenetrable metasurfaces", *IEEE Antennas Wireless Propag. Lett.*, vol. 10, pp. 1499–1502, 2011 (cit. on p. 81).
- [73] C. Caloz and T. Itoh, *Electromagnetic Metamaterials: Transmission Line Theory and Microwave Applications*. Hoboken, NJ, USA: John Wiley & Sons, 2005 (cit. on p. 81).

- [74] D. Blanco, E. Rajo-Iglesias, S. Maci, and N. Llombart, "Directivity enhancement and spurious radiation suppression in leaky-wave antennas using inductive grid metasurfaces", *IEEE Trans. Antennas Propag.*, vol. 63, no. 3, pp. 891–900, 2015 (cit. on p. 81).
- [75] D. Di Ruscio, P. Burghignoli, P. Baccarelli, and A. Galli, "Omnidirectional radiation in the presence of homogenized metasurfaces", *Prog. Electromagn. Res.*, vol. 150, pp. 145–161, 2015 (cit. on p. 81).
- [76] J.-H. Chen, C. Jang, S. Xiao, M. Ishigami, and M. S. Fuhrer, "Intrinsic and extrinsic performance limits of graphene devices on silicon oxide", *Nature Nanotechnol.*, vol. 3, no. 4, pp. 206–209, 2008 (cit. on pp. 81, 116).
- [77] C. Jansen, I. A. Al-Naib, N. Born, and M. Koch, "Terahertz metasurfaces with high Q-factors", *App. Phys. Lett.*, vol. 98, no. 5, p. 051 109, 2011 (cit. on p. 81).
- [78] P. H. Siegel, "Terahertz technology", *IEEE Trans. Microw. Theory Tech.*, vol. 50, no. 3, pp. 910–928, 2002 (cit. on p. 81).
- [79] C. W. Berry, N. Wang, M. R. Hashemi, M. Unlu, and M. Jarrahi, "Significant performance enhancement in photoconductive terahertz optoelectronics by incorporating plasmonic contact electrodes", *Nature Comm.*, vol. 4, p. 1622, 2013 (cit. on p. 81).
- [80] S.-H. Yang and M. Jarrahi, "Spectral characteristics of terahertz radiation from plasmonic photomixers", *Opt. Express*, vol. 23, no. 22, pp. 28 522–28 530, 2015 (cit. on p. 81).
- [81] G. P. Williams, "Filling the THz gap—high power sources and applications", *Rep. Prog. Phys.*, vol. 69, no. 2, p. 301, 2005 (cit. on pp. 81, 156).
- [82] C. Armstrong, "The truth about terahertz", *IEEE Spectrum*, vol. 9, no. 49, pp. 36–41, 2012 (cit. on p. 81).
- [83] P. Mukherjee and B. Gupta, "Terahertz (THz) frequency sources and antennas - A brief review", *Int. J. Infra. Milli. Waves*, vol. 29, no. 12, pp. 1091–1102, 2008 (cit. on pp. 81, 103).
- [84] J. M. Chamberlain, R. E. Miles, C. E. Collins, and D. P. Steenson, "Introduction to terahertz solid-state devices", in *New Directions in Terahertz Technology*, Dordrecht, The Netherlands: Springer, 1997, pp. 3–27 (cit. on p. 81).
- [85] P. H. Siegel, "Terahertz technology in biology and medicine", in *Microwave Symposium Digest, 2004 IEEE MTT-S International*, IEEE, 2004, pp. 1575–1578 (cit. on p. 81).
- [86] M. Tonouchi, "Cutting-edge terahertz technology", *Nature Photonics*, vol. 1, no. 2, pp. 97–105, 2007 (cit. on p. 81).



- [87] E. Pickwell and V. P. Wallace, "Biomedical applications of terahertz technology", *J. Phys. D: App. Phys.*, vol. 39, no. 17, R301, 2006 (cit. on p. 81).
- [88] M. C. Kemp, P. F. Taday, B. E. Cole, J. A. Cluff, A. J. Fitzgerald, and W. R. Tribe, "Security applications of terahertz technology", in *Proc. SPIE*, vol. 5070, 2003, pp. 44–52 (cit. on p. 81).
- [89] L. Viti, J. Hu, D. Coquillat, W. Knap, A. Tredicucci, A. Politano, and M. S. Vitiello, "Black phosphorus terahertz photodetectors", *Advanced Materials*, vol. 27, no. 37, pp. 5567–5572, 2015 (cit. on p. 81).
- [90] C. J. Docherty, P. Parkinson, H. J. Joyce, M.-H. Chiu, C.-H. Chen, M.-Y. Lee, L.-J. Li, L. M. Herz, and M. B. Johnston, "Ultrafast transient terahertz conductivity of monolayer mos<sub>2</sub> and wse<sub>2</sub> grown by chemical vapor deposition", *ACS nano*, vol. 8, no. 11, pp. 11 147–11 153, 2014 (cit. on p. 81).
- [91] H. Raza, *Graphene Nanoelectronics: Metrology, Synthesis, Properties and Applications*. Heidelberg, Germany: Springer Science & Business Media, 2012 (cit. on pp. 81, 85).
- [92] I.-C. Khoo, *Liquid Crystals: Physical Properties and Nonlinear Optical Phenomena*. Hoboken, NJ, USA: John Wiley & Sons, 2007, vol. 64 (cit. on pp. 81, 124, 125).
- [93] P. G. de Gennes and J. Prost, *The Physics of Liquid Crystals*. Oxford, UK: Clarendon Press, 1993 (cit. on pp. 81, 124, 125).
- [94] J. A. Bossard, X. Liang, L. Li, S. Yun, D. H. Werner, B. Weiner, T. S. Mayer, P. F. Cristman, A. Diaz, and I. C. Khoo, "Tunable frequency selective surfaces and negative-zero-positive index metamaterials based on liquid crystals", *IEEE Trans. Antennas Propag.*, vol. 56, no. 5, pp. 1308–1320, 2008 (cit. on p. 81).
- [95] I. C. Khoo, D. H. Werner, X. Liang, A. Diaz, and B. Weiner, "Nanosphere dispersed liquid crystals for tunable negative-zero-positive index of refraction in the optical and terahertz regimes", *Opt. Lett.*, vol. 31, no. 17, pp. 2592–2594, 2006 (cit. on p. 81).
- [96] D. C. Zografopoulos and R. Beccherelli, "Tunable terahertz fishnet metamaterials based on thin nematic liquid crystal layers for fast switching", *Scientific Reports*, vol. 5, 2015 (cit. on pp. 81, 126, 128, 130, 131).
- [97] C.-L. Chang, W.-C. Wang, H.-R. Lin, F. J. Hsieh, Y.-B. Pun, and C.-H. Chan, "Tunable terahertz fishnet metamaterial", *App. Phys. Lett.*, vol. 102, no. 15, p. 151 903, 2013 (cit. on p. 81).
- [98] G. Isić, B. Vasić, D. C. Zografopoulos, R. Beccherelli, and R. Gajić, "Electrically tunable critically coupled terahertz metamaterial absorber based on nematic liquid crystals", *Phys. Rev. App.*, vol. 3, no. 6, p. 064 007, 2015 (cit. on p. 81).



- [99] Y. Du, H. Tian, X. Cui, H. Wang, and Z.-X. Zhou, "Electrically tunable liquid crystal terahertz phase shifter driven by transparent polymer electrodes", *J. Mat. Chem. C*, vol. 4, no. 19, pp. 4138–4142, 2016 (cit. on pp. 81, 95, 131, 136).
- [100] Y. Garbovskiy, V. Zagorodnii, P. Krivosik, J. Lovejoy, R. E. Camley, Z. Celinski, A. Glushchenko, J. Dziaduszek, and R. Dąbrowski, "Liquid crystal phase shifters at millimeter wave frequencies", *J. App. Phys.*, vol. 111, no. 5, p. 054 504, 2012 (cit. on p. 81).
- [101] C.-F. Hsieh, R.-P. Pan, T.-T. Tang, H.-L. Chen, and C.-L. Pan, "Voltage-controlled liquid-crystal terahertz phase shifter and quarter-wave plate", *Opt. Lett.*, vol. 31, no. 8, pp. 1112–1114, 2006 (cit. on p. 81).
- [102] X.-W. Lin, J.-B. Wu, W. Hu, Z.-G. Zheng, Z.-J. Wu, G. Zhu, F. Xu, B.-B. Jin, and Y.-G. Lu, "Self-polarizing terahertz liquid crystal phase shifter", *AIP Advances*, vol. 1, no. 3, p. 032 133, 2011 (cit. on p. 81).
- [103] J. S. Gómez-Díaz, M. Esquius-Morote, and J. Perruisseau-Carrier, "Plane wave excitation-detection of non-resonant plasmons along finite-width graphene strips", *Opt. Express*, vol. 21, no. 21, pp. 24 856–24 872, 2013 (cit. on pp. 81, 83, 84, 93, 104, 116).
- [104] M. Esquius-Morote, J. S. Gómez-Díaz, J. Perruisseau-Carrier, *et al.*, "Sinusoidally modulated graphene leaky-wave antenna for electronic beamscanning at THz", *IEEE Trans. THz Sc. Tech.*, vol. 4, no. 1, pp. 116–122, 2014 (cit. on pp. 81, 83, 84, 91, 93, 95, 104, 111, 116).
- [105] D. Correas-Serrano, J. S. Gómez-Díaz, A. Alù, and A. Á. Melcón, "Electrically and magnetically biased graphene-based cylindrical waveguides: Analysis and applications as reconfigurable antennas", *IEEE Trans. THz Sci. Tech.*, vol. 5, no. 6, pp. 951–960, 2015 (cit. on pp. 81, 83, 104).
- [106] M. Tamagnone, J. S. Gómez-Díaz, J. R. Mosig, and J. Perruisseau-Carrier, "Reconfigurable terahertz plasmonic antenna concept using a graphene stack", *App. Phys. Lett.*, vol. 101, no. 21, p. 214 102, 2012 (cit. on pp. 81, 83, 84, 93, 104, 116).
- [107] M. Tamagnone, J. S. Gómez-Díaz, J. R. Mosig, and J. Perruisseau-Carrier, "Analysis and design of terahertz antennas based on plasmonic resonant graphene sheets", *J. App. Phys.*, vol. 112, no. 11, p. 114 915, 2012 (cit. on pp. 81, 83, 93, 111).
- [108] E. Carrasco and J. Perruisseau-Carrier, "Reflectarray antenna at terahertz using graphene", *IEEE Antennas Wireless Propag. Lett.*, vol. 12, pp. 253–256, 2013 (cit. on pp. 81, 83).
- [109] J. Perruisseau-Carrier, M. Tamagnone, J. S. Gómez-Díaz, M. Esquius-Morote, and J. R. Mosig, "Resonant and leaky-wave reconfigurable antennas based on graphene plasmonics", in *2013 IEEE Antennas and Propagation Society International Symposium (APS-URSI)*, IEEE, 2013, pp. 136–137 (cit. on pp. 81, 83).

- [110] R. Filter, M Farhat, M. Steglich, R. Alaee, C. Rockstuhl, and F. Lederer, “Tunable graphene antennas for selective enhancement of THz-emission”, *Opt. Express*, vol. 21, no. 3, pp. 3737–3745, 2013 (cit. on pp. 81, 83).
- [111] J. M. Jornet and I. F. Akyildiz, “Graphene-based nano-antennas for electromagnetic nanocommunications in the terahertz band”, in *4th Eur. Conf. Antennas Propag. (EuCAP 2010)*, IEEE, Barcelona, Spain, 2010, pp. 1–5 (cit. on pp. 81, 83).
- [112] I. Llatser, C. Kremers, A. Cabellos-Aparicio, J. M. Jornet, E. Alarcón, and D. N. Chigrin, “Graphene-based nano-patch antenna for terahertz radiation”, *Phot. Nano. Fund. App.*, vol. 10, no. 4, pp. 353–358, 2012 (cit. on pp. 81, 83, 89).
- [113] X.-C. Wang, W.-S. Zhao, J. Hu, and W.-Y. Yin, “Reconfigurable terahertz leaky-wave antenna using graphene-based high-impedance surface”, *IEEE Trans. Nanotech.*, vol. 14, no. 1, pp. 62–69, 2015 (cit. on pp. 81, 83, 84, 231).
- [114] W. Fuscaldo, P. Burghignoli, P. Baccarelli, and A. Galli, “Complex mode spectra of graphene-based planar structures for THz applications”, *J. Infrared Milli. Terahz Waves*, vol. 36, no. 8, pp. 720–733, 2015 (cit. on pp. 81, 83, 84, 90, 94, 102, 104, 107–111, 117, 118, 121, 231).
- [115] —, “A reconfigurable substrate–superstrate graphene-based leaky-wave THz antenna”, *IEEE Antennas Wireless Propag. Lett.*, vol. 15, pp. 1545–1548, 2016 (cit. on pp. 81, 83, 84, 104, 114, 121, 123).
- [116] —, “Graphene-based reconfigurable leaky-wave antennas for THz applications”, in *15th Medit. Microw. Symp. (MMS 2015)*, IEEE, Lecce, Italy, 2015, pp. 1–4 (cit. on pp. 81, 83, 231).
- [117] A. K. Geim and K. S. Novoselov, “The rise of graphene”, *Nature materials*, vol. 6, no. 3, pp. 183–191, 2007 (cit. on pp. 83, 85, 86, 123).
- [118] G. W. Hanson, “Dyadic Green’s functions and guided surface waves for a surface conductivity model of graphene”, *J. App. Phys.*, vol. 103, no. 6, p. 064 302, 2008 (cit. on pp. 83, 89).
- [119] —, “Dyadic Green’s functions for an anisotropic, non-local model of biased graphene”, *IEEE Trans. Antennas Propag.*, vol. 56, no. 3, pp. 747–757, 2008 (cit. on pp. 83, 87, 89, 90).
- [120] S. A. Maier, *Plasmonics: Fundamentals and Applications*. New York, NY, USA: Springer Science & Business Media, 2007 (cit. on pp. 83, 91, 99).
- [121] A. Vakil and N. Engheta, “Transformation optics using graphene”, *Science*, vol. 332, no. 6035, pp. 1291–1294, 2011 (cit. on pp. 83, 91).
- [122] —, “Fourier optics on graphene”, *Phys. Rev. B*, vol. 85, no. 7, p. 075 434, 2012 (cit. on p. 83).
- [123] F. Schwierz, “Graphene transistors”, *Nature Nanotechnol.*, vol. 5, no. 7, pp. 487–496, 2010 (cit. on p. 83).

- [124] M. Dragoman, A. A. Muller, D. Dragoman, F. Coccetti, and R. Plana, "Terahertz antenna based on graphene", *J. App. Phys.*, vol. 107, no. 10, p. 104313, 2010 (cit. on p. 83).
- [125] M. Jablan, H. Buljan, and M. Soljačić, "Plasmonics in graphene at infrared frequencies", *Phys. Rev. B*, vol. 80, no. 24, p. 245435, 2009 (cit. on p. 83).
- [126] M. Tamagnone, A. Fallahi, J. R. Mosig, and J. Perruisseau-Carrier, "Fundamental limits and near-optimal design of graphene modulators and non-reciprocal devices", *Nat. Photonics*, vol. 8, no. 7, pp. 556–563, 2014 (cit. on pp. 84, 117).
- [127] M. Tamagnone and J. R. Mosig, "Theoretical limits on the efficiency of reconfigurable and nonreciprocal graphene antennas", *IEEE Antennas Wireless Propag. Lett.*, vol. 15, pp. 1549–1552, 2016 (cit. on pp. 84, 117).
- [128] D. A. Chu, P. W. C. Hon, T. Itoh, and B. S. Williams, "Feasibility of graphene CRLH metamaterial waveguides and leaky wave antennas", *J. App. Phys.*, vol. 120, no. 1, p. 013103, 2016 (cit. on pp. 84, 92, 117).
- [129] V. P. Gusynin, S. G. Sharapov, and J. P. Carbotte, "On the universal AC optical background in graphene", *New Journal of Phys.*, vol. 11, no. 9, p. 095013, 2009 (cit. on pp. 84, 86, 231).
- [130] ———, "AC conductivity of graphene: From tight-binding model to 2+1-dimensional quantum electrodynamics", *Int. J. Mod. Phys. B*, vol. 21, no. 27, pp. 4611–4658, 2007 (cit. on pp. 84, 86).
- [131] O. V. Shapoval, J. S. Gómez-Díaz, J. Perruisseau-Carrier, J. R. Mosig, and A. I. Nosich, "Integral equation analysis of plane wave scattering by coplanar graphene-strip gratings in the THz range", *IEEE Trans. THz Sci. Tech.*, vol. 3, no. 5, pp. 666–674, 2013 (cit. on pp. 84, 118).
- [132] K. S. Novoselov, A. K. Geim, S. V. Morozov, D. Jiang, Y. Zhang, S. V. Dubonos, I. V. Grigorieva, and A. A. Firsov, "Electric field effect in atomically thin carbon films", *Science*, vol. 306, no. 5696, pp. 666–669, 2004 (cit. on p. 85).
- [133] K. S. Novoselov, V. I. Fal, L. Colombo, P. R. Gellert, M. G. Schwab, and K. Kim, "A roadmap for graphene", *Nature*, vol. 490, no. 7419, pp. 192–200, 2012 (cit. on p. 85).
- [134] A. H. C. Neto, F. Guinea, N. M. Peres, K. S. Novoselov, and A. K. Geim, "The electronic properties of graphene", *Reviews of Modern Physics*, vol. 81, no. 1, p. 109, 2009 (cit. on p. 85).
- [135] P. R. Wallace, "The band theory of graphite", *Physical Review*, vol. 71, no. 9, p. 622, 1947 (cit. on p. 85).

- [136] K. I. Bolotin, K. J. Sikes, Z. Jiang, M. Klima, G. Fudenberg, J. Hone, P. Kim, and H. L. Stormer, "Ultrahigh electron mobility in suspended graphene", *Solid State Communications*, vol. 146, no. 9, pp. 351–355, 2008 (cit. on p. 85).
- [137] H. Wang, A. Hsu, J. Wu, J. Kong, and T. Palacios, "Graphene-based ambipolar RF mixers", *IEEE Electron Dev. Lett.*, vol. 31, no. 9, pp. 906–908, 2010 (cit. on p. 85).
- [138] G. Fiori, D. Neumaier, B. N. Szafranek, and G. Iannaccone, "Bilayer graphene transistors for analog electronics", *IEEE Trans. Electron Dev.*, vol. 61, no. 3, pp. 729–733, 2014 (cit. on p. 85).
- [139] G. Lovat, G. W. Hanson, R. Araneo, and P. Burghignoli, "Semiclassical spatially dispersive intraband conductivity tensor and quantum capacitance of graphene", *Phys. Rev. B*, vol. 87, no. 11, p. 115 429, 2013 (cit. on pp. 86, 87, 231).
- [140] G. Lovat, P. Burghignoli, and R. Araneo, "Low-frequency dominant-mode propagation in spatially dispersive graphene nanowaveguides", *IEEE Trans. on Electromagn. Comp.*, vol. 55, no. 2, pp. 328–333, 2013 (cit. on pp. 86, 87, 102).
- [141] T. Fang, A. Konar, H. Xing, and D. Jena, "Carrier statistics and quantum capacitance of graphene sheets and ribbons", *App. Phys. Lett.*, vol. 91, no. 9, p. 092 109, 2007 (cit. on p. 86).
- [142] K. S. Novoselov, A. K. Geim, S. V. Morozov, D. Jiang, M. I. Katsnelson, I. V. Grigorieva, S. V. Dubonos, and A. A. Firsov, "Two-dimensional gas of massless Dirac fermions in graphene", *Nature*, vol. 438, no. 7065, pp. 197–200, 2005 (cit. on pp. 87, 122).
- [143] J. W. McPherson, J. Kim, A. Shanware, H. Mogul, and J. Rodriguez, "Trends in the ultimate breakdown strength of high dielectric-constant materials", *IEEE Trans. Electron Dev.*, vol. 50, no. 8, pp. 1771–1778, 2003 (cit. on pp. 87, 122).
- [144] A. Konar, T. Fang, and D. Jena, "Effect of high- $k$  gate dielectrics on charge transport in graphene-based field effect transistors", *Phys. Rev. B*, vol. 82, no. 11, p. 115 452, 2010 (cit. on pp. 89, 122).
- [145] L. A. Ponomarenko, R. Yang, T. M. Mohiuddin, M. I. Katsnelson, K. S. Novoselov, S. V. Morozov, A. A. Zhukov, F. Schedin, E. W. Hill, and A. K. Geim, "Effect of a high- $k$  environment on charge carrier mobility in graphene", *Phys. Rev. Lett.*, vol. 102, no. 20, p. 206 603, 2009 (cit. on p. 89).
- [146] R. Raccichini, A. Varzi, S. Passerini, and B. Scrosati, "The role of graphene for electrochemical energy storage", *Nature Mat.*, vol. 14, no. 3, pp. 271–279, 2015 (cit. on p. 89).

- [147] W. Zouaghi, D. Voß, M. Gorath, N. Nicoloso, and H. G. Roskos, "How good would the conductivity of graphene have to be to make single-layer-graphene metamaterials for terahertz frequencies feasible?", *Carbon*, vol. 94, pp. 301–308, 2015 (cit. on pp. 90, 116).
- [148] M. Lorente-Crespo and C. Mateo-Segura, "Highly directive Fabry-Perot leaky-wave nanoantennas based on optical partially reflective surfaces", *App. Phys. Lett.*, vol. 106, no. 18, p. 183104, 2015 (cit. on pp. 93, 137, 231).
- [149] P. Berini, "Figures of merit for surface plasmon waveguides", *Opt. Express*, vol. 14, no. 26, pp. 13030–13042, 2006 (cit. on pp. 93, 94).
- [150] D. Comite, P. Burghignoli, P. Baccarelli, D. Di Ruscio, and A. Galli, "Equivalent-network analysis of propagation and radiation features in wire-medium loaded planar structures", *IEEE Trans. Antennas Propag.*, vol. 63, no. 12, pp. 5573–5585, 2015 (cit. on p. 94).
- [151] G. Valerio, D. R. Jackson, and A. Galli, "Fundamental properties of surface waves in lossless stratified structures", in *Proc. Roy. Soc. A - Math. Phys.*, The Royal Society, vol. 466, 2010, pp. 2447–2469 (cit. on pp. 95, 179, 182).
- [152] M. Vosgueritchian, D. J. Lipomi, and Z. Bao, "Highly conductive and transparent PEDOT: PSS films with a fluorosurfactant for stretchable and flexible transparent electrodes", *Advanced functional materials*, vol. 22, no. 2, pp. 421–428, 2012 (cit. on p. 95).
- [153] W. Fuscaldo, G. Valerio, A. Galli, R. Sauleau, A. Grbic, and M. Ettore, "Higher-order leaky-mode Bessel-beam launcher", *IEEE Trans. Antennas Propag.*, vol. 64, no. 3, pp. 904–913, 2016 (cit. on pp. 95, 156, 157, 169, 171, 183, 190, 191, 193).
- [154] P. Lampariello, F. Frezza, and A. A. Oliner, "The transition region between bound-wave and leaky-wave ranges for a partially dielectric-loaded open guiding structure", *IEEE Trans. Microw. Theory Tech.*, vol. 38, no. 12, pp. 1831–1836, 1990 (cit. on pp. 97, 182).
- [155] C. Di Nallo, F. Frezza, A. Galli, P. Lampariello, and A. A. Oliner, "Properties of NRD-guide and H-guide higher-order modes: Physical and nonphysical ranges", *IEEE Trans. Microw. Theory Tech.*, vol. 42, no. 12, pp. 2429–2434, 1994 (cit. on p. 97).
- [156] M. Naftaly and R. E. Miles, "Terahertz time-domain spectroscopy for material characterization", *Proc. IEEE*, vol. 95, no. 8, p. 1658, 2007 (cit. on p. 100).
- [157] D. M. Pozar, *Microwave Engineering*. Hoboken, NJ, USA: John Wiley & Sons, 2009 (cit. on pp. 100, 104, 135, 175, 176, 178).
- [158] N. Laman and D. Grischkowsky, "Terahertz conductivity of thin metal films", *App. Phys. Lett.*, vol. 93, no. 5, p. 051105, 2008 (cit. on p. 101).

- [159] CST products Darmstadt, Germany, 2016. [Online]. Available: <http://www.cst.com> (cit. on pp. 103, 112, 231).
- [160] T. Zhao, D. R. Jackson, J. T. Williams, and A. A. Oliner, "General formulas for 2-D leaky-wave antennas", *IEEE Trans. Antennas Propag.*, vol. 53, no. 11, pp. 3525–3533, 2005 (cit. on pp. 102, 231).
- [161] P. Baccarelli, P. Burghignoli, F. Frezza, A. Galli, P. Lampariello, G. Lovat, and S. Paulotto, "Fundamental modal properties of surface waves on metamaterial grounded slabs", *IEEE Trans. Microw. Theory and Tech.*, vol. 53, no. 4, pp. 1431–1442, 2005 (cit. on p. 104).
- [162] C. Di Nallo, F. Frezza, A. Galli, and P. Lampariello, "Rigorous evaluation of ohmic-loss effects for accurate design of traveling-wave antennas", *J. Electromagn. Waves Appl.*, vol. 12, no. 1, pp. 39–58, 1998 (cit. on pp. 104, 182).
- [163] J. D. Jackson, *Classical Electrodynamics*. Hoboken, NJ, USA: John Wiley & Sons, 1962, vol. 3 (cit. on pp. 109, 172, 182, 214).
- [164] C. A. Balanis, *Advanced Engineering Electromagnetics*. Hoboken, NJ, USA: Wiley Online Library, 2012, vol. 111 (cit. on pp. 117, 166–168, 172, 173, 209, 214, 221).
- [165] A. B. Yakovlev, O. Luukkonen, C. R. Simovski, S. A. Tretyakov, S. Paulotto, P. Baccarelli, and G. W. Hanson, "Analytical modeling of surface waves on high impedance surfaces", in *Metamaterials and Plasmonics: Fundamentals, Modelling, Applications*, Dordrecht, The Netherlands: Springer, 2009, pp. 239–254 (cit. on p. 118).
- [166] F. A. Mas'ud, H. Cho, T. Lee, H. Rho, T. H. Seo, and M. J. Kim, "Domain size engineering of CVD graphene and its influence on physical properties", *J. Phys. D: App. Phys.*, vol. 49, no. 20, p. 205 504, 2016 (cit. on p. 121).
- [167] G. Deokar, J. Avila, I. Razado-Colambo, J.-L. Codron, C. Boyaval, E. Galopin, M.-C. Asensio, and D. Vignaud, "Towards high quality CVD graphene growth and transfer", *Carbon*, vol. 89, pp. 82–92, 2015 (cit. on p. 121).
- [168] X. Li, W. Cai, J. An, S. Kim, J. Nah, D. Yang, R. Piner, A. Velamakanni, I. Jung, E. Tutuc, *et al.*, "Large-area synthesis of high-quality and uniform graphene films on copper foils", *Science*, vol. 324, no. 5932, pp. 1312–1314, 2009 (cit. on p. 121).
- [169] X. Li, Y. Zhu, W. Cai, M. Borysiak, B. Han, D. Chen, R. D. Piner, L. Colombo, and R. S. Ruoff, "Transfer of large-area graphene films for high-performance transparent conductive electrodes", *Nano Lett.*, vol. 9, no. 12, pp. 4359–4363, 2009 (cit. on p. 121).
- [170] H. Wan, W. Cai, F. Wang, S. Jiang, S. Xu, and J. Liu, "High-quality monolayer graphene for bulk laser mode-locking near 2 $\mu$ m", *Optical and Quantum Electronics*, vol. 48, no. 1, pp. 1–8, 2016 (cit. on p. 121).

- [171] X. Wan, N. Zhou, L. Gan, H. Li, Y. Ma, and T. Zhai, "Towards wafer-size strictly monolayer graphene on copper via cyclic atmospheric chemical vapor deposition", *Carbon*, vol. 110, pp. 384–389, 2016 (cit. on p. 121).
- [172] A. M. Ng, Y. Wang, W. C. Lee, C. T. Lim, K. P. Loh, and H. Y. Low, "Patterning of graphene with tunable size and shape for microelectrode array devices", *Carbon*, vol. 67, pp. 390–397, 2014 (cit. on p. 121).
- [173] J. S. Gómez-Díaz, C. Moldovan, S. Capdevila, J. Romeu, L. S. Bernard, A. Magrez, A. M. Ionescu, and J. Perruisseau-Carrier, "Self-biased reconfigurable graphene stacks for terahertz plasmonics", *Nature Communications*, vol. 6, 2015 (cit. on pp. 122, 124).
- [174] L. Ju, B. Geng, J. Horng, C. Girit, M. Martin, Z. Hao, H. A. Bechtel, X. Liang, A. Zettl, Y. R. Shen, *et al.*, "Graphene plasmonics for tunable terahertz metamaterials", *Nature Nanotechnol.*, vol. 6, no. 10, pp. 630–634, 2011 (cit. on p. 122).
- [175] P. Sharma, J. Perruisseau-Carrier, C. Moldovan, and A. M. Ionescu, "Electromagnetic performance of RF NEMS graphene capacitive switches", *IEEE Trans. Nanotechnol.*, vol. 13, no. 1, pp. 70–79, 2014 (cit. on p. 122).
- [176] K. Berdel, J. G. Rivas, P. H. Bolívar, P. de Maagt, and H. Kurz, "Temperature dependence of the permittivity and loss tangent of high-permittivity materials at terahertz frequencies", *IEEE Trans. Microw. Theory. Tech.*, vol. 53, no. 4, pp. 1266–1271, 2005 (cit. on p. 122).
- [177] J. A. Robinson, M. LaBella III, K. A. Trumbull, X. Weng, R. Cavellero, T. Daniels, Z. Hughes, M. Hollander, M. Fanton, and D. Snyder, "Epitaxial graphene materials integration: Effects of dielectric overlayers on structural and electronic properties", *ACS Nano*, vol. 4, no. 5, pp. 2667–2672, 2010 (cit. on p. 122).
- [178] B. J. Kim, H. Jang, S.-K. Lee, B. H. Hong, J.-H. Ahn, and J. H. Cho, "High-performance flexible graphene field effect transistors with ion gel gate dielectrics", *Nano Lett.*, vol. 10, no. 9, pp. 3464–3466, 2010 (cit. on p. 122).
- [179] J. S. Patel, M. A. Saifi, D. W. Berreman, C. Lin, N. Andreadakis, and S. D. Lee, "Electrically tunable optical filter for infrared wavelength using liquid crystals in a Fabry–Perot etalon", *App. Phys. Lett.*, vol. 57, no. 17, pp. 1718–1720, 1990 (cit. on p. 124).
- [180] D. C. Zografopoulos, K. P. Prokopidis, R. Dąbrowski, and R. Beccherelli, "Time-domain modeling of dispersive and lossy liquid-crystals for terahertz applications", *Opt. Mat. Exp.*, vol. 4, no. 3, pp. 449–457, 2014 (cit. on p. 124).
- [181] D. C. Zografopoulos, R. Beccherelli, and E. E. Kriezis, "Beam-splitter switches based on zenithal bistable liquid-crystal gratings", *Phys. Rev. E*, vol. 90, no. 4, p. 042503, 2014 (cit. on pp. 125, 129, 133).



- [182] R. E. Collin, "Field theory of guided waves", 1960 (cit. on pp. 128, 132).
- [183] B. Bellini and R. Beccherelli, "Modelling, design and analysis of liquid crystal waveguides in preferentially etched silicon grooves", *J. Phys. D: App. Phys.*, vol. 42, no. 4, p. 045 111, 2009 (cit. on pp. 129, 131, 133).
- [184] P. A. George, W. Hui, F. Rana, B. G. Hawkins, A. E. Smith, and B. J. Kirby, "Microfluidic devices for terahertz spectroscopy of biomolecules", *Opt. Express*, vol. 16, no. 3, pp. 1577–1582, 2008 (cit. on p. 130).
- [185] M. Reuter, N. Vieweg, B. M. Fischer, M. Mikulicz, M. Koch, K. Garbat, and R. Dabrowski, "Highly birefringent, low-loss liquid crystals for terahertz applications", *APL Materials*, vol. 1, no. 1, p. 012 107, 2013 (cit. on p. 130).
- [186] K. Z. Rajab, M. Naftaly, E. H. Linfield, J. C. Nino, D. Arenas, D. Tanner, R. Mittra, and M. Lanagan, "Broadband dielectric characterization of aluminum oxide (al<sub>2</sub>o<sub>3</sub>)", *J. Microelectronics and Electronic Packaging*, vol. 5, no. 1, pp. 2–7, 2008 (cit. on p. 133).
- [187] ATP Applied Thin Film Products. [Online]. Available: <http://www.thinfilm.com/substrates.html> (cit. on p. 134).
- [188] J. Durnin, "Exact solutions for nondiffracting beams. I. The scalar theory", *J. Opt. Soc. Am. A*, vol. 4, no. 4, pp. 651–654, 1987 (cit. on pp. 143, 147, 148, 152, 156, 159, 201).
- [189] J. Durnin, J. J. Miceli Jr., and J. H. Eberly, "Diffraction-free beams", *Phys. Rev. Lett.*, vol. 58, no. 15, p. 1499, 1987 (cit. on pp. 143, 147, 152, 155, 161, 162, 201).
- [190] G. Chartier, *Introduction to Optics*. New York, NY, USA: Springer Science & Business Media, 2005 (cit. on p. 145).
- [191] H. E. Hernández-Figueroa, M. Zamboni-Rached, and E. Recami, *Localized Waves*. Hoboken, NJ, USA: John Wiley & Sons, 2007, vol. 194 (cit. on pp. 146, 148–150, 154, 160, 178).
- [192] M. Zamboni-Rached, E. Recami, and H. E. Hernández-Figueroa, "New localized superluminal solutions to the wave equations with finite total energies and arbitrary frequencies", *The European Physical Journal D-Atomic, Molecular, Optical and Plasma Phys.*, vol. 21, no. 2, pp. 217–228, 2002 (cit. on pp. 146–148, 160, 162, 202).
- [193] G. Indebetouw, "Nondiffracting optical fields: Some remarks on their analysis and synthesis", *J. Opt. Soc. Am. A*, vol. 6, no. 1, pp. 150–152, 1989 (cit. on p. 147).
- [194] J. Durnin, J. H. Eberly, and J. J. Miceli Jr., "Comparison of Bessel and Gaussian beams", *Opt. Lett.*, vol. 13, no. 2, pp. 79–80, 1988 (cit. on pp. 147, 148, 153).



- [195] P. L. Overfelt and C. S. Kenney, "Comparison of the propagation characteristics of Bessel, Bessel–Gauss, and Gaussian beams diffracted by a circular aperture", *J. Opt. Soc. Am. A*, vol. 8, no. 5, pp. 732–745, 1991 (cit. on p. 148).
- [196] I. M. Besieris, A. M. Shaarawi, and R. W. Ziolkowski, "A bidirectional traveling plane wave representation of exact solutions of the scalar wave equation", *J. Math. Phys.*, vol. 30, no. 6, pp. 1254–1269, 1989 (cit. on pp. 148, 158, 202).
- [197] H. E. Hernández-Figueroa, M. Zamboni-Rached, and E. Recami, *Non-diffracting Waves*. Weinheim, Germany: John Wiley & Sons, 2013 (cit. on pp. 149, 154, 178).
- [198] J. Fagerholm, A. T. Friberg, J. Huttunen, D. P. Morgan, and M. M. Salomaa, "Angular-spectrum representation of nondiffracting X waves", *Phys. Rev. E*, vol. 54, no. 4, p. 4347, 1996 (cit. on pp. 149, 158).
- [199] P. Schemmel, S. Maccalli, G. Pisano, B. Maffei, and M. W. R. Ng, "Three-dimensional measurements of a millimeter wave orbital angular momentum vortex", *Opt. Lett.*, vol. 39, no. 3, pp. 626–629, 2014 (cit. on p. 149).
- [200] B. H. Bransden and C. J. Joachain, *Quantum Mechanics*. London, UK: Pearson Education, 2000 (cit. on p. 149).
- [201] A. M. Yao and M. J. Padgett, "Orbital angular momentum: Origins, behavior and applications", *Adv. Opt. Photonics*, vol. 3, no. 2, pp. 161–204, 2011 (cit. on p. 149).
- [202] K. Volke-Sepulveda, V. Garcés-Chávez, S. Chávez-Cerda, J. Arlt, and K. Dholakia, "Orbital angular momentum of a high-order Bessel light beam", *J. Opt. B: Quantum Semiclassical Opt.*, vol. 4, no. 2, S82, 2002 (cit. on p. 149).
- [203] I. A. Litvin, A. Dudley, and A. Forbes, "Poynting vector and orbital angular momentum density of superpositions of Bessel beams", *Opt. Express*, vol. 19, no. 18, pp. 16 760–16 771, 2011 (cit. on p. 149).
- [204] D. McGloin and K. Dholakia, "Bessel beams: Diffraction in a new light", *Contemporary Phys.*, vol. 46, no. 1, pp. 15–28, 2005 (cit. on pp. 149, 154).
- [205] S. Yan, M. Li, B. Yao, X. Yu, M. Lei, D. Dan, Y. Yang, J. Min, and T. Peng, "Accelerating nondiffracting beams", *Phys. Lett. A*, vol. 379, no. 12, pp. 983–987, 2015 (cit. on pp. 149, 220).
- [206] W. Fuscaldo, S. C. Pavone, G. Valerio, A. Galli, M. Albani, and M. Ettore, "Analysis of limited-diffractive and limited-dispersive X-waves generated by finite radial waveguides", *J. App. Phys.*, vol. 119, no. 19, p. 194 903, 2016 (cit. on pp. 150, 178, 195, 198, 216, 217).

- [207] M. Orniogotti, C. Conti, and A. Szameit, "Effect of orbital angular momentum on nondiffracting ultrashort optical pulses", *Phys. Rev. Lett.*, vol. 115, no. 10, p. 100401, 2015 (cit. on pp. 150, 220).
- [208] D. Mugnai, A. Ranfagni, and R. Ruggeri, "Observation of superluminal behaviors in wave propagation", *Phys. Rev. Lett.*, vol. 84, no. 21, p. 4830, 2000 (cit. on p. 150).
- [209] E. Heyman, "Focus wave modes: A dilemma with causality", *IEEE Trans. Antennas and Propag.*, vol. 37, no. 12, pp. 1604–1608, 1989 (cit. on p. 150).
- [210] E. Heyman, L. B. Felsen, and P. Hillion, "Comments on "nondispersive waves: Interpretation and causality", by P. T. M. Hillion [with reply]", *IEEE Trans. Antennas and Propag.*, vol. 42, no. 12, pp. 1668–1670, 1994 (cit. on p. 150).
- [211] P. T. M. Hillion, "Nondispersive waves: Interpretation and causality", *IEEE Trans. Antennas Propag.*, vol. 40, no. 9, pp. 1031–1035, 1992 (cit. on p. 150).
- [212] K. Wynne, "Causality and the nature of information", *Opt. Commun.*, vol. 209, no. 1, pp. 85–100, 2002 (cit. on p. 150).
- [213] W. Withayachumnankul, B. M. Fischer, B. Ferguson, B. R. Davis, and D. Abbott, "A systemized view of superluminal wave propagation", *Proceedings of the IEEE*, vol. 98, no. 10, pp. 1775–1786, 2010 (cit. on pp. 150, 151).
- [214] T. E. Olson, "Everything is a precursor: The asymptotic singular value decomposition for transmission through absorbing media", in *Int. Conf. Electromagn. Adv. App. (ICEAA, 2011)*, IEEE, 2011, pp. 335–338 (cit. on p. 150).
- [215] C. G. B. Garrett and D. E. McCumber, "Propagation of a Gaussian light pulse through an anomalous dispersion medium", *Phys. Rev. A*, vol. 1, no. 2, p. 305, 1970 (cit. on p. 150).
- [216] L. Brillouin, *Wave Propagation and Group Velocity*. New York, NY, USA: Academic Press, 2013, vol. 8 (cit. on p. 150).
- [217] L.-G. Wang, N.-H. Liu, Q. Lin, and S.-Y. Zhu, "Superluminal propagation of light pulses: A result of interference", *Phys. Rev. E*, vol. 68, no. 6, p. 066606, 2003 (cit. on p. 151).
- [218] J. A. Stratton, *Electromagnetic Theory*. John Wiley & Sons, 1941 (cit. on pp. 152, 166).
- [219] P. Lemaitre-Auger, S. Abielmona, and C. Caloz, "Generation of Bessel beams by two-dimensional antenna arrays using sub-sampled distributions", *IEEE Trans. Antennas Propag.*, vol. 61, no. 4, pp. 1838–1849, 2013 (cit. on pp. 153, 156, 181).

- [220] S. C. Pavone, M. Ettore, and M. Albani, "Analysis and design of Bessel beam launchers: Longitudinal polarization", *IEEE Trans. Antennas Propag.*, vol. 64, no. 6, pp. 2311–2318, 2016 (cit. on pp. 153, 156, 212).
- [221] M. Anguiano-Morales, A. Martínez, M. D. Iturbe-Castillo, S. Chávez-Cerda, and N. Alcalá-Ochoa, "Self-healing property of a caustic optical beam", *Applied optics*, vol. 46, no. 34, pp. 8284–8290, 2007 (cit. on p. 154).
- [222] R. M. Herman and T. A. Wiggins, "Production and uses of diffractionless beams", *J. Opt. Soc. Am. A*, vol. 8, no. 6, pp. 932–942, 1991 (cit. on pp. 154, 156).
- [223] A. Dudley, M. Lavery, M. Padgett, and A. Forbes, "Unraveling Bessel beams", *Optics and Photonics News*, vol. 24, no. 6, pp. 22–29, 2013 (cit. on p. 155).
- [224] M. Ettore and A. Grbic, "Generation of propagating Bessel beams using leaky-wave modes", *IEEE Trans. Antennas Propag.*, vol. 60, no. 8, pp. 3605–3613, 2012 (cit. on pp. 156, 157, 165–167, 169–172, 175–181, 209).
- [225] J. H. McLeod, "The axicon: A new type of optical element", *J. Opt. Soc. Am. A*, vol. 44, no. 8, pp. 592–597, 1954 (cit. on p. 156).
- [226] ———, "Axicons and their uses", *J. Opt. Soc. Am. A*, vol. 50, no. 2, pp. 166–169, 1960 (cit. on p. 156).
- [227] G. Milne, G. D. M. Jeffries, and D. T. Chiu, "Tunable generation of Bessel beams with a fluidic axicon", *App. Phys. Lett.*, vol. 92, no. 26, p. 261 101, 2008 (cit. on p. 156).
- [228] P. Vahimaa, V. Kettunen, M. Kuittinen, J. Turunen, and A. T. Friberg, "Electromagnetic analysis of nonparaxial Bessel beams generated by diffractive axicons", *J. Opt. Soc. Am. A*, vol. 14, no. 8, pp. 1817–1824, 1997 (cit. on p. 156).
- [229] A. Vasara, J. Turunen, and A. T. Friberg, "Realization of general non-diffracting beams with computer-generated holograms", *J. Opt. Soc. Am. A*, vol. 6, no. 11, pp. 1748–1754, 1989 (cit. on p. 156).
- [230] A. J. Cox and D. C. Dibble, "Nondiffracting beam from a spatially filtered Fabry-Perot resonator", *J. Opt. Soc. Am. A*, vol. 9, no. 2, pp. 282–286, 1992 (cit. on p. 156).
- [231] D. K. Hsu, F. J. Margetan, and D. O. Thompson, "Bessel beam ultrasonic transducer: Fabrication method and experimental results", *App. Phys. Lett.*, vol. 55, no. 20, pp. 2066–2068, 1989 (cit. on p. 156).
- [232] Z. Li, K. B. Alici, H. Caglayan, and E. Ozbay, "Generation of an axially asymmetric Bessel-like beam from a metallic subwavelength aperture", *Phys. Rev. Lett.*, vol. 102, no. 14, p. 143 901, 2009 (cit. on p. 156).

- [233] S. Monk, J. Arlt, D. A. Robertson, J. Courtial, and M. J. Padgett, "The generation of Bessel beams at millimetre-wave frequencies by use of an axicon", *Opt. Commun.*, vol. 170, no. 4, pp. 213–215, 1999 (cit. on p. 156).
- [234] J. Salo, J. Fagerholm, A. T. Friberg, and M. M. Salomaa, "Unified description of nondiffracting x and y waves", *Phys. Rev. E*, vol. 62, no. 3, p. 4261, 2000 (cit. on pp. 156, 158, 162).
- [235] M. Ettore, S. M. Rudolph, and A. Grbic, "Generation of propagating Bessel beams using leaky-wave modes: Experimental validation", *IEEE Trans. Antennas Propag.*, vol. 60, no. 6, pp. 2645–2653, 2012 (cit. on pp. 156, 165, 166, 169, 171, 173, 174, 177, 178, 189).
- [236] S. Mishra, "A vector wave analysis of a Bessel beam", *Opt. Comm.*, vol. 85, no. 2, pp. 159–161, 1991 (cit. on pp. 156, 166).
- [237] Z. Bouchal and M. Olivík, "Non-diffractive vector Bessel beams", *J. Modern Optics*, vol. 42, no. 8, pp. 1555–1566, 1995 (cit. on pp. 156, 167).
- [238] F. G. Mitri, "Three-dimensional vectorial analysis of an electromagnetic non-diffracting high-order Bessel trigonometric beam", *Wave Motion*, vol. 49, no. 5, pp. 561–568, 2012 (cit. on p. 156).
- [239] S. Chávez-Cerda, "A new approach to Bessel beams", *J. Modern Opt.*, vol. 46, no. 6, pp. 923–930, 1999 (cit. on pp. 156, 168).
- [240] M. Albani, S. Pavone, M. Casaletti, and M. Ettore, "Generation of non-diffractive Bessel beams by inward cylindrical traveling wave aperture distributions", *Opt. Express*, vol. 22, no. 15, pp. 18 354–18 364, 2014 (cit. on pp. 156, 212, 213, 223).
- [241] M. Ettore, S. Pavone, M. Casaletti, and M. Albani, "Experimental validation of Bessel beam generation using an inward hankel aperture distribution", *IEEE Trans. Antennas Propag.*, vol. 63, no. 6, pp. 2539–2544, 2015 (cit. on pp. 156, 209).
- [242] A. Mazzinghi, M. Balma, D. Devona, G. Guarnieri, G. Mauriello, M. Albani, and A. Freni, "Large depth of field pseudo-Bessel beam generation with a rlsa antenna", *IEEE Trans. Antennas Propag.*, vol. 62, no. 8, pp. 3911–3919, 2014 (cit. on pp. 156, 195, 197, 198, 209, 212).
- [243] M. F. Imani and A. Grbic, "Generating evanescent Bessel beams using near-field plates", *IEEE Trans. Antennas Propag.*, vol. 60, no. 7, pp. 3155–3164, 2012 (cit. on p. 156).
- [244] C. Pfeiffer and A. Grbic, "Controlling vector Bessel beams with metasurfaces", *Phys. Rev. App.*, vol. 2, no. 4, p. 044 012, 2014 (cit. on p. 156).
- [245] B. G. Cai, Y. B. Li, W. X. Jiang, Q. Cheng, and T. J. Cui, "Generation of spatial Bessel beams using holographic metasurface", *Opt. Express*, vol. 23, no. 6, pp. 7593–7601, 2015 (cit. on p. 156).

- [246] M. A. Salem, A. H. Kamel, and E. Niver, "Microwave Bessel beams generation using guided modes", *IEEE Trans. Antennas Propag.*, vol. 59, no. 6, pp. 2241–2247, 2011 (cit. on p. 156).
- [247] J. N. Brittingham, "Focus waves modes in homogeneous maxwell's equations: Transverse electric mode", *J. App. Phys.*, vol. 54, no. 3, pp. 1179–1189, 1983 (cit. on p. 158).
- [248] A. Sezginer, "A general formulation of focus wave modes", *J. App. Phys.*, vol. 57, no. 3, pp. 678–683, 1985 (cit. on p. 158).
- [249] R. W. Ziolkowski, "Exact solutions of the wave equation with complex source locations", *J. Math. Phys.*, vol. 26, no. 4, pp. 861–863, 1985 (cit. on pp. 158, 162).
- [250] R. W. Ziolkowski, I. M. Besieris, and A. M. Shaarawi, "Aperture realizations of exact solutions to homogeneous-wave equations", *J. Opt. Soc. Am. A*, vol. 10, no. 1, pp. 75–87, 1993 (cit. on pp. 158, 161).
- [251] W. A. Rodrigues Jr. and J.-Y. Lu, "On the existence of undistorted progressive waves (UPWs) of arbitrary speeds  $0 \leq \vartheta < \infty$  in nature", *Found. Phys.*, vol. 27, no. 3, pp. 435–508, 1997 (cit. on p. 158).
- [252] E. Heyman, L. B. Felsen, and B. Z. Steinberg, "Spectral analysis of focus wave modes", *J. Opt. Soc. Am. A*, vol. 4, no. 11, pp. 2081–2091, 1987 (cit. on pp. 158, 161).
- [253] A. M. Tagirdzhanov, A. S. Blagovestchenskii, and A. P. Kiselev, "'complex source' wavefields: Sources in real space", *J. Phys. A: Math. and Theoretical*, vol. 44, no. 42, p. 425 203, 2011 (cit. on p. 158).
- [254] G. A. Deschamps, "Gaussian beam as a bundle of complex rays", *Electronics Lett.*, vol. 7, no. 23, pp. 684–685, 1971 (cit. on p. 158).
- [255] R. Donnelly and R. W. Ziolkowski, "Designing localized waves", *Proc. of the Royal Society of London A: Mathematical, Physical and Engineering Sciences*, vol. 440, no. 1910, pp. 541–565, 1993 (cit. on p. 158).
- [256] R. W. Ziolkowski, "Localized transmission of electromagnetic energy", *Phys. Rev. A*, vol. 39, no. 4, p. 2005, 1989 (cit. on p. 158).
- [257] E. Capelas de Oliveira and W. A. Rodrigues, "Finite energy superluminal solutions of maxwell equations", *Phys. Lett. A*, vol. 291, no. 6, pp. 367–370, 2001 (cit. on p. 159).
- [258] P. Ghose and M. K. Samal, "Lorentz-invariant superluminal tunneling", *Phys. Rev. E*, vol. 64, no. 3, p. 036 620, 2001 (cit. on p. 159).
- [259] J.-Y. Lu and A. Liu, "An X wave transform", *IEEE Trans. on Ultrason., Ferroelectr. Freq. Control*, vol. 47, no. 6, pp. 1472–1481, 2000 (cit. on p. 160).
- [260] M. Zamboni-Rached, "Stationary optical wave fields with arbitrary longitudinal shape by superposing equal frequency Bessel beams: Frozen Waves", *Opt. Express*, vol. 12, no. 17, pp. 4001–4006, 2004 (cit. on p. 160).

- [261] C. A. Dartora, K. Z. Nóbrega, A. Dartora, G. A. Viana, and S. Horacio Tertuliano Filho, “A general theory for the Frozen Waves and their realization through finite apertures”, *Opt. Commun.*, vol. 265, no. 2, pp. 481–487, 2006 (cit. on p. 160).
- [262] T. A. Vieira, M. R. R. Gesualdi, and M. Zamboni-Rached, “Frozen waves: Experimental generation”, *Opt. Lett.*, vol. 37, no. 11, pp. 2034–2036, 2012 (cit. on p. 160).
- [263] J.-Y. Lu and J. F. Greenleaf, “Nondiffracting X waves-exact solutions to free-space scalar wave equation and their finite aperture realizations”, *IEEE Trans. Ultrason. Ferroelectr. Freq. Control*, vol. 39, no. 1, pp. 19–31, 1992 (cit. on pp. 161, 162, 178, 202).
- [264] —, “Experimental verification of nondiffracting X waves”, *IEEE Trans. on Ultrason., Ferroelectr. Freq. Control*, vol. 39, no. 3, pp. 441–446, 1992 (cit. on pp. 161, 209).
- [265] P. Saari and K. Reivelt, “Evidence of X-shaped propagation-invariant localized light waves”, *Phys. Rev. Lett.*, vol. 79, no. 21, p. 4135, 1997 (cit. on pp. 161, 162, 209).
- [266] H. Sonajalg and P. Saari, “Suppression of temporal spread of ultrashort pulses in dispersive media by Bessel beam generators”, *Opt. Lett.*, vol. 21, no. 15, pp. 1162–1164, 1996 (cit. on pp. 162, 209).
- [267] A. A. Chatzipetros, A. M. Shaarawi, I. M. Besieris, and M. A. Abdel-Rahman, “Aperture synthesis of time-limited X waves and analysis of their propagation characteristics”, *J. Acoust. Soc. Am.*, vol. 103, no. 5, pp. 2287–2295, 1998 (cit. on p. 162).
- [268] M. A. Porrás, G. Valiulis, and P. Di Trapani, “Unified description of Bessel X waves with cone dispersion and tilted pulses”, *Phys. Rev. E*, vol. 68, no. 1, p. 016613, 2003 (cit. on pp. 162, 209, 210).
- [269] R. F. Harrington, *Time-Harmonic Electromagnetic Fields*. New York, NY, USA: IEEE Press, 2015 (cit. on pp. 166–169, 172, 213).
- [270] S. Chávez-Cerda and G. H. C. New, “Evolution of focused Hankel waves and Bessel beams”, *Opt. Commun.*, vol. 181, no. 4, pp. 369–377, 2000 (cit. on p. 168).
- [271] G. N. Watson, *A Treatise on the Theory of Bessel Functions*. Cambridge, UK: Cambridge University Press, 1995 (cit. on pp. 169, 185).
- [272] M. Abramowitz and I. A. Stegun, *Handbook of Mathematical Functions*. New York, NY, USA: Dover, 1962 (cit. on pp. 169, 203, 211).
- [273] J. A. Kong, *Electromagnetic Wave Theory*. New York, NY, USA: John Wiley & Sons, 1986 (cit. on p. 172).
- [274] *Ansys Corporation, Ansys HFSS version 16.0, 1984-2016*. [Online]. Available: <http://www.ansys.com/Products/Electronics/ANSYS-HFSS> (cit. on pp. 173, 189).

- [275] *Evonik Industries Rohacell structural slab, 31HF Datasheet*. [Online]. Available: <http://www.rohacell.com> (cit. on p. 178).
- [276] *COMSOL Inc., COMSOL Multiphysics version 4.2a, 1998-2016*. [Online]. Available: <http://www.comsol.com/comsol-multiphysics> (cit. on pp. 178, 187).
- [277] G. Valerio, D. R. Jackson, and A. Galli, "Formulas for the number of surface waves on layered structures", *IEEE Trans. Microw. Theory Tech.*, vol. 58, no. 7, pp. 1786–1795, 2010 (cit. on p. 179).
- [278] *Park Electro NELTEC NY9217, Datasheet*. [Online]. Available: <http://www.parkelectro.com/parkelectro/images/n9000a-a4.pdf> (cit. on pp. 182, 189).
- [279] A. B. Yakovlev and G. W. Hanson, "Fundamental modal phenomena on isotropic and anisotropic planar slab dielectric waveguides", *IEEE Trans. Antennas Propag.*, vol. 51, no. 4, pp. 888–897, 2003 (cit. on p. 182).
- [280] P. N. Melezhik, A. Y. Poyedinchuk, Y. A. Tuchkin, and V. P. Shestopalov, "Properties of spectral characteristics of the open two-mirror resonator", in *Dokl. Akad. Nauk SSSR*, pp. 51–54 (cit. on p. 182).
- [281] P. N. Melezhik, A. E. Poedinchuk, Y. A. Tuchkin, and V. P. Shestopalov, "Analytical nature of the vibrational mode-coupling phenomenon", in *Soviet Physics Doklady*, vol. 33, 1988, p. 420 (cit. on p. 182).
- [282] B. H. Fong, J. S. Colburn, J. J. Ottusch, J. L. Visher, and D. F. Sievenpiper, "Scalar and tensor holographic artificial impedance surfaces", *IEEE Trans. Antennas Propag.*, vol. 58, no. 10, pp. 3212–3221, 2010 (cit. on pp. 190, 231).
- [283] *Taconic Advanced Dielectric Division Multilayer non-reinforced prepreg*. [Online]. Available: <http://www.4taconic.com/page/fastrise27-89.html> (cit. on p. 190).
- [284] *SRI Connector Gage Connector 85-131-1000-80*. [Online]. Available: <http://www.sriconnectorgage.com/productDetail.aspx?pid=668> (cit. on p. 190).
- [285] I. Iliopoulos, M. Casaletti, R. Sauleau, P. Pouliguen, P. Potier, and M. Ettore, "3D shaping of a focused aperture in the near field", *IEEE Trans. Antennas Propag.*, 2016 (cit. on p. 191).
- [286] M. Albani, A. Mazzinghi, and A. Freni, "Automatic design of cp-risa antennas", *IEEE Trans. Antennas Propag.*, vol. 60, no. 12, pp. 5538–5547, 2012 (cit. on pp. 195, 197, 198, 212, 213).
- [287] M. Ettore, M. Casaletti, G. Valerio, R. Sauleau, L. Le Coq, S. C. Pavone, and M. Albani, "On the near-field shaping and focusing capability of a radial line slot array", *IEEE Trans. Antennas Propag.*, vol. 62, no. 4, pp. 1991–1999, 2014 (cit. on pp. 197, 198, 212).



- [288] W. Rudin, *Principles of Mathematical Analysis*. New York: McGraw-Hill, 1976 (cit. on p. 204).
- [289] C. Conti, "X-wave-mediated instability of plane waves in Kerr media", *Phys. Rev. E*, vol. 68, no. 1, p. 016 606, 2003 (cit. on p. 209).
- [290] C. Conti and S. Trillo, "X waves generated at the second harmonic", *Opt. Lett.*, vol. 28, no. 14, pp. 1251–1253, 2003 (cit. on p. 209).
- [291] A. Couairon, E. Gaižauskas, D. Faccio, A. Dubietis, and P. Di Trapani, "Nonlinear X-wave formation by femtosecond filamentation in Kerr media", *Phys. Rev. E*, vol. 73, no. 1, p. 016 608, 2006 (cit. on p. 209).
- [292] P. V. Larsen, M. P. Sørensen, O. Bang, W. Krolikowski, and S. Trillo, "Nonlocal description of X waves in quadratic nonlinear materials", *Phys. Rev. E*, vol. 73, no. 3, p. 036 614, 2006 (cit. on p. 209).
- [293] C. Conti, S. Trillo, P. Di Trapani, G. Valiulis, A. Piskarskas, O. Jedrkiewicz, and J. Trull, "Nonlinear electromagnetic X waves", *Phys. Rev. Lett.*, vol. 90, no. 17, p. 170 406, 2003 (cit. on p. 209).
- [294] M. A. Porras, S. Trillo, C. Conti, and P. Di Trapani, "Paraxial envelope X waves", *Opt. Lett.*, vol. 28, no. 13, pp. 1090–1092, 2003 (cit. on p. 209).
- [295] S. C. Pavone, M. Ettore, M. Casaletti, and M. Albani, "Transverse circular-polarized Bessel beam generation by inward cylindrical aperture distribution", *Opt. Express*, vol. 24, no. 10, pp. 11 103–11 111, 2016 (cit. on p. 212).
- [296] R. Piestun and J. Shamir, "Synthesis of three-dimensional light fields and applications", *Proc. IEEE*, vol. 90, no. 2, pp. 222–244, 2002 (cit. on p. 212).
- [297] H. A. Bethe, "Theory of diffraction by small holes", *Physical Review*, vol. 66, no. 7-8, p. 163, 1944 (cit. on p. 213).
- [298] M. Casaletti, R. Sauleau, M. Ettore, and S. Maci, "Efficient analysis of metallic and dielectric posts in parallel-plate waveguide structures", *IEEE Trans. Microw. Theory Tech.*, vol. 60, no. 10, pp. 2979–2989, 2012 (cit. on p. 213).
- [299] M. Casaletti, G. Valerio, J. Seljan, M. Ettore, and R. Sauleau, "A full-wave hybrid method for the analysis of multilayered SIW-based antennas", *IEEE Trans. Antennas Propag.*, vol. 61, no. 11, pp. 5575–5588, 2013 (cit. on p. 213).
- [300] J. Arlt, V. Garces-Chavez, W. Sibbett, and K. Dholakia, "Optical micromanipulation using a Bessel light beam", *Opt. Commun.*, vol. 197, no. 4, pp. 239–245, 2001 (cit. on p. 220).



## LIST OF PUBLICATIONS

- [J.1] **W. Fuscaldo**, P. Burghignoli, P. Baccarelli, and A. Galli, "Complex mode spectra of graphene-based planar structures for THz applications," *J. Infra. Milli. Terahz Waves*, vol. 36, no. 8, pp. 720-733, Aug. 2015.
- [J.2] **W. Fuscaldo**, G. Valerio, A. Galli, R. Sauleau, A. Grbic, and M. Ettore, "Higher-order leaky-mode Bessel-beam launcher," *IEEE Trans. Antennas Propag.*, vol. 64, no. 3, pp. 904-913, Mar. 2016.
- [J.3] **W. Fuscaldo**, P. Burghignoli, P. Baccarelli, and A. Galli, "A reconfigurable substrate-superstrate graphene-based leaky-wave THz antenna," *Antennas Wireless Propag. Lett.*, vol. 15, pp. 1545-1548, Apr. 2016
- [J.4] **W. Fuscaldo**, S. C. Pavone, G. Valerio, A. Galli, M. Albani, and M. Ettore, "Analysis of limited-diffractive and limited-dispersive X-waves generated by finite radial waveguides," *IEEE Trans. Antennas Propag.*, *J. App. Phys.*, vol. 119, no. 19, 194903, May 2016.
- [J.5] **W. Fuscaldo**, P. Burghignoli, P. Baccarelli, and A. Galli, "Graphene Fabry-Perot cavity leaky-wave antennas: plasmonic vs. non-plasmonic solutions," *IEEE Trans. Antennas Propag.*, vol.65, no. 4, DOI:10.1109/TAP.2017.2670520, Apr. 2017.
- [J.6] **W. Fuscaldo**, D. R. Jackson, and A. Galli, "A general and accurate formula for the beamwidth of 1-D leaky-wave antennas," *IEEE Trans. Antennas Propag.*, vol.65, no. 4, DOI: 10.1109/TAP.2017.2670617, Apr. 2017.
- [J.7] **W. Fuscaldo**, P. Burghignoli, P. Baccarelli, and A. Galli, "Efficient 2-D leaky-wave antenna configurations based on graphene metasurfaces," *Int. J. Microw. Wireless Tech.*, accepted for publication.
- [J.8] **W. Fuscaldo**, S. Tofani, D. C. Zografopoulos, P. Baccarelli, P. Burghignoli, R. Beccherelli, and A. Galli, "Tunable Fabry-Perot Cavity THz antenna based on leaky-wave propagation in nematic liquid crystals," *Antennas Wireless Propag. Lett.*, accepted for publication.
- [J.9] D. Comite, **W. Fuscaldo**, S. C. Pavone, G. Valerio, M. Albani, M. Ettore, and A. Galli, "Propagation of localized pulses carrying orbital angular momentum at microwave frequencies," *App. Phys. Lett.*, accepted for publication.
- [J.10] **W. Fuscaldo**, D. R. Jackson, and A. Galli, "Beamwidth Properties of Endfire 1-D Leaky-Wave Antennas," *IEEE Trans. Antennas Propag.*, under review.
- [C.1] **W. Fuscaldo**, G. Valerio, A. Galli, R. Sauleau and M. Ettore, "A millimeter-wave Bessel beam launcher through the excitation of higher-order leaky modes," *Eur. Conf. Antennas Propag. (EuCAP 2014)*, The Hague, The Netherlands, 05-11 Apr. 2014.

- [C.2] **W. Fuscaldo**, G. Valerio, A. Galli, R. Sauleau and M. Ettore, "Bessel beam launchers at millimeter waves using higher-order leaky-wave modes," *IEEE Int. Symp. Antennas Propag./USNC-URSI National Radio Science Meeting (APS-URSI 2014)*, Memphis, TN, USA, 05-11 Jul. 2014.
- [C.3] **W. Fuscaldo**, G. Valerio, A. Galli, R. Sauleau and M. Ettore, "A novel Bessel beam launcher based on higher-order leaky modes," *XX RiNEm*, Padova, Italy, 18-21 Sep. 2014.
- [C.4] M. Ettore, G. Valerio, R. Sauleau, **W. Fuscaldo**, A. Galli, A. Grbic "Generation of non-diffractive Bessel beam using leaky-wave modes," *Eur. Microw. Conf. (EuMC 2014)*, Rome, Italy, 05-10 Oct. 2014.
- [C.5] **W. Fuscaldo**, P. Burghignoli, P. Baccarelli, and A. Galli, "Complex modes of a tunable graphene-based Fabry-Perot cavity THz antenna," *Eur. Conf. Antennas Propag. (EuCAP 2015)*, Lisbon, Portugal, 12-17 Apr. 2015.
- [C.6] B. Errasti-Alcalá, **W. Fuscaldo**, P. Braca, and G. Vivone "Realistic extended target model for track before detect in maritime surveillance," *MTS/IEEE OCEANS 2015*, Genova, Italy, 18-21 May, 2015.
- [C.7] B. Errasti-Alcalá, **W. Fuscaldo**, P. Braca, and G. Vivone "Realistic ship model for extended target tracking algorithms," *IEEE Int. Geoscience Remote Sensing Symp. (IGARSS 2015)*, Milan, Italy, 26-31 Jul. 2015.
- [C.8] P. Burghignoli, P. Baccarelli, D. Comite, D. Di Ruscio, **W. Fuscaldo**, A. Galli, and G. Lovat "Metasurface 2-D leaky-wave antennas," *Int. Congress Adv. Electromagn. Mat. Microw. Opt. (Metamaterials 2015)*, Oxford, United Kingdom, 07-12 Sep. 2015.
- [C.9] **W. Fuscaldo**, P. Burghignoli, P. Baccarelli, and A. Galli, "Graphene-based reconfigurable leaky-wave antennas for THz applications," *IEEE Med. Microw. Symp. (MMS 2015)*, Lecce, Italy, 30 Nov.-02 Dec. 2015.
- [C.10] **W. Fuscaldo**, P. Burghignoli, P. Baccarelli, and A. Galli, "A graphene loaded substrate-superstrate leaky-wave THz antenna," *Eur. Conf. Antennas Propag. (EuCAP 2016)*, Davos, Switzerland, 10-15 Apr. 2016.
- [C.11] **W. Fuscaldo**, S. C. Pavone, G. Valerio, A. Galli, M. Albani, and M. Ettore, "Generation of limited-diffraction electromagnetic pulses at millimeter waves," *Eur. Conf. Antennas Propag. (EuCAP 2016)*, Davos, Switzerland, 10-15 Apr. 2016.
- [C.12] **W. Fuscaldo**, G. Valerio, R. Sauleau, A. Grbic, M. Ettore, and A. Galli, "Design and experimental validation of leaky-wave bessel-beam launcher at millimeter-wave frequencies," *IEEE Int. Symp. Antennas Propag./USNC-URSI National Radio Science Meeting (APS-URSI 2016)*, Fajardo, Puerto Rico, 26 Jun.-01 Jul. 2016.
- [C.13] **W. Fuscaldo**, S. C. Pavone, G. Valerio, A. Galli, and M. Albani, "Parameterization of the nondiffractive features of electromagnetic localized pulses," *IEEE Int. Symp. Antennas Propag./USNC-URSI National Radio Science Meeting (APS-URSI 2016)*, Fajardo, Puerto Rico, 26 Jun.-01 Jul. 2016.

- [C.14] S. C. Pavone, A. Mazzinghi, **W. Fuscaldo**, A. Freni, and M. Albani, "Broadband comparison of standing and traveling wave aperture distribution RLSA Bessel beam launchers for EM pulse generation," *IEEE Int. Symp. Antennas Propag./USNC-URSI National Radio Science Meeting (APS-URSI 2016)*, Fajardo, Puerto Rico, 26 Jun.-01 Jul. 2016.
- [C.15] **W. Fuscaldo**, S. Tofani, P. Baccarelli, P. Burghignoli, D. C. Zografopoulos, R. Beccherelli, and A. Galli, "Reconfigurable Fabry-Perot cavity leaky-wave antennas based on nematic liquid crystals for THz applications," *XXI RiNEm*, Parma, Italy, 12-14 Sep. 2016.
- [C.16] D. Comite, **W. Fuscaldo**, and S. C. Pavone, "Generation of limited-diffractive twisted pulses," *XXI RiNEm*, Parma, Italy, 12-14 Sep. 2016.
- [C.17] **W. Fuscaldo**, S. Tofani, P. Baccarelli, P. Burghignoli, D. C. Zografopoulos, R. Beccherelli, and A. Galli, "Analysis of leaky-wave THz antennas based on graphene," *XXI RiNEm*, Parma, Italy, 12-14 Sep. 2016.
- [C.18] **W. Fuscaldo**, P. Burghignoli, P. Baccarelli, and A. Galli, "Non-plasmonic vs. plasmonic graphene-based THz leaky-wave antennas," *Plasmonica 2016*, Genova, Italy, 14-16 Sep. 2016.
- [C.19] **W. Fuscaldo**, P. Burghignoli, P. Baccarelli, and A. Galli, "Efficient 2-D leaky-wave antenna configurations based on graphene metasurfaces," *Eur. Microw. Conf. (EuMC 2016)*, London, UK, 03-07 Oct. 2016.
- [C.20] **W. Fuscaldo**, D. R. Jackson, and A. Galli, "A new expression for the evaluation of the beamwidth in 1-D leaky-wave antennas: Beyond Oliner's formula," *Eur. Conf. Antennas Propag. (EuCAP 2017)*, Paris, France, 19-24 Mar. 2017, accepted for presentation.
- [C.21] **W. Fuscaldo**, S. Tofani, P. Baccarelli, P. Burghignoli, D. C. Zografopoulos, R. Beccherelli, and A. Galli, "A reconfigurable multilayered THz leaky-wave antenna employing liquid crystals," *Eur. Conf. Antennas Propag. (EuCAP 2017)*, Paris, France, 19-24 Mar. 2017, accepted for presentation.
- [C.22] D. Comite, **W. Fuscaldo**, P. Burghignoli, P. Baccarelli, S. K. Podilchak, and A. Galli, "Bessel Beam Generation by Means of Annular Leaky-Wave Antennas," *Eur. Conf. Antennas Propag. (EuCAP 2017)*, Paris, France, 19-24 Mar. 2017, accepted for presentation.
- [C.23] S. C. Pavone, **W. Fuscaldo**, D. Comite, G. Valerio, A. Galli, M. Ettore, and M. Albani, "Generation of Limited-Diffractive Twisted Pulses at Millimeter Waves," *Eur. Conf. Antennas Propag. (EuCAP 2017)*, Paris, France, 19-24 Mar. 2017, accepted for presentation.
- [C.24] **W. Fuscaldo**, S. C. Pavone, D. Comite, G. Valerio, A. Galli, M. Albani, and M. Ettore, "Nondiffracting Waves: Criteria for designing X-wave launchers," *IEEE Int. Symp. Antennas Propag. (APS-URSI 2017)*, San Diego, CA, USA, 09-14 Jul. 2017, accepted for presentation.
- [C.24] **W. Fuscaldo**, D. R. Jackson, and A. Galli, "Analysis of the radiating properties of endfire 1-D leaky-wave antennas," *IEEE Int. Symp. Antennas Propag. (APS-URSI 2017)*, San Diego, CA, USA, 09-14 Jul. 2017, accepted for presentation.

- [C.26] **W. Fuscaldo**, D. Comite, A. Boesso, P. Baccarelli, P. Burghignoli, and A. Galli, "A new class of nondiffracting pulses based on focusing leaky waves," *Eur. Microw. Conf. (EuMC 2017)*, under review.

## LIST OF AWARDS

[A.1] **Yarman-Carlin Award**

W. Fuscaldo, P. Burghignoli, P. Baccarelli, and A. Galli, "Graphene-based reconfigurable leaky-wave antennas for THz applications," *IEEE Med. Microw. Symp. (MMS 2015)*, Lecce, Italy, 30 Nov.-02 Dec. 2015.

[A.2] **EuMC 2016 Young Engineer Prize**

W. Fuscaldo, P. Burghignoli, P. Baccarelli, and A. Galli, "Efficient 2-D leaky-wave antenna configurations based on graphene metasurfaces," *Eur. Microw. Conf. (EuMC 2016)*, London, UK, 03-07 Oct. 2016.